Report Date: December 31, 2005

Final Report

INVESTIGATION OF EFFICIENCY IMPROVEMENTS DURING CO_2 INJECTION IN HYDRAULICALLY AND NATURALLY FRACTURED RESERVOIRS

DOE Contract No.: DE-FC26-01BC15361

Harold Vance Department of Petroleum Engineering
Texas A& M University
3116 TAMU
College Station, TX 77843-3116
(979) 845-2241

Contract Date:	September 28, 2001
Anticipated Completion Date:	December 31, 2005
Principal Investigator:	David S. Schechter Harold Vance Department of Petroleum Engineering
Contracting Officer's Representative:	Dan Ferguson National Petroleum Technology Office
Report Period:	Sept 28, 2001- Dec. 31, 2005

DISCLAIMER

ABSTRACT

This report describes the final work of the project, "Investigating of Efficiency Improvements during CO_2 Injection in Hydraulically and Naturally Fractured Reservoirs." The objective of this project is to perform unique laboratory experiments with artificial fractured cores (AFCs) and X-ray CT to examine the physical mechanisms of bypassing in HFR and NFR that eventually result in more efficient CO_2 flooding in heterogeneous or fracture-dominated reservoirs. To achieve this objective, we divided the report into two chapters. The first chapter was to image and perform experimental investigation of transfer mechanisms during CO_2 flooding in NFR and HFR using X-ray CT scanner. In this chapter, we emphasized our work on understanding the connection between fracture properties and fundamentals of transfer mechanism from matrix to fractures and fluid flow through fracture systems. We started our work by investigating the effect of different overburden pressures and stress-state conditions on rock properties and fluid flow. Since the fracture aperture is one of important parameter that governs the fluid flow through the fracture systems, the average fracture aperture from the fluid flow experiments and fracture aperture distribution derived from X-ray CT scan were estimated for our modeling purposes. The fracture properties and fluid flow have significant changes in response to different overburden pressures and stress-state conditions. The fracture aperture distribution follows lognormal distribution even at elevated stress conditions. Later, we also investigated the fluid transfers between matrix and fracture that control imbibition process. We evaluated dimensionless time for validating the scheme of upscaling laboratory experiments to field dimensions.

In CO_2 injection experiments, the use of X-ray CT has allowed us to understand the mechanisms of CO_2 flooding process in fractured system and to take important steps in reducing oil bypassed. When CO_2 flooding experiments were performed on a short core with a fracture at the center of the core, the gravity plays an important role in the recovery of oil even in a short matrix block. This results are contrary with the previous believes that gravity drainage has always been associated with tall matrix blocks.

In order to reduce oil bypassed, we injected water that has been viscosified with a polymer into the fracture to divert CO_2 flow into matrix and delay CO_2 breakthrough. Although the breakthrough time reduced considerably, water "leak off" into the matrix was very high. A cross-linked gel was used in the fracture to avoid this problem. The gel was found to overcome "leak off" problems and effectively divert CO_2 flow into the matrix.

As part of our technology transfer activity, we investigated the natural fracture aperture distribution of Tensleep formation cores. We found that the measured apertures distributions follow log normal distribution as expected.

The second chapter deals with analysis and modeling the laboratory experiments and fluid flow through fractured networks. We derived a new equation to determine the average fracture aperture and the amount of each flow through fracture and matrix system. The results of this study were used as the observed data and for validating the simulation model. The idea behind this study is to validate the use of a set of smooth parallel plates that is common in modeling fracture system. The results suggest that fracture apertures need to be distributed to accurately model the experimental results.

In order to study the imbibition process in details, we developed imbibition simulator. We validated our model with X-ray CT experimental data from different imbibition experiments. We found that the proper simulation model requires matching both weight gain and CT water saturation simultaneously as oppose to common practices in matching imbibition process with weight gain only because of lack information from CT scan. The work was continued by developing dual porosity simulation using empirical transfer function (ETF) derived from imbibition experiments. This allows reduction of uncertainty parameter in modeling transfer of fluids from matrix to the fracture. The application of ETF approach not only reduces the computation times but also shows similar results when compared to the results from existing dual porosity simulator.

During the development of our numerical modeling, we found that the grid orientation effect (GOE) is major problem plaguing reservoir simulators that employ finite difference schemes. The GOE is clearly seen when using conventional Cartesian grid blocks during CO_2 flooding or unfavorable mobility ratio presence in the simulation model. We developed hybrid grid block (HGB) to reduce this effect. Using this grid block, the simulation is able to reduce the GOE even for unfavorable mobility ratio.

The last chapter discusses a modeling approach to reduce oil bypassed in CO_2 flood pattern. A fully compositional simulation model was developed to optimize the flood pattern. The simulation model was validated and CO_2 injection rate, slug size, WAG ratio, flood pattern were optimized. In addition, the use of viscous water during the WAG process and placing the polymer in high permeability streak were investigaed. The results show applying viscous water and polymer could significantly increase oil recovery. More details of the abstracts can be found in the following sections that appear in this report.

Chapter I-1 Effect of Overburden Pressure on Unfractured and Fractured Permeability Cores

The fracture aperture and fracture permeability are usually considered to remain the same during the producing life of the reservoir regardless of degree of depletion. Our experimental results show that the fracture aperture and fracture permeability have significant pressure-dependent changes in response to applying variable injection rates and overburden pressures. This paper addresses the laboratory experiments on the effect of fracture aperture and fracture permeability on the fluid flow under different overburden pressure. The equations to quantify the flow through the matrix and the fracture at different overburden pressures are provided. In addition the reservoir simulation was performed to model the laboratory experiments.

Chapter I-2 Investigating the Changes in Matrix and Fracture Properties and Fluid Flow under Different Stress-state Conditions

Laboratory experiments were performed on a Berea core to investigate the changes in rock properties and fluid flow under different stress-state conditions. A comparative study was done to analyze the effect of the various loading systems. The experimental results show that fracture permeability reduces significantly compared to matrix permeability as the stress increases. The hydrostatic and triaxial stresses have greater impacts on permeability reduction compared to the uniaxial stress condition. Flow in the fracture dominates when the applied stress is relatively low. However, the flow in the matrix increases as applied stress increases and dominates at high stress even though the fracture is not completely healed.

Chapter I-3 Investigating Fracture Aperture Distributions under Various Stress Conditions Using X-Ray CT Scanner

Fracture aperture is usually estimated by cubic law, which assumes flow between two smooth parallel plates. However, many researchers have proved that the fracture aperture is not a smooth surface but rather has tortuous paths and roughness and hence the flow behavior is different. Previous research showed that fracture aperture follows lognormal distribution. Nevertheless, there has not been any research conducted to validate the fracture aperture distribution with the change in stress conditions, which is common in fractured reservoirs. With the advent of X-ray CT scanner in the field of petroleum engineering, fracture apertures can be visualized and measured. Since there is no direct calculation for fracture aperture measurement from CT scanner data a calibration curve needs to be established. We developed a calibration curve based on existing calibration techniques, which involves area integration of the fracture region to obtain a correlation between integrated CT numbers and the calibrated fracture aperture. Using this calibration curve, we obtained distribution patterns for fracture apertures along the length of the core for various stress conditions, from about six thousand fracture aperture measurements for each stress condition. The results show that aperture distributions still follow lognormal distribution under various stress conditions.

Chapter I-4 Imbibition Assisted Oil Recovery

Imbibition describes the rate of mass transfer between the rock and the fractures. Therefore, understanding the imbibition process and the key parameters that control the imbibition process is crucial. Capillary imbibition experiments usually take a long time, especially when we need to vary some parameters to investigate their effects. Therefore, this research presented the numerical studies with the matrix block surrounded by the wetting phase for better understanding the characteristic of spontaneous imbibition, and also evaluated dimensionless time for validating the scheme of upscaling laboratory imbibition experiments to field dimensions.

Numerous parametric studies have been performed within the scope of this research. The results were analyzed in detail to investigate oil recovery during spontaneous imbibition with different types of boundary conditions. The results of these studies have been upscaled to the field dimensions. The validity of the new definition of characteristic length used in the modified scaling group has been evaluated. The new scaling group used to correlate simulation results has been compared to the early upscaling technique.

The research revealed the individual effects of various parameters on imbibition oil recovery. Also, the study showed that the characteristic length and the new scaling technique significantly improved upscaling correlations.

Chapter I-5 Application of X-Ray CT for Investigation of CO_2 and WAG Injection in Fractured Reservoirs

Fractured reservoirs have always been considered poor candidates for enhanced oil recovery. This is mainly due to the complexities involved in predicting performance in such reservoirs. A good understanding of multiphase flow in fractures is important to reduce oil bypass and increase recovery in these reservoirs. This paper presents CO_2 flooding experiments in homogeneous and fractured rocks with in-situ saturation and porosity measurements using an X-Ray CT scanner. We found that injection rates played

an important role in the recovery process, more so in the presence of fractures. At high injection rates we observed faster CO_2 breakthrough and higher oil bypass than at low injection rates. But very low injection rates are not attractive from an economic point of view. Hence we injected viscosified water to reduce the mobility of CO_2, similar to the WAG process. Breakthrough time reduced significantly and a much higher recovery was obtained. Saturation measurements were made from the CT scans and were found to be in good agreement with those obtained from effluent data.

Chapter I-6 Analysis of Gravity Drainage Mechanism in a Short Vertically Fractured Core

Gravity drainage is an important oil recovery mechanism in naturally fractured reservoirs. In some cases it is the only mechanism that allows oil recovery and production of oil from the matrix blocks. Oil recovery by gravity drainage strongly depends on the height of the capillary continuity. Hence gravity drainage has always been associated with tall matrix blocks. Our experimental results show that gravity drainage can be an important recovery mechanism even in short matrix blocks. CO_2 flooding experiments were performed on cores with a diameter of 1 inch with a fracture at the center of the core, aligned vertically. A fourth generation CT scanner was used to obtain cross-sectional scans and determine saturations at different points of time. Saturation images indicate that gravity plays an important role in the recovery of oil by CO_2 even in a 1 inch fracture.

Chapter I-7 Investigation of Natural Fracture Aperture Distribution of Tensleep Formation Cores using X-Ray CT Scanner

The Tensleep Formation in Teapot Dome is an intensely fractured rock and considered as a CO_2 sequestration candidate. Fractured reservoirs are ideal candidates for sequestration due to the large volume of CO_2 that can be injected in a short period of time however this is an unproven and risky technology as a result of the high conductivity channels that fractures provide. The ultimate oil recovery in most NFR is very low compared to conventional oil reservoirs thus a significant fraction of the resources are left behind after abandonment. The low recovery inherent in NFR makes such reservoirs ideal candidates for sequestration/EOR carbon cycle projects since the improved cash flow will nurture the desire to apply expensive sequestration technology. However, it has not been clear how the CO_2 would flow through highly conductive fracture network. Therefore, it is critical to know the characteristics of fracture media for the success of the project.

Two cores from the RMOTC 48X28 well, Teapot Dome, were analyzed. One is retrieved from 5565 ft depth (Core-A) and the other one is from 5566 ft depth (Core-B). Both cores contain mineralized fractures and open fractures. The mineralized fractures are filled with high dense mineral such as crystalline dolomite. Some fractures exit the cores and terminations of such fractures cannot be observed.

We applied 4^{th} generation CT scanner to get information on fracture properties such as aperture, mineralization, aperture distribution and permeability distribution without damaging cores. The CT scanner provides CT images, which show the difference between material densities. These images are not the actual physical property of fracture. Thus, it is required to provide a unique calibration curve for the Tensleep rock from these images to obtain aperture size. We found that the measured aperture distributions follow log-normal distribution by comparing measured data with generated data using log-normal probability density function. Aperture of the open fracture of Core-B is wider and

distributes more widely than that of Core-A. Aperture data were converted into permeability values with the assumption of parallel plate model.

Chapter II-1 Experimental and Simulation Analysis of Fractured Reservoir Experiencing Different Stress Conditions

Flow through the fracture is usually estimated by cubic law, which assumes flow to occur between two parallel plates. The cubic law is valid to represent the flow through the fracture system if the matrix permeability is very low to provide any significant flow contribution. However, in high permeability rocks, the flow occurs through both fracture and matrix systems. Flow through matrix may sometimes exceed that through the fractures under increased stress acting on the reservoirs. Under these circumstances, the cubic law should be modified by combining the weighted average of the permeabilities in order to account for flow through matrix. In this paper we present the amount of flow through fracture and matrix system based on modified cubic law equations by conducting a series of laboratory experiments on fractured cores under different stress conditions. The flow rate through fracture and matrix system and the pressure drop were matched using simulation. X-ray CT was used to determine the fracture aperture and saturation distributions. In addition, the saturation distributions from simulation results were compared to X-ray CT Scan results.

Chapter II-2 Modeling Fluid Flow through a Single Fracture using Experimental, Stochastic and Simulation Approaches

In this chapter, sensitivity of fracture modeling, error involved in the experiments and saturation match of fracture imbibition experiments using X-ray CT Scanner are established.

A fracture is usually assumed as a set of smooth parallel plates separated by a constant width. However, the flow characteristics of an actual fracture surface are quite different, affected by tortuosity and the impact of surface roughness. Though several researchers have discussed the effect of friction on flow reduction, their efforts lack corroboration from experimental data and have not converged to form a unified methodology for studying flow on a rough fracture surface. The goal of this research is to examine the effect of surface roughness for flow through fractures and to effectively incorporate them into simulations with the aid of geostatistics.

In this study, we have shown an integrated methodology, involving experiments, stochastics and numerical simulations that incorporate the fracture roughness and the friction factor, to describe flow on a rough fracture surface. Laboratory experiments were performed to support the study in quantifying the flow contributions from the matrix and the fracture under varying confining pressures. The results were used to modify the cubic law through reservoir simulations. Observations suggest that the fracture apertures need to be distributed to accurately model the experimental results.

The methodology successfully modeled fractured core experiments, which were earlier not possible through parallel plate approach. A gravity drainage experiment using an X-ray CT scan of a fractured core has also validated the methodology.

Chapter II-3 Simulation of Fluid Flow through Rough Fractures

Flow through a fracture is usually assumed to take place between two smooth parallel plates. However, it is widely accepted that the fracture has tortuous paths as a result of

surface roughness and hence the flow behavior in these paths compared to that in parallel plates is different. Although previous studies have shown that the fracture aperture follows lognormal distribution, studies have not been conducted to determine the distribution of fracture aperture with changes in stress conditions. In this paper, we present fracture aperture measurements under different stress conditions using an X-Ray CT scanner. We developed a calibration curve to obtain a correlation between CT numbers and fracture aperture since there is no direct calculation of aperture from CT scanner data. Aperture distribution patterns from about six thousand aperture measurements were obtained for each stress condition evaluated. The results of this study show that the apertures follow lognormal distribution even at elevated stress conditions. We then performed waterflood experiments as a precursor to CO_2 injection to validate the use of distributed apertures in simulators. A sensitivity analysis was also performed to analyze the effect of injection rates and fracture roughness on oil recovery.

Chapter II-4 X-Ray Tomography Results Validate Numerical Modeling of Flow in Fractures

Spontaneous imbibition plays a very important role in the displacement mechanism of non-wetting fluid in naturally fractured reservoirs. To quantify this spontaneous imbibition process, we developed a 2D two-phase numerical model. This numerical model was developed because an available commercial simulator cannot be used to model small-scale experiments with different boundary conditions. In building the numerical model, we started with the basic equation of fluid flow and developed a numerical approach of solving the non-linear diffusion saturation equation. We compared our numerical model with the analytical solution of this equation to ascertain the limitations of the assumptions used to arrive at that solution. The unique aspect of this paper is that we validated our model with X-ray computerized tomography (CT) experimental data from a different spontaneous imbibition experiment, where two simultaneously varying parameters of weight gain and CT water saturation were used. This requires us to undertake extensive sensitivity studies on key parameters before a successful match could be obtained. We also successfully captured our own X-ray computerized tomography (CT) laboratory experiment on a fractured core.

Chapter II-5 Simulation of Naturally Fractured Reservoirs Using Empirically Derived Transfer Function

This research utilizes the imbibition experiments and X-Ray Tomography results for modeling fluid flow in naturally fractured reservoirs. Conventional dual porosity simulation requires large number of runs to quantify transfer function parameters for history matching purposes. In this study empirical transfer functions (ETF) are derived from imbibition experiments and this allows reduction in the uncertainty in modeling of transfer of fluids from the matrix to the fracture.

The application of ETF approach is applied in two phases. In the first phase, imbibition experiments are numerically solved using the diffusivity equation with different boundary conditions. Usually only the oil recovery in imbibition experiments is matched, however, with the advent of X-Ray CT the spatial variation of the saturation can also be computed. The matching of this variation can lead to accurate reservoir characterization. In the second phase, the imbibition derived empirical transfer functions are used in developing a dual porosity reservoir simulator. The results from this study are compared with

published results. The study reveals the impact of uncertainty in the transfer function parameters on the flow performance and reduces the computations to obtain transfer function required for dual porosity simulation.

Chapter II-6 A Unique Grid-Block System for Improved Grid Orientation

The grid orientation effect is a long-standing problem plaguing reservoir simulators that employ finite difference schemes. This study develops a unique grid-block assignment where rectangular grid blocks are interspersed with octagonal grid blocks. This grid block system is called the Hybrid Grid Block (HGB) system. The objective of this study is to evaluate the grid orientation effect of the HGB grid to see whether it is an improvement over the conventional Cartesian grid system. In HGB, flow can progress in four directions in the octagonal grid blocks and two in the square grid blocks. The increase in the number of flow directions in the octagonal grid blocks is expected to reduce the grid orientation effect in the model. This study also evaluates the grid orientation effect of the HGB and compares it with the Cartesian grid system.

HGB grid is able to reduce the grid orientation effect even for unfavorable mobility ratio displacement problems (up to M = 50.0), with maximum relative difference in pore volume recovered of 6% between parallel and diagonal HGB grid models for all the cases run in this study. Comparisons between the conventional Cartesian and HGB grid show that the HGB grid is more effective in reducing the grid orientation effect than the Cartesian grid. The HGB grid performs better by consistently giving a smaller relative difference between HGB parallel grid and HGB diagonal grid in pore volume recovered compared to the relative difference between Cartesian parallel grid and Cartesian diagonal grid in pore volume recovered at similar averaged area per grid block for all the four comparison cases studied.

Chapter II-7 Reduced CO_2 Bypassing and Optimized CO_2 Flood Design

This research utilized a modeling approach to reduce oil bypassed in CO_2 flood pattern. A fully compositional simulation model with detailed geological characterization was developed to optimize the flood pattern. The simulation model is a quarter of an inverted nine-spot and covers 20 acres area. The Peng-Robinson equation of state (EOS) was used to describe the phase behavior during CO_2 flooding. Simulation layers represent actual flow units and resemble large variation of reservoir properties. A-34 year production and injection history was matched to validate the model. Then, several sensitivities run including CO_2 injection rate, slug size, WAG ratio, pattern reconfiguration and conformance control were conducted to improve CO_2 sweep efficiency and increase oil recovery.

We found that the optimum CO_2 injection rate is approximately 300 rb (762 MSCF/D). The optimum water-alternating-gas (WAG) ratio is 1:1. This ratio allows an incremental oil recovery up to 18% with an ultimate CO_2 slug of 100% hydrocarbon pore volume (HCPV). If a polymer is placed in high permeability streak during the course of 1:1 WAG ratio, an additional recovery could increase up to 34%. The simulation results also reveal that a pattern reconfiguration change from inverted nine spot to staggered line drive could significantly increase oil recovery.

TABLE OF CONTENTS

LIST OF TABLES

LIST OF FIGURES

ACKNOWLEDGMENTS

Financial support for this work is graciously provided by the United States Department of Energy (NETL/National Petroleum Technology Office).
This support is gratefully acknowledged, as well as that of Eclipse™ and CMG™ which donated software used in this study. I greatly appreciate diligent efforts from the following individuals who contributed to this project: Erwinsyah Putra and Dewi T. Hidayati helped with the technical part of this research along with other students who contributed in this project; Dicman Alfred, Vivek Muralidharan, Deepak Chakravarty, Prassana Tellapaneni, Sandeep Kaul, Emeline Chong, Zuher Syihab, Taehyung Kim, Bulenz Izgec, Pashayev Orkan, and Marilena Garcia.

EXECUTIVE SUMMARY

This report describes the work performed during the second year of the project, "Investigating of Efficiency Improvements during CO_2 Injection in Hydraulically and Naturally Fractured Reservoirs." The objective of this project is to perform unique laboratory experiments with artificial fractured cores (AFCs) and X-ray CT to examine the physical mechanisms of bypassing in HFR and NFR that eventually result in less efficient CO_2 flooding in heterogeneous or fracture-dominated reservoirs.

We are on the verge of an important step in the global understanding of the connection between fracture characterization and fundamentals of fluid flow in fractured systems. The combination of X-Ray CT scanning and basic fluid flow experiments in tandem with numerical simulation has allowed us to take the first steps in making the connection between field observations, simulation and small-scale experiments commonly performed in laboratories. The applications of this research are wide ranging and include the use of X-Ray CT scanning, open hole logs, well test analysis and simulation in order to input realistic fracture networks into reservoir simulators. The profound impact this research has on future engineering applications in naturally and hydraulically fractured reservoirs is immense. Until now, there has been a large disconnect between field performance, interpretation of data collected to characterize fracture networks and the techniques used to simulate and predict fluid flow in fractured systems. We believe this research will eventually provide basic tools that will allow the long-missing connection between laboratory work and theory and actual field performance.

This report provides results of the final report that consists of experiment, numerical modeling, reservoir simulation and field application. We are researching basic fluid flow in single, rough fractures and investigating different levels of stress on fluid flow behavior in the fracture. We have become adept at performing numerical simulations on this type of experiment and closely matching the observed results. An important point is we are no longer relying simply on pressure matches but also saturation distributions in the rock as determined by X-Ray CT scanning and matched with reservoir simulators. This important advancement has provided a plethora of methodologies that will eventually provide the connection between the abundant theoretical work and the numerous observations of fluid flow in naturally and hydraulically fractured reservoirs. The following headings and subsequent findings outline the work that appears in this report.

Chapter I-1 Effect of Overburden Pressure on Unfractured and Fractured Permeability Cores

We performed laboratory experiments to investigate the changes in fracture aperture and fracture permeability in response to applying variable injection rates and overburden pressures. We provided the equation to quantify the flow through matrix and fracture at different overburden pressures. The laboratory results show that the fracture aperture and fracture permeability have significant pressure-dependent changes in response to applying variable injection rates and overburden pressures as expected.

The change in matrix permeability with different injection rates under variable overburden pressures is not significant in contrast with that effect on fracture aperture and fracture permeability. At high overburden pressure the influence of existing fracture permeability on fluid flow contributor in permeable rocks (> 200 md) is not too significant.

Chapter I-2 Investigating the Changes in Matrix and Fracture Properties and Fluid Flow under Different Stress-state Conditions

In this chapter, the laboratory experiments were extended to investigate the changes in rock properties and fluid flow under different stress-state conditions. A comparative study of different stress conditions was conducted to analyze the effect of various loading systems. The experimental results show that as the stress increases, fracture permeability reduces significantly compared to matrix permeability. The hydrostatic and triaxial stresses have greater impacts on permeability reduction compared to applying stress in the uniaxial stress condition. Fluid flow through fracture dominates when applied stress is less. However, the flow through matrix increases as applied stress increases and dominates at high stress even though the fracture still does not heal completely.

Chapter I-3 Investigating Fracture Aperture Distributions under Various Stress Conditions Using X-Ray CT Scanner

This research uses X-ray CT scanner to image the fracture aperture under various overburden pressures. CT scan provides only the density differences between matrix and fracture systems but not a direct fracture aperture description. In order to determine fracture aperture, a calibration curve was developed from known fracture aperture. After the curve was established, the fracture apertures were measured at various points along the length of the core to generate sufficient data for characterizing the distributions of fracture apertures.

Our experimental results show that parallel plate approach of the fractures is no longer valid when the fracture aperture is small due to significant applied overburden pressure. The result of this study confirms the previous studies that fracture aperture distribution is lognormal distribution without overburden pressure. Upon applied overburden pressure, the distribution still follows the common lognormal distribution. The result of this study confirms the previous studies that fracture aperture distribution is lognormal distribution at no overburden pressure. Upon applied overburden pressure, the distribution still follows the common lognormal distribution.

Chapter I-4 Imbibition Assisted Oil Recovery

Different critical aspects of the capillary imbibition process have received a limited treatment in the petroleum literature. None of the recent papers devoted to capillary imbibition studies investigated the numerical scale-up of the process. The objectives of our study were to conduct numerical studies with the matrix block surrounded by the wetting phase for better understanding the characteristic of spontaneous imbibition, and also to evaluate dimensionless time for validating the scheme of upscaling laboratory imbibition experiments to field dimensions. To achieve these objectives, we performed

numerous parametric studies to investigate oil recovery during spontaneous imbibition with different types of boundary conditions. These studies included the effect of varying mobility ratio, different fracture spacing, different capillary pressure, different relative permeabilities, and varying permeability profiles along the core.The results of these studies were upscaled to the field dimensions. The validity of the new definition of characteristic length used in the modified scaling group was evaluated based on our model. The new scaling group used to correlate simulation results was compared to early upscaling technique. We found that (1) the comparative study for different types of boundary conditions revealed the fact that the time required for capillary imbibition until residual oil saturation increases exponentially, as the number of open faces available for imbibition decreases. (2) The comparison of all four types of boundary conditions showed that oil recovery for the All Faces Open type of a model is most efficient and fast, as compared to other cases. (3) The effect of varying permeability profiles along the core on oil recovery showed that when water imbibes in the direction of decreasing permeability, oil recovery is higher than when water imbibes in the direction of increasing permeability. (4) The study of the effect of different water-oil viscosity ratios, at which water imbibed into the core, shows that the lower oil viscosity, the greater the volumes of oil produced from the core as a function of time. (5) As capillary pressure increases the imbibition recovery increases. Oil recovery by imbibition was sensitive to oil relative permeability curves, while no significant effect was observed in changing the water relative permeability curves. (6) The characteristic length described by Ma *et al*. in the equation of dimensionless time improved a correlation between data points for the models with different boundary conditions. (7) The spontaneous imbibition results of this study have been upscaled to the field dimensions. The validity of a new definition of characteristic length used in the modified scaling group has been evaluated. The new scaling group used to correlate simulation results has been compared to the early upscaling techniques. (8) The new technique used for upscaling, significantly improves correlations by taking end-point fluid phase mobilities and the mobility ratios into account. (9) The comparison between the new and the previous dimensionless times proves that even if non-wetting fluid viscosity varies by 3 orders of magnitude, the data could be reduced to a single curve, if we use new dimensionless time definition.

Chapter I-5 Application of X-Ray CT for Investigation of CO_2 and WAG Injection in Fractured Reservoirs

In this chapter, we investigated the displacement of oil by CO_2 using X-ray CT scanner in homogeneous and fractured cores. We conducted the experiments at various injection rates. We quantified the amount of oil bypass due to the effect of different injection rates. We also investigated the fluid transfer between matrix and fracture media. We investigated CO_2 flow in fractures, in the present of water as a mobility control agent. We also performed the experiment with adding a cross-linker to the solution to form a gel. We scanned the entire length of the core in order to obtain saturation distributions at various stages during the course of the experiments, which are important to study fluid transport in the matrix and the fracture. Important conclusions can be drawn from the work include:

1. Injection rate plays an important role in affecting oil recovery and breakthrough.
2. Early breakthrough and higher oil bypass are observed at high injection rates.

3. Low injection rate gives better sweep and higher recovery, but this is not attractive as the recovery is too slow
4. In a fractured system, fluid flow occurs mainly through the fractures and a considerable amount of time is required for the injection fluid to penetrate the matrix.
5. An alternative method like WAG is necessary to reduce the mobility of CO_2 in the fractured system.
6. Coreflood experiments using viscosified water confirmed that WAG can delay CO_2 breakthrough and improve recovery. However, leakoff into the porous rock is very high. This leakoff might be much lower in an oil-wet rock but more work is required to establish this.
7. Formation of gel can eliminate the problem of liquid leakoff into the matrix.
8. Using gel for conformance control results in better sweep and higher recoveries. The type and composition of gel to be used in the presence of CO_2 needs more investigation.

Chapter I-6 Analysis of Gravity Drainage Mechanism in a Short Vertically Fractured Core

We continued our CO_2 experiments to investigate the important mechanisms on oil recovery in a short core. We performed CO_2 experiments on cores with a diameter of 1 inch with a continuous horizontal fracture at the center of the core. CO_2 was injected into the oil saturated core at a low injection rate of about 0.1cc/min to eliminate the effect of viscous forces. A fourth generation CT scanner was used to obtain cross-sectional scans and determine saturations at different points of time. We found that gravity drainage is the main recovery mechanism in this short matrix blocks contrary with previous widely believed that the gravity drainage had always been associated with tall matrix blocks.

Chapter I-7 Investigation of Natural Fracture Aperture Distribution of Tensleep Formation Cores using X-Ray CT Scanner

As part of our technology transfer activity, we collaborated with DOE-RMOTC to implement CO_2 sequestration in Tensleep formation of Teapot Dome. With our expertise in X-Ray CT scanning, we investigated the fracture properties of Tensleep fractured cores. We conducted similar experiments as we did for Berea cores. We found that the Tensleep cores have the following properties:
(1) The cores have open and mineralized fractures, (2) the open and mineralized fractures have totally different fracture aperture sizes, (3) and the open fracture has wider aperture size and more widely distributed apertures than the mineralized fracture. The results of this study will be included in our current effort in modeling and simulating the sequestration process in Teapot Dome.

Chapter II-1 Experimental and Simulation Analysis of Fractured Reservoir Experiencing Different Stress Conditions

In the last topic, the modeling of fluid flow through a single fracture incorporating the effect of surface roughness is conducted. Fracture permeability is usually estimated by a cubic law that is based on the theory of hydrodynamics for the laminar flow between flat plates. However, the cubic law is too simple to estimate the fracture permeability correctly, because the surface of real fracture is much more complicated and rougher than

the surface of flat plate. Several researchers have shown that the flow characteristics of an actual fracture surface would be quite different due to the effect of tortuosity, impact of surface roughness and contact areas. Nonetheless, to date, these efforts have not converged to form a unified definition on the fracture aperture needed in the cubic law. In this study, therefore, we show that the cubic law could still be used to model small-scale and field-scale data as long as it is modeled effectively, accounting for the effect of surface roughness associated with the fracture surface. The goal of this research is to examine the effect of surface roughness for flow through fractures and to effectively incorporate them into simulations with the aid of geostatistics. Since the research has been supported with experimental results, the consistency of the results enabled us to define a methodology for single fracture simulation. This methodology successfully modeled the flow rate and pressure drop from fractured core experiments, which were earlier not possible through parallel plate approach. Observations suggest that the fracture aperture needs to be distributed to accurately model the experimental results. The effect of friction and tortuosity due to surface roughness needs to be taken into account while modeling.

Chapter II-2 Modeling Fluid Flow through a Single Fracture using Experimental, Stochastic and Simulation Approaches

X-ray CT scan reveal that the parallel plate assumption in modeling fluid flow in fracture media seldom reflects the nature of flow through fractures. In this chapter, sensitivity of fracture modeling, error involved in the experiments and saturation match of fracture imbibition experiment using X-ray CT Scanner are established. Important conclusions can be drawn from the work include:

1. The fracture aperture needs to be distributed to accurately model the experimental results.
2. The effect of friction factor due to surface roughness should be considered in modeling fluid flow through rough fracture surface.
3. Fluid flow increases as the variance of the aperture distribution increases. This reiterates the fact that tortuosity in fluid flow is a significant factor.
4. The effective hydraulic aperture is reduced with increased variance of the aperture distribution.
5. Beyond an aperture size of approximately 60 microns, the effect of roughness or tortuosity is found to be insignificant.

Chapter II-3 Simulation of Fluid Flow through Rough Fractures

In this chapter, we investigated waterflooding displacement mechanisms in fractured cores using X-ray CT scanner. We conducted the experiments at various injection rates and scanned the core being flooded at certain times. We recorded oil and water rates at the outlet point. We developed two simulation models where one model describes fracture as parallel plate model and the other model describes it as distributed fracture aperture model. Both results were compared to the experimental data. Once we achieve satisfactory matches, we performed sensitivity studies to analyze the effect of injection rates on oil recovery and breakthrough time. Important conclusions can be drawn from the work include:

1. Simulation results indicate that the parallel plate model fails to duplicate laboratory experiment performance hence this model does not adequately represent a fractured model.
2. On the other hand, satisfactory matches between simulation and experimental data using distributed aperture model shows this model provides an accurate description of a fractured model.
3. The water breakthrough time increases as fracture aperture and injection rate increase.
4. As the injection rate increases the difference in the oil recoveries predicted by the two models increases.
5. At large aperture sizes, the performance of the parallel plate model becomes closer to that of the distributed aperture model. This indicates that there is a certain critical fracture aperture where both models would give similar results.

Chapter II-4 X-Ray Tomography Results Validate Numerical Modeling of Flow in Fractures

This chapter emphasis on modeling spontaneous imbibition experiments in order to understand the spontaneous imbibition process. As a tool to verify this numerical model, the results from X-Ray CT were utilized. We started our modeling development from basic equation and came up with a robust two-dimensional two-phase numerical model that could faithfully reproduce laboratory experiments. This model was rigorously verified with experimental data.

Chapter II-5 Simulation of Naturally Fractured Reservoirs Using Empirically Derived Transfer Function

In previous chapter, we have shown that we are able to model the spontaneous imbibition experiment utilizing the X-Ray CT scan results. We continued our effort by including the imbibition modeling into dual porosity simulation by changing the fluid transfer term. A detail explanation about different transfer functions, derivation of mathematical modeling and dual porosity simulator development using empirical derived transfer function (EDTF) are presented in this report. The results show that dual porosity simulation with EDTF is inherently faster because the number of unknowns per grid block is reduced to two from four. However, “Material Balance” is not conserved to the extent of conventional dual porosity formulations.

Chapter II-6 A Unique Grid-Block System for Improved Grid Orientation

The second chapter is part of our paper that will appear at the SPE Asia Pacific Oil and Gas Conference and Exhibition held in Perth, Australia, 18–20 October 2004. In this chapter, we developed a finite difference IMPES-formulated two dimensional black oil simulator using both Cartesian grid block system and a unique grid block system called Hybrid Grid Model (HGB). We compared the viability of this simulator using Cartesian grid block system with a commercial simulator Eclipse™. We examined the grid orientation in conventional grid block system and then we ran simulation cases using the HGB grid system. Important conclusions can be drawn from the work include: (1) The grid orientation effect was observed in rectangular Cartesian grid models even with isotropic and homogeneous reservoirs with favorable mobility ratio. (2) Grid refinement can help to minimize the grid orientation effect in rectangular Cartesian grid models

when there are favorable mobiliy ratios, ie. M=1.0 or less. However, at an unfavorable mobility ratio, neither the parallel, diagonal grid orientation, nor grid refinement is effective in reducing the grid orientation effect. (3) HGB grid is able to minimize the grid orientation effect even for unfavorable mobility ratio displacement problems, with relative difference of about 6% for all the cases run.

Chapter II-7 Reduced CO_2 Bypassing and Optimized CO_2 Flood Design

All the previous CO_2 flooding studies were conducted in the laboratory scale. As part of our technology transfer activity, in this chapter we focused on investigating CO_2 performance in the field scale dimensions. The effect of heterogeneity in the prominent Wasson Field CO_2 flood in West Texas on the overall sweep efficiency was investigated. A compositional simulation model was developed and then used to optimize CO_2 injection rate, flood patterns, slug sizes, and WAG ratio. The use of a viscous agent in WAG application and polymer injection in conformance control were explored to improve oil recovery. The results show that (1) recovery from a WAG process is a function of the injection rate as well as WAG ratio and the percentage of CO_2 slug size. (2) WAG injection is effective in increasing the sweep efficiency of the CO_2 injection. (3) Increasing viscosity of water injection and placing polymer in high permeability streak result in a positive production response and (4) a pattern reconfiguration change from inverted nine spot to staggered line drive could significantly increase oil recovery.

Project Fact Sheet

Progress work efforts at Project Fact Sheet are listed in the Appendix.

Chapter I-1
Effect of Overburden Pressure on Unfractured and Fractured Permeability Cores

1.1.1 INTRODUCTION

For many years many efforts have been performed in the laboratory experiments to duplicate the reservoir conditions. In this study, we investigated permeability change at different overburden conditions. The reduction in permeability with overburden pressure has been well known. Fatt and Davis (1952) presented the changes in permeability with pressure at a range of 0 to 15,000 psig and found that overburden pressure caused a reduction in permeability of the consolidated, oil-bearing sandstone samples by as much as 50 % at 10,000 psig. Wyble (1958) performed similar experiments on three different sandstone samples to determine the changes in conductivity, porosity, and permeability at a pressure range of 0 to 5,000 psig. His results were consistent with the observation by Fatt and Davis (1952). During the experiments, different overburden pressures (radial force) were applied only to the cylinder core while the axial direction was kept at constant atmospheric pressure.

Gray *et al.* (1963) enhanced the previous experiments by applying axial force and overburden pressure (radial force) to measure the anisotropy permeability changes at more representative reservoir stress-state condition. They showed that permeability reduction subjected to overburden pressure as a function of the ratio of radial to axial stress and the permeability reduction under nonuniform stress (radial pressure ≠ axial pressure) is less than that under uniform stress.

Although extensive work has been established on the effect of overburden pressure and stress state on matrix permeability, some very interesting details of fractured rock behavior under stress have not yet been investigated.

We explored the effect of fracture aperture and fracture permeability on the fluid flow under different overburden pressure as a precursor to investigating fracture apertures

under different stress-state conditions (confining stress, hydrostatic stress, and triaxial stress) and imaging fracture aperture distributions using X-ray computerized tomography (CT scans).

1.1.2 EXPERIMENTAL WORK

For simplicity in applying force in the axial direction, these experiments assume the axial direction is in the atmospheric pressure. Thus, only overburden pressure generated from a hydraulic jack was applied to cylindrical core faces.

Synthetic brine used in the experiments contained NaCl and $CaCl_2.2H_2O$ mixed with distilled water. The clean core was saturated with brine then inserted into a Hassler-type core holder using a confining pressure of 500 psia. Then core flooding was performed at different injection rates. After running set of injection rates at this pressure, we changed to other confining pressures and tested at different injection rates again, then repeated the procedure using a fractured core. Details of the procedure for conducting core flooding experiments can be found in Appendix-A. The procedure can be used for single- and two-phases experiments; the current results are mostly from the single-phase experiments. One experiment has been conducted using two-phase flow (water and kerosene) but the result is not included in our discussion.

The experimental set up shown in Fig. 1.1.1 will be used for future experiments in which the kerosene will be replaced with oil to investigate the fluid interaction through matrix and fracture or vice versa.

A Berea core was used during the core flooding experiments; the core properties are given in the note remark of Table 1.1.1. Two sets of injection rates ranging from 5 cm^3/min to 20 cm^3/min were performed at each overburden pressure. Three different overburden pressures from 500 to 1,500 psia were applied as listed in Tables 1.1.1 and 1.1.2 for both unfractured and fractured Berea core cut using a hydraulic cutter to generate a fracture horizontally along the axis of the core. During the experiments using a fractured core, the pressure drop across the core is lower and the core permeability increases about 3 times those obtained using unfractured cores.

Fig. 1.1.2 shows that the effect of varying overburden pressures on unfractured core is not significant, in contrast with that effect on fractured core. The average permeability of fractured core significantly reduces and even approaches the permeability of unfractured core at 1,500 psia. The pressure drops across unfractured core are parallel to the increase in injection rates; therefore, the permeability remains constant. Meanwhile, an increase in pressure drop causes large changes in average permeability of fractured core, as depicted by Fig. 1.1.3. The result suggests that the effect of stresses may be most pronounced in fractured reservoirs where large pressure changes can cause significant changes in fracture aperture and the related changes in conductivity within a reservoir, as shown by Lorenz (1999).

1.1.3 DATA ANALYSIS

To properly quantify the effect of fracture permeability on the fluid flow, it is important to understand the equations describing the changes of this parameter under different overburden pressures. The equations governing fluid flow through fractures have been widely published in the reservoir engineering literature and are not discussed here. However, the pertinent equations used for our analysis are presented as follows:

The fracture permeability, k_f, is obtained by combining the viscous force and Darcy equation for flow through fractures,

$$k_f = 8.45\times10^9\, w^2 \quad \text{.....(1)}$$

where w is a fracture width in centimeters.

Fracture width is a function of fracture permeability, and those two parameters are unknown. To obtain those parameters, one more equation is needed.

We obtained the average permeability of fracture and matrix, k_{av}, from core flooding experiments using a fractured core and matrix permeability, k_m, using unfractured core. Thus, another fracture permeability equation can be obtained following Eq. 2:

$$k_f = \frac{k_{av}A - k_m(A - wl)}{wl} \quad \text{.....(1.1.2)}$$

where A is matrix area (cm^2) and l is diameter of the core (cm).

Now, we have two equations and two unknowns, combining Eq. 1.1.1 and 1.1.2 can solve the fracture permeability and fracture width. First, Eq. 1.1.3 is applied to solve w, then it is inserted into Eq. 1 to solve k_f.

$$8.45\times10^{9} w^{3} l - k_{av} A + k_m (A - wl) = 0 , \quad \text{..... (1.1.3)}$$

It is also important to determine the contribution of flow rate from the matrix (q_m) and fracture (q_f). We determine the contribution from each zone by applying Darcy's equations. The equation for flow rate in the matrix is

$$q_m = \frac{k_m A \Delta p}{\mu L} , \quad \text{..... (1.1.4)}$$

where q_m is the matrix flow rate (cm^3/sec).

The flow through a smooth conduit, g_f, can be expressed by involving the fracture width (w) and the pressure gradient (Δp):

$$q_f = 9.86\times10^{-9} \frac{w^3 l \Delta p}{12 \mu L} , \quad \text{..... (1.1.5)}$$

where q_f is the fracture flow rate (cm^3/sec), w is the fracture width (cm), l is a lateral extent of the fracture (cm), and L is core length (cm).

1.1.4 ARTIFICIALLY FRACTURED CORE SIMULATION

A numerical model using the CMG™ commercial simulator was used to study the fluid flow through fracture at different overburden pressures. The laboratory process in which the water was injected through the fracture was duplicated in this modeling effort. The rectangular grid block was applied to overcome the difficulty of modeling a

cylindrical core shape [Putra *et al*. (1999)]. A 31x31 grid blocks were used in the x and z directions with 1 grid block in the y direction. The fracture layer is located only in the 16th layer and the rest are matrix layers. The permeability in fracture layer was calculated for two parallel plates without fracture roughness. All the layers were injected with constant water injection of 5 cm^3/hr. At the opposite end, two production points were located in the matrix and fracture layers to quantify the amount of water produced at those two points.

In the experimental process, the core was saturated with the water. Once water injection was started with constant rate, water was produced simultaneously. Then the water that was produced from both matrix and fracture layers at the end point was recorded. In the simulation, however, the initial water saturation condition is assumed zero. Thus, the water saturation change in the matrix and fracture can be observed as illustrated in Fig. 1.1.4.

A few minutes after the injection was started, the flow rate was still in the transient condition and then reached a steady-state condition at later time, as shown in Fig. 1.1.5. At steady-state conditions, we recorded the amount of water produced from matrix and fracture. Similar simulation runs were performed for different overburden pressures. The results were compared with the experimental results as shown in Figs. 1.1.6 and 1.1.7. The dotted lines indicate the experimental results. Even though the quality of the match for both flow rate and pressure drop is less than desirable for the single fracture model, which assumed smooth fracture surface between two parallel plates, the simulation results follows the trend of the laboratory results. To obtain a better result, we extended our research by introducing the fracture aperture heterogeneity along each flow path.

1.1.5 RESULTS AND DISCUSSION

The fracture aperture and fracture permeability are usually considered to remain the same during the producing life of the reservoir regardless of degree of depletion. Our experimental results show that the fracture aperture and fracture permeability have significant pressure-dependent changes in response to applying variable injection rates and overburden pressures.

Figs. 1.1.8 to 1.1.10 show the effect of several injection rates on matrix permeability, fracture aperture, and fracture permeability, respectively, under variable overburden pressures. The effect of several injections on matrix permeability is not significant, in contrast with its effect on fracture aperture and fracture permeability. During constant injection rates of 5 to 20 cm^3/min, the average matrix permeability decreases about 24% at overburden pressure of 1,500 psia from its original value at 500 psia. Meanwhile, the average fracture aperture and fracture permeability decrease about 71% and 91%, respectively, from its original value.

A very different behavior of the curve is observed for the first injection rate than for the injection rates of 10, 15 and 20 cm^3/min, which have similar values. However, after increasing the overburden pressure, the effect of injection rates on fracture aperture is more obvious: the more the overburden pressure increases, at higher injection rates, the more the reduction in fracture aperture. The fracture aperture becomes smaller at higher injection rates, which is the *opposite* of the common thought. The reason behind this phenomenon is that the core has high matrix permeability and is surrounded by constant high confining pressure that does not allow the core to expand. The amount of flow at different injection rates through the fracture drops dramatically, although they flow at similar rates (about 1 cm^3/min) at a confining pressure of 1,500 psia as shown in Fig. 1.1.11. This means that the water mostly flows through the matrix, diverting from the fracture path. At higher injection rates, the pressure drop becomes higher through the matrix and increases the tendency to squeeze the fracture aperture. That is why the fracture aperture becomes smaller at higher injection rates.

The results also indicate that the influence of high stress on axial direction by introducing high injection rates would give high permeability reduction, also as previously reported by Gray *et al.* (1963).

Because the fracture width is a function of fracture permeability, the fracture permeability has a trend similar to fracture width under different overburden pressures. The fracture permeability ranges from about 200 to 700 darcy at 500 psia but reduces to about 9 to 36 darcy at 1,500 psia.

We also calculated the reduction of matrix porosity to investigate the magnitude of rock compaction by adopting the following equation from Jin *et al*., (2000):

$$\frac{k}{k_o} = (\frac{\phi}{\phi_o})^3, \quad \text{(1.1.6)}$$

where N=3, which is commonly used, corresponds to a representation of porous space as an ensemble of flat channels and N=10 is used for real sandstones. The change in porosity with different overburden pressure has been shown to be small compared to significant effect on permeability. The average matrix porosity at different overburden pressures changes only 3%, compared to a 24% change in matrix permeability.

The reduction of fracture permeability in the presence of overburden clearly has a significant effect on reservoir productivity, so we need to quantify the flow through the matrix and the fracture at different overburden pressures. By applying Eqs. 4 and 5, we were able to quantify the contribution of fluid flow from matrix and fracture as shown in Figs. 1.1.11 and 1.1.12 at variable overburden pressures. At 500 psia, the flow is preferential to the high-permeability zone; at the injection range of 5 to 20 cm^3/min, the percentage of fluid flows through the fracture is 72% to 68%. However, after increasing the overburden pressure the fluid flows through the fracture decreases; at 1500 psia, it is only 14% to 2%. At this time most of injected water diverts through the matrix because of significant reduction of permeability in the fracture.

Even though the fracture permeability is still very high (10 to 40 darcy) the volumetric rate of the fracture becomes limited; therefore, most of the water flows through the matrix rock with less permeability (>200 md) but higher volumetric rate.

1.1.6 CONCLUSIONS

1. The laboratory result shows that the change in overburden pressure significantly affects the reservoir properties.
2. The change in matrix permeability with different injection rates under variable overburden pressures is not significant, in contrast with that effect on fracture aperture and fracture permeability.

3. The experimental results of a core-induced fracture with high-permeability matrix reveal that higher injection rates give smaller fracture aperture at constant high confining pressure.
4. The simulation results suggest that a parallel model is insufficient to predict fluid flow in the fracture system. Consequently, the spatial heterogeneity in the fracture aperture must be included in the modeling of fluid flow through the fracture system.
5. The results also imply that the effect of stresses may be most pronounced in fractured reservoirs where large pressure changes can cause significant changes in fracture aperture and related changes in fracture permeability.
6. The change in porosity at different overburden pressure is small compared to its significant effect on permeability.
7. At high overburden pressure, the influence of existing fracture permeability on fluid flow in permeable rocks (> 200 md) is not too significant.

REFERENCES

1. Fatt, I. and Davis, D.H.: "Reduction in Permeability with Overburden Pressure," *Trans.*, AIME (1952) **195**, 329.
2. Gray H. D., Fatt, I., and Bergamini, G.: "The Effect of Stress on Permeability of Sandstone Cores," *SPEJ* (June 1963).
3. Jin, M., Somerville, J. and Smart, B.G.D.: "Coupled Reservoir Simulation Applied to the Management of Production Induced Stress-Sensitivity," paper SPE 64790 presented at the 2000 International Oil and Gas Conference and Exhibition, Cina, Nov 7-10.
4. Lorenz, J.C.: "Stress-Sensitive Reservoirs," *JPT* (Jan 1999), 61.
5. Putra, E., Fidra, Y., and Schechter, D.S.: "Study of Waterflooding Process in Naturally Fractured Reservoirs from Static and Dynamic Imbibition Experiments," paper SCA 9910 presented at the 1999 International Symposium of the Society of Core Analysts, Colorado, August 1-4.
6. Wyble, D.O.: "Effect of Applied Pressure on the Conductivity, Porosity and Permeability on Sandstones," *Trans.*, AIME (1958) **213**, 430.

NOMENCLATURES

A = matrix area (cm^2)

k_m = the matrix permeability (Darcy)

k_f = the fracture permeability (Darcy)

l = core length (cm)

L = diameter of the core (cm)

q_m = the matrix flow rate (cc/sec)

q_f = the fracture flow rate (cc/sec)

w = the fracture width (cm)

Δp = pressure drop across the core (atm)

μ = viscosity (cp)

APPENDIX A – PROCEDURE FOR CONDUCTING CORE FLOODING EXPERIMENT

For single phase experiments:

1. Wash the core before saturating the core at about 350°C for about two days.
2. Saturate the core for about two days before starting the experiment.
3. Make sure the two valves between the pumps and the accumulators are turned off before refilling the pumps.
4. Obtain the desired overburden pressure using a hydraulic jack. This may require several attempts to stabilize, as air will be trapped in line causing a loss of overburden pressure.
5. Fill brine Accumulator 1 with brine and Accumulator 2 with kerosene or oil, if necessary.
6. Turn on the valve between Pump 1 and Accumulator 1, and turn the valves to the on position on the permeameter.
7. Turn the red valve, which connects Accumulator 1 to the core holder, to the on position. Make sure that the black valve connecting Accumulator 2 and the core holder is off.

8. Perform the core flooding experiment with different flow rates and note the pressure difference in the permeameter.
9. Change the overburden pressure and perform the experiment and note the readings.
10. Fracture the core, replace it in the core holder, and apply overburden pressure. Close the black valve and open the red valve again, and perform the core flooding experiment with brine. Note the readings.

For two-phase experiments

Follow the procedure above to Step 9 and continue with the following:

1. Turn the red valve to off position and open the valve between Pump 2 and Accumulator 2.
2. Also open the black valve that connects Accumulator 2 to the core holder.
3. Perform the core flooding experiment.
4. Note the amount of brine coming out of the core when kerosene or oil is injected.
5. Fracture the core, replace it again in the core holder, and apply overburden pressure. Close the black valve and open the red valve again and perform the core flooding experiment with brine.
6. Note the amount of kerosene or oil discharged when brine is injected.

Precautions

1. Filter the brine to avoid any dissolved solids that choke the core.
2. Make sure the experiment is performed without any air trapped in the core.
3. While refilling the accumulators, take care to close the valves between the accumulator and the core holder to avoid any air entering the pipelines.
4. Fracture the core as soon as possible to avoid much loss of fluid.
5. Note the volume of outlet pipeline from the core holder and subtract it from the amount of brine discharged while kerosene is injected.
6. After each flow, allow the pressure to drop close to atmospheric pressure before starting the next flow.

Table 1.1.1 — Overburden experiments for unfractured core.

Pob **psia**	***Dp*** **psia**	k_m **md**	***Q*** **Cm^3/m**
485.7	4.1	299.7	5
506.4	8.1	303.4	10
502.9	12.4	297.2	15
504.4	16.5	297.85	20
501	4.2	292.5	5
504.9	8.5	289	10
501	13	283	15
502	17	289.1	20
1000.4	4.5	273	5
1002.4	9	273	10
1000.5	13.7	269	15
1000.5	18.2	270	20
1000.2	4.8	255.9	5
1003.5	9.7	253.3	10
1002.7	14.5	254.2	15
1004.1	19.2	255.96	20
1500	5.1	240.8	5
1500	10.4	236.3	10
1500.7	16.4	224.7	15
1503.1	22.1	222.4	20
1500.3	5.5	223.4	5
1501	11.2	219.4	10
1501.3	17.3	213	15
1502.3	22.7	216.5	20

Table 1.1.2 — Overburden experiments for fractured core.

Pob **psia**	***Dp*** **psia**	k_{av} **md**	***Q*** **Cm^3/m**
501.3	1.4	877.5	5
500.2	2.8	877.6	10
503.3	4.1	898.9	15
503.3	5.4	910	20
494.8	1	1228.7	5
509.4	2.6	945.1	10
508.8	4.2	877.6	15
509.6	5.8	847.3	20
970.5	2.2	558.4	5
1000.5	4.8	511.9	10
1001	7.6	485	15
1016.7	11.3	434.9	20
1000.8	2.3	534	5
1002.2	5.8	423.6	10
1009.7	9.1	405	15
1002.7	13.9	353.6	20
1500.3	4.2	292.5	5
1504.6	9.3	268.2	10
1507.9	15.1	244.1	15
1504.8	21.4	229.6	20
1500.7	5	245.7	5
1506	10.9	225.4	10
1509.6	17.4	211.8	15
1509.6	22.5	218.4	20

NOTE:

Berea Core Properties

Length	4.9784 Cm
Diameter	2.5146 Cm
Viscosity	1.0 Cp
Area	4.9637 Cm^2
Porosity	23.58%

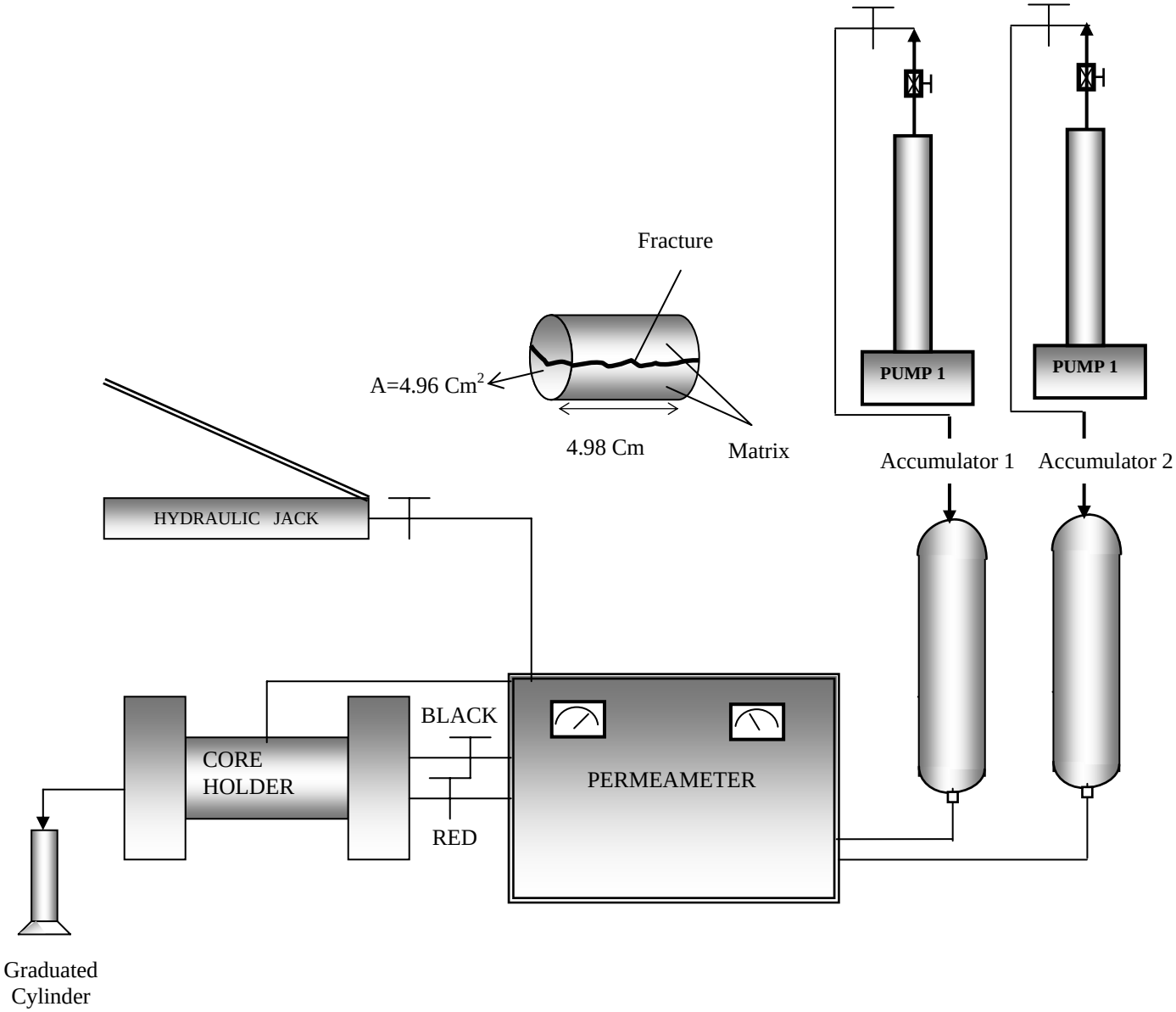

Fig. 1.1.1 — Schematic diagram of the two-phase core flooding experiment.

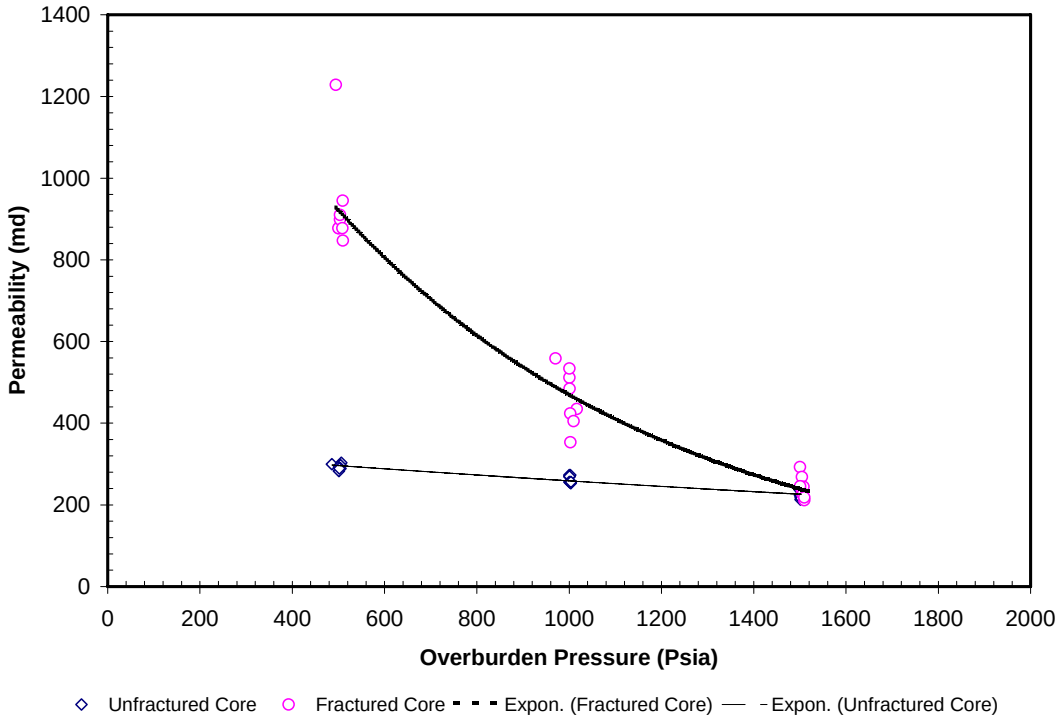

Fig. 1.1.2 — Comparison permeability reduction between unfractured and fractured cores due to increasing overburden pressure.

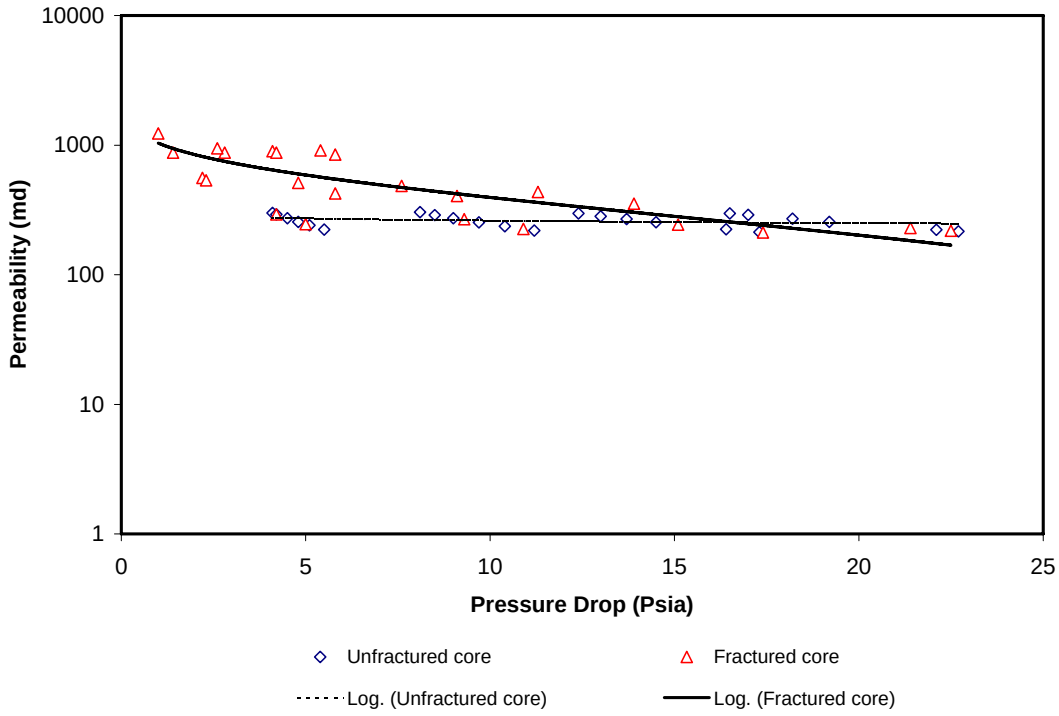

Fig. 1.1.3 — Relationship between pressure drop and permeability.

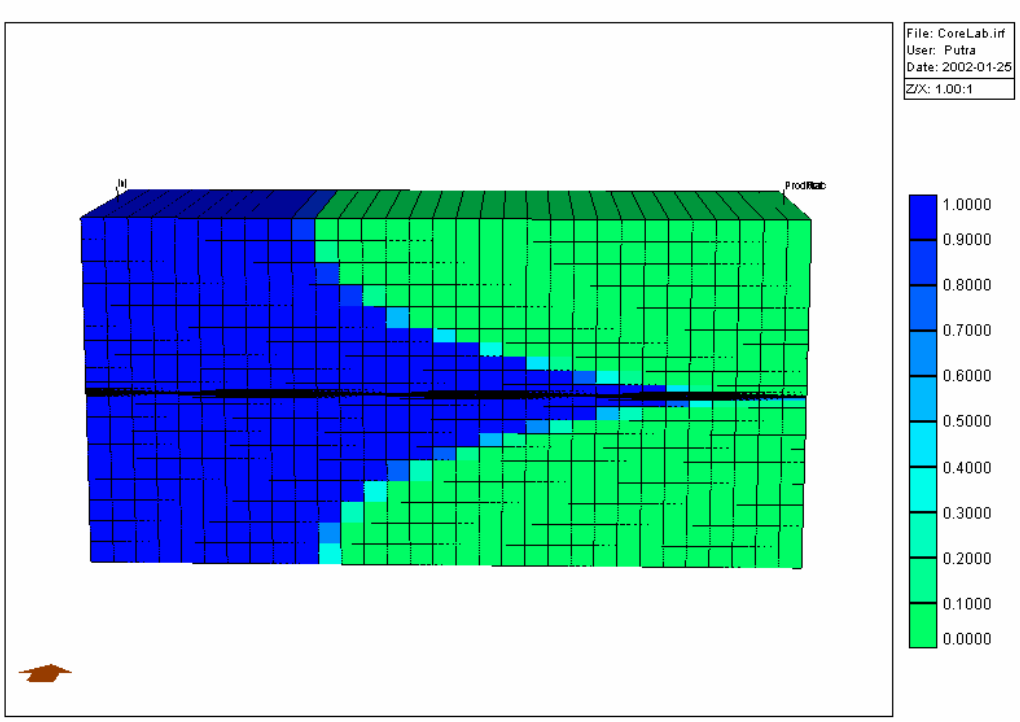

Fig. 1.1.4 — Water saturation change at matrix and fracture at transient flow condition.

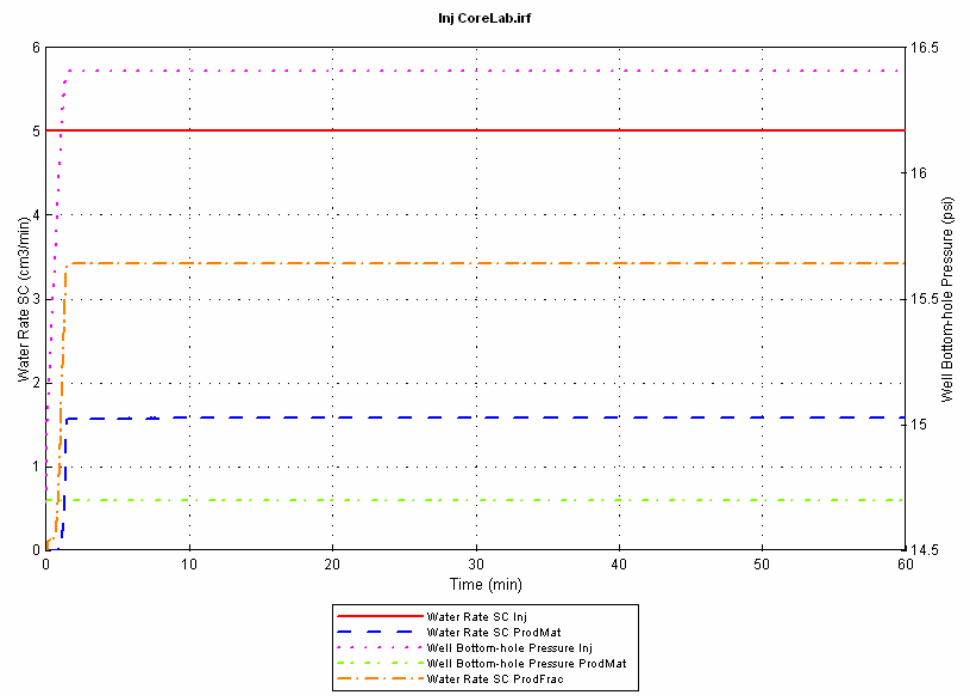

Fig. 1.1.5 — The simulation results of flow rates and pressure drop injected at 5 cm^3/min and overburden pressure of 500 psi.

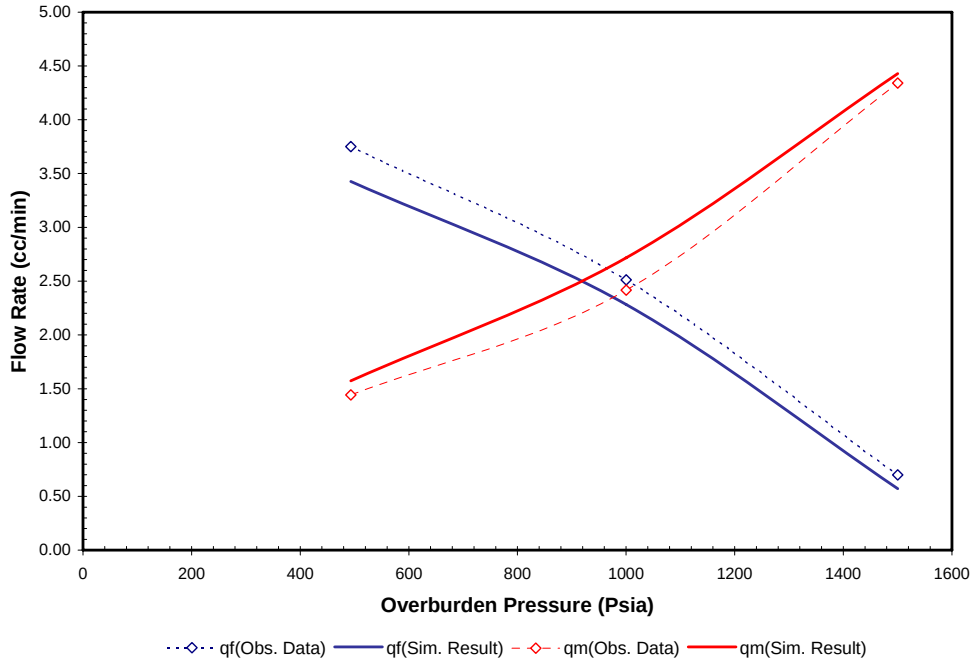

Fig. 1.1.6 — The flow rates comparison between laboratory and simulation results at 5 cm^3/min and each different overburden pressures.

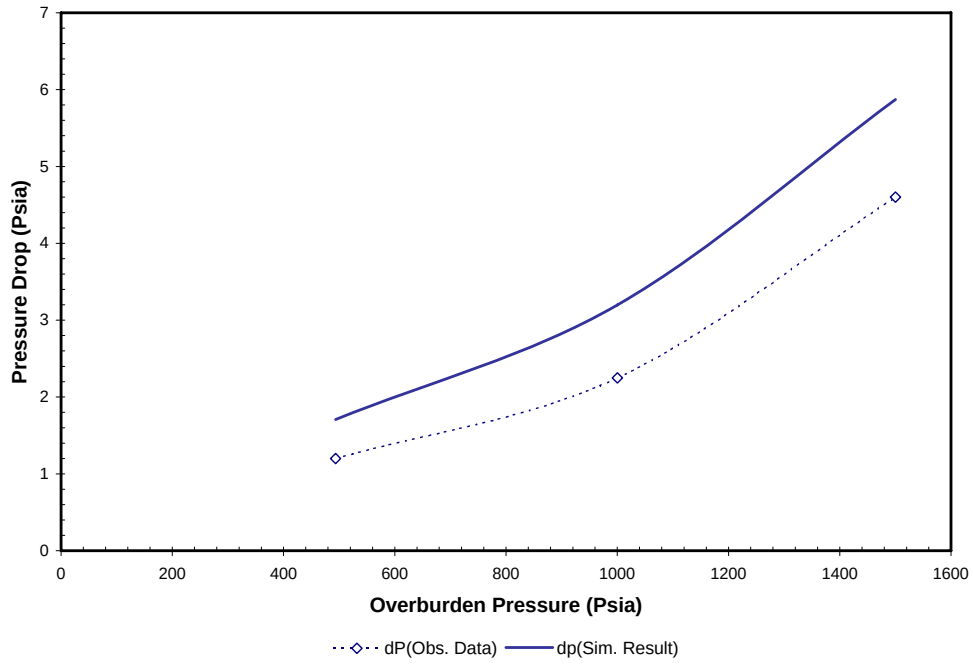

Fig. 1.1.7 — The pressure drop comparison between laboratory and simulation results at 5 cm^3/min and each different overburden pressures.

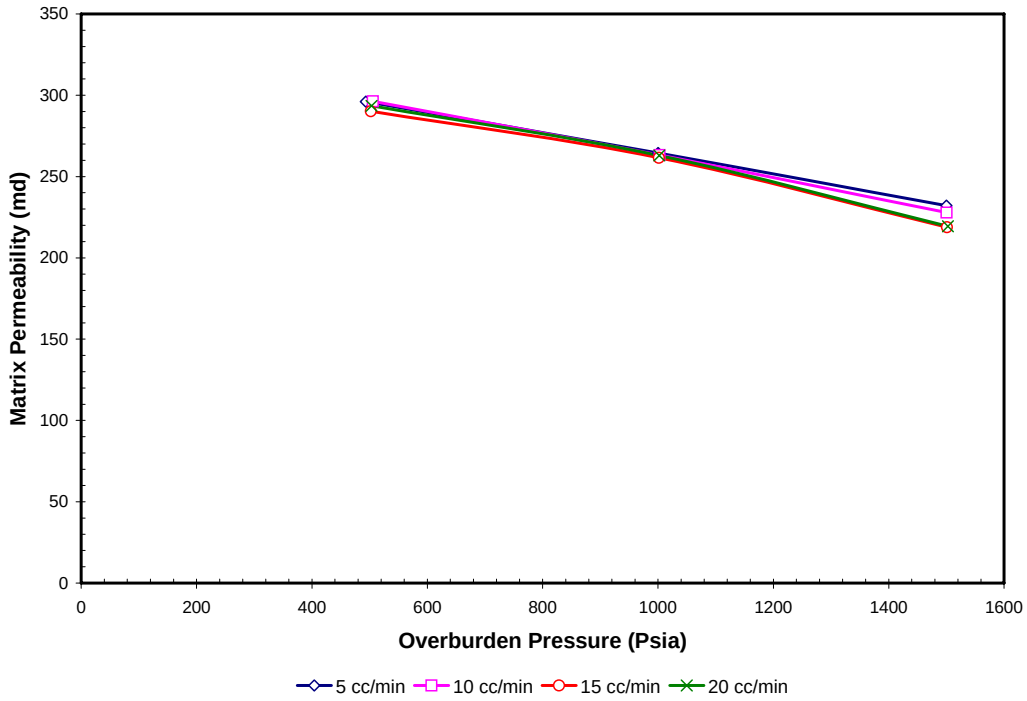

Fig. 1.1.8 — Effect of injection rates on matrix permeability during applying variable overburden pressures.

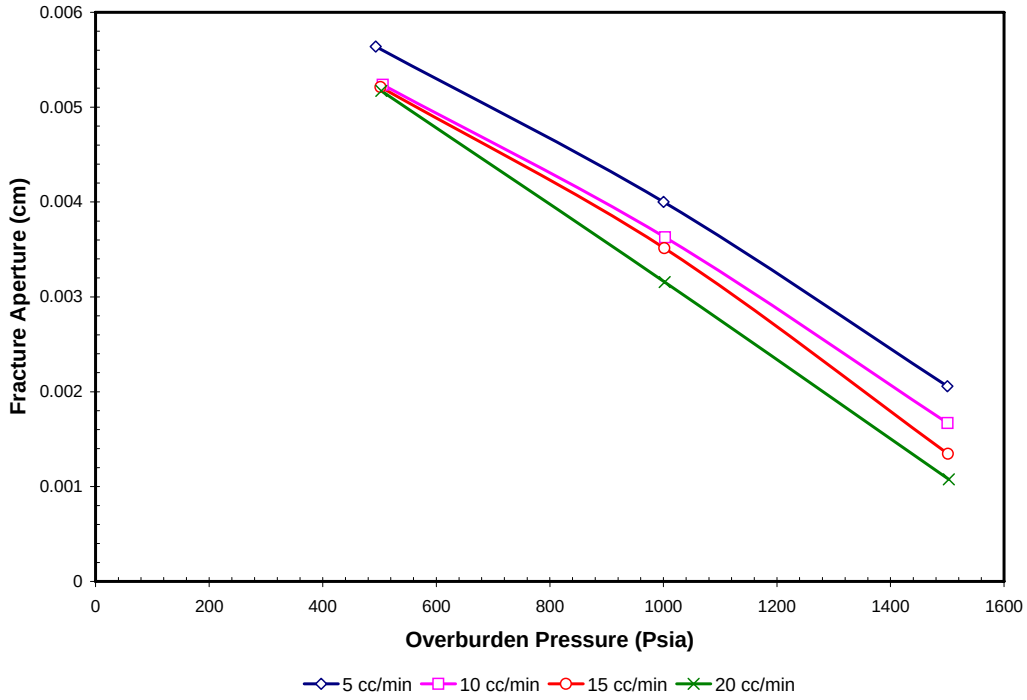

Fig. 1.1.9 — Effect of injection rates on fracture aperture during applying variable overburden pressures.

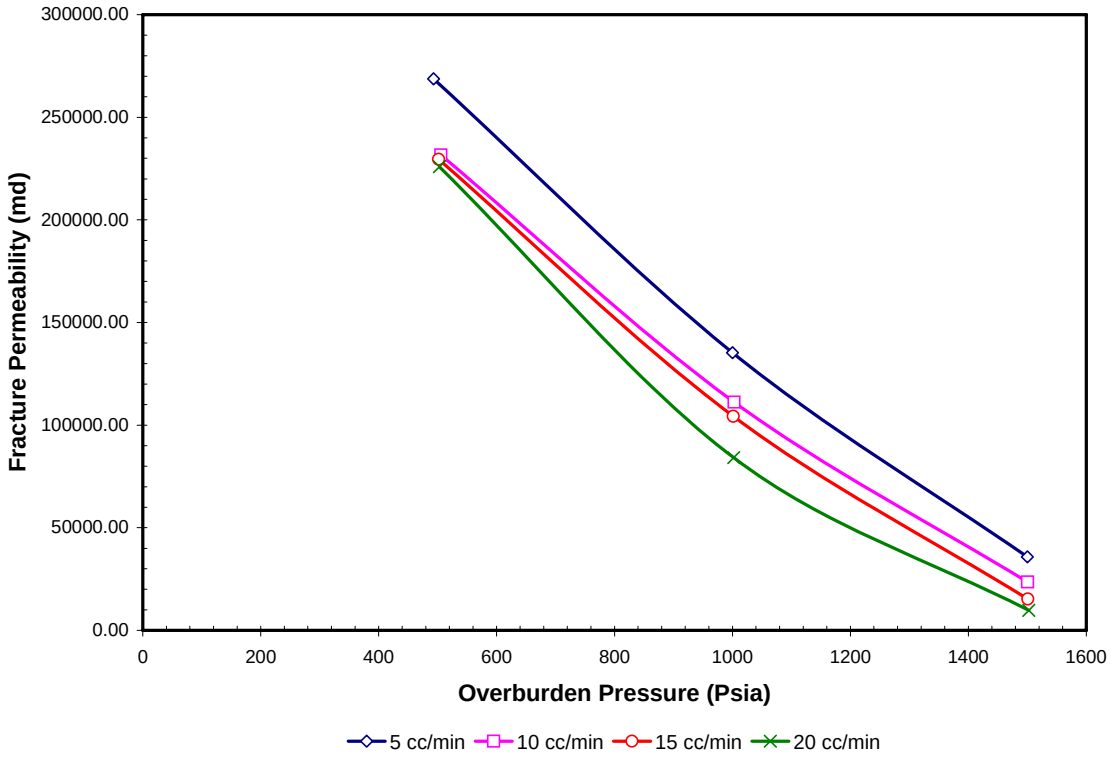

Fig. 1.1.10 — Effect of injection rates on fracture permeability during applying variable overburden pressure.

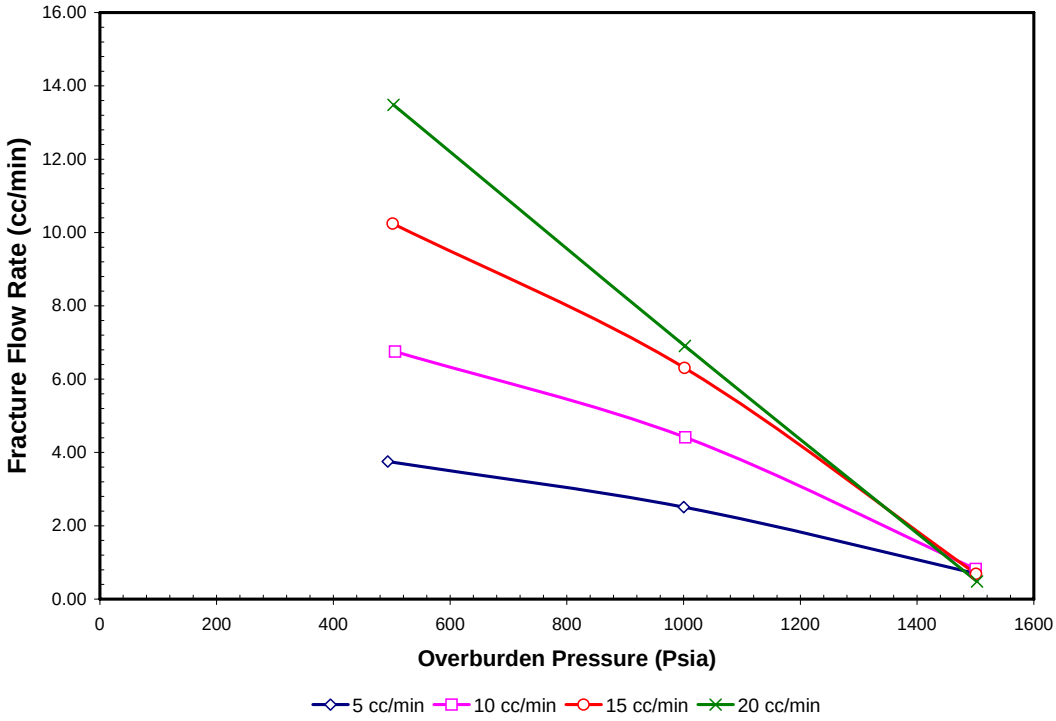

Fig. 1.1.11 — Reduction in fracture flow rate during variable overburden pressures.

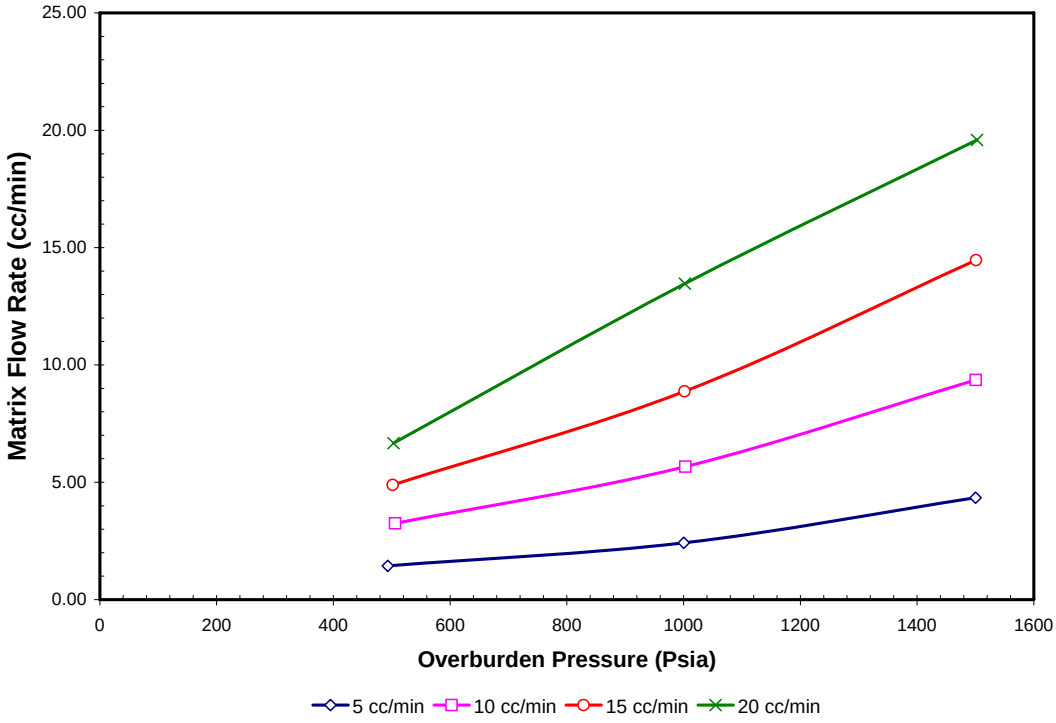

Fig. 1.1.12 – Reduction in matrix flow rate during variable overburden pressures.

Chapter I-2

Investigating the Changes in Matrix and Fracture Properties and Fluid Flow Under Different Stress-State Conditions

1.2.1 INTRODUCTION

Fatt and Davis (1952) observed that a significant decrease in permeability of sandstones occurs at overburden pressures between zero and 3,000 psi; Wyble (1958) observed the same phenomenon at radial pressures of zero and 5,000 psi.

Bergamini (1962) applied radial and axial stresses up to 4,000 psi equally (hydrostatic loading) and then, with axial stress kept constant while the radial pressure increased, observed a reduction of permeability on the order of 10 % for most sandstones. Gray *et al.* (1963) showed that permeability reduction in cylindrical samples of two sandstones, when subjected to mechanical stress, is a function of the ratio between radial and axial stress. Wilhelmi *et al.* (1967) observed that a great reduction in permeability occurred under hydrostatic loading on three outcrop sandstones at several confining pressures and axial stresses up to approximately 80 % of failure stress. A substantial reduction also occur upon application of deviator (triaxial) stress, is $\sigma_y - \sigma_x$, where σ_y is the axial stress and σ_x, which is equal to σ_z, is the lateral stress. The permeability reductions were on the order of 10 to 20 % for Berea sandstone. Holt's (1990) compression and extension tests on Triassic sandstone showed that the single-phase permeability decreased rapidly under nonhydrostatic stress conditions when shear stress [$1/2(|\sigma_{max} - \sigma_{min}|)$] exceeded the yield level.

Jones (1975) showed that fracture permeability is greatly reduced by increasing confining pressure up to 20,000 psi. The fracture permeability behavior governed at lower confining pressures while matrix permeability behavior governed at higher confining pressures. Teufel *et al.* (1993) found that under hydrostatic loading the permeability of unfilled chalk fractures reduced greatly compared to partially filled fractures. Maximum permeability reduction occurred when the stress path remained at hydrostatic pressure.

No research has been carried out to quantify the fracture aperture and permeability of fractures so far. The changes in effective permeability of fractures and matrix have been studied in detail under different effective stress. However, deriving the fracture permeability from the effective permeability to study the permeability of fracture alone has not been considered. Furthermore, no work has evaluated matrix and fracture flowrates under different stress-state conditions. Our research extends the work of previous researchers by quantifying the changes in matrix and fracture permeabilities, fracture aperture, matrix and fracture flowrates under different stress-state conditions (uniaxial, triaxial and hydrostatic stresses). The results of uniaxial stress experiment have been provided in the earlier report (Putra *et al*, 2002); this report mainly discusses the triaxial and hydrostatic experiments and the comparison between the results of uniaxial, triaxial, and hydrostatic experiments.

1.2.2 HYDROSTATIC STRESS EXPERIMENTS

HSEs allow us to explore the effects of even stresses on the sample.

1.2.2.1 Experimental Description

In our HSEs, the core sample was subjected to equal overburden pressure and axial stress. Permeability was evaluated at various confining pressures and at various injection rates. The cores were then fractured and the resulting effective permeability was evaluated at various confining pressures and injection rates. The parameters were plotted against overburden pressure to study the effect of confining stress.

Berea Cores. Berea sandstone was used in this study. Berea sandstone was selected because it is widely used as a standard porous rock for experimental work in the petroleum industry. The cylindrical core sample was cut from 0.5 ft^3 blocks of Berea sandstone. The diameter of the sample was 3.6 cm. The length of the core was 4.88 cm. The bulk volume of the sample was 49.68 cm^3.

Brine Composition. The synthetic brine used in the experiments was prepared by dissolving NaCl and $CaCl_2.2H_2O$ in distilled water. The brine compositions are shown in Table 1.2.1.

Pore Volume and Porosity. The porosity was calculated by the saturation method. The method involves saturating a clean, dry sample with a fluid of known density and

determining the pore volume from the gain in the weight of the sample. For this experiment, the core was saturated with brine. The pore volume was calculated from the following expression:

$$PV = \frac{W_{wet} - W_{dry}}{\rho_b}, \quad (1.2.1)$$

where W_{dry} is the weight of the dry core, W_{wet} is the weight of the core after saturating with brine, and ρ_b is the density of the brine. The pore volume was calculated to be 11.71 cm^3. The calculated porosity was 23.58%.

1.2.2.2 Experimental Procedures

Core Saturation. Dry core samples were weighed on a balance. The core sample was then saturated with deaerated brine using a vacuum pump for at least 12 hours. After saturating the core samples with brine, a period of 3 days was allowed for the brine to achieve ionic equilibrium with the rock.

Core Flooding. The saturated core was inserted in the Hassler-type core holder. Overburden pressure was applied in the radial direction and the axial tension was applied along the axis of the Berea core, perpendicular to the overburden pressure. An initial overburden pressure of 500 psi was applied. This was followed by core flooding with the brine solution at flow rates of 5, 10, 15 and 20 cm^3/min. The pressure drop across the core was recorded by a transducer. The experiments were repeated for overburden pressures of 1,000 psi and 1,500 psi and the corresponding pressure drops were recorded. Then, the core was fractured along the axis and the experiment was repeated for the fractured core. The experimental setup for a two-phase flow experiment is shown in Fig. 1.2.1. This project focused only on single-phase flow.

1.2.2.3 Effect of Hydrostatic Stress on Permeability

Permeability of the rock decreases with increase in applied stress. Fig. 1.2.2 shows the effect of overburden pressure on permeability of both the unfractured and fractured core. In both cases, the permeability is reduced with the increase in stress level; however, the decrease in permeability of the unfractured core is much less than the fractured core.

The resistance to fluid flow in fractures is less compared than in the matrix. The fluid, therefore, tends to take a preferential path through the fractures rather than flowing through the matrix. As a result, the effective permeability of the fractured core is higher than the matrix permeability (unfractured core). The increase in the hydrostatic stress tends to close the fractures and accordingly increase the resistance to fluid flow inside the fracture. Hence, the effective permeability of the fractured core reduces greatly with the increase in hydrostatic stress. The effective permeability value of the fractured core will be close to the matrix permeability at higher hydrostatic stress, although it will still exhibit some effect of fractures. This is because the fractures are not completely healed even at a higher stress, leaving a residual effect of fractures on the effective permeability of the core as is evident from Fig. 1.2.2. Fig. 1.2.3 shows the normalized permeability of both the unfractured and fractured core against overburden pressure at a flowrate of 5 cm^3/min.

1.2.2.4 Effect of Hydrostatic Stress on Fracture Aperture

Fracture permeability depends upon fracture aperture distributions and conductivity of fractures. Fracture aperture, the width between the fracture surfaces, is not uniform along the fractures and depends on the roughness of the fracture surfaces. If the roughness is high, the aperture will vary more; it can be at a maximum at some points and am minimum at other points. Since fracture aperture is not uniform, it is very difficult to quantify it experimentally at all points of the fracture path; hence, the assumption of parallel plates has been (Putra, 2002) used for calculating the mean fracture aperture. The fracture aperture depends on the physical properties of the core, the size of the core sample, and the matrix and the effective fracture permeabilities.

We calculated the fracture aperture for different hydrostatic stress and flowrates. When hydrostatic stress increases, the effective fracture permeability and fracture aperture decrease significantly. The fracture aperture is more dependent on the effective fracture permeability than on the matrix permeability since the variations of the matrix permeability with increase in hydrostatic stress are lower than the effective fracture permeability. The fracture aperture is almost insensitive to the increase in injection rate. Fig. 1.2.4 shows the plot of fracture aperture against overburden pressure.

1.2.2.5 Effect of Hydrostatic Stress on Fracture Permeability

Fracture permeability was determined on the basis of the fracture aperture. Fracture permeability is defined as conductivity of fractures to fluid flow in the fractured core. The effective permeability in a fractured formation is the combination of both fracture permeability and matrix permeability. Fracture permeability is calculated assuming the flow of fluid between parallel plates. Based on this assumption, fracture permeability is proportional to the square of the fracture aperture by combining viscous and Darcy equations for flow. Usually fracture permeability is very high compared to matrix permeability; and hence, fluid tends to flow through the fracture with relative ease as compared to the matrix. However, the fracture permeability decreases significantly with an increase in hydrostatic stress. Fig. 1.2.5 shows reductions of fracture permeability under increased hydrostatic stress.

1.2.2.6 Effect of Hydrostatic Stress on Fracture and Matrix Flow Rates

The fracture flowrate depends on fracture permeability and fracture aperture. Fluid flow in fracture and matrix depends on injection rate. The fluid will rush inside the fractures since the fracture permeability is high compared to the matrix. However, the volumetric area of the fracture region is small compared to the matrix block; hence, some of the fluid diverts to matrix block. The flowrate through the fracture depends on the fracture permeability and fracture aperture. When hydrostatic stress increases, the fracture permeability and aperture decrease, which also decreases the volumetric rate of the fracture region. Therefore at high hydrostatic stress, the fluid flow in the fracture is no longer dominant, although some amount of flow still occurs because the fractures never completely heal. The effects of hydrostatic stress on fracture and matrix flow rates at different injection rate are presented in Figs. 1.2.6 and 1.2.7.

1.2.3 TRIAXIAL STRESS EXPERIMENTS

1.2.3.1 Experimental Description

We subjected the core sample to both overburden pressure and axial stress, keeping the axial stress at one-third of the overburden pressure for the triaxial experiment. After

evaluating matrix permeability at various confining pressures and at various injection rates, we fractured the cores and repeated the tests. We plotted the parameters were plotted against overburden pressure to study the effect of confining stress.

Berea Cores. Berea sandstone was used in this study. The sample was 3.59664 cm diameter and 5.047 cm length. The dimensions, averaged from 3 to 4 measurements using a Vernier caliper. The bulk volume of the sample was 53.23 cm^3. The pore volume and porosity, calculated for hydrostatic loading, 12.55 cm^3 and porosity, 23.58%. The core was saturated as explained before under hydrostatic loading.

Core Flooding. The saturated core sample was inserted into the Hassler-type core holder. Overburden pressure was applied in the radial direction and axial tension was applied along the axis of the core, perpendicular to the overburden pressure. An initial overburden pressure of 500 psi was applied. This was followed by core flooding with the brine solution at flow rates of 5, 10, 15 and 20 cm^3/min. The pressure drop across the core was recorded by a transducer. The experiments were repeated for overburden pressures of 1,000 psi and 1,500 psi and the corresponding pressure drops were recorded. Subsequently, the core was fractured along the axis and the experiment was repeated for the fractured core. The experimental setup for a two-phase flow experiment is shown in Fig. 1.2.8. However, the focus for here is on single-phase flow.

1.2.3.2 Effect of Triaxial Stress on Permeability

Permeability of the rock decreases with increase in applied stress. Fig. 1.2.9 shows the effect of overburden pressure on permeability of both the unfractured and fractured core. The permeability is decreased by the increase in stress level in both cases; however, the reduction in permeability of the unfractured core is much less than in the fractured core.

Increase in triaxial stress tends to close the fractures and increase the resistance to fluid flow. Hence the effective permeability of the fractured core decreases significantly with the increase in triaxial stress. At 1,500 psia, the effective permeability of the fractured core converges to matrix permeability as the fracture aperture closes. Fig. 1.2.10 shows that matrix permeability decreases about 20% from its initial permeability, compared to 80% permeability reduction of the fractured core under the same triaxial stress.

1.2.3.3 Effect of Triaxial Stress on Fracture Aperture

The fracture aperture was calculated for different triaxial stress and flowrates. When triaxial stress increases, the effective fracture permeability and fracture aperture decrease significantly, showing a similar response to previously applied stresses (uniaxial and hydrostatic stresses). Again it shows that fracture aperture is almost insensitive to the increase in injection rate. Fig. 1.2.11 shows the plot of fracture aperture against overburden pressure.

1.2.3.4 Effect of Applied Stress on Fracture Permeability

The fracture permeability decreases significantly with the increase in triaxial stress. Fig. 1.2.12 shows reduction of fracture permeability as triaxial stress increases.

1.2.3.5 Effect of Applied Stress on Fracture Flow Rate

The flow rate through the fracture depends on the fracture permeability and fracture aperture. When triaxial stress increases, the fracture volume becomes small and the flow is no longer dominant in the fracture, although some flow occurs due to the nonhealing nature of the fractures. Hence, the fracture flowrate decreases with increase in triaxial stress. Fig. 1.2.13 shows the plot of fracture flowrate against overburden pressure at various injection rates.

1.2.3.6 Effect of Applied Stress on Matrix Flow Rate

Matrix flowrate depends on the matrix permeability and fracture aperture. The presence of a fracture reduces the flow through the matrix because the resistance to flow is least in the fracture. However, increase in triaxial stress closes the fracture (reducing fracture aperture) and hence the matrix flowrate dominates. Fig. 1.2.14 shows the plot between matrix flowrate and overburden pressure at various injection rates.

1.2.4 COMPARISON OF UNIAXIAL, TRIAXIAL AND HYDROSTATIC RESULTS

1.2.4.1 Effect of Applied Stress on Permeability of Unfractured Core

As mentioned earlier, permeability of the core reduces where applied stress increases. Three types of applied stress used in our experiments are uniaxial, triaxial and hydrostatic

stresses. The difference between those stresses is illustrated in Fig. 1.2.15. Uniaxial stress has uniform confining stress around the body of the core, but no axial stress is applied on the axis of the core. Triaxial stress has confining stress but also has an axial stress applied along the axis of the core. The axial stress is held at one-third of the confining stress. The hydrostatic stress has uniform confining and axial stresses. Fig. 1.2.16 compares matrix permeability reduction under different applied stress. With the permeabilities normalized and plotted against overburden pressure, the figure clearly shows that hydrostatic stress has the highest impact on permeability reduction, followed by triaxial and uniaxial stresses.

1.2.4.2 Effect of Applied Stress on Permeability of Fractured Core

We saw the same effects of pressure when we tested fractured cores (Fig 1.2.17). However, the reduction of effective permeability is higher in the fractured core than in the unfractured core. The residual effects of fracture remain at higher pressure are because the fracture never completely heals even at high stress.

1.2.4.3 Effect of Applied Stress on Fracture Aperture

Fracture aperture depends greatly on applied stress and on the fracturing technique. In the laboratory, cores are fractured using a hydraulic cutter, so the fracture aperture depends on the load applied on the core during cutting. The usual trend is that the fracture aperture decreases significantly as applied stress increases. Fig. 1.2.18 show little difference between the hydrostatic and triaxial stress conditions at flowrate of 5 cm^3/min.

1.2.4.4 Effect of Overburden Pressure on Fracture Permeability

Fracture permeability also decreases greatly as increase in applied stress decreases fracture aperture (Fig. 1.2.19).

1.2.5 CONCLUSIONS

1. Absolute permeability decreases with the increase in applied stresses.
2. Applied stress reduces effective permeability in the fractured core more significantly than in an unfractured core.
3. Applied stress decreases the fracture aperture and fracture permeability.

4. Fracture flow dominates when applied stress is low; however, the matrix flow increases as applied stresses increase and dominates at higher stresses, even if the fracture is not completely healed.
5. Hydrostatic stress has the greatest impact on the reduction of matrix and fracture permeabilities and fracture aperture, followed by triaxial and uniaxial stresses.

REFERENCES

1. Fatt, I and Davis, D. H: "Reduction in Permeability with Overburden Pressure", *Trans.,* AIME (1952) **195**, 329.
2. Fatt, I: "The Effect of Overburden Pressure on Relative Permeability", *Trans.*, AIME (1953) **195**, 329.
3. Mc Latchie, A. S., Hemstock, R. A. and Young, J. W: " The effective Compressibility of Reservoir Rock and Its Effects on Permeability", *Trans.*, AIME (1958) **213**, 386-388.
4. Wyble, D. O: "Effect of Applied Pressure on Conductivity, Porosity and Permeability of Sandstones", *Trans.*, AIME (1958) **231**, 430-432.
5. Dobrynin, V. M: "The Effect of Overburden Pressure on Some Properties of Sandstones", *SPEJ* (Dec 1962) 360-366.
6. Bergamini, G: "The Effect of Non-Uniform Stress on Permeability of Sandstones", Unpublished report, U. of California. Petroleum Engineering Laboratory (May 1962).
7. Gray, D. H., Fatt, I., and Bergamini, G.: "The Effect of Stress on Permeability of Sandstone Cores", *SPEJ* (June 1963) 95-100.
8. Wilhelmi, B. and Somerton, W. H: "Simultaneous Measurement of Pore and Elastic Properties of Rocks Under Triaxial Stress Conditions", paper SPE 1706 (1967).
9. Morita, N. *et al.:* "Rock Property Change During Reservoir Compaction," paper SPE 13059 presented at the 1984 SPE Annual Technical Conference and Exhibition, Houston, Sept. 16-19.
10. Holt, R. M: "Permeability Reduction Induced by a Nonhydrostatic Stress Field", SPE 19595, Presented at the 64th Annual Technical Conference and Exhibition of SPE in San Antonio, TX (1989), 251-258.

11. Keaney, G. M. J., Meredith, P. G. and Murrell, S. A. F: "Laboratory Study of Permeability Evolution in'Tight' Sandstone under Non-Hydrostatic Stress Conditions", SPE/ISRM 47265, presented at the SPE/ISRM Eurock '98 held in Trondheim, Norway, 8-10 July 1998.
12. Hubbert, M. K. and Willis, D.G: "Mechanics of Hydraulic Fracturing", *Trans.*, AIME (1957) **210**, 153-168.
13. Jones, F. O: "A Laboratory Study of the Effects of Confining Pressure on Fracture Flow and Storage Capacity in Carbonate Rocks", SPE 4569, (1975).
14. Teufel, L. W., Rhett, D. W, Farrell, H. E. and Lorenz, J. C.: "Control of Fractured Reservoir Permeability by Spatial and Temporal Variations in Stress Magnitude and Orientation", SPE 26437, presented at the 1993 Annual Technical Conference and Exhibition of SPE in Houston, TX.
15. Putra, E.: "Effect of Overburden Pressure on Unfractured and Fractured Permeability Cores," Semi-Annual Report (DOE Contract No.: DE-FC26-01BC15361), Oct 2001-March 2002.

Table 1.2.1— Synthetic Brine Composition

Salts Content	Concentrations (mg/L)
NaCl	122,699
$CaCl_2.2H_2O$	7,497
Total Dissolved Solids	130,196

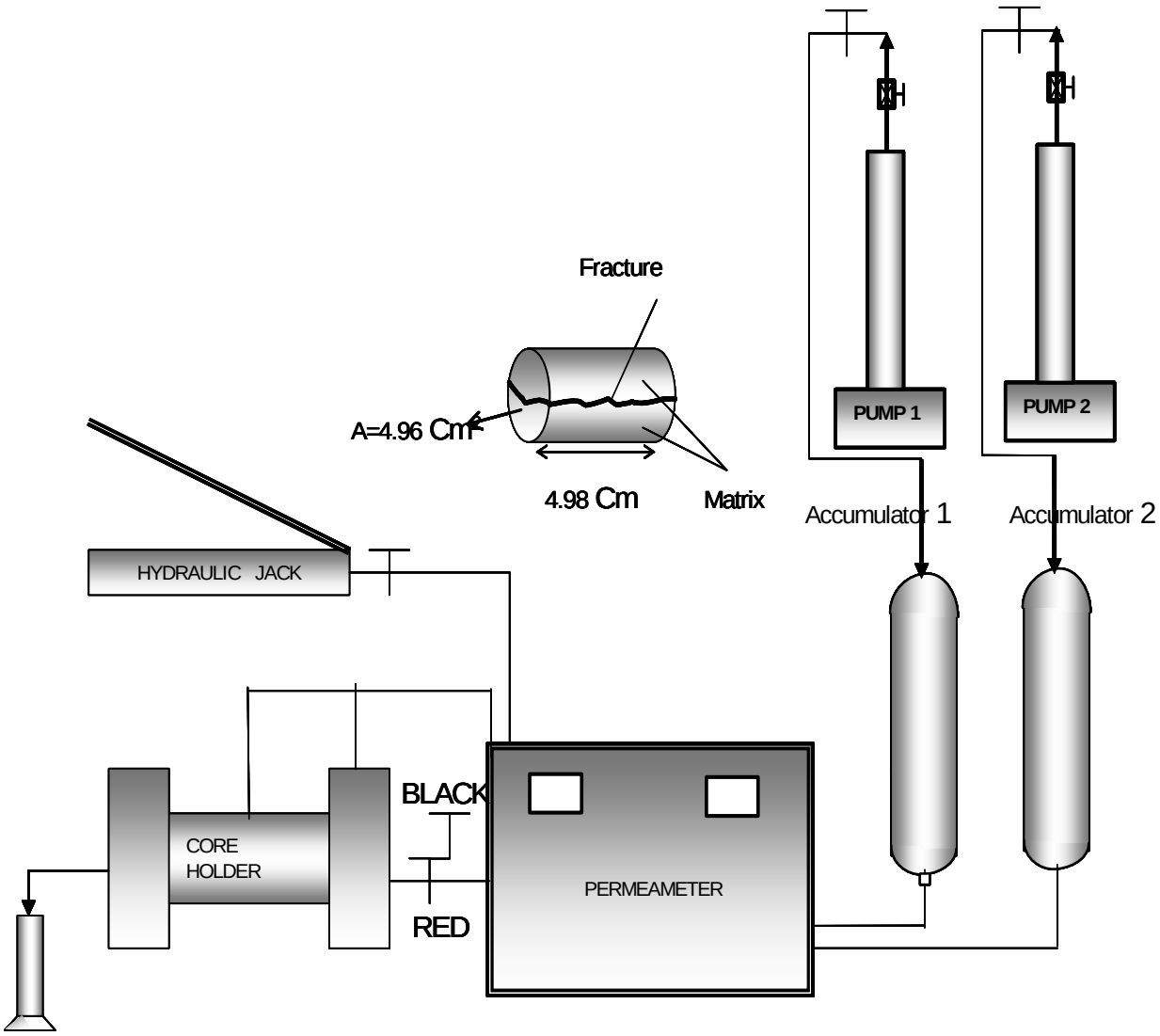

Fig. 1.2.1 — Hydrostatic loading apparatus.

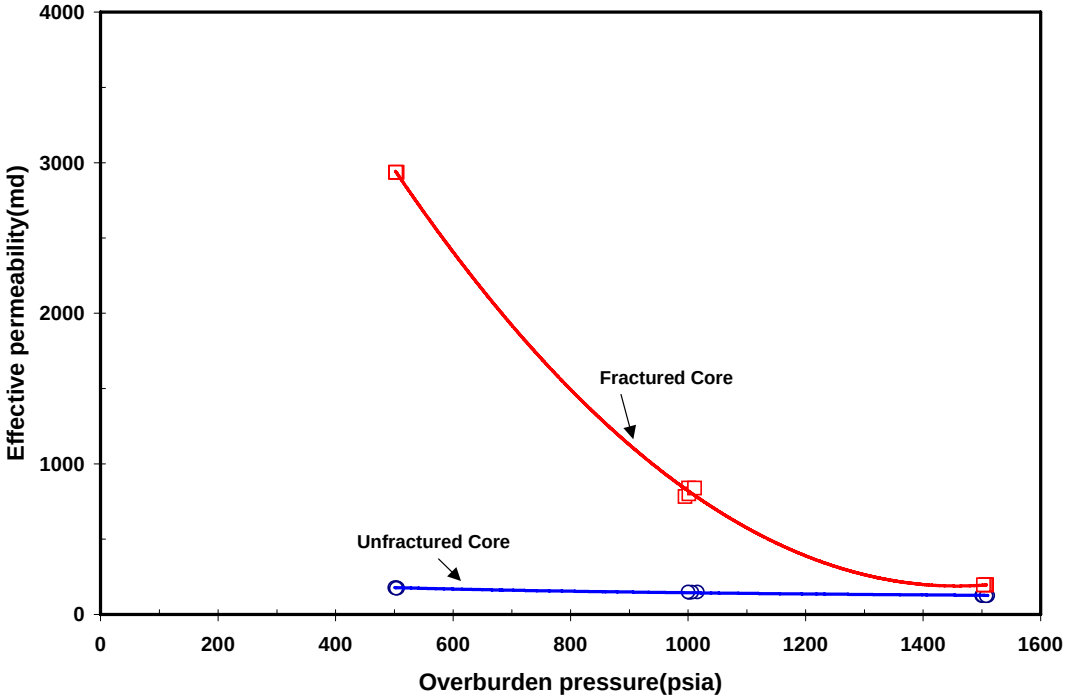

Fig. 1.2.2 — Permeability reduction due to hydrostatic stress.

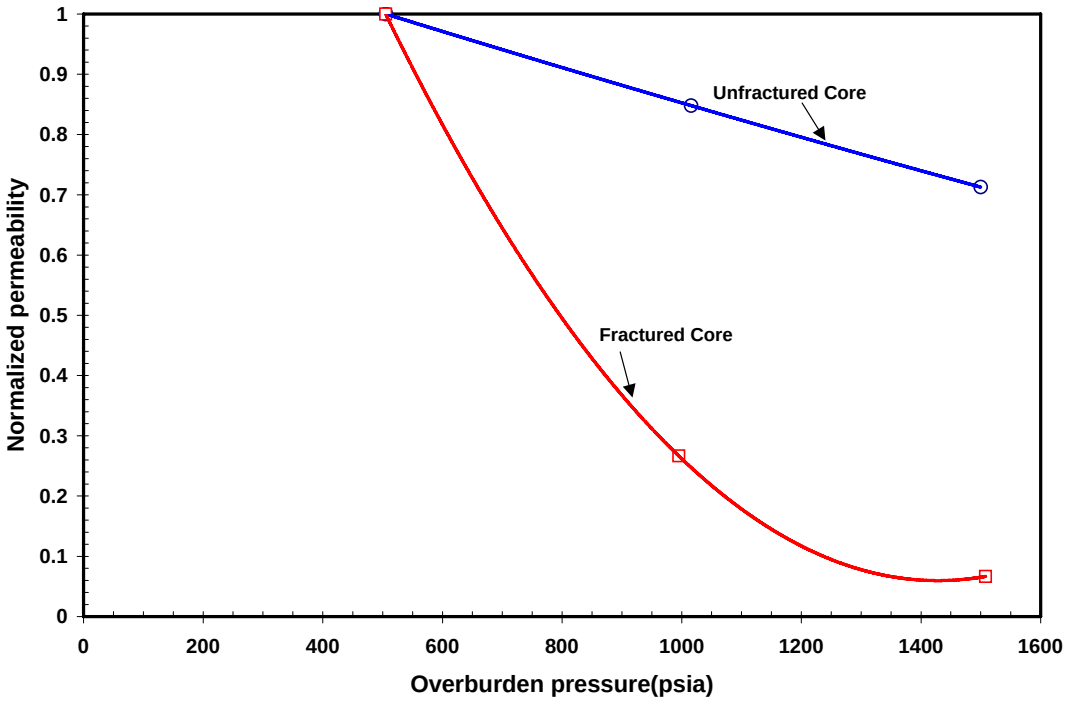

Fig. 1.2.3 — Normalization permeability reduction due to hydrostatic stress at injection 5 cm^3/min.

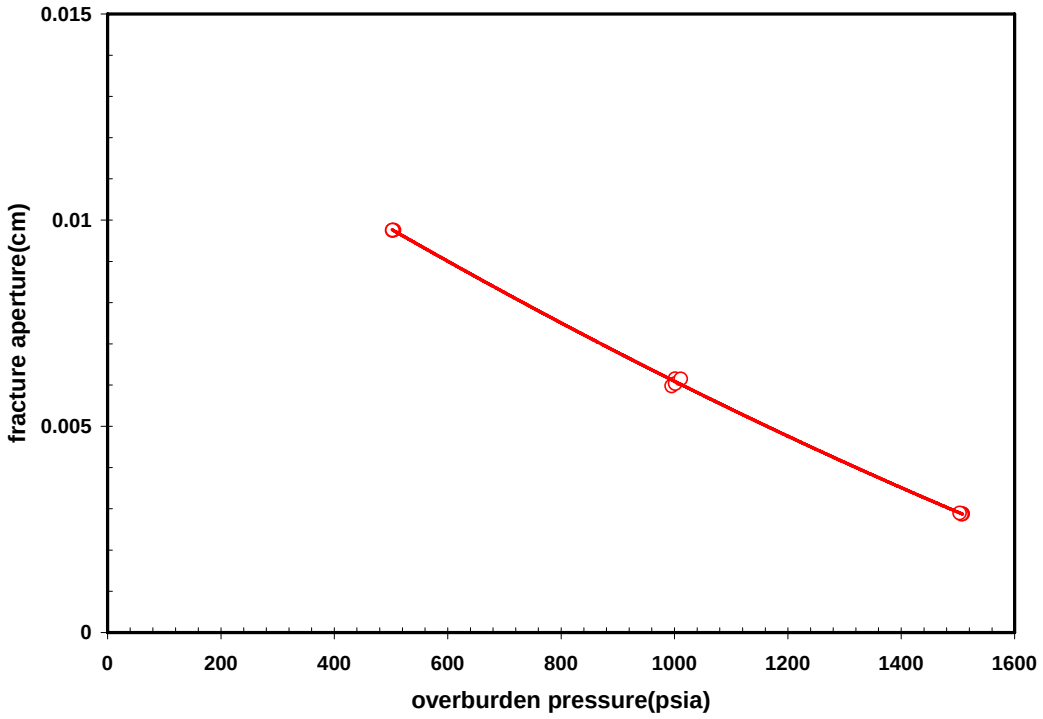

Fig. 1.2.4 — Fracture aperture reduction under hydrostatic stress.

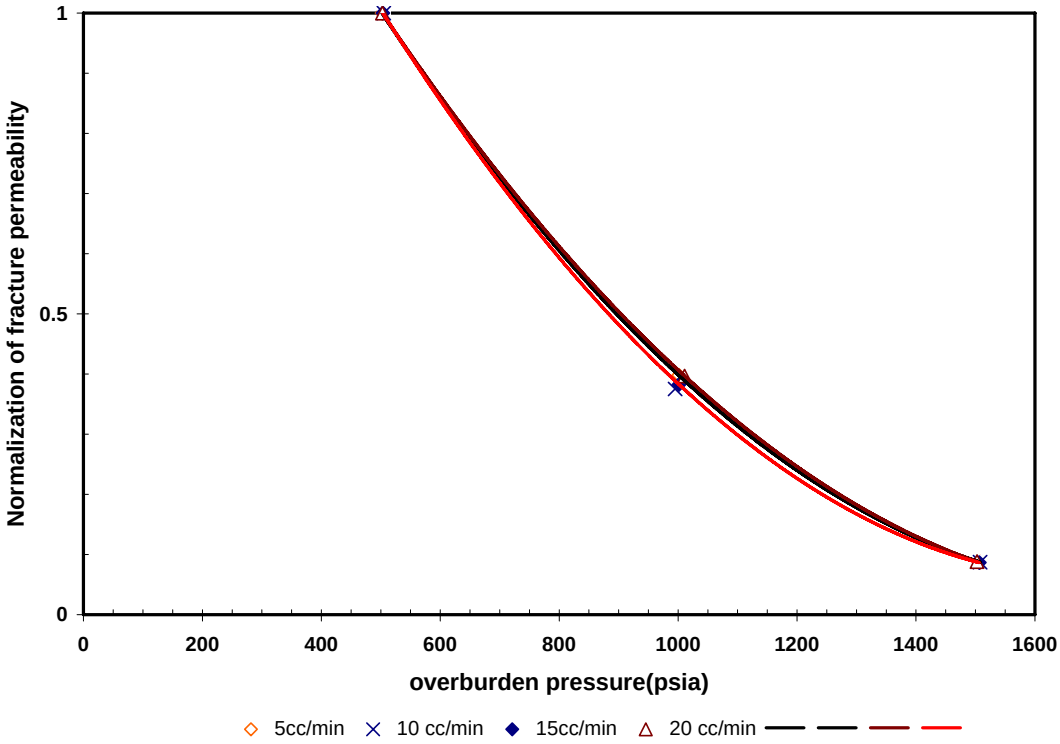

Fig. 1.2.5 — Fracture permeability reduction under hydrostatic stress at different injection rate.

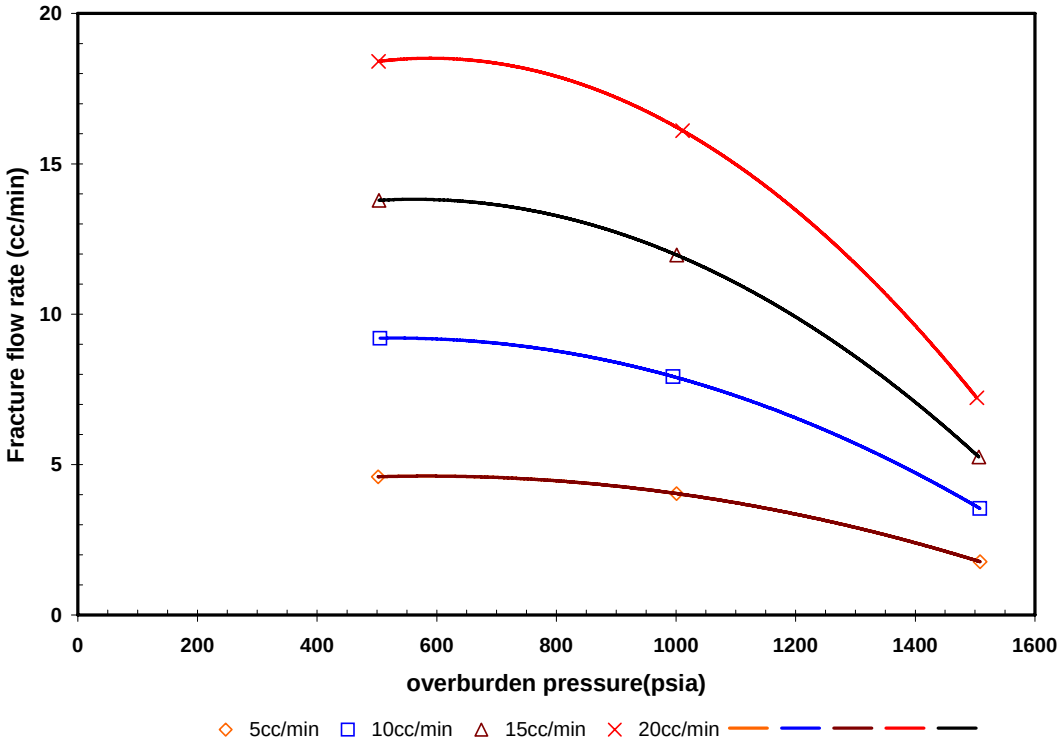

Fig. 1.2.6 — Effect of hydrostatic stress on fracture flow rate at different injection rate.

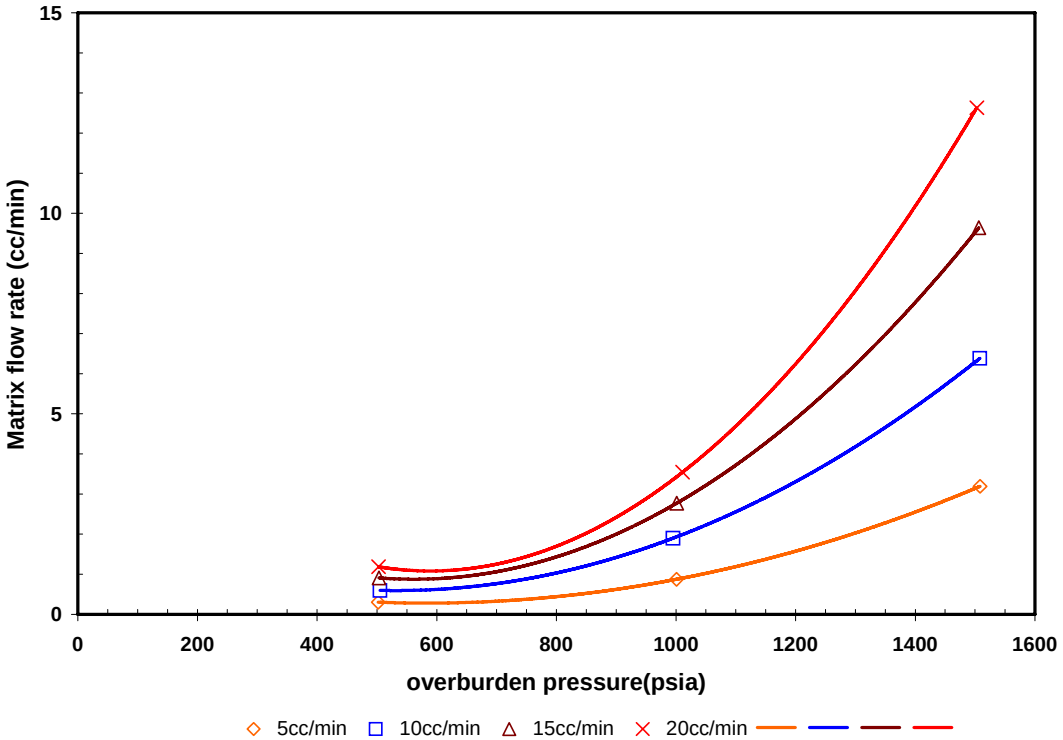

Fig. 1.2.7 — Effect of hydrostatic stress on matrix flow rate at different injection rate.

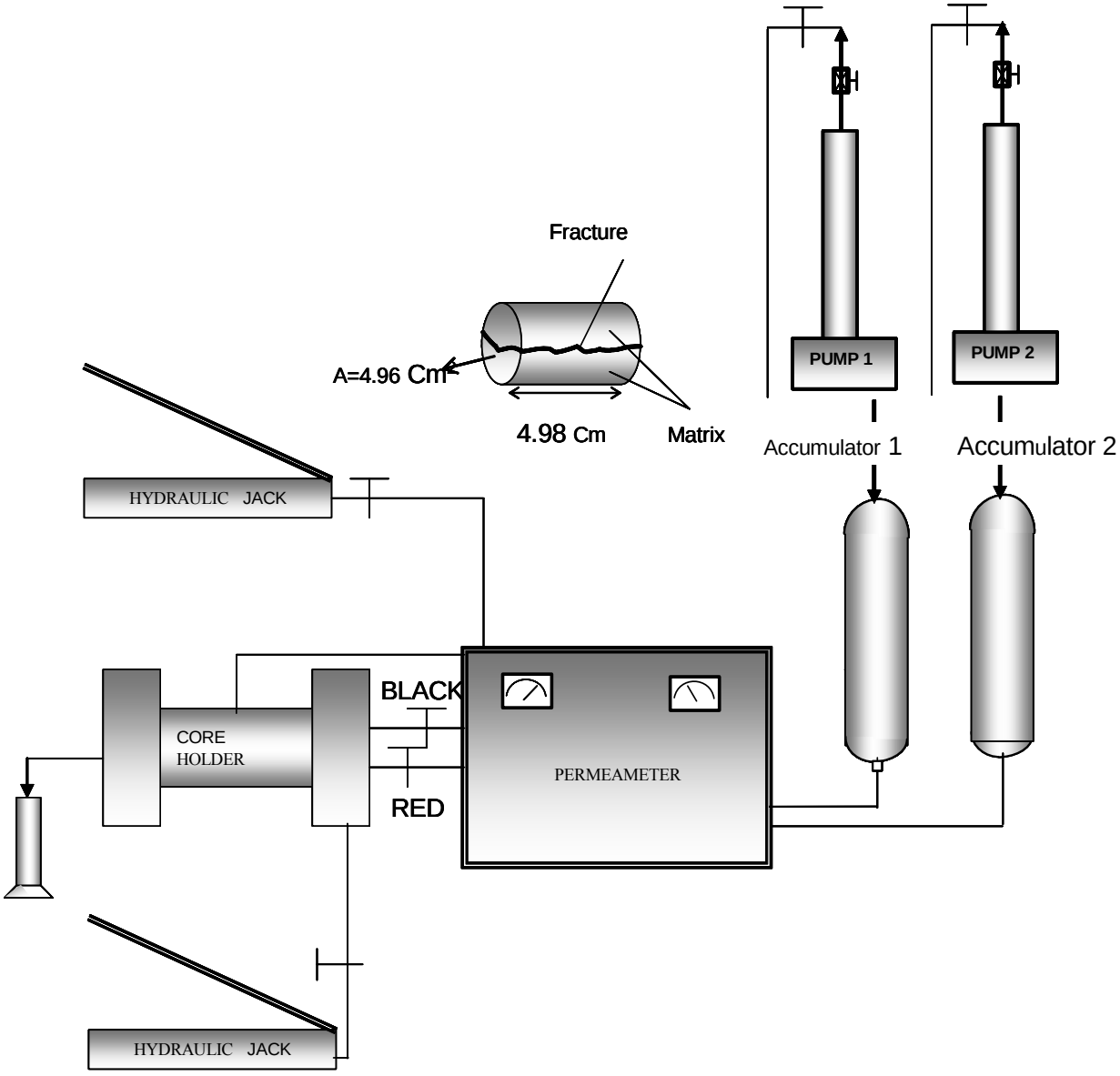

Fig. 1.2.8 — Triaxial stress experiment apparatus.

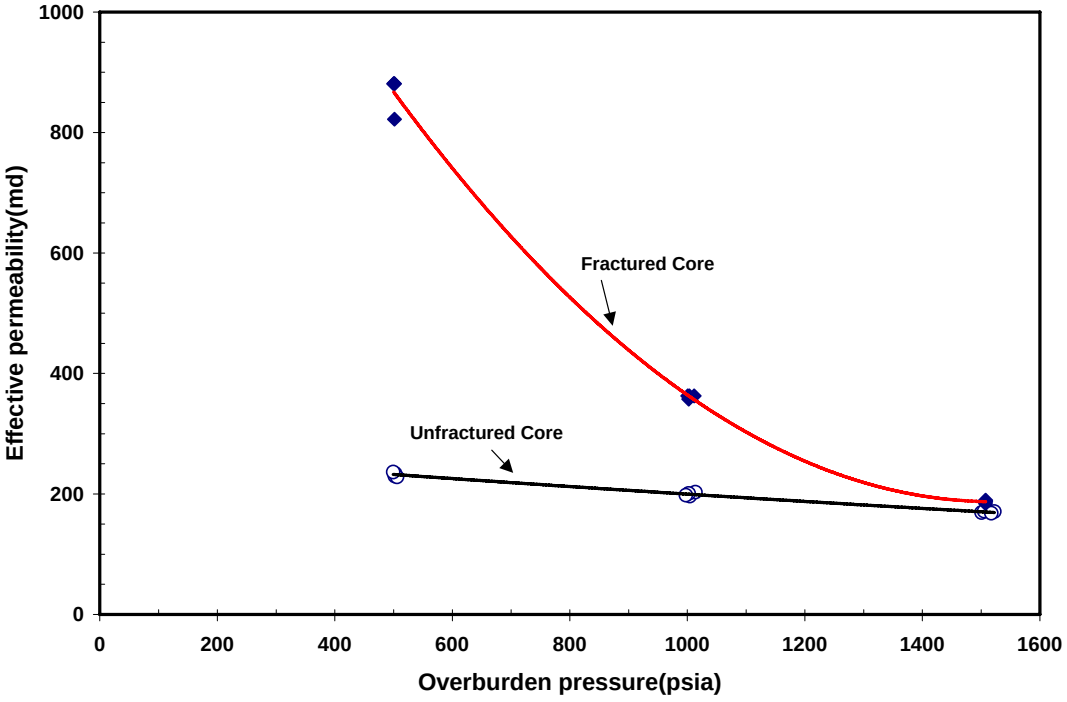

Fig. 1.2.9 — Permeability reduction under triaxial stress.

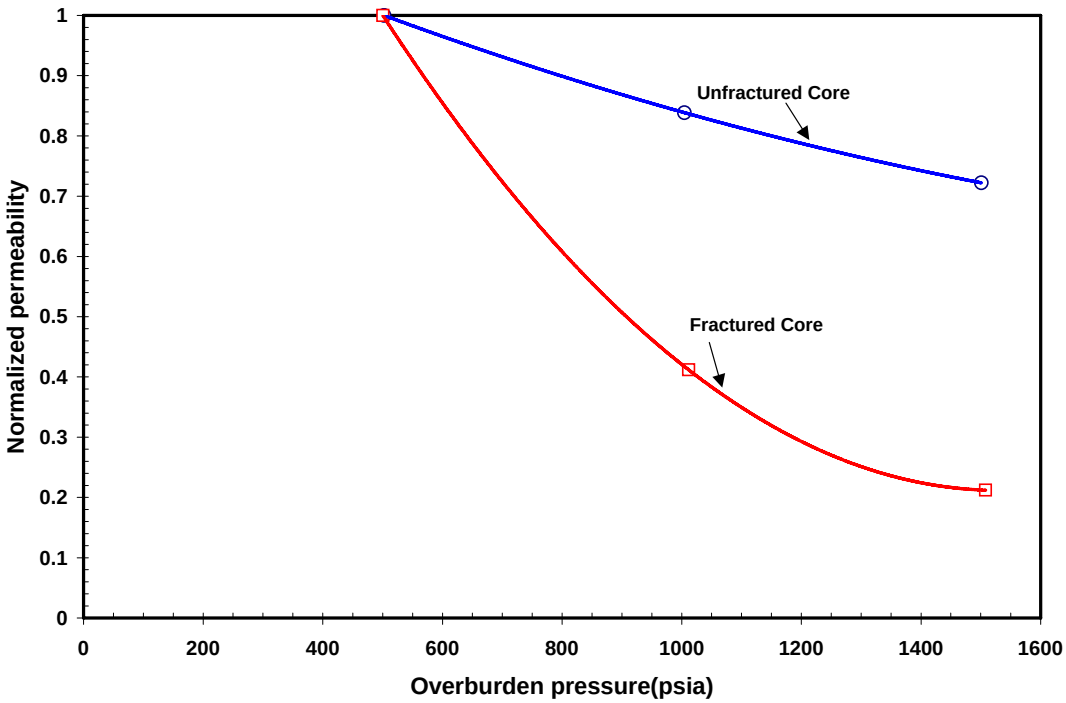

Fig. 1.2.10 — Normalization permeability reduction under triaxial stress.

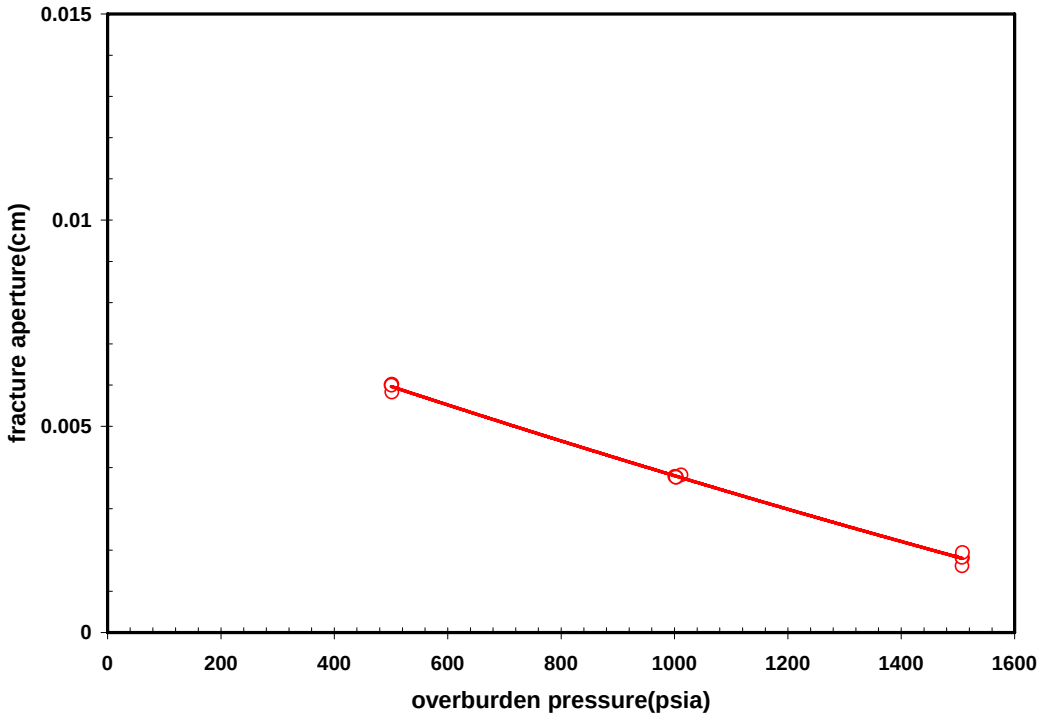

Fig. 1.2.11 — Fracture aperture reduction under triaxial stress.

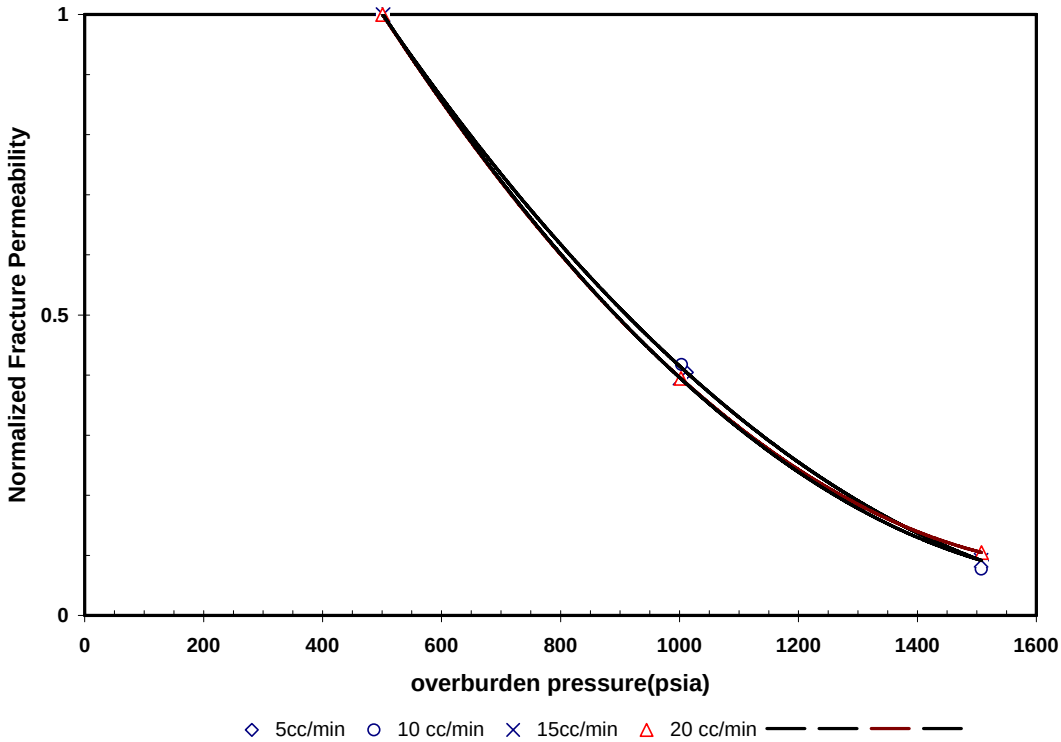

Fig. 1.2.12 — Normalized fracture permeability reduction under triaxial stress.

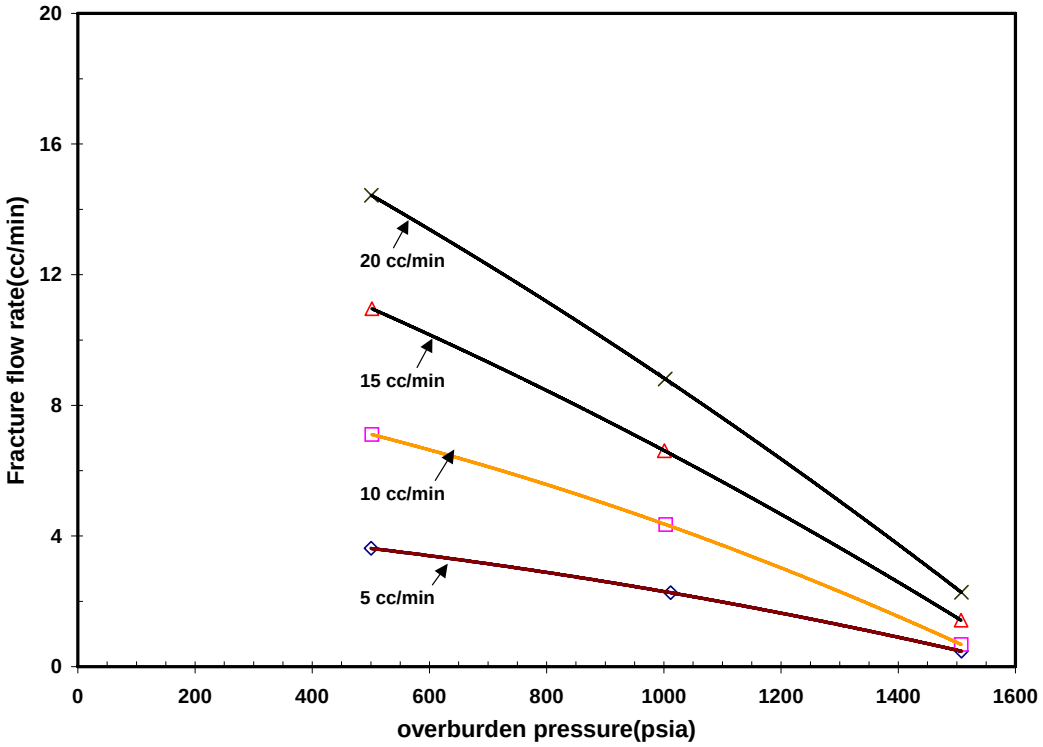

Fig. 1.2.13 — Effect of triaxial stress on fracture flow rate.

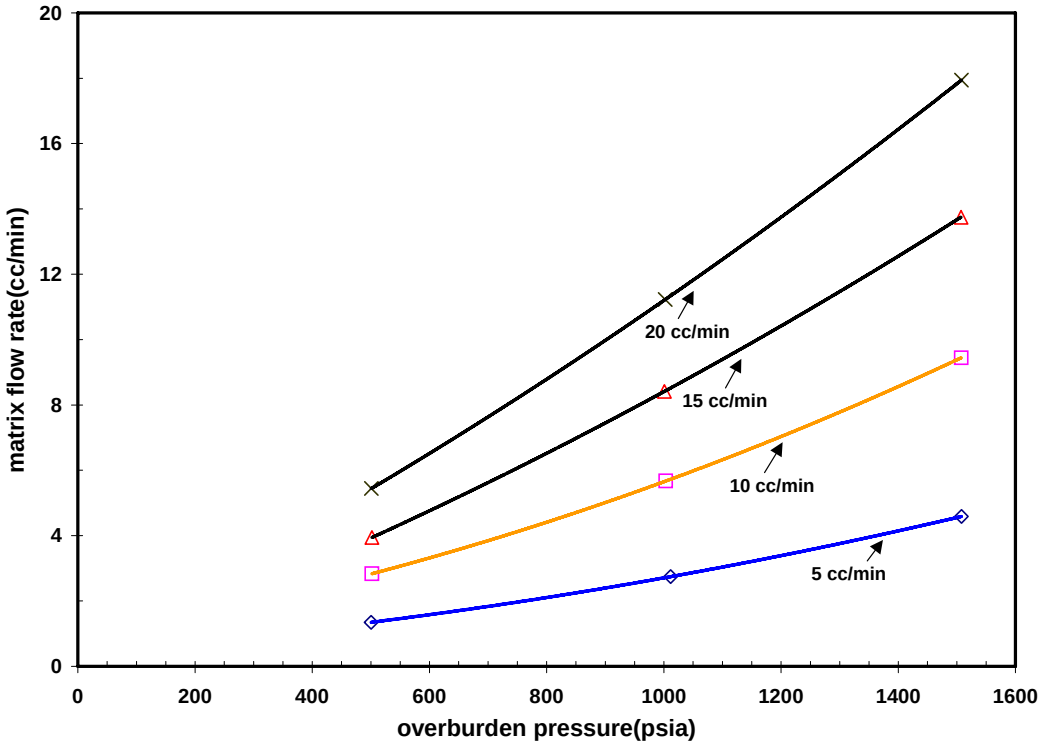

Fig. 1.2.14 — Effect of triaxial stress on matrix flow rate at different injection rates.

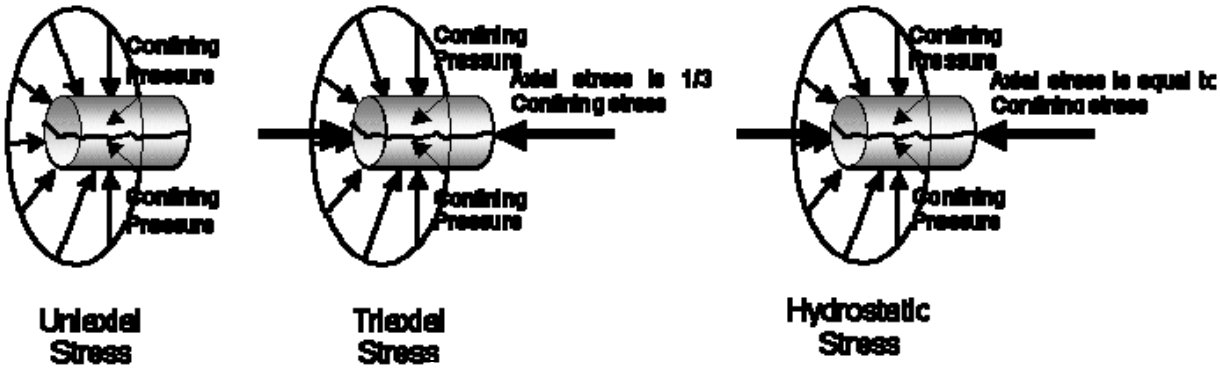

Fig. 1.2.15 — Illustration of uniaxial, triaxial, and hydrostatic stresses.

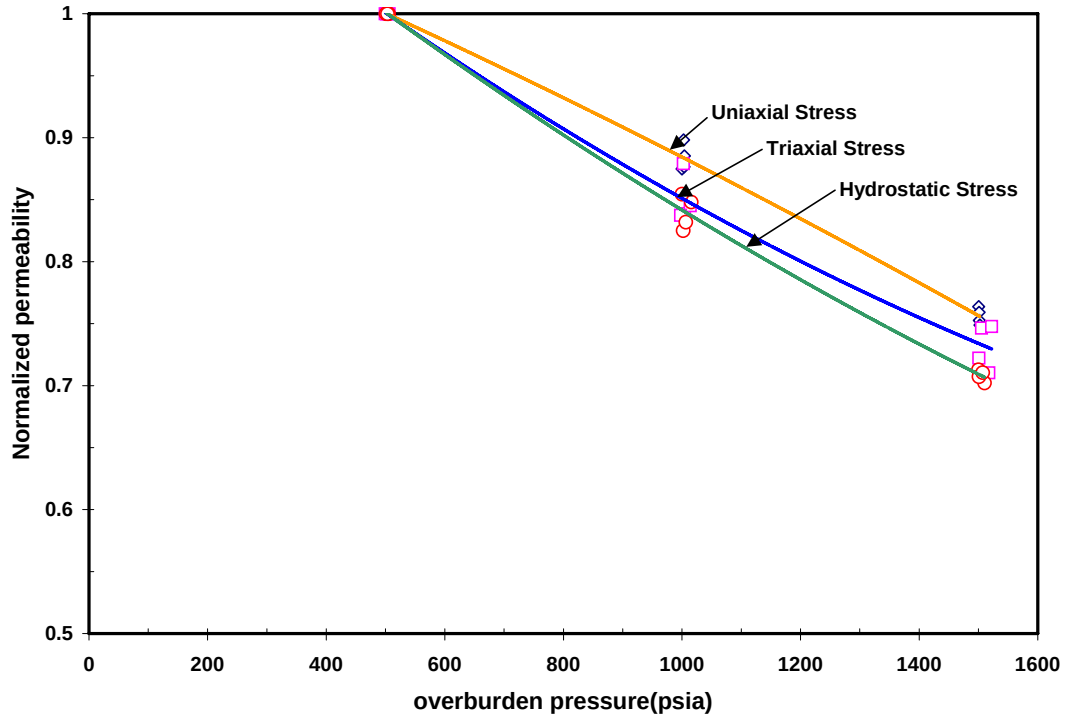

Fig. 1.2.16 — Comparison of matrix permeability reduction under different applied stresses.

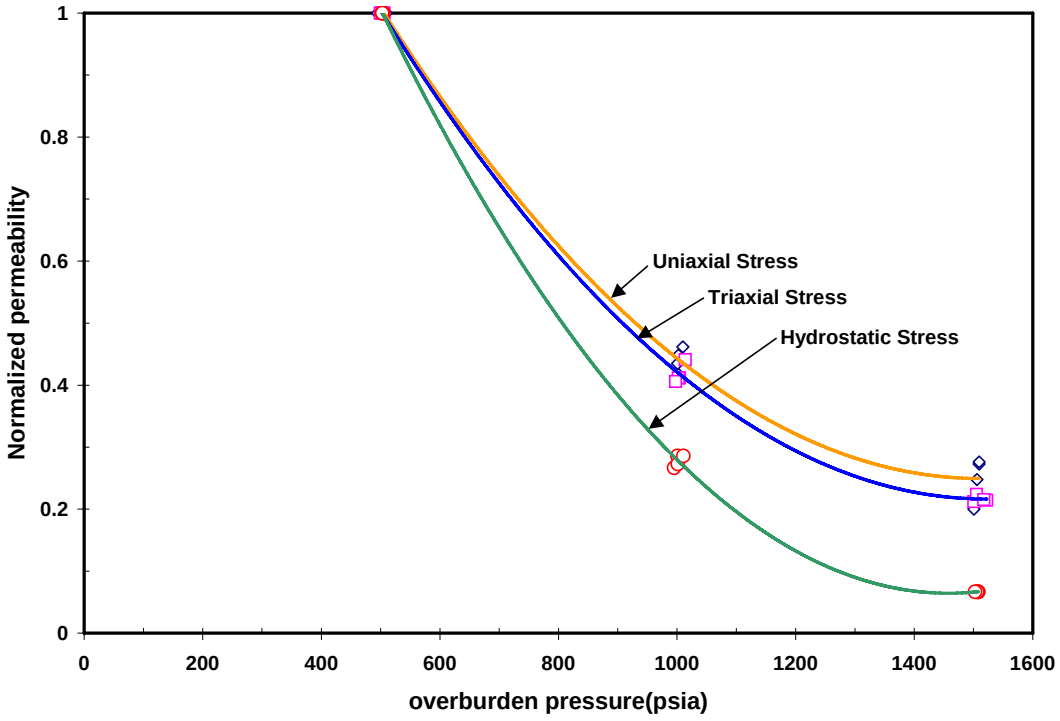

Fig. 1.2.17 — Comparison of effective permeability reduction under different applied stresses.

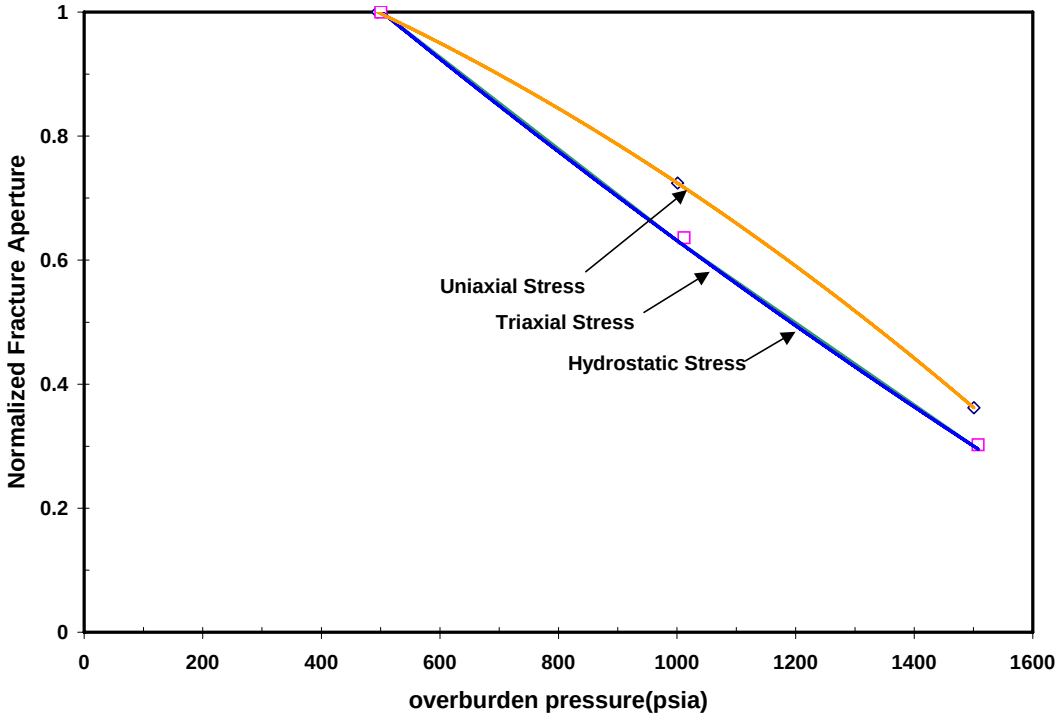

Fig. 1.2.18 — Comparison of fracture aperture reduction under different applied stresses at injection rate of 5 cm^3/min.

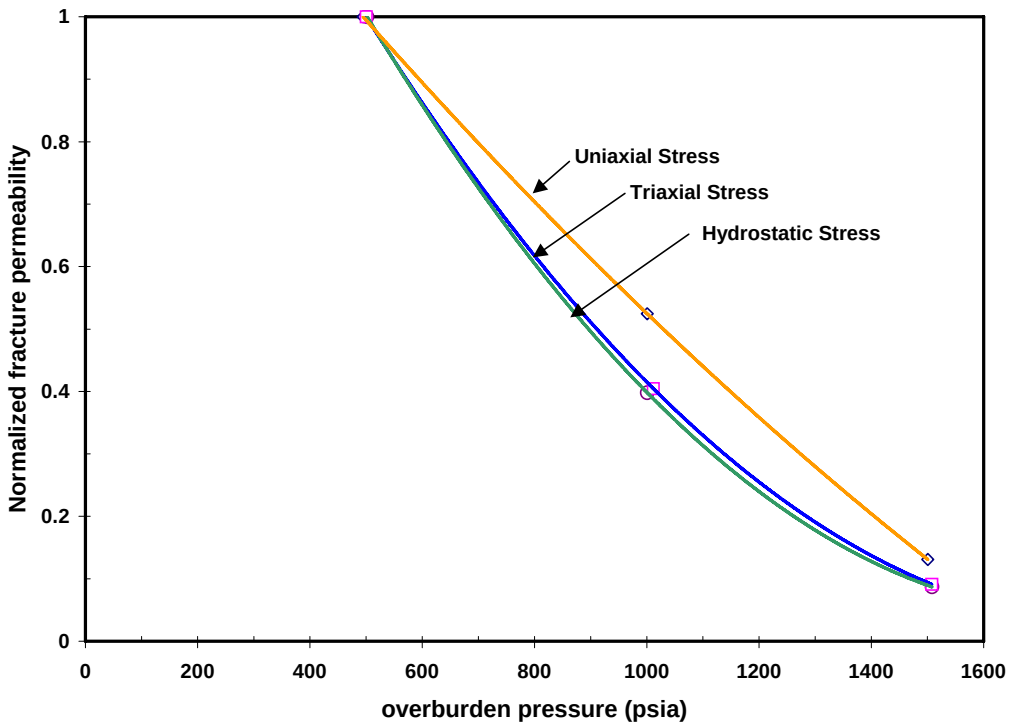

Fig. 1.2.19 — Comparison of fracture permeability reduction under different applied stresses at injection rate of 5 cm^3/min.

Chapter I-3

Investigating Fracture Aperture Distributions under Various Stress Conditions Using X-Ray CT Scanner

1.3.1 INTRODUCTION

Poor knowledge of the fluid flow through naturally fracture reservoirs has left millions of barrels of oil unrecovered. Early researchers[1,2] assumed the fracture model as a set of parallel plates separated by a constant fracture aperture, although mineralization causes the actual fracture surfaces to be very rough. Fluid flow in these tortuous paths tends to follow a preferred path. Pyrak *et al.*[3] (1985) injected molten metal into single fractures at different applied stress conditions. Upon opening the cooled metal in the fracture, they fluid flow in the tortuous paths will be through the larger apertures, which offer least resistance to flow. However, the effect of tortuosity becomes less when the distribution peaks sharply at large apertures with a long tail in the small apertures' which raises the question of whether fracture aperture distribution should follow a particular pattern.

When the parallel plate approach is no longer valid, Tsang and Witherspoon[5] accounted for the variation of apertures in a rough fracture. Later, Tsang[4] modeled the variation of fracture apertures by placing electrical resistors with different resistance values on a two-dimensional grid. The results indicated that small apertures play a key role in depressing fluid flow. When the fracture contact area increases, tortuosity and connectivity of fractures become important.

Field experimentation[6] has shown that flow in a single fracture takes place in a limited number of channels. Results from drilling five holes in the fracture plane and pressurizing each to atmospheric pressure showed that the channels occupied a total area of only about 10% of the fracture plane. Gentier[7] measured fracture surface roughness profiles in a granite fracture and found that the aperture density distribution was approximated by a gamma function given by

$$n(b) = \frac{1}{b_o^2} b \exp(-b/b_o), \quad \text{.....(1.3.1)}$$

where b_o represents the distribution peaks, and the mean aperture is $2b_o$. The same distribution was assumed when considering the channeling of flow through fractured media[8]. Assuming the channel width to be a constant of the same order as the correlation length λ, where correlation length is the spatial length within which the apertures have similar values, the reduction in channel apertures affected the tracer breakthrough curves when normal stress across a fracture increased.

Although gamma distribution has been considered, some authors[6,9] observed the log-normal distribution of fracture apertures from the experiments conducted on cores and well logs. Later Moreno *et al.*[10] followed the same approach when conducting flow and tracer transport models in a single fracture. Using the approach, the flow patterns showed strong resemblance to field observations reported by Bourke.[11] Tsang and Tsang[12] used the log-normal approach to distribute fracture apertures for obtaining the relationship between flow and transport measurements of variable apertures. The frequency of the log-normal distribution is written as follows[13]:

$$f(x) = \frac{1}{x\sqrt{2\pi\beta^2}} \exp\left[\frac{-(\ln x - \alpha)^2}{2\beta^2}\right] \quad \text{.....(1.3.2)}$$

where

$$\beta^2 = \ln\left(1 + \frac{\sigma^2}{\mu^2}\right) \quad \text{.....(1.3.3)}$$

and

$$\alpha = \ln \mu - \frac{\beta^2}{2} \quad \text{.....(1.3.4)}$$

They determined the mean aperture from fluid flow measurements and distributed the aperture using log-normal distribution. The aperture variance was determined from tracer breakthrough. When mercury was injected into the fractures, an isolated patch in the larger aperture region occurred and spatial correlation length became small, which suggests that opportunity for occurrence of isolated patches is more. Alfred *et al.*[13] also assumed log-normal distribution for the fracture apertures upon considering fracture roughness. The parallel plate model could not adequately represent the fluid flow

portrayed from laboratory experiments. Using fracture aperture distribution, they obtained a better match for fluid flow through matrix and fracture system as well as pressure drop at different overburden pressures. They also concluded that beyond a particular value of the mean aperture, the effects of roughness and tortuosity is insignificant.

Keller[14] imaged the fracture apertures using a CT scanner and found that most of the apertures are in the range of 300 to 500 microns with the exception of some aperture value as high as 4,500 microns. Based on the study using three different cores, he concluded that the log-normal distribution is adequate in characterizing the fracture aperture. The smaller aperture regions are confirmed best with the log-normal distribution.

Fracture properties are affected by change in stress conditions; therefore, the effect of stress acting on the reservoirs should be considered in obtaining the fracture aperture distributions. Even though extensive research has been carried out to determine the fracture aperture distributions, the effect of different stresses has not yet been considered. Stress will change aperture size and fracture aperture distribution. Thus, we measured fracture aperture physically under different stress conditions using a CT scanner. The calibration technique was conducted with several known size of feeler gauges to correlate the CT domain into actual domain since, the CT scanner cannot provide direct measurement of fracture aperture. Once the calibration curve was obtained, we measured fracture aperture distributions from a fractured core under different overburden pressures and examined probability distributions of fracture aperture to obtain the mean and variance aperture values. Using those values, we plotted the probability distributions of density function to determine the distribution of fracture aperture at each overburden pressure.

1.3.2 CALIBRATION TECHNIQUE

Research in the field of fractures has been improved with the advent of CT scanning in the petroleum field [14,16]; our is a Picker fourth-generation CT scanner. We used typical power, voltage, and algorithm requirements for a sandstone sample. The CT scanner identifies the density differences between various objects.[15] Since the density of fluid is

less than the density of rock, material filling the fracture with fluid clearly demonstrates the difference in density in fracture and matrix. Although a clear visualization of fracture and matrix can be possible, CT numbers do not represent any aperture size of the fracture as they are mere functions of densities. To obtain the fracture aperture measurement, a calibration technique has to be used to correlate the CT numbers with the actual aperture size. The calibration integrates the CT signal by summing up the differences between a minimum rock CT number and the CT numbers pertaining to the fracture. Keller[17,18] used nonintrusive imaging to obtain aperture curves for granite and sandstone, obtaining fracture apertures as small as 35 μm. We developed our calibration procedure from this existing technique.

The experimental setup consists of two halves of the same rock sample (a Berea core), feeler gauges, and core-holding equipment. The two halves were polished thoroughly to reduce surface roughness as much as possible. Smooth surfaces ensure a proper match between the halves, so that smaller fractures can be measured. Feeler gauges ranging from 38 μm to 813 μm were then placed between the two flat surfaces to create a certain fracture widths (Fig. 1.3.1).

The core sample with fracture was inserted into a sleeve to avoid artifact effects and held in the core holder. A pressure of 500 psi was applied using a hydraulic jack. Multiple scans were then taken along the length of the core, perpendicular to the longitudinal axis. Fig. 1.3.2A shows a typical set of scans for the Berea sample with 38 μm fracture size. The color variations shows variable densities in the sample, with the relatively high density steel feeler gauge set to a bright pink color, the less dense rock material set to a bright orange color and the lower densities set to green, blue, and black in decreasing order of densities. The first scan in Fig. 1.3.2A is taken through the steel feeler gauge placed on one end of core sample, so the color appears brighter in the middle of the core. Both ends of the core sample have one feeler gauge, and scans were taken starting from one feeler gauge to the start of the next feeler gauge at intervals of 5 mm. The next three scans show a fracture aperture of 38 μm along the length of the core. The CT number of the matrix core ranges from 1,400 to 1,440 (Fig. 1.3.3). The CT number variation of the core material reflects its heterogeneity; however, the difference is not appreciable since Berea is not a highly heterogeneous rock. The dip in CT numbers in the

middle indicates the location of the fracture region. The CT number in the fracture is close to 1,230. This clearly distinguishes the fracture from the matrix. Although we can clearly identify the fracture and measure the CT number, the measurement does not directly provide fracture aperture value. However, since the dip of CT number in Fig. 1.3.3 corresponds to the 38 μm fracture aperture, the fracture aperture can be obtained by integrating the value of CT number. The dip is not abrupt, but rather a smooth transition from matrix to fracture, caused by finite beam width and oversampling.

"Oversampling" refers to the unexpected difference between the CT number of a fracture and that of air; the presence of rock around the fracture causes the higher value. Fig. 1.3.2B shows the fracture aperture size of 51 μm, along the length of the core. As the increment in fracture aperture size is small, there is no appreciable difference between Figs. 1.3.2A and 1.3.2B. Sample scans for aperture sizes of 64 μm, 76 μm, and 102 μm are shown in Figs. 1.3.2C to 1.3.2E. As the aperture size increases, the CT number increases and the fracture aperture can be seen clearly in the middle of the core, with darker color. Fig. 1.3.4 compares the average CT number curves obtained for various fracture sizes. As the aperture size increases, the dip increases and the size of the dip widens.

1.3.2 CALIBRATION CURVE

We plotted CT number versus pixel number from the CT numbers from each scan and developed an average CT number plot to account for minor variations in fracture sizes caused by surface roughness. An example of such plot is shown in Fig. 1.3.5. From this plot, we identified a threshold CT number, which essentially is the minimum rock CT number. All the CT numbers in the area below the minimum rock CT number are subtracted from the rock CT number and the differences are used to obtain the integrated CT signal for the fracture size. The integrated CT signals are calculated for each pixel number and are given an index starting from 1 to *n* as shown in Fig. 1.3.5. The area of integrated CT region is calculated from the following formula:

For index *i* equal to 1 to *c*,

$$Area\ (i) = IntCT\ (i-1) + \frac{1}{2}[IntCT\ (i) - IntCT\ (i-1)] \quad \text{.. .....} \quad (1.3.5)$$

For index i equal to c+1 to n,

$$Area\ (i) = IntCT\ (i) + \frac{1}{2}[IntCT\ (i-1) - IntCT\ (i)] \quad \text{.....(1.3.6)}$$

After measuring nine different feeler gauges, we obtained a calibration curve for fracture aperture (Fig. 1.3.6). The graph shows a linear relationship between the integrated CT signal and fracture aperture. The linear relationship still holds, even for smaller fracture aperture. The equation obtained from this calibration curve is,

$$y = 8.7616x + 460.7 \quad \text{.....(1.3.7)}$$

By rearranging the equation we can calculate fracture aperture, if the integrated CT signal is known, as follows:

$$x = 0.1141y - 52.582 \quad \text{.....(1.3.8)}$$

Given this calibration curve, fracture aperture from any fracture samples can be measured by extrapolating the integrated CT signal obtained from the CT scanner.

1.3.3 FRACTURE APERTURE DISTRIBUTION

For this specific experiment we used a 1-inch diameter by 2.36-inch length of Berea core. The core was fractured mechanically in the laboratory using a hydraulic cutter. The artificially fractured core was then imaged in the CT scanner. Images were taken at every 1 mm along the length of the core. The core was then subjected to overburden pressure of 500 psi and again scanned at the same locations. This procedure was repeated for overburden pressures of 1,000 psi and 1,500 psi. Fig. 1.3.7 shows the images taken with and without overburden pressures; about 6,000 data points were taken for each overburden condition. The resulting CT numbers from the images were then converted to the aperture values using the calibration curve as discussed in the previous section.

The fracture aperture dataset was plotted in the probability chart for each stress condition as shown in Figs. 8 to 11. Table 1.3.1 shows the range and frequencies of the apertures with and without overburden pressure. The mean, variance, and standard deviation for each dataset are given in Table 1.3.2. The result of a comparative study for different overburden pressures is plotted in Fig. 1.3.12.

1.3.4 DISCUSSION

The apertures are distributed in the range of 0 to 2,000 microns, with probable apertures in the range of 100 to 500 microns, as shown in Fig. 1.3.12. The tail of the aperture distribution is long and the aperture distribution is right skewed, which suggests that the distribution might follow either gamma or log-normal distribution as given in the earlier studies.[7,8,14] The tail of the aperture controls the fluid flow as fluid will tend to flow through preferred channels of least resistance.[13] Since most apertures fall in the range of 100 to 500 microns, the permeability measurements will be largely controlled by small apertures. The presence of some large apertures in the range of 600 to 2,000 microns may provide the main path for the fluid flow if they are interconnected. The calculation of flow rate based on this measured permeability will be different from the calculation using the single mean permeability as assumed by parallel plate approach which assumed the fracture is separated by two smooth, parallel plates at constant width.

Using mean and variance aperture values obtained from the probability distribution plot for each overburden pressure, the distributions of probability density function can be obtained by applying Eq. 1.2.2. The distribution plots are presented in Fig. 1.3.13. By comparing the actual dataset to the calculated distribution obtained from Eq. 1.3.2., we found that the distributions of probability density function follow log-normal distribution at all conditions.

Without overburden pressure, the probability density function that follows log-normal distribution has mean aperture value of 370.53 microns and variance of 44,847 (Fig. 1.3.13). This log-normal distribution confirms the previous findings.[4,8,10,12-14,16] The most probable aperture value calculated from log-normal distribution is 326.783 microns. This value is less than the mean aperture value because of the large variance of the aperture values.

As overburden pressure increases, the mean and variance apertures decrease, suggesting that permeability decreases under increased overburden pressures. The mean apertures dramatically decreased from 370.53 microns to 197.997 microns when an initial overburden pressure of 500 pasi was applied (Table 1.3.2).

The fracture surfaces are rough and have many contact points along the path. If the apertures sizes are larger, the contact points become weak and tend to break down under

overburden stress. The decrease in aperture sizes is not significant with further increase in overburden pressures. Since each reservoir experiences different overburden pressures, this research will be important to identify some of the uncertainties in predicting fluid flow through fractured reservoirs.

1.3.5 CONCLUSIONS

1. The result of this study confirms that fracture aperture distribution follows log-normal distribution under no overburden pressure.
2. Under overburden pressure, the distribution still follows the common log-normal distribution with longer tail and more right skewed aperture distribution.
3. As the overburden pressure increases, the fracture aperture decreases as indicated by reduction of mean and variance aperture distribution.

NOMENCLATURE

$Area(i)$ = area of section i

b_o = distribution peak

b = aperture size

c = index of lower CT number

$f(x)$ = frequency of apertures

$IntCT(i)$ = integrated CT area for section i

n = index of higher CT number

$n(b)$ = probability density distribution

x = fracture aperture

y = total integrated CT signal

α = log-normal mean

β = log-normal standard deviation

μ = mean of the aperture sizes

σ = standard deviation

REFERENCES

1. Snow, D. T., Anisotropic Permeability of Fractured Media; *Water Resources Research, 5(6), 1273-1289, 1969.*
2. Wilson, C. R., An Investigation of Laminar Flow in Fractured Porous Rocks; *Ph.D. thesis, Univ. of California, Berkeley, 1970.*
3. Pyrak, L. R., Myer, L. R., and Cook, N. G. W., Determination of Fracture Void Geometry and Contact Area at Different Effective Stress; *Eos Trans. AGU (abstract), 66(46), 903, 1985.*
4. Tsang, Y. W., The Effect of Tortuosity on Fluid Flow Through a Single Fracture; *Water Resources Research, 20(9), 1209-1215, 1984.*
5. Tsang, Y. W., and Witherspoon, P. A., The Dependence of Fracture Mechanical and Fluid Properties on Fracture Roughness and Sample Size; *J. Geophys. Res., 88(B3), 2359-2366, 1983.*
6. Bourke, P. J., Dunance, E. M., Heath, M. J., and Hodgkinson, D. D., Fracture Hydrology Relevant to Radionuclide Transport; *AERE Rep. 11414, Atomic Energy Res. Estab., Harwell, United Kingdom, 1985.*
7. Gentier, S., Morphologie et comportement hydromécanique d'une fracture naturelle dans un granite sous contrainte normale; *doctoral thesis, Univ. d'Orléans, France, 1986.*
8. Tsang, Y. W. and Tsang, C. F., Channel Model of Flow through Fractured Media; *Water Resources Research, 23(3), 467-479, 1987.*
9. Bianchi, L., and Snow, D., Permeability Crystalline Rock Interpretated from Measured Orientations and Apertures of Fractures*; Annu. Arid Zone, 8(2), 231-245, 1968.*
10. Moreno, L., Tsang, Y. W., Tsang, C. F., Hale, F. V., and Neretnieks, I., Flow and Tracer Transport in a Single Fracture: A Stochastic Model and Its Relation to Some Field Observations; *Water Resources Research, 24(12), 2033-2048, 1988.*
11. Bourke, P. J., Channeling of Flow through Fractures in Rock; *in Proceedings of GEOVAL-87 International Symposium, Swed. Nucl. Power Inspectorate, Stockholm, Sweden, 1987.*

12. Tsang, Y. W. and Tsang, C. F., Hydrological Characterization of Variable-Aperture Fractures; *Rock Joints, Barton & Stephansson (eds), Balkema, Rotterdam, 1990.*

13. Alfred, D., Putra, E., and Schechter, D.S., Modeling Fluid Flow through Single Fractures Using Experimental, Stochastic and Simulation Approaches; paper SPE/DOE 89442 will be presented at 2004 Improved Oil Recovery Symposium, OK, Tulsa, 17–21April.

14. Keller, A. A., Single and multiphase flow and transport in fractured porous media; *PhD thesis, Stanford University (1996).*

15. Wellington, S. L. and Vinegar, H. J., CT Studies of Surfactant- Induced CO2 Mobility Control; *paper SPE 14393 presented at the 1985 SPE Annual Technical Conference and Exhibition, Las Vegas, September 22-25.*

16. Johns, R. A., Steude, J. D., Castanier, L. M., and Roberts, P. V., Non-destructive Measurements of Fracture Aperture in a Crystalline Rock Using X-ray Computed Tomography; *J. Geophysical Research (1993), 98, 1899-1900.*

17. Keller, A.A., High Resolution CAT Imaging of Fractures in Consolidated Materials; *Int. J. Rock Mech. Min. Sci. (1997), 34 (3/4), 358-375.*

18. He, M., Application of X-ray Tomography to Measurement of Fractures in Rocks; *M.S. Thesis, Stanford University (1998).*

TABLE 1.3.1 — Data Range and Frequency for Various Overburden Pressure Conditions.

Range	Count	Range	Count	Range	Count	Range	Count
0 - 100	68	0 - 100	1508	0 - 100	2558	0 - 100	2892
100 - 200	353	100 - 200	2393	100 - 200	1999	100 - 200	1890
200 - 300	2139	200 - 300	1287	200 - 300	812	200 - 300	684
300 - 400	2119	300 - 400	368	300 - 400	261	300 - 400	193
400 - 500	832	400 - 500	176	400 - 500	125	400 - 500	109
500 - 600	226	500 - 600	102	500 - 600	85	500 - 600	84
600 - 700	134	600 - 700	79	600 - 700	56	600 - 700	63
700 - 800	85	700 - 800	38	700 - 800	59	700 - 800	36
800 - 900	61	800 - 900	43	800 - 900	54	800 - 900	38
900 - 1000	34	900 - 1000	25	900 - 1000	29	900 - 1000	16
1000 - 1100	27	1000 - 1100	33	1000 - 1100	8	1000 - 1100	4
1100 - 1200	22	1100 - 1200	15	1100 - 1200	1	1100 - 1200	0
1200 - 1300	25	1200 - 1300	4	1200 - 1300	0	1200 - 1300	1
1300 - 1400	19	1300 - 1400	3	1300 - 1400	0	1300 - 1400	0
1400 - 1500	13	1400 - 1500	0	1400 - 1500	0	1400 - 1500	0
1500 - 1600	16	1500 - 1600	0	1500 - 1600	0	1500 - 1600	0
1600 - 1700	7	1600 - 1700	0	1600 - 1700	0	1600 - 1700	0
1700 - 1800	6	1700 - 1800	0	1700 - 1800	0	1700 - 1800	0
1800 - 1900	14	1800 - 1900	0	1800 - 1900	0	1800 - 1900	0
1900 - 2000	5	1900 - 2000	0	1900 - 2000	0	1900 - 2000	0
2000 - 2100	0	2000 - 2100	0	2000 - 2100	0	2000 - 2100	0
2100 - 2200	1	2100 - 2200	0	2100 - 2200	0	2100 - 2200	0

TABLE 1.3.2 — Statistical Parameters for Different Overburden Conditions.

		Overburden Pressure		
	0 psi	**500 psi**	**1000 psi**	**1500 psi**
Mean	370.53	197.99	157.42	138.66
Variance	44847.63	29781.35	26372.15	22599.1
Std deviation	211.77	172.57	162.39	150.33

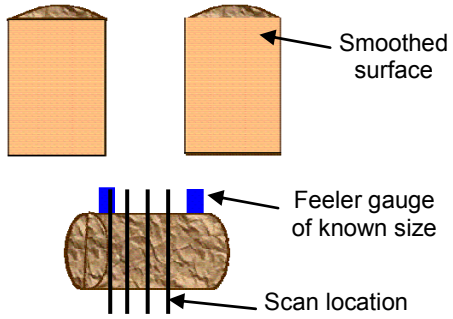

FIGURE 1.3.1 — Experimental procedure showing feeler gauges and scan locations.

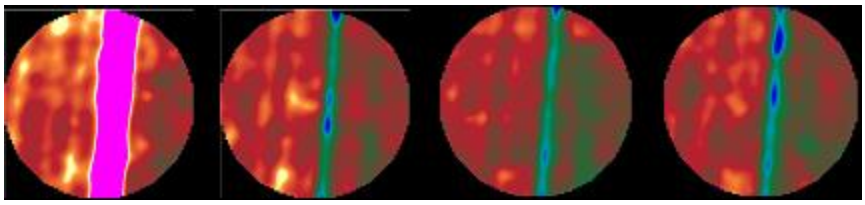

A. 38 µm feeler gauge

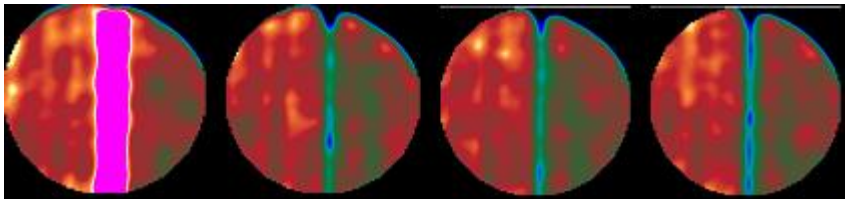

B. 51 µm feeler gauge

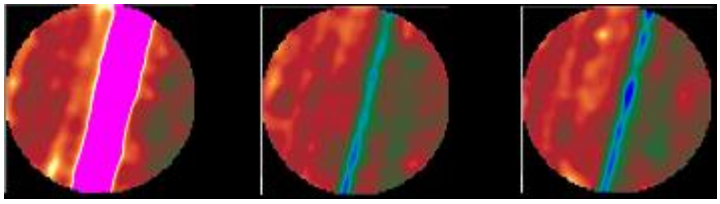

C. 64 µm feeler gauge

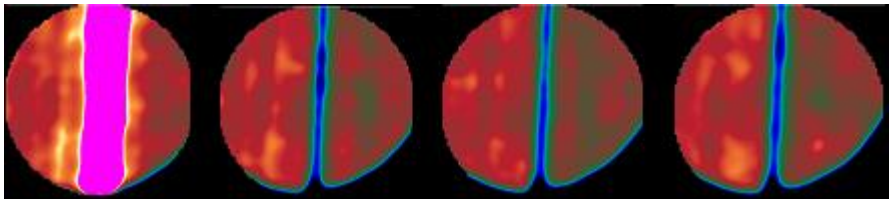

D. 76 µm feeler gauge

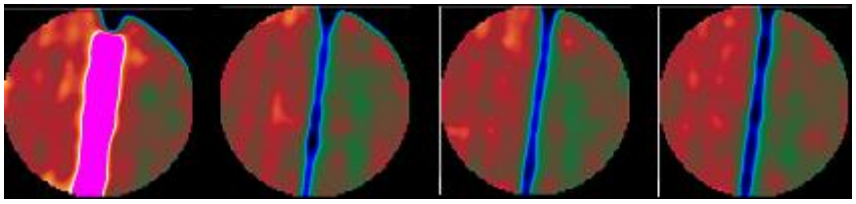

E. 102 µm feeler gauge

FIGURE 1.3.2 — Scans taken along the length of the core for various feeler gauges.

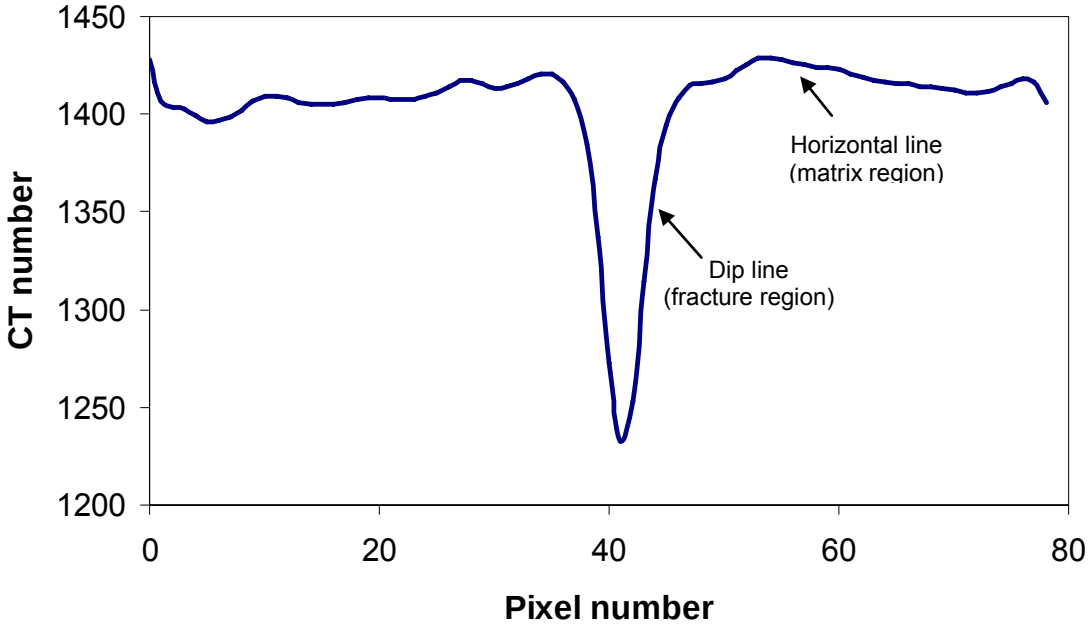

FIGURE 1.3.3 — Average CT number plot for 38-μm feeler gauge.

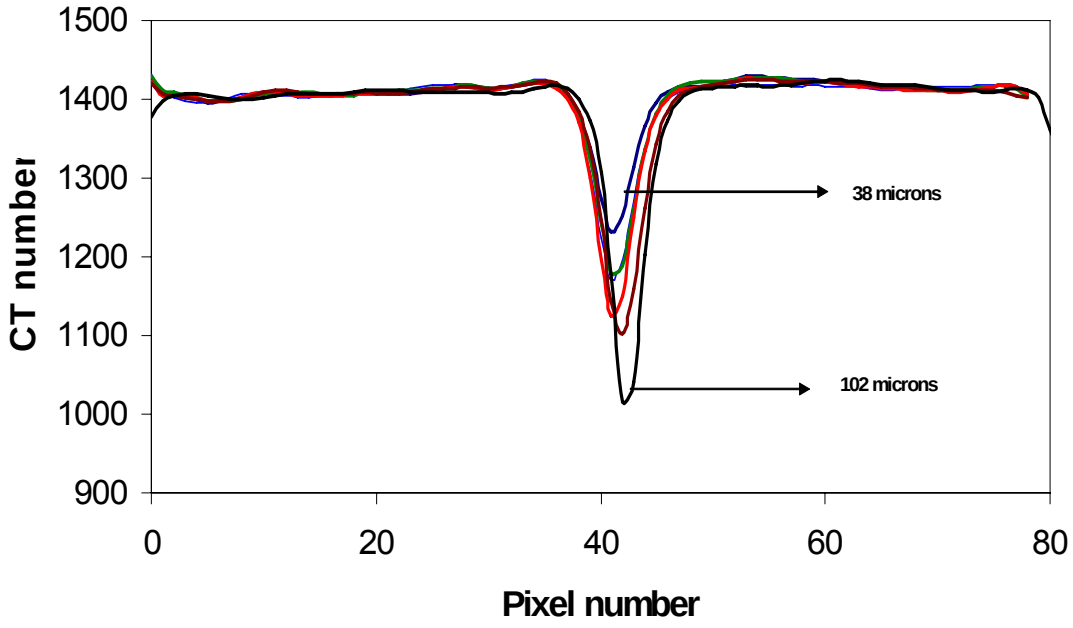

FIGURE 1.3.4 — Comparison of CT number plots for different fracture sizes.

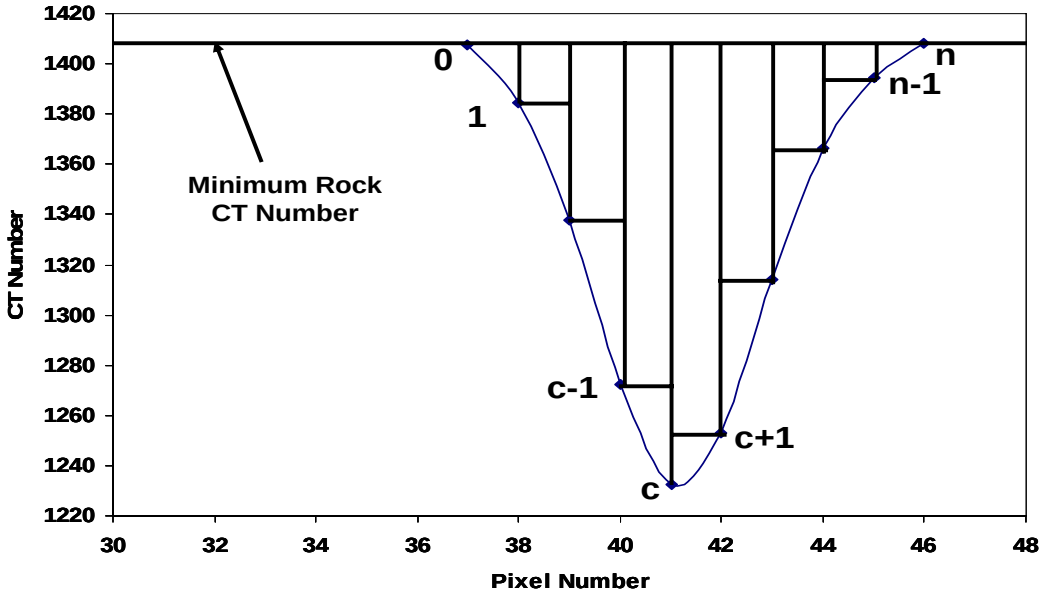

FIGURE 1.3.5 — Integrated area in the fracture region showing the index of integrated CT.

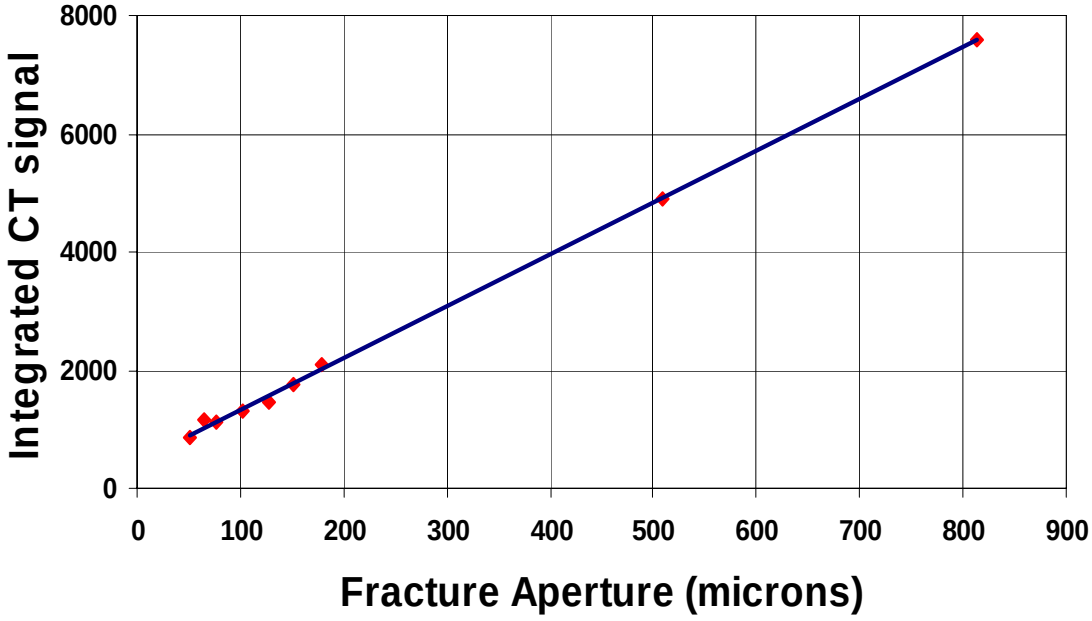

FIGURE 1.3.6 — Calibration curve between integrated CT signal and fracture aperture.

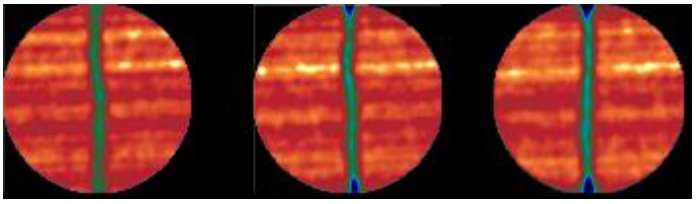

A. No overburden pressure

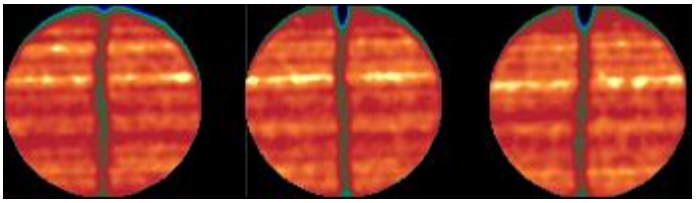

B. 500 psi overburden pressure

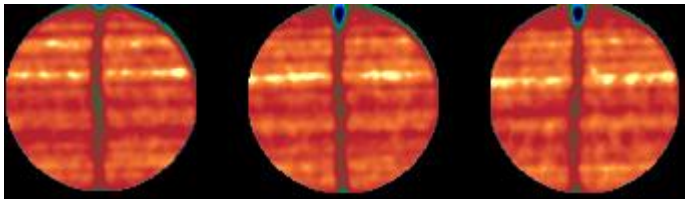

C. 1000 psi overburden pressure

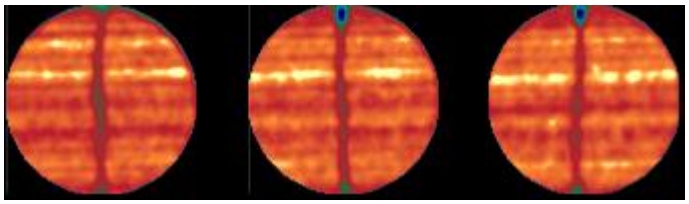

D. 1500 psi overburden pressure

FIGURE 1.3.7 — Sample scans taken along the length of the core with different overburden pressures.

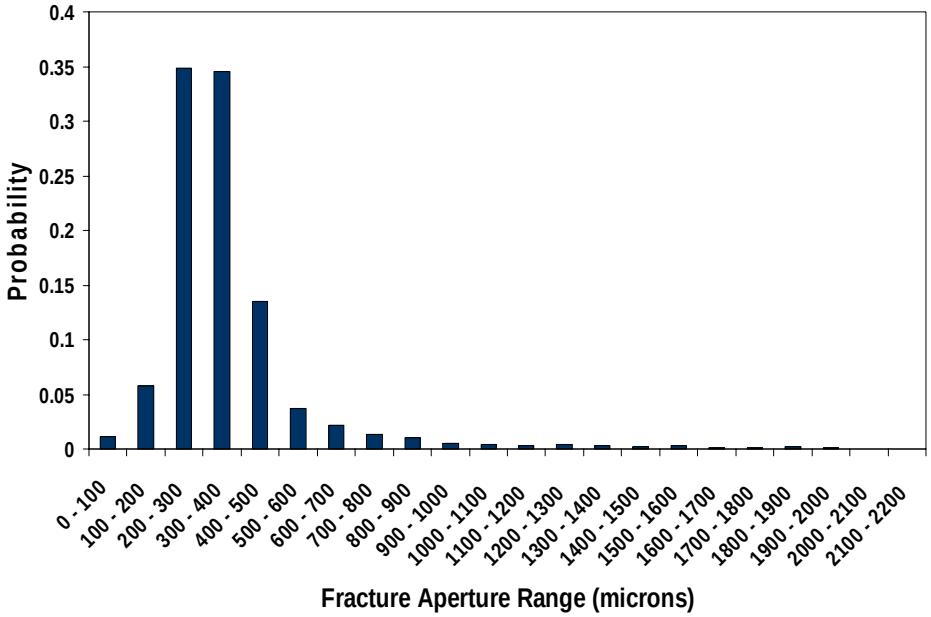

FIGURE 1.3.8 — Probability distribution of fracture apertures without overburden pressure.

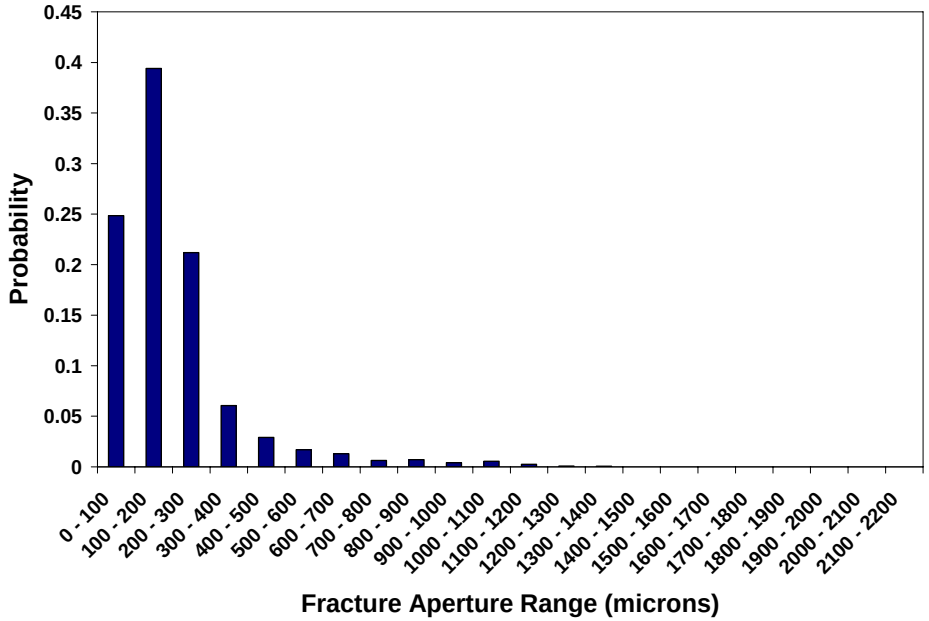

FIGURE 1.3.9 — Probability distribution of fracture apertures at 500 psi overburden pressure.

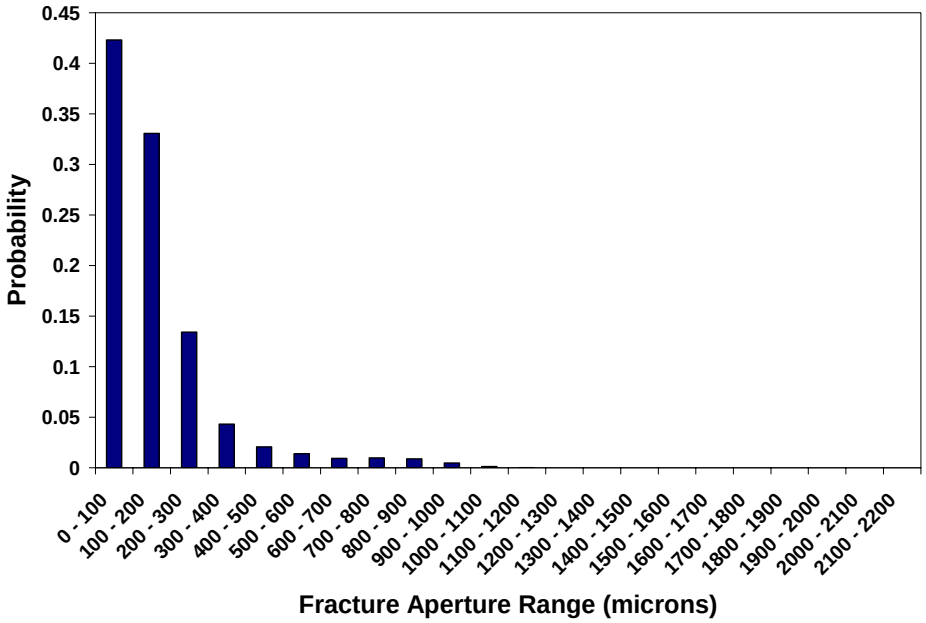

FIGURE 1.3.10 — Probability distribution of fracture apertures at 1,000 psi overburden pressure.

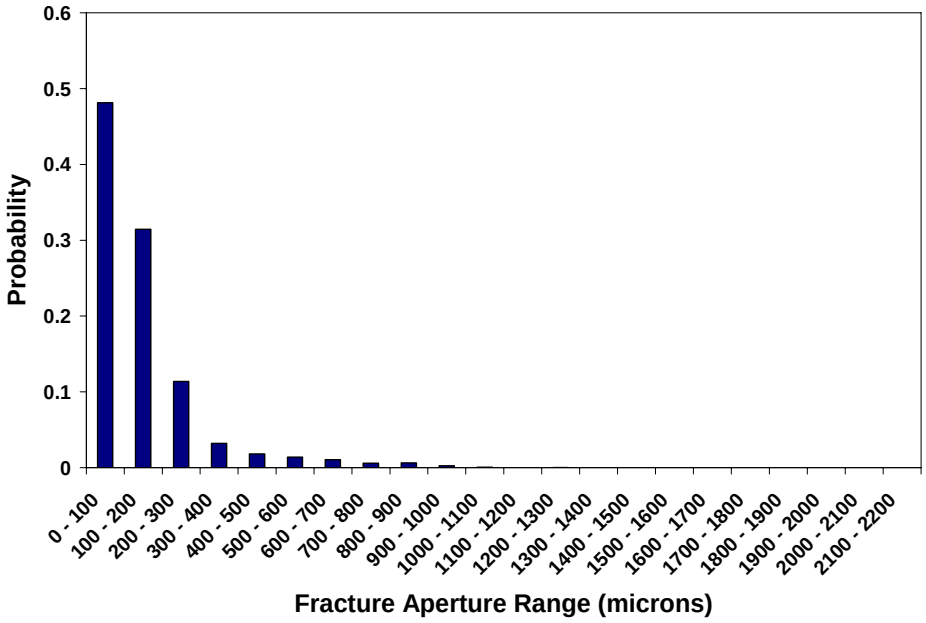

FIGURE 1.3.11 — Probability distribution of fracture apertures at 1,500 psi overburden pressure.

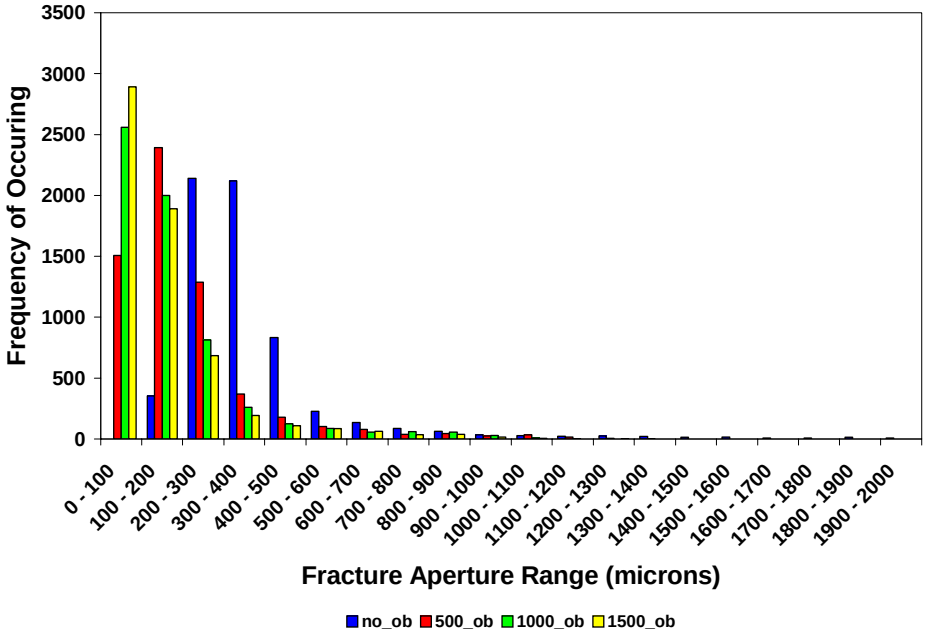

FIGURE 1.3.12 — Comparative study of fracture aperture distribution under various overburden pressures.

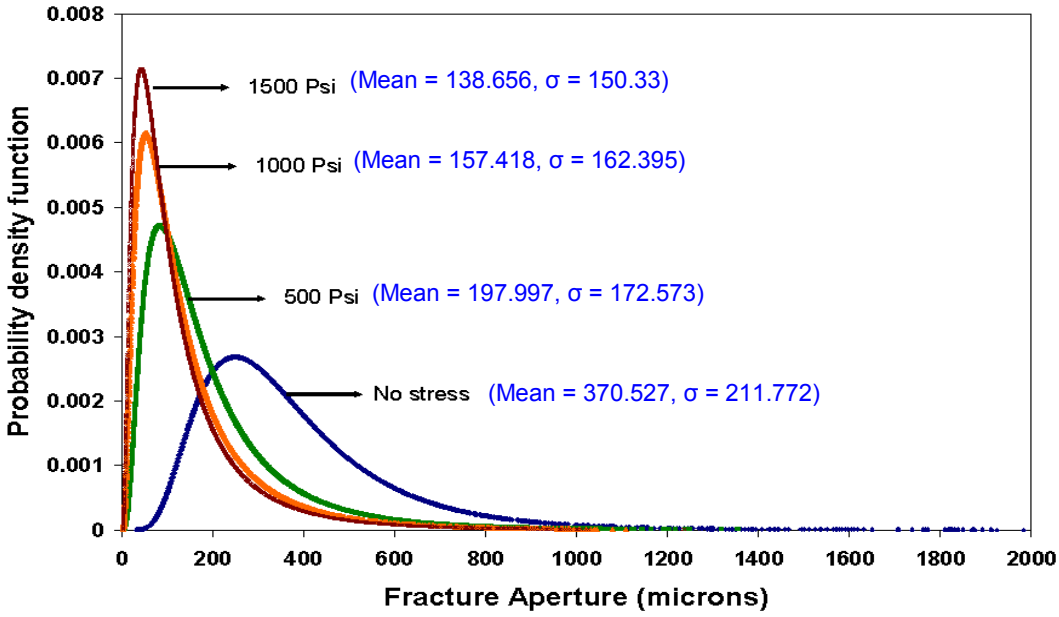

FIGURE 1.3.13 — Comparison of aperture distribution curves for various overburden pressures.

Chapter I-4
Imbibition Assisted Oil Recovery

1.4.1 BACKGROUND

As much as 30% of the oil production of the world comes from naturally fractured reservoirs. Naturally fractured reservoirs are typically considered as dual-porosity systems, composed of two distinct media: the matrix and the fractures. The matrix has high porosity but low permeability, and the fractures have very high permeability and low porosity. This combination means that most of oil and gas is stored in the matrix, and the fracture system provides the main channel for fluid flow. A successful recovery process is one that recovers hydrocarbons from the low-permeability/high-porosity matrix. Because of the interactions between the matrix and the fracture, the characteristics of the fluid flow in the naturally fractured reservoirs are quite different from those of conventional single-porosity reservoirs. Some of the tasks in the recent modeling studies of naturally fractured reservoirs include: geological fracture characterization, hydraulic characterization of fractures, upscaling of fractured reservoir properties, and fractured reservoir simulation.

In the dual-porosity model, the fluid flow between the matrix blocks and the surrounding fractures is characterized by the transfer functions, which must accurately describe the multiphase flow between the matrix and the surrounding fractures. The expulsion of oil from the matrix blocks to the surrounding fractures by capillary imbibition of water is one of the most important oil recovery mechanisms in naturally fractured reservoirs with low-permeability rock matrices, since in such reservoirs the conventional methods of production, such as building a pressure difference across matrix blocks, fail because of the high-permeability fracture network.

Water imbibition is a primary component of fluid transfer from the matrix to the fracture. Two approaches are generally used to describe the flow from the matrix blocks to the fractures and within the matrix blocks themselves: numerical and analytical. Numerical modeling requires intensive computer programming. The relations among the model parameters are often obscured inside complex nonlinear expressions. Analytical solutions may provide more necessary physical insights about the effect of the model parameters and help better understand imbibition mechanisms

to predict and optimize oil recovery. In turn, this can help to refine existing numerical models and/or develop better models in the future.

The importance of capillary imbibition was identified by the early investigators. Brownscombe and Dye[1] suggested that imbibition flooding could contribute to oil production from the Spraberry trend of west Texas. Their study established that successful imbibition flood required the rock to be preferentially water-wet and the rock surface exposed to imbibition to be as large as possible. Kleppe and Morse[2] suggested a two-dimensional numerical model to simulate flow of water and oil in the matrix block as well as in the fractures. The fractures were represented by horizontal and vertical flow channels surrounding the matrix blocks.

Published studies have been concerned with different conditions under which water imbibition occurs. Geometrical shape and size of the samples, boundary conditions, effects of gravity, type of fluids, and flowing conditions of the fluid surrounding the rock blocks are among the many factors that have been considered. Oil recovery by water imbibition displacement has concentrated on evaluating the relationship between time and oil production rate.

1.4.2 MOTIVATION AND OBJECTIVES

Different critical aspects of the capillary imbibition process have received a limited treatment in the petroleum literature. None of the recent papers devoted to capillary imbibition studies has investigated the numerical scale-up of the process. Most authors checked the validity of their numerical models against data from the imbibition tests involving the same boundary conditions. Early scaling studies of spontaneous imbibition mostly focused on the shape factor, putting no emphasis on endpoint mobilities. Large discrepancies among the scaled curves brought up the effect of sample heterogeneity, which is not well-studied yet.

To validate the scheme of upscaling laboratory imbibition experiments to field dimensions we conducted numerical studies with the matrix block surrounded by the wetting phase to better understand the characteristics of spontaneous imbibition and to evaluate dimensionless time. This allowed us to isolate the individual effects of various parameters on imbibition recovery and emphasize the importance of characterizing the imbibition mechanism for analysis of reservoir performance.

1.4.3 METHODOLOGY

For numerical modeling of the spontaneous imbibition experiment, we used a two-phase black-oil commercial simulator (CMG™) and acquired the experimental results from water static imbibition experiments.[3]

We performed numerous parametric studies and analyzed the results in detail to investigate oil recovery during spontaneous imbibition with different types of boundary conditions. These studies included the effect of varying mobility ratio, different fracture spacing, different capillary pressure, different relative permeabilities, and varying permeability profiles along the core.

After upscaling the results of these studies to the field dimensions, we evaluated the validity of the new definition of characteristic length and used the new scaling group to correlate simulation results with early upscaling techniques.

1.4.3.1 Available Data.

The spontaneous imbibition tests were performed using an imbibition apparatus shown in Fig. 1.4.1.[3] The apparatus is a simple glass container equipped with a graduated glass cap. To perform an imbibition test, a core sample was immersed in the glass container filled with preheated brine. The container was then covered with a graduated cap. After filling the cap full with brine, we stored the container in an air bath that had been set at constant temperature of 138°F. Capillary imbibition action, displaced oil from the core sample with the imbibing brine. The displaced oil accumulated in the graduated cap by gravity segregation. During the experiment, the volume of produced oil was recorded against time. The physical properties of the core sample and synthetic brine are listed in Table 1.4.1. Fig. 1.4.2 presents the cumulative oil production from the core sample as a function of time. The portion of the oil recovery curve corresponding to the early times represents maximum rate of imbibition; and the curve deviates as the major channels of flow are filled and the imbibition rate slows down. Later, the curve completely bends over and the rate of imbibition is drastically reduced. At this stage, a very slow change in water saturation with time is observed in the core. The final water saturation in the core reached 55.32%.

1.4.4 NUMERICAL MODELING

1.4.4.1 Discretization and Grid Sensitivity Analysis

The core was completely surrounded by a wetting phase. Therefore, all faces of the core were at a constant water saturation of 1.0. All the rest of the core, prior to the experiment, was at constant initial water saturation, as indicated by the initial conditions. Hence, the boundary conditions for this experiment were:

$$\begin{aligned} &S_w(x, y, z, t) = 1, x = 0 \\ &S_w(x, y, z, t) = 1, y = 0 \\ &S_w(x, y, z, t) = 1, z = 0 \\ &S_w(x, y, z, t) = 1, x = 1 \\ &S_w(x, y, z, t) = 1, y = 1 \\ &S_w(x, y, z, t) = 1, z = 1 \end{aligned} \quad \ldots\ldots\ldots\

gridblocks, which corresponds to the grid size of 20×20×20. Therefore, based on the grid sensitivity analysis, we chose the 20×20×20 grid size. As shown in Fig. 1.4.4, it took around 90 seconds to simulate this case. Additional information of this model is presented in Table 1.4.3.

1.4.4.2 Matching Experimental Results

In general, initial simulation input data do not match historical reservoir performance to a level that is acceptable for making an accurate future forecast; the final matched model is not unique. In other words, several different matched models may provide equally acceptable matches to past reservoir performance, but may yield significantly different future predictions. However, matching as much production data as available and adjusting only the least known reservoir data within the acceptable ranges should yield a better match.[44]

In our case, the only available data we had was the cumulative oil production from the core sample as a function of time. These data were matched by trial and error estimates of relative permeability and capillary pressure. Fig. 1.4.5 illustrates a very poor match of observed oil recovery vs. simulated oil recovery.

1.4.4.2.1 Relative Permeability and Capillary Pressure

We modeled relative permeability with the power law correlations built in the commercial simulator CMG™, varying the values of end-point permeabilities to obtain the best match. The capillary pressure was modeled by trial and error solution. Table 1.4.4 shows the relative permeabilities and the capillary pressure values obtained for this match. The match of the recovery is shown in Fig. 1.4.6. The distance of the water imbibed into the core plug is demonstrated by the water saturation profile as shown in Fig. 1.4.7. As time increases, more water is imbibed into the core plug and, in turn, more oil is recovered.

1.4.4.2.2 Boundary Conditions

Once we had a satisfactory model, we studied different types of boundary conditions and investigated oil recoveries by spontaneous imbibition model for the following boundary conditions:

1. All Faces Open (AFO): The base case had an "all faces open" boundary condition. This meant that all faces of the core were open to imbibition, i.e., a wetting phase could be imbibed into the core from all sides.
2. Two Ends Open (TEO): the "two ends open" boundary condition was applied to the base-case model. This imbibition model refers to a matrix block with only two faces at the top and bottom open to imbibition. The sides of the core were closed for a wetting phase to imbibe. The boundary conditions for this model were as follows:

$$S_w(x, y, z, t) = 1, x = 0$$
$$S_w(x, y, z, t) = 1, y = 0 \quad \ldots\ldots\ldots\ldots\ldots\ldots\ldots\ldots\ldots\ldots\ldots\ldots\ldots\ldots\ldots\ldots\ldots\ldots \quad (1.4.2)$$
$$S_w(x, y, z, t) = 1, x = L_x$$
$$S_w(x, y, z, t) = 1, y = L_y$$

3. Two Ends Closed (TEC): the "two ends closed" boundary condition refers to the imbibition model with two impermeable faces at the top and the bottom. For this type of imbibition, the flow occurs simultaneously through four faces of the matrix block. The boundary conditions for this type of the model were as follows:

$$S_w(x, y, z, t) = 1, z = 0 \quad \ldots\ldots\ldots\ldots\ldots\ldots\ldots\ldots\ldots\ldots\ldots\ldots\ldots\ldots\ldots\ldots\ldots\

this, we adjusted the Bond number, B_o. Bond number is a measure of relative effect of gravity forces to that of capillary forces:

$$B_o = \frac{g(\rho_1 - \rho_2)H^2}{\sigma}, \quad \text{..... (1.4.5)}$$

where g is gravitational acceleration, ρ_1 and ρ_2 are the densities of a wetting and a nonwetting phase, respectively, H is the height of the core, and σ is surface tension. When $B_o >> 1$, capillarity pressure is negligible, if $B_o << 1$, then gravity is negligible.

Although the height of the core was very small, we decided to reduce the effect of the gravity by making the density difference equal to zero. We changed the density of water from 1 g/cm^3 to 0.8635 g/cm^3, which was equal to the density of oil. This way the value of the Bond number has been set to zero, which meant that the gravity effect is negligble. Fig. 1.4.9 shows the effect of the gravity on oil recovery. From the figure we observed that the gravity effect was negligible and neglecting it did not significantly affect the oil recovery.

1.4.4.3 Rates of Imbibition

We compared spontaneous imbibition rates of water for different types of boundary conditions, based on the total surface area available for imbibition and corresponding times taken for saturating a core until residual oil saturation. Fig. 1.4.10 shows oil recovery curves for four types of boundary conditions: AFO, TEO, TEC, and OEO. The figure shows that the OEO boundary condition exhibits the smallest oil recovery, while the AFO boundary condition exhibits the largest value of oil recovery. The OEO boundary condition has only one face of the core available for imbibition, while the AFO boundary condition has six faces of the core open for imbibition.

Fig. 1.4.11 shows that the time required for saturating a core with water until residual oil saturation increases exponentially, as the number of faces available for imbibition decreases. The comparison of all four types of boundary conditions shows that a nonwetting recovery for the AFO model is most efficient and fast, as compared with all other cases.

1.4.4.3.1 Effect of Heterogeneity on the Imbibition Oil Recovery

Because the effect of heterogeneities on oil recovery has received limited treatment in the petroleum literature, we investigated the effect on oil recovery of varying permeability profiles along the core. Under the influence of capillary forces, water imbibes from the more permeable zones of the porous medium into the less permeable zones and displaces oil. However, without experimental or numerical studies, it is difficult to determine oil displacement from the more permeable zone into the less permeable. The same problem arises when water displaces oil from highly permeable oil lenses into the less-permeable zones of a porous medium. For further investigation of the problem, we performed numerical analyses.

To formulate the problem, we considered a core with only one imbibing face open to fluid flow, varying the permeability along the core. Particularly, two cases have been considered. The first case is when oil has been displaced by water and the permeability of the core decreased from the bottom to the top of the core; the second case is when permeability increased from the bottom to the top. A schematic of both cases is shown in Fig. 1.4.12. The core on the scheme has been conditionally divided into four parts to illustrate the permeability change along the core. For computational ease, the permeability variance along the core was distributed linearly (Fig. 1.4.13). This study was based on numerical simulation and the previously matched model of spontaneous imbibition. The gravity effect was neglected.

The following *J*–function was used to scale capillary pressures to account for the differences in block permeability:

$$J(S_W) = \frac{P_c}{\sigma \cos\theta}\sqrt{\frac{k}{\phi}} \quad \text{..... (1.4.6)}$$

The *J*-function has the effect of normalizing all curves to approach a single curve. The results of numerical analyses are shown in Fig. 1.4.14, which shows that oil recovery curves for both cases have generally known shape but different oil recovery values. Clearly, capillary displacement of oil by water is more efficient for a case when water imbibes into the core in the direction of decreasing permeability.

The explanation lies in understanding the mechanism of capillary displacement and also realizing that capillary pressure is an inversely proportional function of permeability, which means that when permeability decreases, the capillary pressure increases, or vice versa. So when water imbibes in the direction of decreasing permeability, it reaches the boundary of two different permeability zones and without

any difficulty moves into the next zone. This unhampered movement occurs because water moves from the zones of low capillary forces into the zones with high capillary forces.

The case is different when the permeability of a porous medium increases in the direction of water imbibition. Water imbibed into the low-permeability zone of the core moves ahead under the influence of capillary forces and, finally, reaches the boundary of the highly permeable zone. At this point, the further movement of water is hindered because water moves into the zone with low capillary forces. So the analyses indicated that oil displacement from a porous medium, consisting of the sequential zones of different permeabilities, is more efficient if imbibition occurs in the direction of decreasing permeability than in the direction of increasing permeability.

1.4.5 PARAMETRIC STUDY

This parametric study was based on numerical simulation, using the previously matched model of spontaneous imbibition. The gravity effect was neglected. The first series of computer runs was conducted to study the change in imbibition recovery, which was expected with the change in viscosities of the reservoir fluids. The second series considered the changes caused by different capillary pressure and relative-permeability curves. The third set of computer runs was conducted to examine oil recoveries for the models with different fracture spacing. Other reservoir and fluid properties were held constant.

1.4.5.1 Effect of Water-Oil Viscosity Ratio

Fluid viscosity can significantly affect the rate of imbibition. We examined the effect of different water/oil viscosity ratios at which water imbibed into the core. The original water/oil ratio used in the base case model was 0.68:3.52, and we made the simulation runs for two different oil viscosities: 0.352 and 50 cp. The water viscosity was held constant at 0.68 cp. The first case, with 0.68:0.352 water/oil viscosity ratio, simulated the case with favorable fluid flow mobility. The second case, with 0.68:50 water/oil viscosity ratio, simulated the case with unfavorable fluid flow mobility.

The effect of different oil viscosities on the oil recovery for the AFO spontaneous imbibition model is shown in Fig. 1.4.15, which shows that the lower the oil viscosity,

the bigger the volumes of oil produced from the core as a function of time. As oil viscosity increases, less and less water is imbibed into the core plug. Exactly the same picture has been observed with three other types of imbibition models.

1.4.5.2 Effect of Capillary Pressure and Relative Permeability

Capillary pressure is a function of pore sizes and the interfacial tension between the fluids in the matrix and the driving force during spontaneous imbibition. In general, the smaller the pore size, or the higher the interfacial tension, the stronger the capillary pressure.

To investigate the sensitivity of imbibition capillary pressure on the imbibition oil recovery, we used two different capillary pressures by multiplying the matching results of capillary pressure by 0.1 (Case 1) and 10 (Case 2) in the AFO model. These series of simulation runs were made to determine the effect on imbibition of changing capillary pressure. AFO type of the spontaneous imbibition model was used. Other data used in the simulator remained unchanged.

Changes in the imbibition oil recovery for these cases are clearly demonstrated in Fig. 1.4.16. The change from the Base Case to Case 1 caused a decrease in the oil recovery, and the change of capillary pressure from the Base Case to Case 2 caused an increase in spontaneous imbibition oil recovery.

Capillary pressure is assumed to be the only driving force in the spontaneous imbibition process. Thus, increasing the capillary pressure increased the imbibition recovery as shown in Fig 1.4.16. Likewise, the decrease of imbibition oil recovery from the Base Case to Case 1 was also based on the fact that capillary pressure of Case 1 was lower than that of the Base Case.

To investigate the sensitivity of relative permeability curves on the imbibition oil recovery, we ran two cases representing relative permeabilities as results of multiplication of 0.1 and 0.5 to the matching results of relative permeability. The results in **Figs. 1.4.17** and 1.4.18 show that oil recovery by imbibition is sensitive to the oil relative permeability curves, while no significant effect was observed in changing the water relative permeability curves. The imbibition oil recovery was sensitive to the oil relative permeability. This can be explained by the fact that a capillary diffusion coefficient is a function of the square of oil relative permeability and, thus, affects the imbibition process much more.

1.4.5.3 Effect of Fracture Spacing

The effect of different fracture spacing was investigated on the TEO model. Fracture spacing is the distance between parallel fracture planes. The top and the bottom of the model, which were open to water imbibition, were assumed as fracture planes, and the distance between the top and the bottom of the model was varied to study the effect on oil recovery. Different fracture spacing was obtained by multiplying original fracture spacing by 2, 4, and 8.

Fig. 1.4.19 presents a comparative study of time rates of spontaneous imbibition of water for different fracture spacing. The comparison here was based on the fracture spacing and the corresponding times taken to saturate the core until residual oil saturation. As the fracture width increases, the time required for saturating a core with water until residual oil saturation increases linearly.

1.4.6 SCALING OF STATIC IMBIBITION DATA

Spontaneous imbibition is an important phenomenon in oil recovery from fractured reservoirs, where the rate of mass transfer between the rock matrix and the fractures determines the oil production. Imbibition is also important in evaluation of wettability of a fluid/liquid/porous media system. The rate of imbibition depends primarily on the porous media, the fluids, and their interactions. These include relative permeabilities, matrix shapes, boundary conditions, fluid viscosity, interfacial tension (IFT), and wettability. Laboratory results need to be scaled to estimate oil recovery from the reservoir matrix blocks that have shapes, sizes, and boundary conditions different from those of the laboratory core samples. Upscaling of imbibition oil recovery from the small reservoir core sample allows us to predict field performance.

The basic requirements for scaling laboratory data to field conditions were investigated by Rapoport.[4] In scaling imbibition results for different oil/brine/rock systems or in predicting field performance from laboratory measurements, Mattax and Kyte[5] proposed the following scaling group:

$$t_D = t\sqrt{\frac{k_m}{\phi}}\frac{\sigma}{\mu_w}\frac{1}{L^2}, \quad \text{..... (1.4.7)}$$

where t_D is dimensionless time, t is imbibition time, k_m is matrix permeability, ϕ is porosity, σ is interfacial tension, μ_w is water viscosity, and L is core length. The assumptions made in deriving this equation were that the sample shapes must be identical, the oil/water viscosity ratio must be duplicated, the gravity effects must be neglected, initial fluid distribution must be duplicated, the capillary pressure functions must be related by direct proportionality, and the relative permeability functions must be the same.

In oil production from fractured reservoirs, the systems with different matrix sizes, shapes, and boundary conditions will give different mass transfer rates between the fractures and the rock matrix. The smaller the ratio of a volume to open surface area, the faster the imbibition rate. So, based on the work of Mattax and Kyte[5] and Kazemi *et al*.[6] a characteristic length was proposed by Ma *et al*.,[7] which was defined as follows:

$$L_C = \sqrt{\frac{V}{\sum_{i=1}^{n} \frac{A_i}{x_{Ai}}}}, \quad \text{..... . (1.4.8)}$$

where V is the bulk volume of the matrix, Ai is the area open to the imbibition at the ith direction, and xAi is the length defined by the shape and boundary conditions of the matrix block. Because one of the assumptions in deriving Eq. 1.4.7 is that viscosity ratios are identical, Ma *et al*.[7]also proposed to use oil viscosity in Eq. 1.4.7, provided that the viscosity ratio is constant, taking into consideration from the recent studies that for water/oil systems imbibition rate is proportional to the geometric mean of the water and oil phase viscosities:

$$\mu_g = \sqrt{\mu_o \mu_w} \quad \text{..... (1.4.9)}$$

So, to account for both the effect of viscosity ratio and boundary conditions, the following modified scaling group was proposed by Ma *et al*.:[7]

$$t_D = t\sqrt{\frac{k_m}{\phi}}\frac{\sigma}{\mu_g}\frac{1}{L_C^{\,2}} \quad \text{..... (1.4.10)}$$

1.4.6.1 Scaling for Different Types of Boundary Conditions

We tested the applicability of Eq. 1.4.10 through extensive numerical study of the effect of two boundary conditions, OEO and TEO. Then we used the results from numerical studies of spontaneous imbibition mechanism to compare between Eq. 1.4.7 and Eq. 1.4.10 on a semilog plot of oil recovery vs. dimensionless time.

Fig. 1.4.20 shows results for different boundary conditions using Eq. 1.4.7. Fig. 1.4.21 shows results for different boundary conditions using the characteristic length in Eq. 1.4.10. Comparison of both figures revealed that the points are more scattered in Fig. 1.4.20 than in Fig. 1.4.21, which proved that using characteristic length in the equation of dimensionless time improves the correlation for the models with different boundary conditions.

1.4.6.2 Scaling for Variable Mobility Ratios

We compared the new scaling group proposed to correlate simulation results to the early upscaling technique. The previous scaling studies of spontaneous imbibition did not focus on the varying mobilities of the fluids. Therefore, we decided to study this effect and compare results from the previous upscaling technique (Eq. 1.4.10) to the results from the newly developed scaling equation.

The newly developed scaling technique was proposed by Zhou *et al.*[8] They included characteristic mobilities of a wetting and a nonwetting phase into the equation of dimensionless time:

$$t_D = t\sqrt{\frac{k_m}{\phi}}\frac{\sigma}{L_C^{\,2}}\sqrt{\lambda_W \lambda_{NW}}\,\frac{1}{\sqrt{M}+1/\sqrt{M}}, \quad \text{..... (1.4.11)}$$

where

$$\lambda = \frac{k}{\mu} \quad \text{..... (1.4.12)}$$

and

$$M = \frac{\lambda_W}{\lambda_{NW}} \quad \text{..... (1.4.13)}$$

The parameter λ is characteristically mobility for a wetting and a nonwetting phase, and **M** is a characteristic mobility ratio. Here, end-point relative permeabilities are used when calculating λ and *M*. The mobility ratios also depend on the viscosity of fluids. The equation is valid only if relative permeability and capillary pressure

functions are similar for all of the measurements. Figs. 1.4.22 and 1.4.23 compare the newly proposed upscaling method (Eq. 1.4.11) with the previous upscaling technique (Eq. 1.4.10, TEO and OEO boundary conditions.

We considered three mobility ratios. The first case was with favorable mobility ratio, the second case was with unit mobility ratio, and the third case was with unfavorable mobility ratio. In all cases, oil viscosity has been altered, and water viscosity remained unchanged. The curves fall into a narrow range when we use the newly developed scaling technique; the scaling is almost perfect with slight differences at late times. These differences probably result from the influence of the boundary of the porous medium on imbibition. When using a previous scaling equation, the data are more scattered.

We observed a very good correlation for the results of spontaneous imbibition with the new scaling technique. The recovery curves agree reasonably well for all mobility ratios. The data are reduced to a single curve in spite of the fact that nonwetting fluid viscosity varies by three orders of magnitude. The results indicate that the new dimensionless time can significantly improve the scaling of spontaneous imbibition.

1.4.7 CONCLUSIONS

1. The comparative study of time rates of water spontaneous imbibition for different types of boundary conditions revealed that the time required for capillary imbibition to reach residual oil saturation increases exponentially as the number of faces available for imbibition decreases.
2. The comparison of all four types of boundary conditions showed that oil recovery for the AFO model is most efficient and fast, as compared with all other cases.
3. The effect on oil recovery of varying permeability profiles along the core showed that when water imbibes in the direction of decreasing permeability, oil recovery is higher than when water imbibes in the direction of increasing permeability.
4. The study of the effect of different water/oil viscosity ratios at which water imbibed into the core showed that the lower the oil viscosity, the greater the volumes of oil produced from the core as a function of time.
5. Increasing the capillary pressure increased imbibition recovery. Oil recovery by imbibition was sensitive to oil relative permeability curves, while no significant effect was observed in changing the water relative permeability curves.

6. A comparative study of time rates of spontaneous imbibition of water for different fracture spacing showed that the time required for capillary imbibition until residual oil saturation increased linearly as the fracture space increased.
7. The characteristic length described by Ma's equation of dimensionless time improved a correlation between data points for the models with different boundary conditions.
8. The spontaneous imbibition results of this study have been upscaled to field dimensions. The new definition of characteristic length used in the modified scaling group has been Validated, by comparison with the early upscaling techniques.
9. The new technique used for upscaling significantly improved correlations by taking end-point fluid-phase mobilities and the mobility ratios into account. The comparison between the new and the previous dimensionless times proved that even if nonwetting fluid viscosity varies by 3 orders of magnitude, the data could be reduced to a single curve if we use new dimensionless time definition.

Nomenclatures

A = total area, ft2
B_o = bond number
D = diameter, ft
g = gravitational acceleration, ft/sec2
H = height, ft
$J(S_w)$ = leverett J-function
k = permeability, md
k_{ro} = oil relative permeability
k_{rw} = water relative permeability
L = length, ft
L_c = characteristic length, ft
M = mobility ratio
P_c = capillary pressure, psi
P_{nw} = pressure of non-wetting phase, psi
P_w = pressure of wetting phase, psi
r = pore radius, ft
R = oil recovery, %
R_∞ = ultimate recovery, %
R_{imb} = imbibition oil recovery, %
S_w = water saturation, fraction
S_{wi} = irreducible water saturation, fraction
S_{nwr} = residual saturation, fraction
S_e = effective water saturation, fraction
t = time, min

t_d = dimensionless time
t_c = dimensionless time for high capillary gravity ratio
t_g = dimensionless time for low capillary gravity ratio
V = volume, ft3
μ_o = oil viscosity, cp
μ_w = water viscosity, cp
μ_g = geometric mean of the water and oil phase viscosities, cp
ρ = density, ft/lb3
ϕ = porosity, fraction
σ = interfacial tension, dynes/cm
θ = contact angle, degrees
λ = phase mobility, md/cp

References

1. Brownscombe, E.R., and Dyes, A.B.: "Water-Imbibition Displacement… Can it Release Reluctant Spraberry Oil?," Oil and Gas J. (17 November 1952) 264-265.
2. Kleppe, J., and Morse, R.A.: "Oil Production from Fractured Reservoirs by Water Displacement," paper SPE 5084 presented at the SPE-AIME 49th Annual Fall Meeting, Houston, Texas, 6-9 October.
3. Putra, E., Fidra, Y. and Schechter, D.S.: "Study of Waterflooding Process in Naturally Fractured Reservoirs from Static and Dynamic Imbibition Experiments" paper SCA 9910 presented at the 1999 International Symposium of the Society of Core Analysts, Colorado, Aug. 1-4.
4. Rapoport, L.A.: "Scaling Laws for Use in Design and Operation of Water/Oil Flow Models," Trans., AIME (1955) 204, 143.
5. Mattax, C.C., and Kyte, J.R.: "Imbibition Oil Recovery from Fractured, Water-Drive Reservoirs," SPEJ (June 1962) 177-184; Trans., AIME, 225.
6. Kazemi, H., Gilman, J.R., and Elsharkawy, A.M.: "Analytical and Numerical Solution of Oil Recovery from Fractured Reservoirs with Empirical Transfer Functions," paper SPE 6192 presented at the 1976 SPE Annual Technical Conference and Exhibition, New-Orleans, Louisiana, 3-6 October.
7. Ma, S., Zhang, X., and Morrow, N.R.: "Experimental Verification of a Modified Scaling Group for Spontaneous Imbibition," paper SPE 30762 presented at the 1995 SPE Annual Technical Conference and Exhibition, Dallas, Texas, 22-25 October.

8. Zhou, D., Jia, L., Kamath, J., and Kovscek, A.R.: “An Investigation of Counter-Current Imbibition Process in Diatomite,” paper SPE 68837 presented at the 2001 SPE Western Regional Meeting, Bakersfield, California, 26-30 March.

Table 1.4.1 — Physical Properties of the Core and Brine

Property	Value	Unit
Dimensions of the core	3.2 x 3.2 x 4.9	cm
Porosity	15.91	%
Permeability	74.7	md
Initial water saturation	41.61	%
Viscosity of oil	3.52	cp
Density of oil	0.8635	g/cm^3
API	31	°
Viscosity of water	0.68	cp
Density of water	1	g/cm^3

Table 1.4.2 — Table of Grid Sizes Investigated in the Grid Sensitivity Analyses

Number of Simulation Run	No. of gridblocks in I, J and K directions			Total number of gridblocks
	I-Direction	J-Direction	K-Direction	
1	7	7	7	343
2	12	12	12	1,728
3	16	16	16	4,096
4	20	20	20	8,000
5	20	20	25	10,000

Table 1.4.3 — Properties of the Core for Numerical Simulation

Property	Value	Unit
Number of grid blocks in X-Direction	20	-
Number of grid blocks in Y-Direction	20	-
Number of grid blocks in Z-Direction	20	-
Grid block dimension X-Direction	0.178	cm
Grid block dimension Y-Direction	0.178	cm
Grid block dimension Z-Direction	0.242	cm
Density of oil	0.8635	g/cm^3
Density of water	1	g/cm^3
Viscosity of oil	3.52	cp
Viscosity of water	0.68	cp
Permeability	74.7	md
Porosity	0.1591	-
Initial water saturation	(2-19x2-19x2-19)*0.4161	-
Boundary condition	All sides	-

Table 1.4.4 — Table of Relative Permeabilities and Capillary Pressure

Water Saturation, Fraction	Water Relative Permeability	Oil Relative Permeability	Capillary Pressure, Psi
0.4161	0	0.9	1.7537
0.4338	0.0007	0.7787	1.555
0.4516	0.003	0.6331	1.445
0.4693	0.0067	0.5069	1.375
0.4871	0.0119	0.3967	1.273
0.5048	0.0186	0.3071	1.164
0.5226	0.0268	0.2307	1.078
0.5403	0.0365	0.1682	0.976
0.5581	0.0476	0.1181	0.922
0.5758	0.0603	0.0791	0.828
0.5935	0.0744	0.0498	0.733
0.6113	0.09	0.0288	0.651
0.6290	0.1071	0.0148	0.547
0.6468	0.1257	0.0062	0.345
0.6645	0.1458	0.00018	0.254
0.6823	0.1674	0.00015	0.134
0.7	0.2	0	0

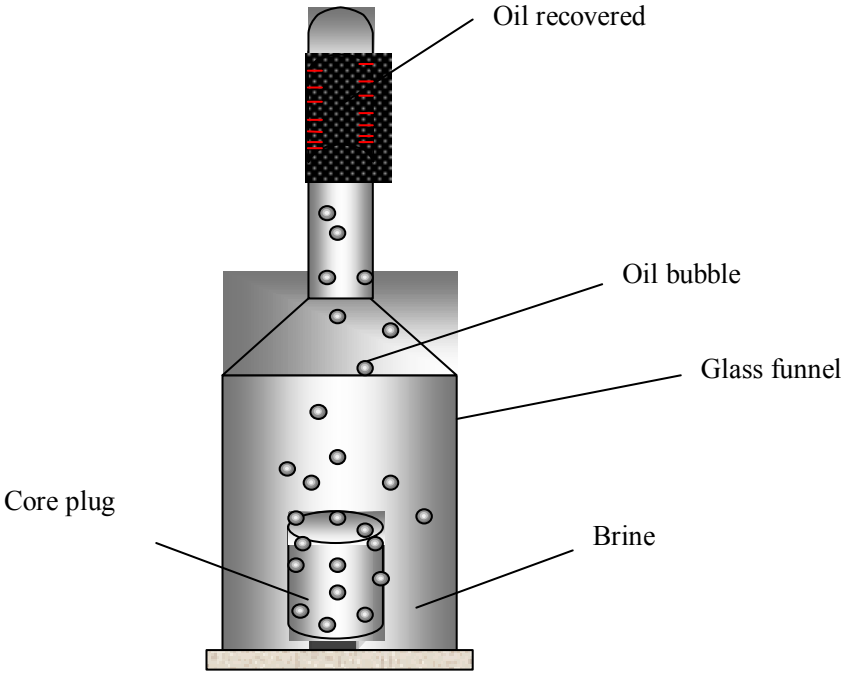

Fig. 1.4.1 — Spontaneous Imbibition Cell.[3]

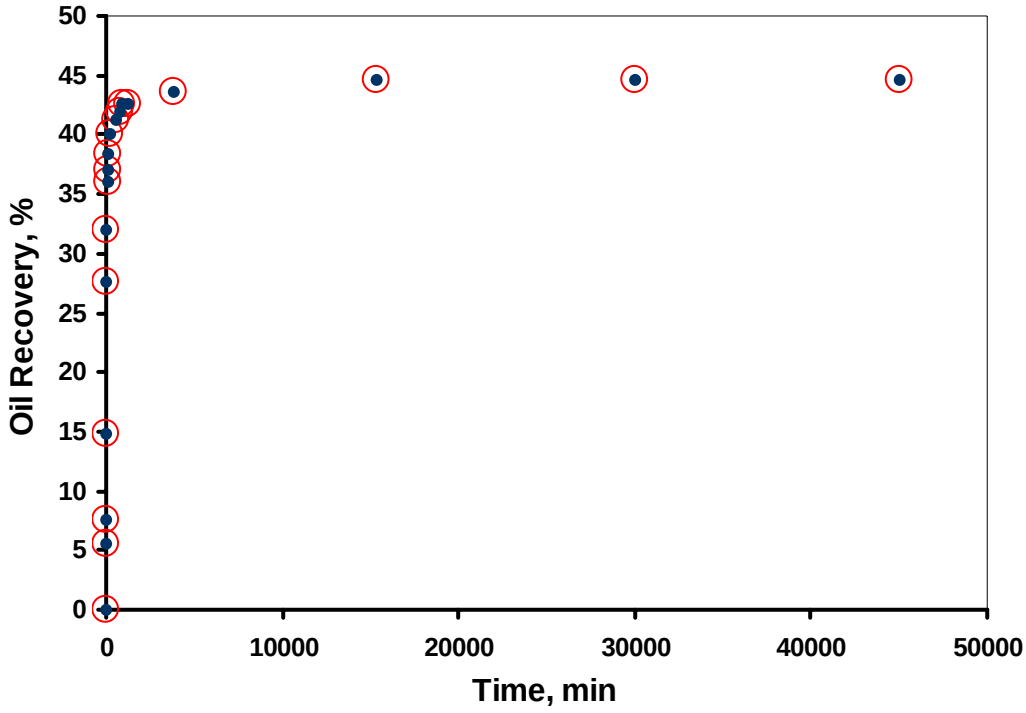

Fig. 1.4.2 — Oil recovery curve from static imbibition experiment.

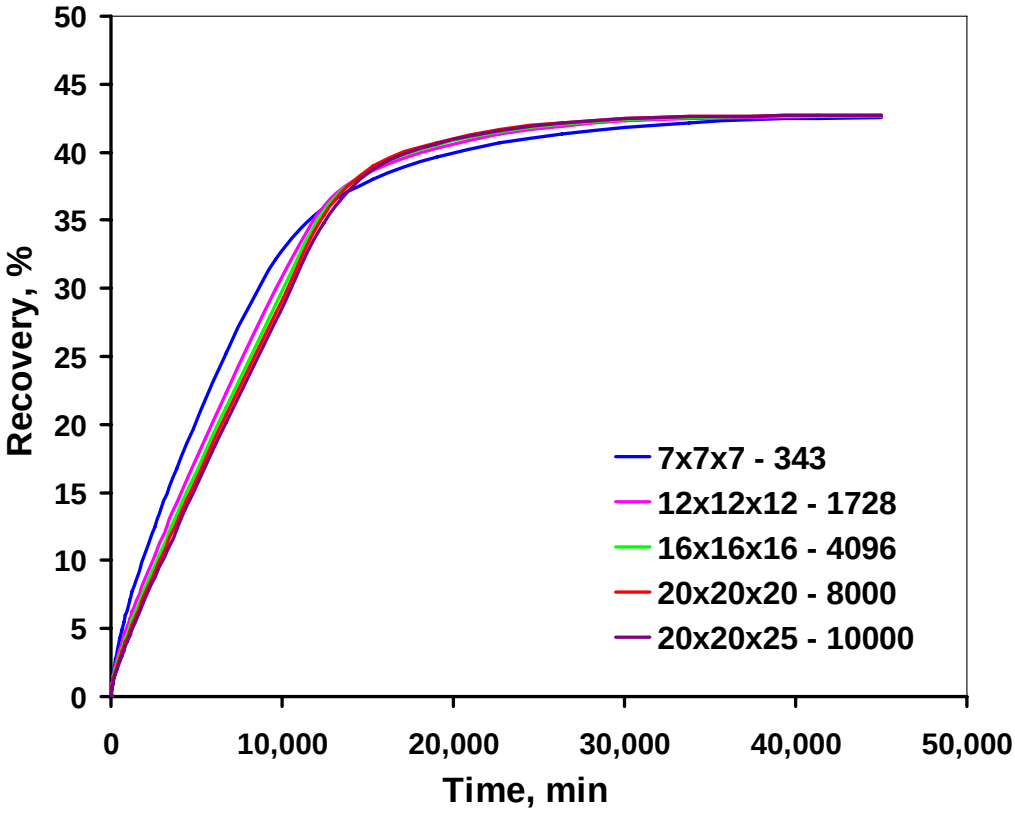

Fig. 1.4.3 — Grid size effect on oil recovery from static imbibition experiment.

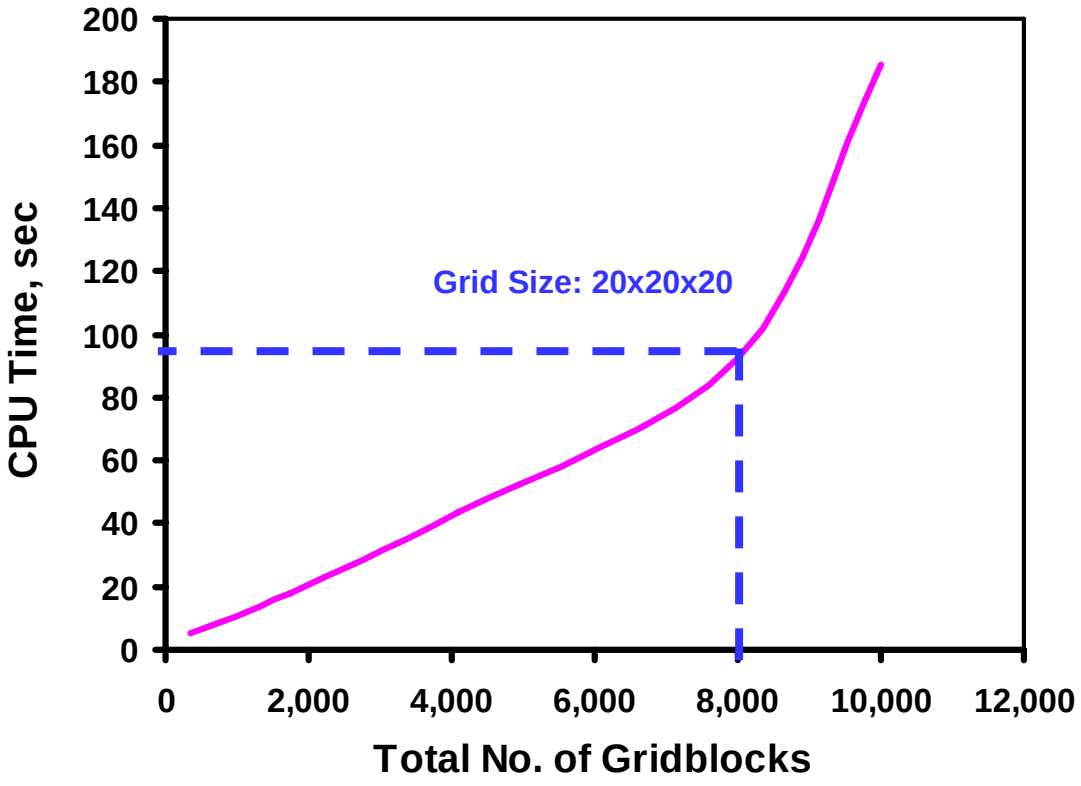

Fig. 1.4.4 — Simulation times for different grid sizes.

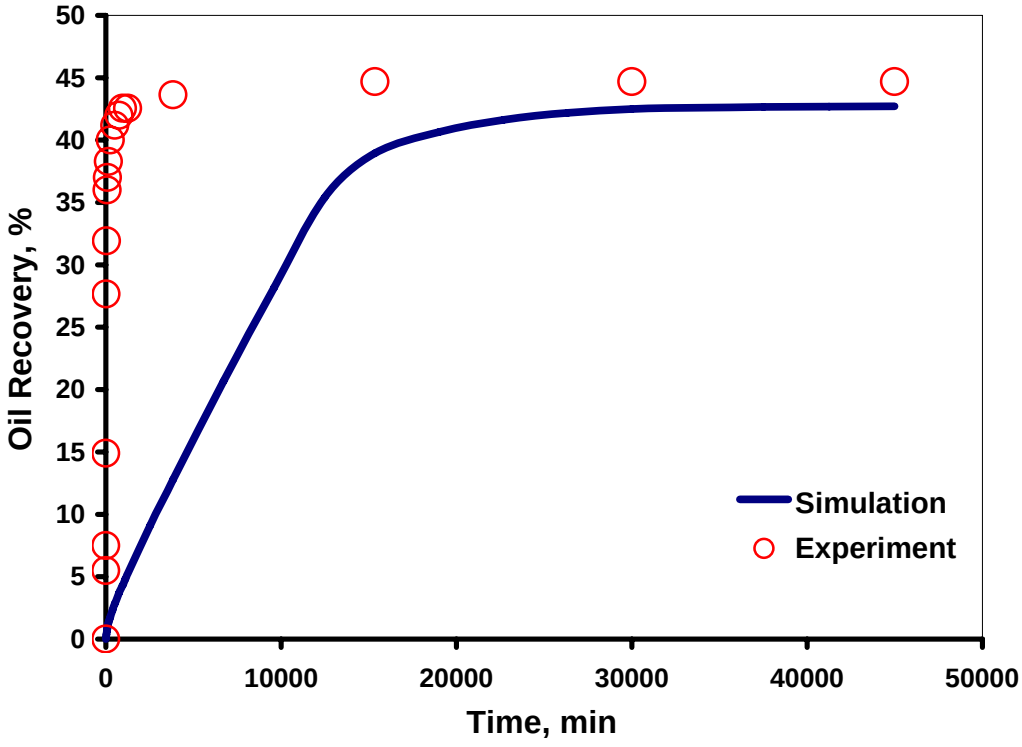

Fig. 1.4.5 — Observed oil recovery vs. simulated before adjustment of reservoir data.

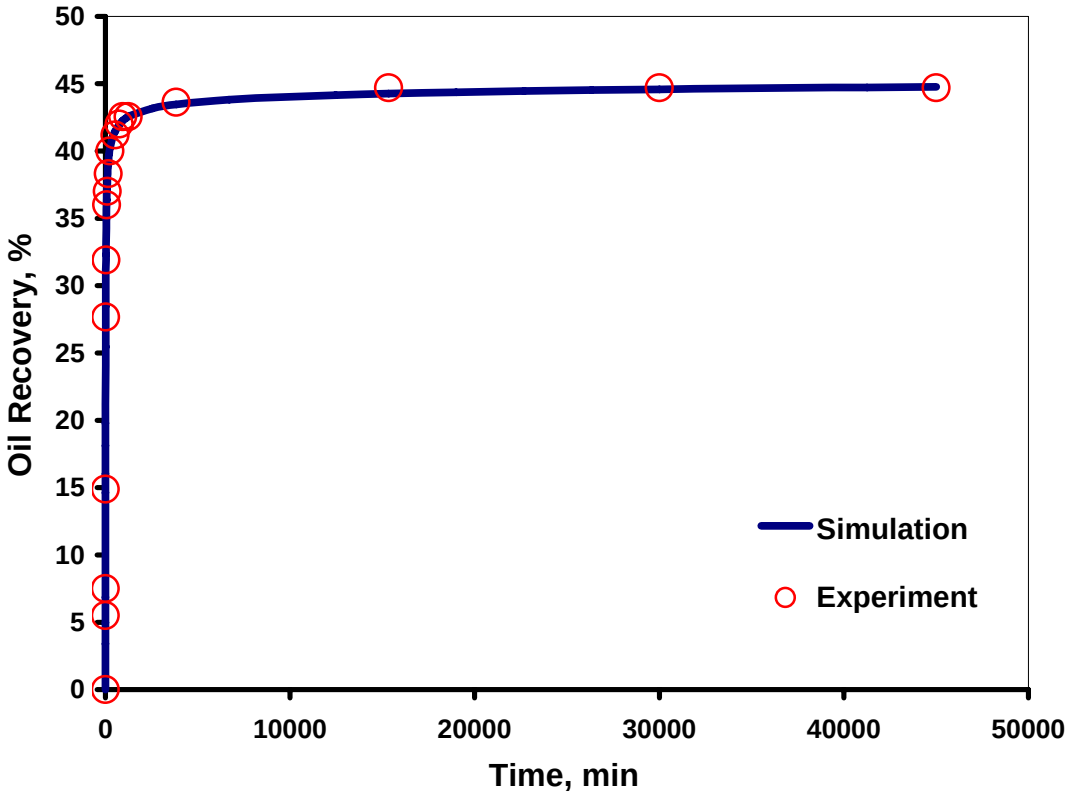

Fig. 1.4.6 — Match of the simulated oil recovery with the observed oil recovery.

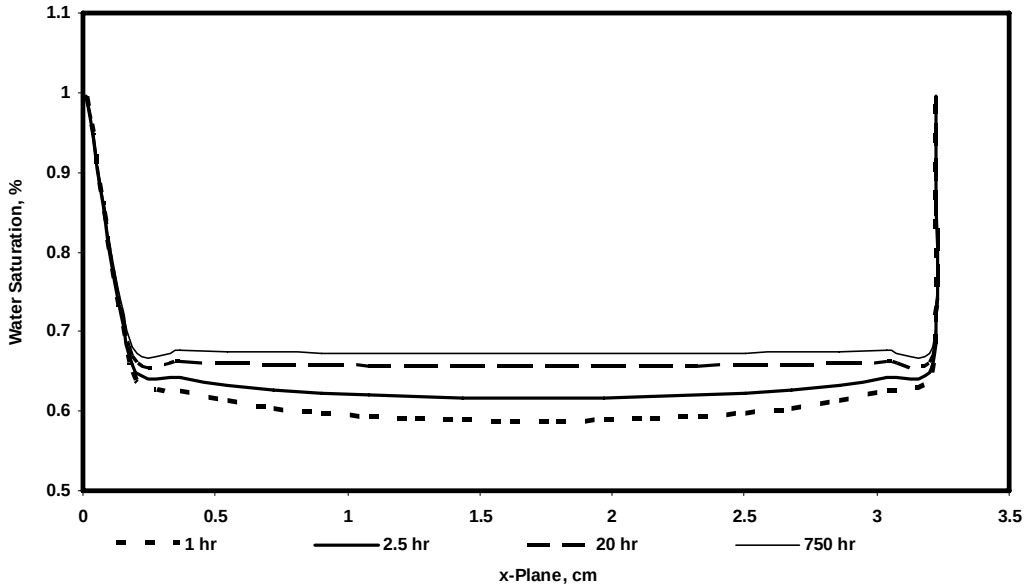

Fig. 1.4.7 — Water distribution at different imbibition times from x-plane view.

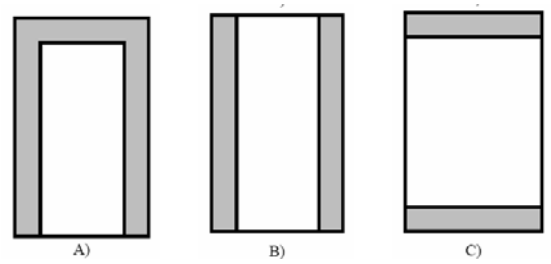

Fig. 1.4.8 — Schematic representation of imbibition in cores with different boundary conditions: A) One End Open, B) Two Ends Open, and C) Two Ends Closed.

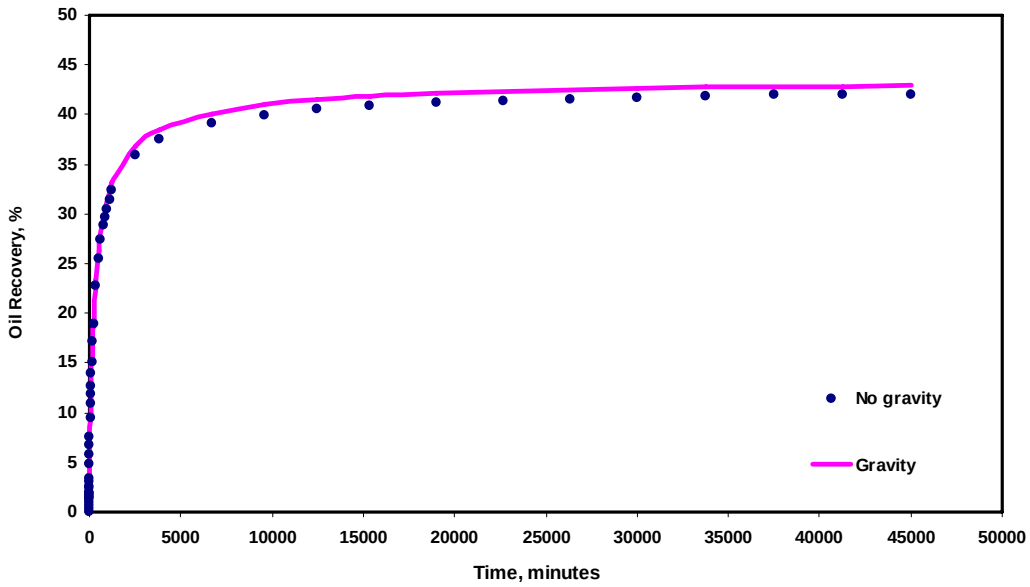

Fig. 1.4.9 — Effect of gravity on imbibition response.

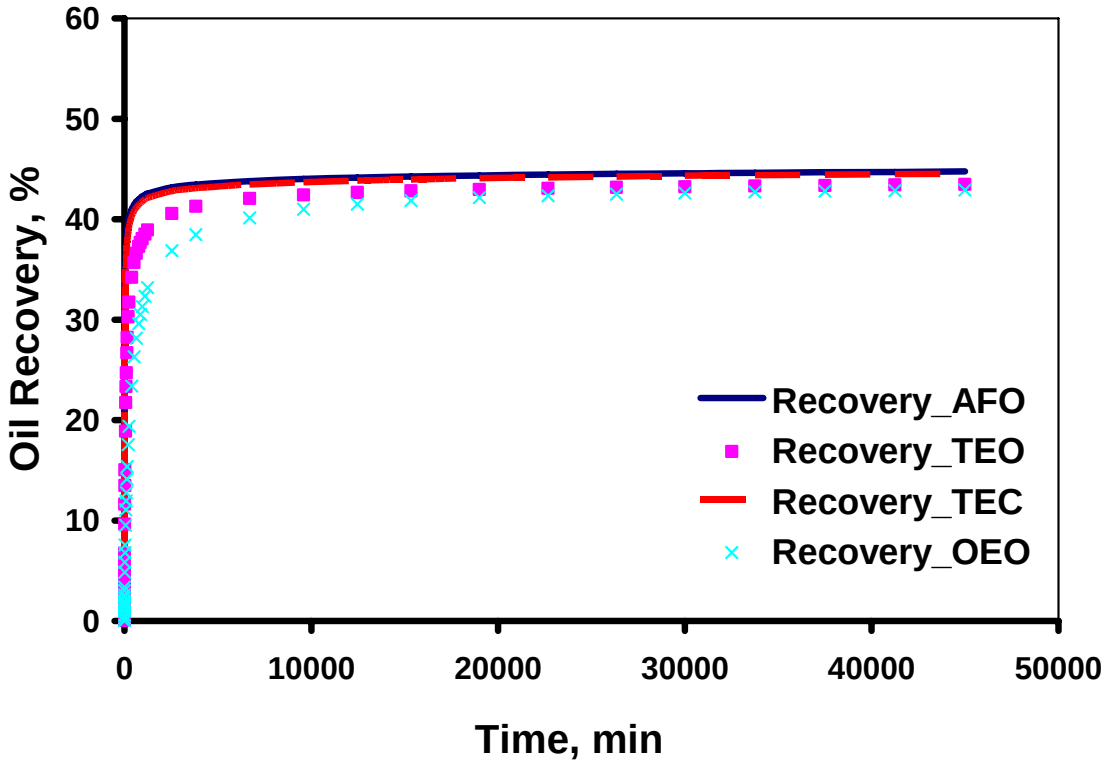

Fig. 1.4.10 — Oil recoveries for All Faces Open, Two Ends Closed, Two Ends Open, and One End Open boundary conditions.

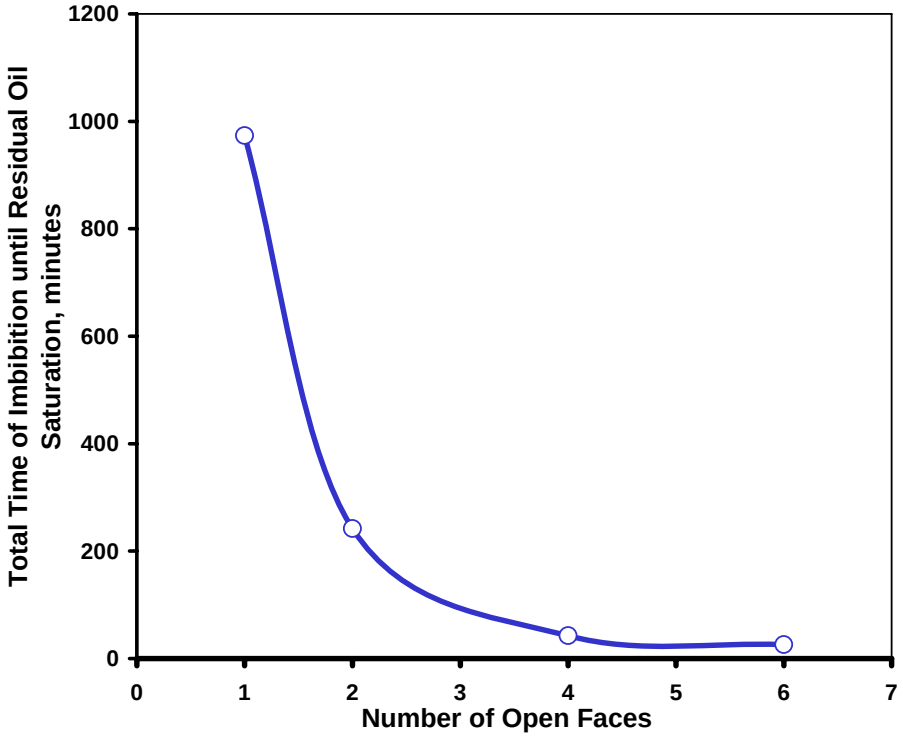

Fig. 1.4.11 — Absolute time for imbibition to reach Sor as a function of the faces available for imbibition.

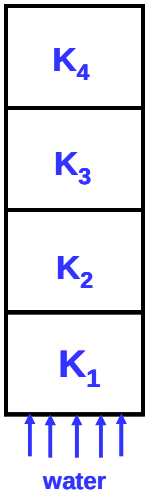

Fig. 1.4.12 — OEO imbibition model: first case $k_1>k_2>k_3>k_4$ and second case $k_1<k_2<k_3<k_4$.

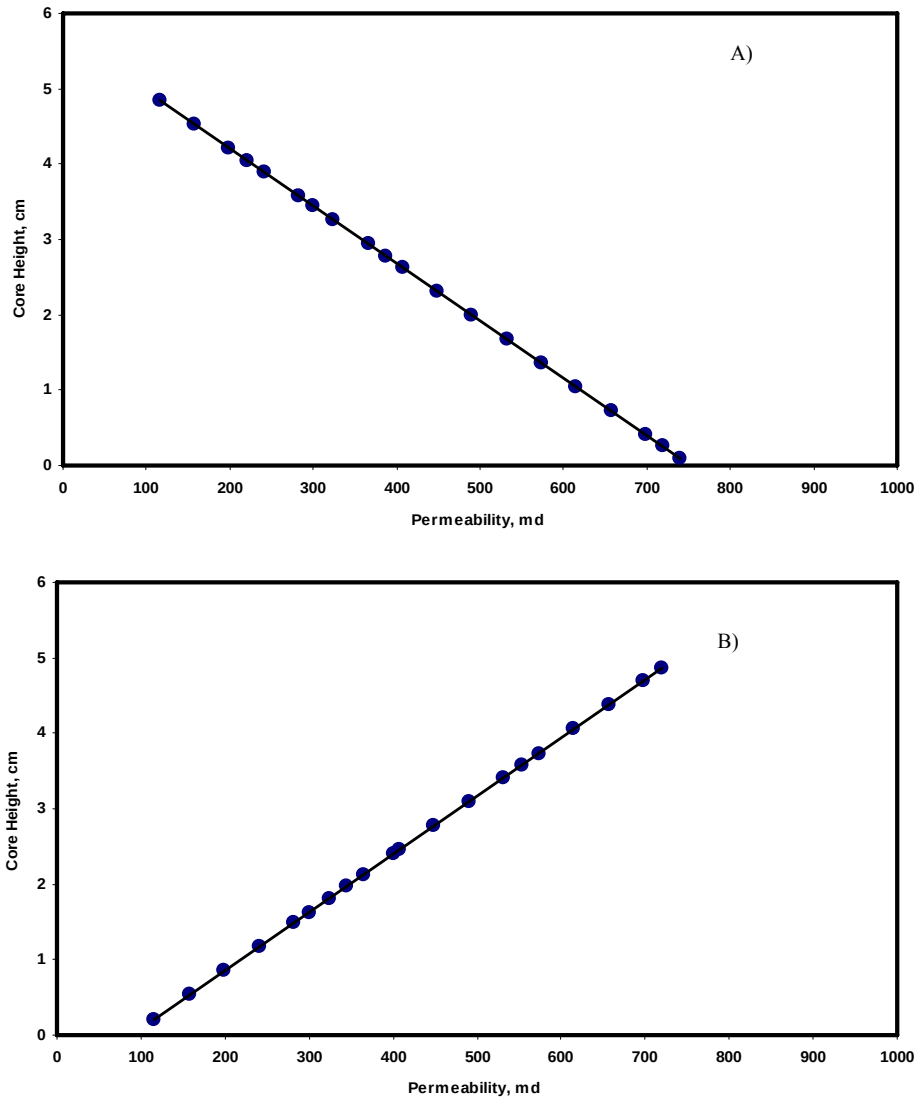

Fig. 1.4.13 —Permeability profiles along the core: A) $k_1>k_2>k_3>k_4$, B) $k_1<k_2<k_3<k_4$.

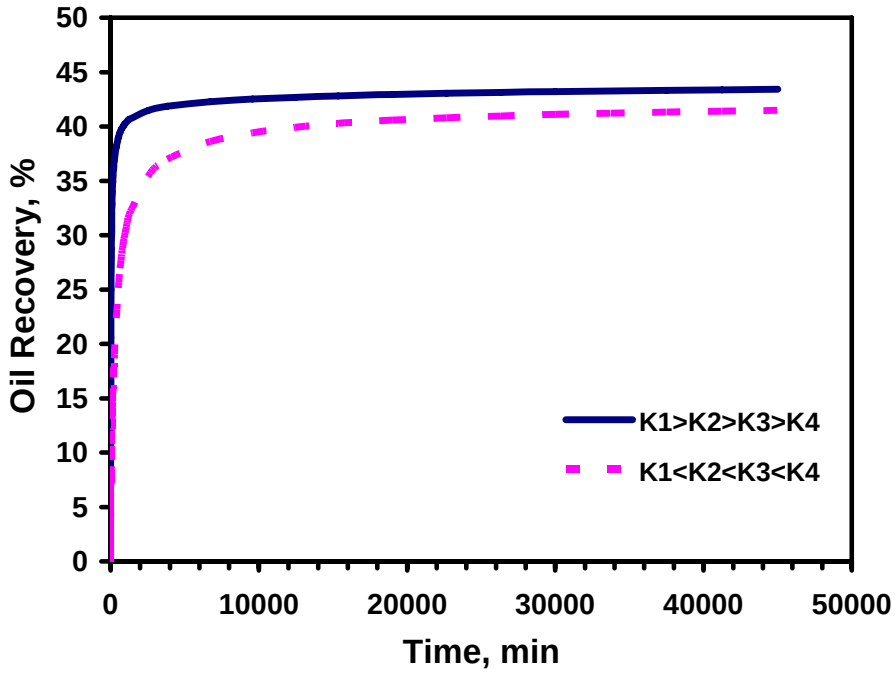

Fig. 1.4.14 — Oil recovery curves for different permeability profiles along the core.

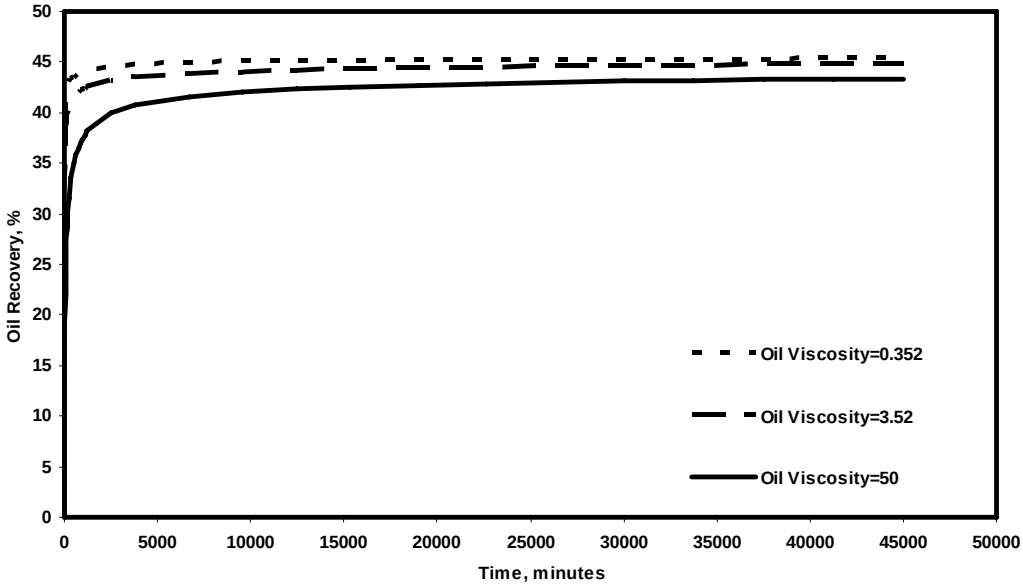

Fig. 1.5.15 — Oil recovery curves with different oil viscosities.

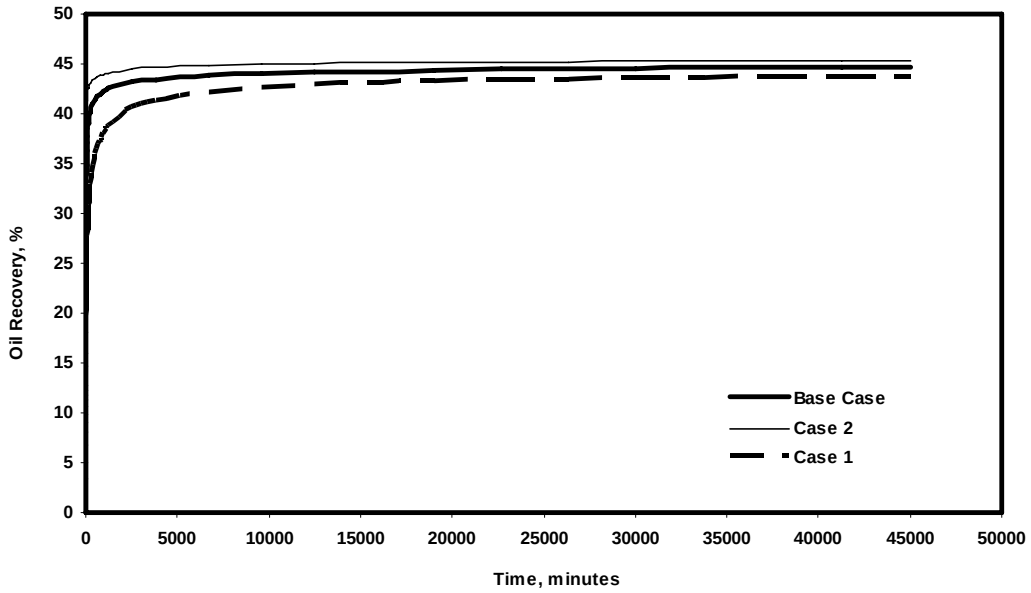

Fig. 1.4.16 — Effect of different capillary pressure on oil recovery.

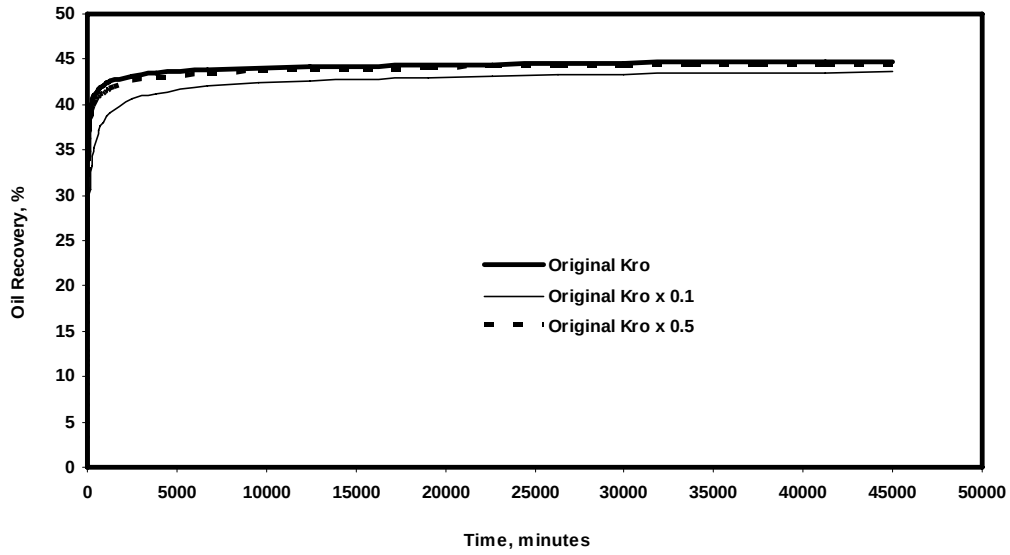

Fig. 1.4.17 — Effect of different oil relative permeabilities on oil recovery.

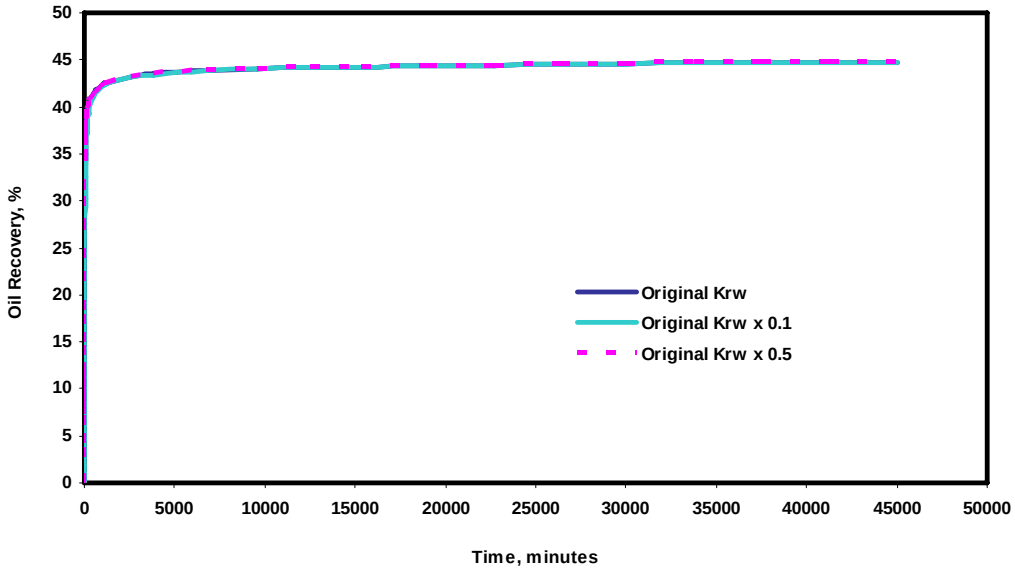

Fig. 1.4.18 — Effect of different water relative permeabilities on oil recovery.

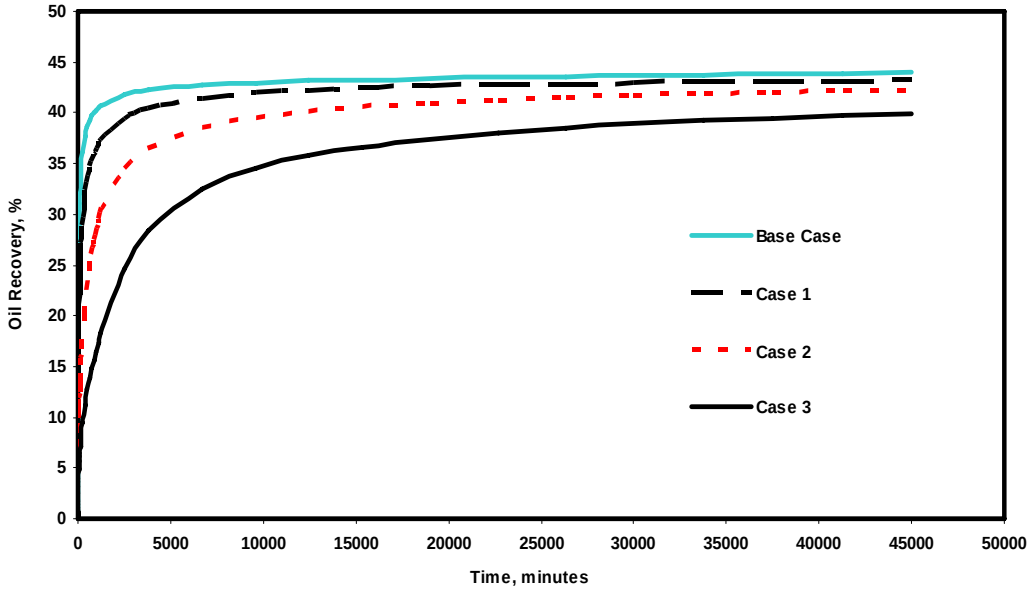

Fig. 1.4.19 — Effect of different fracture spacing on oil recovery.

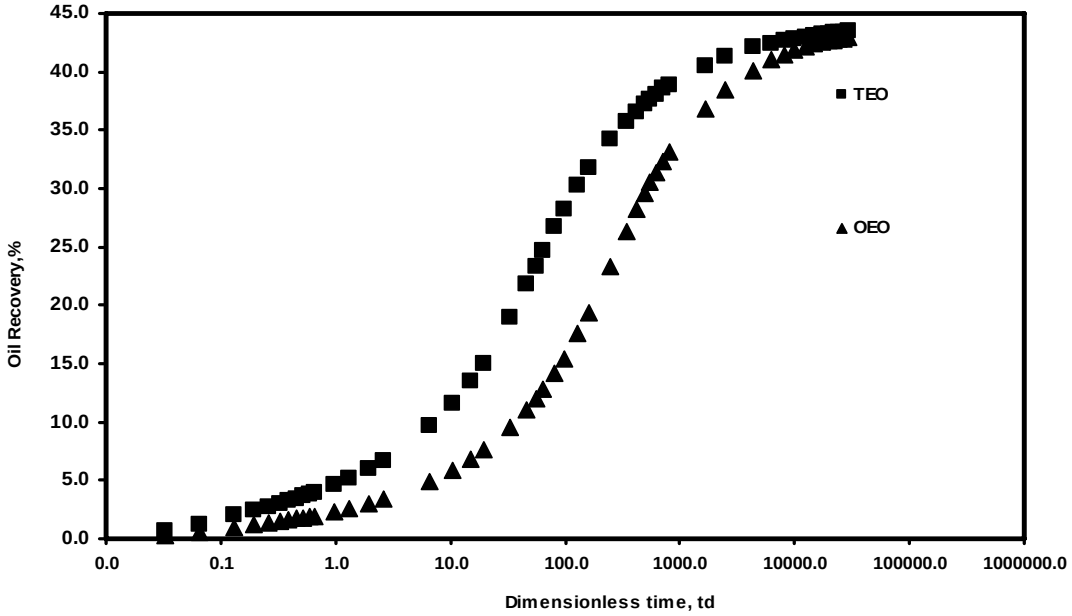

Fig. 1.4.20 — Correlation of the results for the systems with different boundary conditions, using the length of the core in the equation of dimensionless time.

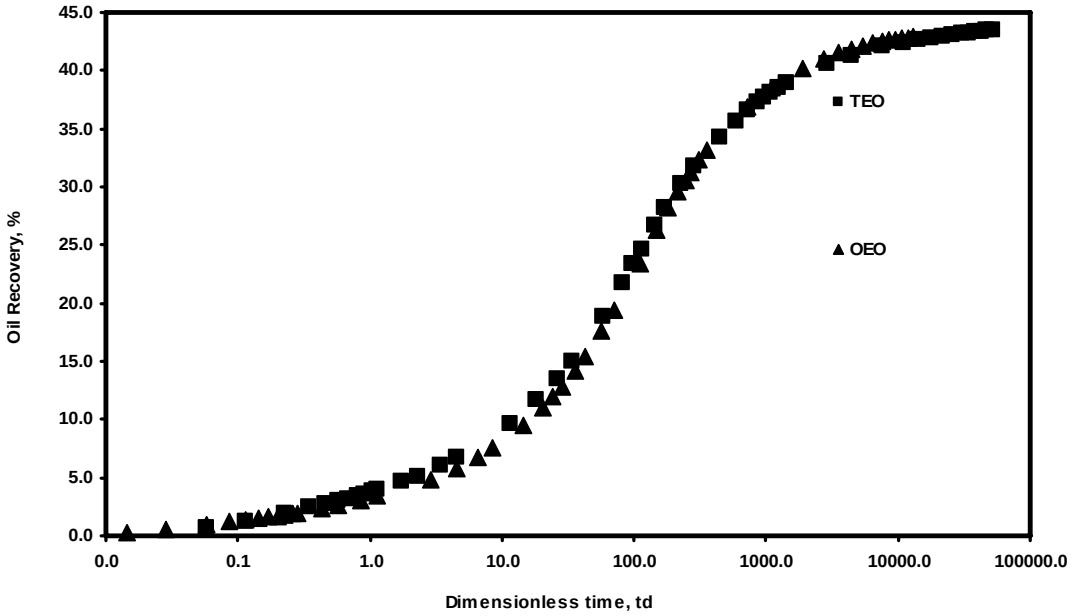

Fig. 1.4.21 — Correlation of the results for the systems with different boundary conditions, using the characteristic length in the equation of dimensionless time.

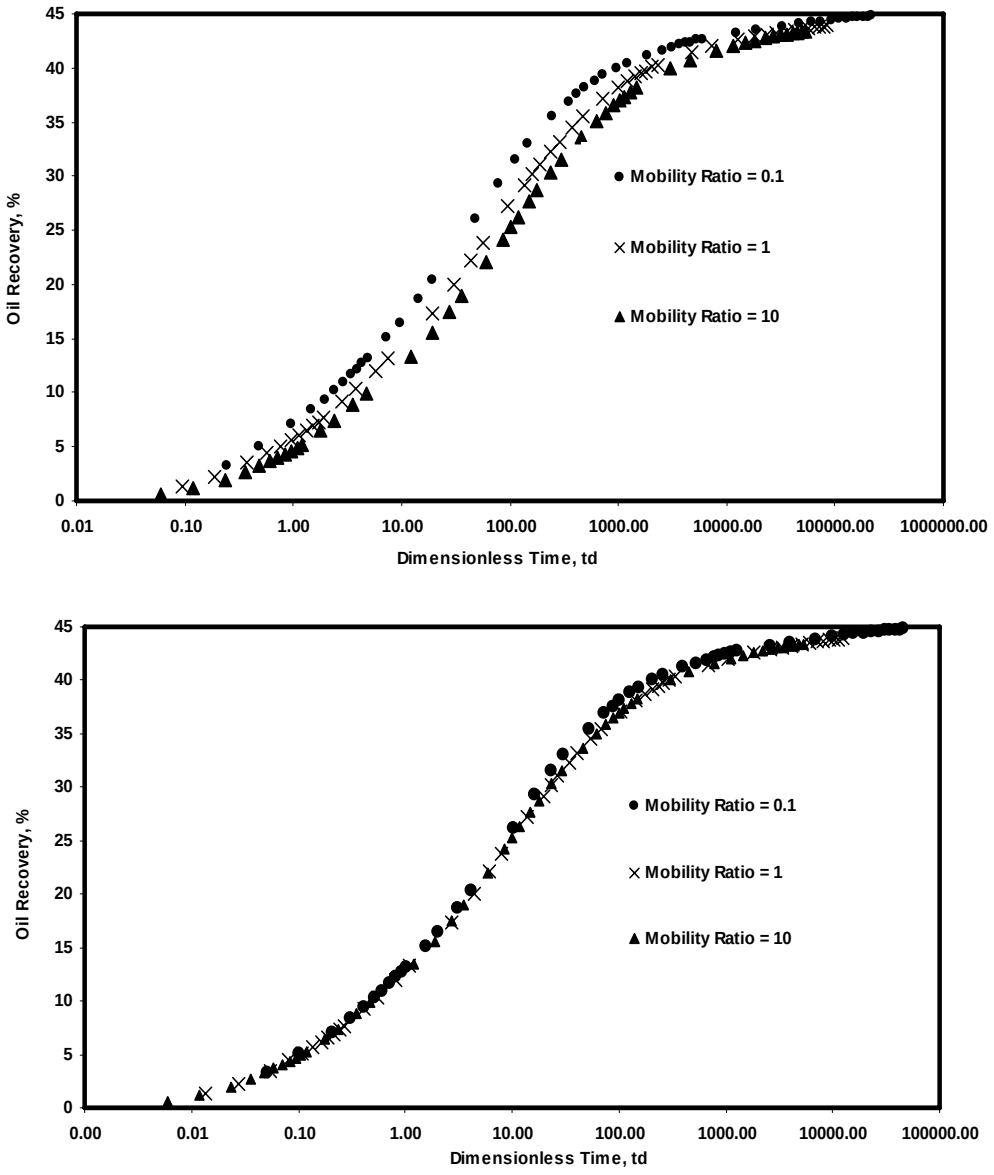

Fig. 1.4.22 — Comparing correlation of the results for the systems with different mobility ratios using Eq. 1.4.10 and Eq. 1.4.11 – Two Ends Open.

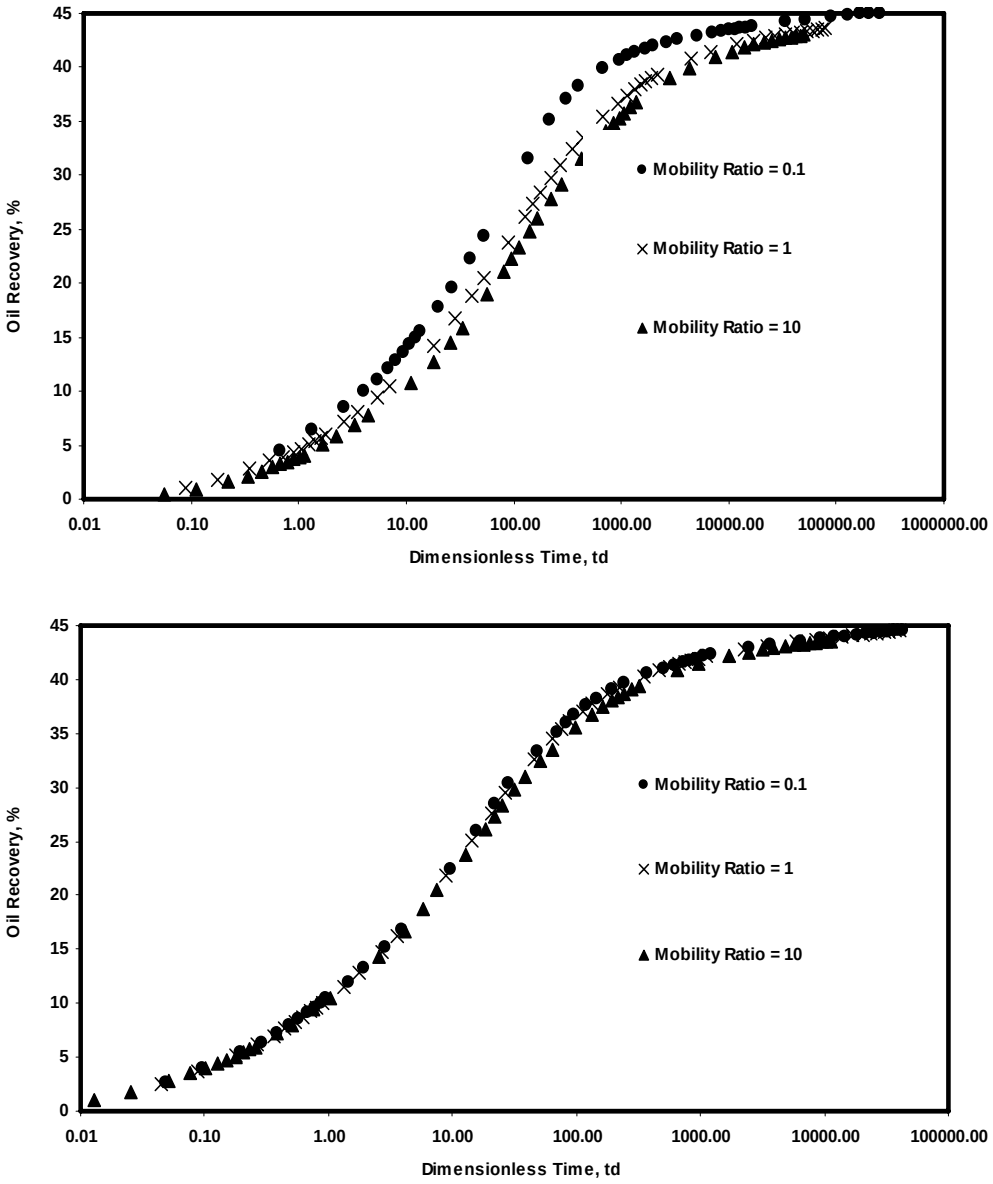

Fig. 1.4.23 — Comparing correlation of the results for the systems with different mobility ratios using Eq. 1.4.10 and Eq. 1.4.11 – One End Open.

Chapter I-5

Application of X-Ray CT for Investigation of CO_2 and WAG Injection in Fractured Reservoirs

1.5.1 INTRODUCTION

Fractured reservoirs form a large percentage of the world's hydrocarbon reserves. However, in spite of their wide occurrence and huge reserves, the oil recovery from most of these reservoirs is extremely low. This can be attributed to their poor response to both secondary and tertiary recovery operations. In a fractured system, the displacement process is dependent on the fracture/matrix geometry, size, and interaction apart from other physical phenomena. [1] Uleberg and Hoier [2] suggest that the injection fluid tends to flow through the highly permeable fractures, often resulting in early breakthrough and poor sweep efficiency. This is especially true when the displacing phase is a highly mobile fluid like CO_2. To improve the sweep efficiency and delay breakthrough, the mobility of the displacing fluid in fractures has to be controlled.

Several field cases [3-6] and laboratory experiments [7-9] indicate that the water-alternating-gas (WAG) process has been an effective mobility control method in most cases. In a fairly homogeneous system, water invades the zones previously invaded by the gas, subsequently diverting the gas into other zones. [10] But a completely different situation prevails in the presence of extreme heterogeneities like fractures. In such a case, the conformance control agent must be able to effectively divert the fluid into the matrix, thereby delaying breakthrough and reducing oil bypass. But the performance of WAG in terms of mobility control in fractures has not been adequately studied.

We investigated CO_2 flow in fractures, in the presence of water as a mobility control agent. Immiscible CO_2 flooding experiments were first conducted using homogeneous cores (in the absence of fracture) at different injection rates to serve as a comparison for the fractured core experiments. The cores were then fractured using a core splitter. Experiments were then conducted in fractured cores with continuous CO_2 injection and injection of specific pore volumes of water and CO_2. One experiment was also performed

after adding a cross-linker to the solution to form a gel. During each injection, CT scans covering the entire length of the core were taken in order to study fluid transport in the matrix and the fracture. Saturation distributions were obtained at various stages during the course of the experiment.

1.5.2 EXPERIMENTAL SETUP

The experimental setup consists of five main components – the injection system, the coreflood cell, the CT scanner, the production system and the data acquisition system. A brief description of each of the components is given below.

The injection system consists of two sets of 1-liter accumulators, one each for the oil and water, and one 2-liter accumulator for CO_2. All the accumulators are connected to an ISCO 5000 D syringe pump**.** The pump is equipped with a programmable controller that can be set to deliver at a constant flow rate or a constant pressure. Water is injected below the piston in the accumulator, and this increases the pressure of the fluid above the piston to the desired level. A flow switching valve is used to inject oil, water, or CO_2 into the coreflood cell.

The core holder measuring 21 in. long is made up of aluminum for use with the CT scanner. It is capable of holding cores up to 1 ft. in length and 1 in. in diameter. A Viton Hassler sleeve surrounds the core and is secured to plungers at the ends of the core holder. The coreflood cell has an inlet for hydraulic oil that is used to apply overburden pressure. A pump is used to pressurize the cell by injecting hydraulic oil into the Hassler sleeve – inner wall annulus, and pressures up to 7,000 psi can be obtained in this manner.

The CT scanner is a fourth generation Universal systems HD 200 system with a resolution of 0.3 mm x 0.3 mm. This scanner can be used to scan a maximum diameter of 48 cm with a maximum scan time of 4 sec per scan. Cross-sectional scans of the core sample are made at regular intervals during the experiment. The data obtained from the CT scanner is transferred to the image-processing system installed in a Sun workstation. The cross-sectional images can then be used for porosity and saturation determination or reconstructed for flow visualization.

The outlet end of the core holder is connected to a precision needle valve which serves as the backpressure regulator and is used to increase pressure in the system. Also

connected is a high-precision metering valve to allow minute adjustments to the fluid flow rate. The produced fluid is collected in a graduated cylinder and any gas produced is measured using a wet test meter.

Two Omega pressure transducers, one each at the inlet and the outlet, are used in conjunction with an Omega OMB 55 data acquisition system. The pressures can be observed and acquired real time from the personal computer connected to the DAQ.

A schematic of the experimental setup is shown in Fig. 1.5.1.

1.5.3 EXPERIMENTAL PROCEDURE

The oil used for the experiments is a mixture of refined Soltrol 130^{TM} and 1-iodohexadecane. Previous measurements have shown that the iodohexadecane serves only as the doping phase and does not alter the interfacial tension between the fluids. [11] The cores used were Berea sandstones with a diameter of 2.5 cm (1 inch) and a length of about 10 cm (3.9 inch). Porosity measurements made using CT scanner revealed that the cores have porosity in the range of 18 to 21%. The pressure and temperature were maintained at 800 psi and 25º C for all experiments. These parameters were important to ensure that the displacements were immiscible and also obtain a clear contrast between the fluids in the CT scans. Fluids were injected into cores at constant rates or at rates that were varied to maintain constant pressure. Produced fluids were collected in graduated cylinders. The displacement processes were studied during the experiment where the injection rates, production volumes, and pressure drops were measured. Fluid saturation distributions were also indirectly measured using CT scanning. The overall efficiency of the process was analyzed by combining the CT measurements and the external effluent volume measurements. A general outline of the experimental procedure is given below:

1. The core is first heated to about 150º F for a sufficient period of time to remove all residual water saturation and evacuated using a vacuum pump.
2. The evacuated dry core is scanned at a confining pressure of about 1,000 psi.
3. For a fractured core experiment, these steps are repeated after fracturing the core.
4. The core is flooded with CO_2 at the desired temperature and pressure to obtain the scans at 100% CO_2 saturation.
5. The core is then evacuated again in the vacuum chamber.

6. The evacuated core is saturated with doped oil in the vacuum chamber for a period of 48 hr.
7. The oil saturated core is transferred to the aluminum core holder and about 15 pore volumes of oil are injected to ensure complete saturation.
8. The backpressure regulator at the outlet is fully closed and the pressure in the core holder is allowed to build up. Care is taken that the overburden pressure is always at least 300 psi higher than the pressure inside the sleeve.
9. Once the desired pressure is reached, oil injection is stopped.
10. The oil-saturated core is now scanned again.
11. The pressure in the CO_2 accumulator is increased to be about 50 psi higher than the pressure in the coreflood cell to prevent backflow of oil.
12. CO_2 is now allowed to enter the coreflood cell and any excess pressure above the desired pressure is released through a valve available for this purpose.
13. Injection is then started at the desired rate.
14. The core is scanned at various times to visualize fluid flow and determine saturations at various times.
15. For a WAG experiment, doped/viscosified water is injected when desired and the core is scanned during the injection process.
16. For the experiment with the cross-linker, the gel is injected into the fracture prior to CO_2 injection.

1.5.4 RESULTS AND DISCUSSIONS

Three types of experiments were performed in this study – continuous CO_2 injection in unfractured cores, continuous CO_2 injection in fractured cores, and CO_2 injection in fractured cores in the presence of viscosified water. For the viscosified water case, experiments were conducted with and without the presence of a cross-linker. A discussion of each of the experiments is given below.

1.5.4.1 Homogeneous Core Experiments

Two experiments were conducted using homogeneous (unfractured) cores: a high injection rate case where CO_2 was injected at about 1 cm^3/min and a low injection rate case where CO_2 was injected at 0.03 cm^3/min. The goal of these two experiments was to

investigate bypassing mechanisms at the two injection rates and also observe the difference in sweep in the two cases.

1.5.4.1.1 High Injection Rate

Fig. 1.5.2 depicts the cross-sectional scans taken at different times during the experiment. Fig. 1.5.2a represents the dry core scans, with the first scan being the injector end and the last scan being the producer end. In these scans the bright blue color represents regions of high density, whereas the dark blue represents regions of low density. The same kind of difference can also be seen in the oil-saturated core scans (Fig. 1.5.2b) where the red color shows regions of high density. Once injection is started, CO_2 can be seen as a blue spot (Fig. 1.5.2c) and a decrease in the CT number (a number dependent on density, characteristic of a particular material) indicates an increase in CO_2 saturation (Fig. 1.5.3). The last set of scans (Fig. 1.5.2e) taken after about 1 hour of injection, show that the core is now almost fully saturated with CO_2. At this point, the produced fluid was only CO_2 and about 95% of the oil had been recovered. However, more than 5 p.v. of CO_2 had to be injected to obtain this recovery.

Fig. 1.5.4, showing the reconstructions of the cross-sectional images, gives a better picture of the fluid flow in the core during CO_2 injection. The injected CO_2 enters the core, sweeping most of the oil near the injection port (left), but tends to flow through the center of the core near the producing port (right), hence bypassing a considerable amount of oil. Continuous injection of CO_2 for a sufficient amount of time allowed CO_2 to contact all regions of the core and squeezed the oil out of those regions. This type of flow commonly occurs in homogeneous cores. However, Fig. 1.5.4 shows that even in a supposedly homogeneous core, some degree of heterogeneity is still present. The red colored spots on the side of the producing port (right) in Fig. 1.5.4 represent regions of higher density and lower porosity. The CO_2 flow line thins down at particular regions and remains that way for some time. This phenomenon is also observed in the cross-sectional images and the saturation distributions of CO_2 at different stages, obtained from the scans.

1.5.4.1.2Low Injection Rate

Fig. 1.5.5 represents the horizontal reconstructions of the cross-sectional images at different times for the low injection rate case. These images clearly depict the effect of

injection rate on sweep and use of CO_2. At this injection rate, CO_2 does not bypass oil and a very good sweep is obtained. This is because of the long time allows CO_2 to diffuse uniformly into all parts of the core. Also, the breakthrough time of CO_2 reduced considerably compared to the previous case. The effect of heterogeneity in the core is the same as in the previous case. Saturation distributions along the length of the core were obtained from the CT scans. Fig. 1.5.6, the CO_2 saturations from the injector end to the producer end for both the injection rates, shows that breakthrough occurs after about 0.57 p.v. of CO_2 injection for the low injection rate, whereas in the high injection rate case breakthrough occurred at only about 0.3 p.v. of injection. The figure also shows that the final recovery obtained in both cases is consistently above the 90% range, although the difference in the amount of CO_2 used to obtain such a high recovery is huge. Such a high value of oil recovery obtained even when the displacement is immiscible can be attributed to the light, low viscosity oil used in the experiments. Although the sweep in the low injection rate case is very good, the time required to obtain the final recovery value is very high. Hence, we must optimize the injection rate before beginning injection. Fig. 1.5.7 shows the oil recovery obtained using CT saturations for the two cases.

1.5.4.2 Fractured Core Experiments

1.5.4.2.1Continuous CO_2 Injection

The permeability of a fracture is typically about 103 to 106 times greater than the permeability of the porous rock. In a fractured system, the tendency of the fluid would be to flow through the high permeability fracture, which leads to early breakthroughs. This phenomenon was observed during CO_2 injection in the fractured core where breakthrough occurred after about 10 minutes of CO_2 injection (0.09 p.v.). Fig. 1.5.8 shows the cross-sectional scans of the oil-saturated core and the scans at various stages of CO_2 injection. In these scans the color scale has been chosen such that the blues indicate the lowest CT numbers while red and pink indicate the highest CT numbers, with green and yellow being the intermediates. Thus, with an increase in CO_2 saturation, the CT number decreases and hence the color changes to a dark shade of blue. These scans show that CO_2 moves through the fracture while simultaneously displacing small amounts of oil from the matrix. In such a case, some amount of CO_2 always breaks through without contacting any oil, thus greatly reducing the sweep efficiency. The diffusion process is

very slow, but given a large amount of time and CO_2, a good recovery may be obtained. In this experiment, the recovery obtained after 2.2 p.v. of injection is about 58%.

1.5.4.2.2WAG Experiment

To prevent early breakthrough of CO_2 and improve sweep efficiency, some kind of conformance control agent is required in the fracture. Although water-alternating-gas (WAG) has been the most widely used method for mobility control, its success has not been universal. So we conducted a set of experiments to analyze the performance of WAG in the presence of fractures. The first experiment tested water mobility in the core. Brine tagged with both sodium iodide and potassium iodide was used to improve the contrast between the fluids. Water was injected at a rate of about 0.1 cm^3/min into an oil-saturated core. During the experiment we observed that the water mobility in the core was very high and the breakthrough occurred at about 0.4 p.v. of injection. From the results of this experiment, we concluded that brine by itself cannot delay the breakthrough of CO_2 from the fracture. So we decided to increase the viscosity of water with the aim of reducing its mobility. A conventional WAG process involves alternate injection of specific pore volumes of gas and water to reduce the relative permeability of the gas and hence its mobility. But here, our aim is to delay CO_2 breakthrough, so we decided to inject the viscosified water into the fracture to "heal" it to some extent so as to the reduce CO_2 mobility in fracture. We used Xanthan gum to increase the viscosity of water because of its good injectivity and relative insensitivity of its viscosity to salinity. [12] Sufficient Xanthan was added to the iodated brine to increase the viscosity to about 20 cp. This was then injected into the core with the injection port aligned with the fracture. Although no problems were encountered with the injectivity of the liquid, we found that once the viscous liquid entered the core, a considerable amount of "leakoff" occurred into the matrix. The main reason for this leakoff is that the cores we used were strongly water wet and imbibition of water into the porous matrix was an extremely quick process. By the time the liquid filled the entire fracture and breakthrough occurred, a considerable quantity had leaked off into the rock and more than 65% of the oil had already been recovered. Fig. 1.5.9 shows the scans taken at liquid breakthrough where the red color represents the viscous liquid with a higher CT number because of the iodated brine. At this point, liquid injection was stopped and CO_2 injection was started. The liquid

remaining in the flow lines was first displaced into the core by CO_2 and when CO_2 contacted the core, about 80% of the oil had been recovered. This was considered to be the residual oil saturation for the core to water. CO_2 injection resulted in an incremental recovery of about 4.5%. In this case we observed that the breakthrough of CO_2 was delayed considerably in the presence of the viscous phase. Although the overall recovery obtained was higher than that obtained by continuous CO_2 injection, the viscous water, not the CO_2 was responsible for most of the recovery possibly because of the strong water-wet nature of the cores used. Using a liquid of higher viscosity (about 30 cp) also gave us similar results. Liquid leakoff into the porous rock can be minimized by using suspended particulate matter. [13, 14] Also, in an oil-wet core, the amount of water imbibing into the porous rock would obviously be less, and hence the viscous liquid can remain in the fracture, healing it to some extent. But this liquid can still flow and would be produced when CO_2 flows through the fracture. So CO_2 and liquid have to be injected alternately, similar to the WAG process. Another method suggested in the literature to minimize leakoff is the addition of a cross-linker to form a gel, when its propagation becomes extremely slow or negligible. [13]

1.5.4.2.3Experiment with Gel

In this experiment, we used cross-linked gel was used to delay breakthrough and improve recovery, assuming that any gel that can heal the fracture effectively would serve the purpose. We chose guar with a borate cross linker because of their easy availability. One of the important considerations in using a gel for conformance is the injection pressure. Once the gel is formed by the cross-link process, it has a huge increase in the resistance to flow. [15] But Seright [13] proved that gels with low resistance factors can be injected into the fracture without too much “screenout.” The gel was injected directly into the fracture at high pressure, with pressure drop of about 90 psi/ft. Once the fracture was filled with the gel, we allowed a 16-hour setting time before the start of CO_2 injection. Fig. 1.5.10 shows the scans taken before the start of injection, at breakthrough, and at the end of the experiment with their corresponding ortho reconstructions. We can see a preferential movement of CO_2 in one half of the core compared to the other. Investigation after the experiment showed that two of the grooves on one side of the injection face were blocked by the gel. This caused most of the injected CO_2 to flow to

the other half of the injection face (open grooves). This also led to a much earlier breakthrough than we had expected, it clearly shows that a good sweep has been obtained on both halves of the core. The final recovery in this case was about 95% after approximately 2.5 p.v. of injection. Fig. 1.5.11, a comparison of the recoveries obtained from the different experiments, shows that the highest recovery is obtained from the experiment using the gel for conformance control.

1.5.5 CONCLUSIONS

1. Injection rates play an important role in affecting oil recovery and breakthrough.
2. Early breakthrough and higher oil bypass are observed at a high injection rate while, low injection rate gives better sweep and lesser utilization of CO_2.
3. Injection rates must be optimized prior to beginning injection.
4. In a fractured system, fluid flow occurs mainly through the fractures. Considerable time is required for the injection fluid to penetrate the matrix and obtain a good recovery.
5. Coreflood experiments using viscosified water confirmed that WAG can delay CO_2 breakthrough and improve recovery. However, leakoff into the porous rock is very high. This leakoff might be much lower in an oil-wet rock, but more work is required to establish this.
6. Formation of gel can eliminate the problem of liquid leakoff into the matrix.
7. Using gel for conformance control results in better sweep and higher recoveries. The type and composition of gel to be used in the presence of CO_2 needs more investigation.

REFERENCES

1. Yaghoobi, H., Tsau, J.S., Heller, J.P., Improving CO_2 Floods in Heterogeneous Media, *paper SPE 35403 presented at the 1996 SPE/DOE Tenth Symposium on Improved Oil Recovery, Tulsa, 21-24 April.*
2. Uleberg, K. and Hoier L., Miscible Gas Injection in Fractured Reservoirs, *paper SPE 75136 prepared for presentation at SPE/DOE Improved Oil Recovery Symposium, Tulsa, Oklahoma ,April 13-17,2002.*

3. Hsie, J.C. and Moore, J.S., The Quarantine Bay 4RC CO_2-WAG Pilot Project: A Post Flood Evaluation, paper SPE 15498 presented at the 1986 SPE Annual Technical conference and Exhibition, New Orleans, 5-8 October.
4. Holm, L.W, O'Brien, L.J., Carbon-Dioxide Test at the Mead-Strawn Field, *paper SPE 3103;Journal of Petroleum Technology, pp. 431-432, April 1971.*
5. Kane, A.V., Performance Review of a Large-Scale CO_2-WAG Enhanced Recovery Project; SACROC Unit- KELLY SNYDER, *JPT 217, Trans., AIME 267, Feb.1979.*
6. Aarra, M.G, Skauge, A., Martinsen, H.A., FAWAG: A Breakthrough for EOR in the North Sea, *paper SPE 77695 presented at the SPE Annual Technical Conference and Exhibition, San Antonio, TX, September 29 – October2, 2002.*
7. Christensen, J.R., Stenby, E.H., and Skauge, A., Review of WAG Field Experience, *paper SPE71203; SPE Reservoir Evaluation & Engineering Journal, pp 97-106, April 2001.*
8. Prieditis, J., Wolle, C.R. and Notz, P.K., A Laboratory and Field Injectivity Study: CO_2 WAG in the San Andres Formation of the West Texas, *paper SPE 22653 presented at the 66th Annual Technical Conference and Exhibition, Dallas, TX, October 6-9.*
9. Akervoll, I., Talukdar, M.S., Midtlyng, S.H., Torsaeter, O., WAG Injection Experiments With In-Situ Saturation Measurements at Reservoir Conditions and Simulations, *paper SPE 59323 presented at the SPE/DOE Improved Oil Recovery symposium, Tulsa, OK, April 3-5, 2000.*
10. Holm, L.W., CO_2 FLOODING: Its Time has Come, *paper SPE 11592; Journal of Petroleum Technology, pp. 2739-2745, December 1982.*
11. Wellington, S.L. and Vinegar, H.J., X-Ray Computerized Tomography, *paper SPE 16983; Journal of Petroleum Technology, pp. 885-898, August 1987.*
12. Cannella, W.J., Huh, C. and Seright, R.S., Prediction of Xanthan Rheology in Porous Media, *paper SPE 18089 prepared for presentation at 63rd Annual Technical Conference and Exhibition, Houston, October 2-5.*
13. Seright, R.S., Gel Placement in Fractured Systems, *paper SPE 27740, SPE Production & Facilities Journal pp 241-248, November1995.*

14. Seright, R.S. and Liang, J., A Comparison of Different Types of Blocking Agents, *paper SPE 30120 prepared for presentation at the European Formation Damage Conference, The Hague, The Netherlands, May 15-16, 1995.*
15. Shahab, H., Jousset, F., Green, D.W., McCool, C.S., Willhite, G.P., Permeability Reduction by a Xanthan/Chromium (III) System in Porous Media , *paper SPE 19634; SPERE, pp. 299-304, November 1993.*

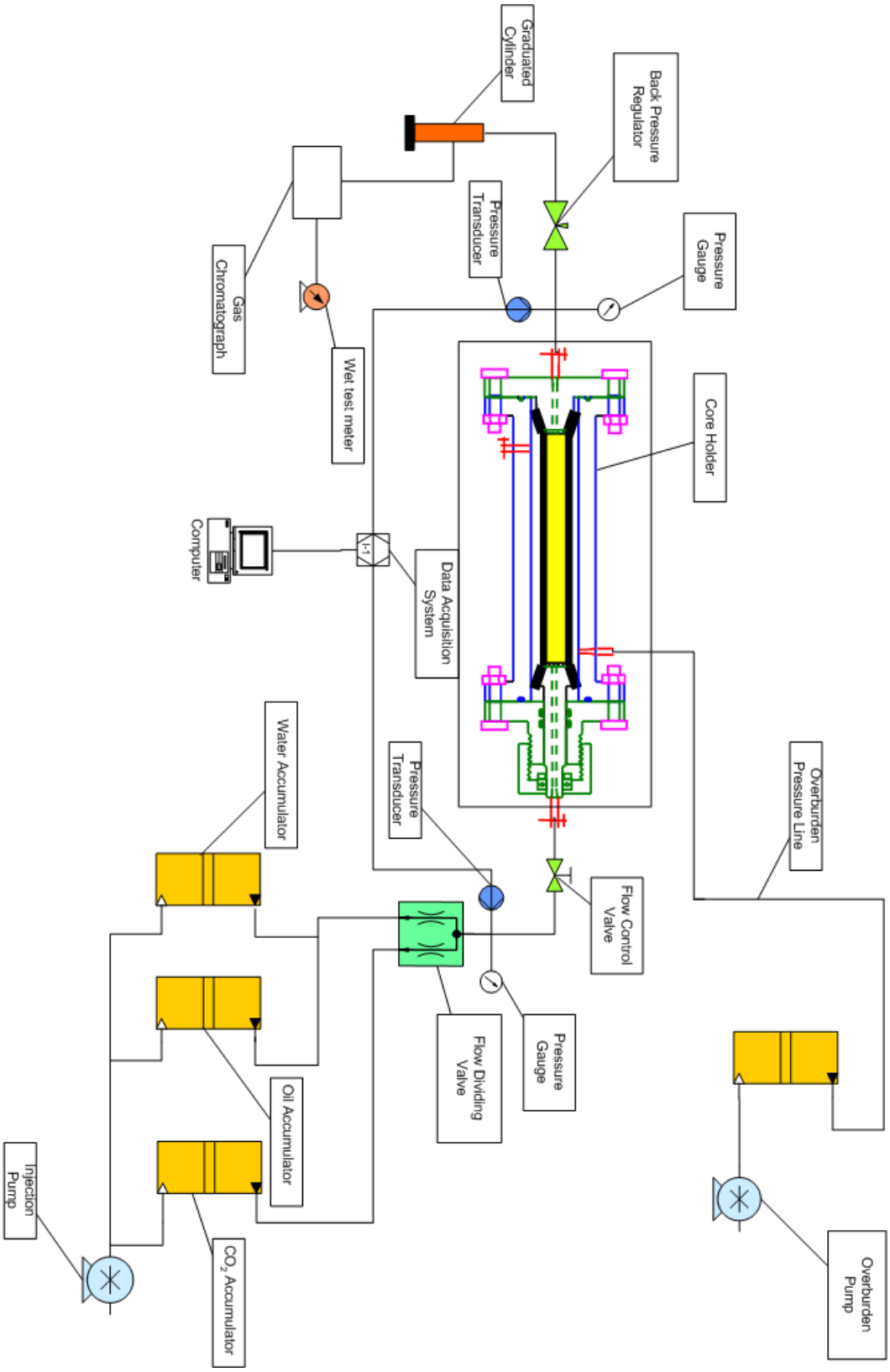

Fig. 1.5.1 — Schematic of the experimental setup.

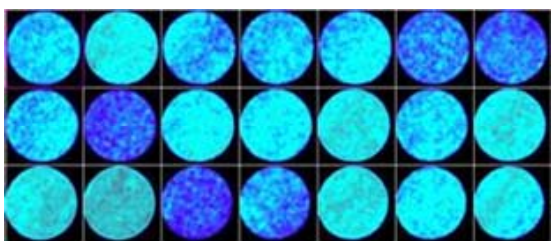

(a) Dry core scans

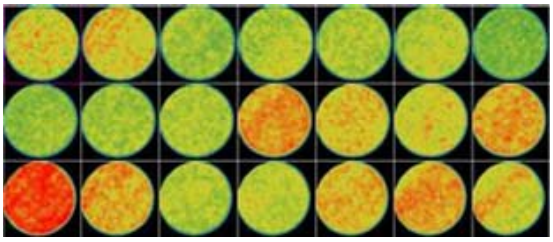

(b) Oil saturated core

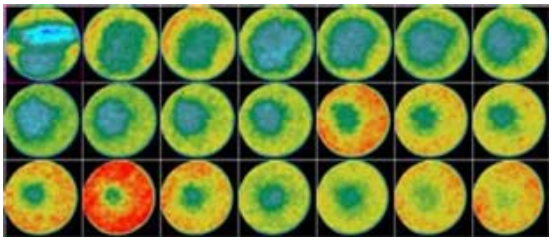

(c) 3 minutes of CO_2 injection

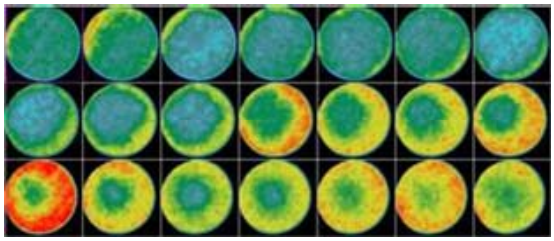

(d) 5 minutes of CO_2 injection

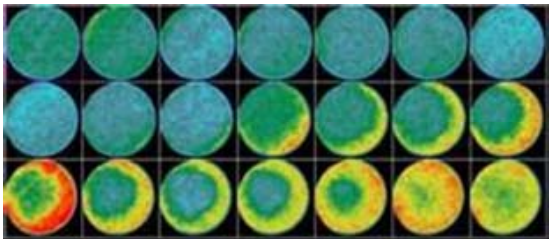

(d) 15 minutes of CO_2 injection

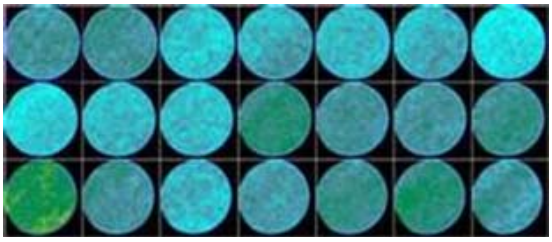

(e) 60 minutes of CO_2 injection

Fig. 1.5.2 — Cross-sectional scans taken at various stages during the experiment.

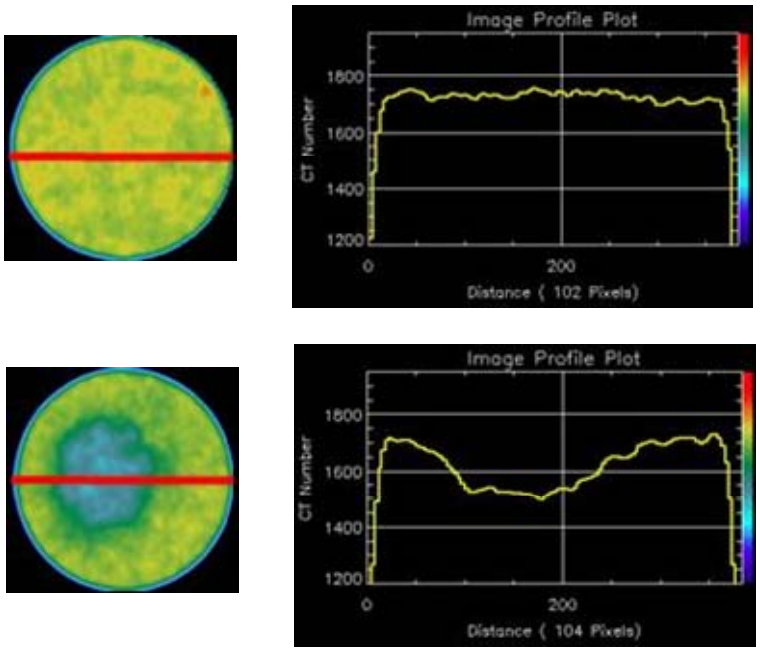

Fig. 1.5.3 — CT number decreases with increase in CO_2 saturation.

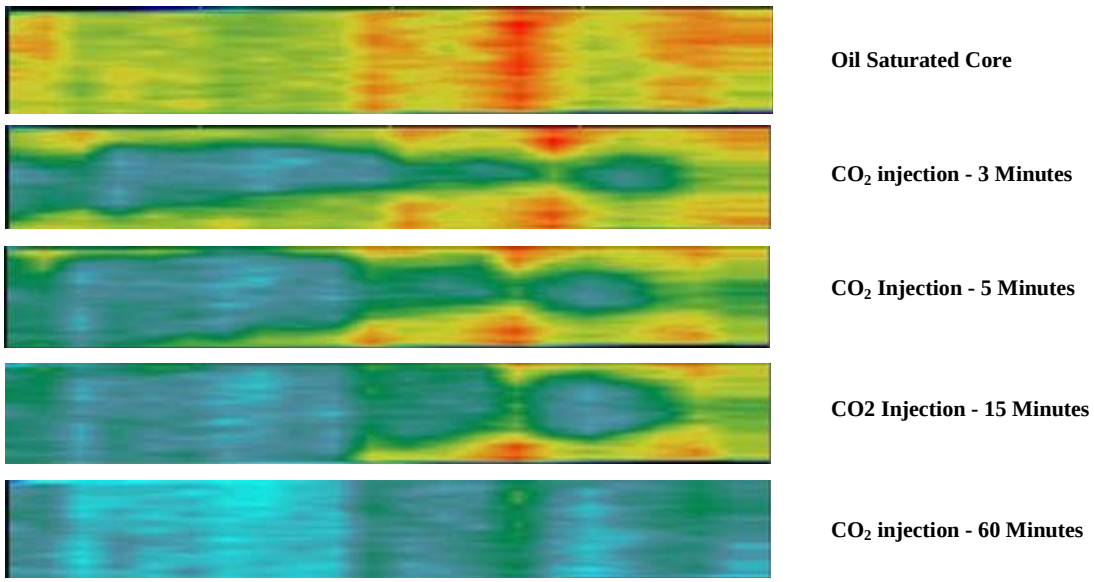

Fig. 1.5.4 — Reconstructions of cross-sectional scans for high injection rate case.

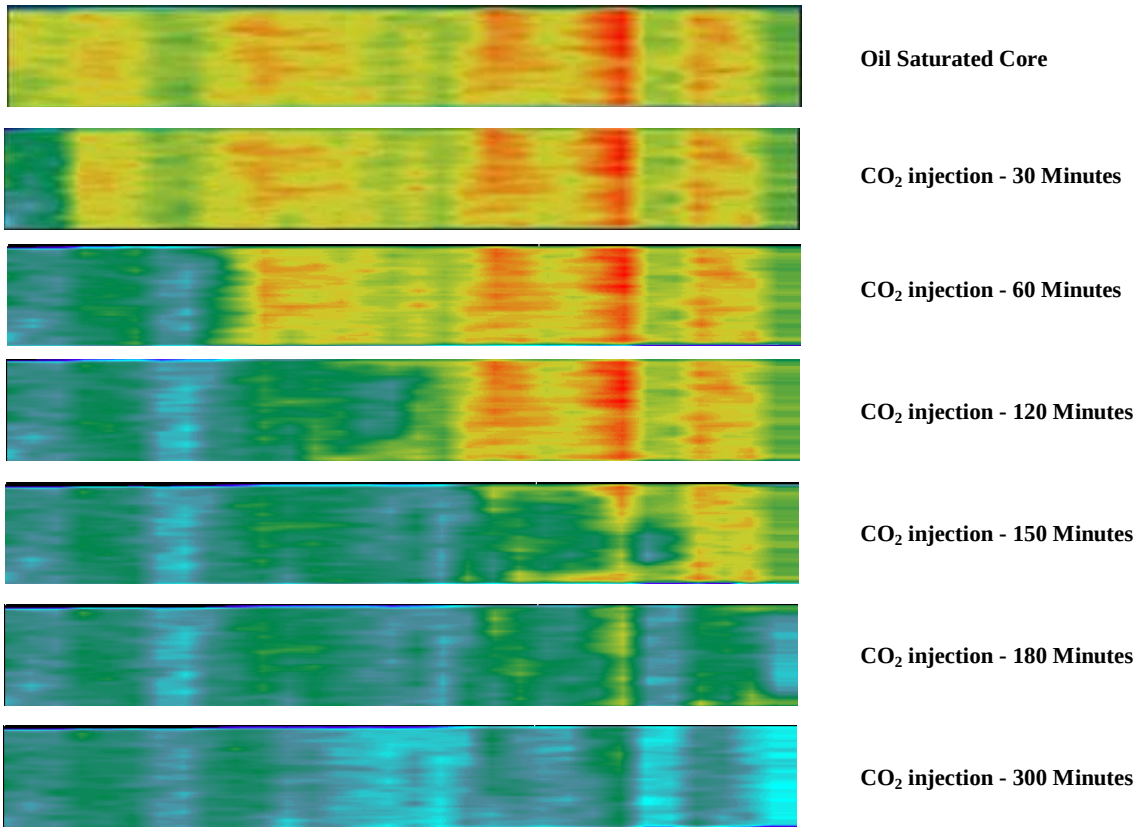

Fig. 1.5.5 — Reconstructions of cross-sectional scans for low injection rate case shows good sweep.

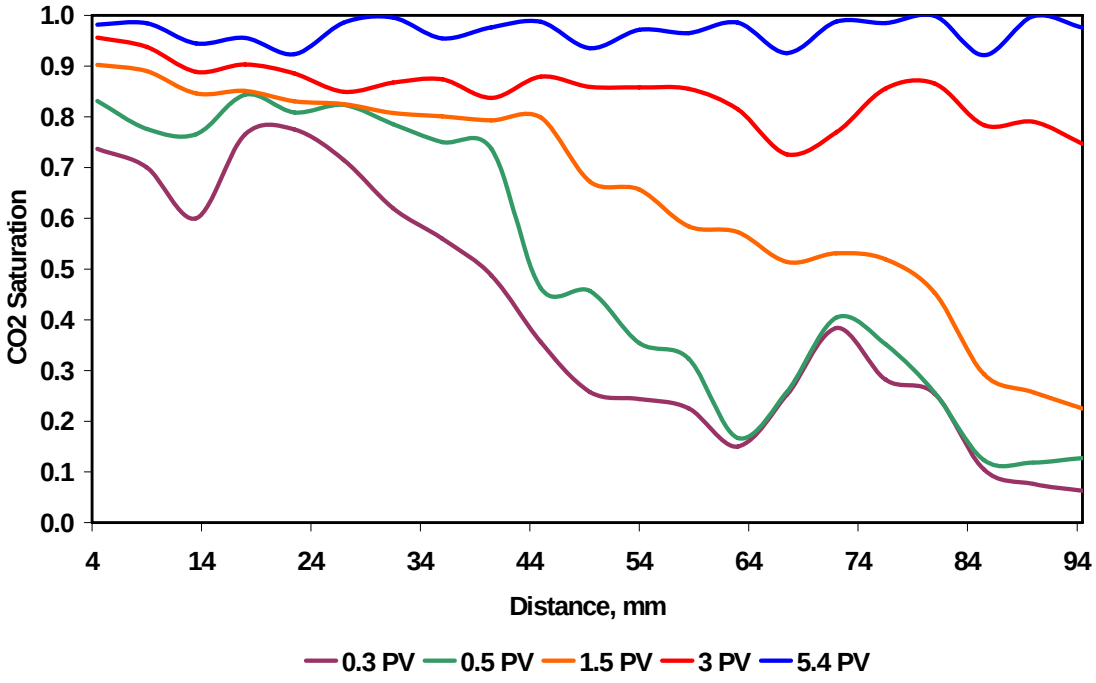

(a). High injection rate

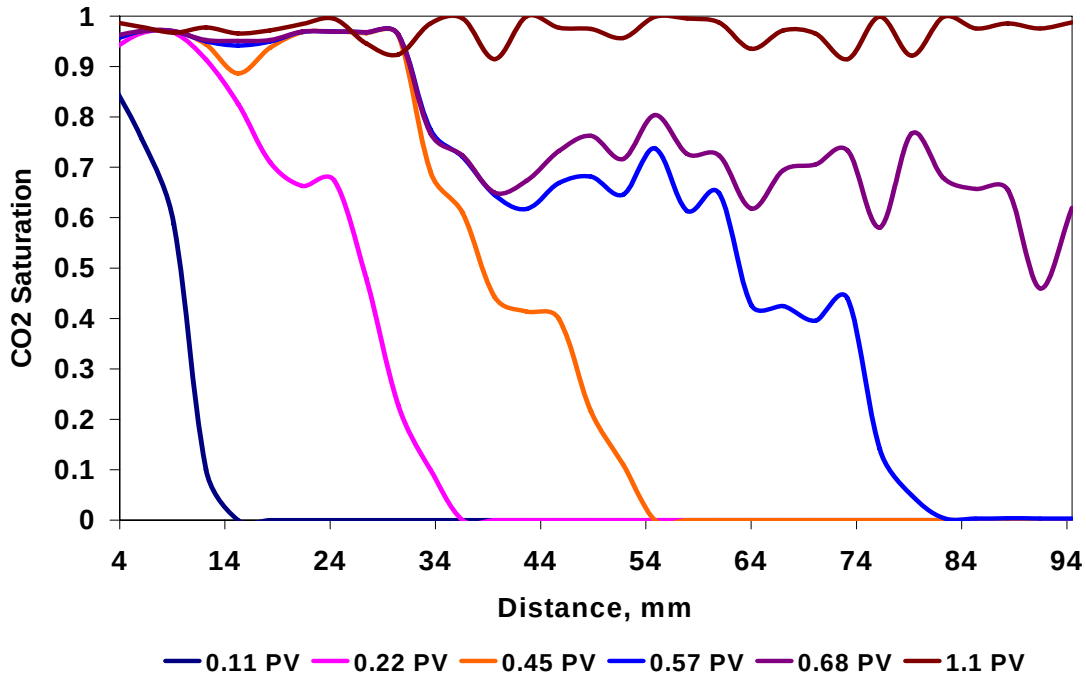

(b). Low injection rate

Fig. 1.5.6 — CO_2 saturations along the length of the core at different stages of injection.

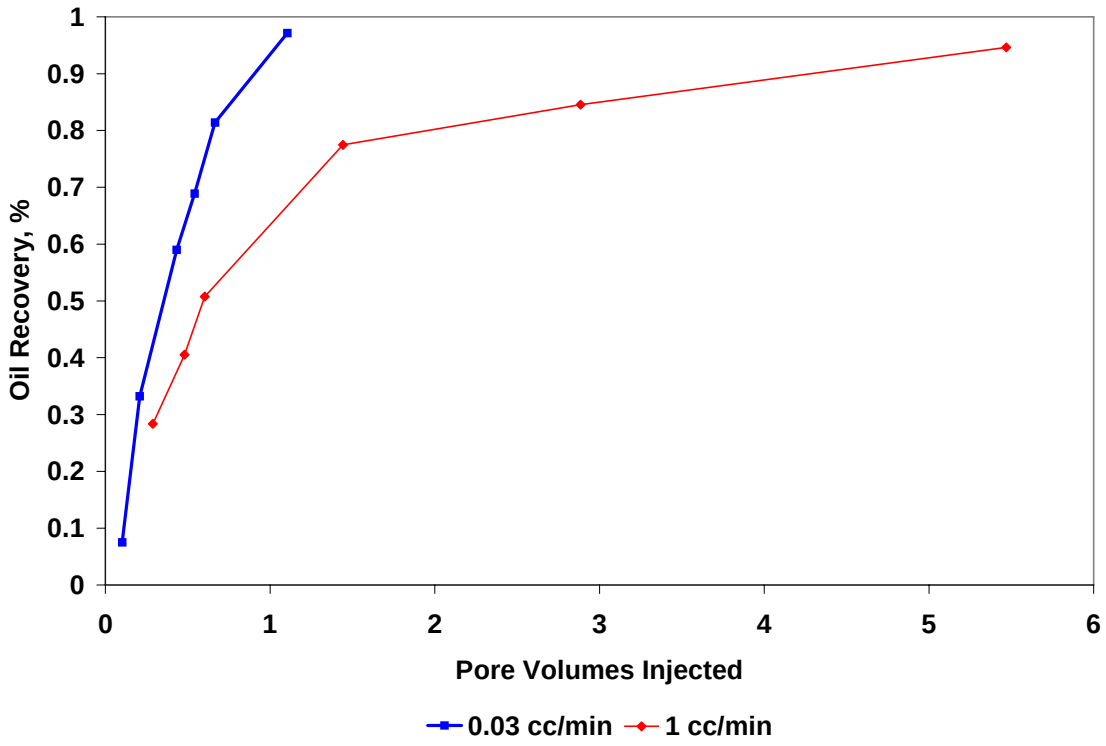

Fig. 1.5.7 — Higher oil recovery is obtained for lesser pore volumes injected in the low injection rate case.

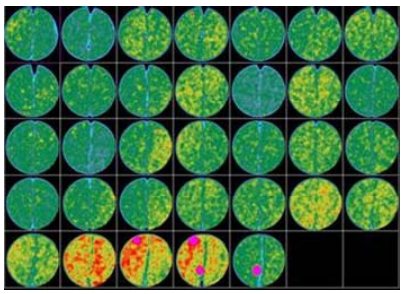

(a). Oil saturated core

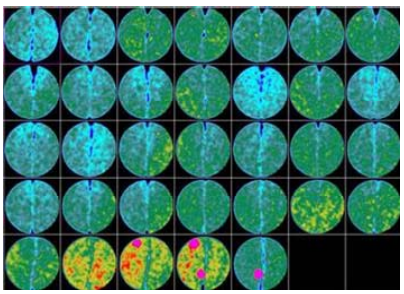

(a). CO_2 breakthrough indicated by increase in CO_2 saturation in the fracture

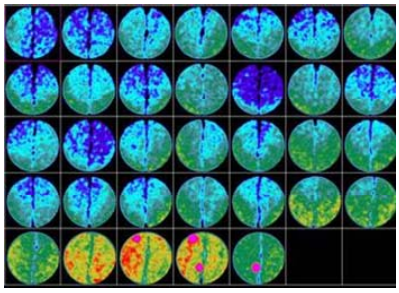

(c). CO_2 saturation after about 1.3 PV of injection

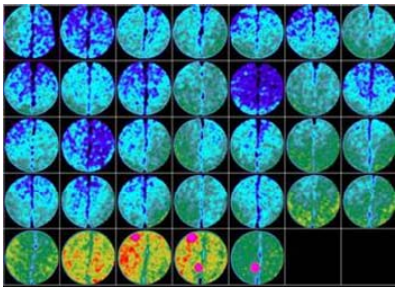

(c). CO_2 saturation at the end of experiment

Fig. 1.5.8 — Cross-sectional scans taken during the continuous CO_2 injection experiment.

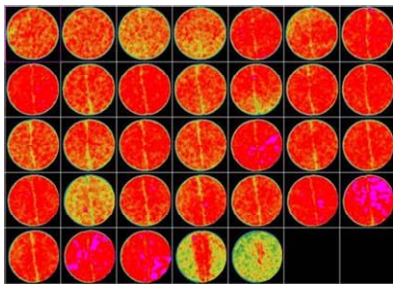

(a). Cross-sectional scans at water breakthrough

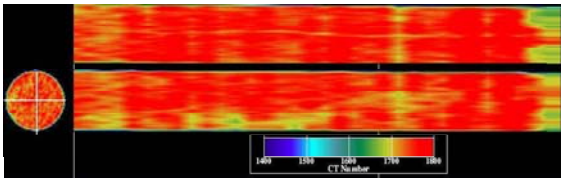

(b). Reconstructions of Cross-sectional scans

Fig. 1.5.9 — Scans taken at water breakthrough where red color indicates water.

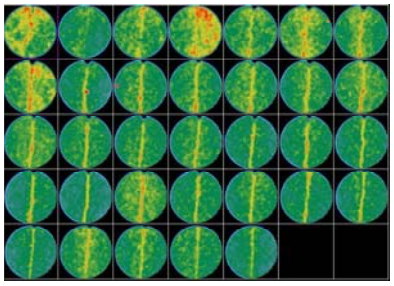

(a). Cross-sectional scans before iniection

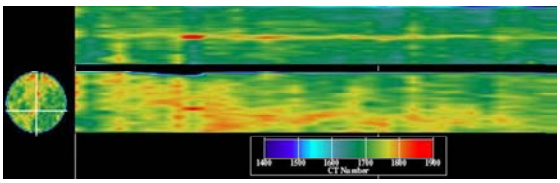

(b). Ortho reconstruction showing gel in the fracture (top) and on the fracture surface (bottom)

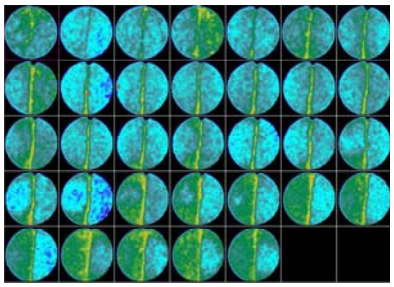

(c). Cross-sectional scans taken at CO_2 breakthrough

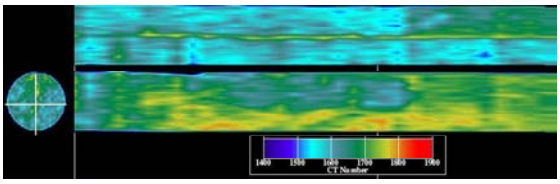

(d). Reconstructions of cross-sectional scans showing preferential movement of CO_2 on one half of the core

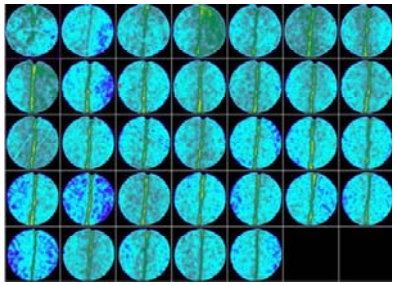

(e). Cross-sectional scans taken at end of injection

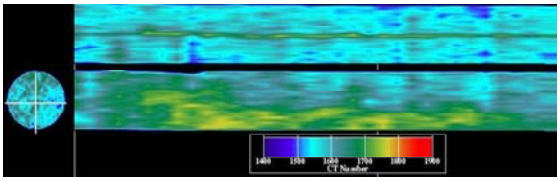

(f). Ortho reconstructions showing gel intact at the end of the experiment

Fig. 1.5.10 — Scans taken at various stages of the experiment in the presence of gel.

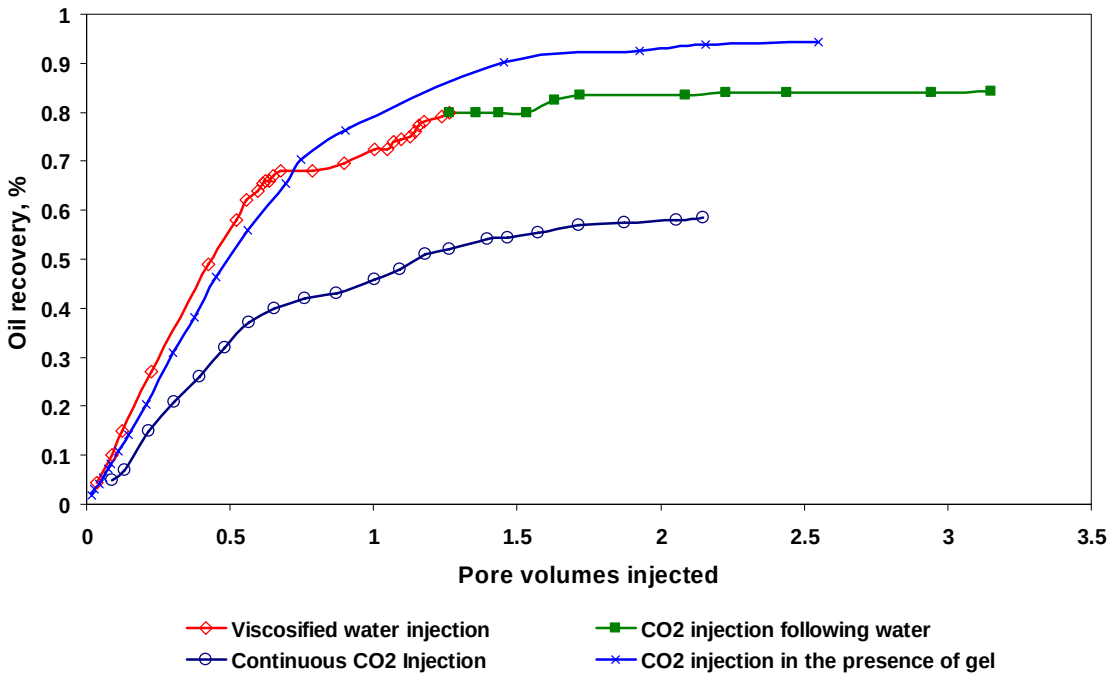

Fig. 1.5.11 — Recovery curves for the various cases showing highest recovery in the presence of gel.

Chapter I-6
Analysis of Gravity Drainage Mechanism in a Short Vertically Fractured Core

1. 6. 1 INTRODUCTION

Gravity drainage is the name given to the recovery process in which gravity acts as the main driving force and gas replaces the voidage volume from which oil has been displaced. In other words, gravity is the dominating force in this type of gas/oil displacement. Gravity drainage can occur during primary depletion phase because of gas cap expansion, or during secondary and tertiary depletion phases when gas is supplied from an external source.[1] Several experiments have proved that the oil recovery due to gravity drainage can be unexpectedly high. Dumore and Schols[2] found that the residual oil saturation in high-permeability sandstone cores with connate water was extremely low (5%) after invasion by gas. This low saturation was also observed in sandpack experiments. Thompson and Mungan[3] reported that gravity drainage under miscible conditions can be a very efficient process, especially in unfractured systems. Hagoort[1] also found that gravity drainage can play an important role in recovering oil from water-wet reservoirs. Espie *et al.*[4] studied the interaction of various forces with gravity drainage. They concluded that this kind of interaction between forces can result in higher oil recoveries than what can be expected from a waterflood. Li *et al.*[5] experimentally investigated CO_2 gravity drainage in the low-permeability fractured Spraberry reservoir and concluded that CO_2 gravity drainage could significantly improve oil recovery after a waterflood. Many field successes have also been reported where gravity drainage was the dominating recovery mechanism. Haldorsen *et al.*[6] investigated the effect of gravity drainage in the Prudhoe Bay field using a repeat compensated neutron log (CNL) and concluded that gravity drainage in the field was very time-effective and provided high displacement efficiencies. Donnelly[7] analyzed the Hilda Lake steam-assisted gravity drainage pilot project and reported that the recoveries obtained from the field were high, as expected from simulation forecasts. Several efforts have attempted to model gravity

drainage. A review of various gravity drainage models by Schechter and Guo[8] summarized four main models for gravity drainage. These include the Caldwell-Parson-Dkystra (CPD),[9] Nenniger-Storrow (NS) model,[8] Pavon-Bruzzi-Verre (PBV) model,[8] and Luan[10] model. Schechter and Guo[8] also presented their own model of gravity drainage. Later, Li and Horne[11] presented their model for predicting the initial oil production rate and average residual oil saturation under free-fall gravity drainage. All these studies, suggest that gravity drainage has traditionally been associated with reservoirs having a large dip angle, largely because researchers lacked proper visualization tools. But with the increasing usage of CT scanners in the petroleum industry, it is now easy to calculate exactly the variation of oil and gas saturations as functions of both space and time. Our laboratory experiments using horizontal cores with a short vertical fracture in the center indicate that gravity drainage can occur even when the effective height is as low as 1 inch. The porosity of the core and the saturations were measured at real time during the course of the experiment. The experimental setup, procedure, and results are described in the following sections.

1.6.2 EXPERIMENTAL SETUP

The experimental setup for these tests is the same as in Section 1.5.2.

1.6.3 EXPERIMENTAL PARAMETERS

The Berea cores used were cut from a single block of Berea sandstone. The properties of the cores used are given in Table 1.6.1. The oil used for the experiment, a mixture of Soltrol 130^{TM} and 1-iodohexadecane. 1-iodohexadecane, was used as the doping phase to artificially increase the CT number of the refined oil and obtain a clear contrast between the different phases during the course of the experiment. We chose 1-iodohexadecane for its similar structure to our refined oil. Previous measurements have shown that the iodohexadecane serves only as the doping phase and does not alter the interfacial tension between the fluids. The only problem associated with this doping phase is that it is sensitive to light and the attenuation properties decrease with constant exposure to bright light. This problem can be eliminated by using bromodecane, despite the fact that the attenuation coefficient for bromodecane is not as high as for

iodohexadecane. The pressure and temperature for the experiments were maintained at 800 psi and 25º C for all experiments to ensure that the displacements were immiscible and to obtain a clear contrast between the fluids in the CT scans. A plot of density versus pressure at the experimental conditions is shown in Fig. 1.6.2.

In the experiments, cores were fully saturated with oil, and no connate water saturation was considered. The displacing phase, CO_2, was used as a secondary recovery agent. Fluids were injected into cores at constant rates or at rates that were varied to maintain a constant pressure. Produced fluids were collected in graduated cylinders. The displacement processes were studied during the experiment where the injection rates, production volumes, and pressure drops were measured. The overall efficiency of the process was analyzed by combining the CT measurements and the external effluent volume measurements.

1.6.4 EXPERIMENTAL PROCEDURE

The general outline of the experimental procedure is given below.

1. The core is first heated at about 150ºF for a sufficient period of time to remove all residual water saturation.
2. The entire core is then evacuated using a vacuum pump.
3. The evacuated dry core is scanned at a confining pressure of about 1,000 psi.
4. For the fractured core experiment, steps 1 to 3 are repeated after fracturing the core.
5. The core is flooded with CO_2 at a desired temperature and pressure to obtain the scans at 100% CO_2 saturation.
6. The core is then evacuated again in the vacuum chamber.
7. The evacuated core is saturated with doped oil in the vacuum chamber for a period of 48 hours.
8. The oil saturated core is transferred to the aluminum core holder and about 15 pore volumes of oil are injected to ensure complete saturation.
9. The backpressure regulator at the outlet is fully closed and the pressure in the core holder is allowed to build up. Care is taken that the overburden pressure is at least 300 psi higher than the pressure inside the sleeve at all times.
10. Once the desired pressure is reached, the oil injection is stopped.

11. The oil-saturated core is now scanned again.
12. The pressure in the CO_2 accumulator is maintained at about 50 psi higher than the pressure in the coreflood cell to prevent back flow of oil.
13. CO_2 is now allowed to enter the coreflood cell, and any excess pressure above the desired pressure is released through a valve available for this purpose.
14. Injection is then started at a desired rate.
15. The core is scanned at various times to visualize the fluid flow and to determine the saturations at various times.

Porosity was calculated before the start of the experiment. Two methods were employed to calculate the porosity. First, a core from a set of cores was used to calculate the porosity by material balance method. This resulted in the porosity of about 19%. We calculated the porosity from the CT scans of the dry core and the fluid saturated core. The CT scanner results show that the average porosity of the core is in the range of 18% with a few regions having more than 20% porosity. The 3D porosity images are shown in Figs. 1.6.3 and 1.6.4.

1.6.5 RESULTS AND DISCUSSION

In this experiment, CO_2 was injected into the oil-saturated core at the injection rate of about 0.1 cm^3/min. The CT scan images obtained during the experiment can be seen from Figs. 1.6..5 to 1.6.8. These images represent the initial condition when the core was oil saturated and the various stages of CO_2 injection. In Fig. 1.6.5, the top left cross-section represents the injector end of the core while the bottom right image represents the producer end. The changes in color along the length represent the variations in density along the core caused by the heterogeneity.

In these scans the color scale has been chosen such that the blue color indicates the lowest CT numbers, red and pink indicate the highest CT numbers, green and yellow are the intermediates. Thus, with an increase in CO_2 saturation, the CT number decreases and hence the color changes to a dark shade of blue. The color scale for these CT numbers is shown in Fig. 1.6.9.

The images shown above only represent changes in density and do not convey any physical meaning. To better understand the displacement process and calculate the saturations, the CT number images were converted to saturations and the 3D images were also obtained using these saturations. The CO_2 saturations from the continuous CO_2 injection process are shown in Figs. 1.6.10 to 1.6.13. These images represent the actual values of CO_2 saturation and provide a clear indication of the displacement process that takes place inside the core. In these images, the red color indicates higher values of saturation, the dark blue represents the lowest values, and green and yellow are the intermediates. The saturation images can be better understood by looking at the color scale shown in Fig. 1.6.13. The highest values of CO_2 saturation are along the fracture, which provides a high-permeability path for fluid to flow. The CO_2 saturations along the length of the core appear to be very irregular. This is due to the heterogeneity of the core, which seems to be an important controlling factor. The most important observation from the saturation images is the role played by the gravity in the recovery process.

In Fig. 1.6.10, the CO_2 saturation is initially high at the upper part of the core. These were the regions first contacted by CO_2. As time progresses, CO_2 seems to move downward, as indicated by the increase in CO_2 saturation along the lower part of the core. This kind of variation is observed as a function of both time and space. This clearly indicates that gravity drainage can take place even in a 1-in. high matrix block. The force required for CO_2 to flow horizontally into the matrix is provided by the viscous drive mechanisms. Thus the displacement is seen to be a combination of gravity and viscous forces. Although CO_2 has invaded a large portion of the core, the recovery of oil from these regions is not complete, mainly because the presence of a fracture that runs from the injector to the producer end. The 3D saturations of CO_2 can be seen from Figs. 1.6.14 to 1.6.17. The images are presented such that they represent all regions that have a particular minimum value of CO_2 saturation at some point during the injection process.

These images are then converted to the actual values of saturations and plotted to show the spatial variation of saturation. The plot representing this variation is shown in Fig. 1.6.18. The calculated saturations represent the average saturations from approximately 65,000 points per cross-section. The average of these points would give us the total average saturation at any particular time, and this in turn can be converted to the

corresponding oil recovery. But the only problem with this approach would be the low resolution of the curve associated with the CT scanner tube, which heats up after a certain number of scans and has to be cooled off before starting another scan.

The oil recovery curve from the displacement process is shown in Fig. 1.6.19. This curve shows that the recovery is high initially then reduces as time progresses. Towards the end of the experiment, the recovery becomes constant. In this kind of displacement, some amount of CO_2 breaks through without contacting any oil, thus greatly reducing the sweep efficiency. Although the diffusion process is extremely slow, a good recovery may be obtained given enough time and CO_2. The final recovery obtained in this experiment is about 58% after about 2.2 p.v. of injection. For the process efficiency to increase, there must be some kind of conformance control technique must prevent early breakthrough of CO_2 from the fracture and hence increase the sweep efficiency.

1.6.6 CONCLUSIONS

1. Oil recovery by gravity drainage is not limited to thick matrix blocks. Experimental results and visualization using the CT scanner prove that gravity drainage is possible even in a 1-inch high system.

2. Although the recovery due to gravity drainage can be significantly high, the presence of fractures leads to early breakthrough and hence lowers the sweep efficiency.

3. Some kind of conformance control technique like polymer gel or viscosified gelant is required to improve the sweep efficiency of the system.

REFERENCES

1. Hagoort, J.: “Oil Recovery by Gravity Drainage,” paper SPE 7424, *SPEJ* (June 1980), pp. 139-150.
2. Dumoré, J.M. and Schols, R.S.: “Drainage Capillary Pressure Function and the Influence of Connate Water”, paper SPE 4096, *SPEJ* (October 1974)**,** 437.

3. Thompson, J.L., Mungan, N.: “A Laboratory Study of Gravity Drainage in Fractured Systems Under Miscible Conditions,” paper SPE 2232 presented at the 1969 Annual Fall Meeting, Houston, Sep 29 – Oct 2.
4. Espie, A.A *et al*: “A Laboratory Investigation of Gravity Drainage/Waterflood Interaction in Prudhoe Bay,” paper SPE 28614 presented at the 69th Annual Technical Conference and Exhibition, New Orleans, 25-28 September.
5. Li, H., Putra, E., Schechter, D.S., and Grigg, R.B. : “Experimental Investigation of CO2 Gravity Drainage in a Fractured System,” paper SPE 64510 presented at the 2000 SPE Asia Pacific Oil and Gas Conference, Brisbane, Australia, 16-18 October.
6. Halderson, H.H *et al*: “An Evaluation of the Prudhoe Bay Gravity Drainage Mechanism by Complementary Techniques,” paper SPE 13651 presented at the 1985 SPE California Regional Meeting, Bakersfield , California, 27-29 March.
7. Donnelly, J.K.: “Hilda Lake a Gravity Drainage Success,” paper SPE 54093 presented at the 1999 International Thermal Operations and Heavy Oil Symposium, Bakersfield, California, 17-19 March.
8. Schechter, D.S. and Guo, B.: “Mathematical Modeling of Gravity Drainage after Gas Injection into Fractured Reservoirs,” paper SPE 35170, presented at the, 1996 SPE/DOE Improved Oil Recovery Symposium, Tulsa, Oklahoma, April 22–24.
9. Dykstra, H. : “Prediction of Oil Recovery by Gravity Drainage,” paper SPE 6548, *JPT* (May 1978), 818-830.
10. Luan, Z.: “Some Theoretical Aspects of Gravity Drainage in Naturally Fractured Reservoirs,” paper SPE 28641 presented at the 69th Annual Technical Conference and Exhibition, New Orleans, Louisiana, September 25-28, 1994
11. Li, K. and Horne, R. N.: “Prediction of Oil Production by Gravity Drainage,” paper SPE 84184 presented at the 2003 SPE Annual Technical Conference and Exhibition, Denver, Colorado, 5-8 October.

Table 1.6.1—Berea core properties.

Berea Core Properties	
Length	13 cm
Diameter	2.5146 cm
Area	4.963 cm^2
Porosity	19 - 23 %
Permeability	200 md

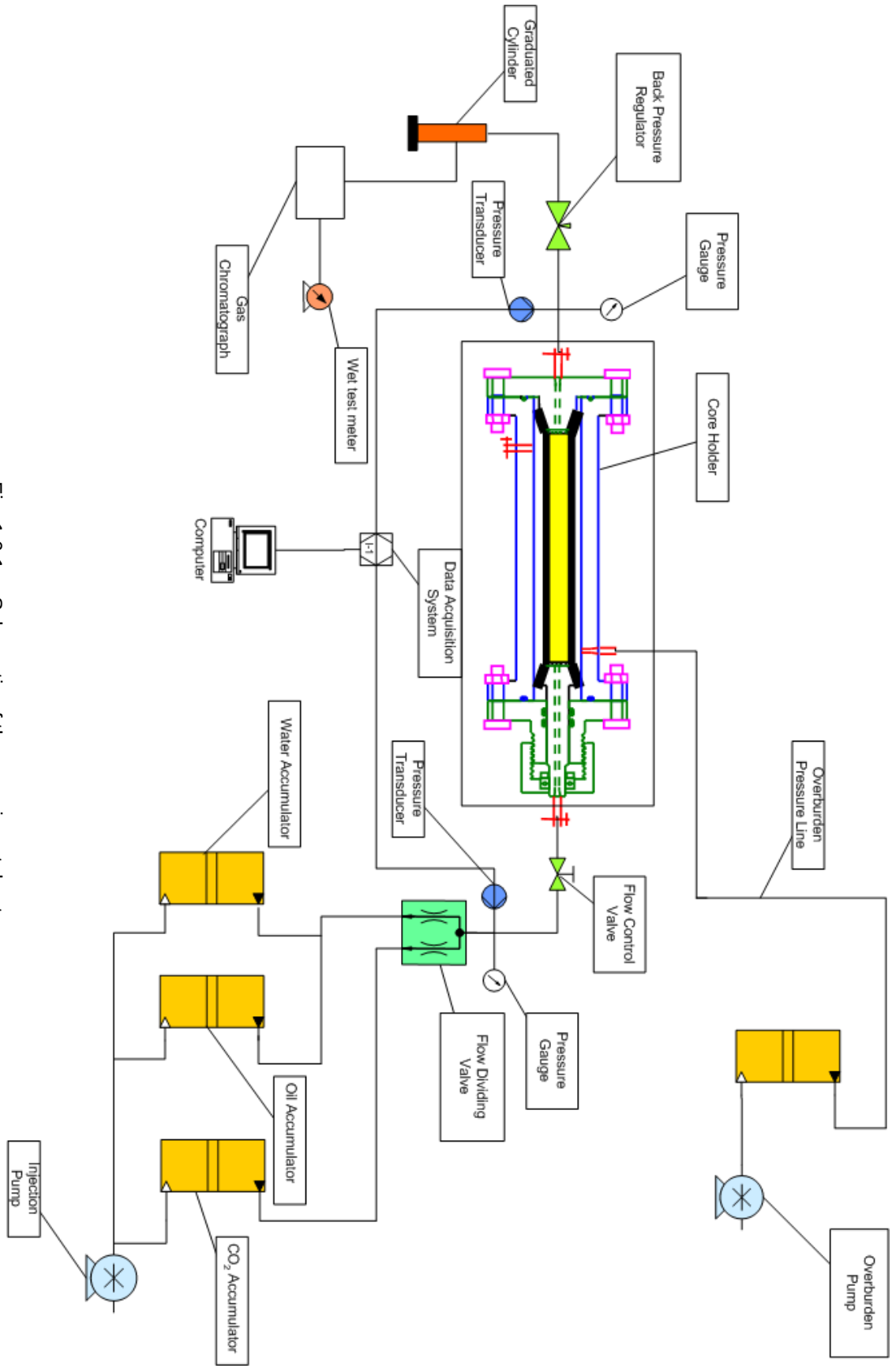

Fig. 1.6.1— Schematic of the experimental setup.

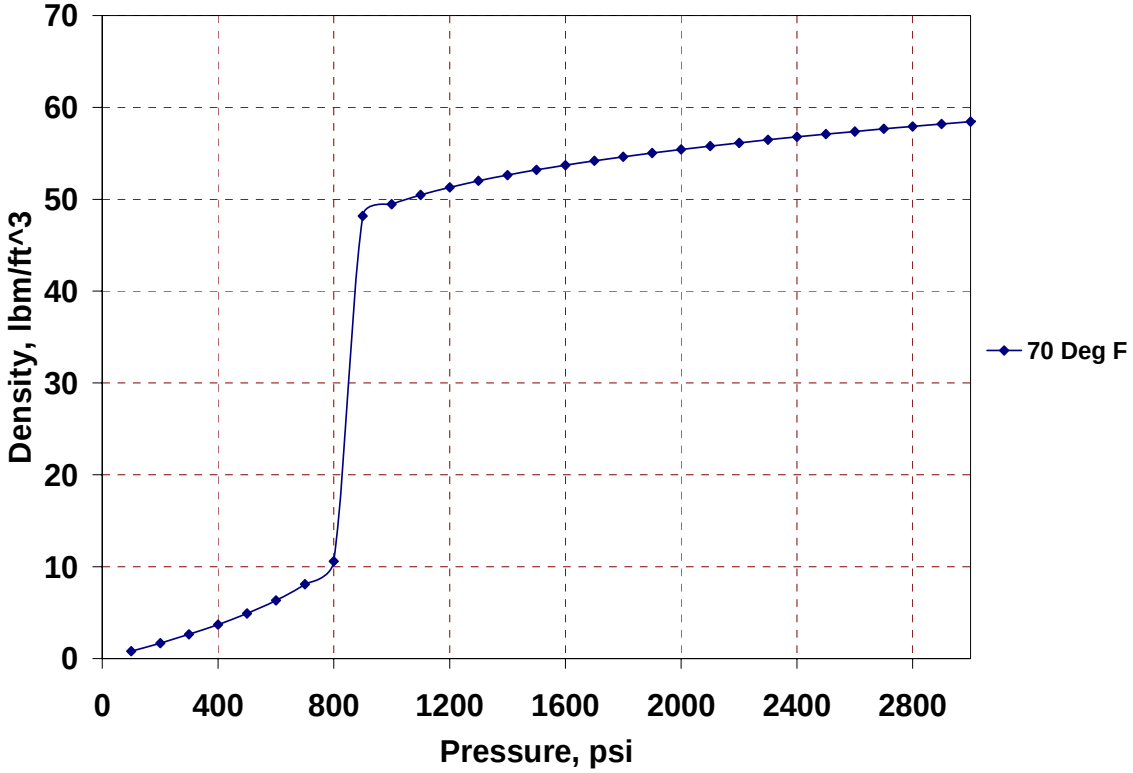

Fig. 1.6.2—Density of CO_2 at experimental conditions.

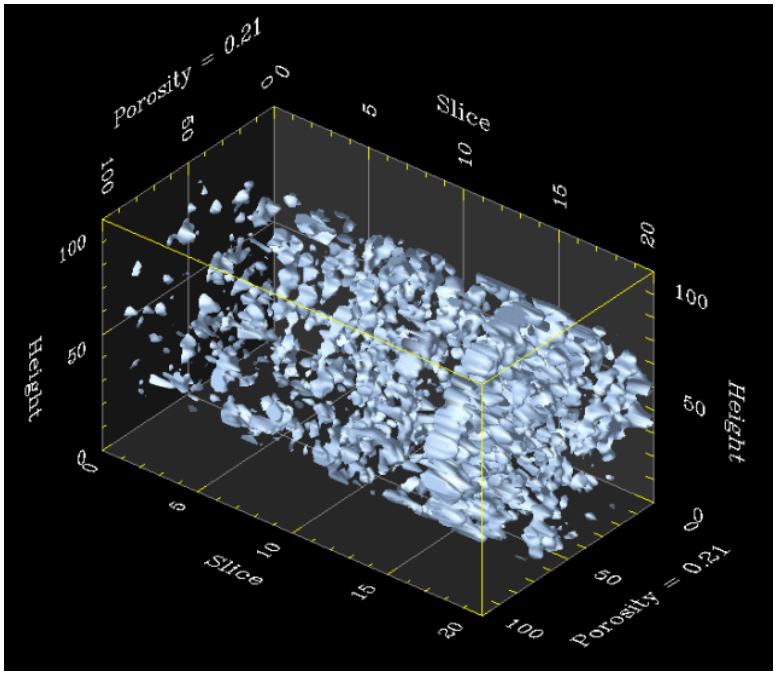

Fig. 1.6.3—Regions with porosity value in the range of 21%.

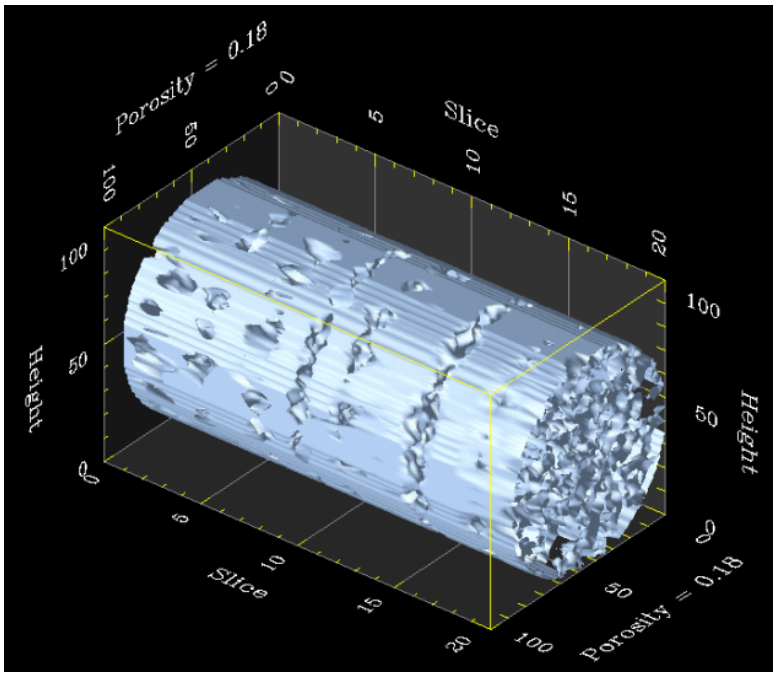

Fig. 1.6.4—Regions with a porosity value of at least 18%.

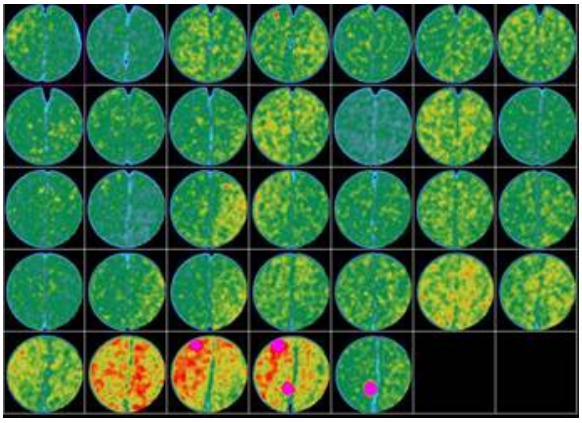

Fig. 1.6.5—Oil saturated core scans during continuous CO_2 injection.

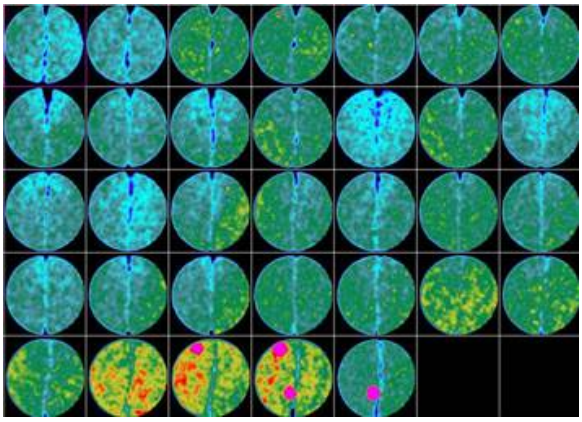

Fig. 1.6.6—Scans taken at about 0.7 p.v. of injection indicate irregular saturation of CO_2 and breakthrough from fracture.

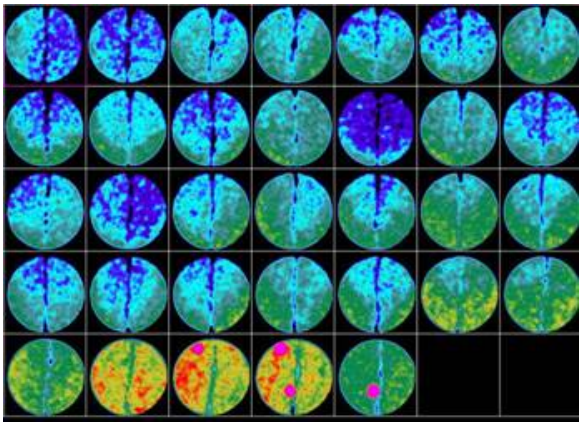

Fig. 1.6.7—Scans taken at about 1.3 p.v. of injection.

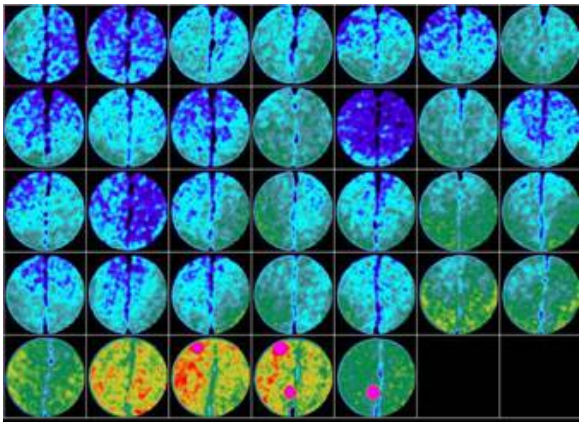

Fig. 1.6.8—Scans taken at the end of the experiment.

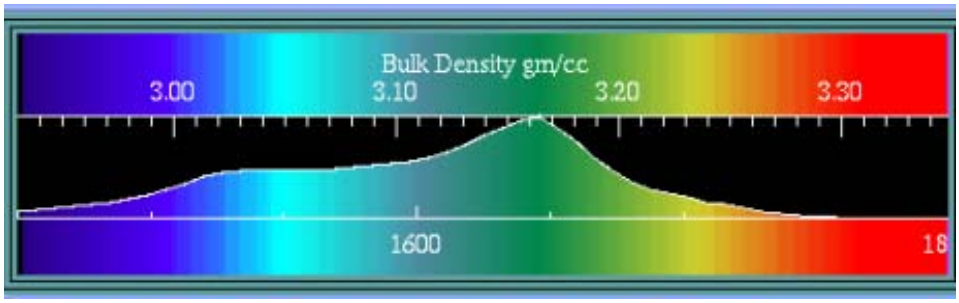

Fig. 1.6.9—Scale showing colors and their corresponding CT numbers.

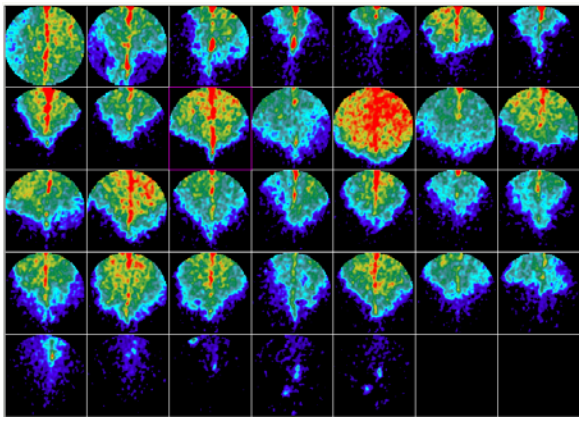

Fig. 1.6.10—CO_2 saturations at 0.7 p.v. of injection.

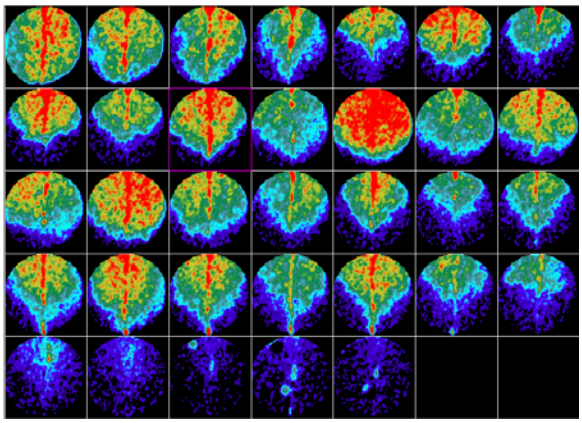

Fig. 1.6.11—CO_2 saturations at 1.3 p.v. of injection.

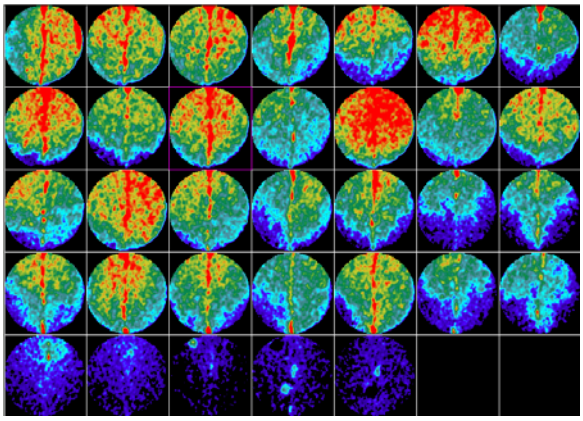

Fig. 1.6.12—CO_2 saturations at the end of the experiment.

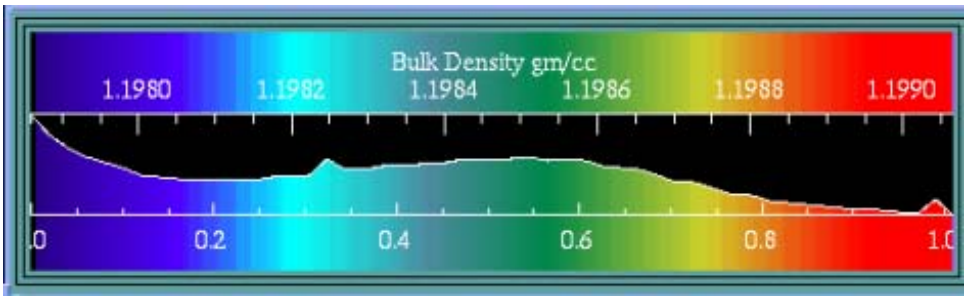

Fig. 1.6.13—Color scale indicating red color with high values of saturation.

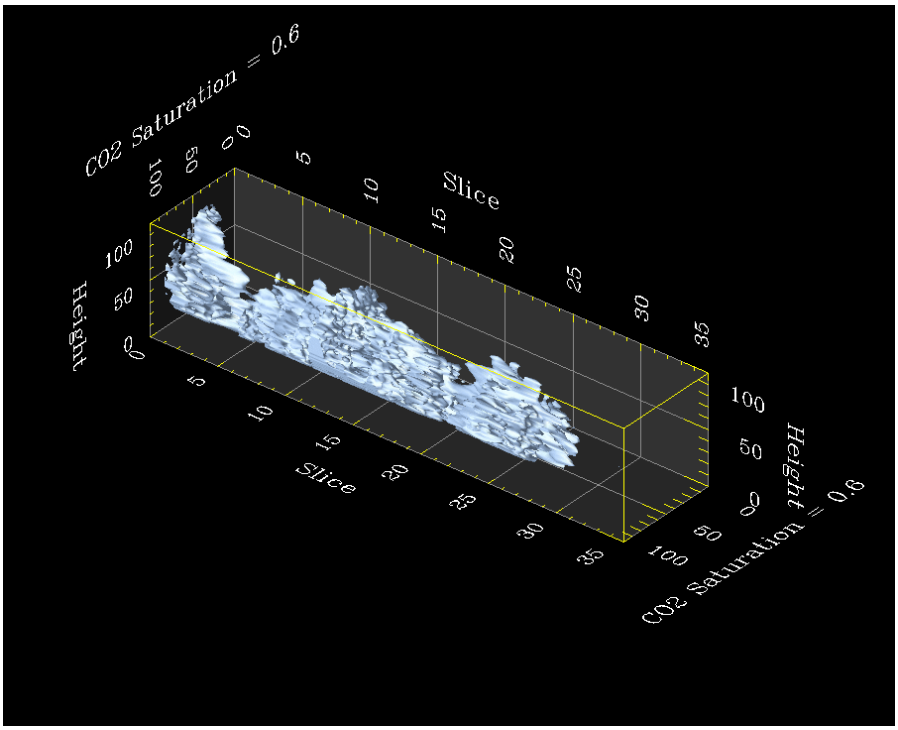

Fig. 1.6.14—Regions with minimum saturation of 60% at 0.7 p.v. of injection.

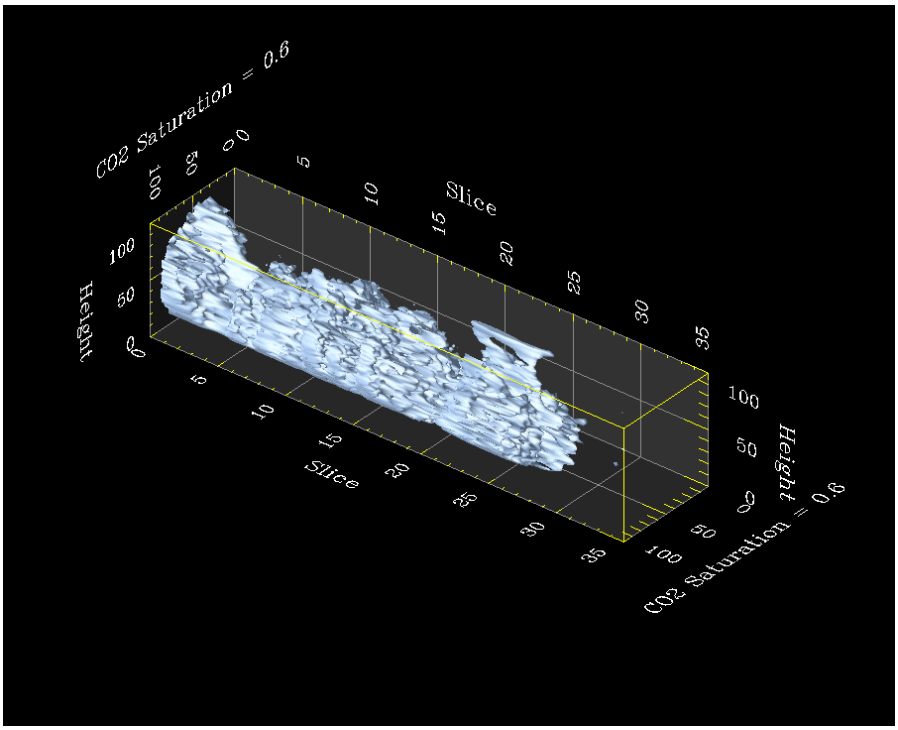

Fig. 1.6.15—Regions with minimum saturation of 60% at 1.3 p.v. of injection.

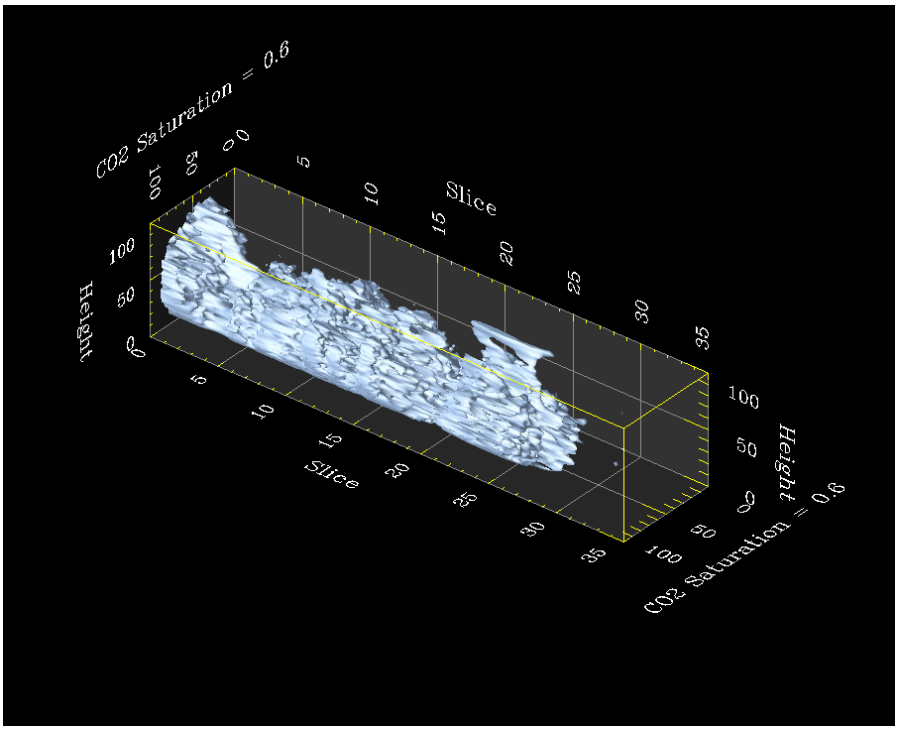

Fig. 1.6.16—Regions with minimum saturation of 60% at 1.7 p.v. of injection.

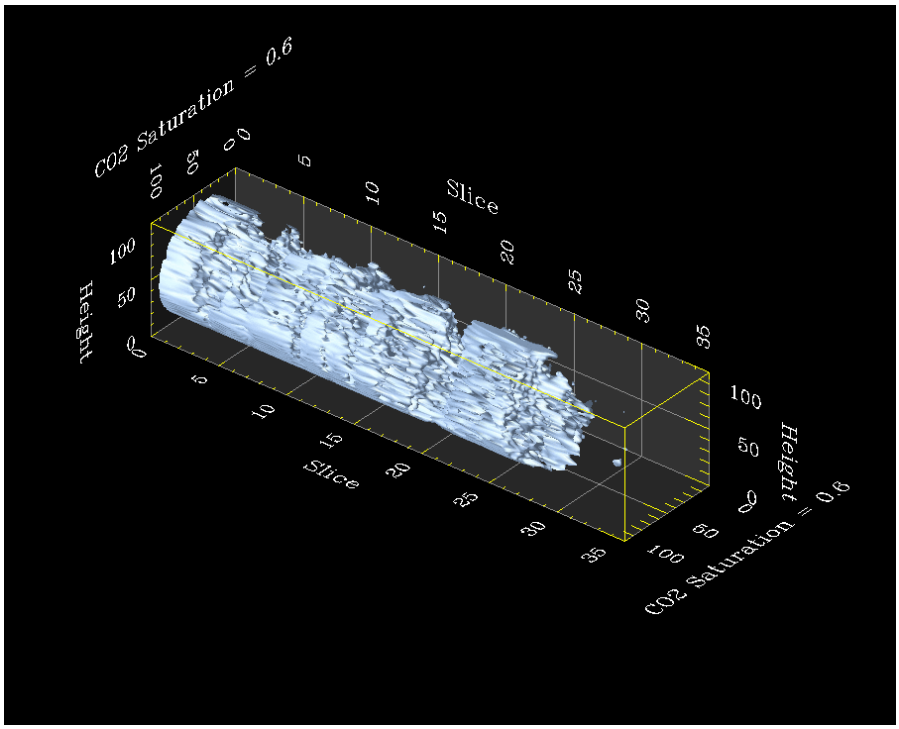

Fig. 1.6.17—Regions with minimum saturation of 60% at the end of the experiment.

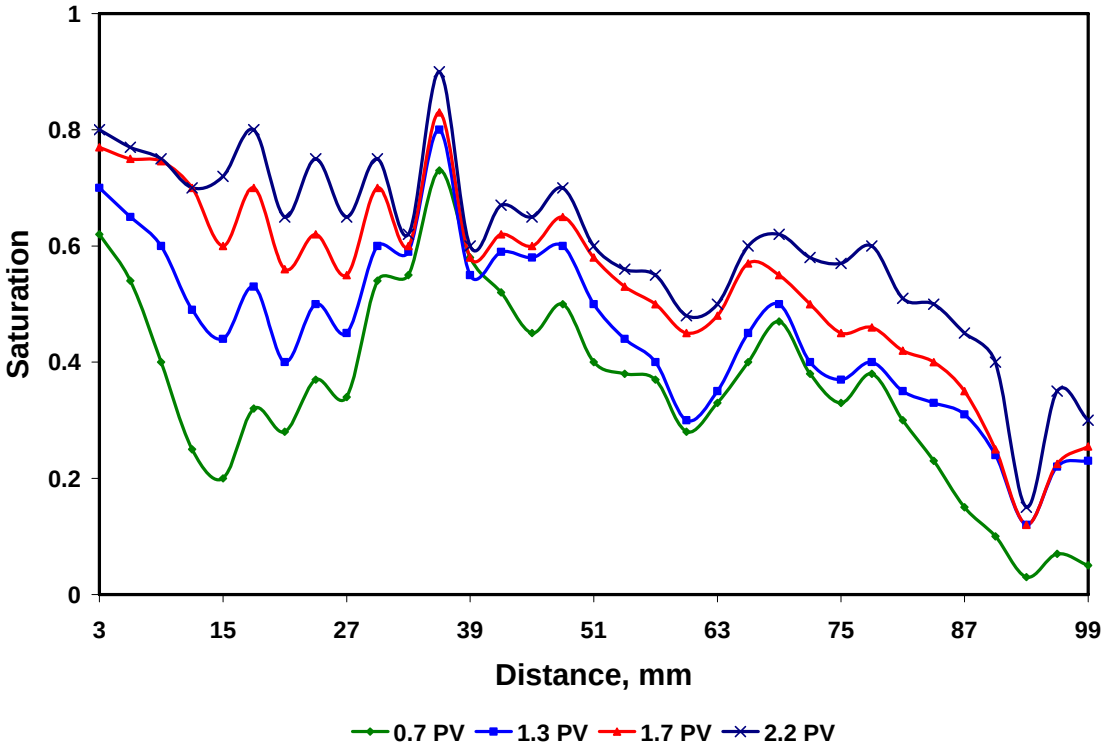

Fig. 1.6.18—Spatial variation of saturation at various p.v. of injection.

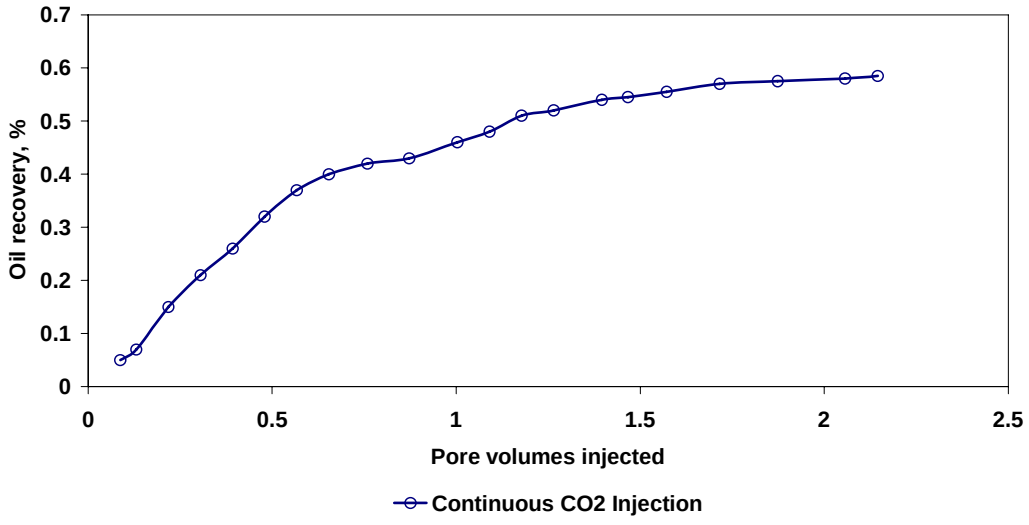

Fig. 1.6.19—Oil recovery vs. pore volumes injected for continuous CO_2 injection.

Chapter I-7

Investigation of Natural Fracture Aperture Distribution of Tensleep Formation Cores using X-Ray CT Scanner

1.7.1 INTRODUCTION

The Teapot Dome formation is an elongated anticline, striking NNW-SSE, probably produced by a reverse fault whose strike is also NNW-SSE, located in the southwestern part of the anticline (Fig. 1.7.1).[1] This reverse fault dips roughly to the NE, and is considered the main fault. Three small faults represent accommodation faults produced after the movement of the main fault, and as a response to that movement. Most fractures generally terminate vertically at bedding planes and stylolites.

The Tensleep sandstone is heavily fractured (Fig. 1.7.2). Most of the fractures are less than a millimeter in total width, and much of that width is occluded in the smaller fractures by partial mineralization of quartz and/or dolomite. Nevertheless, significant porosity, 10 to 80%, remains in most fractures, especially within the larger ones.[2] The larger fractures also typically splits the rock, and the core is no longer intact across the fracture plane, indicating that mineralization provides only an incomplete and weak seal between fracture faces. A zone of inclined fractures is present between 5,591 ft and 5,595 ft, and these fractures are suggestive of a conjugate shear system similar to that seen in Tensleep outcrops immediately south of the Alcova reservoir.[2] A short of interval of white, micritic dolomite with numerous bitumen-stained natural fractures is present between 5,495 and 5,498 ft overlying the oil-saturated reservoir facies.[2]

We characterized the Tensleep rock and assessed the potential for bypassing during CO_2 injection in the Teapot Dome oilfield, currently operated by the Rocky Mountain Oilfield Testing Center (RMOTC). As shown by recent core analysis, the Tensleep formation in Teapot Dome is heavily fractured and the reservoir is considered as a good candidate for CO_2 sequestration. For the success of CO_2 sequestration, knowing the characteristics of fractures is crucial. Our CT scanner enables us to obtain fracture properties such as fracture aperture, fracture mineralization, aperture distribution, and permeability distribution without damaging the core.

1.7.2 EXPERIMENTAL PROCEDURES

We characterized fractures of two cores recovered from RMOTC 48X28 well. The scanner (Fig. 1.7.3) is able to scan as fast as 1 sec/scan and has 75-cm diameter gantry. It can analyze a core plug up to 81 cm long and gives a spatial resolution of 0.35mm.[3] To characterize Tensleep rock, we used the procedures of the experiment are follows:

(1) Artificially cut the core.
(2) Use different known feeler sizes to develop calibration curves for Tensleep sandstone and then use calibration curves to convert the CT number into fracture aperture size.
(3) Develop matrix calibration curves to compensate the beam hardening effect.
(4) Take CT images of Core-A and Core-B.
(5) Use the calibration curve to obtain fracture aperture size and generate permeability contour maps based on the aperture maps.

Details of the calibration curve, CT scanning and analysis of the fracture aperture using log normal density function are described below.

1.7.2.1 Calibration Curve

The CT scanner identifies the density differences between various objects.[4] The density of a fracture that is filled with air is less than the density of the rock matrix. Thus CT images can differentiate between matrix and fracture. The CT numbers do not represent aperture size of the fracture as they are mere functions of densities. To obtain the fracture aperture, we apply a calibration technique to correlate the CT numbers with the actual aperture size.[5, 6]

The experimental setup consists of two halves of a rock specimen, feeler gauges and a core holder. The rock specimen was obtained from an unfractured part of a Tensleep core. Then it was cut using a diamond saw along the longitudinal direction. Cut faces were ground in a grinding machine to reduce surface roughness as much as possible. Smooth faces ensure a proper match between the halves so that an accurate small fracture aperture can be obtained. Feeler gauges of known sizes (Fig. 1.7.4) were then inserted between the halves.

The feeler gauge inserted into the core was placed in the core holder and 500 psi overburden pressure was applied. Multiple CT scans were taken in the middle of the core between the two feeler gauges along the longitudinal direction. Fig. 1.7.5 shows typical

sets of scans of a Tensleep core with various feeler gauges. The more dense area is shown with an orange color and the less dense area is shown green, blue, and black in decreasing order of density. The feeler gauge is made from the steel; therefore, the density of this material is very high. The feeler gauges were placed at the both ends, and some images were affected by these gauges if CT scan were taken close to these gauges, which we usually identified as the beam-hardening effect; the affected CT images are slightly bent. These images were not used in calibration calculation. Fig. 1.7.6 is an example of CT number plot for the 203-μm fracture size. Horizontal lines represent rock matrix and a dip of a CT number in the middle of the plot represents the fracture. Although the matrix and the fracture can be clearly distinguished with the CT number, it is impossible to determine the aperture size with CT number only. However, the CT numbers correspond to the known fracture size of 203 μm. Thus, the aperture size can be calculated using this relationship. The dip of the CT number plot near the fracture is not abrupt, but rather has a smooth transition from matrix to fracture. This effect reflects dispersion of CT numbers caused by the finite beam width and oversampling. Fig. 1.7.7 shows CT number plots for different feeler-gauge sizes. We found that if the feeler-gauge size increases the CT numbers of the fracture decrease and thus the dip of CT numbers is deeper and wider. Since the CT number difference reflects density difference, the CT number of a fracture filled with air would be expected to have similar CT number to the air. This is true for large void space, but not for a narrow space like a rock fracture. The CT number of fracture is affected by surrounding rock in an effect usually called “oversampling”.[5]

A plot of CT number based on the CT numbers obtained from each scan (Fig. 1.7.8) yields an average CT number plot that accounts for minor variation in fracture size and matrix heterogeneity. From this plot, the minimum rock CT number is identified. All CT numbers that are smaller than the minimum rock CT number are subtracted from the minimum rock CT, number and the differences are used to obtain the integrated CT signal for the fracture size. The integrated CT signals are calculated for each pixel number and are given indexes from 1 to *n* (Fig. 1.7.8). The area of the integrated CT region is calculated using the following formulae[5, 6]:

For index *i* equals to 1 to *c*,

$$Area(i) = IntCT(i-1) + \frac{1}{2}[IntCT(i) - IntCT(i-1)] \quad \text{.....(1.7.1)}$$

For index *i* equals to *c+1* to *n*,

$$Area(i) = IntCT(i) + \frac{1}{2}[IntCT(i-1) - IntCT(i)] \quad \text{.....(1.7.2)}$$

After calculating areas for different feeler gauges, plots of integrated CT signal versus aperture size shows a linear relationship, as seen in Fig. 1.7.9. The correlation of aperture size derived from this calibration curve is expressed by the following formula.

$$Fracture \quad Aperture = \frac{IntCT - 360.99}{6.5458} \quad \text{.....(1.7.3)}$$

1.7.2.2 CT Scanning

The cores scanned (Fig. 1.7.10) were retrieved from depths of 5,565 ft (Core-A) and 5,566 ft (Core-B). Diameter of both cores is 2.52 in. and the length of Core-A and Core-B are 5.55 in. and 7.64 in., respectively. CT images of the cores were taken under no overburden pressure condition.

1.7.2.3 Log-normal distribution

Once the cores were scanned, the results were converted to fracture aperture maps. Then, we determined the fracture aperture distribution using a log-normal density function.[5,6] A random variable *x* has a log-normal probability distribution if ln *x* is normal. In this case, the density function of *x* is expressed as follows.[8]

$$f(x) = \frac{1}{\sqrt{2\pi}\varsigma} Exp\left[-\frac{1}{2}\left(\frac{ln\ x - \lambda}{\varsigma} \right)^2 \right] \quad 0 \le x < \infty \text{ .....(1.7.4)}$$

where

$$\lambda = \ln\ \mu - \frac{1}{2}\varsigma^2 \text{ .....(1.7.5)}$$

$$\varsigma^2 = \ln\left(1 + \frac{\sigma^2}{\mu^2} \right) \text{.....(1.7.6)}$$

μ and σ represent mean and standard deviation of a random variable *x*, respectively.

1.7.3 RESULTS AND DISCUSSIONS

A total of 30 scans were taken for Core-A, including 15 images containing the information of fracture (Fig. 1.7.11). For Core-B, 17 images contained fracture information among a total of 50 scans (Fig. 1.7.12). Figs. 1.7.13 and 1.7.14 show the 3D images of fracture inside the cores.

Fig. 1.7.11 reveals that the fracture of Core-A does not extend to the outside of the core. Mineral does not precipitate inside of the fracture. The upper part of the CT images shows mineralized fractures that have red or orange colors as observed in Fig. 1.7.13. These fractures extend to the side of the core with a large void space as indicated

in CT images from 16 to 18. This void space is seen as a cloud-like shape, and the open fracture looks like a board in 3D imaging (Fig. 1.7.14). Core-B shows a set of open fractures and a set of mineralized fractures. As discussed in core analysis, Core-B fractures were precipitated with highly dense minerals like dolomite (Figs. 1.7.12 and 1.7.15). Mineralized fractures extend to the outside of the core. These fractures begin parallel, then join together. The open fracture also extends to the side of the core and terminates at the mineralized fracture (Fig. 1.7.15). The open fracture appears to be a secondary set or caused by drilling. Fig. 1.7.16 shows a 3D image of the open fracture.

As mentioned earlier, a minimum rock CT number is required to determine the aperture size of a fracture. To get a proper value, we used the minimum rock CT number from the function of pixel position as shown in Fig. 1.7.17. This figure shows different CT numbers present at different pixel positions in the core. Once the minimum CT numbers were obtained, the area below the minimum CT line was calculated. All the CT images were then analyzed, and the fracture distribution obtained was plotted in distribution function (Fig. 1.7.18). Using the mean and standard deviation following Eq. 1.7.4, we generated the log-normal distribution to fit the experimental data (Fig. 1.7.18). The generated value and the experimental data show a close agreement. This matching result confirms that the aperture distribution follows log-normal distribution (Table 1.7.1). Fig. 1.7.19 shows the aperture distributions of both cores. The figure shows that the open fracture of Core-B is wider and distributes more evenly than the open fracture of Core-A. For use in our future simulation work, we also plotted the fracture aperture distribution of Core-A and Core-B in 2D plane views as shown in Figs. 1.7.20 and 1.7.21, respectively. The fracture aperture data can be converted to fracture permeability (Figs. 1.7.22 and 1.7.23) by the following equation[7]:

$$k_f = 8.45\times10^9 w^2 \quad [md] \qquad \text{.....(1.7.6)}$$

where, w is in microns.

1.7.4 CONCLUSIONS

1. CT images taken from two RMOTC 48X28 cores show open fracture and mineralized fractures.
2. The measured fracture aperture distribution follows log-normal distribution.
3. The fracture aperture sizes and distribution from both cores are totally different. The aperture size of Core-B is bigger and more widely distributed than that of Core-A.
4. Permeability contour maps of Core-A and Core-B clearly show preferential flow paths.

REFERENCES

1- Schechter, D.S. *et al.*: “Reservoir Modeling of CO_2 Sequestration and Enhanced Oil Recovery in Teapot Dome,” Project Narrative, U.S. DOE/NPTO Contract No. DE-PS26-04NT42249-1D (Oct. 5, 2004).

2- Lorenz, J. and Cooper, S.: “Fractures in the Core from RMOTC 48X28 Core,” internal report to RMOTC, June 24, 2004.

3- Universal Systems Website (http://www.universal-systems.com/HD_350.asp).

4- Wellington, S.L. and Vinegar, H. J.: “CT Studies of Surfactant-Induced CO_2 Mobility Control,” paper SPE 14393 presented at the 1985 SPE Annual Technical Conference and Exhibition, Las Vegas, Sep. 22-25.

5- Muralidharan, V., Chakravarty, D., Putra, E. and Schechter, D.S.: “Investigating Fracture Aperture Distribution under Various Stress Conditions Using X-Ray Scanner,” paper CIPC 2004-230 presented at 2004 Annual Technical Meeting of the Petroleum Society, Calgary, Canada, Jun. 8-10.

6- Muralidharan, V., Chakravarty, D., Putra, E. and Schechter, D.S.: “Simulation of Fluid Flow thorough Rough Fractures,” paper SPE 89941 presented at the 2004 SPE International Petroleum Conference, Puebla, Mexico, Nov. 8-9.Witherspoon, P.A., Wang, J.S.Y., Iwai, K. and Gale, J.e.: “Validity of Cubic Law for Fluid Flow in a Deformable Rock Fracture,” Water Resources Research, 16(6), 1016-1024, 1980.

8- Ang, A. and Tang, W.H.: “Probability Concepts in Engineering Planning and Design,” John Wiley & Sons, 1975.

Table 1.7.1—Values of statistical parameters

	Mean [μm]	Standard Deviation [μm]
Core-A	222.17	577.50
Core-B	536.90	756.60

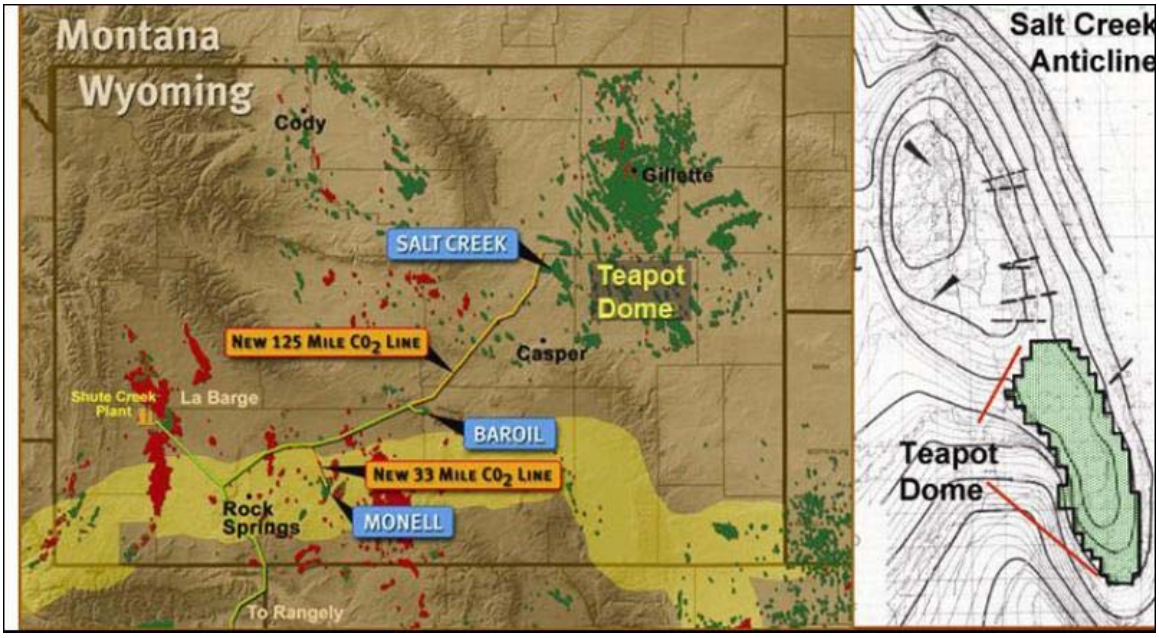

Fig. 1.7.1—Teapot Dome, NE Natrona Co., central Wyoming, 30 mi/48 km NNE of Casper, Wyoming. The teapot-shaped rock formation is also shown.[1]

(a) A natural fracture face that is partially covered with crystalline dolomite

(b) Highly fractured Tensleep sandstone

Fig. 1.7.2—Cores from Tensleep formation.[2]

Fig. 1.7.3—Universal Systems HD-350E.

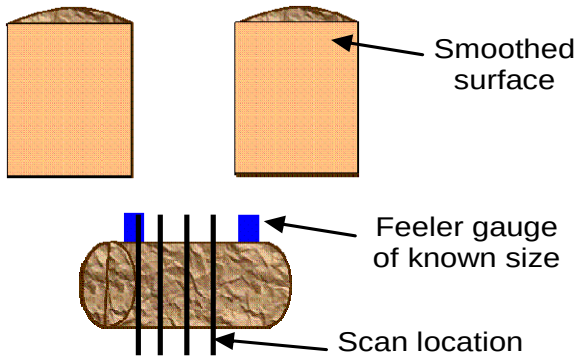

Fig. 1.7.4—Schematic view of feeler gauge locations and scanning locations.[5]

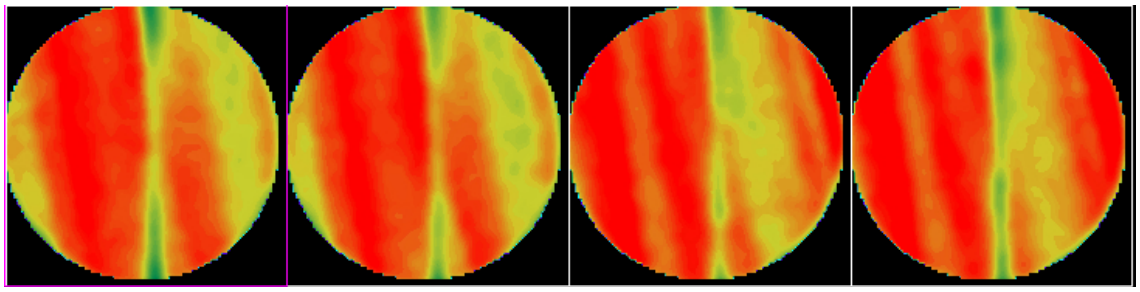

(a) 51-µm feeler gauge

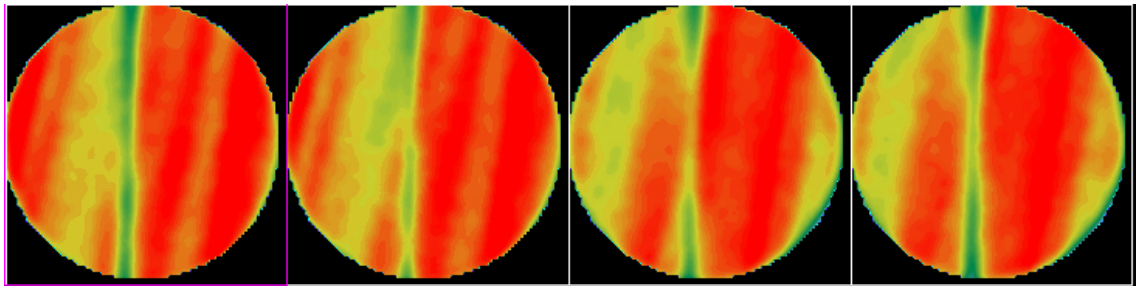

(b) 76-µm feeler gauge

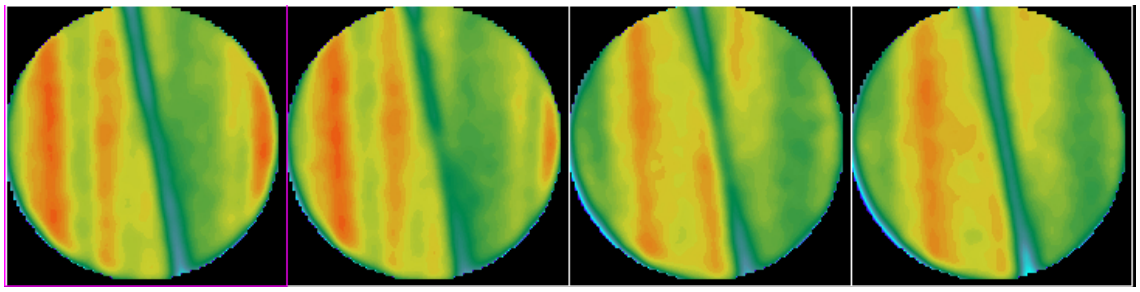

(c) 127-µm feeler gauge

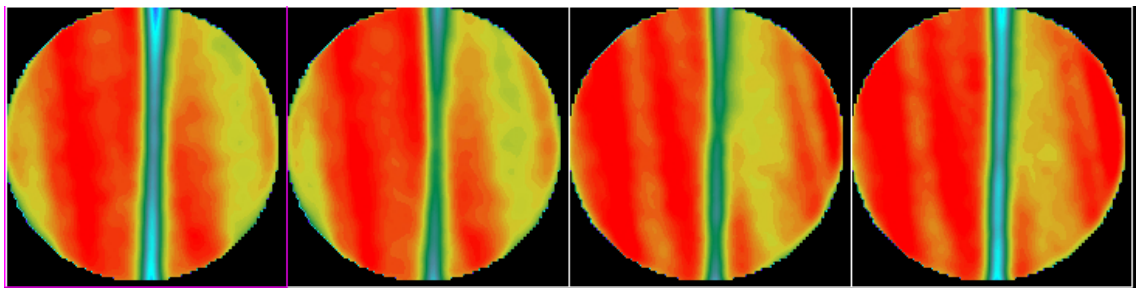

(d) 203-µm feeler gauge

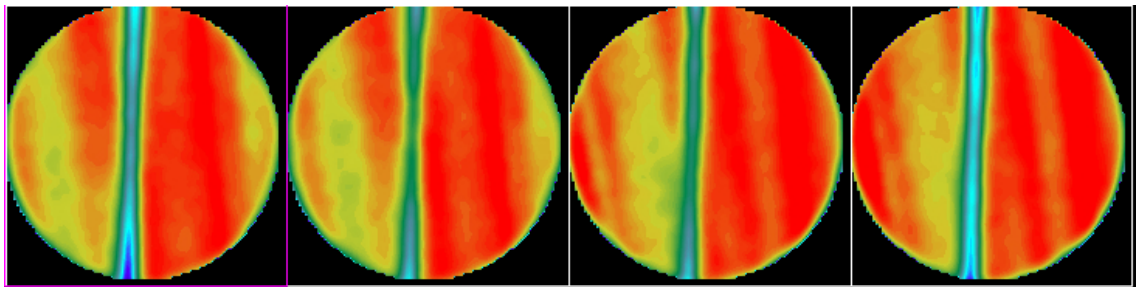

(e) 279-μm feeler gauge

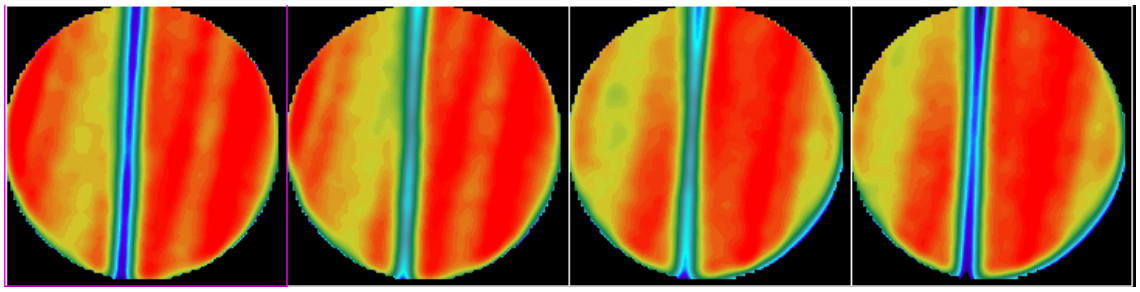

(f) 330-μm feeler gauge

Fig. 1.7.5—Scanning images with various feeler gauge sizes.

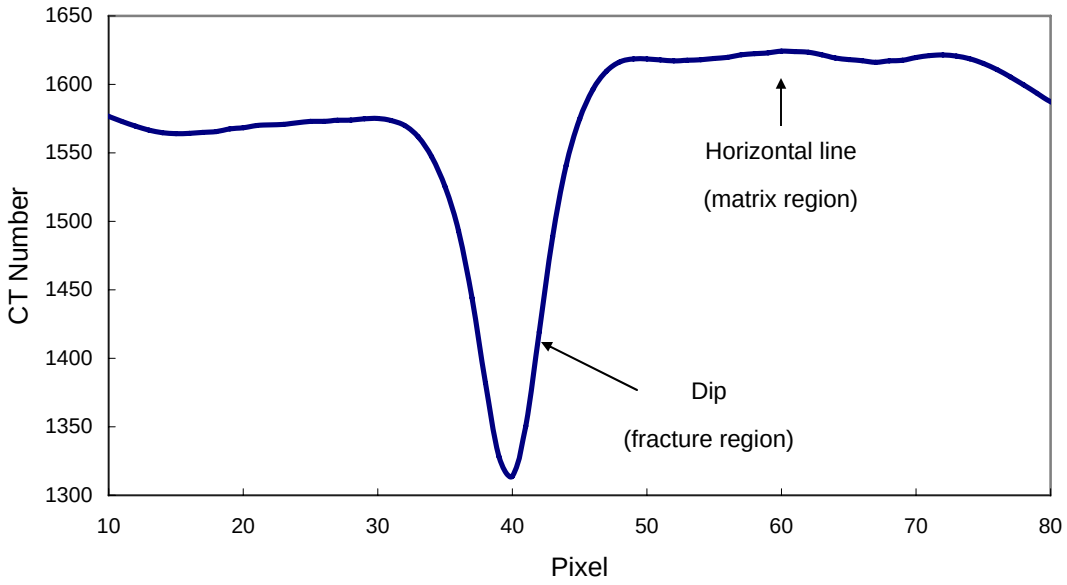

Fig. 1.7.6—Average CT number plot of 203-μm feeler gauge.

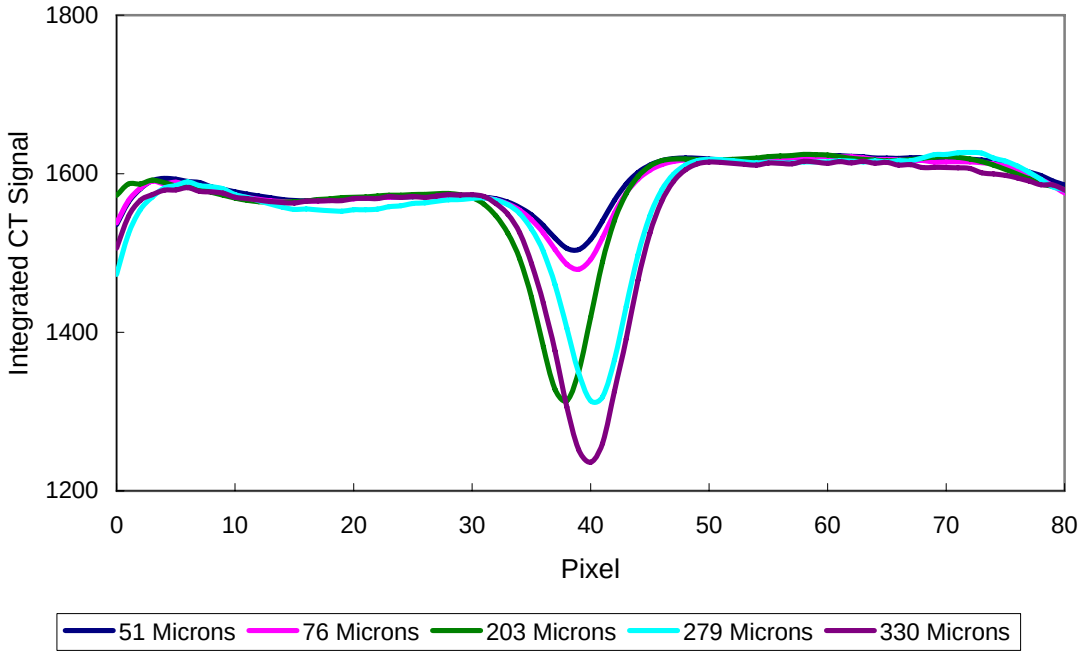

Fig. 1.7.7—Comparison of CT number plots for various fracture size.

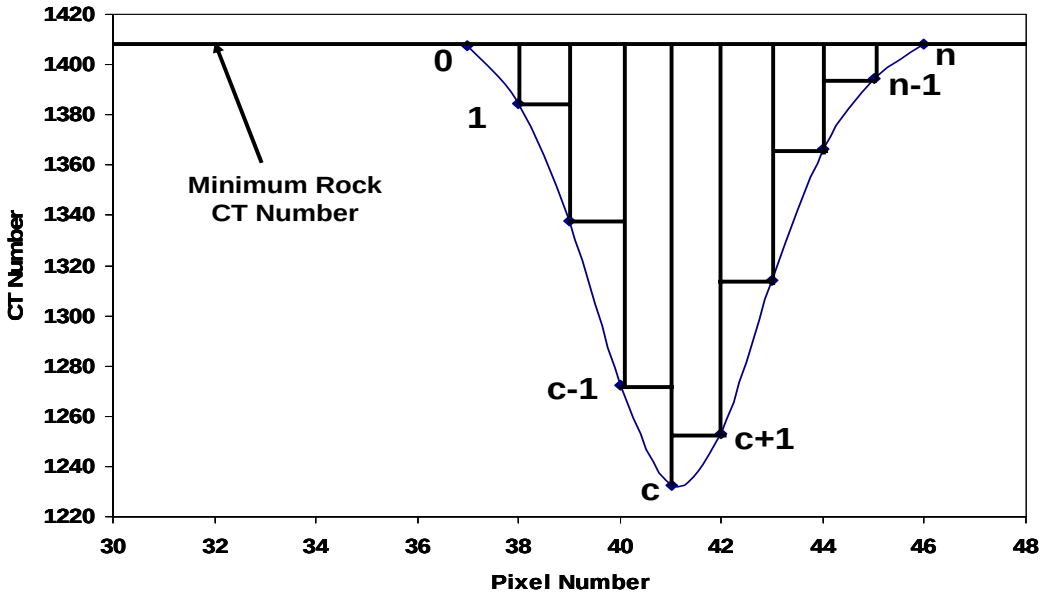

Fig. 1.7.8—Integrated area of fracture region.[5]

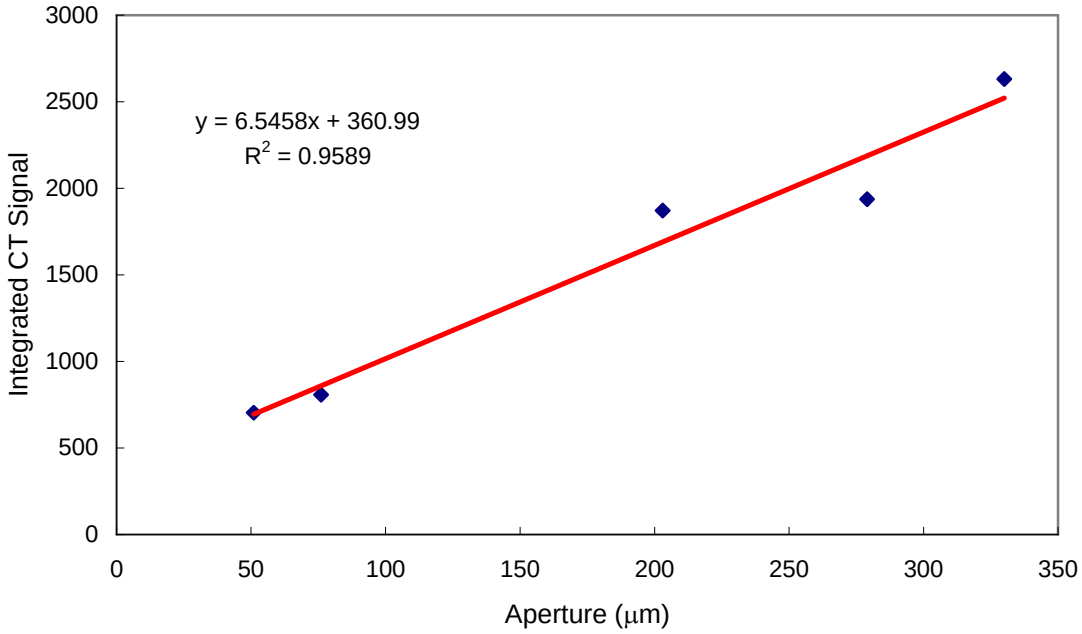

Fig. 1.7.9—Calibration between Integrated CT signal and fracture aperture.

(a) Core-A

(b) Core-B

Fig. 1.7.10—Measured cores from Tensleep Formation.

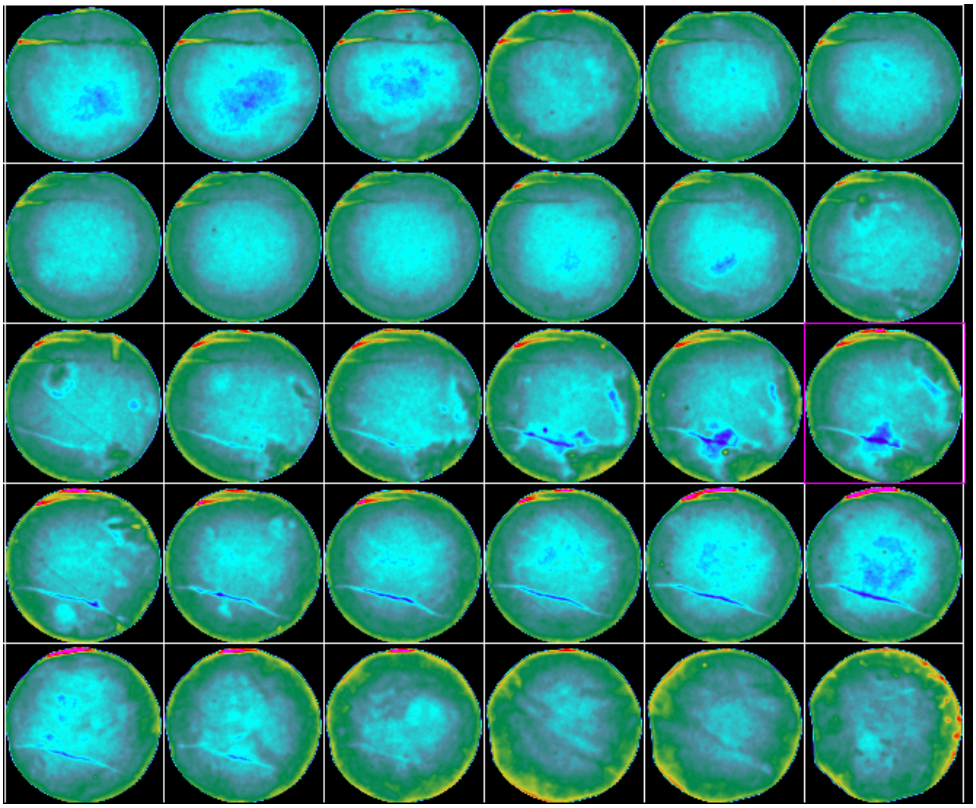

Fig. 1.7.11—CT images of Core-A

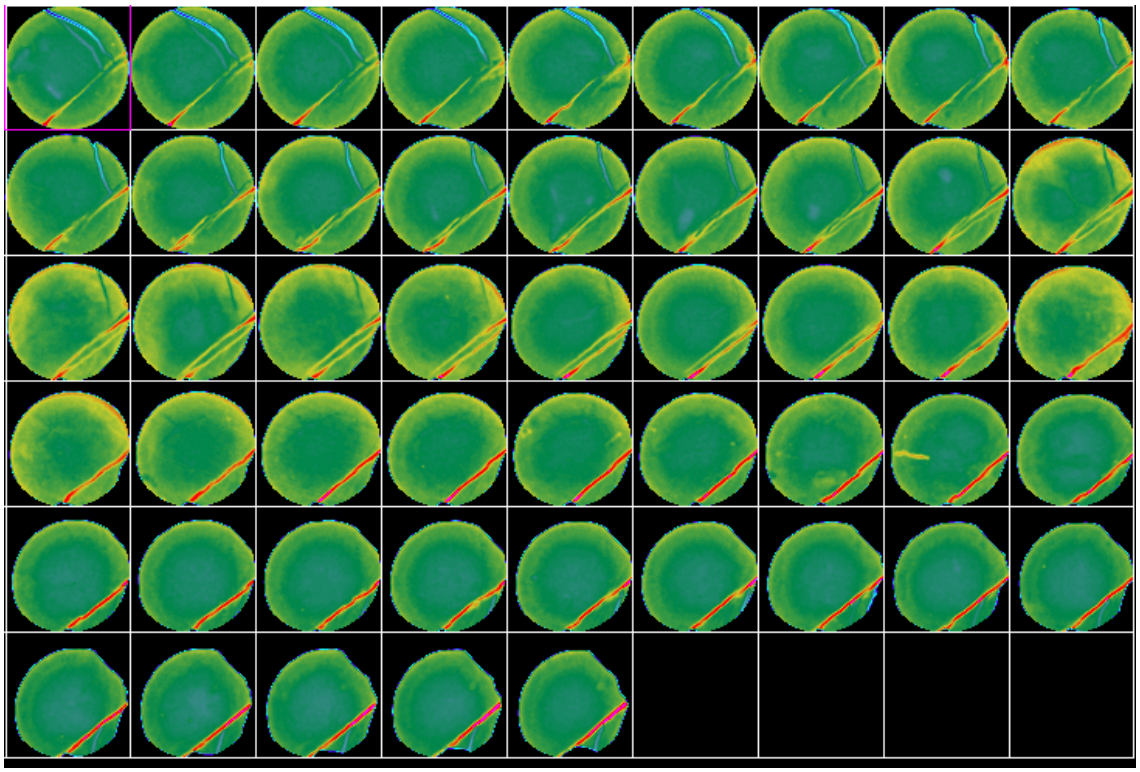

Fig. 1.7.12—CT images of Core-B

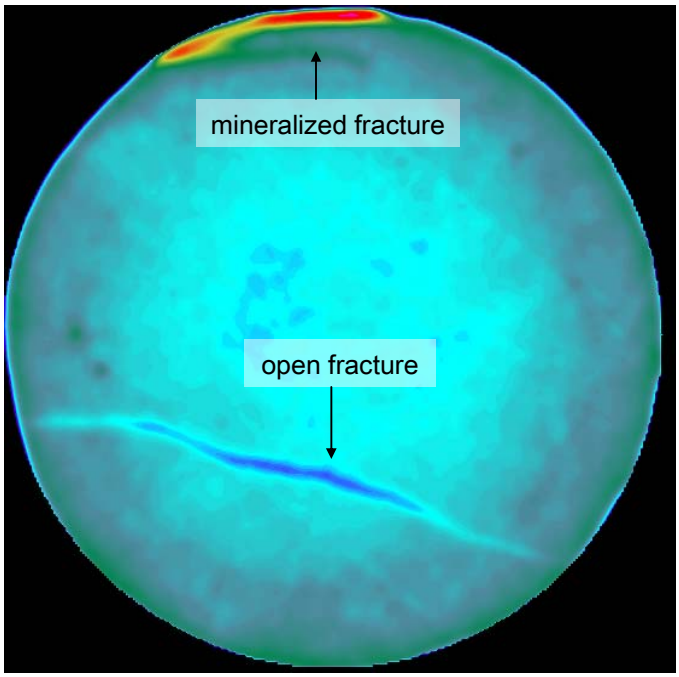

Fig. 1.7.13—Single CT image of Core-A.

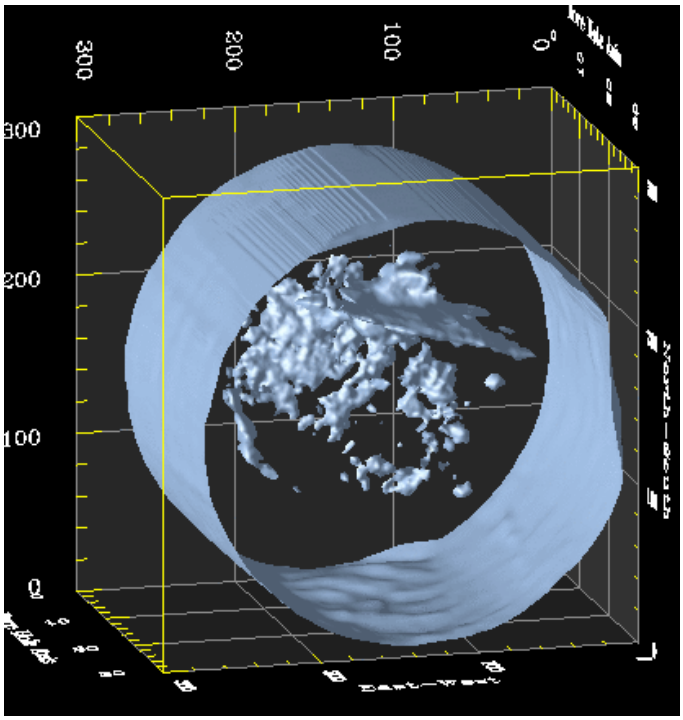

Fig. 1.7.14—3D image of fracture of Core-A

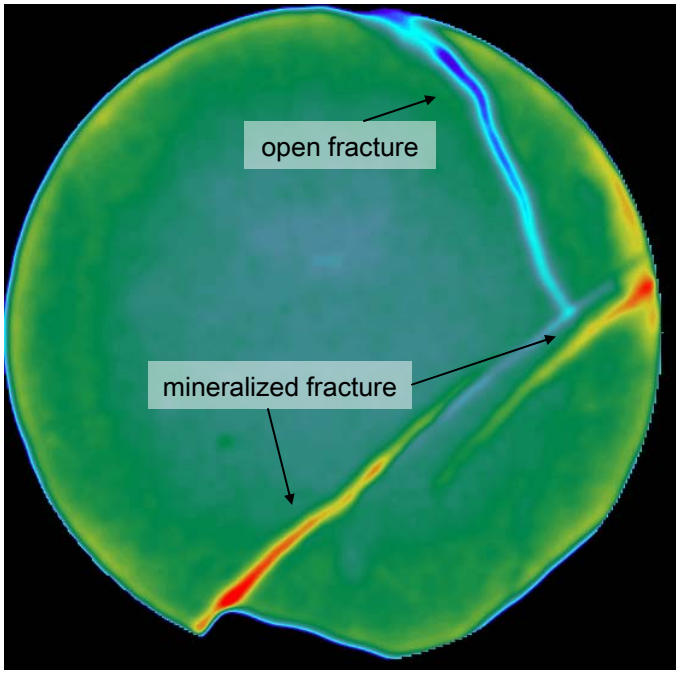

Fig. 1.7.15— Single CT image of Core-B.

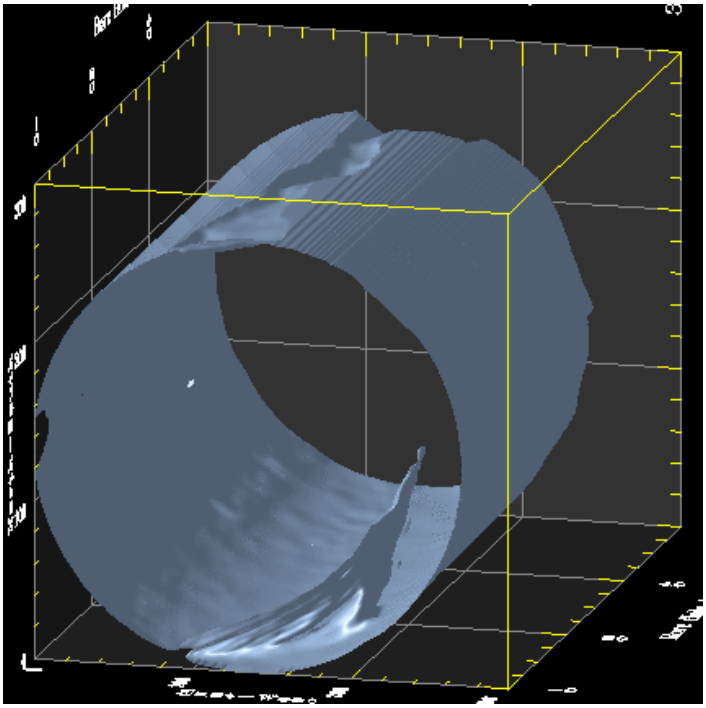

Fig. 1.7.16—3D image of fracture of Core-B.

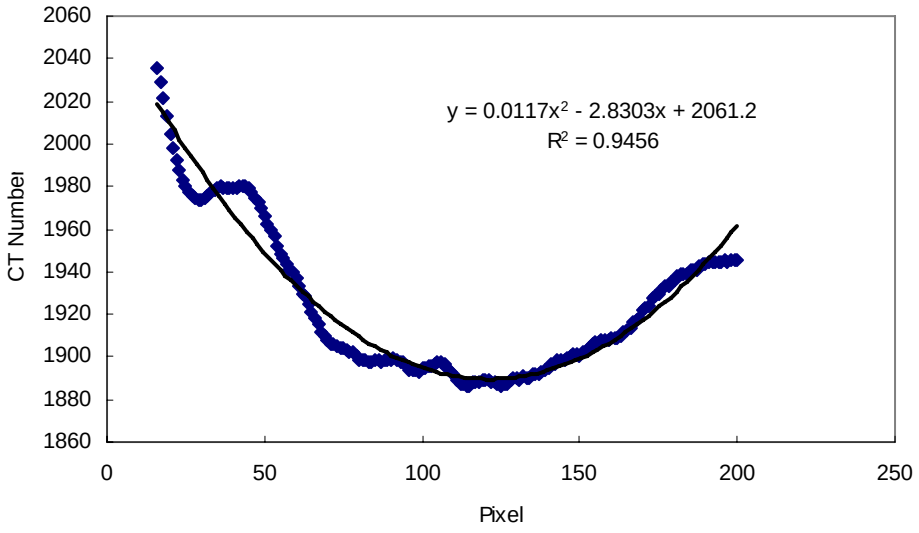

(a) Core-A

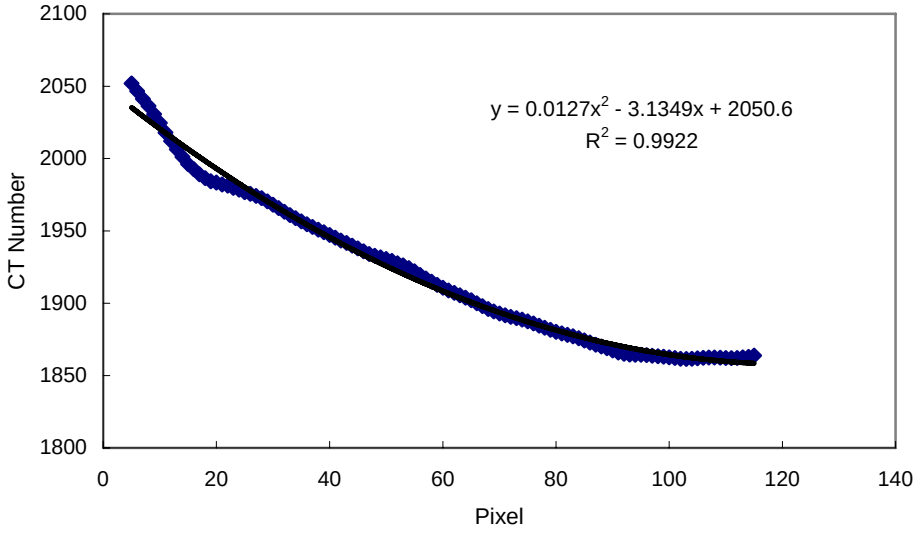

(b) Core-B

Fig. 1.7.17—Minimum CT number according to locations.

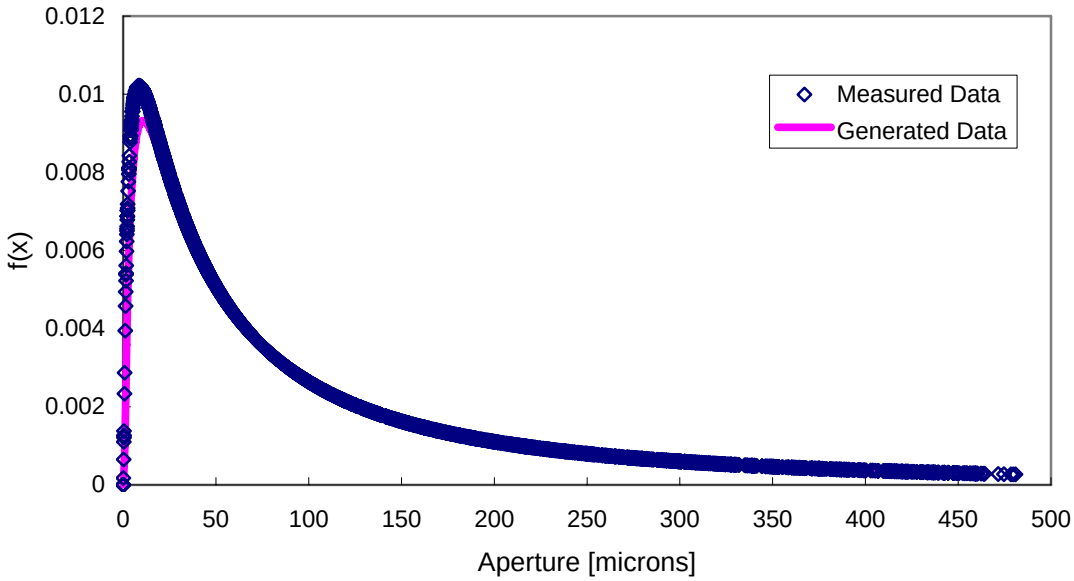

Fig. 1.7.18—Distribution of Measured Data & Generated Data (Core-A).

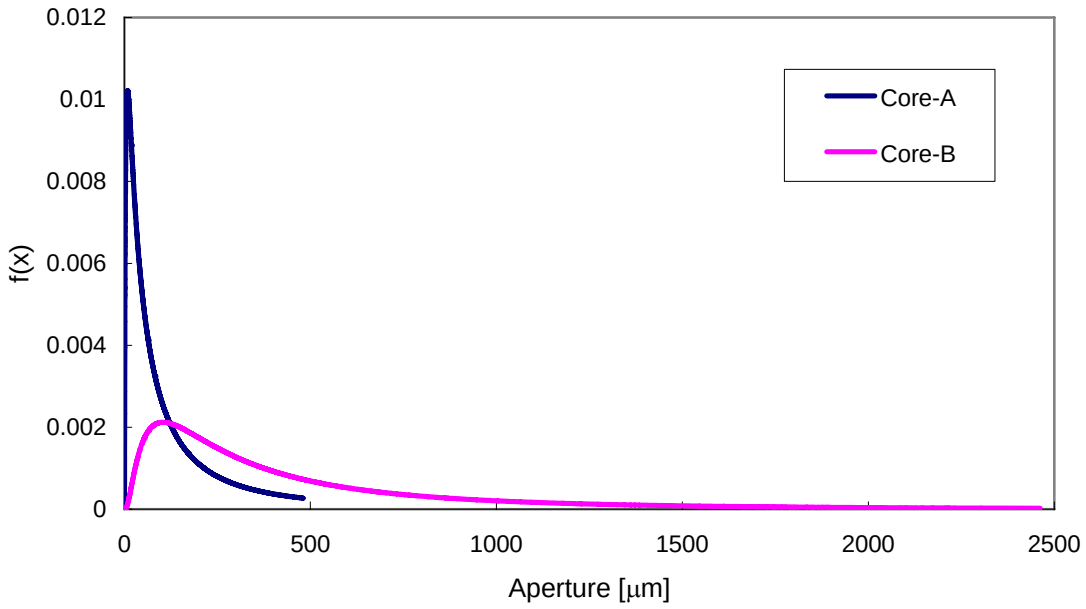

Fig. 1.7.19—Comparison of Aperture Distributions between Core-A and Core-B.

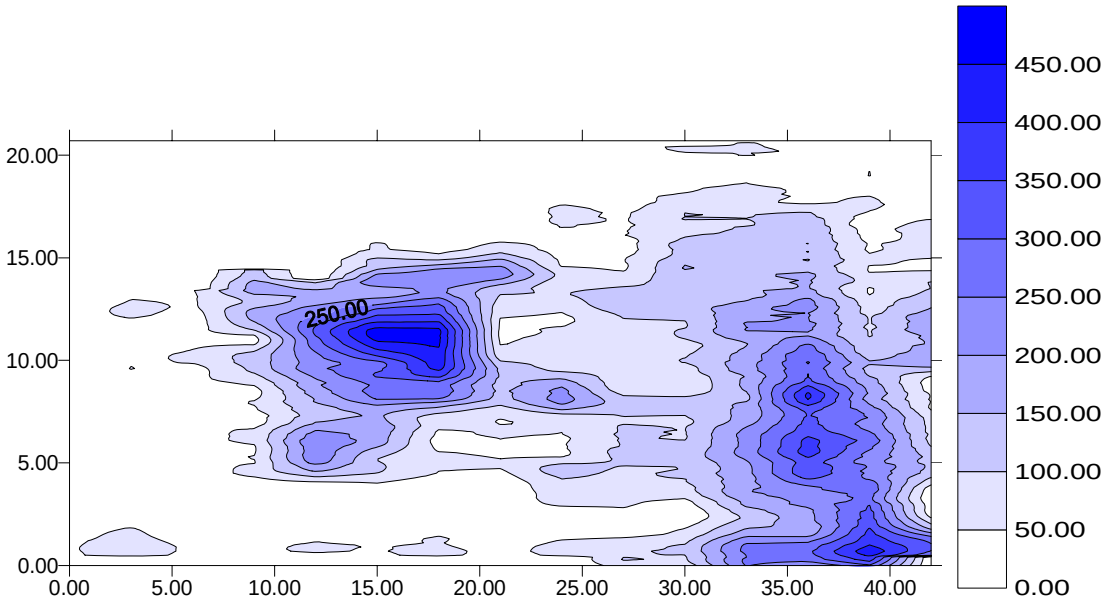

Fig. 1.7.20—Aperture contour map of Core-A in μm.

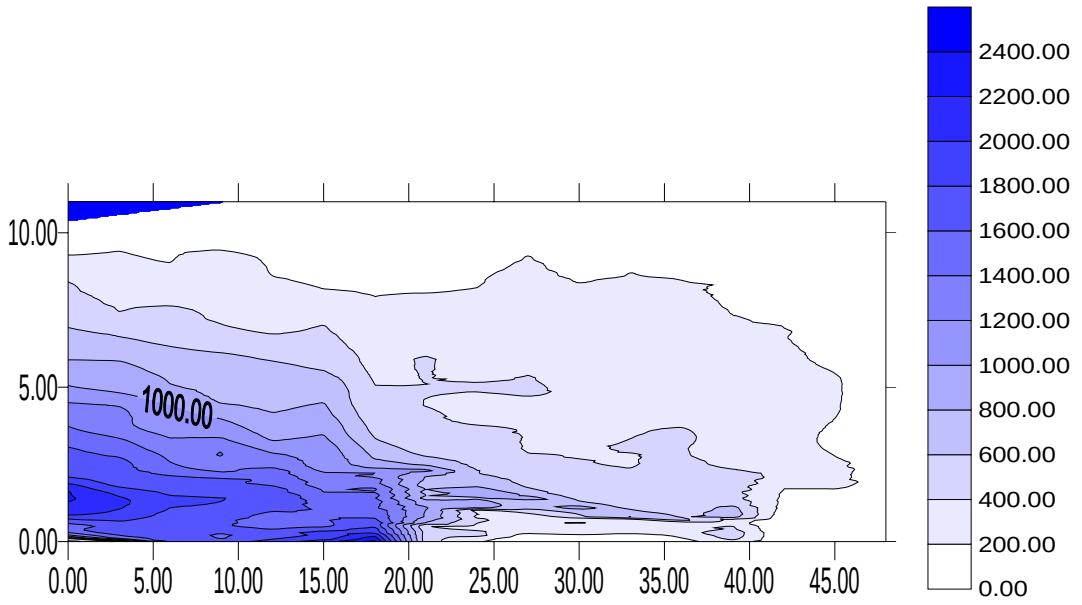

Fig. 1.7.21—Aperture contour map of Core-B in μm.

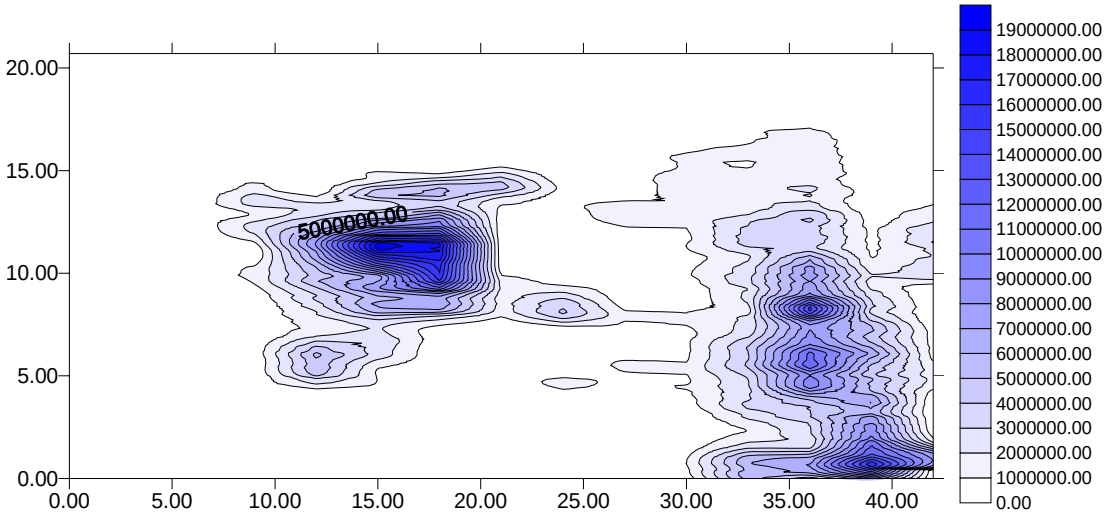

Fig. 1.7.22—Permeability contour map of Core-A in md.

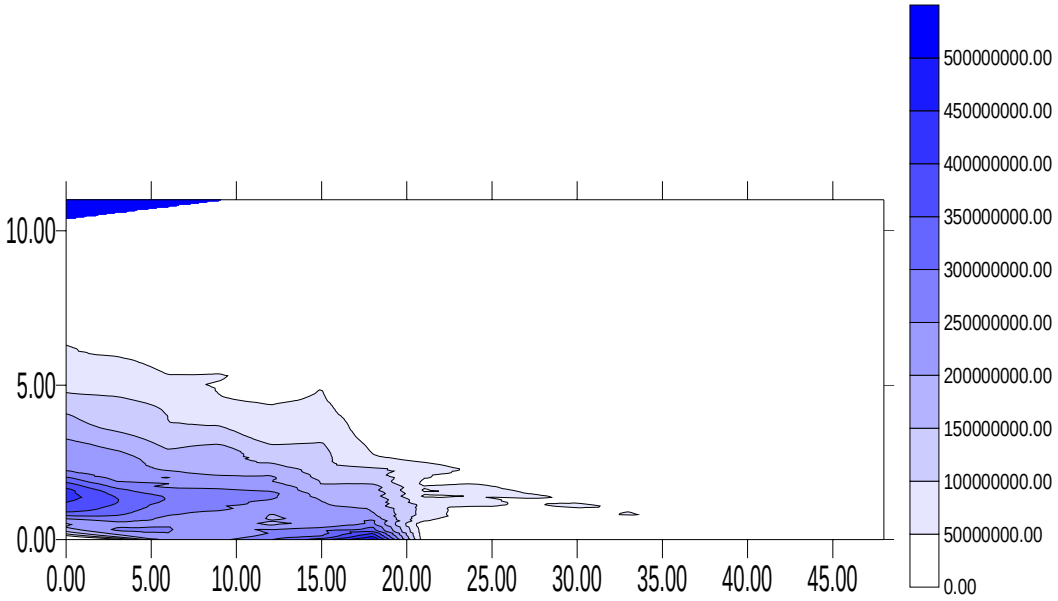

Fig. 1.7.23—Permeability contour map of Core-B in md.

Chapter II-1

Experimental and Simulation Analysis of Fractured Reservoir Experiencing Different Stress Conditions

2.1.1 INTRODUCTION

In the first comprehensive work on flow through open fractures, Lomize[1], used parallel glass plates and demonstrated the validity of cubic law for laminar flow. He modeled fluid flow with different fracture shapes and investigated the effects of changing the fracture walls from smooth to rough. Later comprehensive fluid flow studies[2,3] were conducted through a single fracture to investigate the validity of cubic law. Idealized fracture models were constructed by assuming that the fracture planes had contact area and roughness.

The flow in a fracture is usually characterized by the classical cubic law equation,[4]

$$Q = 5.11 \times 10^{6}\left[\frac{d\Delta P w^{3}}{L\mu}\right]. \quad \text{..... (1)}$$

This equation neglects the matrix permeability as a part of the fracture permeability. As a result, the classical cubic law does not account for any flow occurring through the matrix and assumes that the flow occurs entirely through the fracture. This assumption holds for low permeability reservoirs. However, in high-permeability reservoirs the classical cubic law is no longer valid and has to be modified by considering the effect of matrix permeability.[5] Flow might also be diverted from the fracture to matrix where fracture aperture size decreases under increasing stress conditions.[6]

The cubic law equation is valid only for steady-state laminar flow between two parallel-plates. This equation assumes that the walls of the fracture are smooth. Witherspoon *et al.*[4] validated parallel-plate theory in the laboratory and showed that the parallel-plate approximation tends to break down at higher normal stress (>10 MPa) across the fracture. Alfred[5] also confirmed that the parallel-plate assumption is not valid to adequately model the fluid-flow experiments when overburden pressure is significant. The flow in a single fracture does not progress uniformly as assumed by parallel-plate theory; rather, it flows through a limited number of channels.[7,8,9] Several authors[7,9,10] measured fracture aperture directly without any applied stresses and found that fracture apertures follow log-normal distribution. Muralidharan *et al.*[11] extended the previous work[12,13] by measuring fracture

aperture under different stresses using a CT scanner and found that the fracture apertures still follow log-normal distribution for all stress conditions.

In this study, we performed fluid flow experiments on homogeneous and fractured cores with different overburden pressures and injection rates to obtain mean fracture aperture and to measure fluid flow through matrix and fracture under different overburden pressures. To obtain fracture apertures from these experiments, we derived analytical equations by combining cubic law and weighted average of the permeabilities. Once the mean fracture apertures were obtained, we then used them to calculate the fluid flow through matrix and fracture. The mean fracture apertures were distributed for each overburden pressure using log-normal distributions following our previous results.[11] We used these aperture distributions and the matrix permeability calculated from the experiments as input data, and the measured pressure drop and calculated flow rates through matrix and fracture as observed data for our simulation modeling.

Once a match between simulation result and experimental data was obtained, we also compared the simulation result with parallel-plate model to prove that the parallel-plate model is not valid for modeling fluid flow through rough surfaces. The parallel-plate model has only mean fracture aperture without distributing the apertures on the fracture surface. In addition we validated our approach using our distributed aperture model on gravity drainage experiments. We used our CT scanner to obtain saturation distribution during fluid flow in the core and matched the fluid flow profile and average water saturations.

2.1.2 EXPERIMENTAL PROCEDURE

Synthetic brine was used in the experiments. The brine contains NaCl and $CaCl_2.H_2O$ mixed with distilled water. The clean core was saturated with brine then inserted into a Hassler-type core holder using a confining pressure of 500 psia. Then, core flooding was performed with different injection rates. After running a set of injection rates at this pressure, we changed to other confining pressures and performed with different injection rates again. A similar procedure was performed using a fractured core. The experimental set up is shown in Fig. 2.1.1.

Berea core was used during the core flooding experiments. The core properties are given in Table 1.2.1. Injection rates ranging from 5 cm^3/min to 20 cm^3/min were performed at each overburden pressure. Three different overburden pressures (500 to 1,500 psia) were applied for both unfractured and fractured cores. The core was cut using a hydraulic cutter to generate a single fracture horizontally along the axis of the core.

2.1.3 ANALYTICAL EQUATIONS

When water was injected through the homogeneous core with a fully water-saturated matrix and at steady-state conditions, we obtained a pressure difference between injecting and producing ends. According to Darcy's law, matrix permeability can be calculated by:

$$k_m = \frac{\mu QL}{A\Delta P}. \quad \text{..... (2.1.2)}$$

When water was injected through the fractured core, we obtained the average pressure difference due to the presence of fracture. According to Darcy's law, average permeability in the fractured core can be calculated by:

$$k_{avg} = \frac{\mu QL}{A\Delta P_{avg}}. \quad \text{..... (2.1.3)}$$

Tables 1.2.2 and 1.2.3 show the results obtained from experiments with unfractured and fractured cores and the calculated permeability values. Fig. 2.1.2 shows that the effect of varying overburden pressures on the unfractured core is not significant, in contrast with that effect on the fractured core. The average permeability of the fractured core reduces significantly and is almost similar to permeability of unfractured core at 1,500 psia. The results suggests that the effect of stresses may be most pronounced in fractured reservoirs where large pressure changes can cause significant changes in fracture aperture and the related changes in conductivity within a reservoir.

From experimental analysis, we obtained matrix and average permeabilities as discussed previously. The fracture permeability, k_f, obtained from the parallel-plate model is[4]

$$k_f = 8.45 \times 10^9 w^2. \quad \text{..... (2.1.4)}$$

Fracture width is a function of fracture permeability, but both parameters are unknown. To obtain those parameters, another equation is needed. By the concept of parallel flow, we obtained the equation for total flow rate (or injection rate) as follows:

$$Q = Q_f + Q_m. \quad \text{..... (2.1.5)}$$

Since the flow rates were measured at steady-state conditions, the pressure drop in the matrix and fracture would be the same. Thus, Eq. 2.1.5 can be simplified to weighted average permeabilities as follows:

$$k_{avg}A = k_f A_f + k_m A_m. \quad \text{..... (6)}$$

In this equation A represents total area of the core, A_f represents area of the fracture which is equal to wd, and A_m represents area of the matrix which is equal to $A - wd$. In the parallel-plate assumption, k_m is assumed to be zero; therefore the fracture permeability is the same as the average permeability in a fractured core. But, in conditions of high matrix permeability, the weighted average permeabilities should be combined with cubic law equation to represent the fluid flow in a fractured reservoir. By rearranging Eq. 2.1.6 we obtain an expression for calculating fracture permeability, k_f as given below:

$$k_f = \frac{k_{avg} A - k_m (A - wd)}{wd}. \quad \text{..... (2.1.7)}$$

Now, we have two equations and two unknowns. So, combining Eqs. 2.1.4 and 2.1.7, we arrive at Eq. 2.1.8:

$$8.45 \times 10^9 w^3 d - k_{avg} A + k_m (A - wd) = 0. \quad \text{..... (2.1.8)}$$

This equation can be solved iteratively to obtain fracture width. Once the fracture width is obtained, the fracture permeability can be calculated either using Eqs. 2.1.4 or 2.1.7.

Fig. 2.1.3 shows the variation of mean aperture size with various overburden pressures and injection rates. The effect of several injection rates on the matrix permeability is not significant, in contrast with the effect of overburden pressures on mean fracture aperture. The average mean fracture aperture decreases about 71% from its original value when the overburden pressure changes from 500 psia to 1,500 psia. We can see the effect of hysteresis on fracture aperture for various injection rates. At higher injection rates, the pressure drop becomes higher through the matrix and increases the tendency to squeeze the fracture aperture. Hence, the fracture aperture becomes smaller at higher injection rates. Fig. 2.1.4 shows the variation of mean fracture permeability with various overburden pressures and injection rates. During the constant injection rates of 5 to 20 cm^3/min, the average fracture permeability decreases about 91% at the overburden pressure of 1,500 psia from its original value at 500 psia. The trend of fracture permeability with overburden pressure is the same for all injection rates.

It is also important to determine the flow rate through matrix (Q_m) and fracture (Q_f). We determine the flowrate from each zone by applying Darcy's equations. The equation for flow rate in the matrix is given below:

$$Q_m = \frac{k_m A \Delta P_{avg}}{\mu L}. \quad \text{..... (2.1.9)}$$

The flow through a smooth conduit can be expressed by involving the fracture width (w) and the pressure gradient (Δp_{avg}):

$$q_f = \left(\frac{1}{9.86 \times 10^{-9}} \right) \frac{w^3 d\Delta p_{avg}}{12 \mu L}. \quad \text{..... (2.1.10)}$$

Fig. 2.1.5 shows the trend of fracture flowrate with the change in overburden pressure. The fracture flowrate decreases with the increase in overburden pressure. For example, the fracture flowrate at 500 psi overburden pressure and at 5 cm^3/min injection rate is about 4 cm^3/min. This means around 80% of the flow is through the high-permeability fractures. The amount of flow at different injection rates through the fracture drops dramatically to similar rates at confining pressure of 1,500 psi (about 1 cm^3/min). This means that most of the water flows through the matrix, diverting from the fracture path (Fig. 2.1.6). Even though the fracture permeability is still very high (10 to 40 darcy), the volumetric rate of fracture becomes limited. Most of the water flows through the matrix rock of less permeability (200 md). The reduction of the fracture permeability clearly has significant effects on reservoir productivity.

2.1.4 PARALLEL PLATE SIMULATION MODEL

We used a commercial simulator (CMG™) to study the fluid flow through fracture at different overburden pressures, duplicating the laboratory process in which the water was injected through the fracture and using the parallel-plate assumption. We used a rectangular grid block to overcome the difficulty of modeling a cylindrical core shape.[14] The mean fracture aperture and mean fracture permeability obtained from analytical solution were constant values in all the grid blocks in our 10x10x15 simulation model (Fig. 2.1.7). An injector was placed in the fracture block from which water was injected and producers were placed in fracture and matrix blocks (Fig. 2.1.8).

Fig. 2.1.9 shows the fluid movement through fracture surface using the parallel-plate model for 5 cm^3/min injection rate under various overburden pressures. The fluid flows uniformly in each grid block. We observed different data and simulation results for flowrate through matrix and fracture (Fig. 2.1.10 and 2.1.11) and pressure drop. The simulated fracture rate is higher than the observed fracture flowrate due to constant fracture permeability in the grid-block simulation model.

2.1.5 DISTRIBUTED SIMULATION MODEL

The distributed simulation model was constructed with the same number of grid blocks and sizes. The fracture apertures in the fracture layer were distributed in a log-normal distribution for various

stress conditions found in our earlier study[11]. The frequency of the log-normal distribution[15] is written as follows:

$$f(x) = \frac{1}{x\sqrt{2\pi\beta^2}} \exp\left[\frac{-(\ln x - \alpha)^2}{2\beta^2}\right], \quad \text{..... (2.1.11)}$$

where,

$$\beta^2 = \ln(1 + \frac{\sigma^2}{\delta^2}) \text{..... (2.1.12)}$$

and

$$\alpha = \ln \delta - \frac{\beta^2}{2}. \quad \text{..... (2.1.13)}$$

The fracture apertures were then converted to fracture permeability using the relation between aperture and permeability (Eq. 2.1.4). The aperture maps for the fracture layer were then constructed for each overburden pressure by generating log-normal fracture apertures using the mean fracture aperture obtained from the analytical solution.

The relationship between the mean and the variance of apertures was derived from our previous paper.[11] The values of mean apertures obtained from analytical solution were 56.15, 40.4, and 20.57 microns for 500, 1,000, and 1,500 psi, respectively. The corresponding values of variance were 9,417.8, 5,934.8, and 1,296.9. We can see that the variance decreases as the mean aperture decreases. The variance in the parallel-plate model is zero; therefore there is no preferential path for the fluid. The fluid flows in a block-type pattern, resulting in more flow than we had observed. If the fracture apertures are distributed, then variable apertures control the fluid flow in the fracture. The fluid flows to the path of least resistance and interconnected large apertures. The smaller apertures have less volumetric rate, which creates barriers to fluid flow through the fracture. Thus, the fluid diverts to the matrix blocks. Since the fluid flow follows the preferred path through the rough surfaces, then the rate of fluid through fracture and matrix blocks (Fig. 2.1.12) and the pressure drop can be matched adequately with the experimental results (Fig. 2.1.13).

2.1.6 GRAVITY DRAINAGE EXPERIMENT

We performed a gravity drainage experiment with a CT scanner to differentiate the fluid flow through parallel-plate and distributed-aperture models. Water was injected on top of a fractured core at a rate of 0.5 cm^3/min. Cross-sectional scans were taken from 0 to 12 minutes, as shown in Fig.

2.1.14. The first five scans were taken at 0.5-min interval, the next four scans at 1-min intervals, and the last three scans at 2-min intervals.

Using the parallel-plate simulation model, the fluid flow profiles were not able to match the profile from CT scan results (Fig. 2.1.14). The fluid in this model falls rapidly through the high, single-fracture permeability. As a result, average water saturation also did not adequately represent the CT result (Fig. 2.1.15). Using the distributed aperture model in which the apertures were distributed in a log-normal distribution using Eq. 11, the fluid flow profiles match the CT scan profiles (Fig. 2.1.16). A good agreement of average water saturation was also shown between observed data and simulated results (Fig. 2.1.17).

2.1.7 CONCLUSIONS

1. Cubic law has to be modified by combining the weighted average of permeabilities to account for the flow through the matrix for high-permeability, fractured reservoirs.
2. The parallel-plate assumption with a single fracture aperture is not valid for modeling fluid flow through fractured reservoirs.
3. The distributed-fracture-aperture model adequately represents the fluid flow behavior in fractured reservoirs.

NOMENCLATURE

A	=	area of core, cm^2
A_f	=	area of fracture, cm^2
A_m	=	area of matrix, cm^2
d	=	core diameter, cm
$f(x)$	=	frequency of apertures
k_{avg}	=	average permeability in fractured core, md
k_m	=	matrix permeability, md
k_f	=	fracture permeability, md
L	=	core length, cm
Q	=	injection rate, cm^3/min
Q_f	=	flowrate through fracture, cm^3/min
Q_m	=	flowrate through matrix, cm^3/min

w = mean fracture aperture, cm

x = fracture aperture

ΔP = pressure drop, psia

ΔP_{avg} = av. pressure drop in fractured core, psia

α = log-normal mean

β = log-normal standard deviation

δ = mean of the aperture sizes

μ = viscosity of Brine, cp

σ = standard deviation

REFERENCES

1. Lomize, G. M., Seepage in Fissured Rocks; *State Press, Moskow-Leningrad, 1951.*
2. Iwai, K., Fundamental Studies of Fluid Flow Through a Single Fracture; *Ph. D. Thesis, Univ. of Calif. Berkeley, 1976.*
3. Neuzil, C. E., and Tracy. J. V., Flow Through Fractures; *Water Resources Research, 16 (6), 1016-1024, 1980.*
4. Witherspoon, P. A., Wang, J. S. Y., Iwai, K., and Gale, J. E., Validity of Cubic Law for Fluid Flow in a Deformable Rock Fracture; *Water Resources Research, 16(6), 1016-1024, 1980.*
5. Alfred, D., Modeling Fluid Flow Through a Single Fracture Using Experimental, Stochastic and Simulation Approaches; *master's thesis, Texas A&M University, 2003.*
6. Putra, E., Muralidharan, V., and Schechter, D.S., Overburden Pressure Affects Fracture Aperture and Fracture Permeability in a Fracture Reservoir; *Saudi Aramco Journal of Technology, Fall 2003.*
7. Pyrak, L. R., Myer, L. R., and Cook, N. G. W., Determination of Fracture Void Geometry and Contact Area at Different Effective Stress; *Eos Trans. AGU (abstract), 66(46), 903, 1985.*
8. Tsang, Y. W., The Effect of Tortuosity on Fluid Flow Through a Single Fracture; *Water Resources Research, 20(9), 1209-1215, 1984.*
9. Tsang, Y. W., and Witherspoon, P. A., The Dependence of Fracture Mechanical and Fluid Properties on Fracture Roughness and Sample Size; *J. Geophys. Res., 88(B3), 2359-2366, 1983.*
10. Tsang, Y. W. and Tsang, C. F., Hydrological Characterization of Variable-Aperture Fractures; *Rock Joints, Barton & Stephansson (eds), Balkema, Rotterdam, 1990.*

11. Muralidharan, V., Putra, E., and Schechter, D.S., Investigating Fracture Aperture Distributions under Various Stress Conditions Using X-Ray CT Scanner; *Canadian International Petroleum Conference to be held in Calgary, Canada, June 2004.*
12. Keller, A. A., Single and multiphase flow and transport in fractured porous media; *PhD thesis, Stanford University (1996).*
13. Keller, A.A., High Resolution CAT Imaging of Fractures in Consolidated Materials; *Int. J. Rock Mech. Min. Sci. (1997), 34 (3/4), 358-375.*
14. Putra, E., Fidra, Y., and Schechter, D.S., Study of Waterflooding Process in Naturally Fractured Reservoirs from Static and Dynamic Imbibition Experiments; *paper SCA 9910 presented at the 1999 International Symposium of the Society of Core Analysts, Colorado, 1-4 August.*
15. Alfred, D., Putra, E., and Schechter, D.S., Modeling Fluid Flow through Single Fractures Using Experimental, Stochastic and Simulation Approaches; paper SPE/DOE 89442 will be presented at 2004 Improved Oil Recovery Symposium, OK, Tulsa, 17–21April.

TABLE 2.1.1— Berea Core Properties

Length	4.9784 Cm
Diameter	2.5146 Cm
Viscosity	1.0 Cp
Area	10.9637 Cm^2
Porosity	23.58%

TABLE 2.1.2 — Experimental Observations for Unfractured Core

Pob **psia**	***Dp*** **psia**	k_{av} **md**	***Q*** **Cm^3/min**
501.3	1.4	877.5	5
500.2	2.8	877.6	10
503.3	4.1	898.9	15
503.3	5.4	910	20
494.8	1	1228.7	5
509.4	2.6	945.1	10
508.8	4.2	877.6	15
509.6	5.8	847.3	20
970.5	2.2	558.4	5
1000.5	4.8	511.9	10
1001	7.6	485	15
1016.7	11.3	434.9	20
1000.8	2.3	534	5
1002.2	5.8	423.6	10
1009.7	9.1	405	15
1002.7	13.9	353.6	20
1500.3	4.2	292.5	5
1504.6	9.3	268.2	10
1507.9	15.1	244.1	15
1504.8	21.4	229.6	20
1500.7	5	245.7	5
1506	10.9	225.4	10
1509.6	17.4	211.8	15
1509.6	22.5	218.4	20

TABLE 2.1.3— Experimental Observations for Fractured Core.

Pob **psia**	***Dp*** **psia**	k_m **md**	***Q*** **Cm³/m**
485.7	4.1	299.7	5
506.4	8.1	303.4	10
502.9	12.4	297.2	15
504.4	16.5	297.85	20
501	4.2	292.5	5
504.9	8.5	289	10
501	13	283	15
502	17	289.1	20
1000.4	4.5	273	5
1002.4	9	273	10
1000.5	13.7	269	15
1000.5	18.2	270	20
1000.2	4.8	255.9	5
1003.5	9.7	253.3	10
1002.7	14.5	254.2	15
1004.1	19.2	255.96	20
1500	5.1	240.8	5
1500	10.4	236.3	10
1500.7	16.4	224.7	15
1503.1	22.1	222.4	20
1500.3	5.5	223.4	5
1501	11.2	219.4	10
1501.3	17.3	213	15
1502.3	22.7	216.5	20

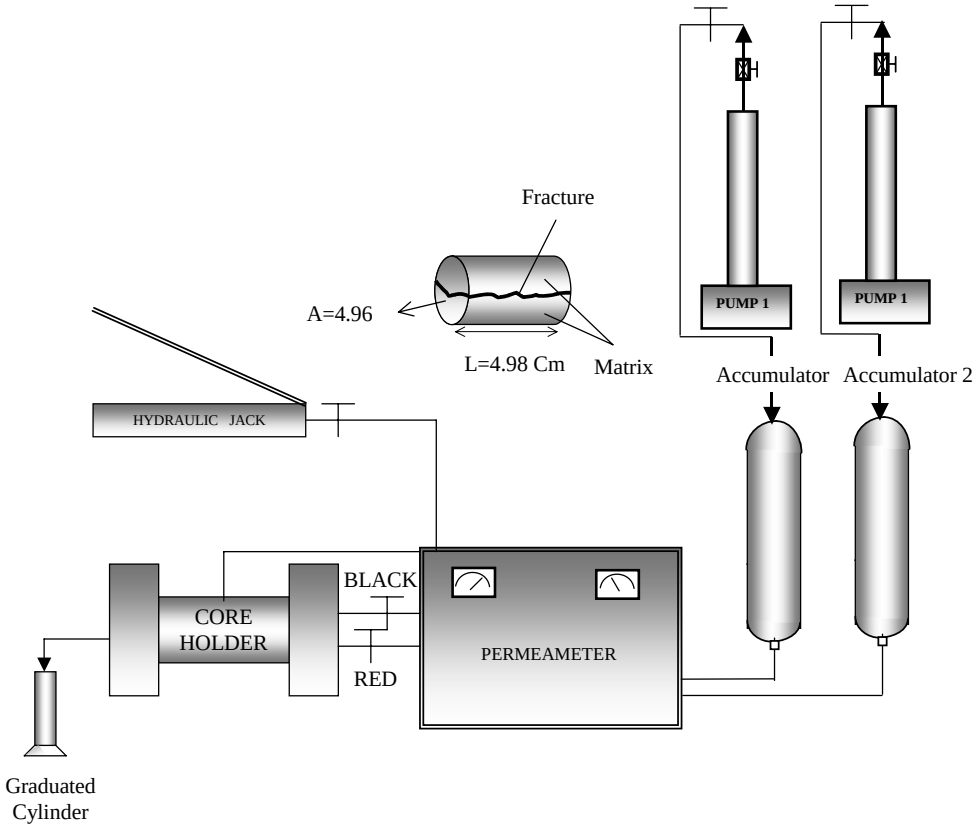

Fig. 2.1.1— Schematic diagram of the core-flooding experiment.

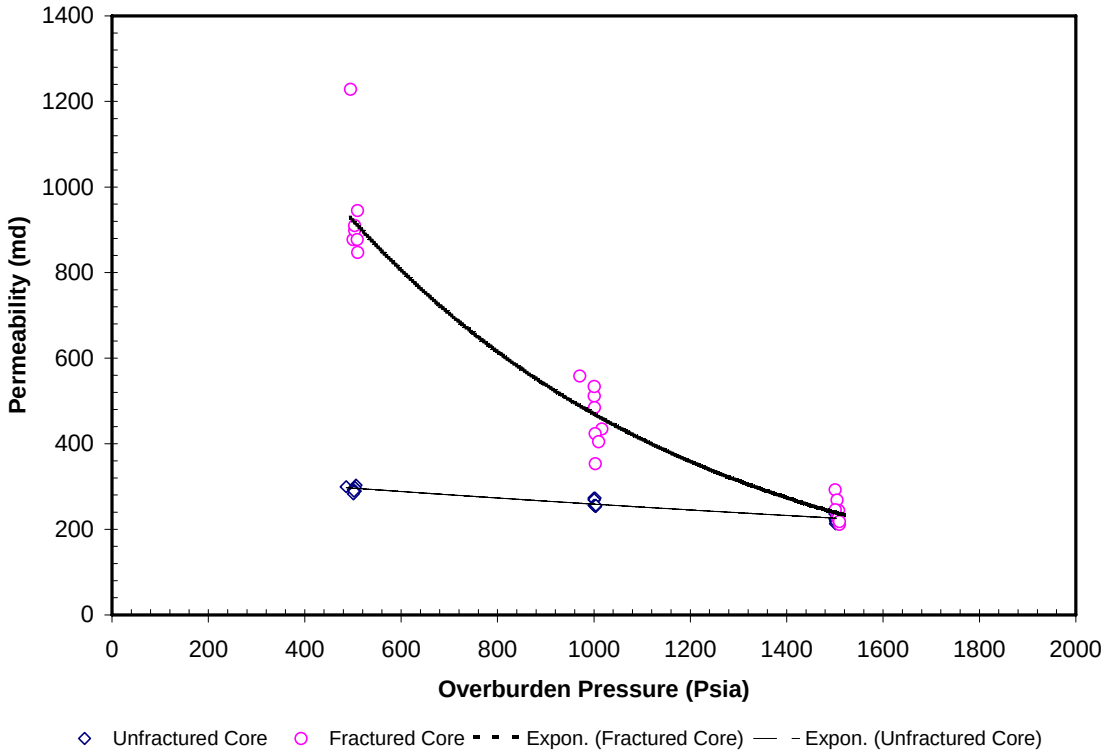

Fig. 2.1.2— Comparison of permeability reduction between unfractured and fractured cores under increasing overburden pressures.

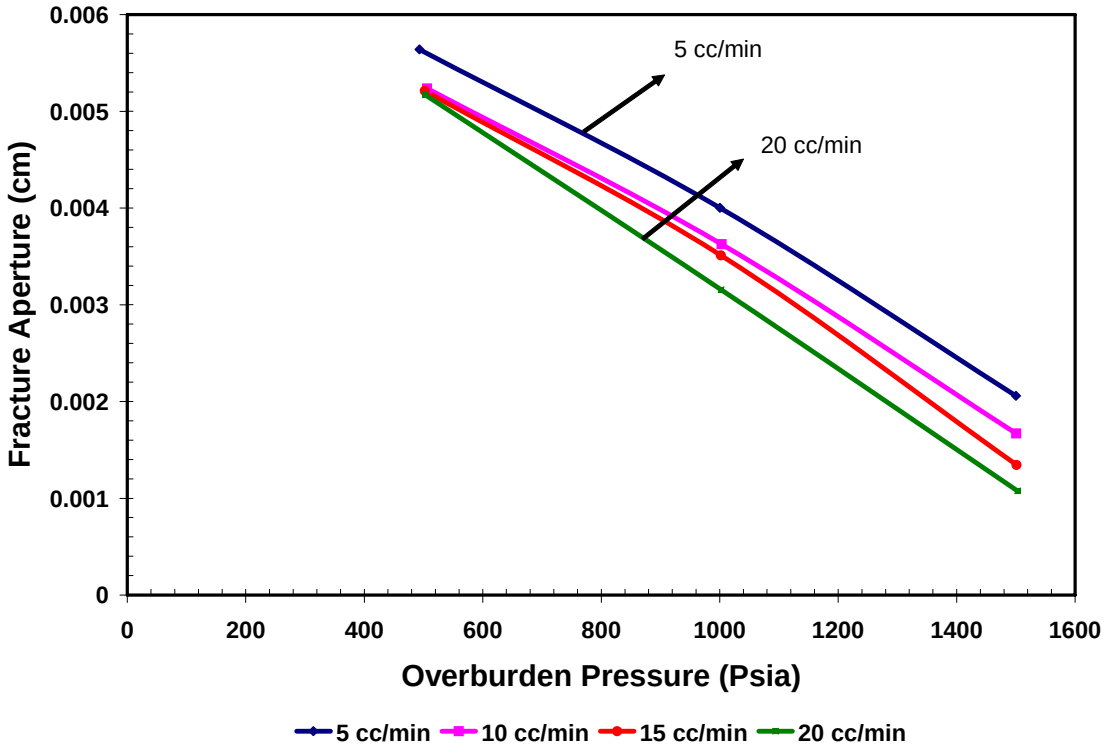

Fig. 2.1.3 — Effect of injection rates on fracture aperture at variable overburden pressures.

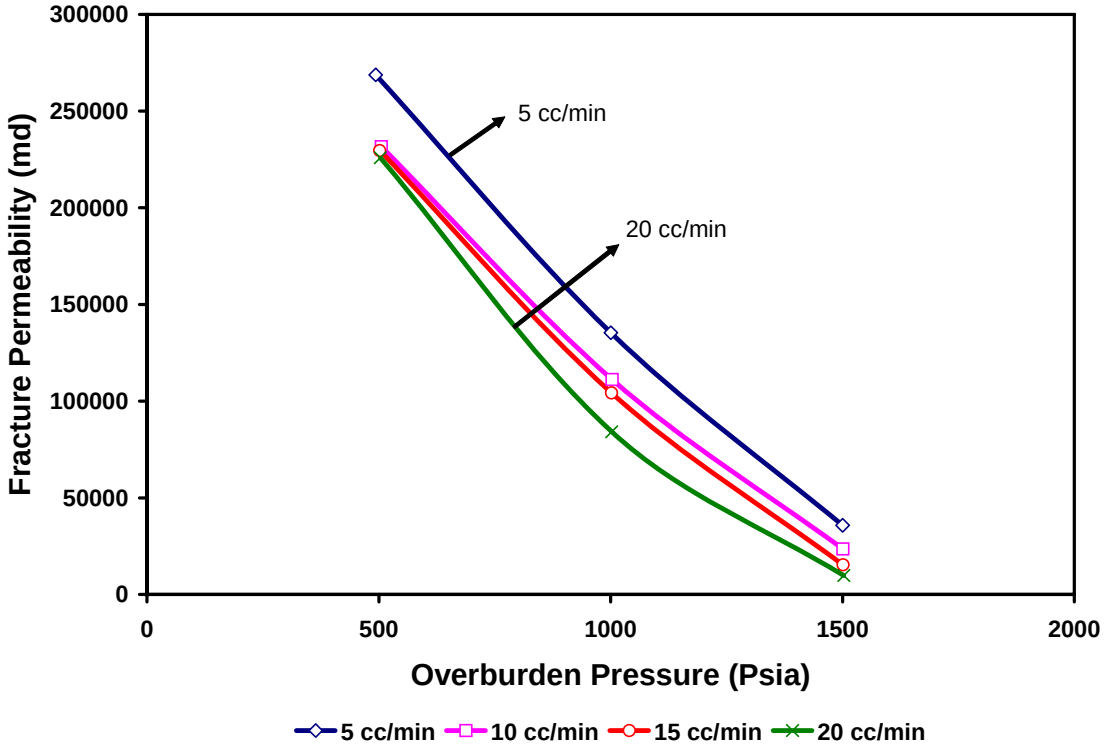

Fig. 2.1.4— Effect of injection rates on fracture permeability at variable overburden pressures.

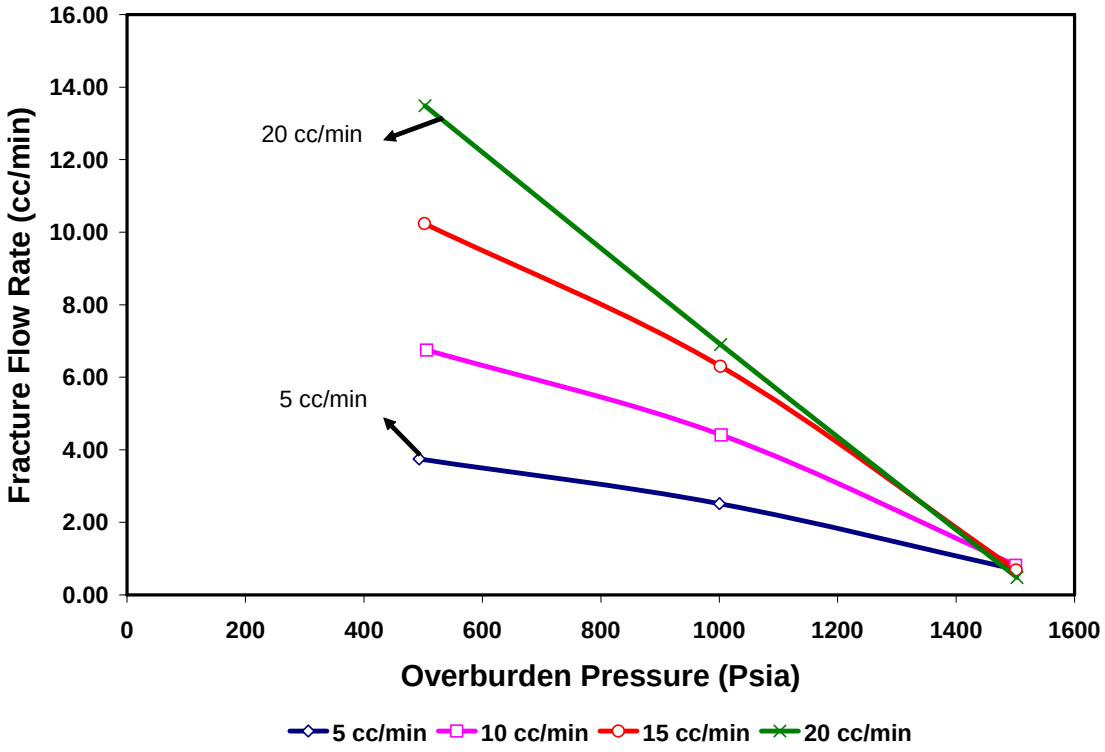

Fig. 2.1.5 — Effect of overburden pressures on fracture flowrates.

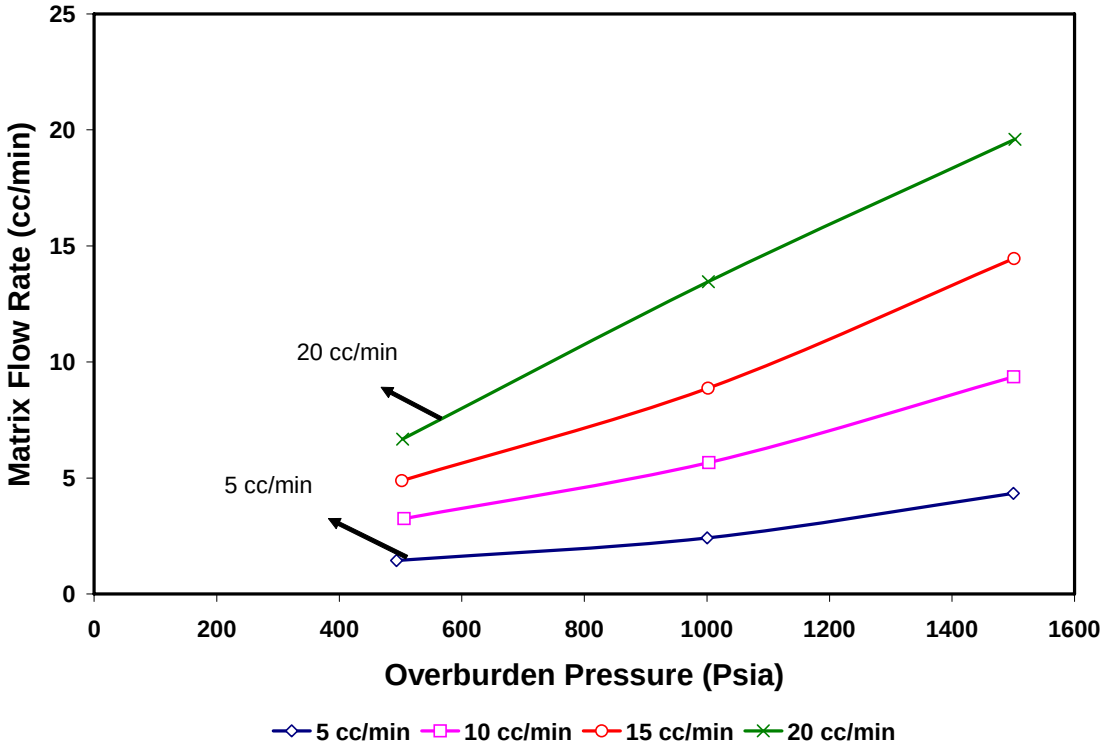

Fig. 2.1.6 — Effect of overburden pressures on matrix flowrates.

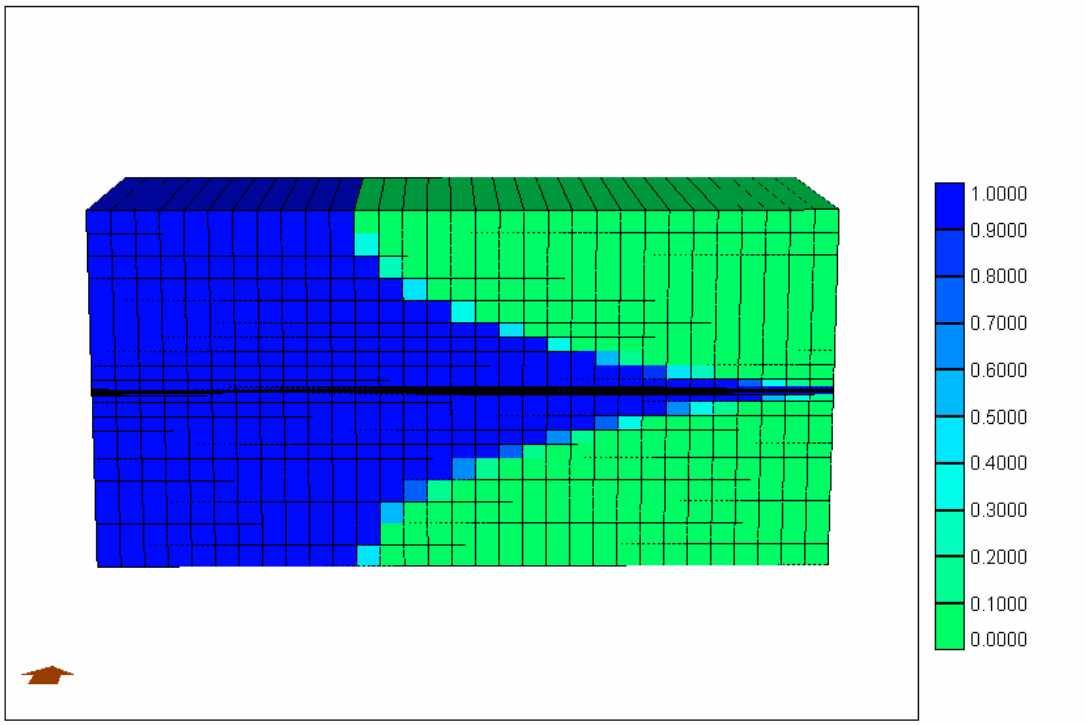

Fig. 2.1.7— Water saturation change in matrix and fracture at transient flow condition.

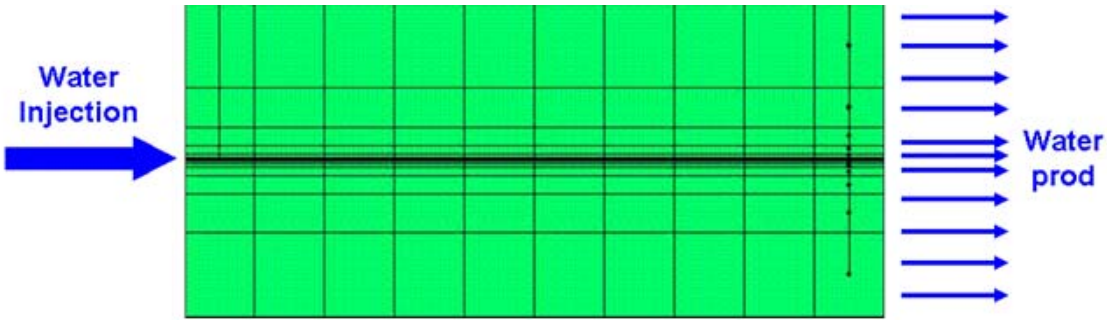

Fig. 2.1.8 — Simulation model showing injector and producers.

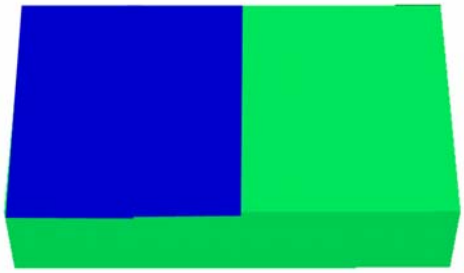

Fig. 2.1.9— Flow through fracture surface in parallel-plate model.

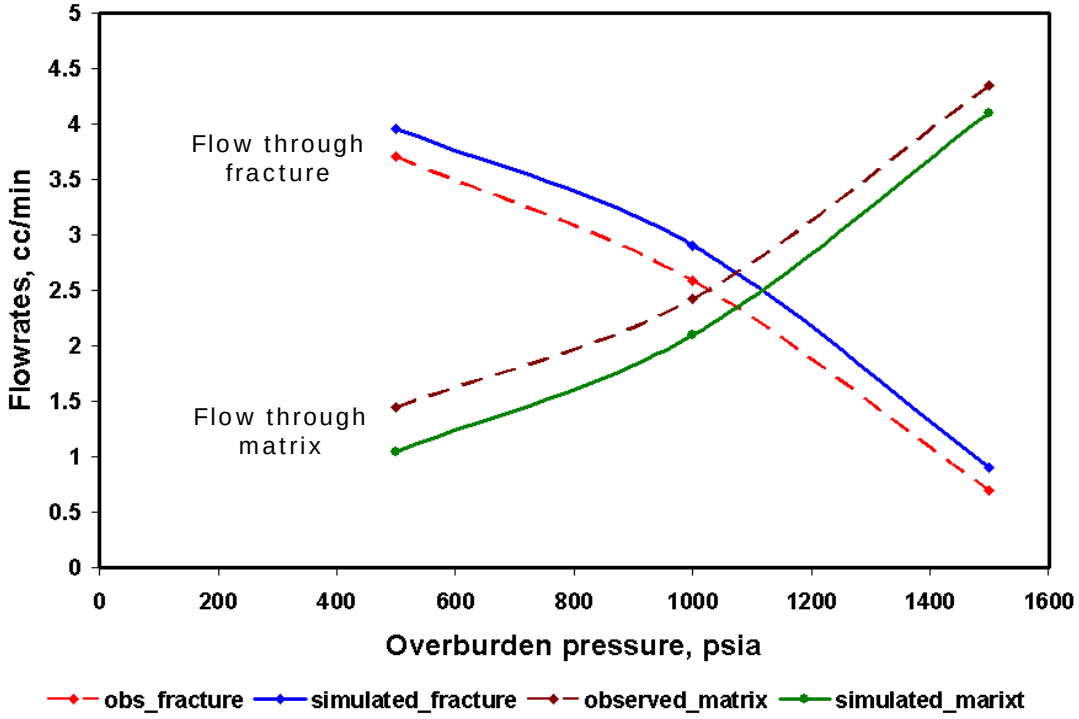

Fig. 2.1.10 — Simulation results of matrix and fracture flowrate at 5 cm^3/min injection rate under various overburden pressures.

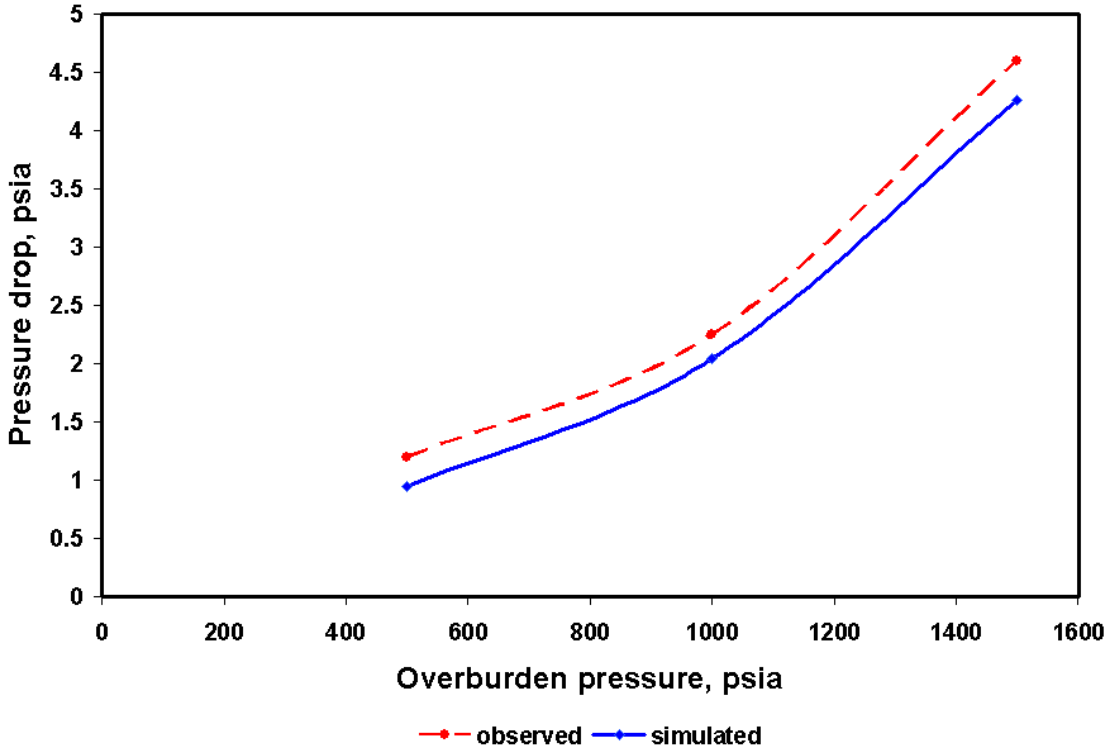

Fig. 2.1.11 — Simulation results of matrix and fracture flowrate at 5 c^3/min injection rate under various overburden pressures.

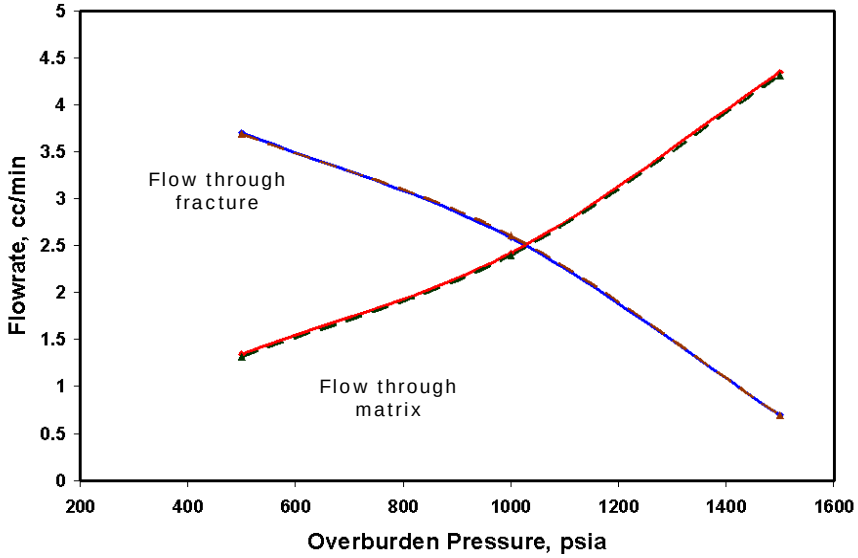

Fig. 2.1.12 — Simulation results of matrix and fracture flowrate at 5 cm^3/min injection rate under various overburden pressures using distributed simulation model.

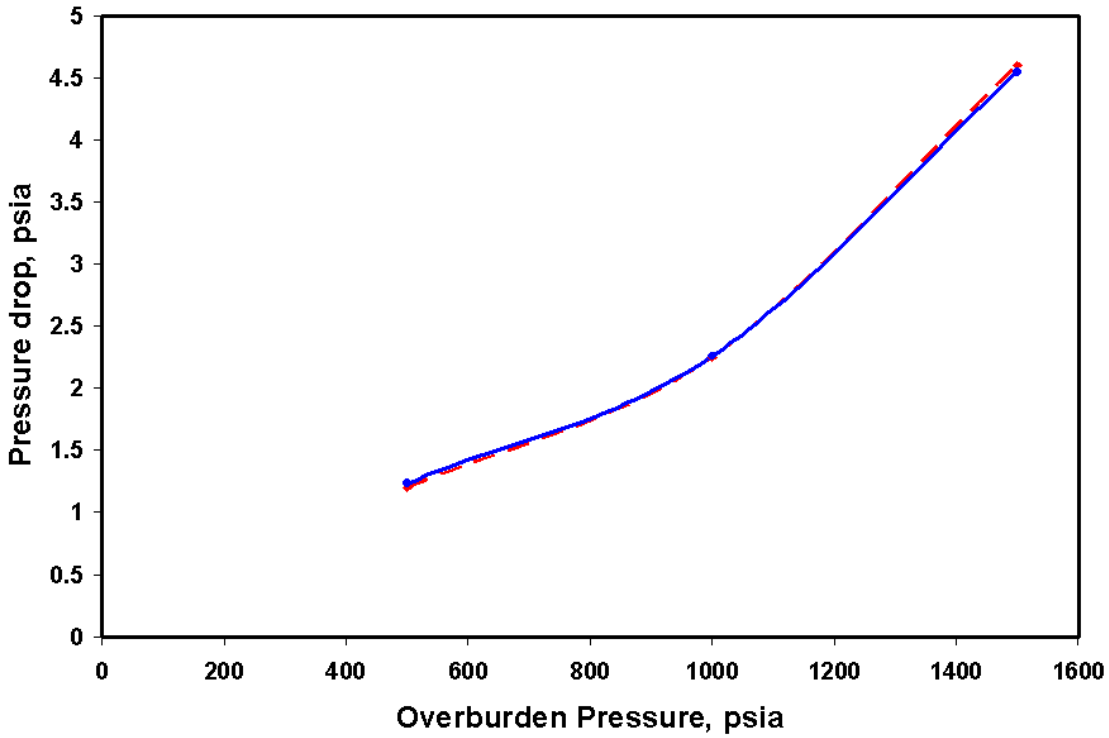

Fig. 2.1.13 — Simulation results of observed and simulated pressure drop using distributed model at 5 cm^3/min injection rate under various overburden pressures.

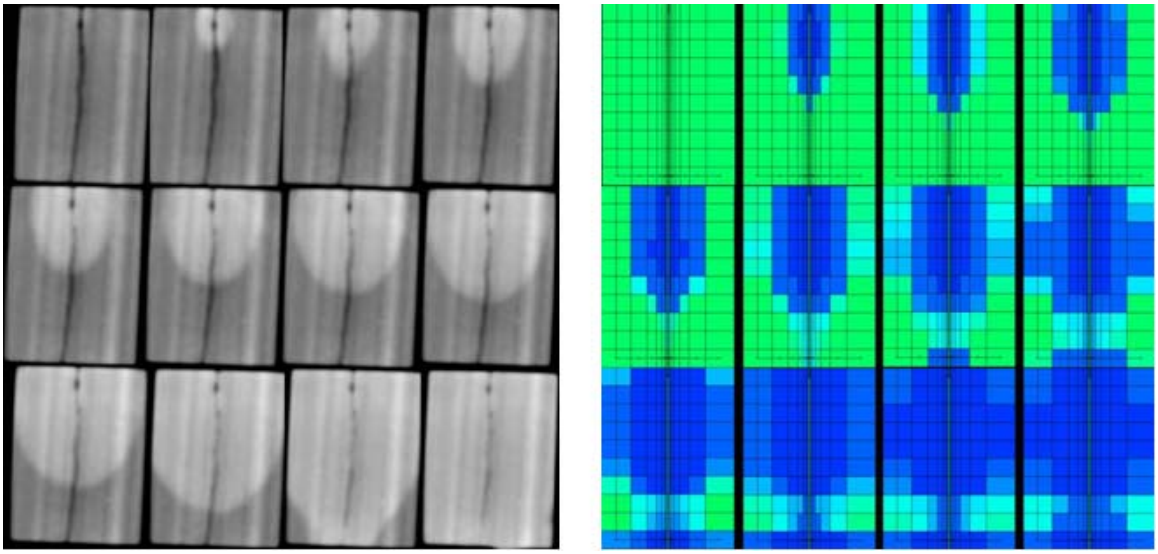

Fig. 2.1.14 —Modeling water saturation profile using parallel-plate simulation model.

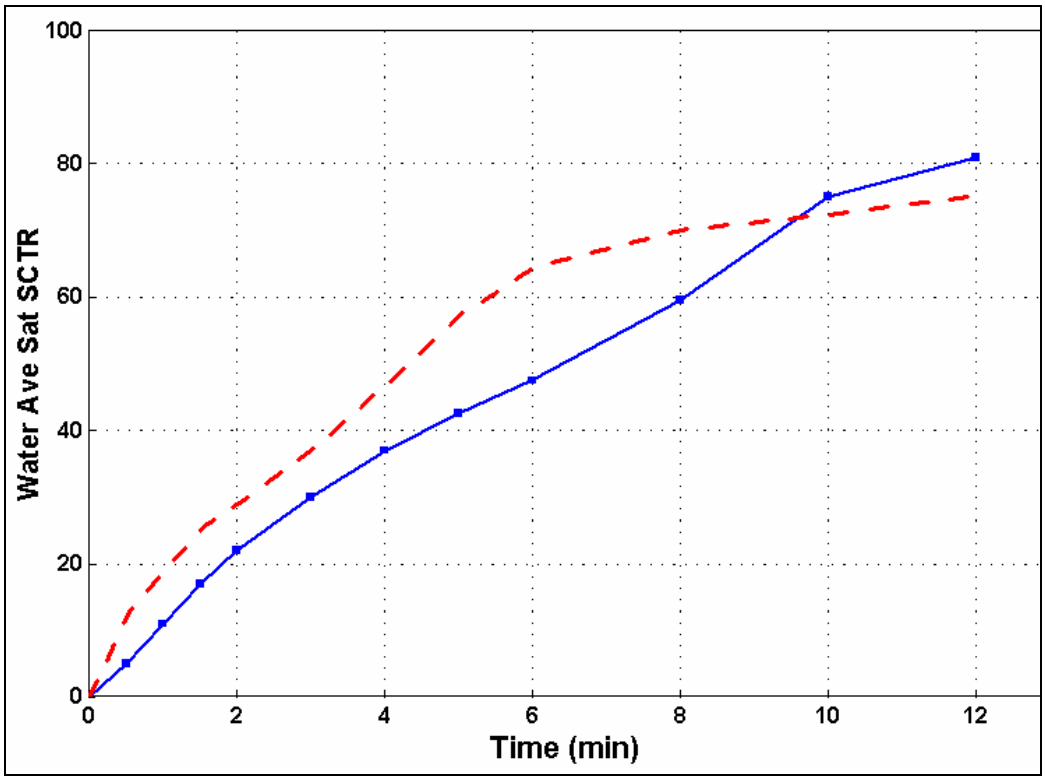

Fig. 2.1.15—Match of average water saturation using parallel-plate simulation model.

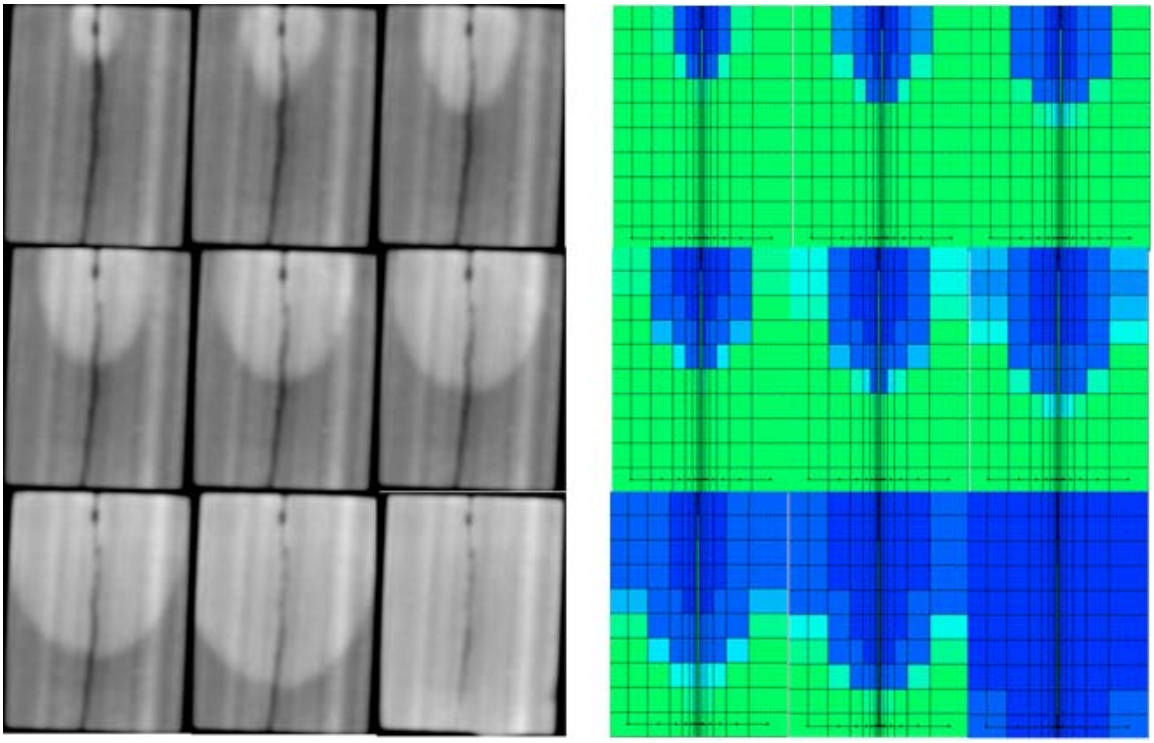

Fig. 2.1.16—Modeling water saturation profile using distributed simulation model.

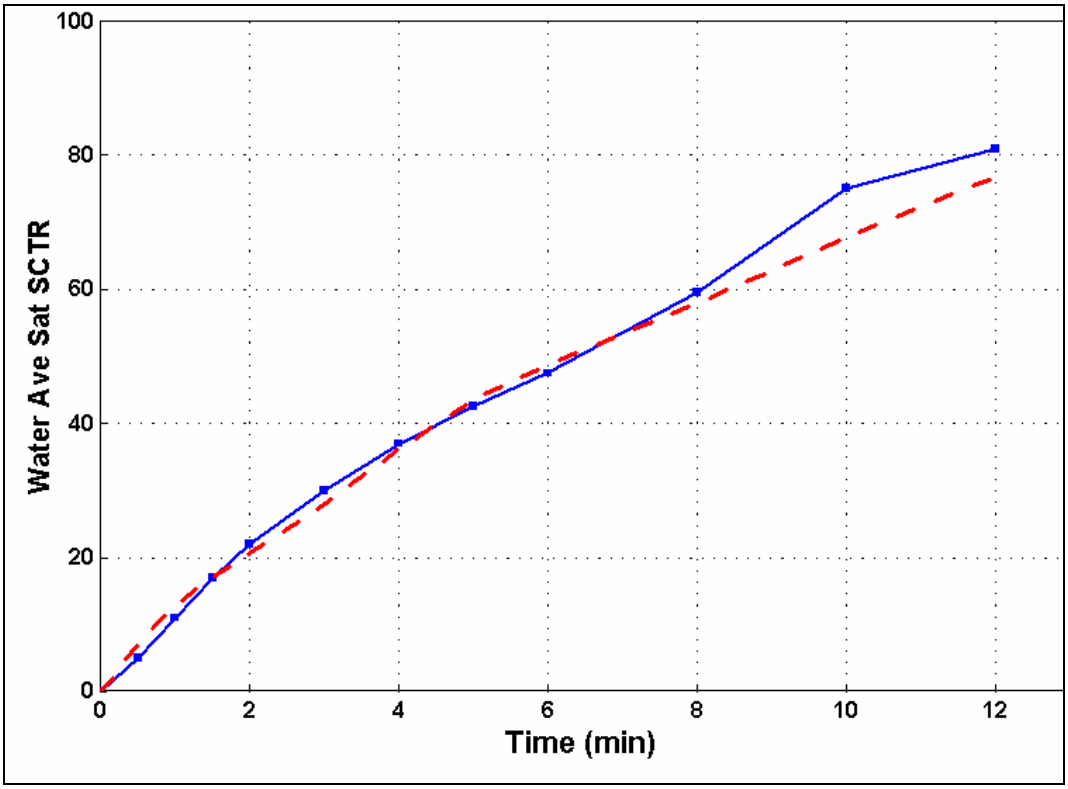

Fig. 2.1.17— Match of average water saturation using distributed simulation model.

Chapter II-2
Modeling Fluid Flow through a Single Fracture using Experimental, Stochastic and Simulation Approaches

2.2.1 INTRODUCTION

We have shown that fracture modeling using a parallel-plate approach is inadequate to reproduce our experimental observations.[1] In this chapter, we establish the sensitivity of fracture modeling, error involved in the experiments, and saturation match of fracture imbibition experiments using a CT scanner.

We again used a numerical model in a commercial simulator to study the fluid flow through fractures at different overburden pressures. The laboratory process in which the water was injected through the fracture was duplicated in this modeling effort. Rectangular grid blocks were used to overcome the difficulty of modeling a cylindrical core shape,[2,3] with 31x31 grid blocks in the x and z directions and 1 grid block in the y direction. The fracture layer is located only in the 16th layer and the rest are matrix layers. The permeability in the fracture layer was calculated as two parallel-plates without fracture roughness. All the layers were injected with constant water injection of 5 cm^3/hr. At the opposite end, two production points were located in the matrix and fracture layers to quantify the amount of water produced at those two points.

In the experimental process, the core is saturated with water. Once water injection was initiated at a constant rate, water was produced simultaneously. Then the water that was produced from both matrix and fracture layers at the end point was recorded. In the simulation, however, the initial water saturation condition is assumed zero to visualize the movement of water through a single fracture. The water saturation change in the matrix and fracture during the transient state can be observed in Fig. 2.2.1.

A few minutes after the injection was started, the flow rate was still in the transient condition and then reached a steady-state condition at later time, as shown in Fig. 2.2.2. At steady-state, the amount of water produced from matrix and fracture was recorded. Similar simulation runs were performed for different overburden pressures.

2.2.2 ERROR ANALYSIS

Any experimental data is subject to errors, so an error analysis was performed using the experimental data to quantify the range of error in the calculation of matrix and fracture flow rates. The summary of the error analysis for the injection rate case of 5 cm^3/min is presented in Table 2.2.1. The parameter fracture flow rate (Q_f) in Table 2.2.1 was calculated by subtracting the matrix flow rate from the total injection rate. From the table we find that the errors involved in the calculation of fracture flow rates are relatively small (< 8%), at lower overburden pressures (500 and 1,000 psia) when compared to the high overburden pressure case (1,500 psia).

This indicates that the values obtained at high overburden pressure have a large degree of uncertainty, possibly because, at high overburden pressures, the characteristics of the matrix have a dominant influence on fracture flow. The high levels of uncertainty at higher overburden pressures have not been explored or taken into account while modeling; this is an area where more analysis could be done in the future.

The results for the 5 cm^3/min injection case were compared with the experimental results as shown in Figs. 2.2.3 and 2.2.4. The dotted lines indicate the experimental results.

Even though the quality of the match for both flow rate and pressure drop are not very good with the single-fracture model, which assumed a smooth fracture surface between two parallel-plates, the simulation results follow the trend of the laboratory results.

To make sure that neither assumptions nor the error caused the discrepancies in flow rates, we attempted to match the experimental observation. Figs. 2.2.5 and 2.2.6 show the matching between experimental and simulated results for average pressure drop and flow rates across the core. The aperture widths and their corresponding permeabilities with overburden pressures for the pressure drop match are given in Table 2.2.2. From the resulting average fracture flow rates, the effective aperture width was back-calculated from cubic law. The results of the effective aperture width calculated from fracture flow rates and the comparison to the effective aperture widths inferred from experiments is given in Table 2.2.3. The results reveal that the effective fracture aperture

widths obtained by matching the average pressure drop (the actual measured parameter in the experiments) is outside the range of effective aperture widths inferred from experiments. So the deviations from the cubic law did not arise from the assumption or the error involved but could reflect the rough nature of the fracture surface. Even if we assumed that the deviation in flow rates resulted from error, we could not achieve a simultaneous match for the average pressure drop and the average flow rates.

2.2.3 CT SCANNER RESULTS

In an attempt to study the movement of brine in a fractured core, we conducted a simple experiment with a CT scanner. The experimental procedure involved injecting water at a rate of 0.5 cm^3/min from the top center of the core, through the fracture. The movement of brine on a cross section perpendicular to the fracture observed through the CT Scan is presented in Fig. 2.2.7.

The experiment was modeled using a commercial simulator. The fracture was modeled as smooth plates with a constant permeability layer. Since the low resolution prevented us from establishing the aperture value through the scan pictures, we assumed an aperture value of 50 microns. From the observations, we found that the smooth fracture assumption failed to recreate the saturation-front movement seen through scans (Fig. 2.2.8). The fluid moved through the fracture quickly because of its high permeability. Hence, for modeling purposes a parallel-plate approach for fractures fails to portray the true nature of flow. The flow on a smooth fracture surface is different from flow on a rough fracture surface. As could be observed from scans and modeling results, the shape of sweep occurring in a plane perpendicular to the fracture is not adequately described by parallel-plate modeling and we need to model fractures quite differently from what has been done in the past.

2.2.4 SIMULATION OF CT SCANNER EXPERIMENTS

Once we concluded that smooth fracture modeling could not replicate the movement and the average saturation calculated from CT scans, we implemented our integrated methodology. This time the fracture apertures were distributed and roughness

accounted for through a friction factor. Fig. 2.2.9 illustrates the result of this kind of modeling.

The distributed fracture modeling also adequately matched the average water saturation inferred from CT-scans (Fig. 2.2.10). The parallel-plate model neither reproduced the movement of the water front nor matched the average water saturation obtained from the CT scans. As a result of this match, fracture aperture was estimated to be around 120 microns and the aperture distribution had a variance of 260 micron.[2]

2.2.5 SENSITIVITY STUDIES

2.2.5.1 Effect of variance of aperture distribution on fracture flow rate

For sensitivity studies, we used a core model with 31x15 grid block size in the x and y directions with 15 layers in the z direction. The fracture layer was incorporated in the 8th layer and the rest are matrix layers. The modified permeability layer was used for the fracture layer, while the matrix layers had a constant permeability. All the layers were subjected to constant-rate water injection of 5 cm^3/min through injection points located at one extreme end and penetrating through all the layers. At the opposite end were two production points, one for the matrix layers and the other for the fracture layer, to quantify the amount of water produced at those two points. For this study, a single phase was used.

Initially, with a constant mean aperture size of 56.4 μm, the fracture aperture distribution was generated solely through a log-normal distribution. Aperture distributions were obtained for different variances (100, 200, 600, 1,000 $micron^2$). From the simulation results, we found that the increased variance in the fracture aperture distribution leads to a reduction in the mean hydraulic aperture size. The hydraulic aperture is the value of the aperture required to produce the observed pressure drop across the core. This observation can be explained from previous observations by Dagan,[4] who approximated the change in effective hydraulic aperture as a result of roughness through

$$h_{eff}{}^3 \approx h_{hyd}{}^3 (1 - 1.5\ \sigma_h{}^2 / \langle h_{hyd} \rangle^2) . \qquad (2.2.1)$$

where h_{eff} is the effective hydraulic aperture as a result of roughness (microns) and $\sigma_h{}^2$ is the variance of hydraulic aperture $microns^2$, and $<h_{hyd}>$ is the mean hydraulic aperture. In

our simulation, experiments show the same trend as observed by Dagan. Fig. 2.2.11 illustrates the log-normal realizations of aperture distributions with constant width and different variances, while Fig. 2.2.12 shows the comparative plots between simulated and Dagan's approximation of hydraulic aperture reduction as a result of increased roughness (variance).

2.2.5.2 Determination of critical aperture size

To establish the limitation or restriction of this approach, we conducted simulation runs maintaining a constant variance and different aperture widths. Fig. 2.2.13 illustrates the log-normal realizations of constant aperture variance but different aperture widths; in other words, the aim of this sensitivity study was to determine the critical aperture width beyond which rough fracture surfaces could be treated as smooth parallel-plates. Fig. 2.2.14 compares flow rates from fracture between the simulation runs of distributed fracture apertures, accounting for roughness and parallel-plate assumptions. In parallel-plate assumptions, the fracture layer was assumed to be uniform rather than being distributed log-normally. Hence it had a constant permeability throughout. The figure shows that as the aperture size increases, the effect of rough surfaces also gradually decreases. From the observations we infer that beyond an aperture size approximately of 60 microns, the effects of roughness or tortuosity are insignificant. This is rooted in the fact that larger aperture size means lower overburden pressure. So it could be inferred that as over burden pressure increases, the effect of roughness becomes more predominant.

2.2.5.3 Effect of matrix permeability

The permeability of the Berea core used in the experiments is about 300 md. Usually in fractured reservoirs the matrix permeability varies in the range of 1 to 10 md, so we conducted a sensitivity study to determine if matrix permeability had any impact in determining flow rates through fractures. Simulation runs were performed varying the permeability range from 0.001 to 1000 md. The size of the fracture aperture was 40 microns and the variance of the aperture distribution was 200. The injection rate of water was 5 cm^3/min. From the results, we inferred that the pressure drop across the core

reduced considerably only if the matrix permeability increased to beyond 1,000 md. When considering a moderate permeability matrix (k = 1 md) embedded with high fracture permeability ($k \approx$ 135,000 md in this case), there is a significant pressure drop across the core. This pressure drop reduces significantly only when the matrix permeability increases beyond 1,000 md. Fig. 2.2.15 illustrates this phenomenon. Much as would be expected, the fracture flow followed the same trend (Fig. 2.2.16).

Sensitivity studies were also conducted to observe the impact of matrix permeability between rough fracture surfaces and smooth parallel-plates. Fig. 2.2.17 compares the fracture flow rates between smooth and rough fractures for different matrix permeabilities.

Although the impact on fracture flow rates was insignificant, the effect on pressure drop was quite significant. For a range of matrix permeability between 0.001 md and 10 md, the difference in the pressure drop between rough fracture surfaces and smooth parallel-plates varied from 7 to 6.2 psia. Thus, distributing the fracture apertures mainly affects the pressure distribution in the core. Fig. 2.2.18 illustrates the difference in pressure drop across the core between rough fractures and smooth fractures. The difference is almost negligible at a matrix permeability of 1,000 md; however, in reality we seldom find a naturally fractured reservoir with that high matrix permeability.

2.2.5.4 Effect of matrix heterogeneity

The Berea core we used is known to be fairly homogeneous with high matrix permeability. The true effect of matrix heterogeneity can only be established after having studied the core with a CT scanner. The porosity distribution of the core can be established through CT scans. But for permeability distribution, some kind of empirical correlation has to be used, since matrix permeability heterogeneity cannot be established through CT scans. In this research, we attempted to study the effect of matrix heterogeneity on flow through the fractures. Two cases were run to study the effect. The first case had a single value for matrix permeability (100 md) and in the second case the matrix permeabilities were distributed randomly in the range of 80 to 130 md. In both cases the fracture permeability layer was distributed through the log-normal distribution (mean aperture = 60 microns and variance = 500 micron^2). Figs. 2.2.19 and 2.2.20 show

the distribution of permeabilities used in the matrix (Case 2) and the fracture layer respectively.

The total area of the matrix in this study was 5 cm x 5 cm x 5 cm. The simulation grid size used was 15x15x15. The fracture layer was introduced in the 8th layer in the z-direction. An injection rate of 5 cm^3/min was applied at one end and was produced at the other end. The fracture flow rates obtained from both the cases were 3.76 cm^3/min (Case 1) and 3.82 cm^3/min (Case 2). The difference in the flow rates was 0.04 cm^3/min, which is about a 1% change from the case of constant matrix permeability. Therefore, matrix heterogeneity of a core with high matrix permeability (100 md in this case) does not play a significant role in affecting flow contributions through a fracture.

2.2.5.5 Simulator testing

Sensitivity studies were also performed to test whether the simulator provides accurate results when confronted with a very high-permeability region (fracture) among surrounding matrix blocks (low-permeability regions). A one-dimensional model was established in which serial flow was modeled across blocks of moderate permeability (10 md) with a high permeability block embedded in the center. The values for high permeability were varied from 100 md to 10,000 darcy. An example of the model is shown in Fig. 2.2.21, where the value of the high permeability region is 10 darcy. The model was injected from one end and produced at the other end. The injection rate used in this case was 5 cm^3/min. The producer was operated at atmospheric pressure. The pressure drops obtained from simulations were compared with those obtained from Darcy's law,

$$\Delta p = \frac{Q\mu l}{\bar{k} A} \tag{2.2.2}$$

The average permeability $\bar{k}$ for this model can be obtained through [1]:

$$\bar{k} = \frac{L}{\sum \frac{l_i}{k_i}} \tag{3}$$

where L is the total length of the core, l_i is the length of the grid block (x-dir) and k_i is the corresponding grid-block permeability.

The results of simulation testing are given in Fig. 2.2.22. The pressure drops obtained from simulation are compared with those obtained from Darcy's law. The comparison shows the values obtained from simulation are consistent with Darcy's law. The maximum deviation was about 0.25 psi, which is less than 1% of the actual value. Accurate results can be obtained from increased griding.

2.2.6 CONCLUSIONS

Even though much work still remains to procure all the necessary analysis and data to provide a detailed modeling procedure for flow through single fractures, the proposed methodology is able to model flow experiments through single fractures fairly well. So far, the following conclusions can be drawn from on the work:

1. Quantification of effective aperture widths is possible through proper experimental design.
2. The effect of surface-roughness friction needs to be taken into account while modeling. In these experiments friction reduced the flow through the fractures by approximately 24%. In addition to the reduction of flow, the pressure drop observed across the core is quite different from the one that would result from smooth parallel-plate modeling.
3. The effective hydraulic aperture is reduced with increased variance of the aperture distribution.
4. Beyond an aperture size of approximately 60 microns, the effects of roughness and tortuosity are insignificant.
5. The sensitivity studies on matrix permeability show that the fracture has to be modeled with a two-dimensional aperture distribution regardless of the value of matrix permeability. Even though the flow rates may appear to be the same, the pressure drop across the core is different.
6. Matrix heterogeneity in cores with high permeability does not affect the flow rate through fracture significantly.
7. The simulator gives consistent results when a very high-permeability region is embedded among moderate-permeability blocks.

8. The simulation results suggest that a parallel-plate model is insufficient to predict fluid flow in the fracture system. Consequently, the spatial heterogeneity in the fracture aperture must be included in modeling fluid flow through the fracture system.
9. The results also imply that the effect of stresses may be most pronounced in fractured reservoirs where large pressure changes can cause significant changes in fracture aperture and related changes in fracture permeability.
10. At high overburden pressures the influence of existing fracture permeability is not too significant. This conclusion is limited to the Berea core, which has high matrix permeability.
11. CT scans reveal that parallel-plate modeling of fractures seldom reflects the true nature of flow through fractures.
12. Though effective aperture successfully modeled experimental results using the integrated methodology, the value of the fracture aperture is only a close estimate. The correct value of the fracture aperture can be obtained with high accuracy using an a CT scanner.
13. Modeling flow through fractures is an area of active research. The methodology described in this work could open more perspectives in fracture modeling. Improvements could be made to this model by distributing porosity in the core scale and also considering the effect of matrix heterogeneity.

NOMENCLATURE

A = matrix area (cm^2)

f = friction factor

k_m = matrix permeability (Darcy)

k_f = fracture permeability (Darcy)

L = core length (cm)

l = diameter of the core (cm)

q_m = matrix flow rate (cm^3/sec)

q_f = fracture flow rate (cm^3/sec)

w = effective fracture width (cm)

Δp = pressure drop across the core (atm)

μ = viscosity (cp)

REFERENCES

1. Schechter, D.S.: “Investigation of Efficiency Improvements during CO2 Injection in Hydraulically and Naturally Fractured Reservoirs,” Second Semi-Annual Technical Progress Report, US DOE Contract No.: DE-FC26-01BC15361, (October 2002).
2. Putra, E., Fidra, Y., and Schechter, D.S.: “Study of Waterflooding Process in Naturally Fractured Reservoirs from Static and Dynamic Imbibition Experiments,” paper SCA 9910 presented at the 1999 International Symposium of the Society of Core Analysts, Colorado, 1-4 August.
3. Alfred, D.: “Modeling Fluid Flow through a Single Fracture Using Experimental, Stochastic and Simulation Approaches,” Master’s Thesis, Texas A&M University, 2003.
4. Zimmerman R.W. and Bodvarsson, G.S.: "Hydraulic Conductivity of Rock Fractures" Transport in Porous Media (1996), 23, 1-30.

Table 2.2.1—Experimental Error Analysis

Overburden Pressure, psia	K_m, md	Pressure Drop psia	Q_m cm3/min	Q_m cm3/min		Q_f cm3/min		Error in Q_f, %
				mean	Std dev	mean	Std dev	
500.00	max = 299.96	1.00	1.21	1.44	±0.27	3.56	±0.27	7.59
		1.40	1.70					
	min= 292.44	1.00	1.18					
		1.40	1.66					
1000.00	max = 273.02	2.20	2.44	2.41	±0.11	2.59	±0.11	4.25
		2.30	2.55					
	min = 255.41	2.20	2.28					
		2.30	2.39					
1500.00	max = 240.12	4.20	4.11	4.34	±0.47	0.66	±0.47	70.68
		5.00	4.90					
	min = 222.23	4.20	3.80					
		5.00	4.53					

Table 2.2.2—Fracture Properties Obtained From Pressure Drop Match

Overburden Pressure (psia)	Fracture aperture (microns)	Average Kf (md) dp match
498.05	74.5	470,000.00
985.65	57.6	280,000.00
1500.5	41.3	146,500.00

Table 2.2.3—Fracture Properties From Simulation and Experimental Results

Qinj	Pressure	Aperture width (experiments)		Aperture width (simulation)
cm3/min	psia	mean (microns)	σ (microns)	microns
5	500	56.15	±4.73	74.51
	1000	40.40	±0.59	54.62
	1500	20.57	±5.80	41.36

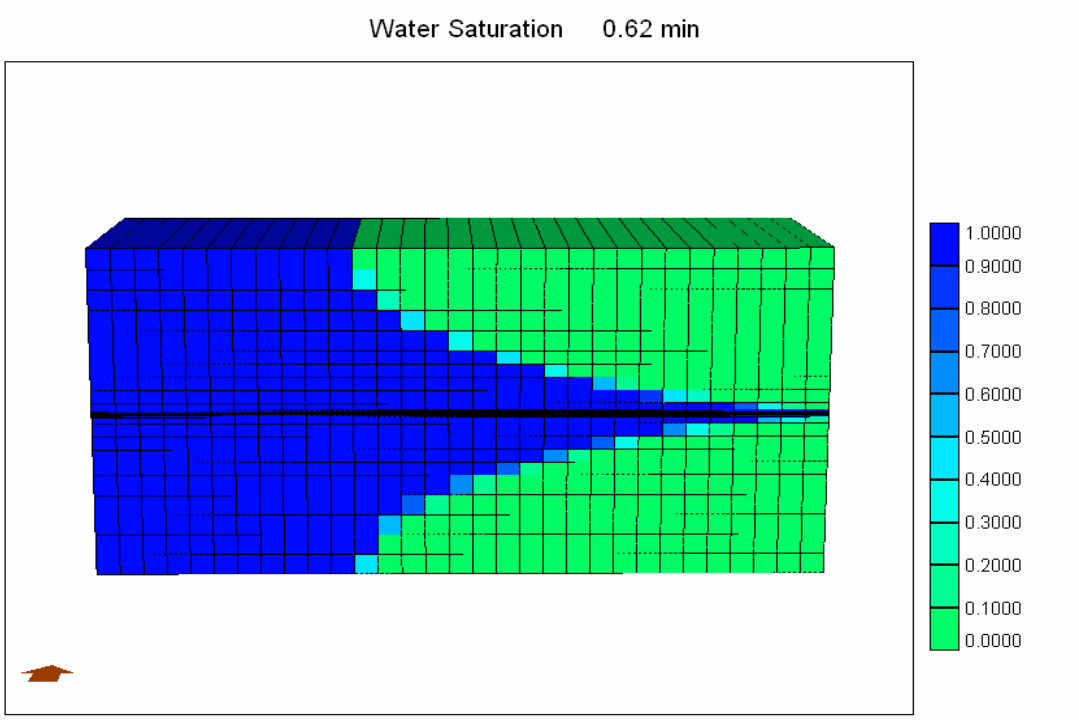

Fig. 2.2.1—Water saturation change in matrix and fracture at transient flow condition.

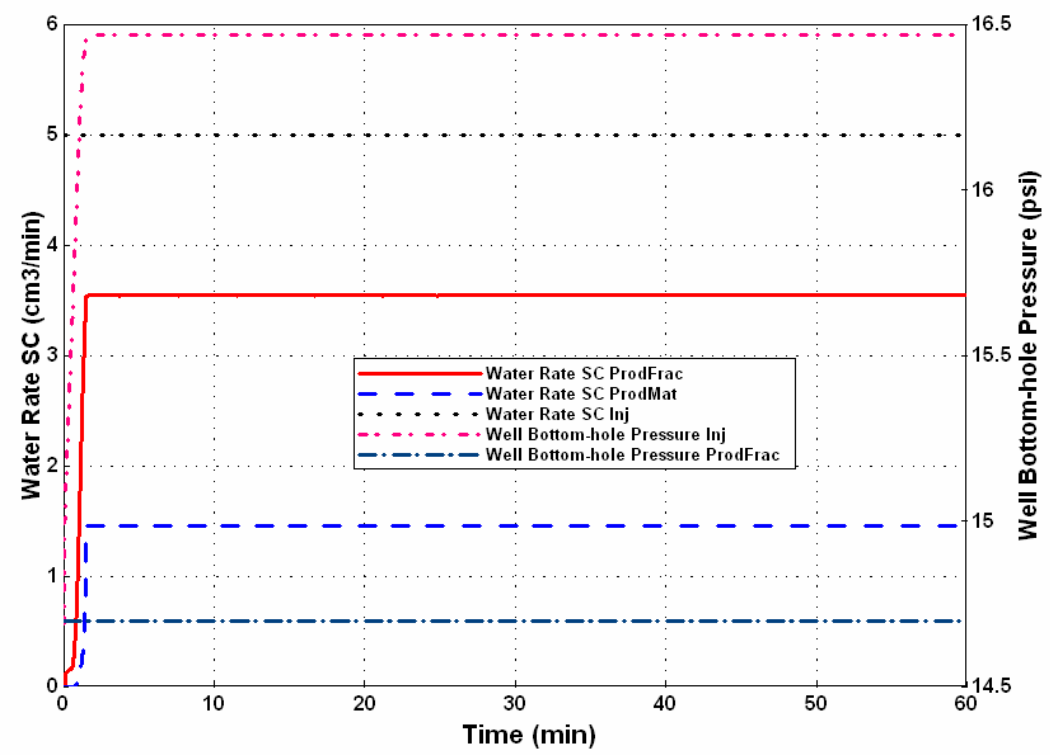

Fig. 2.2.2—Simulation results of flow rates and pressure drop injected at 5cm^3/min and overburden pressure of 500 psi.

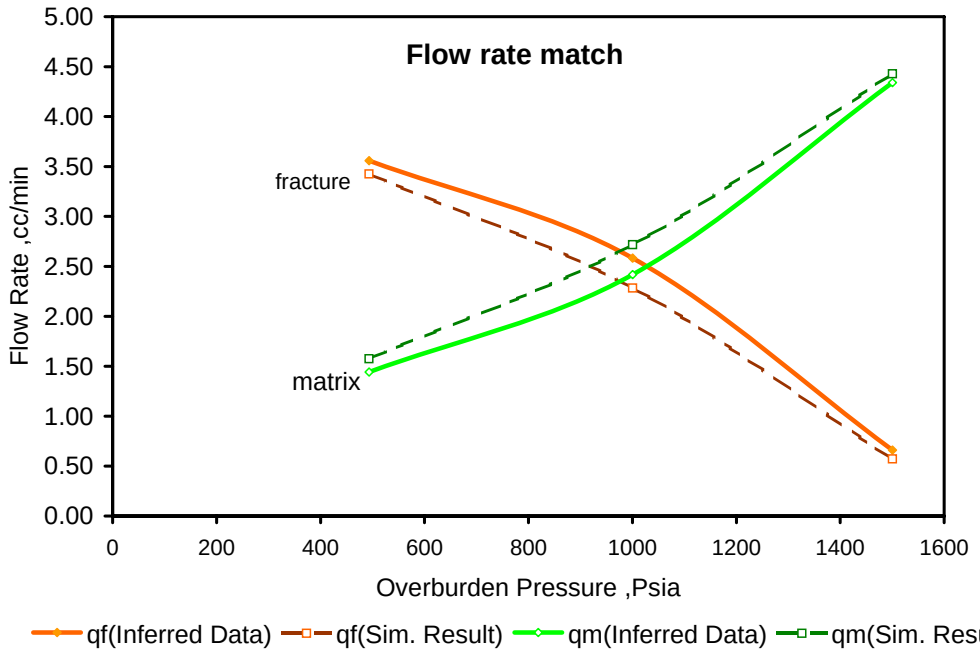

Fig. 2.2.3—Average flow rate comparison between laboratory and simulation results at 5 cm^3/min and each different overburden pressure.

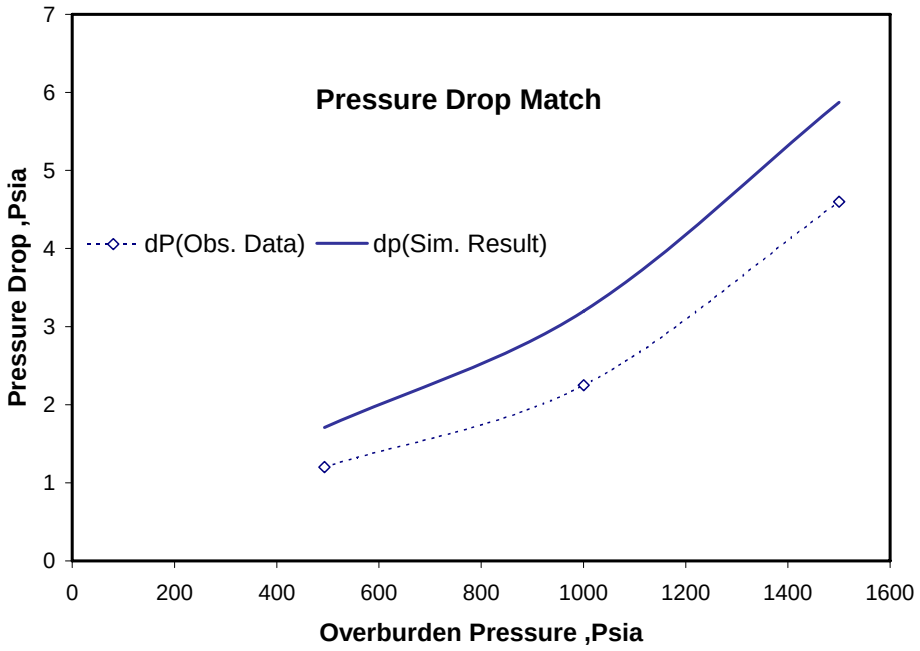

Fig. 2.2.4—Average pressure drop comparison between laboratory and simulation results at 5 cm^3/min and each different overburden pressure.

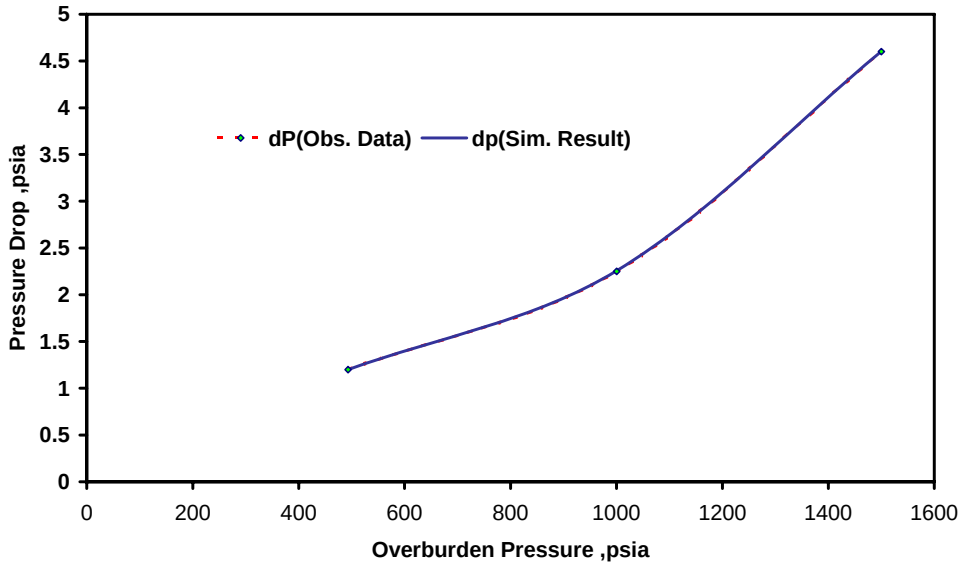

Fig. 2.2.5—Average pressure drop match between observed and simulation results for the fractured core experiment for 5 cm^3/min injection rate.

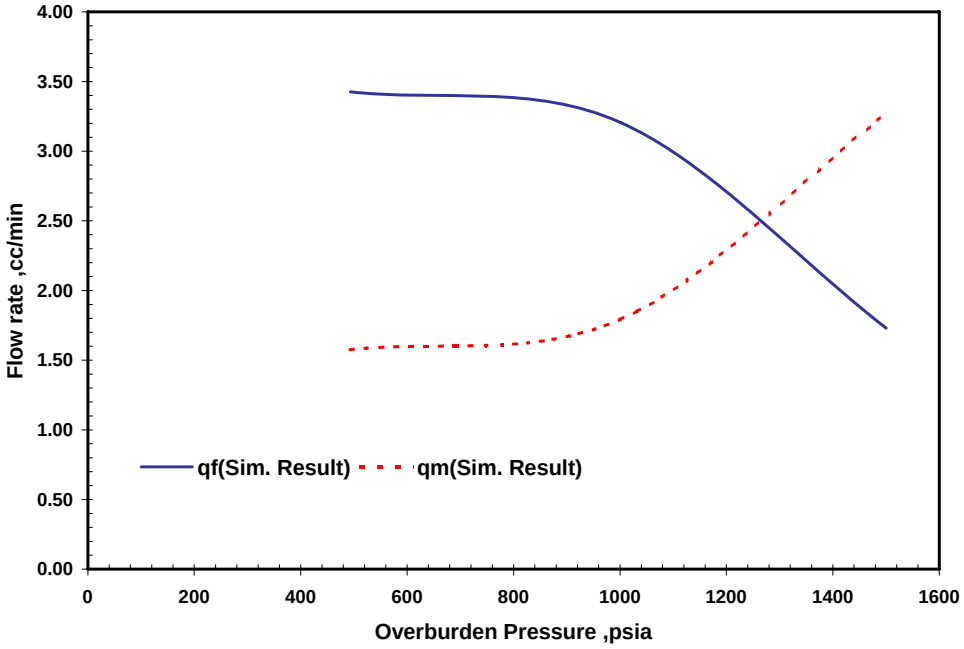

Fig. 2.2.6—Average flow rates observed for the corresponding average pressure drop match across the core at 5 cm^3/min injection rate.

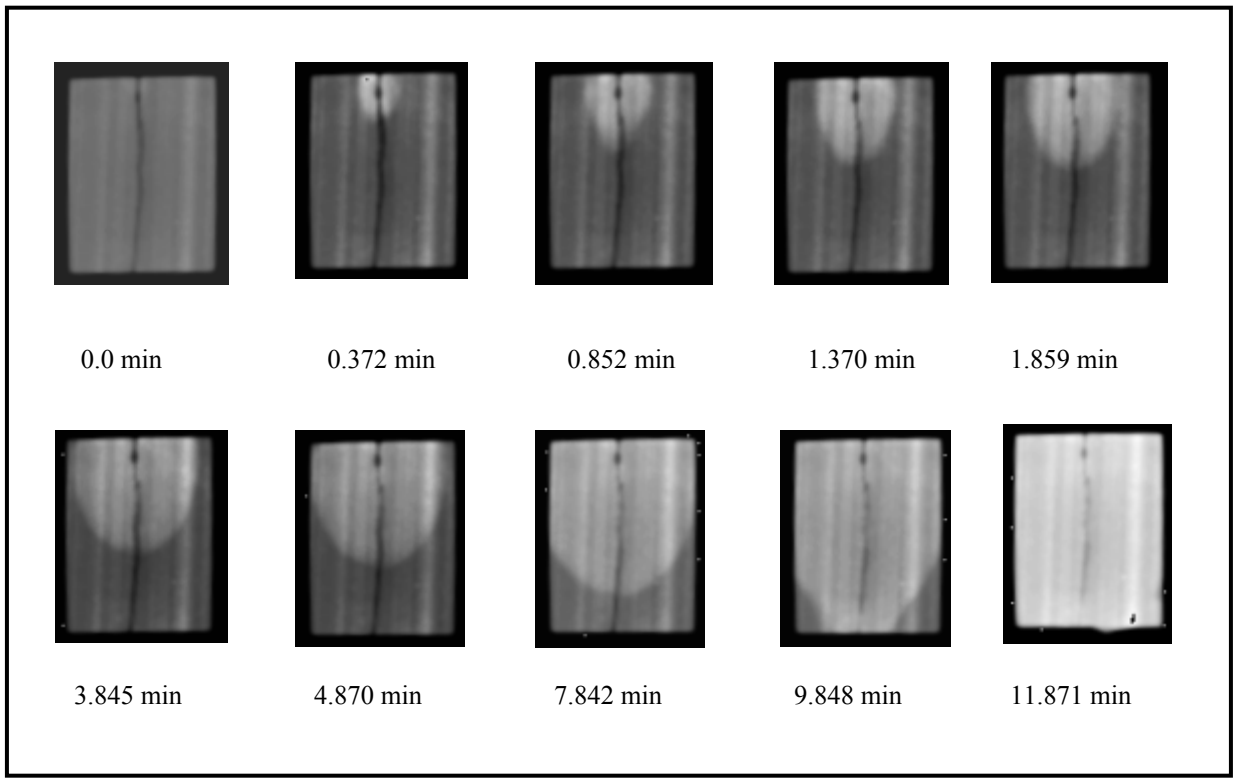

Fig. 2.2.7—CT scans (perpendicular to the fracture) of single-phase gravity drainage experiment through a fractured core.

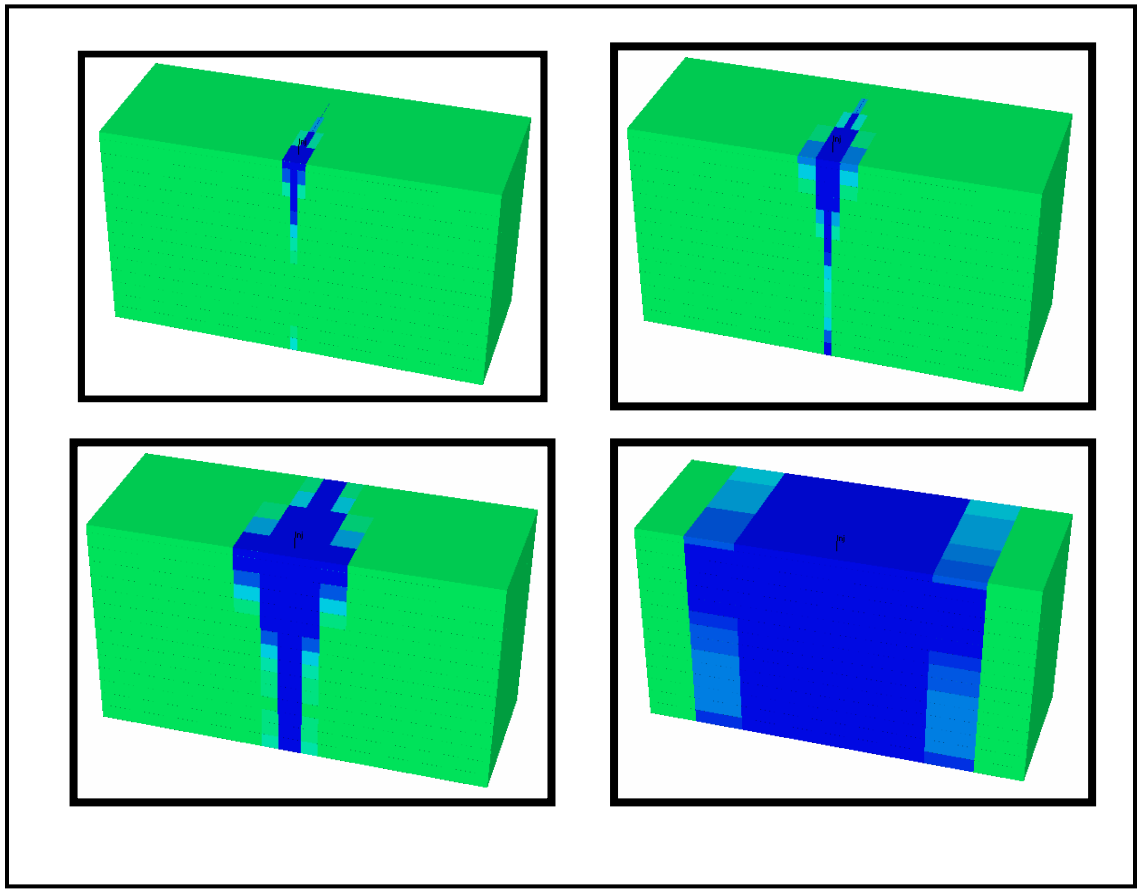

Fig. 2.2.8—Fluid movement through a core with smooth fracture.

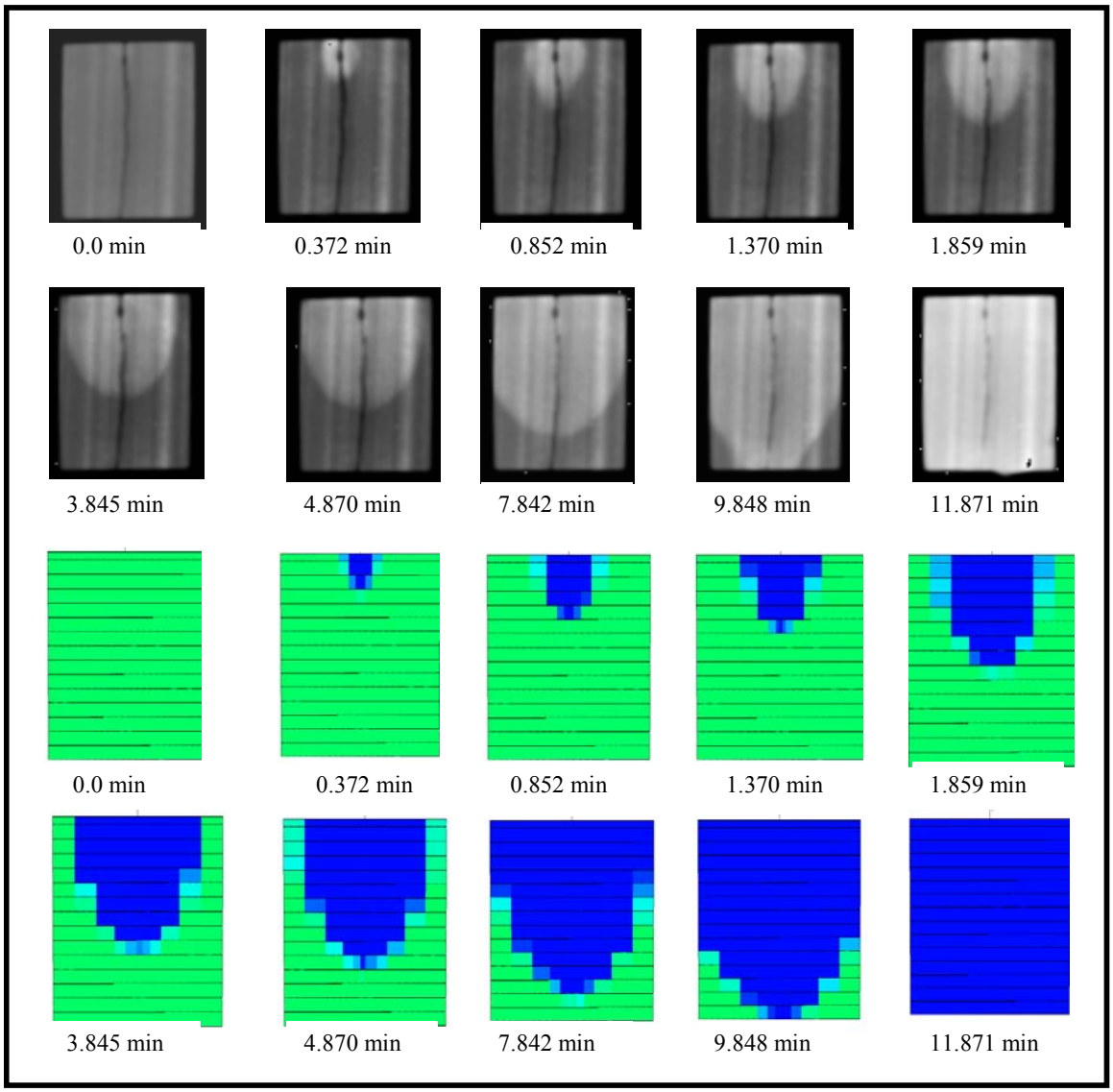

Fig. 2.2.9 —Fluid front movement through a core with a distributed fracture surface.

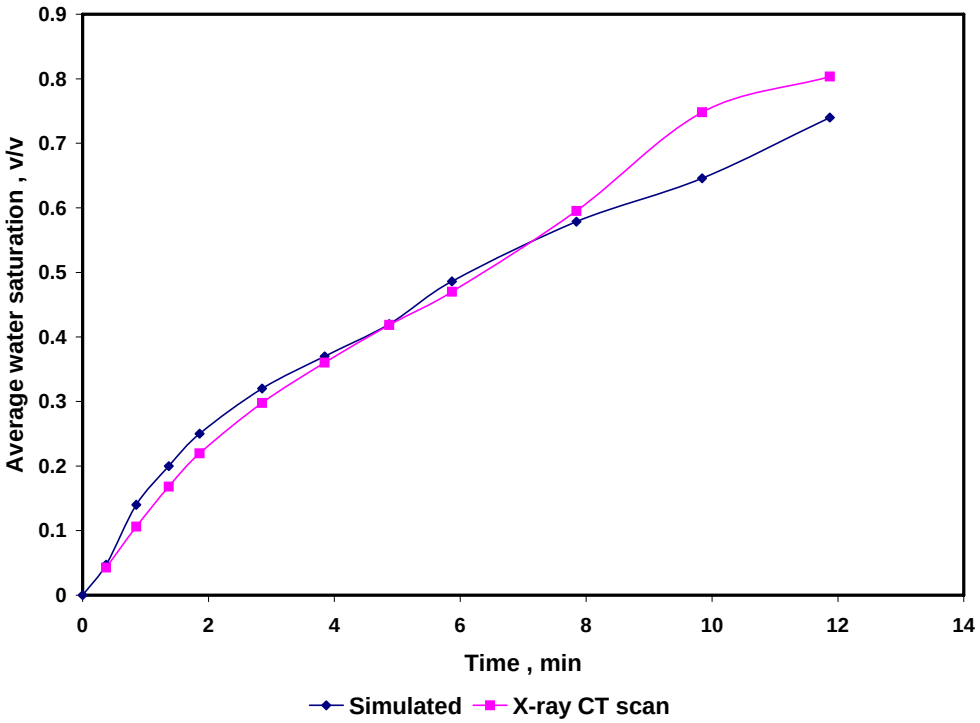

Fig. 2.2.10—Average water saturation match between simulation and X-ray CT scan.

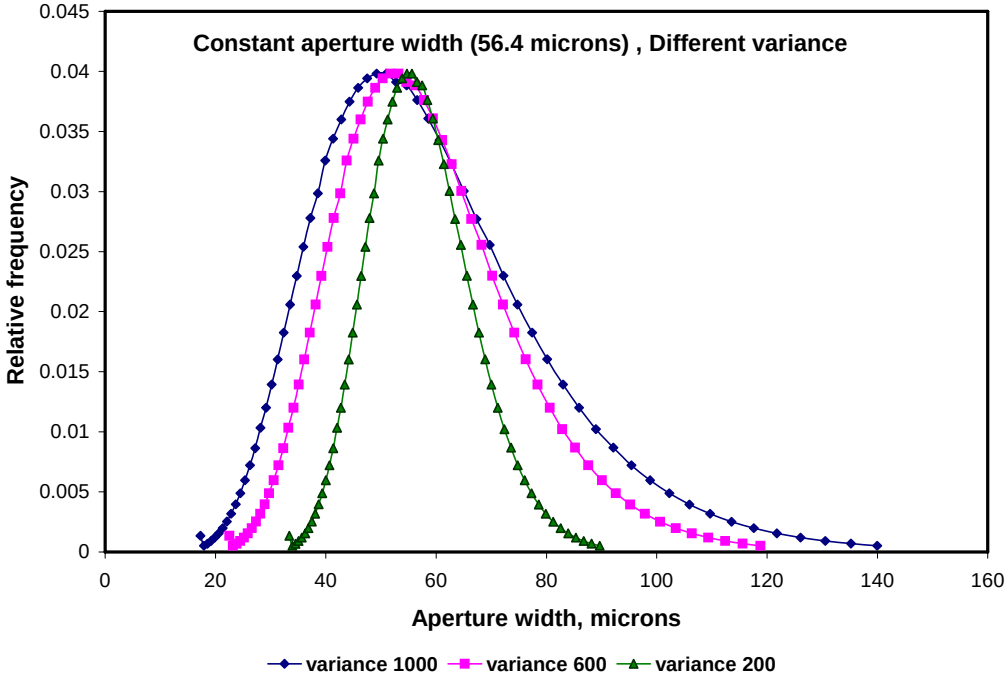

Fig. 2.2.11—Log-normal distribution for constant aperture width, different variances.

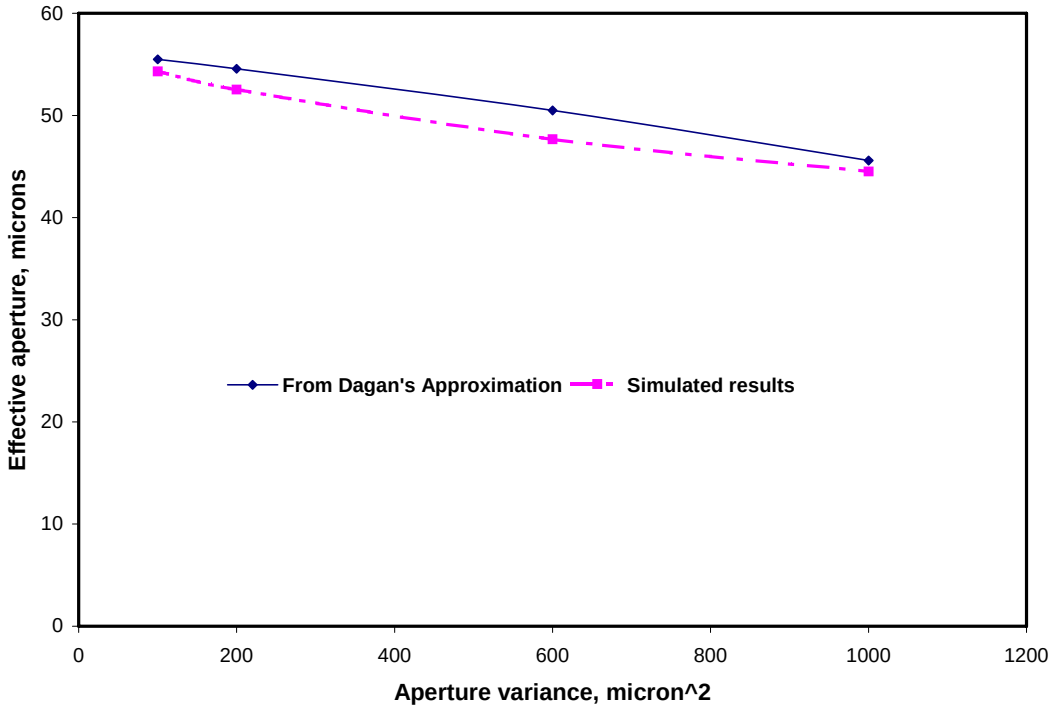

Fig. 2.2.12—The comparative plots of hydraulic aperture reduction as a result of increased roughness (variance)

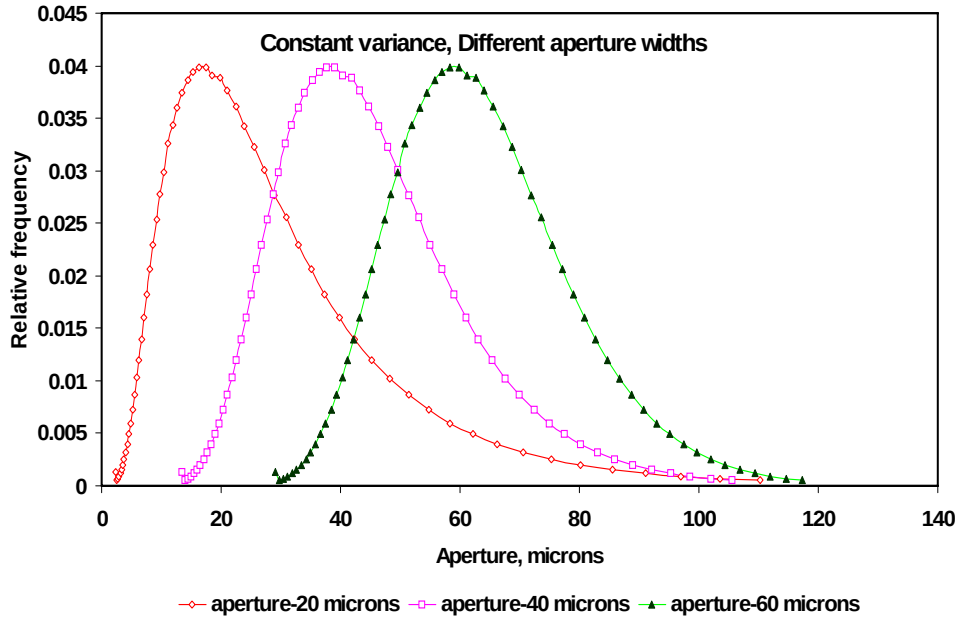

Fig. 2.2.13 —Log-normal distribution for constant variance, different aperture widths.

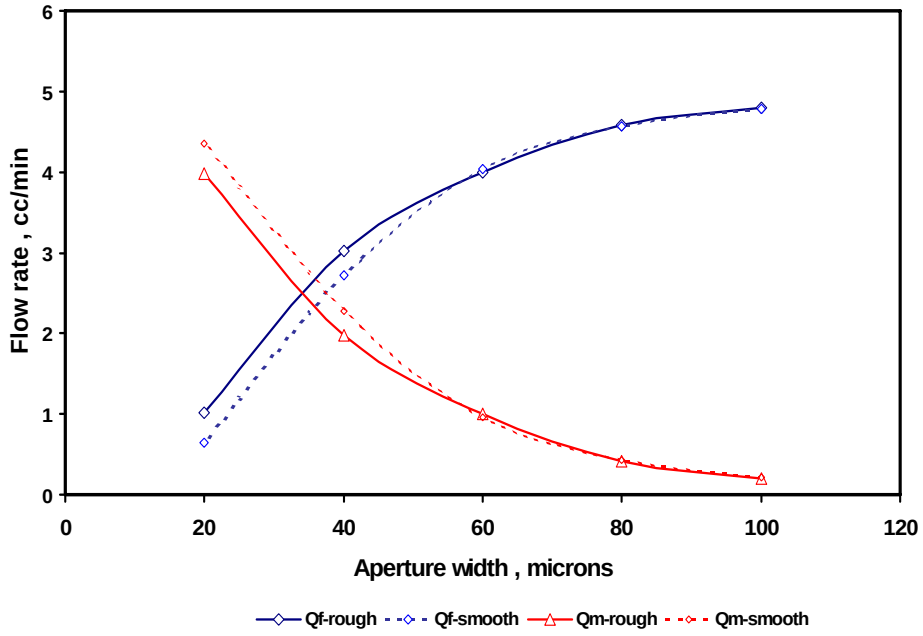

Fig. 2.2.14—Comparison between parallel-plate (smooth) and distributed aperture flow (rough) for different apertures.

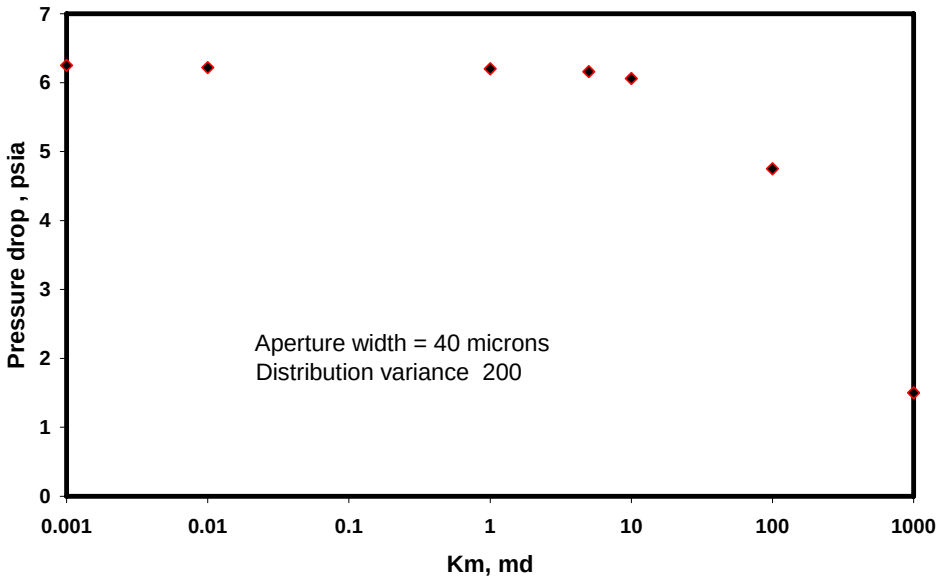

Fig. 2.2.15—Effect of matrix permeability on pressure drop across the core.

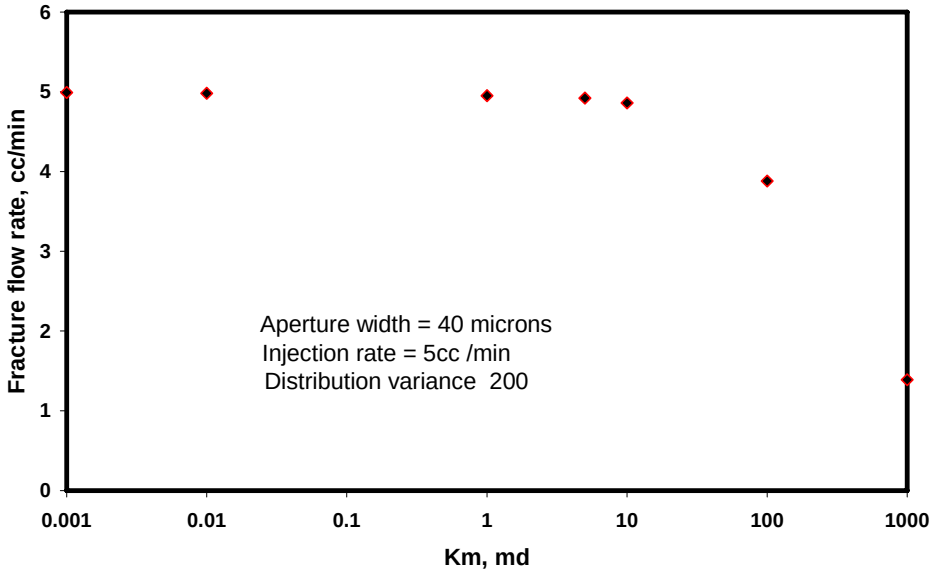

Fig. 2.2.16—Effect of matrix permeability on fracture flow rate.

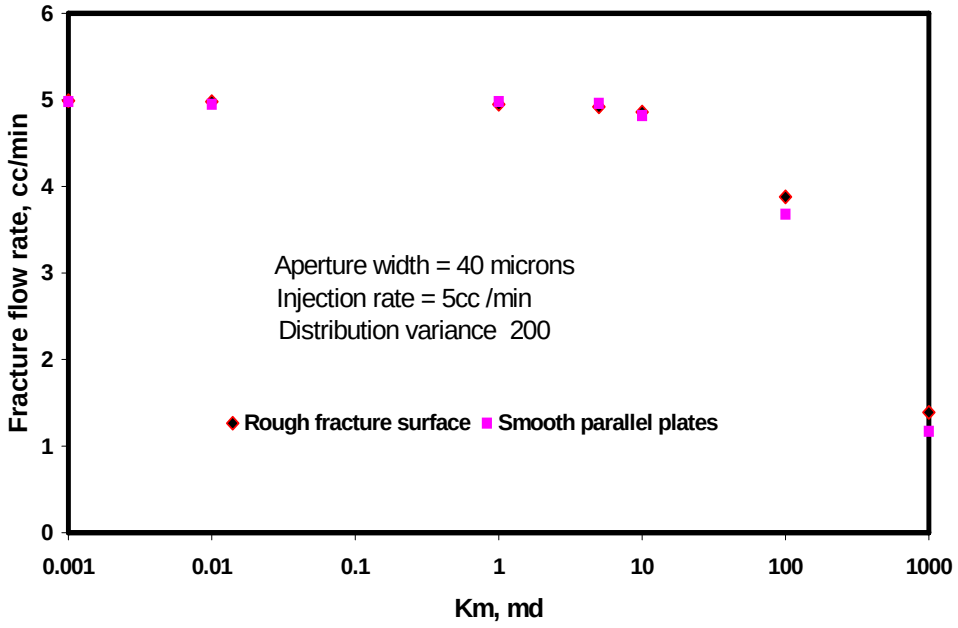

Fig. 2.2.17—Comparison of fracture flow rates between smooth and rough fractures for different matrix permeabilities.

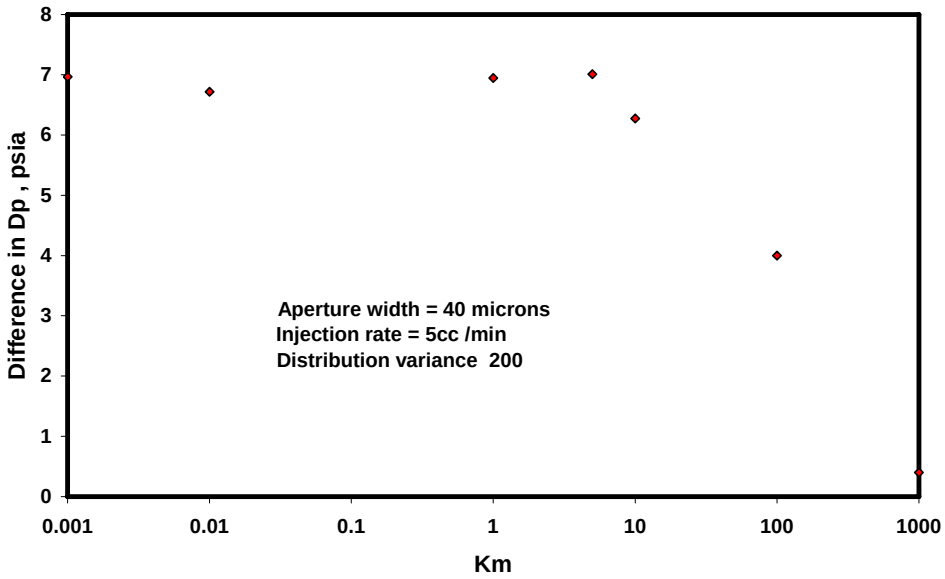

Fig. 2.2.18—Difference in pressure drop across the core between smooth and rough fractures at different matrix permeabilities.

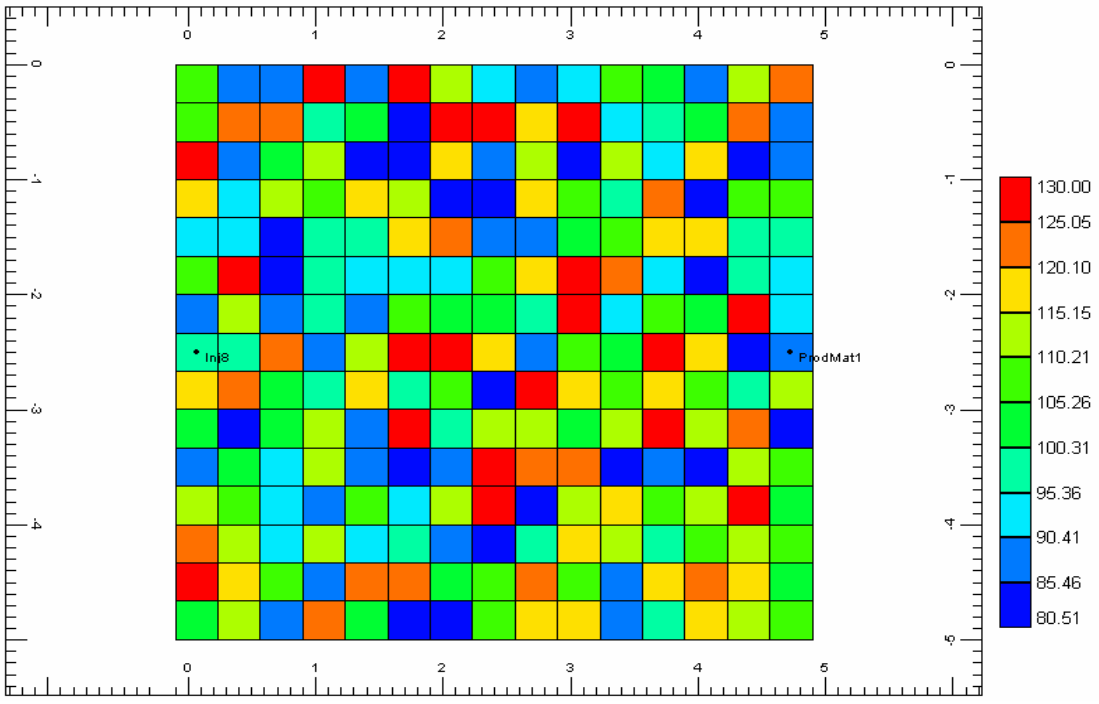

Fig. 2.2.19—Distribution of matrix permeability layer (Case 2).

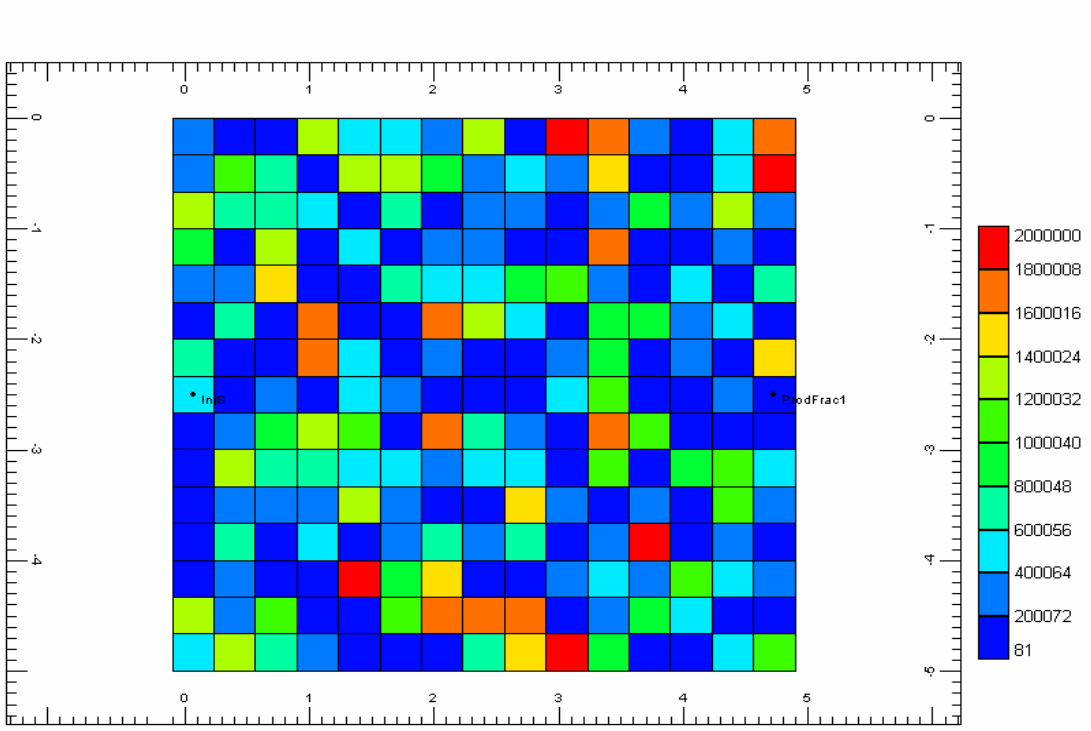

Fig. 2.2.20—Distribution of fracture permeability layer (Cases 1 and 2).

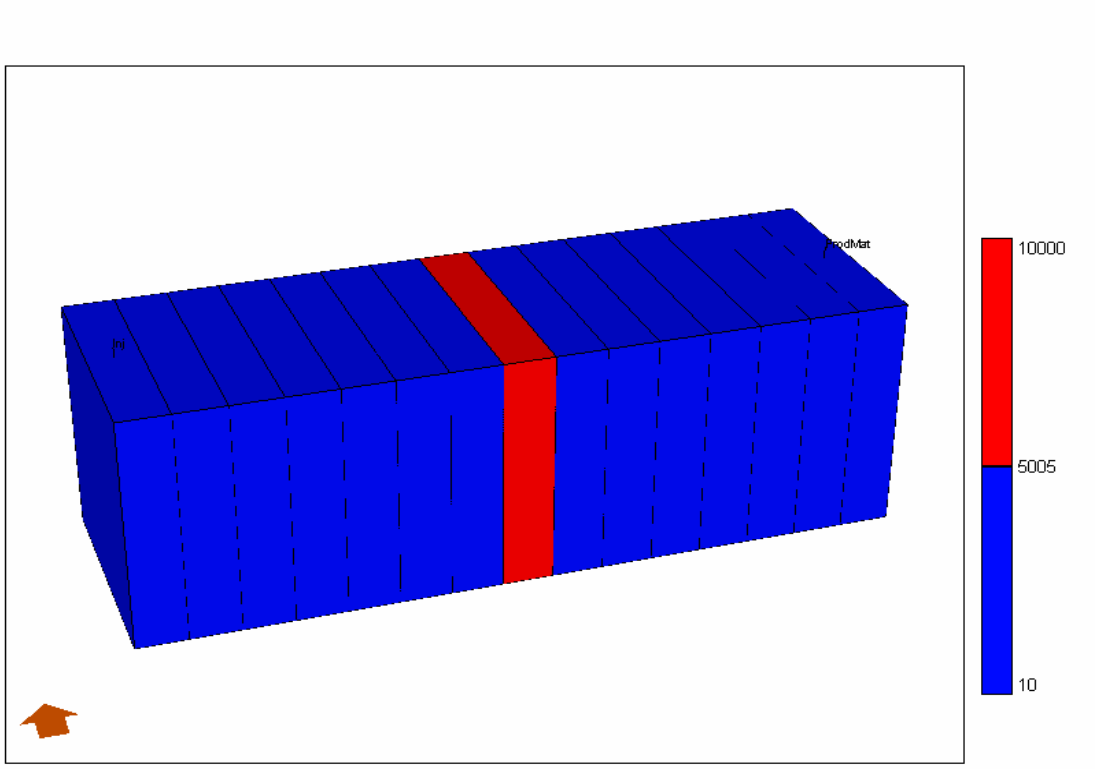

Fig. 2.2.21—One-dimensional model employed in simulation testing.

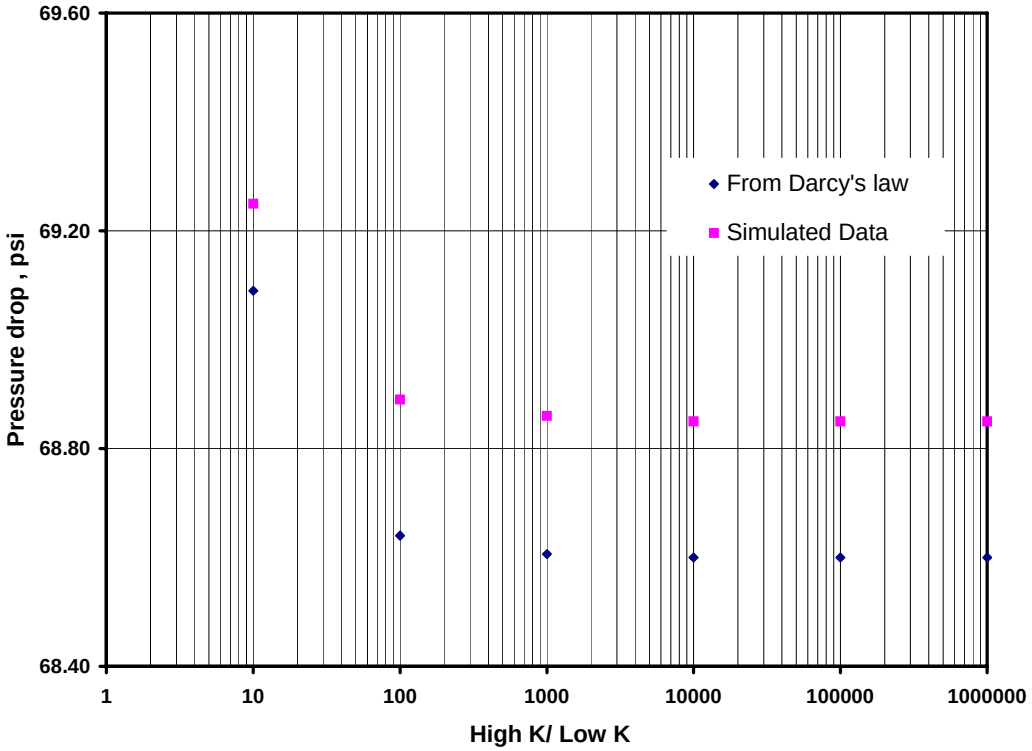

Fig. 2.2.22—Comparative plot of pressure drops observed from simulation and through Darcy's law.

Chapter II-3
Simulation of Fluid Flow through Rough Fractures

2.3.1 INTRODUCTION

Modeling of fluid flow through rough fractures has gained importance over the years. This can be attributed to the extremely low ultimate recoveries obtained from naturally fractured reservoirs, in spite of their huge reserves. Attempts are being made to develop efficient models to better formulate depletion plans. The first comprehensive work on flow through open fractures was done by Lomize,[1] who used parallel glass plates and demonstrated the validity of cubic law for laminar flow. He modeled fluid flow with different fracture shapes and investigated the effects of changing the fracture walls from smooth to rough.

Witherspoon *et al.*[2] showed that the parallel-plate approximation tends to break down at higher normal stress (>10 MPa) across the fracture. Alfred[3] also confirmed that the parallel-plate assumption is not valid to adequately model the fluid flow experiments when overburden pressure is significant. The flow through a single fracture does not progress uniformly as assumed by parallel-plate theory; rather, it flows through a limited number of channels.[4,5] Hence, the fluid flow in these tortuous channels tends to follow a preferred path. Pyrak *et al.*[6] injected molten metal into single fractures at different applied stress conditions and observed direct evidence of tortuous paths upon opening the cooled metal in the fracture. They established that the fluid flow in these paths will be through the larger apertures which offer least resistance to flow.

When the parallel-plate approach was proved invalid, Tsang and Witherspoon[5] accounted for the variation of apertures in a rough fracture. Later, Tsang[4] modeled the variation of fracture apertures by electrical resistors with different resistance values placed on a two-dimensional grid. The results indicated that smaller apertures play a key role in restricting fluid flow. When the fracture contact area increases, tortuosity and connectivity of fractures become important. The flow through a single fracture took place in a limited number of channels, which was evident from the field experiment carried out in a single

fracture,[7] Gentier[8] measured fracture surface roughness profiles in a granite fracture, plotting the apertures, and approximating the aperture density distribution by a gamma function. The density distribution is given by

$$n(b) = \frac{1}{b_o^2} b \exp(-b/b_o), \quad \text{.....(2.3.1)}$$

where b_o represents the distribution peaks, and the mean aperture is $2b_o$. The same distribution was assumed when considering the channeling of flow through fractured media.[9] Tsang and Tsang[9] assumed the channel width to be a constant of the same order as the correlation length λ, where correlation length is the spatial length within which the apertures have similar values. The reduction in channel apertures affected the tracer breakthrough curves when normal stress across a fracture was increased.

Although gamma distribution was considered, some authors[7,10] observed a log-normal distribution of fracture apertures from well logs and experiments conducted on cores. Later Moreno *et al.*[11] followed the log-normal approach when modeling flow and tracer transport in a single fracture. Using the approach, the flow patterns showed strong resemblance to field observations reported by Bourke.[12] Tsang and Tsang[13] used the log-normal approach to distribute fracture apertures for obtaining a relationship between flow and transport measurements of variable apertures. The frequency of the log-normal distribution is written as follows[14]:

$$f(x) = \frac{1}{x\sqrt{2\pi\beta^2}} \exp\left[\frac{-(\ln x - \alpha)^2}{2\beta^2}\right], \quad \text{.....(2.3.2)}$$

where

$$\beta^2 = \ln\left(1 + \frac{\sigma^2}{\delta^2}\right) \text{.....(2.3.3)}$$

and

$$\alpha = \ln\delta - \frac{\beta^2}{2}. \quad \text{.....(2.3.4)}$$

The mean aperture was determined from fluid flow measurements and used to distribute the apertures log-normally. The aperture variance was determined from tracer breakthrough. Alfred *et al.*[14] also assumed log-normal distribution for fracture apertures to

account for fracture roughness. Keller[15] imaged fracture apertures using an X-ray CT scanner. Based on the study using three different cores, he concluded that the fractures follow a log-normal distribution.

Fracture properties are strongly affected by changes in stress conditions, and therefore the effect of stress acting on the reservoirs should be considered in obtaining fracture-aperture distributions. Even though extensive research has been done on fracture aperture distributions, the effect of varying stress conditions has not yet been investigated. Stress changes aperture size and might have an effect on the distribution of fracture apertures. Thus, we measured fracture apertures under different stress conditions using a CT scanner. Several feeler gauges were used to create fractures of known size and obtain a calibration curve. Once the calibration curve was obtained, fracture aperture distributions from a fractured core were measured under different overburden pressures. Probability distributions of fracture apertures were examined to obtain the mean aperture and variance values. Using those values, the probability distributions of the density function were plotted to determine the distribution of fracture apertures at each overburden pressure.

Waterflooding a fractured core validated the use of the log-normal approach for fracture apertures and showed that the parallel-plate model is not valid for modeling fluid flow through rough surfaces.

2.3.2 CALIBRATION TECHNIQUE

We imaged the core samples in a CT scanner with power, voltage, and algorithm requirements set for a typical sandstone sample. The CT scanner identifies density differences between various objects.[16] As the density of a fluid is less than to the density of rock, the scans can be used to clearly distinguish a fluid-filled fracture from the matrix. Although a clear visualization of fracture and matrix is possible, the CT numbers (dimensionless numbers that are functions of densities) do not represent any physical characteristic. To obtain the fracture aperture measurement, we used a calibration technique to correlate the CT numbers with the actual aperture size. Keller[17] used nonintrusive imaging to obtain aperture calibration curves for granite and sandstone, measuring fracture apertures as small as 35μm; he[18] used a similar technique. Both

techniques use the integrated CT signal to determine fracture aperture by summing up the differences between a minimum rock CT number and the CT numbers pertaining to the fracture. Our calibration curve was developed from this existing technique.

The experimental setup consists of two halves of the rock sample (Berea core), feeler gauges, and core-holding equipment. The two halves were polished thoroughly to reduce surface roughness as much as possible. Smooth surfaces ensure that a proper match between the halves, and hence smaller fractures can be measured. Feeler gauges ranging from 38 μm to 813 μm were then placed between the two flat surfaces to create different fracture widths (Fig. 2.3.1).

The core sample with fracture was inserted into a sleeve to avoid artifact effects then held in the core holder. Multiple scans were then taken along the length of the core, perpendicular to the longitudinal axis. Fig. 2.3.2A shows a typical set of scans for the Berea sample with 38 μm fracture size. The color variations indicate variable densities in the sample, with the relatively high-density steel feeler gauge set to bright pink, the less dense rock material set to a bright orange, and the lower densities set to green, blue and black in decreasing order of densities. The first scan in Fig. 2.3.2A is taken through the steel feeler gauge placed on one end of the core sample; hence the color appears brighter in the middle of the core. Both ends of core sample have a feeler gauge, and scans were taken starting from one feeler gauge to the start of the next feeler gauge, at intervals of 5 mm. The next three scans show a fracture aperture of 38 μm along the length of the core. The dip in CT number curve in the middle corresponds to the location of the fracture region, and this clearly distinguishes the fracture from the matrix. Since this dip (Fig. 2.3.3) corresponds to a fracture size of 38 μm, a correlation can be obtained between the area enclosed by the curve and the fracture size. The dip is not abrupt, but rather a smooth transition from matrix to fracture. This effect reflects dispersion of CT numbers, which is caused by a finite beam width and oversampling. Fig. 2.3.2B shows the fracture aperture size of 102 μm, along the length of the core. As the aperture size increases, the CT number decreases and the fracture aperture can be seen clearly in the middle of the core, with a darker color. Fig. 2.3.4 shows a comparison of the average CT number curves obtained for various fracture sizes.

2.3.3 CALIBRATION CURVE

A plot of CT number versus the pixel number was made from the CT numbers obtained from each scan. An average CT number plot was obtained to account for minor variations in fracture sizes caused by surface roughness. An example of such plot is shown in Fig. 2.3.5. From this plot, we identified a threshold CT number, which essentially is the minimum rock CT number. All the CT numbers in the area below the minimum rock CT number are subtracted from the rock CT number and the differences are used to obtain the integrated CT signal for the fracture size. The integrated CT signals are calculated for each pixel number and are given an index starting from 1 to *n* as shown in Fig. 2.3.5. The area of integrated CT region is calculated from the following formula:

For index *i* equal to 1 to *c*,

$$Area(i) = IntCT(i-1) + \frac{1}{2}[IntCT(i) - IntCT(i-1)] . \quad \text{.....} (2.3.5)$$

For index *i* equal to *c*+1 to **n**,

$$Area(i) = IntCT(i) + \frac{1}{2}[IntCT(i-1) - IntCT(i)] . \quad \text{.....} (2.3.6)$$

After measuring nine different feeler gauges, we obtained a calibration curve for fracture aperture (Fig. 2.3.6). The plot shows a linear relationship between the integrated CT signal and fracture aperture. The linear relationship holds even at small fracture apertures. The equation obtained from this calibration curve is,

$$y = 8.7616x + 460.7 . \quad \text{.....} (2.3.7)$$

By rearranging the equation, we can calculate fracture aperture, using the integrated CT signal as follows:

$$x = 0.1141y - 52.582 . \quad \text{.....} (2.3.8)$$

Given a fracture sample, the fracture apertures can be measured using the calibration curve.

2.3.4 FRACTURE APERTURE DISTRIBUTION

For this specific experiment we used a 1-in. diameter by 2.36-in. length of Berea core. The core was fractured mechanically in the laboratory. The artificially fractured core was then imaged using the CT scanner. Images were taken at 1-mm intervals along the length

of the core. The core was then subjected to overburden pressure of 500 psi, and scans were taken at the same locations. This procedure was repeated for overburden pressures of 1,000 psi and 1,500 psi. Fig. 2.3.7 shows the images taken with and without overburden pressures. About 6,000 data points were taken for each overburden condition. The resulting CT numbers from the images were then converted to the aperture values using the calibration curve as discussed in the previous section. Mean, variance, and standard deviation were obtained for each dataset. A comparative study was made for different overburden pressures. The results are plotted in Fig. 2.3.8.

The apertures are distributed in the range of 0 to 2,000 microns as shown in Fig. 2.3.8. The tail of the aperture distribution is long and the aperture distribution is right skewed which suggests that the distribution might follow either gamma or log-normal distribution as given in the earlier studies.[8,9,15] The tail of the apertures controls the fluid flow, as fluid will tend to flow through preferred channels of least resistance.[14] Since most apertures fall in the range of 100 to 500 microns, the permeability measurements will largely be controlled by small apertures. The presence of some large apertures in the range of 600 to 2,000 microns may provide the main path for the fluid flow if they are interconnected. The calculation of flow rate based on these measured permeabilities will be different from the calculation using a single mean value of permeability as assumed by the parallel-plate approach.

Using the mean and variance of the aperture values obtained from the probability distribution plot for each overburden pressure, the distributions of probability density function (PDF) can be obtained by applying Eq. 2.3.2. The distribution plots are presented in Fig. 2.3.9. Comparison of the actual dataset to calculated distribution reveals that the distribution of PDF follows log-normal distribution at all stresses.

Without applying an overburden pressure, the PDF that follows log-normal distribution has a mean aperture value of 370.53 micron and a variance of 44,847 (Fig. 2.3.9). This log-normal distribution confirms the previous findings.[4,11,13,14,15] As the overburden pressure increases, the mean and variance of the apertures decrease, suggesting that the permeability decreases with increase in overburden pressures. The mean of the apertures decreases sharply from 370.53 microns to 197.997 microns when an initial overburden pressure of

500 psi is applied.

The fracture surfaces are rough and have many contact points along the fracture. The contact points tend to break down under overburden stress. The decrease in aperture sizes is not significant with further increase in overburden pressures. Since each reservoir experiences different overburden pressures, this research will be important to identify some of the uncertainties in predicting fluid flow through fractured reservoirs.

2.3.5 WATERFLOODING EXPERIMENT

A clean, dry core was artificially fractured in the laboratory using the Brazilian technique. Fracture apertures were then determined using the method suggested in the previous sections. The core was then saturated with refined oil and inserted into a Hassler-type core holder with a confining pressure of 500 psia. Water was then injected at a rate of 0.2 cm^3/min. The core properties are given in Table 2.3.1. CT scans were taken before, during and at the end of the injection process. The first set of scans in Fig. 2.3.10 represents the cross-sectional CT images of the oil-saturated core. The CT numbers for the oil-saturated core are found to be in the range of 1,450. When water injection is started, the water invasion can be seen as an increase in the CT numbers, as identified by a change in color (Fig. 2.3.10). Water injection was continued till residual oil saturation was reached. CT numbers of the water-saturated core are seen to be in the range of 1,650 to 1,700. Due to high permeability of the fracture, water is seen to preferentially flow along the fracture plane. Fig. 2.3.11 shows the 3D water saturations along the length of the core.

2.3.5.1 PARALLEL PLATE SIMULATION MODEL

We used a commercial simulator to analyze the fluid flow through fracture during waterflooding. The laboratory process in which water was injected through the fracture was duplicated in this modeling effort, using the parallel-plate assumption. The mean fracture aperture and the mean fracture permeability obtained from the CT scanner data were treated as constant value in all the grid blocks in the fracture plane. The simulation model used 34x10x15, with a well placed in gridblock 1,5,8 that served as the water injector, while the producers were placed on the matrix and the fracture layers at the outlet end.

Fig. 2.3.12 shows the comparison of fluid movement through fracture surface using the CT profile and the simulated profile using the parallel-plate model. As we can see from the figure, the water-saturation profiles predicted by the parallel-plate model indicate higher saturations than the CT profile. This difference can be attributed to the single mean value of fracture permeability used in the fracture. In this case, the fracture surface is devoid of roughness and contact points, which allows the water to move freely without any resistance to flow. This also results in an earlier breakthrough than was observed during the experiment. The oil recovery was also lower than the experimental value (Fig. 2.3.13). Most of the injected water flows through the fracture and hence the predicted watercut is also higher than the observed watercut (Fig. 2.3.14).

2.3.5.2 DISTRIBUTED APERTURE SIMULATION MODEL

The distributed-aperture simulation model was constructed with the same number of grid blocks and sizes as used in the parallel-plate model. Actual aperture data was obtained from CT scanner results. Fig. 2.3.15 shows the 3D distribution of apertures along the fracture plane. The mean aperture size is 198 micron. Darker colors in the distribution pattern indicate higher aperture values.

The fracture aperture values were then converted to their corresponding fracture permeability values using the relation between fracture aperture and permeability[19] and introduced into the fracture layer with 34 x 10 gridblocks.

In this case, the fluid flows through the path of least resistance offered by the interconnected large apertures. The smaller apertures have lesser volumetric rate and offer resistance to flow, which diverts some amount of fluid into the matrix blocks. Fig. 2.3.16 shows the comparison of fluid flow profile obtained from the CT scanner and that obtained from simulation using the distributed-aperture model. As can be seen from the figure, the water-saturation profiles predicted by the distributed-aperture model are in good agreement with the CT profiles. Figs. 2.3.17 and 2.3.18 show that a good match is obtained between the observed and simulated oil recovery and water breakthrough. Fig. 2.3.18 also shows an improvement in the water cut match compared to the previous case. Fig. 2.3.19 shows the match obtained between observed and predicted cumulative water production.

2.3.5.3 SENSITIVITY ANALYSIS

A sensitivity analysis was performed to analyze the effect of injection rates and aperture distributions on oil recovery and water breakthrough. Three different injection rates (0.2, 0.5, and 0.8 cm^3/min) were used with different aperture sizes for both parallel-plate and distributed-aperture model. About 2 p.v. of water was injected in each case. The oil recoveries obtained for each case have been tabulated in Tables 2.3.2 and 2.3.3. Fig. 2.3.20 shows the effect of different injection rates on oil recovery. The oil recovery obtained is seen to decrease with an increase in the injection rate. This is due to an increase in the viscous forces, which causes the fluid to flow preferentially through the fracture layer with high values of permeability resulting in early breakthrough and poor sweep. At low injection rates, dominance of capillary forces over viscous forces results in delayed breakthrough and hence better recovery.

Changes in aperture distributions are also seen to affect oil recovery. The mean and variance values shown in Fig. 2.3.9 were used. For each distributed-model case, the corresponding parallel-plate model was constructed with the same value of mean and zero variance. Fig. 2.3.20 shows that, as the fracture aperture increases, the performance of the parallel-plate model becomes closer to the distributed-aperture model. The reason for this is the decrease in resistance to flow that was previously offered by the smaller apertures. Although the two models are in closer agreement at lower injection rates, the parallel-plate model underestimates the oil recovery that can be obtained from the system. This shows that the oil recovery is very sensitive to the variance of aperture sizes, making the parallel-plate model invalid for performance predictions.

2.3.6 CONCLUSIONS

The main conclusions derived from this study can be summarized as follows:

1. Fracture apertures follow log-normal distribution at all stress conditions.
2. Simulation results indicate that the parallel-plate model does not adequately represent a fractured reservoir system.
3. The profile match obtained using the distributed-aperture model shows that this model can be used to provide accurate descriptions of fractured systems.

4. Analysis of sensitivity to injection rates shows that, as the injection rate increases, the difference in the oil recoveries predicted by the two models also increases.
5. At higher injection rates, higher viscous forces cause early breakthrough from the fracture and hence the oil recovery obtained is lesser.
6. For large aperture sizes, the performance of the parallel-plate model becomes closer to that of the distributed-aperture model. The sensitivity of oil recovery to variance of aperture sizes makes the parallel-plate model invalid.

NOMENCLATURE

$Area(i)$	= area of section i
b_o	= distribution peak
b	= aperture size
c	=index of lower CT number
$f(x)$	= frequency of apertures
i	= index
$IntCT(i)$	= integrated CT area for section i
n	= index of higher CT number
$n(b)$	= probability density distribution
x	= fracture aperture
y	= total integrated CT signal

REFERENCES

1. Lomize, G. M.: “Seepage in Fissured Rocks,” State Press, Moskow-Leningrad, 1951.
2. Witherspoon, P. A., Wang, J. S. Y., Iwai, K., and Gale, J. E.: “Validity of Cubic Law for Fluid Flow in a Deformable Rock Fracture,” *Water Resources Research*, 16(6), 1016-1024, 1980.
3. Alfred, D.: “Modeling Fluid Flow through a Single Fracture Using Experimental, Stochastic and Simulation Approaches,” master’s thesis, Texas A&M University, 2003.

4. Tsang, Y. W.: “The Effect of Tortuosity on Fluid Flow through a Single Fracture,” *Water Resources Research*, 20(9), 1209-1215, 1984.
5. Tsang, Y. W. and Witherspoon, P. A.: “The Dependence of Fracture Mechanical and Fluid Properties on Fracture Roughness and Sample Size,” *J. Geophys. Res.*, 88(B3), 2359-2366, 1983.
6. Pyrak, L. R., Myer, L. R., and Cook, N. G. W.: “Determination of Fracture Void Geometry and Contact Area at Different Effective Stress,” *Eos Trans.* AGU (abstract), 66(46), 903, 1985.
7. Bourke, P. J., Dunance, E. M., Heath, M. J., and Hodgkinson, D. D.: “Fracture Hydrology Relevant to Radionuclide Transport, AERE *Rep.* 11414, Atomic Energy Res. Estab., Harwell, United Kingdom, 1985.
8. Gentier, S.: “Morphologie et comportement hydromécanique d’une fracture naturelle dans un granite sous contrainte normale,” doctoral thesis, Univ. d’Orléans, France, 1986.
9. Tsang, Y. W. and Tsang, C. F.: “Channel Model of Flow Through Fractured Media,” *Water Resources Research*, 23(3), 467-479, 1987.
10. Bianchi, L. and Snow, D.: “Permeability Crystalline Rock Interpretated from Measured Orientations and Apertures of Fractures*,” Annu. Arid Zone*, 8(2), 231-245, 1968.
11. Moreno, L., Tsang, Y. W., Tsang, C. F., Hale, F. V., and Neretnieks, I.: “Flow and Tracer Transport in a Single Fracture: A Stochastic Model and Its Relation to Some Field Observations,” *Water Resources Research*, 24(12), 2033-2048, 1988.
12. Bourke, P. J.: “Channeling of Flow Through Fractures in Rock,” in *Proceedings* of GEOVAL-87 International Symposium, Swed. Nucl. Power Inspectorate, Stockholm, Sweden, 1987.
13. Tsang, Y. W. and Tsang, C. F.: “Hydrological Characterization of Variable-Aperture Fractures,” *Rock Joints*, Barton & Stephansson (eds), Balkema, Rotterdam, 1990.
14. Alfred, D., Putra, E., and Schechter, D.S.: “Modeling Fluid Flow through Single Fractures Using Experimental, Stochastic and Simulation Approaches,” paper SPE/DOE 89442 presented at 2004 Improved Oil Recovery Symposium, OK, Tulsa, 17–21April.

15. Keller, A. A.: “Single and multiphase flow and transport in fractured porous media,” PhD dissertation submitted to Stanford University (1996).
16. Wellington, S. L. and Vinegar, H. J.: “CT Studies of Surfactant- Induced CO_2 Mobility Control,” paper SPE 14393 presented at the 1985 SPE Annual Technical Conference and Exhibition, Las Vegas, September 22-25.
17. Keller, A.A.: “High Resolution CAT Imaging of Fractures in Consolidated Materials,” *Int. J. Rock Mech. Min. Sci*. (1997), 34 (3/4), 358-375.
18. He, M.: “Application of X-ray Tomography to Measurement of Fractures in Rocks,” M.S. Thesis, Stanford University (1998).
19. Putra, E., Muralidharan, V., and Schechter, D.S.: “Overburden Pressure Affects Fracture Aperture and Fracture Permeability in a Fracture Reservoir,” *SA Journal of Technology* (Fall 2003), pp 57-63.

Table 2.3.1 — Properties of Berea core

Core Properties	
Length	10.414 cm
Diameter	2.413 cm
Porosity	22.53%
Permeability	248 md

Table 2.3.2 — Oil Recovery Obtained at Different Injection Rates Using Distributed Fracture Aperture Model

	Inj rate, cc/min	Oil recovery, %IOIP
mean = 138.6 μm σ = 150.3	0.2	69.77633588
	0.5	69.04828244
	0.8	68.37442748
mean = 157.4 μm σ = 162.4	0.2	69.5019084
	0.5	68.5240458
	0.8	67.75658397
mean = 198 μm σ = 172.6	0.2	68.9879771
	0.5	67.64169847
	0.8	66.51412214
mean = 370.5 μm σ = 211.8	0.2	68.48177481
	0.5	66.69589695
	0.8	64.69914122

Table 2.3.3 — Oil Recovery Obtained at Different Injection Rates Using Smooth Fracture Aperture (Parallel Plate) Model

	Inj rate, cc/min	Oil recovery, %IOIP
mean = 138.6 μm	0.2	68.17461832
	0.5	66.08416031
	0.8	64.28244275
mean = 157.4 μm	0.2	68.18568702
	0.5	65.83969466
	0.8	63.74045802
mean = 198 μm	0.2	68.08778626
	0.5	65.62977099
	0.8	63.07251908
mean = 370.5 μm	0.2	67.90076336
	0.5	65.36259542
	0.8	62.21374046

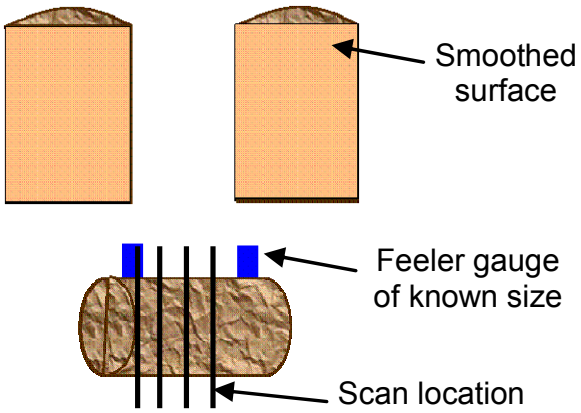

Fig. 2.3.1 — Experimental procedure showing feeler gauges and scan locations

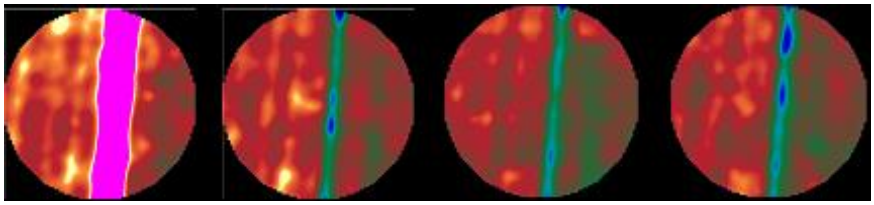

A. 38 µm feeler gauge

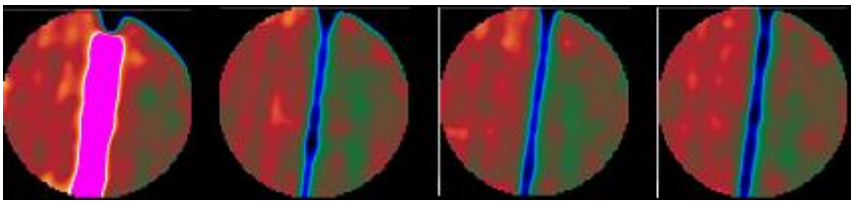

B. 102 µm feeler gauge

Fig. 2.3.2 — Scans taken along the length of the core for various feeler gauges

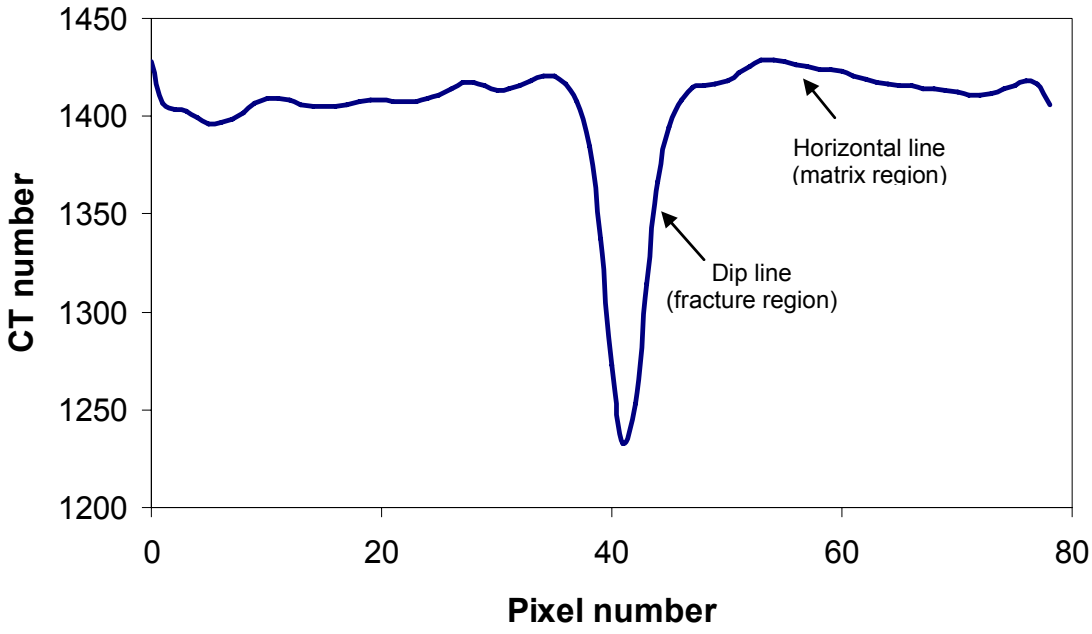

Fig. 2.3.3 — Average CT number plot for 38 μm feeler gauge

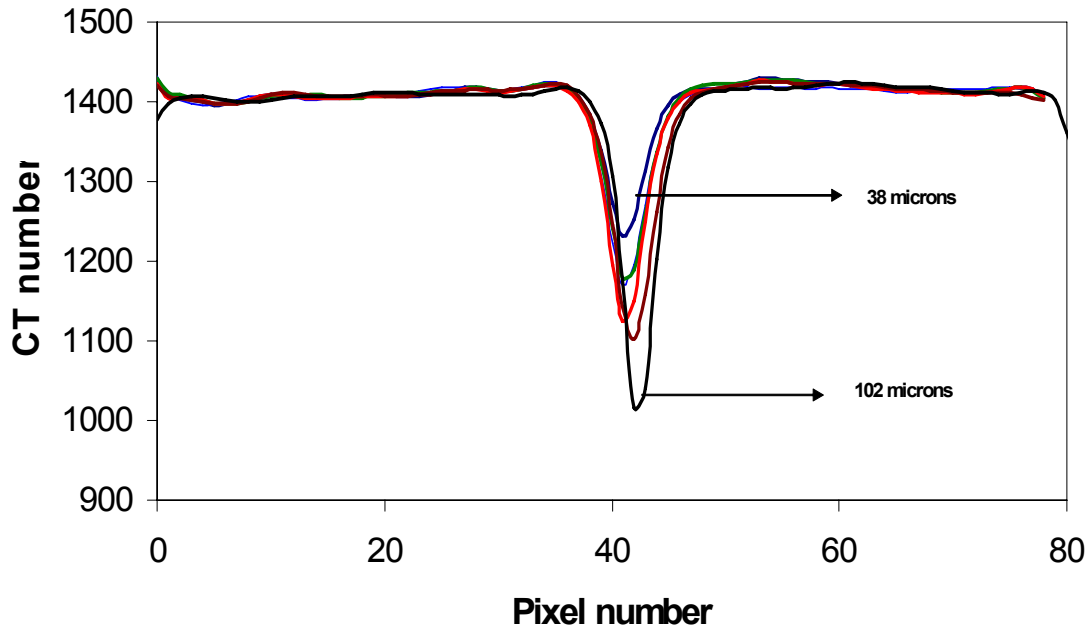

Fig. 2.3.4 — Comparison of CT number plots for different fracture sizes

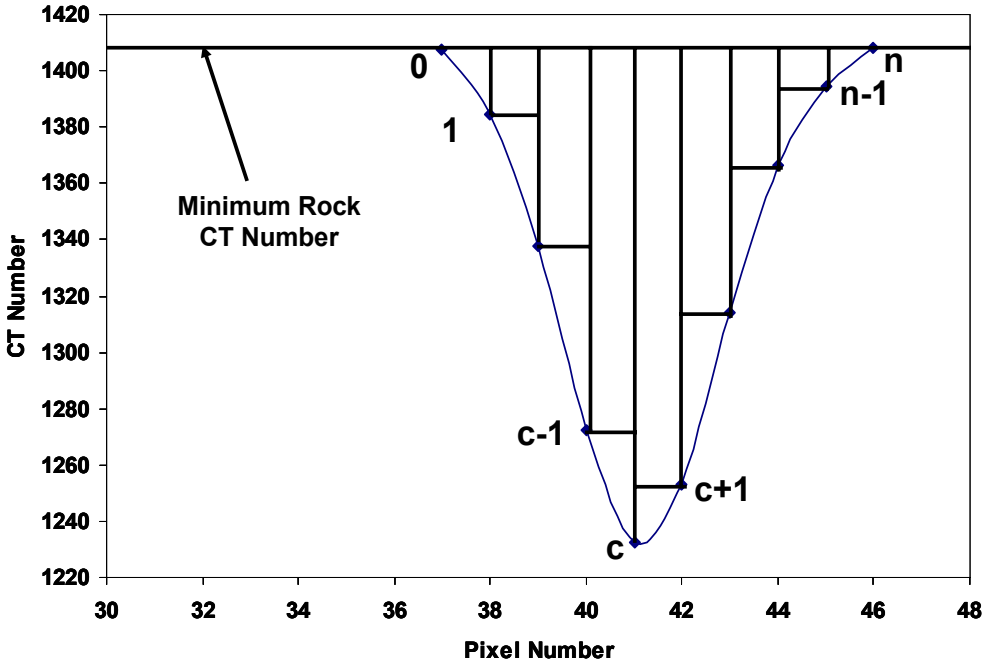

Fig. 2.3.5 — Integrated area in the fracture region showing the index of integrated CT

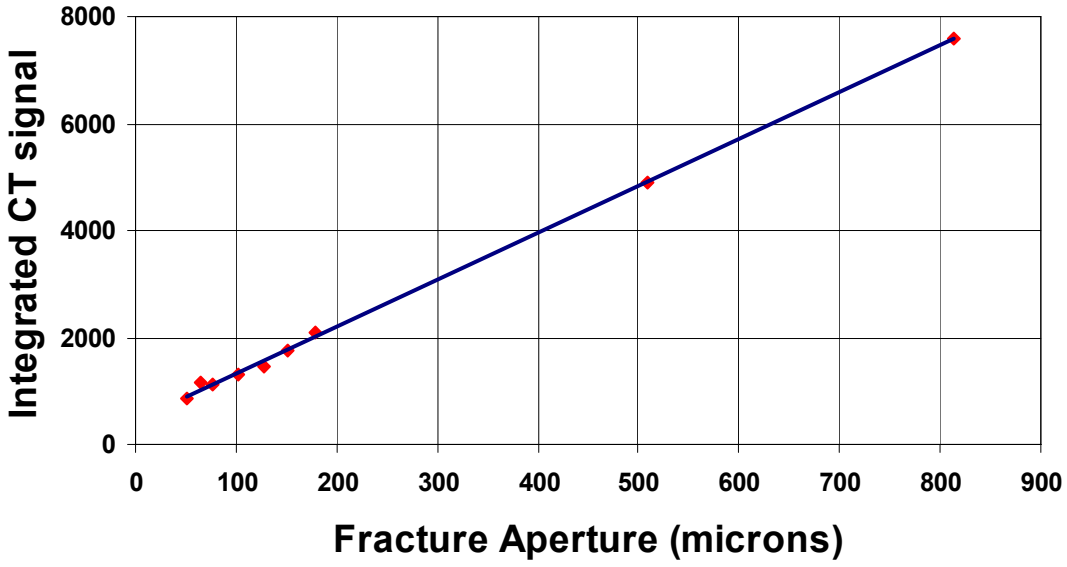

Fig. 2.3.6 — Calibration curve between integrated CT signal and fracture aperture

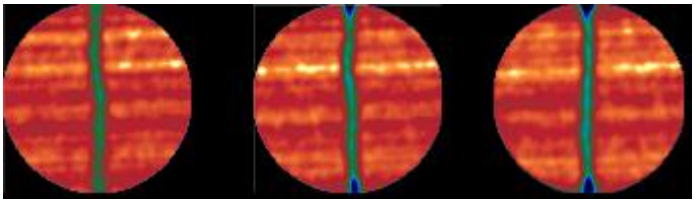

A. No overburden pressure

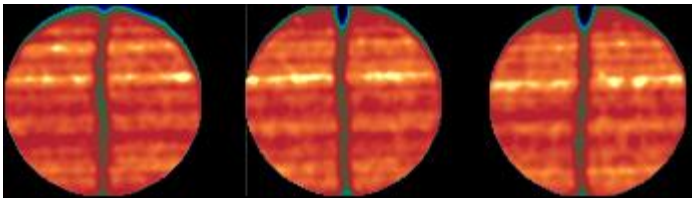

B. 500 psi overburden pressure

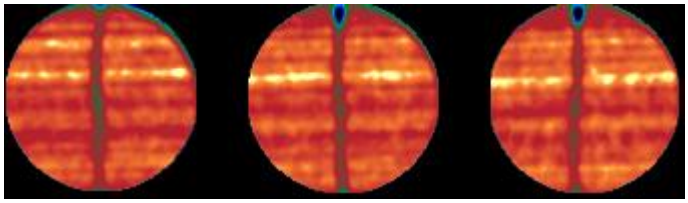

C. 1000 psi overburden pressure

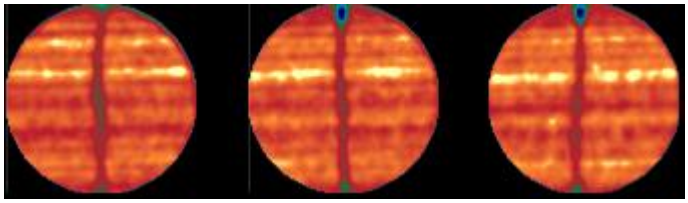

D. 1500 psi overburden pressure

Fig. 2.3.7 — Sample scans taken along the length of the core with different overburden pressures

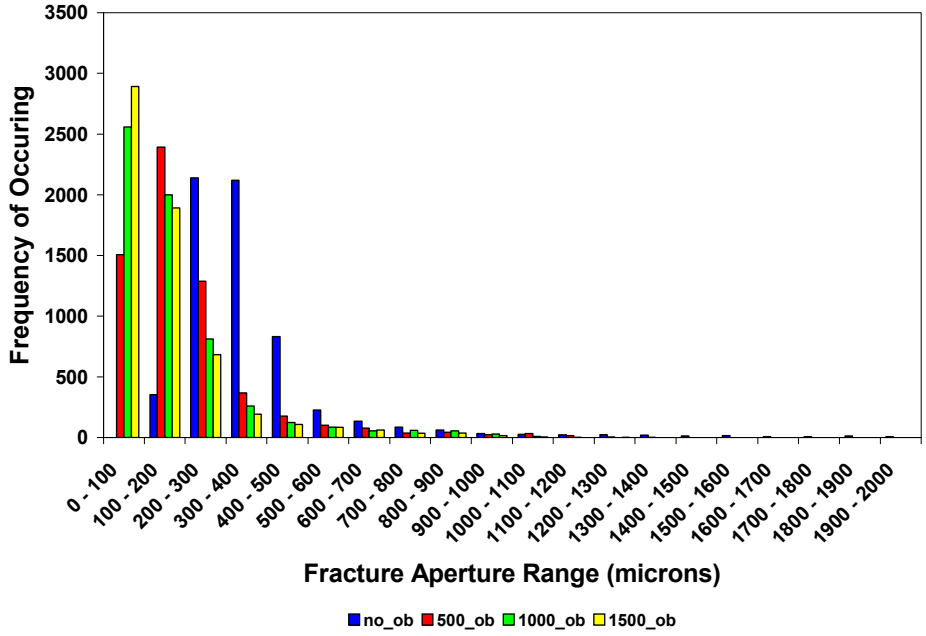

Fig. 2.3.8 — Comparative study of fracture aperture distribution under various overburden pressures

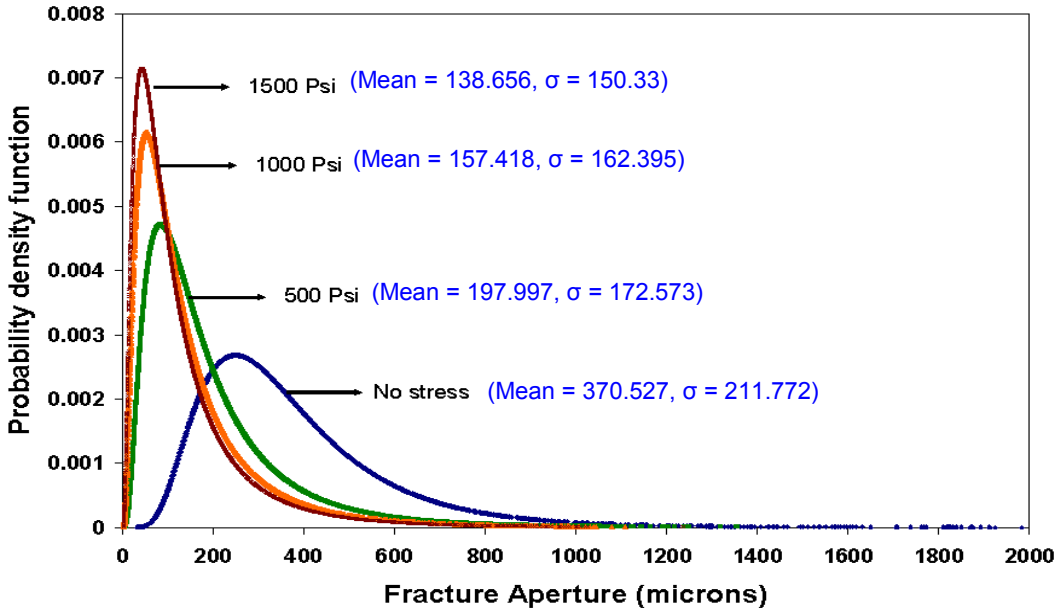

Fig. 2.3.9 — Comparison of aperture distribution curves for various overburden pressures

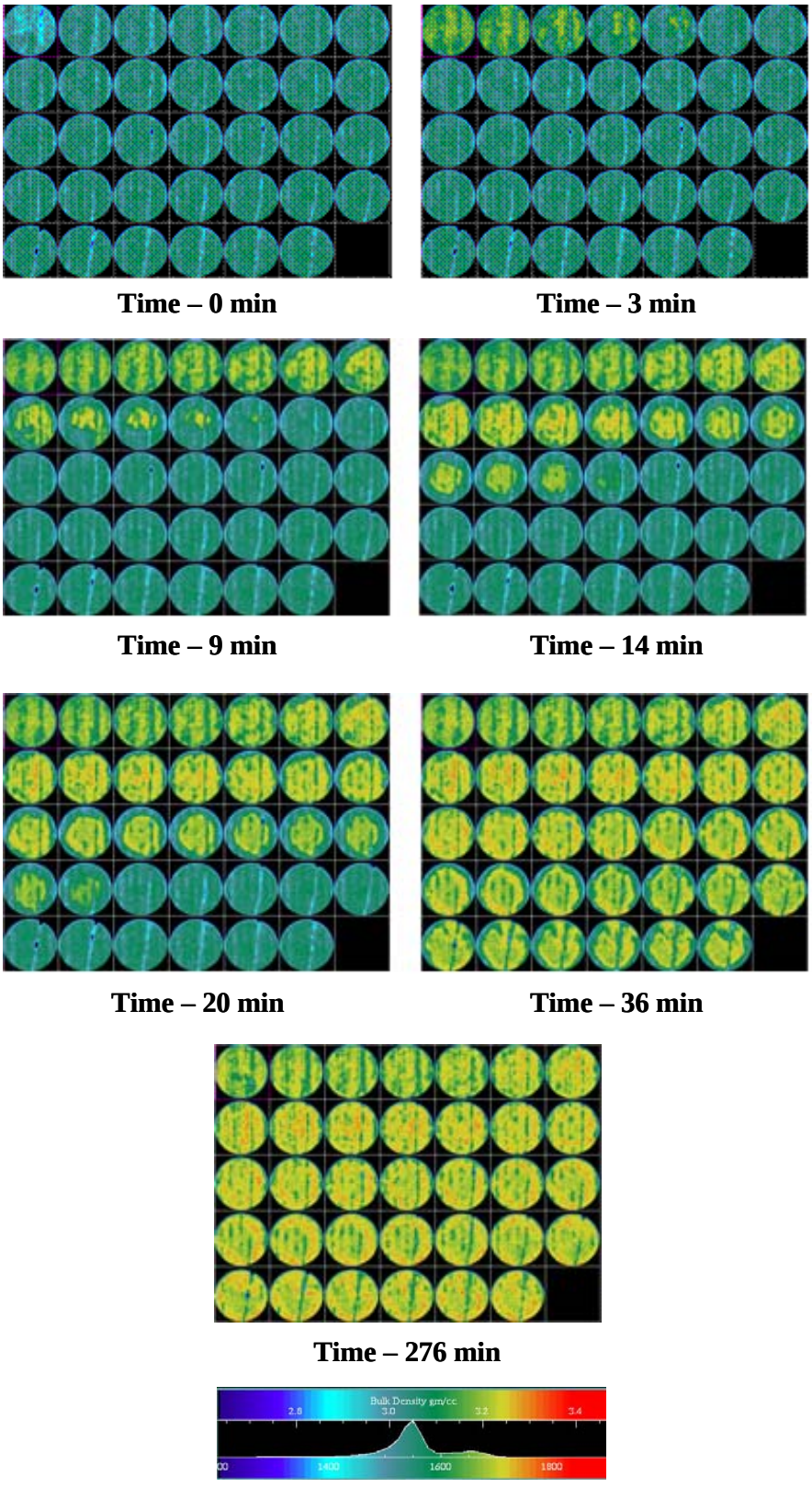

Fig. 2.3.10 — CT scan images during waterflooding at various timesteps

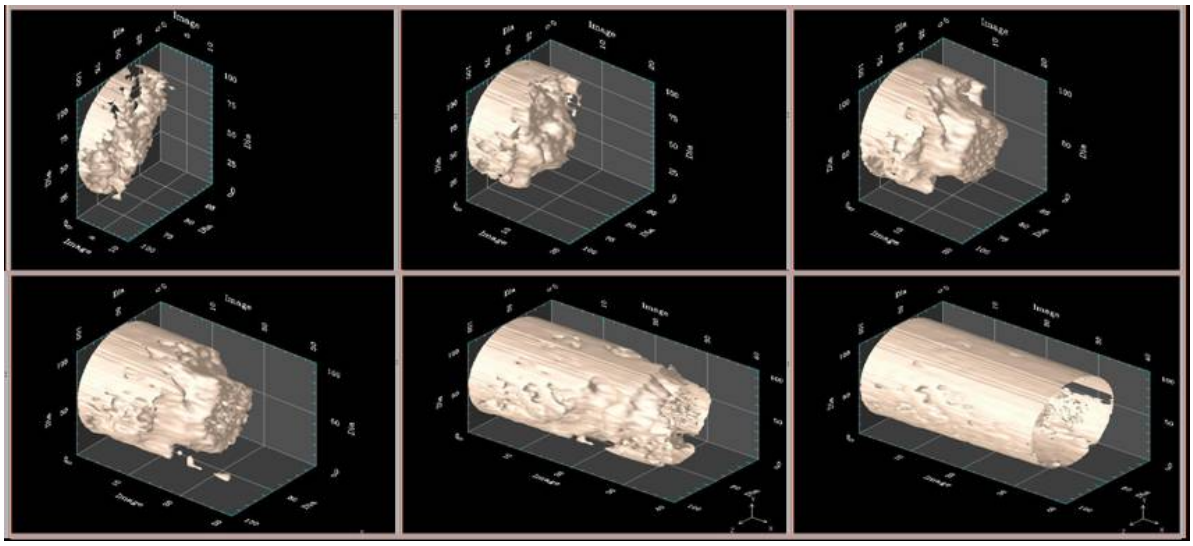

Fig. 2.3.11 — 3D images of water saturation during waterflooding at various timesteps

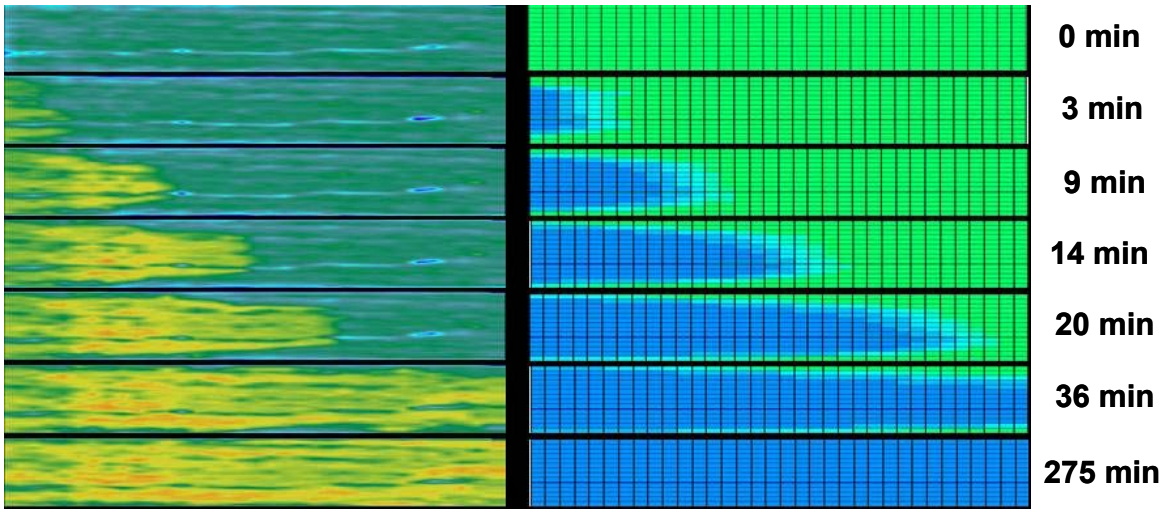

Fig. 2.3.12 — Comparison between CT and simulated water progression using parallel-plate model

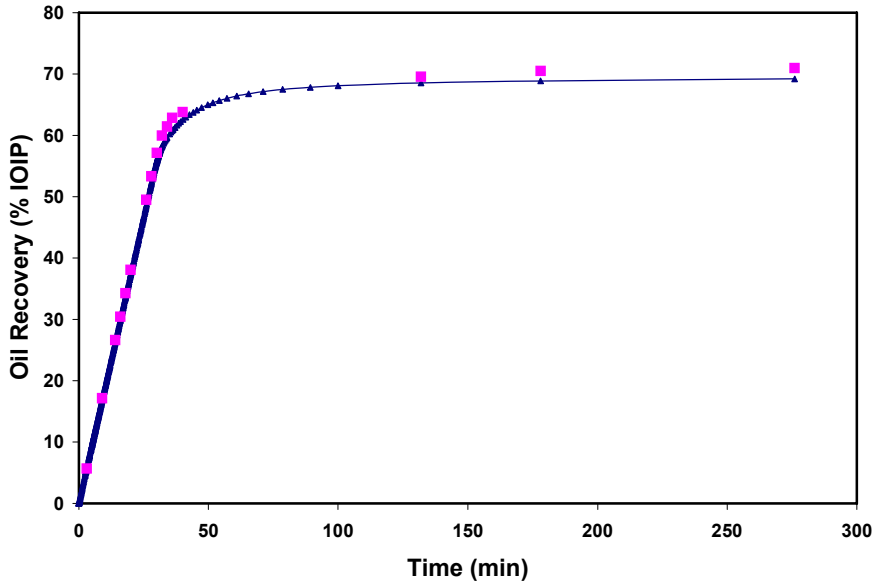

Fig. 2.3.13 — Comparison between observed and simulated oil recovery using parallel-plate model

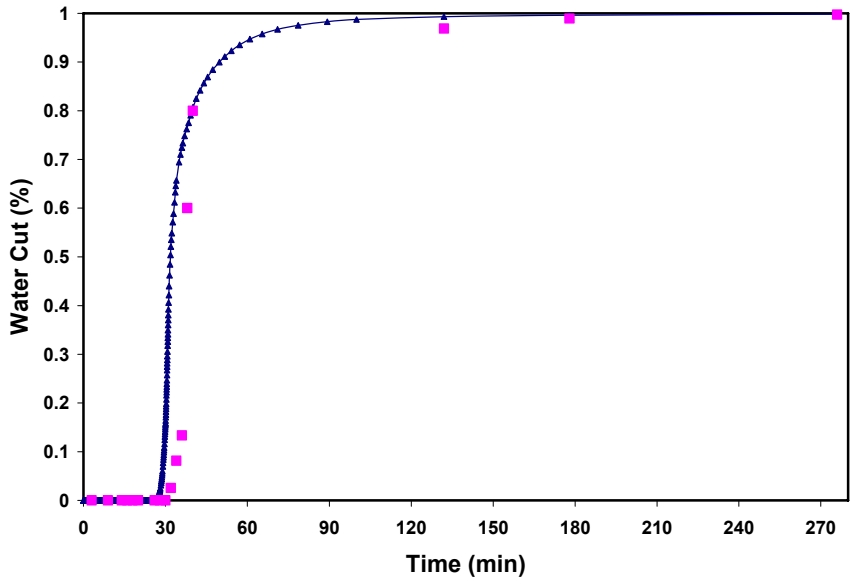

Fig. 2.3.14 — Comparison between observed and simulated water cut using parallel-plate model

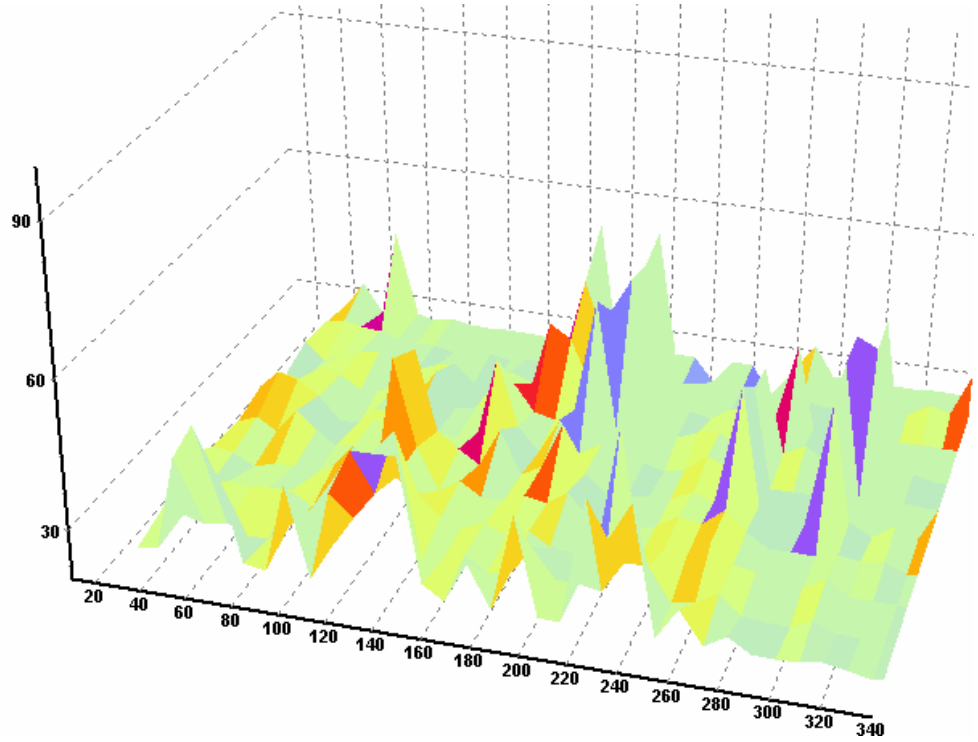

Fig. 2.3.15 — 3D map of aperture distribution

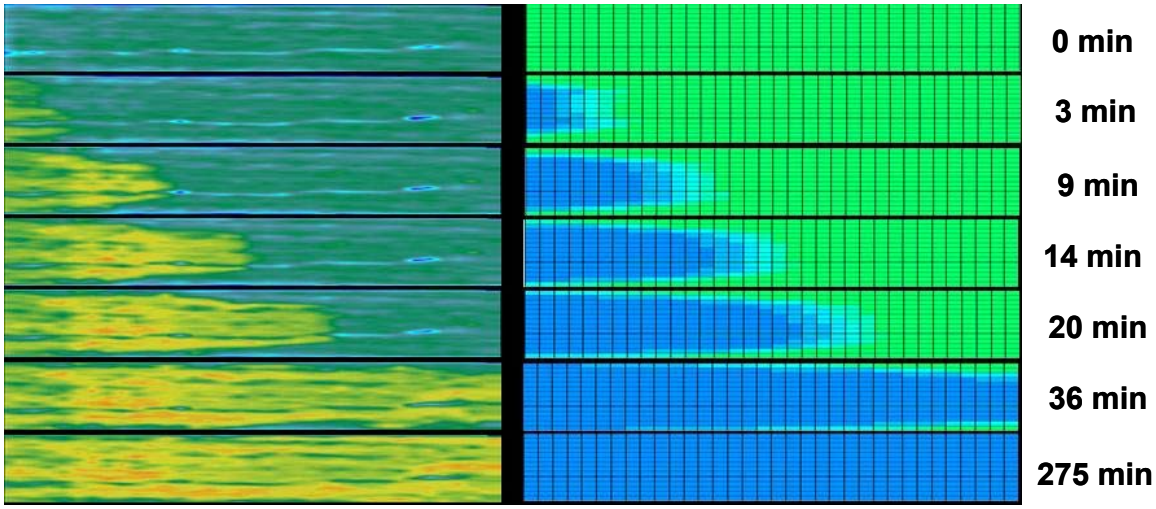

Fig. 2.3.16 — Comparison between CT and simulated water progression using distributed-aperture model

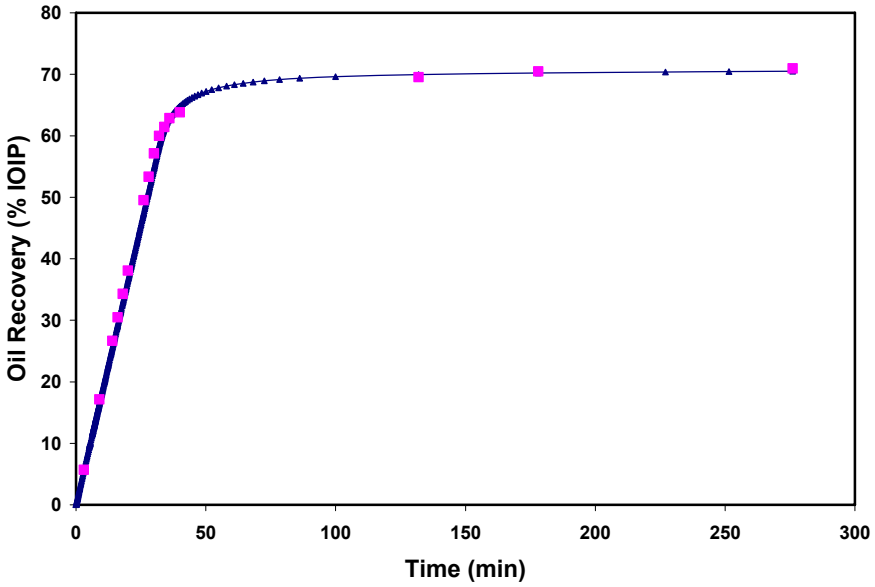

Fig. 2.3.17 — Comparison between observed and simulated oil recovery using distributed-aperture model

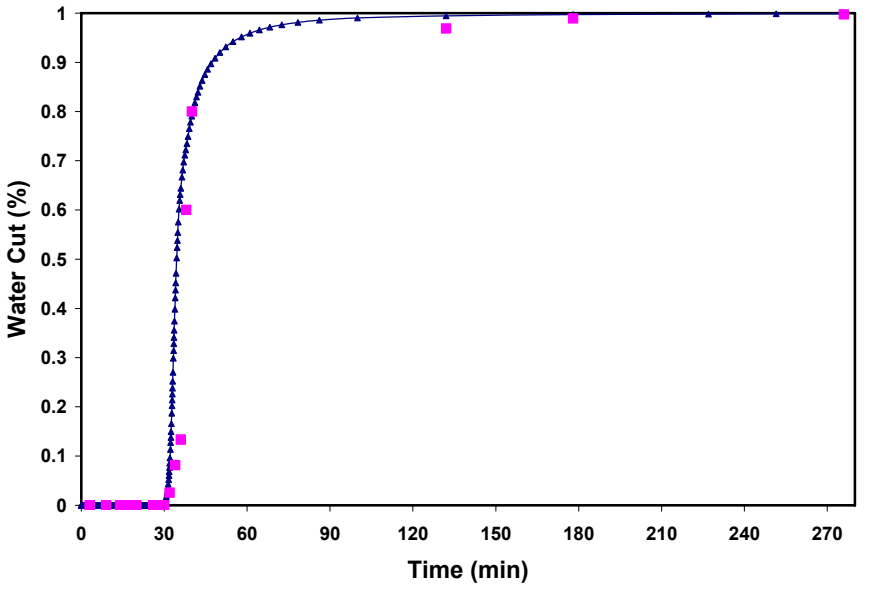

Fig. 2.3.18 — Comparison between observed and simulated water cut using distributed-aperture model

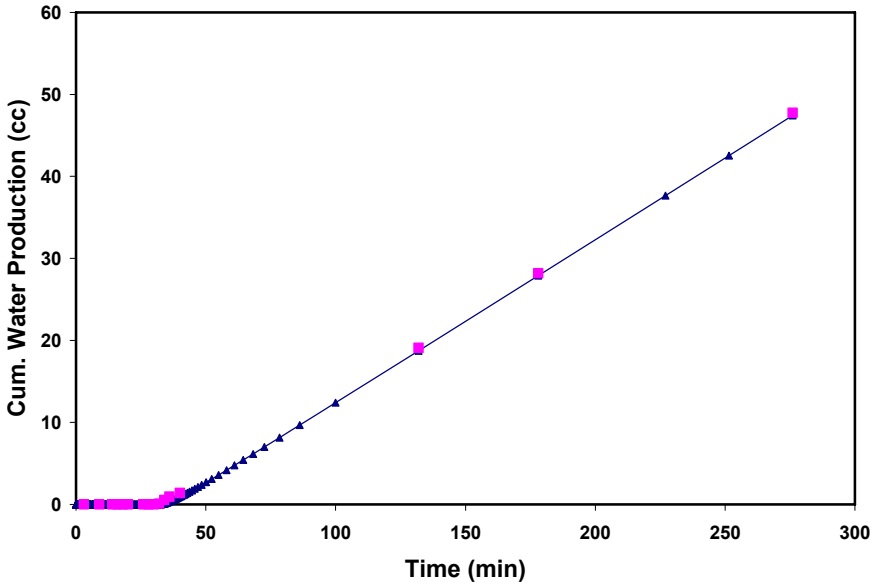

Fig. 2.3.19 — Comparison between observed and simulated cumulative water production using distributed-aperture model

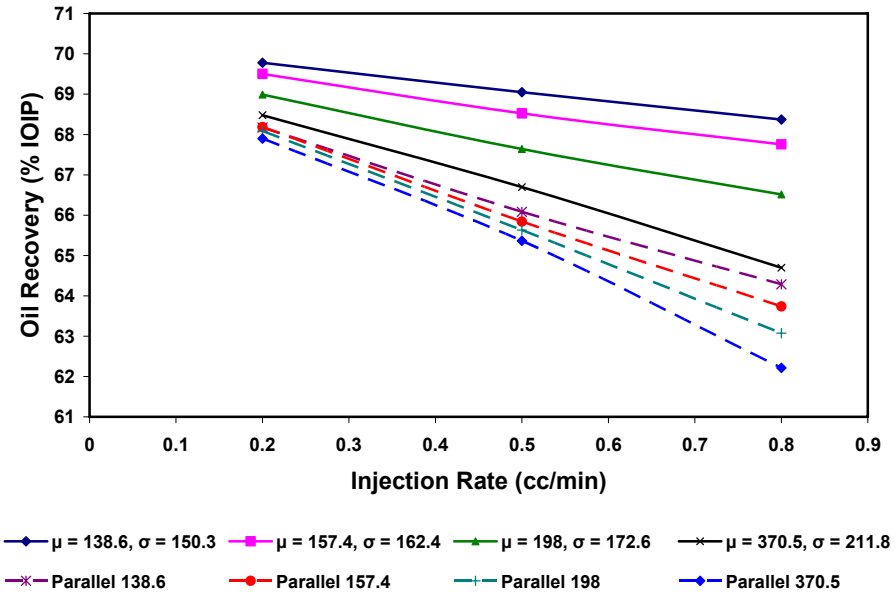

Fig. 2.3.20 — Sensitivity of oil recovery to fracture aperture size, distribution, and injection rates

Chapter II-4
X-Ray Tomography Results Validate Numerical Modeling of Flow in Fractures

2.4.1 INTRODUCTION

The quest to produce more oil has led various researchers to evaluate more complex reservoirs such as naturally fractured ones. The complexity of fluid flow in these types of reservoirs arises from the fact that two principal media, the matrix flow and the fracture network, allow fluid flow. At the heart of this phenomenon lies the problem of interaction between these two flow media. In naturally fractured reservoirs, the matrix acts as a source where hydrocarbons are present, whereas the fractures facilitate in fast recovery of these hydrocarbons. Hence it is important to study what makes the matrix produce more oil. Water is used as a means to efficiently displace oil, but fluid flow in porous media, which is determined primarily by capillary force, is relatively difficult to quantify. Handy,[2] Garg *et al.,*[3] Babadagli and Ershaghi,[4] Li and Horne,[5] Akin and Kovscek,[6] Reis and Cil,[7] Zhou *et al.*,[8] have all investigated this problem. Also, depending on the geometry of the fracture, the fracture network may or may not have any capillary force. This force is responsible for imparting the spontaneity to fluid flow within naturally fractured reservoirs. Given the complexity of quantifying the spread of fractures, it is even difficult to ascertain the limits where the fracture flow acts as an independent flow entity instead of being a part of porous matrix.

Fluid flow in fractured media in our work deals exclusively with the study of this spontaneous phenomenon that helps displace oil out of matrix. With the help of a numerical model, our experimental study quantifies spontaneous imbibition processes in both unfractured and fractured cores having negligible capillary pressure in the fracture.

To understand the spontaneous imbibition process on the laboratory scale, then, we developed our own numerical model which is flexible enough to examine the effect of various parameters on spontaneous imbibition process can be studied in depth.

2.4.2 PRINCIPLE OF X-RAY TOMOGRAPHY

CT scanning was introduced for medical purposes in the 1970s and it was introduced for industrial purposes in the 1980s. In this nondestructive imaging technique, Fig. 2.4.1 emits a fan-shaped beam, that is moved to different positions around the object. All the data generated, in each voxel, is then accumulated and processed with the help of a computer algorithm which generates a 3D CT image. The digital detector measures the linear attenuation coefficient, μ, the units of which are in form of a dimensionless number called a *Hounsfield unit*. The value of μ, depends on the density and the atomic composition of the matter in which X-ray propagates.

For a homogeneous object, the receptor reading, as per Huang[1], is given by:

$$I = I_0 e^{-\mu x} . \quad \text{..... (2.4.1)}$$

Although slower than radiography, CT scanning is superior when it comes to revealing interior details of the imaged object. The scale of CT numbers, N_{CT}, has two fixed values independent of photon energy. For vacuum, air, or body gas, N_{CT} = -1000 and for water, N_{CT} = 0.

The common method used for calculating porosity from CT images is:

$$\phi = \frac{N_{CT100\%Sat} - N_{CTDry}}{N_{CTWater} - N_{CTAir}} . \quad \text{..... (2.4.2)}$$

If water displaces air in the core, then saturation is given by:

$$S_w = \frac{N_{CTMat} - N_{CTDry}}{N_{CT100\%Sat} - N_{CTDry}} . \quad \text{..... (2.4.3)}$$

2.4.3 MATHEMATICAL MODEL

To form a mathematical model, we have to start from the basic equations. For a one-dimensional, two-phase system, such as an oil/water system, the governing equations of fluid flow in porous media is given by Darcy's law:

Nonwetting phase: $$u_{nw} = -\frac{kk_{rnw}}{\mu_{nw}}\left(\frac{\partial p_{nw}}{\partial x} + g\rho_{nw}\sin\alpha\right) . \quad \text{..... (2.3.4)}$$

Wetting phase: $$u_w = -\frac{kk_{rw}}{\mu_w}\left(\frac{\partial p_w}{\partial x} - g\rho_w \sin\alpha\right). \quad \text{.....} \quad (2.4.5)$$

Here it is assumed that water is displacing oil. We use the capillary pressure equation,

$$P_c = p_{nw} - p_w. \quad \text{.....} \quad (2.4.6)$$

For counter-current imbibition we have,

$$u_w = -u_{nw}. \quad \text{.....} \quad (2.4.7)$$

Combining Eqs. 2.4.4 to 2.4.7 and further reduction gives the following:

$$u_w\left(\frac{\mu_w k_{rnw} + \mu_{nw} k_{rw}}{kk_{rw}k_{rnw}}\right) = \left(\frac{\partial P_c}{\partial x}\right) + g\left(\rho_w - \rho_{nw}\right)\sin\alpha. \quad \text{.....} \quad (2.4.8)$$

Again, for a given volume of porous medium, as per the law of conservation of mass, for a two-phase system having boundaries at x and $x + \Delta x$, we have:

$$q_{nw}\rho_{nw}\big|_x - q_{nw}\rho_{nw}\big|_{x+\Delta x} = A\phi\Delta x\frac{\partial}{\partial t}\left(S_{nw}\rho_{nw}\right). \quad \text{.....} \quad (2.4.9)$$

$$q_w\rho_w\big|_x - q_w\rho_w\big|_{x+\Delta x} = A\phi\Delta x\frac{\partial}{\partial t}\left(S_w\rho_w\right). \quad \text{.....} \quad (2.4.10)$$

Here we assumed that the pore volume and fluid properties remain constant. This leads to cancellation of densities on both sides of these two equations; expressing flow rate in terms of velocity, they reduce to:

$$\frac{\partial u_{nw}}{\partial x} + \phi\frac{\partial S_{nw}}{\partial t} = 0. \quad \text{.....} \quad (2.4.11)$$

and

$$\frac{\partial u_w}{\partial x} + \phi\frac{\partial S_w}{\partial t} = 0. \quad \text{.....} \quad (2.4.12)$$

For two-phase flow, we have:

$$S_{nw} = 1 - S_w. \quad \text{.....} \quad (2.4.13)$$

and this implies:

$$\partial S_{nw} = -\partial S_w . \quad \text{..... (2.4.14)}$$

Thus combining Eqs. 2.4.11 to 2.4.14 we have:

$$\frac{\partial u_{nw}}{\partial x} - \phi \frac{\partial S_w}{\partial t} = 0 . \quad \text{..... (2.4.15)}$$

$$\frac{\partial u_w}{\partial x} + \phi \frac{\partial S_w}{\partial t} = 0 . \quad \text{..... (2.4.16)}$$

Combining Darcy's law with the equations from the law of conservation of mass and on reduction, we have:

$$\phi \frac{\partial S_w}{\partial t} = -\frac{\partial}{\partial x}\left[\frac{k k_{rw} k_{rnw}}{\left(\mu_w k_{rnw} + \mu_{nw} k_{rw}\right)} \left(\left(\frac{dP_c}{dS_w} \right) \frac{\partial S_w}{\partial x} \right) \right] - \frac{\partial}{\partial x}\left[\frac{k k_{rw} k_{rnw}}{\left(\mu_w k_{rnw} + \mu_{nw} k_{rw}\right)} \right] g \Delta\rho \sin\alpha ,$$

..... (2.4.17)

which is the non-linear diffusion saturation equation and forms the basic equation of spontaneous imbibition. The first part of Eq. 2.4.17 is the diffusion term *D*, which is determined by capillary forces whereas the latter, gravity term *V*, is determined by the gravitational forces. For simplicity, Eq. 2.4.17 is written in the form:

$$\phi \frac{\partial S_w}{\partial t} = -\frac{\partial}{\partial x}\left[D\left(\frac{\partial S_w}{\partial x} \right) \right] - \frac{\partial}{\partial x}[V] \Delta\rho \sin\alpha . \quad \text{.....(2.4.18)}$$

where

$$[D] = \left[\frac{k k_{rw} k_{rnw}}{\left(\mu_w k_{rnw} + \mu_{nw} k_{rw}\right)} \left(\frac{dP_c}{dS_w} \right) \right] . \quad \text{..... (2.4.19)}$$

$$[V] = \left[\frac{k k_{rw} k_{rnw}}{\left(\mu_w k_{rnw} + \mu_{nw} k_{rw}\right)} \right] g . \quad \text{..... (2.4.20)}$$

Extending this from a 1D to 2D form we have the general form of Eq. 2.4.18 as:

$$\phi \frac{\partial S_w}{\partial t} = -\frac{\partial}{\partial x}\left[D\left(\frac{\partial S_w}{\partial x} \right) \right] - \frac{\partial}{\partial y}\left[D\left(\frac{\partial S_w}{\partial y} \right) \right] - \frac{\partial}{\partial x}[V] \Delta\rho \sin\alpha - \frac{\partial}{\partial y}[V] \Delta\rho \sin\alpha .$$

..... (2.4.21)

2.4.4 FINITE DIFFERENCE NUMERICAL MODEL

To arrive at a solution of Eq. 2.4.21, we have to solve it numerically. The most common of the assumptions is to assume the effect of gravity to be small and hence neglected. Also, if the nonwetting phase is assumed to be air, then mobility of air is much higher than mobility of water and the mobility ratio of water to air is almost zero. This simplifies the Eq. 2.4.21 to:

$$\phi \frac{\partial S_w}{\partial t} = -\frac{\partial}{\partial x}\left[D\left(\frac{\partial S_w}{\partial x} \right) \right] - \frac{\partial}{\partial y}\left[D\left(\frac{\partial S_w}{\partial y} \right) \right] . \quad \text{(2.4.22)}$$

and its finite difference equivalent, central difference in space and forward difference in time, is given by:

$$\frac{D^n_{i-\frac{1}{2},j}}{\Delta x_{i-\frac{1}{2},j}} \frac{\left((S_w)^{n+1}_{i-1,j} - (S_w)^{n+1}_{i,j} \right)}{\Delta x_{i,j}} + \frac{D^n_{i+\frac{1}{2},j}}{\Delta x_{i+\frac{1}{2},j}} \frac{\left((S_w)^{n+1}_{i+1,j} - (S_w)^{n+1}_{i,j} \right)}{\Delta x_{i,j}}$$

$$+ \frac{D^n_{i,j-\frac{1}{2}}}{\Delta x_{i,j-\frac{1}{2}}} \frac{\left((S_w)^{n+1}_{i,j-1} - (S_w)^{n+1}_{i,j} \right)}{\Delta x_{i,j}} + \frac{D^n_{i,j+\frac{1}{2}}}{\Delta x_{i,j+\frac{1}{2}}} \frac{\left((S_w)^{n+1}_{i,j+1} - (S_w)^{n+1}_{i,j} \right)}{\Delta x_{i,j}} = -\phi_{i,j} \frac{\left((S_w)^{n+1}_{i,j} - (S_w)^{n}_{i,j} \right)}{\Delta t},$$

.....(2.4.23)

where following the discretization process the diffusion term is calculated, for example, at the face of the grid block as:

$$D_{i-\frac{1}{2},j} = \frac{(k_w)_{i-\frac{1}{2},j}}{\mu_w} \left(\frac{dP_c}{dS_w} \right)_{i-\frac{1}{2},j} . \quad \text{(2.4.24)}$$

The capillary pressure term is calculated as:

$$\left(\frac{dP_c}{dS_w} \right)_{i-\frac{1}{2},j} \approx \left(\frac{P_c(S_w + \Delta S) - P_c(S_w)}{\Delta S} \right)_{i-1,j} . \quad \text{(2.4.25)}$$

and the distance to one of the faces of the grid block with respect to center is given by:

$$\Delta x_{i-\frac{1}{2},j} = \Delta x_{i,j} - \Delta x_{i-1,j} . \quad \text{(2.4.26)}$$

In Eq. 2.4.24 the magnitude of the relative permeability is governed by the upstream value whereas the absolute permeability at the face is taken as the harmonic average of the two different absolute permeability values across the face. With the help of Eq. 2.4.23

a numerical code is generated, which is flexible enough to take into account various desired boundary conditions.

2.4.5 THEORETICAL BACKGROUND AND VERIFICATION TASKS

2.4.5.1 Handy's[2] Experiment of Spontaneous Imbibition

Eq. 2.4.22 has been used by many researchers such as Babadagli and Ershaghi[4] and Li and Horne[5] to describe spontaneous imbibition. One of the earliest attempts with air-water system was made by Handy,[2] who assumed that the capillary term varied linearly with distance. This is true as long as we assume a piston-type displacement of the non-wetting phase by the wetting phase and the potential, generated by the capillary forces, provides the driving force. With these assumptions, Eq. 2.4.22 for cylindrical cores reduces to the following form:

$$Q_w^2 = \left(\frac{2P_c k_w \phi A^2 S_w}{\mu_w} \right) t \,. \quad \text{..... (2.4.27)}$$

This is the equation of a line, and a plot of the square of the water imbibed versus time will pass through the origin.

We chose Handy's data to verify our numerical code. The reason for doing this is to prove that our simulator could exactly match that data as well as bring forth the limitation of the initial assumption that capillary pressure varies linearly with distance. This is true for early time, but the relationship breaks down as time progresses. If imbibition is allowed to prolong into late time, it levels off and stops. This is shown in Fig. 2.4.2, which shows the results of our numerical simulation run. We plotted one of the outputs of our simulator, a plot of capillary pressure versus distance, and as it is clear from Fig. 2.4.3, that the relationship is a not a linear one.

2.4.5.2 Spontaneous Imbibition Experiment of Unfractured Core

Garg *et al.*[3] solved Eq. 2.4.21 for one-dimensional saturation data measured with the help of CT. They set up a mechanism with which they could simultaneously measure the weight of the water imbibed and the water saturation with the help of the CT scanner. We

chose to compare the validity of our code with the help of two simultaneously varying data, the first being weight gain of the imbibed water expressed as a fraction of total water imbibed and the other being water saturation measured with the CT scanner. As is with all multiple parameters, a match with one does not necessarily guarantee a match with the other, and this leads to lot of iterative effort before both can be matched. Out of the two, the data collected for weight gain was a tricky one as buoyancy forces interfered because the match does not start from the origin. We started with a power expression for relative permeability and found that an exponent of n = 8.5, gave us a close match as can be seen in Fig. 2.4.4. Table 2.4.1 a shows summary of key parameters used in the simulation to match CT water saturation. Next we varied the different values of end-point relative permeability to arrive at an adequate match for saturation. We found that this value was more sensitive to saturation than the amount of water imbibed, which was almost the same in all cases of different exponents. Figs. 2.4.5 and 2.4.6 shows the effect of various values of saturation exponent and Figs. 2.4.7 and 2.4.8 gives shows the effect of various values of end-point relative permeability values. Hence:

$$k_{rw} = 0.045 S_w^{8.5}. \quad \text{(2.4.28)}$$

We used a variable capillary pressure curve as shown in Fig. 2.4.9 as input. Our sensitivity study on gridblock size and the time steps used in the simulation found that 15 gridblocks and time step of 2 seconds were enough to adequately run our model. The output from the code can track the saturation front in one dimension as shown in Fig. 2.4.10, where saturation for each grid block in a section are plotted. A difference in methodologies between our experimental study and experimental work conducted by Garg *et al.*[3] is that they used the following logarithmic capillary pressure relation:

$$P_c = P_c^o \ln S. \quad \text{(2.4.29)}$$

where P_c^o is the threshold capillary pressure and S is the normalized saturation. They have used a power expression for air/water relative permeability as given by:

$$k_{rw} = k_{rw}^o S^n, \qquad n \geq 1. \quad \text{(2.4.30)}$$

Again k_{rw}^o is the end point relative permeability, and they matched the experimental data with n = 2.5. We have gone further than this, and our code can

incorporate a variable capillary pressure data and a variable relative permeability data even though we have used a similar kind of relationship.

The departure from the experimental data initially in Figs. 2.4.6 and 2.4.8 is on account of high imbibition rate. The anomaly at the top of the core, we believe, is due to diffraction, which produces artifacts (areas of high CT numbers). The sides of the core were covered by epoxy and hence shielded from this effect.

Garg *et al.*[3] incorporated the effect of gravity, which we have neglected because of the small size of the core. We had to alter horizontal permeability as well, at normalized height of 0.6, to 80 md so as to match the experimental results at 360 seconds. Having matched the 1D data, we compared the 2D saturation front pictures with our simulator output. Here also we got an adequate match on a picture-by-picture basis, as shown in Fig. 2.4.11. To the left are the pictures appearing in Garg *et al.'s*[3] paper and to the right are our simulator results.

2.4.5.3 Spontaneous Imbibition Experiments with Fractured Core

We also carried out our own experiments with fractured Berea core. The aim was to again put to test the validity of the code and its faithful reproduction of the experiment. For the experiment we used Berea core, 1.5 in. in diameter and 2.5 in. in height with an average permeability of around 200 md. It was first dried for 24 hours and then put in a water bath at the beginning of the experiment. Great care was taken so that the constant level of water was maintained at the bottom. The experiment was conducted at room temperature and normal tap water was used in the water bath. As can be seen from Fig. 2.4.12, as soon as the experiment was started the clock reported the actual time of the experiment. It took close to half an hour for the imbibition saturation front to travel from bottom to top. Initially, CT images were taken at one-minute time intervals, but those were be increased near the end of the experiment, as shown in Fig. 2.4.12. The energy level used in the scanning process was 120 keV, which gave us the best resolution. The step-by-step match is shown in Fig. 2.4.13. The obvious point to be noticed here is that both Figs. 2.4.12 and 2.4.13 have the same number of time steps. Once again we used a variable capillary pressure curve and a variable relative permeability curve and obtained an adequate match.

2.4.6 CONCLUSIONS

Our aim in this paper was to start from basics and come up with a robust two-dimensional two-phase numerical model for spontaneous imbibition that could faithfully reproduce laboratory experiments. This model was rigorously verified by experimental data. With this model we have successfully accomplished the following three experimental objectives:

1. Validated the experimental data of Handy and proved the limitations of the most common assumption used to solve Eq. 2.4.22 analytically.
2. Matched the results of the Garg *et al.*[3] CT experiment, with two simultaneously varying parameters of weight gain and water saturation.
3. Reproduced accurately our own experiment of a fractured core.

With this numerical model, we will study capillary pressure and relative permeability during spontaneous imbibition on a more detailed basis for an oil/water system.

Nomenclature

I_0 = receptor reading without the object

μ = linear attenuation coefficient for the object

x = object thickness along the path of that ray

$N_{CT100\%Sat}$ = CT number of 100% saturated voxel

N_{CTDry} = CT number of dry voxel

$N_{CTWater}$ = CT number of water = 0.0

N_{CTAir} =CT number of air = -1000.0

N_{CTMat} = CT number of the matrix

ϕ = porosity of the matrix

S_{nw} = saturation of nonwetting phase

S_w = saturation of wetting phase

u_{nw} = velocity of nonwetting phase

u_w = velocity of wetting phase

μ_{nw} = viscosity of nonwetting phase

μ_w = viscosity of wetting phase

k = absolute permeability of rock

k_{rnw} = viscosity of nonwetting phase

k_{rw} = viscosity of wetting phase

p_{nw} = pressure of nonwetting phase

p_w = pressure of wetting phase

ρ_{nw} = density of nonwetting phase

ρ_w = density of wetting phase

g = acceleration due to gravity

α = angle, measured counter-clockwise, with the horizontal

P_c = capillary pressure

q_{nw} = flow rate of nonwetting phase

q_w = flow rate of wetting phase

A = area of control volume in Eqs. 2.4.9 and 2.4.10/ area of core in Eq. 2.4.27

x, y = linear dimensions along principal axes

i,j = grid block directions along principal axes

n = time step number

ΔS = change of saturation of wetting phase

REFERENCES

1. Huang, H.K., Elements of digital radiology: A professional handbook and guide, Prentice-Hall, New Jersey (1987).
2. Handy, L.L.: "Determination of Effective Capillary Pressures for Porous Media from Imbibition Data," Petroleum Transactions AIME, Vol. 219, 1960, 75-80.
3. Garg, A., Zwahlen, E. and Patzek, T.W.: "Experimental and Numerical Studies of One-Dimensional Imbibition in Berea Sandstone," paper presented at the 16th Annual American Geophysical Union Hydrology Days, Fort Collins, Colorado, 15-18 Apr, 1996.

4. Babadagli, T. and Ershaghi, I.: “Imbibition Assisted Two-Phase Flow in Natural Fractures,” paper SPE 24044 presented at the 1992 SPE Western Regional Meeting, Bakersfield, California, Mar 30-Apr 1.
5. Li, K. and Horne, R.N.: “Characterization of Spontaneous Water Imbibition into Gas-Saturated Rocks,” paper SPE 62552 presented at the 2000 SPE/AAPG Western Regional Meeting, Long Beach, California, 19-23 June.
6. Akin, S. and Kovscek, A.R.: “Imbibition Studies of Low-Permeability Porous Media,” paper SPE 54590 presented at the 1999 SPE Western Regional Meeting, Anchorage, Alaska, 26-27 May.
7. Reis, J.C. and Cil, M.: “A Model for Oil Expulsion by Counter-Current Water Imbibition into Gas-Saturated Matrix Blocks,” J. Pet. Sci. & Eng., **10**: 97-107.
8. Zhou, D., Kamath, J., and Kovscek, A. R.: “An Investigation of Counter-Current Imbibition Process in Diatomite,” Paper SPE 68837 presented at the 2001 SPE Western Regional Meeting, Bakersfield, California, 26-30 Mar.

Table 2.4.1 – Summary of Key Parameters

Parameters	Value
k	300 md
K_{rw}^{o}	0.045
P_{c}^{o}	2.5 psia
ϕ	0.22
n	8.5
S_{wi}	0.1

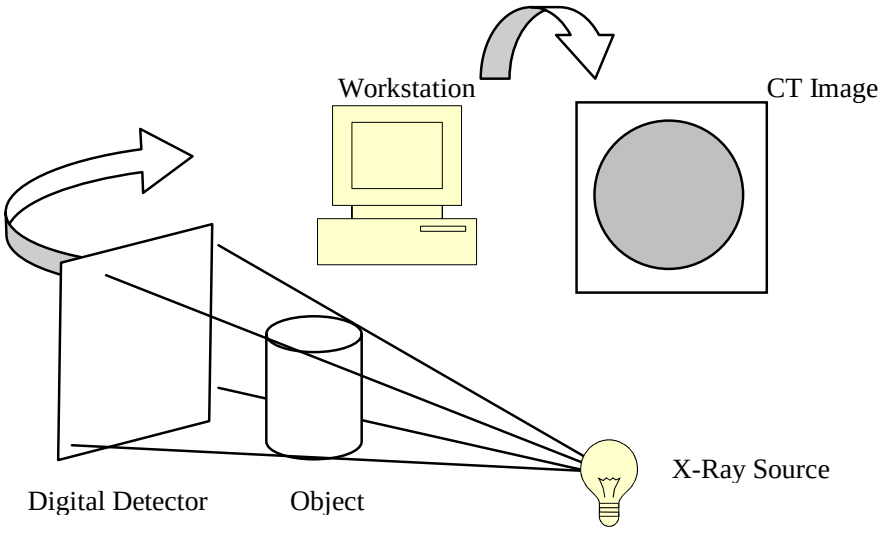

Fig. 2.4.1 – Conceptual representation X-Ray computerized tomography

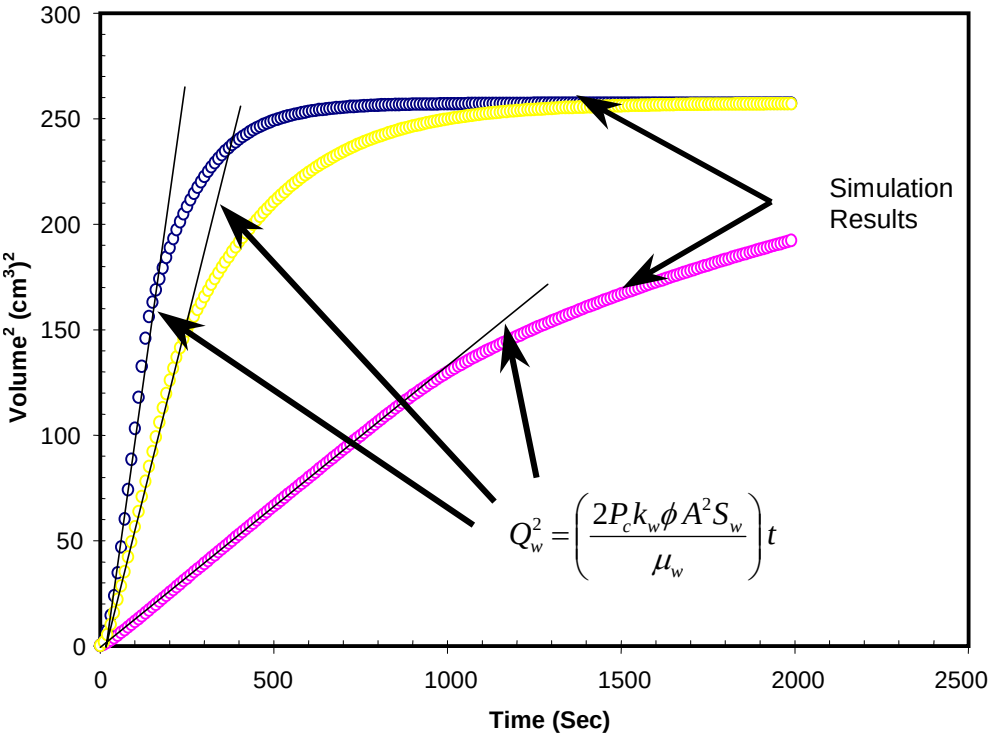

Fig. 2.4.2 – Comparison of Handy's data with numerical simulation

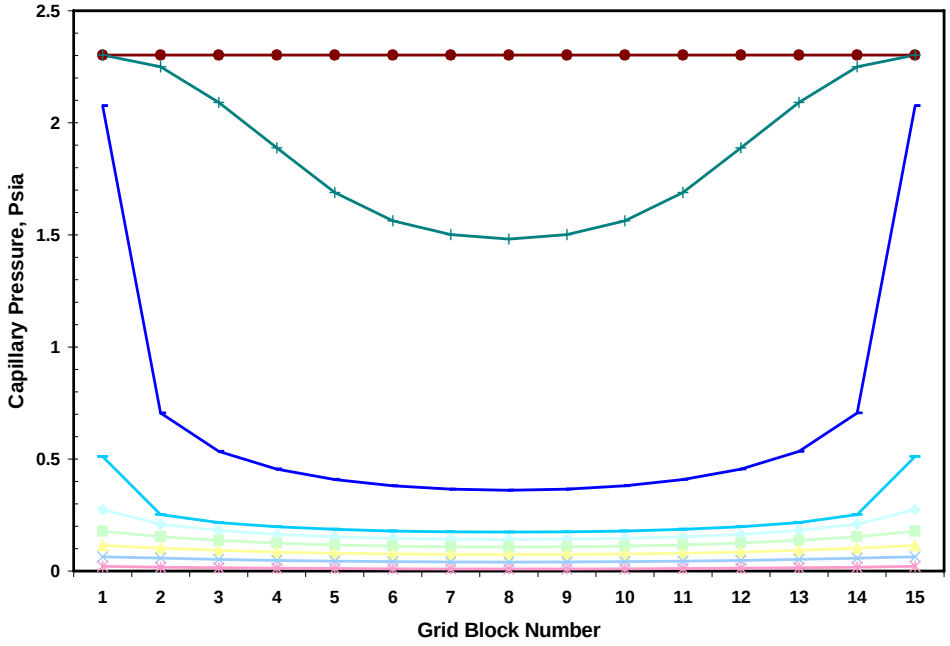

Fig. 2.4.3 – Capillary pressure shows a nonlinear relationship at different times

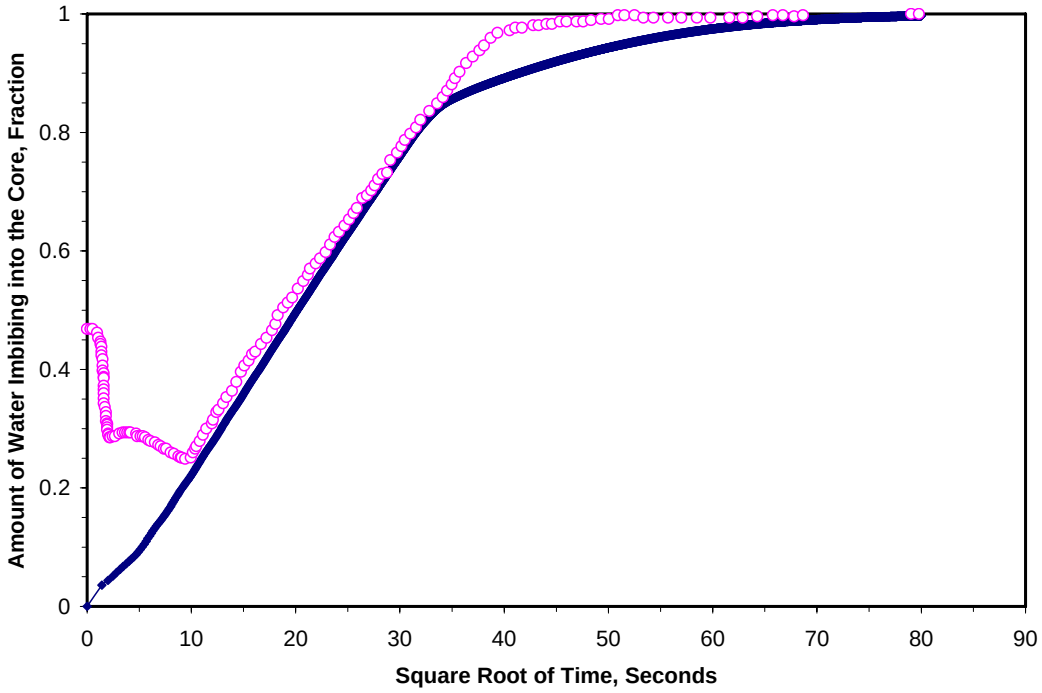

Fig. 2.4.4 – Weight-gain match between laboratory and simulation results

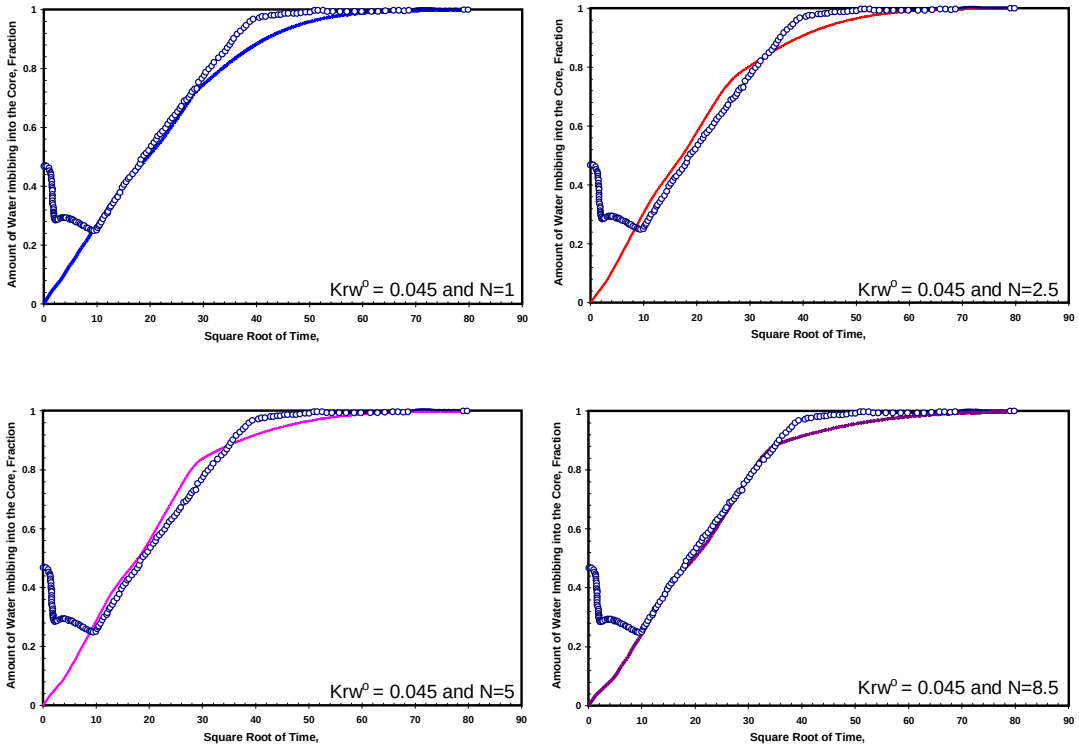

Fig. 2.4.5 – Effect of different saturation exponents on amount of water imbibing into the core

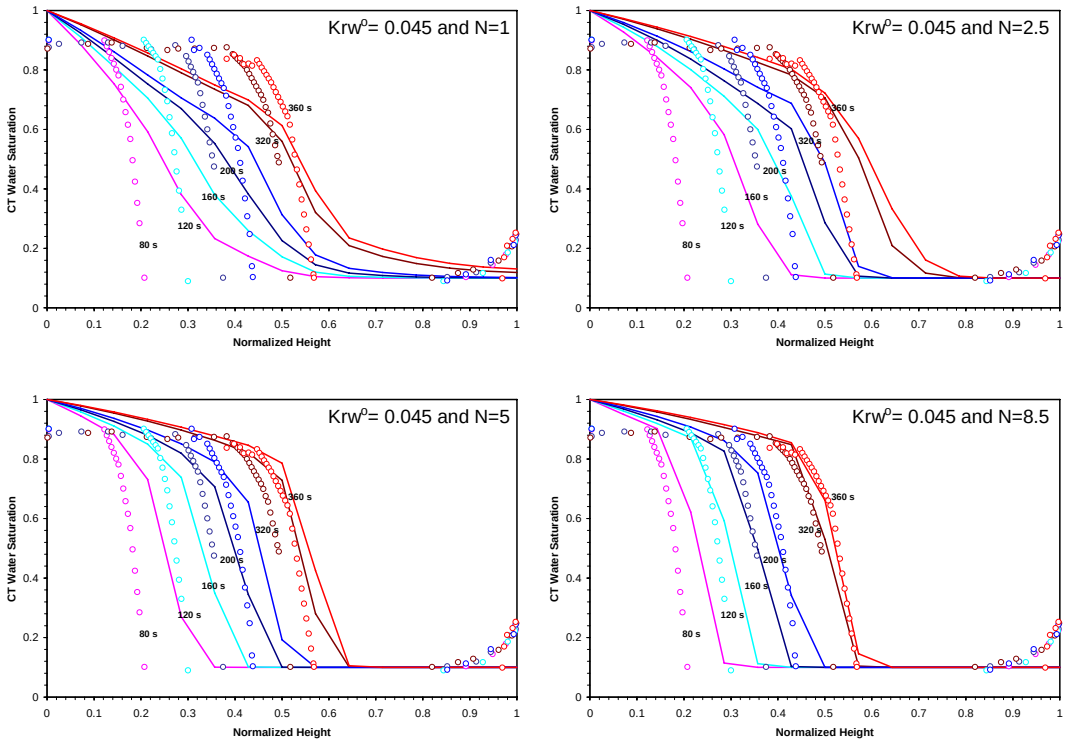

Fig. 2.4.6 – Effect of different saturation exponents on water saturation distribution

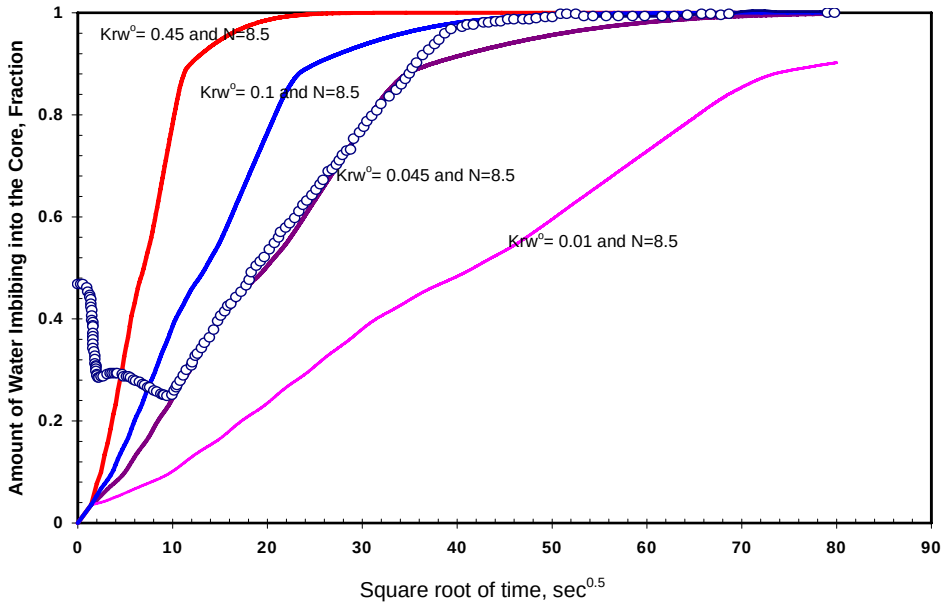

Fig. 2.4.7 – Effect of different initial water relative permeability on amount of water imbibing into the core

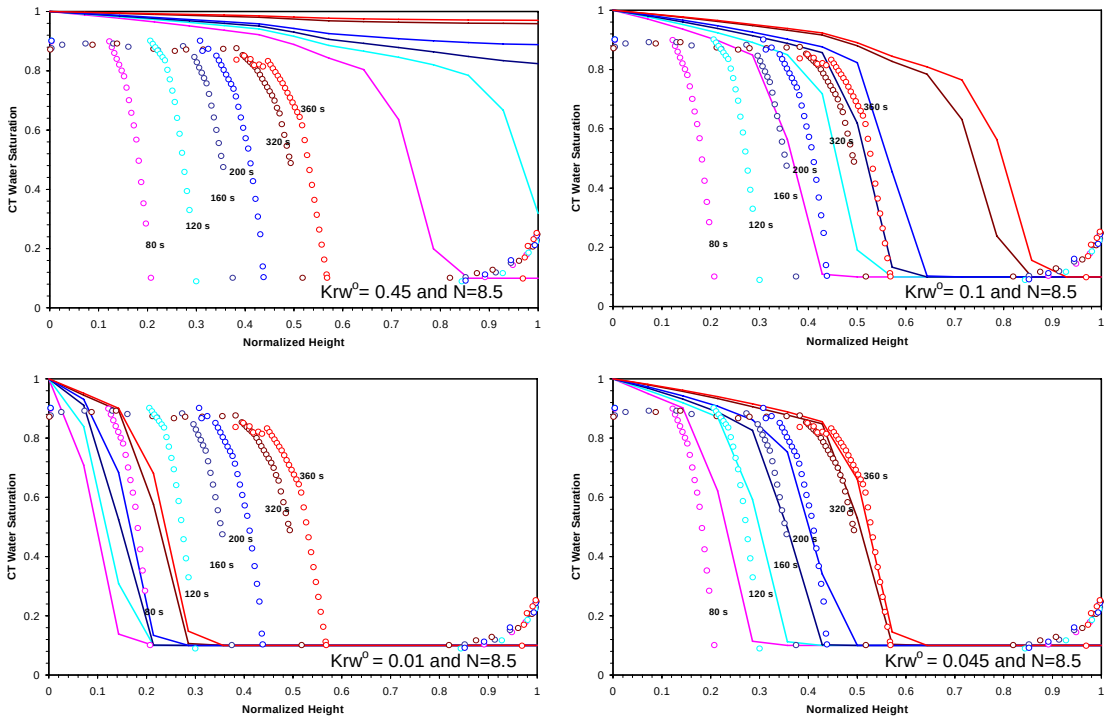

Fig. 2.4.8 – Effect of different initial water relative permeability on water saturation distribution

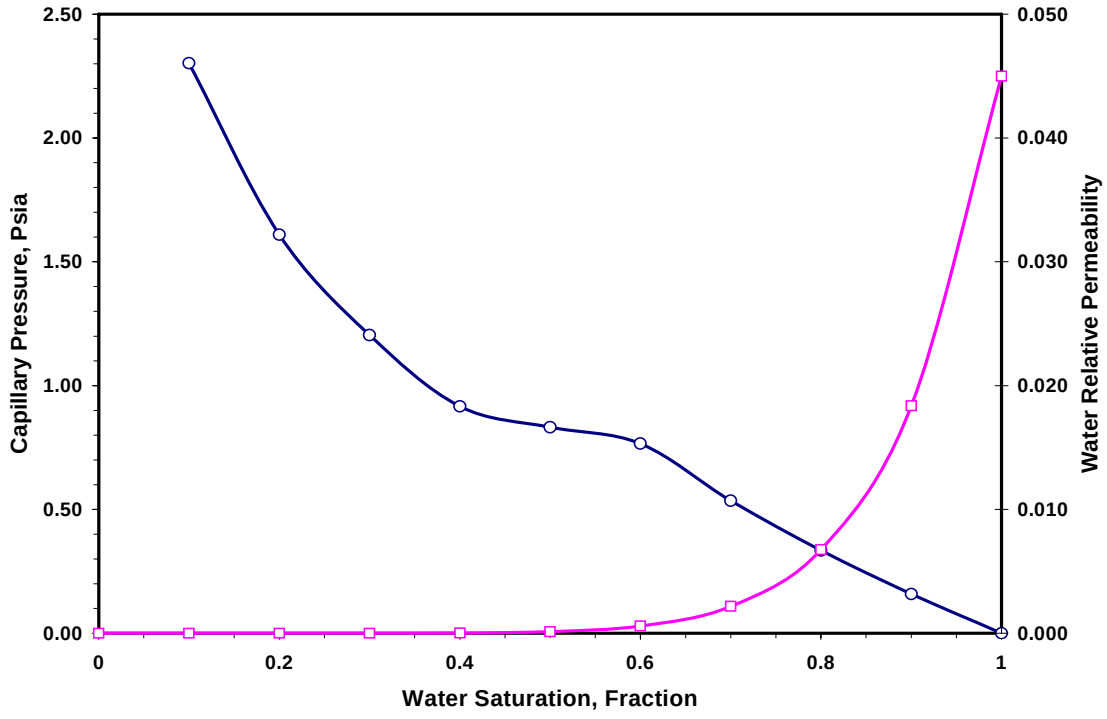

Fig. 2.4.9 – Final capillary pressure and relative permeability data used in simulation model

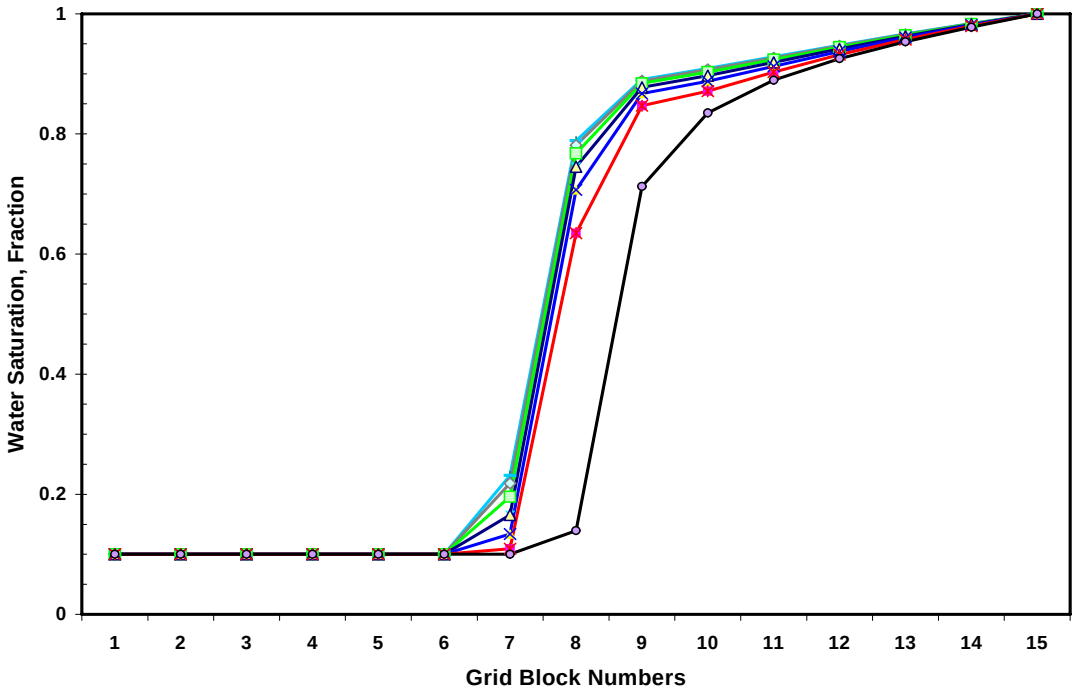

Fig. 2.4.10 – Water saturation distribution versus distance (front is moving from left to right)

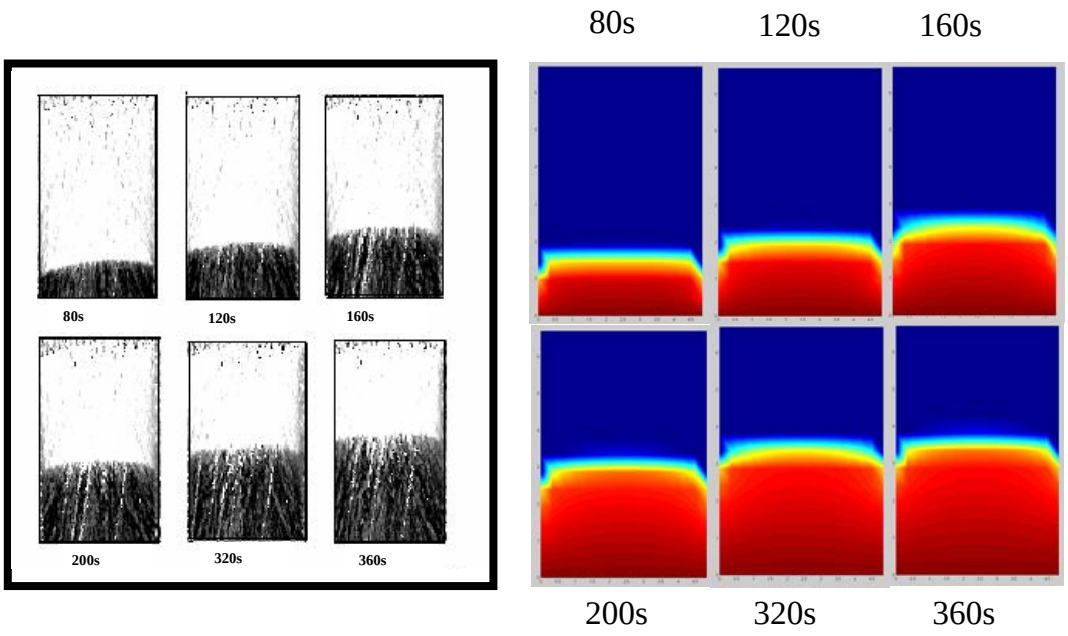

Fig. 2.4.11 – 2D comparison of water saturation front movement between CT scan and simulation results

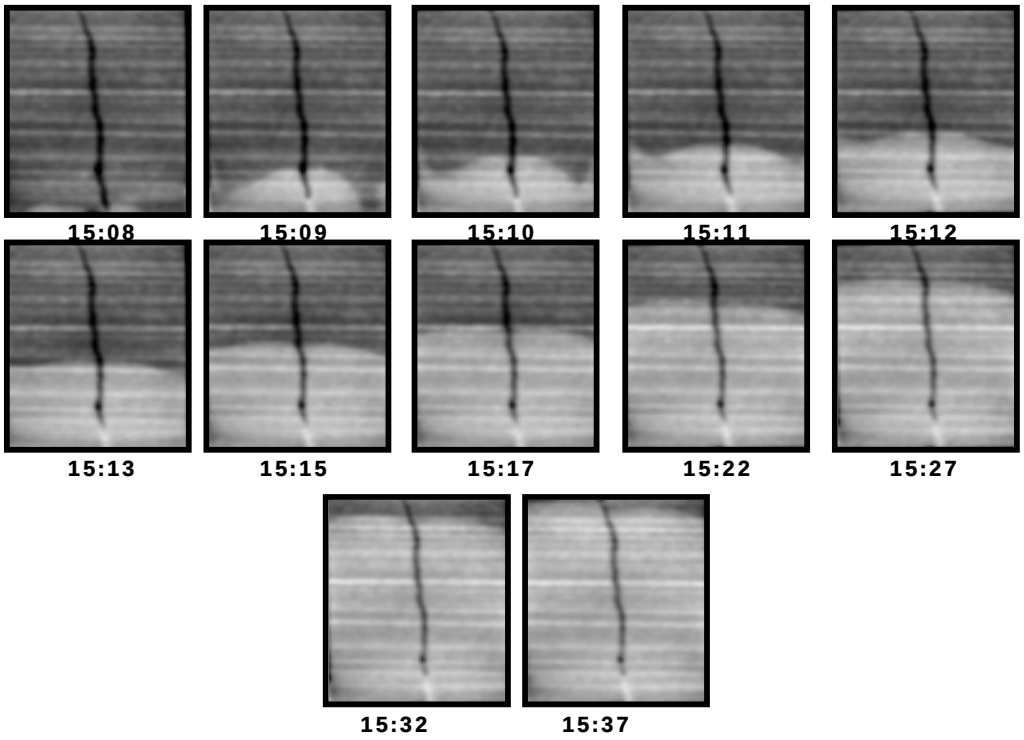

Fig. 2.4.12 –Water saturation front movement in fractured core from CT scan

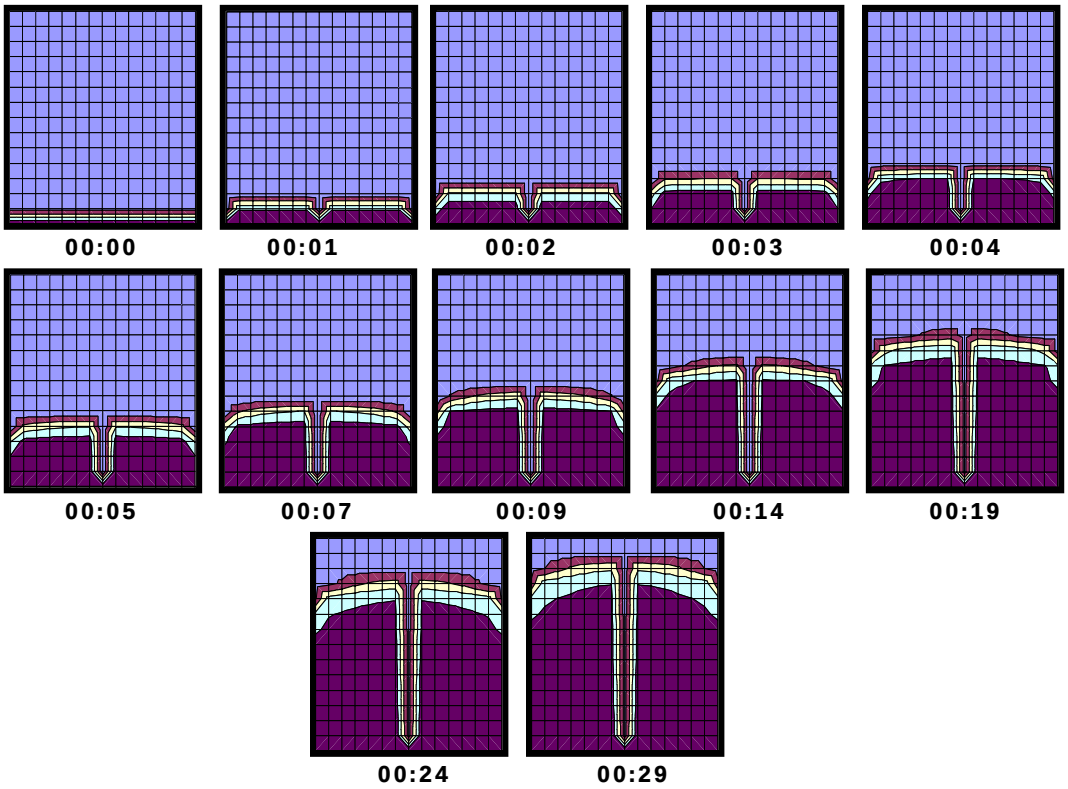

Fig. 2.4.13 – Water saturation front movement in fractured core from 2D simulation result

Chapter II-5
Simulation of Naturally Fractured Reservoirs Using Empirically Derived Transfer Function

2.5.1 INTRODUCTION

Proper simulation and modeling of naturally fractured reservoirs is a challenging issue in reservoir engineering.[1-3] Fractures play an important role in fluid distribution and flow in a naturally fractured reservoir. Hence proper characterization is of great significance to the validity of simulation results. Two divergent approaches are available for the proper simulation of naturally fractured reservoirs, single-continuum methods and dual-continuum methods.

Single-continuum methods treat the matrix and fracture as one. Grid blocks are assigned high permeability and low porosity values, to represent fractures. Although this method yields accurate results, it is usually very slow and taxes both computational speed and memory.

Dual-continuum methods decouple the pore space into fractures and matrix. Dual-porosity methods, probably synonymous with dual-continuum methods, were first introduced by Warren and Root[4] and result in simplified computational techniques. Dual-porosity models assume that the fracture medium is the main flow path and the matrix provides fluid storage only. Fluid flow and exchange between fracture and matrix medium are coupled by a factor called the transfer function, which physically represents the flow of fluids from the matrix to the fracture.

Dual-Continuum methods, to date, use statistics and history matching to estimate the value of the shape factor. This shape factor is essentially the coupling factor between the matrix and fracture[5] and is the key for transfer between fracture and matrix. The equations for the single- and dual-continuum methods are provided in the next section.

Lab imbibition experiments provide an estimate of the relative permeability and capillary pressures necessary to model performance in naturally fractured reservoirs.[6, 7] In these experiments the core can be idealized as matrix and the adjoining wetting phase as the fracture. The rate of change of water saturation in the core gives us an estimate of the

rate of change of matrix saturation when surrounded by a fracture filled with wetting phase. This, in essence, is the rate of transfer of fluids from matrix to the fracture. Imbibition experiments using CT scans provide us with the saturation of the nonwetting phase within the core. In addition to the recovery, the saturation vs. time also needs to be matched to establish an accurate transfer function. Our laboratory experiments on recovery of the nonwetting phase demonstrate the efficacy of using the transfer function term in the dual-porosity simulation.

2.5.2 LITERATURE REVIEW AND PRESENT STATUS

With increasing deepwater exploration, more fractured, vugular, and heterogeneous reservoirs are being explored and developed. This has increased the interest the petroleum industry towards more fractured reservoir modeling. With the advent of faster computers with large amounts of memory storage, the industry is now able to model complex reservoirs faster and with increasing accuracy. This section reviews commonly used approaches for naturally fractured reservoir modeling and interporosity flow estimation. Fluid flow in naturally fractured reservoirs can be broadly classified into the following models[6-9]:

1. Discrete fracture network models.
2. Hybrid models.
3. Equivalent continuum models.

Discrete networks consist of modeling a population of fractures. Equivalent continuum methods model reservoirs by assigning equivalent rock and fluid parameters to large rock masses. Hybrid models are a combination of both discrete fracture networks and equivalent continuum methods. The selection of any particular model depends not only on the reservoir and the type of fluid flow behavior to be numerically simulated, but also on the amount of computer memory and processor power available for the project. In general, the equivalent continuum modeling approach is the favored approach to model naturally fractured reservoirs because of the ease of computation. Whenever large models with accurate data need to be solved with a high degree of accuracy, the other two models may be applied. The equivalent continuum method is sufficient to model reservoir rocks

that have undergone multiple and extensive deformations (high fracture density) and/or any formations where matrix permeabilities are large enough that fluid flow is not influenced by any individual fracture or series of fractures that form a conducting channel[10]. Because of the focus to this study, the most important equivalent continuum models – single-porosity and dual-porosity models – are briefly reviewed.

Single-Porosity Modeling. Single-porosity modeling is the common method of modeling nonfractured reservoirs. This model does not differentiate between the matrix and the fracture continua, and the equivalent rock and fluid properties are assigned to both the continuum. Agarwal *et al.*[11] used the single-continuum method to model a carbonate reservoir with large number of fractures in the North Sea. Since this methodology doesn't differentiate any part of the continuum, it can be safely said to be the most accurate modeling method. But its accuracy is dependent on the number of grid blocks used. Most of the single-porosity modeling of naturally fractured reservoirs is done with a large number of grid blocks for greater accuracy, and thus can lead to large computational times.

To circumvent this problem, Agarwal *et al.*[11] used pseudorelative-permeability functions. In developing these pseudorelative-permeability curves, they use dual-porosity simulation on a stack of matrix blocks and then matched the relative permeabilities developed were matched with fine grid simulation. This method deserves special consideration because of its ease of computation. The problem with the method was that new sets of dynamic pseudofunctions had to be calculated for changes in operating conditions.

Dual-Porosity Modeling. Dual-porosity simulation is the mathematical modeling of fluid flow in reservoirs with significant secondary porosity. The fluid flow model requires spatial definition of the secondary porosity. Since this process is inherently complex and cannot be easily quantified, Barenblatt *et al*[12] proposed an idealization that consisted of dividing the porous media into two superimposed media, a continuous system of fractures (secondary porosity) and a discontinuous matrix (primary porosity) system. The fracture system is further assumed to have negligible storage capacity, but to be the primary flow path. Meanwhile the matrix (primary porosity) is assumed to be the storage medium of the system but has negligible flow capacity. This idealization was

introduced by Warren and Root,[4] who presented an analytical solution for single-phase radial flow in a reservoir with significant contribution of the secondary porosity towards flow. The idealization made the following assumptions:

- The primary porosity is isotropic and is contained in a symmetric array of identical parallelepipeds.
- All the secondary porosity is contained in a set of orthogonal fractures, which are oriented in a direction parallel to the axis of permeability.
- Flow can occur in the secondary porosity and from the primary porosity to the secondary porosity, but not within the primary porosity.

The idealization can be visualized in Fig. 2.5.1. Both the primary and fracture porosity are not consistent in orientation or continuity in Fig. 2.5.1a. The actual reservoir is idealized as shown in Fig. 2.5.1b. The idealized reservoir can be viewed as a series of primary porosities contained in the parallelepipeds, which are disconnected from each other, by a series of continuous secondary porosities.

Other idealizations include parallel horizontal fracture[13] and matchstick column models.[4] Multiporosity models are a special case of dual porosity models, which assume that the fracture set interacts with two groups of matrix blocks with distinct permeabilities and porosities.[14]

2.5.3 TRANSFER FUNCTION

The primary and secondary porosities are coupled by a factor called the transfer function or the interporosity flow. Physically this can be defined as the rate of fluid flow between the primary and the secondary porosities. Since the secondary porosity is the only fluid path and fluid storage is negligible, the dual-porosity simulation method can be imagined as a system of secondary porosity with the primary porosity as the major source for the fluid. The transfer function can be regarded as the “heart” of a dual-porosity simulation. The transfer function is the parameter that is changed to effect the transition from the actual reservoir as shown in Fig. 2.5.1a to the ideal reservoir as shown in Fig. 2.5.1b**.** Transfer functions can be broadly classified into four types

1. Empirical transfer functions.
2. Scaling transfer functions.

3. Diffusivity transfer functions.
4. Transfer functions that use Darcy's law.

2.5.3.1 EMPIRICAL TRANSFER FUNCTIONS

Empirical models assume the transfer or interporosity flow can be attributed to the imbibition phenomenon during water injection. They assume a function is used to describe the time rate of exchange of oil and water for a single matrix block when surrounded by fractures with high water saturation. Empirical transfer functions usually consist of two parts:

1. A curve-fitting expression to describe recovery as a function of time.
2. A scaling equation to express the time in terms of rock and fluid properties.

The first empirical oil recovery function was given by Aronofsky.[15] He showed that the rate of transfer of fluids from the matrix can be approximated by an exponential decline function as shown:

$$R = R_{\infty}(1-e^{-\lambda t}). \quad \text{..... (2.5.1)}$$

De Swaan[16] used that relation to derive an analytical expression for the water/oil ratio and the cumulative oil production from a linear reservoir during water injection. His theory also accounts for the fact that in a fractured reservoir exploited by waterflooding, the matrix blocks downstream from the waterfront are subject to varying degrees of saturation within the fractures because of water imbibition of the matrix blocks upstream. His theory modifies the well-known Buckley-Leverett formulation by addition of a term for the interporosity flow or the transfer function.

$$-\frac{\partial q}{\partial x} = h\phi\frac{\partial S_w}{\partial t} + \frac{N_{ma}}{\tau_1}\int_o^t e^{-(t-\theta)/\tau 1}\frac{\partial S_w}{\partial \theta}d\theta. \quad \text{.....(2.5.2)}$$

Also assuming that the fractional flow coefficient is the same as the mobile water saturation, de Swaan derived an analytical solution for the equation. The analytical solution contains an integro-differential term to account for the interporosity flow:

$$S_w = \begin{cases} 0, t < t_{Lf} \\ 1-e^{-t/\tau}\int e^{-y} I_o(2\sqrt{ty/\tau})dy, t > t_{LF} \end{cases}. \quad \text{.....(2.5.3)}$$

Kazemi *et al.*[17] solved the analytical expression derived by deSwaan by using explicit finite difference and the trapezoidal rule. Reis and Cil[27] proposed a new relation for the transfer function

$$R = R_{\infty}(1-e^{-0.69(\lambda t)^n}) . \quad \text{.....(2.5.4)}$$

Civan[19] extended the Arfonsky relation by addition of an exponential term as shown in Eq. 2.5.5:

$$R = R_{\infty}(1-e^{-\lambda t_1}-e^{-\lambda_2 t}) . \quad \text{.....(2.5.5)}$$

The second exponential term was justified by the fact that the collection of oil droplets in the fracture consists of two different, irreversible processes, namely:

1. Expulsion of oil droplets from the matrix into the fracture.
2. Entraining of the oil droplets in the fracture by the fluid present in the fracture.

Eq. 2.5.5 was used in the Buckley-Leverett equation, similar to de Swaan, and a numerical solution was developed. This numerical solution used the quadrature solution. Civan[28] showed that the quadrature solutions are easier to compute than the finite difference solutions for the case of end-point mobilities. Gupta and Civan [20] proposed an additional term to the Eq. 2.5.5 as shown below:

$$R = R_{\infty}(1-e^{-\lambda t_1}-e^{-\lambda_2 t}-e^{-\lambda_3 t}) . \quad \text{.....(2.5.6)}$$

The third term was added to include the “dead-end” pores of the matrix but the results obtained did not justify the need for the inclusion of this third term.[21] These empirical methods suffer from the following fallacies:

1. This methods are limited to waterflooded reservoirs.
2. The role of capillary pressure in oil recovery is neglected.
3. Gravity is neglected.
4. The methods are limited to only two phases.

2.5.3.2 SCALING TRANSFER FUNCTIONS

Scaling transfer functions are used to predict recovery in field-size cases, together with the results from lab experiments. Rapoport[22] proposed the “scaling laws” applicable in the case of water/oil flow. Using these laws, Mattax and Kyte[23] presented the

dimensionless time to scale up laboratory data to field size cases. The dimensionless time is given as:

$$t_D = t\sqrt{k/\phi}\left(\frac{\sigma}{\mu_w L^2{}_c}\right). \quad \text{.....(2.5.7)}$$

Du Prey[24] performed centrifuge imbibition experiments on cores to account for gravity effects on imbibition. He showed that the dimensionless time defined by the previous Eq. 2.5.7 couldn't be used to model the experiments. He also showed that the dimensionless equation couldn't be used for matrix blocks of different sizes. He defined three more dimensionless parameters

- Dimensionless shape factor.
- Dimensionless mobility.
- Capillary/gravity ratio.

The dimensionless time was defined for two low-capillary gravity ratios and for a high capillary/gravity ratio. His definitions are as follows:

$$t_c = \frac{H^2 \phi \Delta S \mu_o}{P_{ct} k_{o\max}} \quad . \quad \text{.....(2.5.8)}$$
$$t_g = \frac{H\ \phi \Delta S \mu_o}{\Delta \rho g k_{o\max}}$$

where t_c is the dimensionless time factor for high capillary/gravity ratio and t_g is the dimensionless time factor for low capillary/gravity ratio.

Ma *et al.*[25] studied the relationship between water wetness and the oil recovery from imbibition. The characteristic length to scale up time was also defined for various cases. The authors also defined "effective viscosity" to remove the issue of comparable viscosities between the lab and field cases.

$$t_D = t\sqrt{\frac{k}{\phi}}\frac{\sigma}{\mu_g}\frac{1}{L_c^2}. \quad \text{.....(2.5.9)}$$

where

$$\mu_g = \sqrt{\mu_w \mu_{nw}} \ . \quad \text{.....(2.5.10)}$$

Although the scaling transfer functions are the best representations of transfer functions, the following are the requirements for the correct formulation of scaling transfer functions:

1. The shapes of the matrix blocks for the field and lab cases must be the same.
2. The fluid mobilites must be comparable.
3. The initial and boundary conditions for both the lab and field cases must be the same.
4. The capillary pressures must be directly proportional.

Because of these inherent assumptions, scaling transfer functions are not widely used.

2.5.3.3 TRANSFER FUNCTION USING DARCY LAW

Transfer functions that use Darcy's law assume that the transfer of fluids from the matrix to the fracture can be adequately be described with an appropriate geometric factor that accounts for the characteristic length and the flow area between the matrix and the fracture.

The first model is analgous to a model used for heat transfer in a heterogeneous medium. Barenblatt *et al.*[12] assumed that the outflow of fluids from matrix blocks into the fractures is steady-state and that the fluid transfer rate is a function of the viscosity of the fluid, the pressure drop between the matrix and fracture systems, and matrix-rock properties related to geometry and interconnectivity of the fractures and matrix. Their fluid transfer rate per unit volume of rock is:

$$q = \frac{\sigma K_m}{\mu}(p_m - p_f) \ . \quad \text{.....(2.5.11)}$$

where σ is a shape factor related to the specific surface of the fractures, p_m and p_f are the average pressures in the matrix and fracture domains, respectively, and q is the fluid transfer rate between the matrix and fracture. Although this transfer function is the most popular, there is hardly any agreement among various researchers regarding the shape factor. Table 2.5.1 is a modified version of the Bourbiaux table[26] as reported by Penula-Pineda.[27]

Although the transfer functions of this family are the most popular, they suffer from the following problems

1. They assume a linear gradient of pressures between the matrix and the fracture centers.
2. They also assume that the whole storage is present in the matrix blocks only.
3. They lack a lab oratory background that the other methods enjoy.
4. They assume that all the matrix blocks exist at the same saturation.
5. Recovery from *n* number of matrix blocks is equal to *n* times the recovery from a single matrix block.
6. They assumed linear relative permeability in the fracture media.

2.5.3.4 DIFFUSIVITY TRANSFER FUNCTIONS

These transfer functions assume that the interporosity flow can be approximated by "diffusion" phenomenon. These functions are based on incompressible flow and assume that diffusivity equation[28] is sufficient to model the interporosity flow between the matrix and the fractured media. Hernandez and Rosales[29] proposed the first diffusivity transfer function. They developed an analytical equation for the oil production from waterflooded reservoirs which they verified from imbibition experiments on Berea cores.

$$N_{pn} = 1 - \frac{8}{\pi^2} \sum_{n=0}^{\alpha} \frac{1}{(2n+1)^2} \exp[-(2n+1)^2 t_D] \,. \quad \text{.....(2.5.12)}$$

Hayashi and Rosales[30] developed a technique for making visual observations of water imbibition processes in porous media saturated with oil. They found that spontaneous penetration of water by imbibition was similar to the diffusion phenomenon. Also based on experimental results, they proposed a theoretical model for explaining imbibition processes:

$$N_{pn} = 1 - [\frac{8}{\pi^2} \sum_{n=0}^{\alpha} \frac{1}{(2n+1)^2} \exp[-\frac{D(2n+1)^2 \pi^2 t}{L^2} \ ]^2 \,. \quad \text{.....(2.5.13)}$$

D is a coefficient to be estimated by trial and error.

2.5.3.5 COMPARISON OF THE TRANSFER FUNCTIONS.

Reis and Cil[18] compared the various transfer functions on several imbibition experiments with different boundary conditions and found the following:

1. The match between the diffusivity models and the experimental data were good except at early times.
2. The scaling function matched the experiments within experimental errors.
3. The empirical function had a good agreement with the experimental values.

For single-phase interporosity flow, Najurieta[31] showed that de Swaan's analytical model results were equivalent to numerical solutions provided by Kazemi, which accounted for pressure-transient effects by assuming non steady-state flow at the matrix/fracture interface.

Our procedure developed is intended for implementation in existing simulators without significantly increasing computational work yet representing pressure transient and saturation gradient effects on the interporosity flow as accurately as possible.

2.5.3.6 FLOW VISUALIZATION USING X-RAY TOMOGRAPHY

CT scanning is a nondestructive technique that uses X-rays and mathematical reconstruction algorithms to generate a cross-sectional slice of an object.[32]

A detailed explanation of the principles and application of CT can be found in the literature.[33]

2.5.4 METHODOLOGY - PROCEDURE OF STUDY

2.5.4.1 SIMULATOR TO MODEL THE IMBIBITION EXPERIMENTS

Imbibition or transfer of fluids can be treated as a diffusion phenomenon. Thus, by discretizing the diffusion equation (as shown below), a simulator can be developed to match the recovery of the nonwetting phase with time and the spatial variation of saturation.

$$D(S_w) = -\left(\frac{k}{\phi}\frac{\lambda_w\lambda_o}{\lambda_w+\lambda_o}\right)\frac{dP_c}{dS_w} \qquad \frac{\partial}{\partial t}\left(\frac{\phi S_w}{B_w}\right) + \nabla\left(\frac{kk_{rw}}{\mu_w B_w}\nabla P_c\right) = 0$$

Conventionally, only the ultimate recovery versus time is matched to obtain the relative permeability and capillary pressure information.[15] However, with the advent of

the CT Scanner, saturations can be quantified, as a function of time and space. Matching not only the recovery but also the saturations can lead to identification of heterogeneity in the core, and thus can be effective in modeling of vugs and microfractures.[16, 17]

2.5.4.2 DUAL POROSITY SIMULATOR

We developed a dual-porosity simulator that uses the recovery of the nonwetting phase with time data as the transfer function. The derivation of the flow equations are as given below.

2.5.4.2.1 FRACTURE FLOW EQUATIONS

Stating Darcy's law for multiphase flow in porous media, we have:

$$\vec{u}_w = -\frac{k\,k_{rw}}{\mu_w}\nabla\Phi_w = -\frac{k\,k_{rw}}{\mu_w}\nabla(p_w + \rho_w gh) \quad . \quad \text{.....(2.5.14)}$$

$$\vec{u}_o = -\frac{k\,k_{ro}}{\mu_o}\nabla\Phi_o = -\frac{k\,k_{ro}}{\mu_o}\nabla(p_o + \rho_o gh) \quad . \quad \text{.....(2.5.15)}$$

Since the primary flow path in a dual-porosity formations is through the fracture, we have Darcy's law as follows:

$$\vec{u}_{wf} = -\frac{k_f k_{rwf}}{B_{wf}\mu_{wf}}\nabla(p_{wf} + \rho_w gh). \quad \text{.....(2.5.16)}$$

$$\vec{u}_{of} = -\frac{k_f k_{rof}}{B_{of}\mu_{of}}\nabla(p_{of} + \rho_o gh). \quad \text{.....(2.5.17)}$$

From the definition of capillary pressure, the water-phase pressure can be expressed in terms of oil-phase pressure as:

$$P_c = p_o - p_w = P_c(S_w)\,;\; p_w = p_o - P_c. \quad \text{.....(2.5.18)}$$

Thus, Eq. 2.5.14 can be rewritten as:

$$\vec{u}_{wf} = -\frac{k_f k_{rwf}}{B_{wf}\mu_{wf}}\nabla(p_{of} - P_{cf} + \rho_w gh). \quad \text{.....(2.5.19)}$$

Consider a control volume (secondary porosity) of dimensions Δx, Δy as shown in Fig. 2.5.2. For the sake of brevity, the subscript *f* is dropped in the derivation of the conservation of mass.

From conservation of mass principle, we have that:

[Rate of change of mass in Control Volume = Rate of Net Influx]

Consider the control volume in Fig. 2.5.2. For the water phase we have:

Rate of change of mass of water in the *x* direction:

$$\rho_w \vec{u}_{wx} \Delta y - (\rho_w \vec{u}_{wx} + \frac{\partial}{\partial x}(\rho_w \vec{u}_{wx})\Delta x)\Delta y$$

Similarly, for the *y* direction:

$$\rho_w \vec{u}_{wy} \Delta x - (\rho_w \vec{u}_{wy} + \frac{\partial}{\partial x}(\rho_w \vec{u}_{wy})\Delta y)\Delta x$$

Rate of accumulation of water:

$$\frac{\partial}{\partial t}(\phi S_w \rho_w \Delta x \Delta y) + \tau$$

where τ is the rate of flow of water from the matrix to the fracture, since the primary porosity also contributes to the accumulation of water in the fractures.

Thus the conservation of mass can be written in the following form:

$$\frac{\partial}{\partial t}(\phi S_w \rho_w \Delta x \Delta y) + \tau = (\rho_w \vec{u}_{wy} \Delta x - (\rho_w \vec{u}_{wy} + \frac{\partial}{\partial x}(\rho_w \vec{u}_{wy})\Delta y)\Delta x) + (\rho_w \vec{u}_{wx} \Delta y - (\rho_w \vec{u}_{wx} + \frac{\partial}{\partial x}(\rho_w \vec{u}_{wx})\Delta x)\Delta y) \quad . \quad \text{.....(2.5.20)}$$

Simplifying Eq. 2.5.20 similar to the conservation of mass as described in the earlier section, we have,

$$\phi \frac{\partial}{\partial t}(S_w) + \tau_w = \nabla.(\vec{u}_w) \, . \quad \text{.....(2.5.21)}$$

Similarly, for oil phase we have:

$$\phi \frac{\partial}{\partial t}(S_o) + \tau_o = \nabla.(\vec{u}_o)\,. \quad \text{.....(2.5.22)}$$

Substituting Eqs. 2.5.17 and 2.5.18 in Eqs. 2.5.21 and 2.5.22, we have that:

$$\phi \frac{\partial}{\partial t}(S_{wf}) + \tau_w = \nabla.(-\frac{k_f k_{rwf}}{B_{wf}\mu_{wf}}\nabla(p_{of} - P_{cf} + \rho_w gh))\,. \quad \text{.....(2.5.23)}$$

$$\phi \frac{\partial}{\partial t}(S_{of}) + \tau_o = \nabla.(-\frac{k_f k_{rof}}{B_{of}\mu_{of}}\nabla(p_{of} + \rho_o gh))$$

We know that the sum of the saturations is unity. Hence:

$$S_o + S_w = 1; S_o = 1 - S_w; \frac{\partial S_o}{\partial t} = -\frac{\partial S_w}{\partial t}\,. \quad \text{.....(2.5.24)}$$

Simplifying Eq. 2.5.23 and using 2.5.24 in 2.5.23, we have that:

$$-\phi \frac{\partial}{\partial t}(S_{wf}) + \tau_o = \nabla.(-\frac{k_f k_{rof}}{B_{of}\mu_{of}}\nabla(p_{of} + \rho_o gh))\,. \quad \text{.....(2.5.25)}$$

$$\phi \frac{\partial}{\partial t}(S_{wf}) + \tau_w = \nabla.(-\frac{k_f k_{rwf}}{B_{wf}\mu_{wf}}\nabla(p_{of} - P_{cf} + \rho_w gh))\,. \quad \text{.....(2.5.26)}$$

Multiplying both sides of the equation by the bulk volume we have:

$$V_p \frac{\partial}{\partial t}(S_{wf}) - V_b\tau_o = \nabla.(a_o\nabla(p_{of} + \rho_o gh))\,. \quad \text{.....(2.5.27)}$$

$$-V_p \frac{\partial}{\partial t}(S_{wf}) - V_b\tau_w = \nabla.(a_w\nabla(p_{of} - P_{cf} + \rho_w gh)) \quad \text{.....(2.5.28)}$$

Where *a* is the symmetric coefficient defined as:

$$a_w = \frac{k_f k_{rwf}}{B_{wf}\mu_{wf}} V_b$$

These equations don't consider source and sink terms such as injection wells and production wells. To include wells into Eqs. 2.5.27 and 2.5.28 the flow rate is added to the right-hand side with the convention of positive for production and negative for an injector. Therefore, Eqs. 2.5.27 and 2.5.28 can be rewritten as:

$$V_p \frac{\partial}{\partial t}(S_{wf}) - V_b \tau_o - q_o = \nabla.(a_o \nabla(p_{of} + \rho_o gh)) . \quad \text{.....(2.5.29)}$$

$$-V_p \frac{\partial}{\partial t}(S_{wf}) - V_b \tau_w - q_w = \nabla.(a_w \nabla(p_{of} - P_{cf} + \rho_w gh)) . \quad \text{.....(2.5.30)}$$

2.5.4.2.2 MATRIX FLOW EQUATIONS

Consider a matrix control volume similar to Fig. 2.5.2. The rate of inflow into the matrix is zero as there is no flow into the matrix; including the rate of outflow from the matrix into the transfer function, the conservation of mass can be written as:

$$0 - \tau = \frac{\partial}{\partial t}(\phi S) . \quad \text{.....(2.5.31)}$$

$$-\tau_w = \frac{\partial}{\partial t}(\phi S)_{wma} . \quad \text{.....(2.5.32)}$$

$$-\tau_o = \frac{\partial}{\partial t}(\phi S)_{oma} . \quad \text{.....(2.5.33)}$$

2.5.4.2.3 EMPIRICAL TRANSFER FUNCTION

The empirical equations are derived from the imbibition experiments that are conducted on the matrix core. To scale the time from the imbibition experiments to the field size, Mattax and Kyte[32] proposed the following transformation:

$$\left(t \frac{\sigma}{\mu_w L^2} \sqrt{\frac{k}{\phi}} \right)_{model} = \left(t \frac{\sigma}{\mu_w L^2} \sqrt{\frac{k}{\phi}} \right)_{matrixblock} . \quad \text{.....(2.5.34)}$$

Therefore, actual time can be converted to dimensionless time as:

$$t_D = \left(t \frac{\sigma}{\mu_w L^2} \sqrt{\frac{k}{\phi}} \right) . \quad \text{.....(2.5.35)}$$

From the imbibition data, we obtained a table of the recovery versus time. The time from the imbibition experiments can be converted to dimensionless form as given by Eq. 2.5.35, and also the recovery can be converted into dimensionless form using the following equation:

$$R_D = \frac{R}{V_R}. \quad \text{.....(2.5.36)}$$

Therefore, we can build a table of the recovery and time in dimensionless units can from the numerical simulation of the imbibition experiment. Now the problem is resolved by expressing the dimensional recovery in terms of the transfer function.

De Swaan proposed that the rate of imbibition into the fracture from the matrix could be expressed as:

$$\tau = R_\alpha \lambda \int_o^t e^{-(t_D-\varepsilon)\lambda} \frac{\partial S_{wf}}{\partial \varepsilon} d\varepsilon . \quad \text{.....(2.5.37)}$$

He also derived the Buckley-Leverett solution for the 1D, two-Phase water flooding displacement process. Considering the integral as shown above, the transfer function can be written as:

$$\tau = R_\alpha \lambda \sum_{j=0}^{n} \left\{ [S_{wf}(t_{j+1}) - S_{wf}(t_j)] \prod_{k=j}^{n} e^{-\lambda \Delta t_k} \right\}. \quad \text{.....(2.5.38)}$$

Simplifying Eq. 2.5.38 we have,

$$\tau = R_\alpha \lambda \left\{ Sum^{n-1} e^{-\lambda \Delta t_{Dn}} \right\}, \quad \text{.....(2.5.39)}$$

where,

$$Sum^{n-1} = Sum^{n-2} + (S_{wf}{}^{n} - S_{wf}{}^{n-1}) e^{-\lambda \Delta t_{Dn-1}} . \quad \text{.....(2.5.40)}$$

Eqs. 2.5.29 and 2.5.30 combined with Eq. 2.5.39 can be written as:

$$-V_p \frac{\partial}{\partial t}(S_{wf}) - \sum R_\alpha \lambda \left\{ Sum^{n-1} e^{-\lambda \Delta t_{Dn}} \right\} - q_o = \nabla.(a_o \nabla(p_{of} + \rho_o g h)) \text{ .....(2.5.41)}$$

$$V_p \frac{\partial}{\partial t}(S_{wf}) - \sum R_\alpha \lambda \left\{ Sum^{n-1} e^{-\lambda \Delta t_{Dn}} \right\} - q_w = \nabla.(a_w \nabla(p_{of} - P_{cf} + \rho_w g h)) \text{ ...(2.5.42)}$$

Therefore the problem is reduced to a two-unknown, two-equation problem.

2.5.4.2.4 DISCRETIZATION OF THE EQUATIONS

Eqs. 2.5.41 and 2.5.42 can be discretized as shown in the previous chapter using the finite- difference technique, and the following equation can be derived:

$$\Delta a_o \Delta \Phi_o = - \frac{V_p / B_o}{\Delta t} \delta S_w + q_o + \sum R_\alpha \lambda \{ Sum^{n-1} e^{-\lambda \Delta t_{Dn}} \} \quad . \text{ ..... (2.5.43)}$$

$$\Delta a_w \Delta \Phi_w = \frac{V_p / B_w}{\Delta t} \delta Sw + q_w + \sum R_\alpha \lambda \{ Sum^{n-1} e^{-\lambda \Delta t_{Dn}} \} \quad . \text{ .....(2.5.44)}$$

Where

a	= symmetric coefficient
Φ	= potential, defined as
$\Delta \Phi_w$	$= \Delta (p\text{-}P_c) - \rho_w g \Delta H$
$\Delta \Phi_o$	$= \Delta (p) - \rho_o g \Delta H$
Δ	$= \Delta = \frac{\partial}{\partial x} + \frac{\partial}{\partial y}$

Writing Eqs. 2.5.43 and 2.5.44 after finite-difference discretization, neglecting gravity we have

$$a_{ow\,i\text{-}1}^{n+1} (\Phi_{i\text{-}1}^{n+1} - \Phi_i^{n+1}) + a_{oE\,i}^{n+1} (\Phi_{i+1}^{n+1} - \Phi_i^{n+1}) + a_{oS\,j}^{n+1} (\Phi_{j\text{-}1}^{n+1} - \Phi_j^{n+1}) + a_{oN\,j}^{n+1} (\Phi_{j+1}^{n+1} - \Phi_j^{n+1})$$
$$= - \frac{V_p / B_o}{\Delta t} (Sw^{n+1} - Sw^n) + q_o + \sum R_\alpha \lambda \{ Sum^{n-1} e^{-\lambda \Delta t_{Dn}} \} \quad . \text{ (2.5.45)}$$

$$a_{ww\,i\text{-}1}^{n+1} (\Phi_{i\text{-}1}^{n+1} - \Phi_i^{n+1}) + a_{wE\,i}^{n+1} (\Phi_{i+1}^{n+1} - \Phi_i^{n+1}) + a_{wS\,j}^{n+1} (\Phi_{j\text{-}1}^{n+1} - \Phi_j^{n+1}) + a_{wN\,j}^{n+1} (\Phi_{j+1}^{n+1} - \Phi_j^{n+1})$$
$$= \frac{V_p / B_w}{\Delta t} (Sw^{n+1} - Sw^n) + q_w + \sum R_\alpha \lambda \{ Sum^{n-1} e^{-\lambda \Delta t_{Dn}} \} \quad . \text{ (2.5.46)}$$

Eqs. 2.5.45 and 2.5.46 are highly nonlinear. With the advent of faster computers, the conventional IMPES formulation of the equation above is not necessary as the IMPES methods are known for their stability problems. Hence, the fully implicit option is applied. To solve these equations, Newton-Raphson's method of solution can be applied.

Newton-Raphson's Solution of NonLinear Equations. Consider Eqs. 2.5.45 and 2.5.46. They can be posed in the matrix form as shown below:

$$\vec{A}\vec{X} = \vec{b}\,, \quad \text{.....(2.5.47)}$$

where

$$\vec{X} = \begin{bmatrix} \Phi_f \\ S_{wf} \\ \cdot \\ \cdot \\ \Phi_f \\ S_{wf} \end{bmatrix}$$

$\vec{A}$ = coefficient Matrix

$\vec{b}$ = right-hand-side Matrix

Since both the *A* and *b* matrices in Eqs. 2.5.47 are functions of the *x* matrix the system of equations is nonlinear. Rewriting the equation:

$$\vec{R} = \vec{A}\vec{X} - \vec{b}\,, \quad \text{.....(2.5.48)}$$

Where the *R* matrix is called the *residual matrix*. Using the Taylor series expansion, the residual matrix can be written as:

$$\vec{R}^{n+1} = \vec{R}^{n} + \left(\frac{\partial \vec{R}}{\partial x}\right)^{n} (\vec{x}^{n+1} - \vec{x}^{n})\,. \quad \text{.....(2.5.49)}$$

Setting R^{n+1} to zero, as the objective is to reduce the residual to zero, the following equation can be derived:

$$\vec{R}^{k} = -\left(\frac{\partial \vec{R}}{\partial x}\right)^{k} \Delta\vec{x}^{k+1}, \quad \text{.....(2.5.50)}$$

where

Δx^{k+1} = x^{k+1}-x^{k}

k = iteration counter

Eq. 2.5.50 is similar to Eq. 2.5.47. Therefore, Eqs. 2.5.45 and 2.5.46 can be posed in the form of residuals, and the partial derivative in Eq. 2.5.50 can be computed as the coefficient of the change in residual with respect to a variable; then the difference matrix can to be computed.

To solve Eq. 2.5.50, at the beginning of every time step the value of the iteration counter is set to unity and the residuals are computed at the previous time step. Then the Jacobian matrix is computed at the iteration level. Then Eq. 2.5.50 is solved. With the new difference matrix, the variables are updated and checked for convergence. If the variables have not converged, the iteration counter is increased and the process is repeated till convergence. A flow diagram is presented in Fig. 2.5.3.

Posing Equations in the Residual Form. We know that both the relative permeability and capillary pressures are a function of water saturation. Therefore the coefficient *a* is not a constant but is a spatial variable of water saturation. Therefore, we can use the equation:

$$k_{ro}^{n+1} = k_{ro}^{k} + \left(\frac{k_{ro}^{n+1} - k_{ro}^{k}}{S_w^{n+1} - S_w^{k}} \right) (S_w^{n+1} - S_w^{k}) \quad \text{.....(2.5.51)}$$

$$= k_{ro}{}^{k} + k_{ro}{}' (Sw^{n+1} - Sw^{k}), \quad \text{.....(2.5.52)}$$

where

n	= time-step counter
k	= iteration counter
`	= prime operator

Therefore, the symmetric coefficient can be written as

$$a_{oE}^{n+1} = a_{oE}^{k} + a_{oE}{}' (Sw^{n+1} - Sw^{k}) \quad . \quad \text{.....(2.5.53)}$$

Similarly

$$a_{wE}^{n+1} = a_{wE}^{k} + a_{wE}{}' (Sw^{n+1} - Sw^{k}) \quad . \quad \text{.....(2.5.54)}$$

And Eq. 2.5.45 can be written (ignoring gravity) as:

$$\left[a^k_{oW\,i} + a_{oW}{}'_i\,(S^{n+1}_{w\,i} - S^k_{wi})\right]\left(p^{n+1}_{i-1} - p^{n+1}_i\right) + + \left[a^k_{oE\,i} + a_{oE}{}'_i\,(S^{n+1}_{w\,i} - S^k_{wi})\right]\left(p^{n+1}_{i+1} - p^{n+1}_i\right)$$
$$+\left[a^k_{oS\,j} + a_{oS}{}'_j\,(S^{n+1}_{w\,j} - S^k_{wi})\right]\left(p^{n+1}_{j-1} - p^{n+1}_j\right) + + \left[a^k_{oN\,j} + a_{oN}{}'_j\,(S^{n+1}_{w\,j} - S^k_{w\,j})\right]\left(p^{n+1}_{j+1} - p^{n+1}_j\right)$$

$$= -\frac{V_p / B_o}{\Delta t}(S_{w_i}{}^{n+1} - S^n_{wi}) + q_o + \sum R_\alpha \lambda \left\{Sum^{n-1} e^{-\lambda \Delta t_{Dn}}\right\} \quad . \quad \text{.....(2.5.55)}$$

Now converting the unknowns to difference terms, we have:

$$S^{n+1}_w = S^k_w + S^*_w \,. \quad \text{.....(2.5.56)}$$

$$p^{n+1} = p^k + p^* \,. \quad \text{.....(2.5.57)}$$

Rewriting Eq.2.5.55 in terms of these unknowns we have:

$$\left[a^k_{oW\,i} + a_{oW}{}'_i\,S^*_{wi}\right]\left(p^k_{i-1} - p^k_i + p^*_{i-1} - p^*_i\right) + \left[a^k_{oE\,i} + a_{oE}{}'_i\,S^*_{wi}\right]\left(p^k_{i+1} - p^k_i + p^*_{i+1} - p^*_i\right)$$
$$+\left[a^k_{oS\,j} + a_{oS}{}'_j\,S^*_{w\,j}\right]\left(p^k_{j-1} - p^k_j + p^*_{j+1} - p^*_j\right) + \left[a^k_{oN\,j} + a_{oN}{}'_j\,S^*_{w\,j}\right]\left(p^k_{j+1} - p^k_j + p^*_{j+1} - p^*_j\right)$$

$$= -\frac{V_p / B_o}{\Delta t}(S_{w_i}{}^k + S^*{}_{wi} - S^n_{wi}) + q_o + \sum R_\alpha \lambda \left\{Sum^{n-1} e^{-\lambda \Delta t_{Dn}}\right\} \quad \text{.....(2.5.58)}$$

Now consider the first term on the left-hand side of Eq. 2.5.58:

$$\left[a^k_{oW\,i} + a_{oW}{}'_i\,S^*_{wi}\right]\left(p^k_{i-1} - p^k_i + p^*_{i-1} - p^*_i\right)$$
$$= a^k_{oW\,i}(p^k_{i-1} - p^k_i) + a^k_{oW\,i}(p^*_{i-1} - p^*_i) + a_{oW}{}'_i\,S^*_{wi}(p^*_{i-1} - p^*_i) + a_{oW}{}'_i\,S^*_{wi}(p^k_{i-1} - p^k_i)$$

The third term is a product of two differences, and as the differences are small, the third term can be neglected. Expanding each term in Eq. 2.5.58 and bringing the unknowns to the left-hand side, the equation can be rewritten as

$$a^k_{oW\,i}(p^*_{i-1} - p^*_i) + a_{oW}{}'_i\,S^*_{wi}(p^k_{i-1} - p^k_i) + a^k_{oE\,i}(p^*_{i+1} - p^*_i) + a_{oE}{}'_i\,S^*_{wi}(p^k_{i+1} - p^k_i)$$
$$+ a^k_{oS\,j}(p^*_{j-1} - p^*_j) + a_{oS}{}'_j\,S^*_{w\,j}(p^k_{j-1} - p^k_j) + a^k_{oN\,j}(p^*_{j+1} - p^*_j) + a_{oN}{}'_j\,S^*_{w\,j}(p^k_{j+1} - p^k_j) + \frac{V_p / B_o}{\Delta t}(S^*{}_w)$$

$$a^k_{oW_i}(p^k_{i-1} - p^k_i) + a^k_{oE_i}(p^k_{i+1} - p^k_i) + + a^k_{oS_j}(p^k_{j-1} - p^k_j) + a^k_{oN_j}(p^k_{j+1} - p^k_j)$$
$$= + \frac{V_p / B_o}{\Delta t}(S^k{}_w - S^n{}_w) + q_o + \sum R_\alpha \lambda \{Sum^{n-1} e^{-\lambda \Delta t_{Dn}}\} \quad . \quad \text{.....(2.5.59)}$$

The right-hand side of Eq. 2.5.59, which doesn't contain any unknowns, can be construed as being the residual. Thus the equation can be written as

$$\vec{R}^k = -\left(\frac{\partial \vec{R}}{\partial x}\right)^k \Delta \vec{x}^{k+1}, \text{ .....(2.5.60)}$$

where

$$\Delta \vec{X} = \begin{bmatrix} p^* \\ S^*{}_w \\ . \\ . \\ p^* \\ S^*{}_w \end{bmatrix}$$

The Jacobian matrix can be computed from the coefficients of individual variables in Eq. 2.5.59. A similar equation for the water phase is

$$a^k_{wW_i}(p^*_{i-1} - p^*_i) + a_{wW}{}'_i S^*_{wi}(p^k_{i-1} - p^k_i) + a^k_{wE_i}(p^*_{i+1} - p^*_i) + a_{wE}{}'_i S^*_{wi}(p^k_{i+1} - p^k_i)$$
$$+ a^k_{wS_j}(p^*_{j-1} - p^*_j) + a_{wS}{}'_j S^*_{wj}(p^k_{j-1} - p^k_j) + a^k_{wN_j}(p^*_{j+1} - p^*_j) + a_{wN}{}'_j S^*_{wj}(p^k_{j+1} - p^k_j) - \frac{V_p / B_o}{\Delta t}(S^*{}_w)$$
$$a^k_{wW_i}(p^k_{i-1} - p^k_i) + a^k_{wE_i}(p^k_{i+1} - p^k_i) + + a^k_{wS_j}(p^k_{j-1} - p^k_j) + a^k_{wN_j}(p^k_{j+1} - p^k_j)$$
$$= - \frac{V_p / B_w}{\Delta t}(S^k{}_w - S^n{}_w) + q_w + \sum R_\alpha \lambda \{Sum^{n-1} e^{-\lambda \Delta t_{Dn}}\} \quad . \quad \text{.....(2.5.61)}$$

Numerical Method of Estimating the Jacobian. The Jacobian matrix can be estimated from numerical methods rather than analytical methods. Consider Eqs. 2.5.59 and 2.5.61. The Jacobian matrix for Eq. 2.5.59 (only 2.5.59 is considered for brevity) can be written as

$$\vec{J} = \begin{bmatrix} \frac{\partial R_1}{\partial p_1^*} & \frac{\partial R_1}{\partial S_{w1}^*} & \cdots & \frac{\partial R_1}{\partial p_n^*} & \frac{\partial R_1}{\partial S_{wn}^*} \\ \frac{\partial R_{1w}}{\partial p_1^*} & \frac{\partial R_{1w}}{\partial S_{w1}^*} & \cdots & \frac{\partial R_{1w}}{\partial p_n^*} & \frac{\partial R_{1w}}{\partial S_{wn}^*} \\ \vdots & \vdots & \cdots & \vdots & \vdots \\ \frac{\partial R_n}{\partial p_1^*} & \frac{\partial R_n}{\partial S_{w1}^*} & \cdots & \frac{\partial R_n}{\partial p_n^*} & \frac{\partial R_n}{\partial S_{wn}^*} \\ \frac{\partial R_{nw}}{\partial p_1^*} & \frac{\partial R_{nw}}{\partial S_{w1}^*} & \cdots & \frac{\partial R_{nw}}{\partial p_n^*} & \frac{\partial R_{nw}}{\partial S_{wn}^*} \end{bmatrix}. \quad \text{.....(2.5.62)}$$

Consider the term in Row 1 and Column 1 of the Jacobian matrix. By definition, the partial differential can be written as

$$\frac{\partial R_1}{\partial p^*_1} = \underset{h \to 0}{Lt}\left(\frac{R_1(p^*_1 + h) - R_1(p^*_1)}{h} \right) = \underset{h \to 0}{Lt}\left(\frac{R_1(p_1 + h) - R_1(p_1)}{h} \right). \quad \text{..(2.5.63)}$$

The user can specify the value of *h* in the equation and the limit of the ratio can be approximated as the ratio, since the residual is continuous at zero. Therefore the partial differential can be written as

$$\frac{\partial R_1}{\partial p^*_1} = \left(\frac{R_1(p_1 + h) - R_1(p_1)}{h} \right). \quad \text{.....(2.5.64)}$$

The other elements in the Jacobian matrix can also be written in that form.

Method of Solution of the System of Equations. To solve the system of equations as posed by Eq. 2.5.60 for both the water and the oil phases, we propose Gaussian elimination, which is briefly described in this section.

To solve a system of equations as shown below,

$$\begin{cases} a_{11}x_1 + a_{12}x_2 + ...a_{1n}x_n = b_1 \\ a_{21}x_1 + a_{22}x_2 + ...a_{2n}x_n = b_2 \\ \quad\quad\quad\quad . \\ a_{n1}x_1 + a_{n2}x_2 + ...a_{nn}x_n = b_n \end{cases}, \quad .....(2.5.65)$$

The objective of Gaussian elimination is to rewrite the equation in the following form

$$\begin{cases} \alpha_{11}x_1 + \alpha_{12}x_2 + ...\alpha_{1n}x_n = \beta_1 \\ \quad\quad \alpha_{22}x_2 + ...\alpha_{2n}x_n = \beta_2 \\ \quad\quad\quad\quad . \\ \quad\quad\quad \alpha_{nn}x_n = \beta_n \end{cases} . \quad .....(2.5.66)$$

To obtain this transformation the following matrix rules are applied:

1. No interchanging of the order of the equations.
2. No multiplication of any equation by a nonzero number.
3. No addition of any equation with a multiple of any other.

After the system of equations is posed in the form indicated by 2.5.66, the value of x_n is first calculated using the last equation of the system, then x_{n-1} and so on till x_1 is calculated.

The following algorithm is used to achieve the transformation:

1. Starting with the first equation, divide the equation by a_{11} to get one in the first term.
2. Subtract a_{1i} times the first equation from all the equations below the first equation to make the first term in all those equations zero.
3. Repeat the step for the second equation and so on until the last equation consists of only one term.

2.5.5 DISCUSSIONS

We used the imbibition simulator to match the recovery and spatial variation of saturation. To validate this simulator we modeled two experimental cases.

Garg *et al.* Garg *et al.*[34] developed scans of saturation across the core at various time steps in a one-dimensional imbibition experiment. To model these experiments, the recovery and saturation distributions are necessary to be modeled. Various petrophysical properties that were used for this model are shown in Table 2.5.2. The relative permeabilities were modeled using Corey's equation:

$$k_{rw} = k_{rw}^{o} S^{n}{}_{w}. \quad \text{.....(2.5.67)}$$

The capillary pressures were modeled using

$$P_c = P_c^{\,0} \ln S_w. \quad \text{.....(2.5.68)}$$

By varying the relative permeability *n*, krw^0 and $P_c^{\,0}$ values, they obtained a match between the lab and simulated data. Fig. 2.5.4 shows the insignificant effect of gravity on imbibition response in the small core. Fig. 2.5.5 shows the magnitude of the capillary and gravity forces. The effect of relative permeability exponent *n* can be seen in Fig. 2.5.6. Similarly, the effect of end point capillary pressure can be seen in Fig. 2.5.7. By trial and error, the recovery and saturation distributions were matched as shown in Figs. 2.5.8 and 2.5.9. The parameters used to obtain this match are shown in Table 2.5.3.

Muralidharan *et al.* Muralidharan *et al.*[35] performed two-dimensional imbibition experiments with oil-saturated core completely surrounded by water. Since CT scanning was not used to model the saturation distribution, only the recovery of oil could be matched (Fig. 2.5.10). The core petrophysical properties are as provided in Table 2.5.4. The capillary pressure values and relative permeability values obtained for this match are tabulated in Tables 2.5.5 and 2.5.6.

By modeling these two imbibition experiments successfully, the veracity of the simulator is verified.

Dual-Porosity Simulation. We developed a dual-porosity simulator using empirical transfer functions, as shown in the previous section, and verified the results from some test cases using Eclipse™. Eclipse models used the conventional transfer functions; i.e,

they assumed that the transfer of fluids was governed by the difference in pressures of the matrix and the fracture media.

To perform numerical simulation, the imbibition simulator was run for a matrix block and empirical parameters were estimated using curve-fitting techniques. Then these were input into the dual-porosity simulator and compared with Eclipse under different production schemes.

One-Dimensional Model. We compared the pressure and water saturation for a 10x1x1 grid, with 1 well. The well was produced at the low production rate of 1 bbl/day. Fig. 2.5.11 presents the fracture pressure and water saturation results for this model compared with Eclipse; a good match can be seen between the two models. Fig. 2.5.12 presents the comparison with a very high production rate of 10 bbls/day. The empirical model simulator reports the pressure and saturation to be less than 1% off when compared to Eclipse.

Dual-Dimensional Model. The same reservoir model was extended to a 10x10x1 grid with one well located at 5x5x1. This well was produced at a high production rate and the pressure and water saturations compared with Eclipse. Figs. 2.5.13 and 2.5.14 are the pressure profiles along a line drawn parallel to the X-axis and Y-axis respectively. Fig. 2.5.15 shows the material balance error of both oil and water phases for the two-dimensional case. The water-phase material balance increases initially but becomes constant after 6 days, but the oil-phase material-balance error increases with time continuously. This is probably due to the empirical transfer function (Fig. 2.5.16). Fig. 2.5.17 shows the fitting of the imbibition recovery data with curve-fitting parameters.

Comparison With Subdomain Method. Kazemi and Gilman[17] presented a 5-spot waterflooding case. From this case, a matrix block was selected and synthetic imbibition experiments were performed. The matrix was initially filled with recoverable oil and completely surrounded by fractures. The fracture spacing was selected in such a manner that the matrix block is of the same size as the grid block. Fractures that surround the matrix block were saturated with water and a field size imbibition case was thus created. A graphical representation of this model is shown in Fig. 2.5.18.

Fig. 2.5.19 shows the matrix simulation results from a commercially available simulator and our empirical-transfer-function, dual-porosity simulator. We used a five-

level subdomain method, which is a refinement of dual-porosity simulation, for this test case. The subdomain method reports a matrix saturation slightly less than that of the conventional, dual-porosity simulation. This is because of matrix block refinement in the subdomain method. We divided the matrix into five different blocks and, the average saturation among these divisions was reported as the matrix saturation.

The empirical transfer function model compares well with both these models. The initial portion of Fig. 2.5.19, shows the empirical transfer function's results are within the error tolerances of the subdomain method while offset from the conventional dual-porosity results. This is because the conventional transfer functions formulations do not honor the initial time behavior of transfer of fluids.[36] The later time behavior of empirical transfer function model is within acceptable limits of both the conventional transfer function model and subdomain models.

2.5.6 CONCLUSIONS

The following conclusions can be derived from this study.

1. The diffusivity equation is sufficient to model imbibition experiments.
2. Imbibition experiments provide us with empirical transfer functions that can be used to model dual-porosity simulation.
3. Empirical dual-porosity simulation is inherently faster, because the number of unknowns per grid block is reduced to two from four.
4. Material balance is not conserved to the extent of conventional dual-porosity formulations.

REFERENCES

1. Nelson, R: *Geological Analysis of Naturally Fractured Reservoirs*, second edition, Gulf Professional Publishing, St. Louis (2003).
2. Jaeger, J.S. and Cook, N.G.W.: *Fundamentals of Rock Mechanics*, third edition, Chapman and Hall Ltd., New York City (1979).
3. Aguilera, R.: *Naturally Fractured Reservoirs*, second edition, PennWell Pub. Co., Tulsa (1995).

4. Warren, J.E. and Root, P.J.: “The Behavior of Naturally Fractured Reservoirs,” *SPEJ* (Sep. 1963) 245-255.
5. Gilman, J.R. and Kazemi, H.: “Improvements in Simulation of Naturally Fractured Reservoirs,” *SPEJ* (Aug. 1983) 695-707.
6. Nelson, R.A.: *Geologic Analysis of Naturally Fractured Reservoirs*, Golf. Pub. Co., Houston (1985).
7. *Rock Fractures and Fluid Flow: Contemporary Understanding and Applications*, Committee on Fracture Characterization and Fluid Flow, National Academy Press, Washington, D.C. (1996).
8. Reiss, L.H.: *The Reservoir Engineering Aspects of Fractured Reservoirs*, Golf. Pub. Co., Houston (1980).
9. van Golf-Racht, T.D.: *Fundamentals of Fractured Reservoir Engineering*, Elsevier Scientific Pub. Co., Amsterdam (1982).
10. Lawn, B. and Wilshaw, R. “Indentation Fracture: Principles and Applications”, J. Mater. Sci. (UK) **10** (June 1975) 1049-81.
11. Agarwal, B., Hermansen, H., Sylte, J.E., and Thomas, L.K.: “Reservoir Characterization of Ekofisk Field: A Giant, Fractured Chalk Reservoir in the Norwegian North Sea – History Match,” *SPEREE* (Dec. 2000), 534-543.
12. Barenblatt, G.I., Zheltov, I.P., and Kochina, I.N.: “Basic Concepts in the Theory of Seepage of Homogenous Liquids in Fissured Rocks (Strata),” *J. Appl. Math. Mech.* (1960) 24, 1286-1303.
13. Kazemi, H.: “Pressure Transient Analysis of Naturally Fractured Reservoirs with Uniform Fracture Distribution,” *SPEJ* (Dec. 1969) 451-462; *Trans.*, AIME, **246**.
14. Abdassah, D. and Ershaghi, I.: “Triple-Porosity Systems for Representing Naturally Fractured Reservoirs,” *SPEFE* (April 1986) 113-127.
15. Aronofsky, J.S., Masse, L., and Natanson, S.G.: “A Model for the Mechanism of Oil Recovery from the Porous Matrix Due to Water Invasion in Fractured Reservoirs,” *Trans.*, AIME (1958) **213**, 17-19.
16. de Swaan, A.: “A Theory of Waterflooding in Fractured Reservoirs,” *SPEJ* (April 1978) 117-122; *Trans.*, AIME, **265**.

17. Kazemi, H., Gilman, J.R., and Elsharkawy, A.M.: “Analytical and Numerical Solution of Oil Recovery From Fractured Reservoirs With Empirical Transfer Functions,” *SPERE* (May 1992) 219-227.
18. Reis, J.C., and Cil, M.: “A Model for Oil Expulsion by Counter-Current Water Imbibition Into Gas-Saturated Matrix Blocks,” *J. Pet. Sci. & Eng.* (1993) No. 10: 97.
19. Civan, F.: “Waterflooding of Naturally Fractured Reservoirs: An Efficient Simulation Approach,” paper SPE 25449 presented at the Production Operations Symposium, Oklahoma City, March 21-23, 1993.
20. Gupta, A. and Civan, F.: “An Improved Model for Laboratory Measurement of Matrix to Fracture Transfer Function Parameters in Immiscible Displacement,” paper SPE 28929 presented at the SPE Annual Technical Conference and Exhibition, New Orleans, Sep. 25-28, 1994.
21. Civan, F.: “Quadrature Solution for Waterflooding of Naturally Fractured Reservoirs,” *SPEREE* (April 1998) 141-147.
22. Rapoport, L.A.: “Scaling Laws for Use in Design and Operation of Water/Oil Flow Models,” *Trans*., AIME (1955) 204, 143.
23. Mattax, C.C. and Kyte, J.R.: “Imbibition Oil Recovery from Fractured, Water-Drive Reservoirs,” *SPEJ* (June 1962) 177-184; *Trans.*, AIME, **225**.
24. Du Prey, E. L.: “Gravity and Capillary Effects on Imbibition in Porous Media” *Soc. Pet. Eng. J.* (June, 1978) 195-206.
25. Ma, S., X. Zhang, and N.R. Morrow: “Influence of Fluid Viscosity on Mass, Transfer Between Rock Matrix and Fractures,” paper presented at the 1995 Annual Technical Meeting of The Petroleum Society of CIM in Banff, Alberta, Canada, May 14-17.
26. Bourbiaux, B. and Kalaydjian, F.J.: “Experimental Study of Cocurrent and Countercurrent Flows in Natural Porous Media,” *SPERE* (Aug. 1990) 361-368.
27. Peñuela-Pineda, G.: “Modeling Interporosity Flow For Improved Simulation Of Naturally Fractured Reservoirs,” Ph.D. thesis (2002), University of Oklahoma, Norman, OK.

28. Chen, J., M,A, Miller, and K. Sepehrnoori: “Theoretical Investigation of Countercument Imbibition in Fractured Reservoir Matrix Blocks,” paper SPE 29141 presented at 1995 SPE Symposium on Reservoir Simulation, San Antonio, TX, Feb. 12-15.
29. Hemandez J.C. and C.P. Resales: “Imbibition as a Dispersion Process,” paper SPE 23748 presented at the 1992 SPE Latin American Petroleum Engineering Conference, Caracas, Venezuela, March 8-11.
30. Hayashi, J.A. and C.P. Resales: “Visual Investigation of Imbibition Process,”, paper SPE 23745 presented at the 1992 SPE Latin American Petroleum Engineering Conference, Caracas, Venezuela, March 8-11.
31. Najurieta, H.L.: “A Theory for Pressure Transient Analysis in Naturally Fractured Reservoirs,” *JPT* (July 1980) 1241-1250.
32. Siddiqui, S., Hicks, P.J., Grader, A.S: “Verification of Buckley-Leverett Three Phase Theory Using Computerized Tomography”, *J. Pet. Sci. and Engg.* 15 (1996) 1-21.
33. Hunt, P.K., Engler, P. and Bajsarowicz, C.: “Computerized Tomography as a Core Analysis Tool: Applications, Instrument Evaluation and Image Improvement Techniques”, *Soc. Pet. Eng. J., Formation Evaluation* (Sep. 1988), 1203-1210.
34. Garg, A., Zwahlen, E., and Patzek, T.W.: “Experimental and Numerical Studies of One-Dimensional Imbibition in Berea Sandstone,” paper presented at the 16th Annual Geophysical Union Hydrology Days, Fort Collins, CO, 15-18 April.
35. Muralidharan, V., Putra, K., and Schechter, D.S.: “Experimental and Simulation Analysis of Fractured Reservoirs Experiencing Different Stress Conditions,” CIPC Paper No. 2004-229, 55th Annual Technical Meeting for the Canadian International Petroleum Conference, Calgary, CA, June 8-10.
36. Aziz, K. and Lim, K.T.: “Matrix-Fracture Transfer Shape Factors for Dual Porosity Simulators,” *J. Pet. Sci. and Eng.* **13** (1995) 169-178.

Table 2.5.1—Shape Factors as Reported by Penula-Pineda

Mathematical Approximations	Slab Geometry	**Square Geometry**	**Cube Geometry**
Warren And Root	12	32	60
Kazemi et al	4	8	12
Thomas et al[37]	-	-	25
Coats[38]	8	16	24
Kazemi and Gilman[39]	-	-	29.6
Limm and Aziz[40]	9.9	19.7	29.6
Quintard and Whitaker[41]	12	28.4	49.6
Noetinger et al[42]	11.5	27.1	-
Bourbiaux et al	-	20	-

Table 2.5.2—Modeled Garg *et al*. Core Properties.

Property	**Value**	**Units**
Number of grids blocks in X-Direction	1	-
Number of grids blocks in Y-Direction	1	-
Number of grids blocks in Z-Direction	11	-
Grid Block Dimension X-Direction	4.83	cm
Grid Block Dimension Y-Direction	4.83	cm
Grid Block Dimension Z-Direction	0.67	cm
Density of Oil	0.0006	Lb/cu.ft
Density of Water	62.4	Lb/cu.ft
Permeability X-Direction	300	md
Permeability Z-Direction	300	md
Porosity	0.22	-
Initial Water Saturation	10*0.1, 1.0	-
Boundary Condition	Bottom Most	-

Table 2.5.3—Parameters for Match of Imbibition Response (Garg *et al.*).

Property	**Value**	**Units**
Relative Permeability Exponent	8	-
End Point Relative Permeability	0.045	-
End Point Capillary Pressure	40	psi

Table 2.5.4—Properties of the Core for Numerical Simulation (Vivek *et al.*)

Property	Value	Units
Number of grids blocks in X-Direction	12	-
Number of grids blocks in Y-Direction	1	-
Number of grids blocks in Z-Direction	12	-
Grid Block Dimension X-Direction	0.3130493	cm
Grid Block Dimension Y-Direction	3.19214817	cm
Grid Block Dimension Z-Direction	0.4621	cm
Density of Oil	48.0	Lb/cu.ft
Density of Water	62.4	Lb/cu.ft
Permeability X-Direction	68	md
Permeability Z-Direction	68	md
Porosity	0. 2092	-
Initial Water Saturation	12*1,10*(1,10*0.46,1), 12*1	-
Boundary Condition	All Sides	-

Table 2.5.5—Capillary Pressure Obtained From the Match.

Water Saturation (Fraction)	Capillary Pressure (psi)
0.14	2.0
0.2	1.71
0.4	0.91
0.5	0.653
0.6	0.518
0.635	0.46
0.76	0.11
0.8	0.1

Table 2.5.6—Relative Permeability Obtained for the Match.

Water Saturation	Water Relative Permeability	Oil Relative Permeability
0.0	0.33	0.
0.2	0.22	0.15
0.4	0.18	0.37
0.5	0.1	0.4
0.635	0.	0.44
0.76	0.	0.44
0.8	0.	0.44

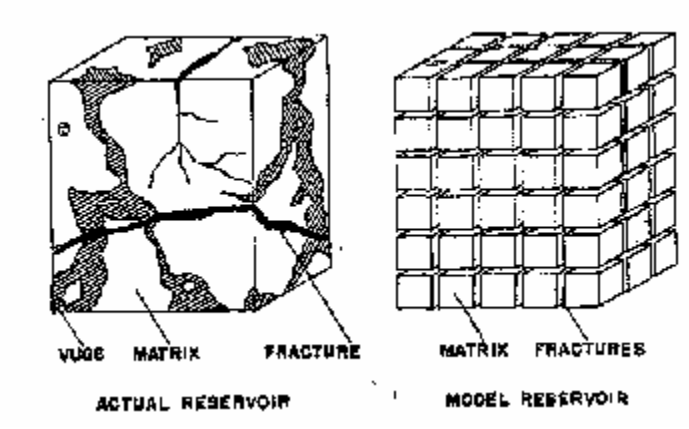

Fig. 2.5.1— (a) Actual Reservoir (b) Idealized Reservoir.

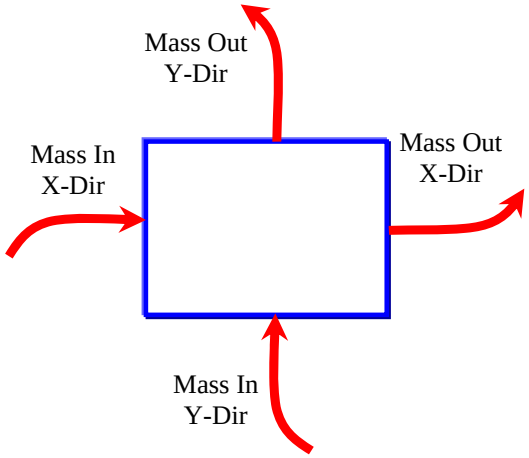

Fig. 2.5.2—Conservation of mass in a control volume.

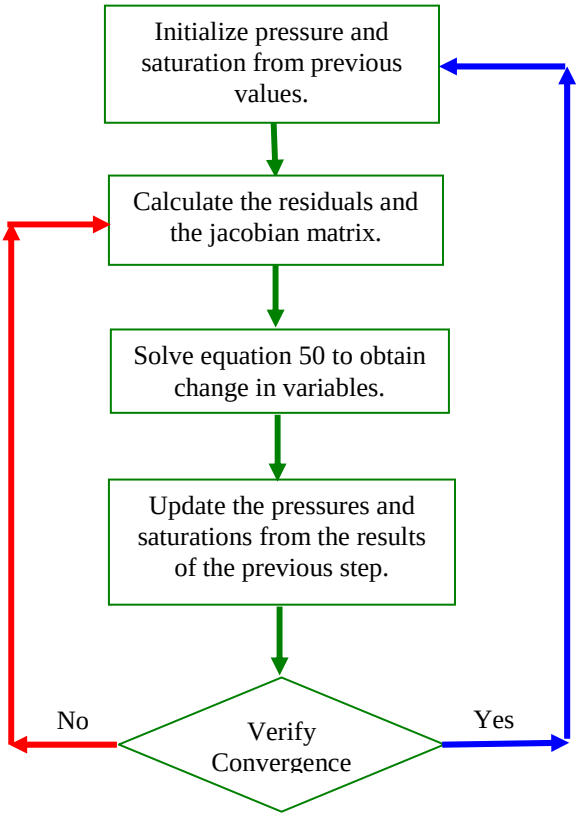

Fig. 2.5.3—Flow Chart for Newton-Raphson's method of solution.

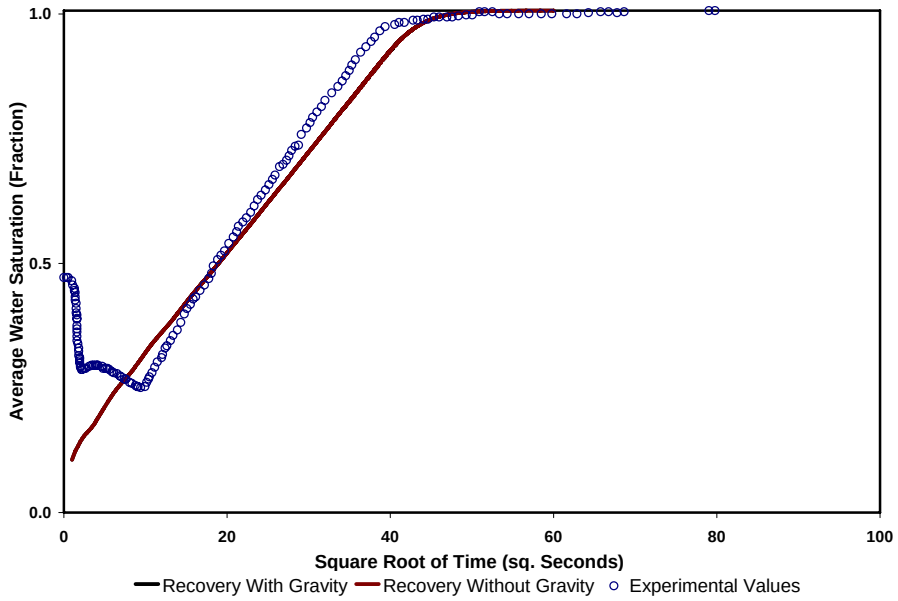

Fig. 2.5.4—Effect of gravity on imbibition response.

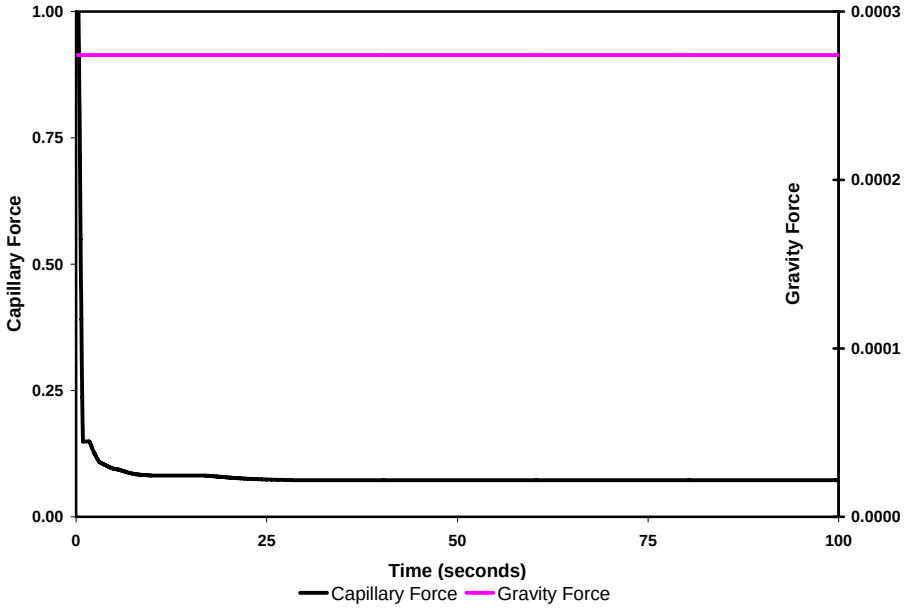

Fig. 2.5.5—Gravity and capillary forces as a function of time during imbibition.

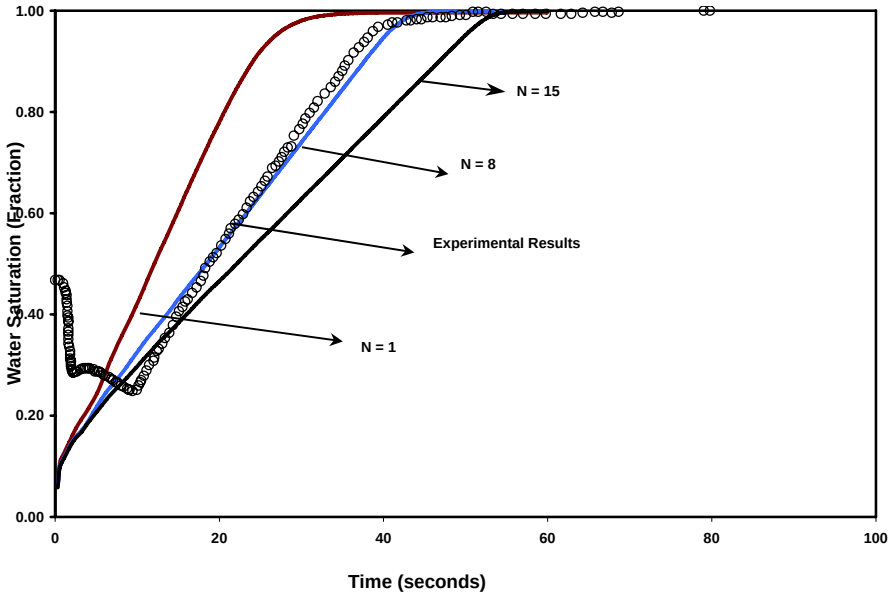

Fig. 2.5.6 —Effect of relative permeability exponent on imbibition recovery.

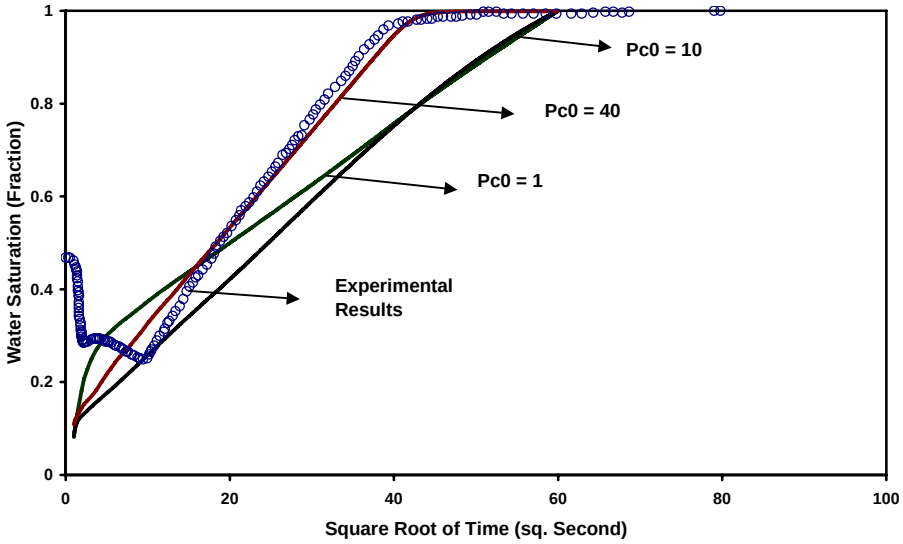

Fig. 2.5.7—Effect of end-point capillary pressure on imbibition response.

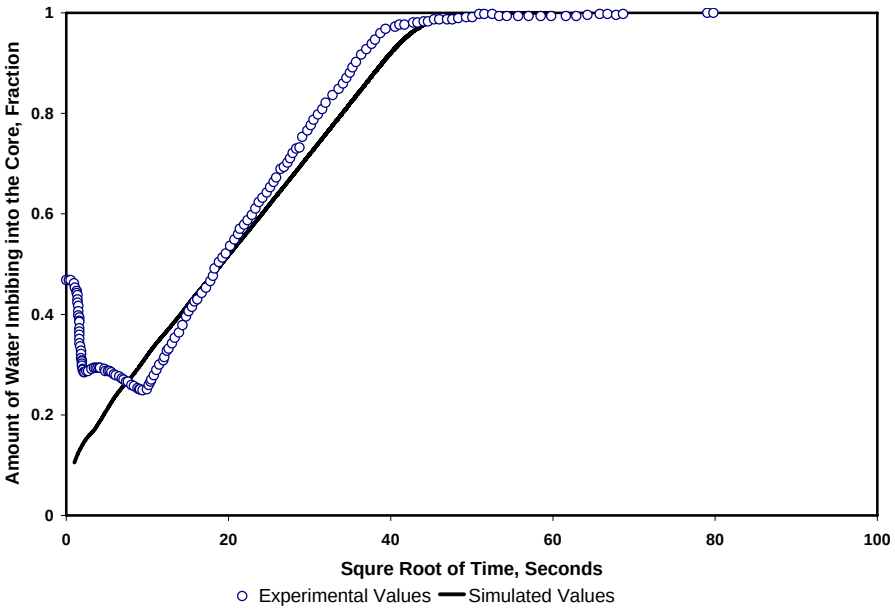

Fig. 2.5.8—Match of experimental recovery with simulated recovery.

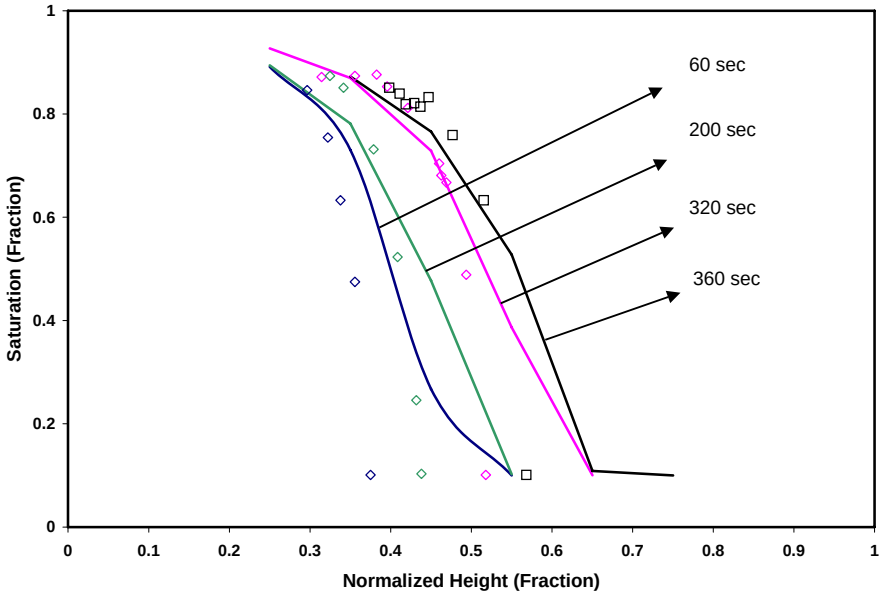

Fig. 2.5.9—Match of experimental and simulated saturations.

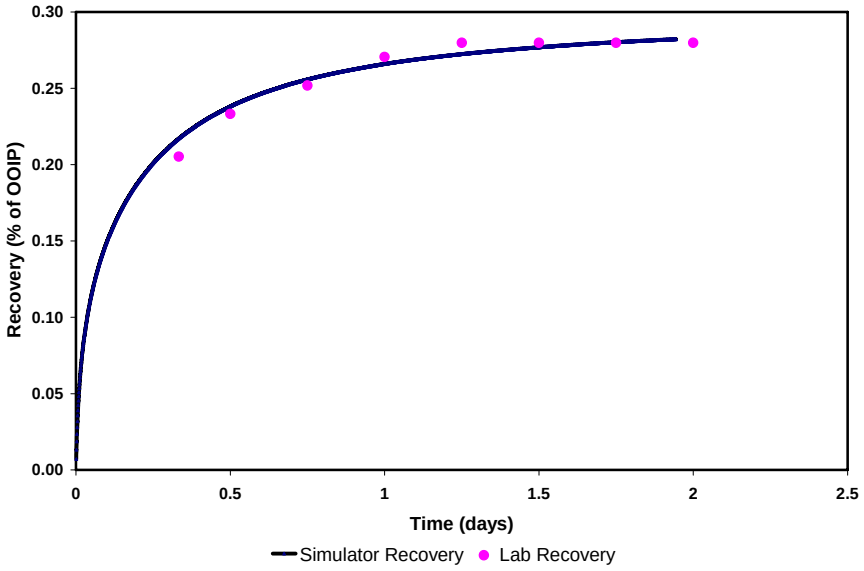

Fig. 2.5.10— Match of experimental and simulated recovery.

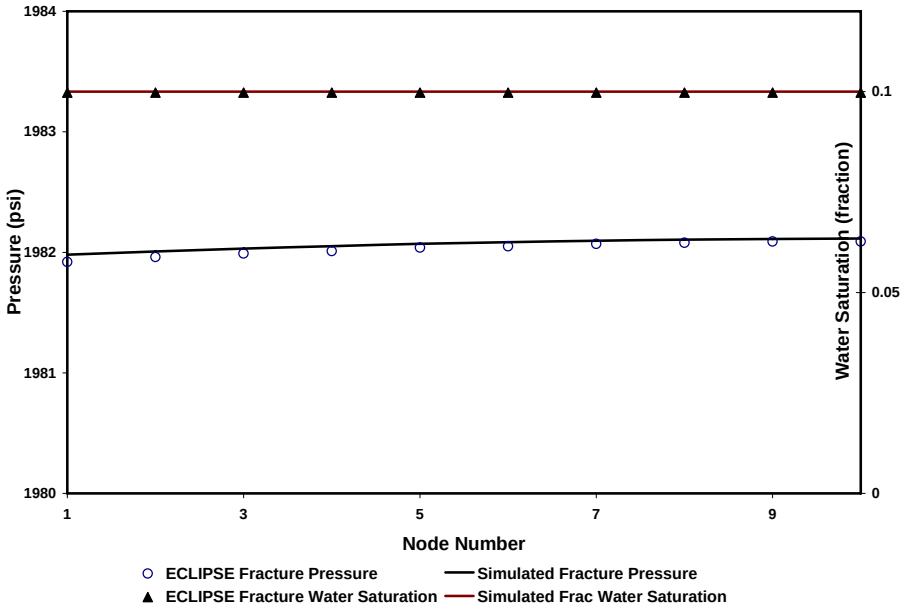

Fig. 2.5.11— One-dimensional, low-production-rate-pressure- and water-saturation profiles.

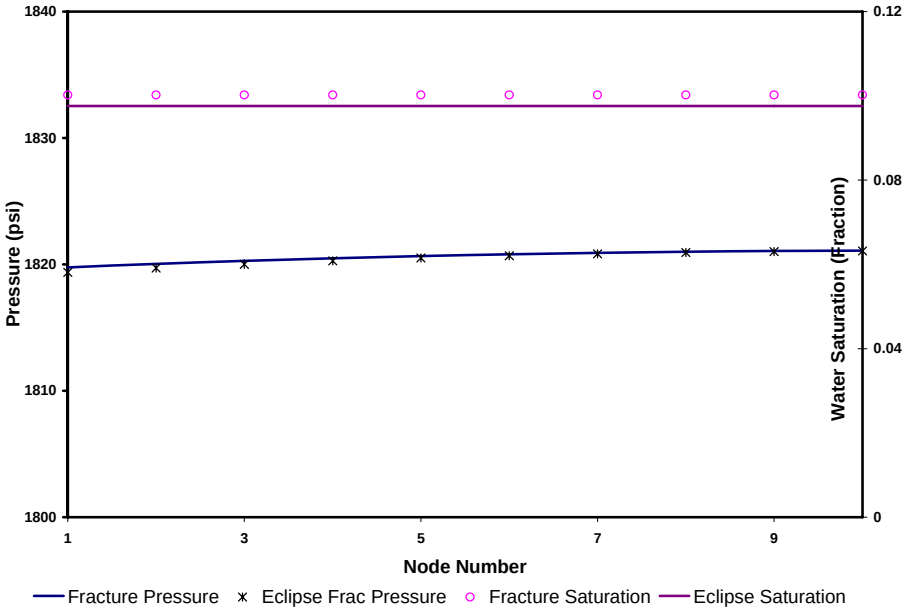

Fig. 2.5.12—One-dimensional, high production, pressure- and water-saturation profiles.

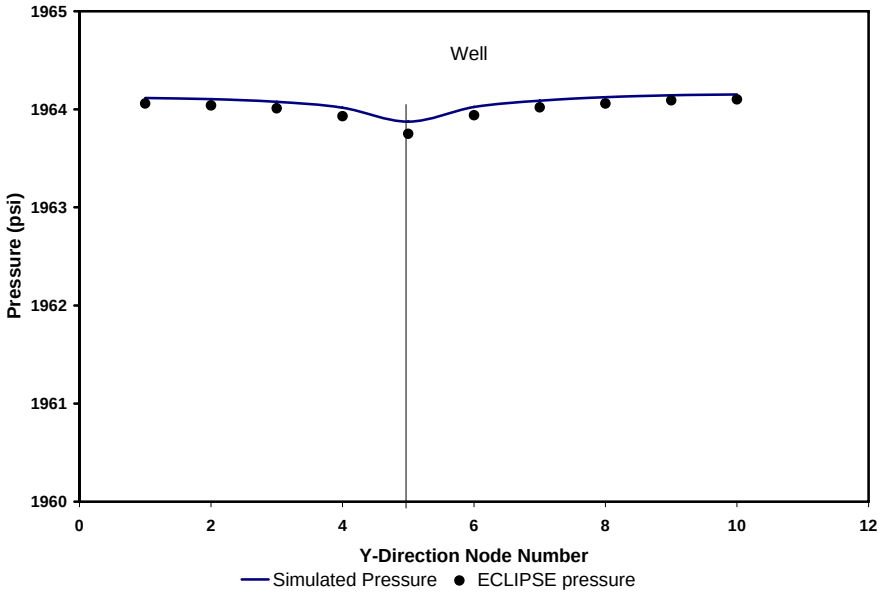

Fig. 2.5.13—Pressure profile along a line parallel to Y axis.

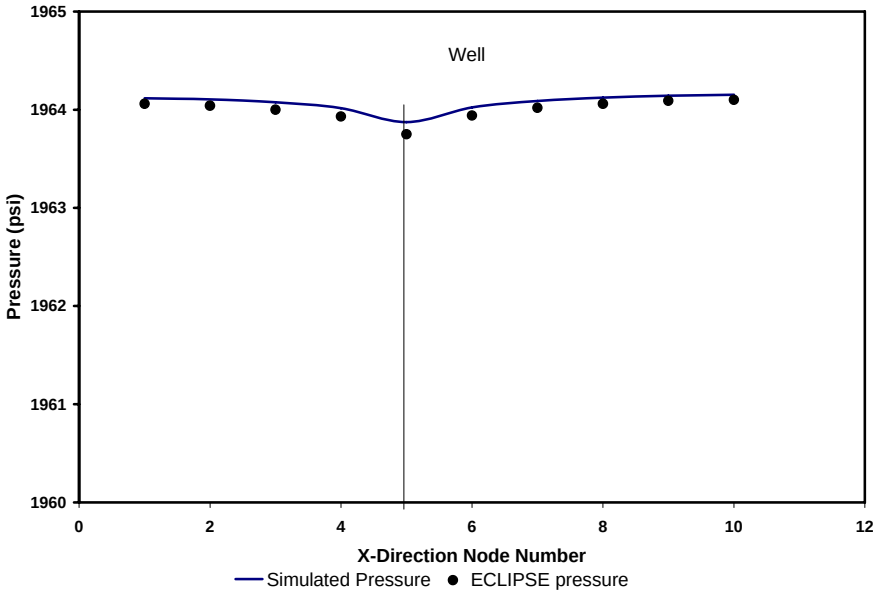

Fig. 2.5.14—Pressure profile along a line parallel to X axis.

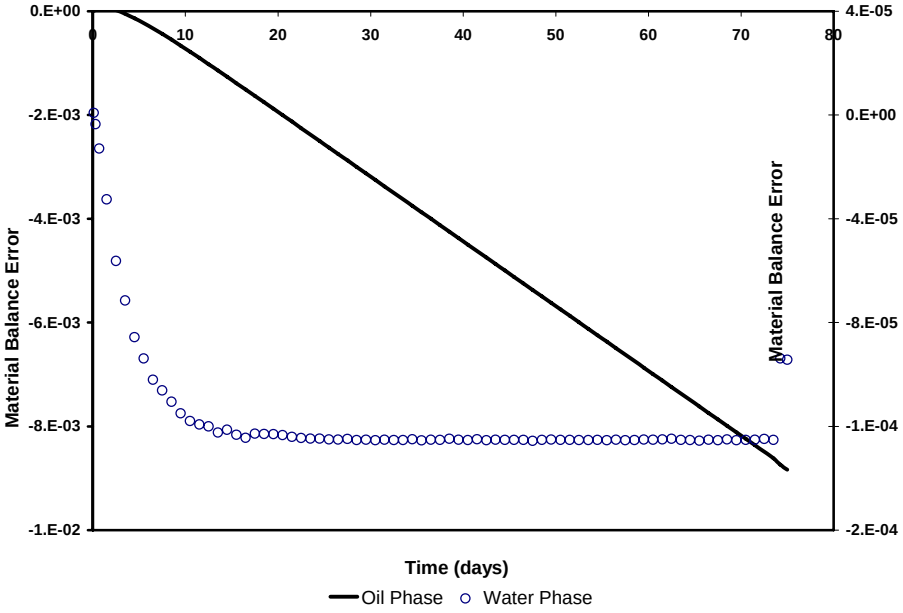

Fig. 2.5.15—Material balance error for the empirical model, 2D case.

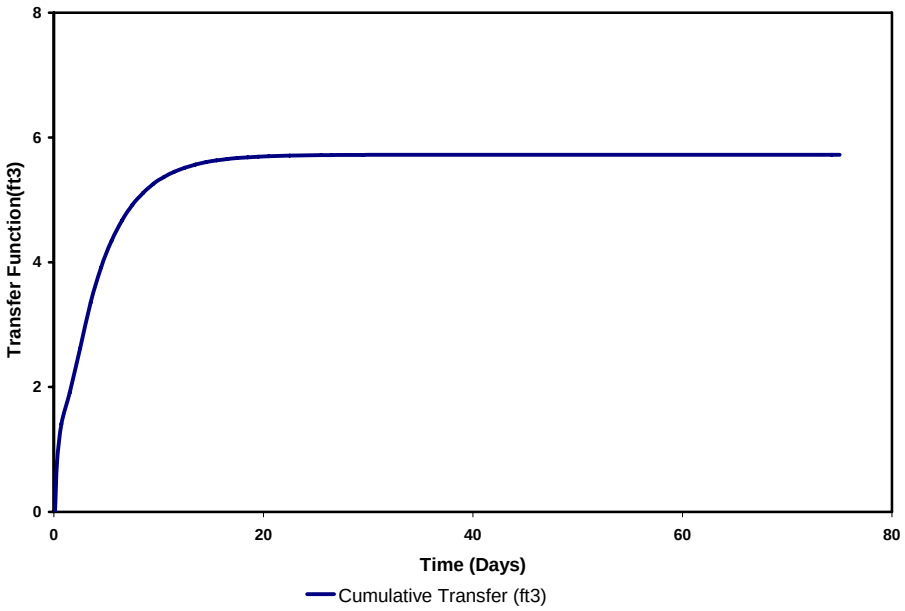

Fig. 2.5.16—Empirical transfer function as a function of time

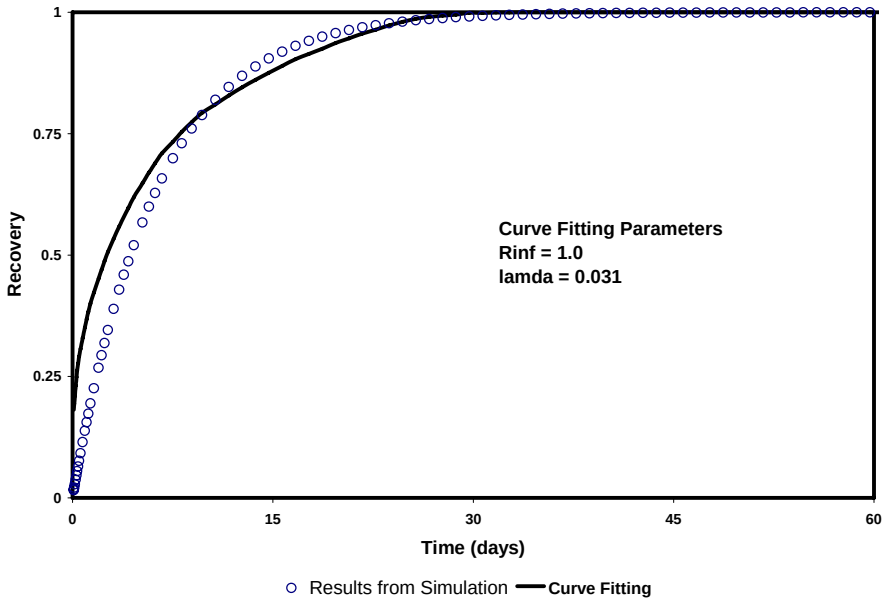

Fig. 2.5.17—Imbibition simulator response.

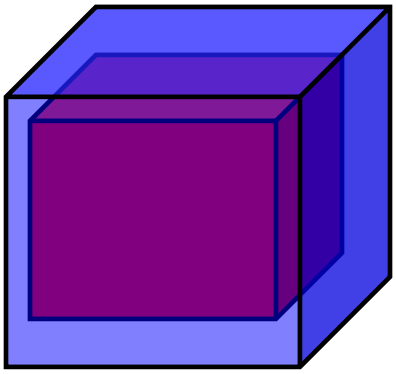

Fig. 2.5.18—Representation of the matrix block surrounded by water.

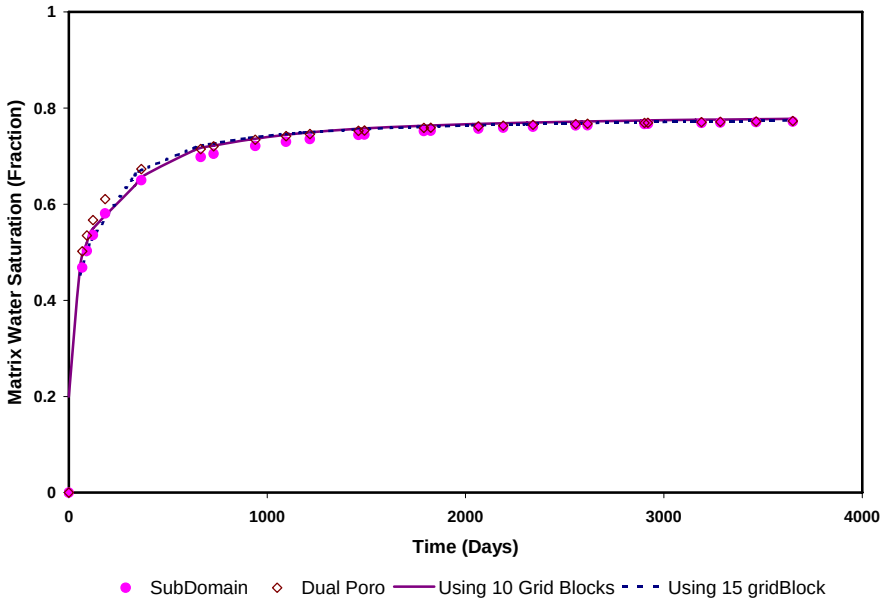

Fig. 2.5.19—Comparison of empirical transfer function with subdomain method and dual-porosity methods.

Chapter II-6
Hybrid Grid Block Reduces Grid Orientation Effect

2.6.1 INTRODUCTION

Most commonly used grids are constructed by aligning the grid-block along orthogonal coordinate directions and then distorting the grid to fit major reservoir features. It is generally believed that heterogeneous reservoirs could also be represented if grids are made sufficiently small. Even though the Cartesian grids have been widely used, they are not always suitable for the simulation of complex reservoirs. Some shortcomings of Cartesian grids include their inflexibility in the description of faults, pinchouts, and discontinuities in reservoirs and the influence of grid-orientation on the results.

In principle, if extremely fine grids could be created, it would be possible to represent heterogeneous reservoirs easily. However, the number of grids in a model is practically limited by computer capacity and CPU time. To solve this problem, the concept of local grid refinement has been introduced.

Local grid refinement involves using a fine grid inside a coarse-based grid. This is usually done for regions with large pressure changes near the wellbore, in areas of wide variation in saturation, in regions of interest which require finer resolution, and in highly heterogeneous regions. This might reduce the computation time but it should yield results which are very similar to a fine-based grid in accuracy. Nevertheless, the banded structure of the matrix is lost, so the matrix-solving procedure may be less efficient. For example, to model radial flow near a well, hybrid local grid refinement was proposed by Pedrosa and Aziz.[1] Orthogonal curvilinear grids are used in the well region and Cartesian grids are used in the rest of the reservoir.

Different types of locally refined grids have been presented throughout the literature. Reservoir simulations are normally being performed on rectangular Cartesian grids; the radial grid was developed later to simulate flow near the wellbore. Local grid refinement was developed to achieve better accuracy in high flow regions.[1-2]

Development of the corner-point geometry grid[3-4] enables the use of nonrectangular grid-blocks. This provides the ability to model faults and other complex geological

features. Before then, all grids were structured where the neighbors of a grid-block could be easily identified from their *i,j,k* indices.

In the last decade, unstructured grids[5-10] were introduced. In unstructured grids, the connections between grid-blocks are flexible, and a connection list is used to keep track of the connected grid-blocks. More and more reservoir simulators have flexible grid capabilities already available or in development. More studies should be done to determine whether these techniques are reliable and accurate, and whether they can allow a significant computer time saving during a reservoir simulation run.

2.6.1.1 Literature Review on Grid Orientation Effect

Several methods have been proposed to reduce the grid-orientation effect. The literature can be divided into several major groups in terms of the approach taken to reduce the grid-orientation effect.

The grid-orientation effect in reservoir simulation caused by conventional rectangular five-point discretization scheme was reported by Todd *et al*.[11] The orientation of the grid relative to the lines of flow influenced results from the scheme involving five-point differencing and single-point upstream weighting. They attributed the problem to single-point upstream weighting and proposed the use of two-point upstream mobility weighting in place of the generally used single-point approximation. They reported a reduction of both numerical dispersion of flood fronts and the sensitivity of predicted areal displacement performance to grid-orientation.

Holloway *et al*.[12] presented an approach to reduce the grid-orientation effect by modifying phase transmissibilities and the two-point upstream weighting method proposed by Todd *et al*.[11] that permitted diagonal flow, but their modifications only resulted in marginal improvement over the original two-point weighting. Meanwhile, a generalization of upstream weighting proposed by Frauenthal *et al*.[13] involves using a weighting parameter between the two mobilities instead of the simple single-point weighting. The main attraction of these techniques is that they can be easily implemented into existing computer codes and do not add significantly to computational time. However, based on the studies done by Vinsome and Au,[14] they concluded that in an extreme case of unfavorable mobility ratio, the upstream formulation predicts a pressure

drop across a shock front that is much smaller than it is supposed to be, and vice versa in the case of favorable mobility ratio.

The second group of the literature developed around the method of using a nine-point finite-difference discretization scheme, which was initially proposed by Yanosik and McCracken.[15] This scheme is based on adding diagonal transmissibilities in the areal (X-Y) direction to reduce grid-orientation effects when the flow is not aligned with the grid. They introduced weighting factors, of four and one for the diagonal and parallel grids respectively. Various forms of nine-point schemes were also introduced by subsequent authors.[15-21] Ko and Au[16] concluded that the nine-point scheme proposed by Yanosik and McCracken could not solve the problem of grid-orientation for all mobility ratios since the weighting factor used in this method is a function of mobility ratio itself. In addition, as the nine-point scheme is a weighted interpolation between the two five-point grids with a common center point and its diagonal transmissibilities, it lacks physical justification.

In single-point upstream mobility weighting, the mobility term is discretized using a first-order scheme. It is generally believed that the grid-orientation effect is partly caused by numerical dispersion in low-order techniques such as this. Also, truncation error manifests itself as a numerical dispersion, which will cause smearing of the flood front. Coarser grids will have larger truncation errors and more dispersion. On the contrary, finer grids will have smaller truncation error and less dispersion. However, as stated by Brand *et al.,*[22] "…in general the GOE (Grid Orientation Effect) cannot be overcome with grid refinement….When the grid is refined, the solutions still depend on the size and orientation of the underlying grid, as long as numerical diffusion dominates over physical dispersion and diffusion."

The third group concerns mainly the numerical implications[23-26] of the finite-difference solutions using higher-order finite-difference methods, generally known as high-order techniques (HOT). For example, Chen *et al*.,[23] Pinto and Correa,[24] and Wolcott *et al*.[25] proposed using the Total Variation Diminishing (TVD) methods. Wolcott *et al*.[25] used a combination of nine-point scheme and the third order Taylor's series expansion TVD scheme. The authors reported that this method was able to reduce numerical dispersion and produce sharper saturation fronts.

A type of uniform triangular grids was also introduced in the early 1980s.[27] This method requires the use of the point-distributed grid system, where the grid generation is more complicated than the conventional grid system. The advantage of this grid is that the grid boundaries are not aligned in one particular direction or the other. On the other hand, Pruess and Bodvarsson[26] proposed the use of a seven-point discretization scheme, which is essentially a structured and uniform hexagonal grid-block model. They investigated steam injection problems with relatively coarse grids and concluded that the hexagonal grid can reduce the grid-orientation effect.

The use of hexagonal grids was further supported by Heinemann *et al.*[28] in their Perpendicular-bisector grid model. They also reported the unrealistic saturation front produced by the hexagonal grid and by the Cartesian grid with the nine-point formulation for $M = 50$. The current trend includes the development of flexible gridding to alleviate the problem associated with grid-orientation effects resulting from using rectangular Cartesian grid. Even so, the generation and construction of unstructured grids are not as simple as Cartesian grids. For example, the construction of an unstructured grid for a reservoir is feasible only if it is done by a numerical grid generation procedure.

2.6.1.2 Motivation

Finite difference solutions of 2D frontal displacement problems can be strongly influenced by the orientation of the underlying grid. In multidimensional models, numerical dispersion leads to a phenomenon where calculated performance is influenced by the orientation of the grid relative to the locations of injection and production wells. This is called the grid-orientation effect.

The grid-orientation effect has been found to be particularly pronounced in simulations where the displacing phase is much more mobile than the displaced phase. Fig. 2.6.1 illustrates the problem. It is a sketch of part of the Cartesian grid system of a model for simulating water flooding in an oil reservoir. This part of the model contains one production well and two injection wells. In the simulator, water from Well A will move in a direct path to the producer. However, water from Well B will follow a zig-zag path to the producer. Not only is the flow path from Well B longer, but water from Well

B will sweep the reservoir more efficiently than water from Well A. However, if the grid is rotated 45°, the performances calculated for the two wells would be reversed.

To complicate matters, grid-orientation may distort and affect the accuracy of calculated pressures and saturations.[29] Thus, the grid-orientation effect has become one of the important factors in evaluating different types of grids. In general, neither parallel nor diagonal orientation can be used reliably for displacements at highly unfavorable mobility ratios. Numerous attempts to eliminate the grid-orientation effect in finite-difference simulators have been made, and the latest method being attempted is the use of flexible or unstructured gridding methods.

2.6.2 METHODOLOGY

We developed a novel approach to reduce the effect of grid-orientation on computed numerical results in finite-difference reservoir simulation. This method uses a unique grid-block assignment where rectangular grid-blocks are interspersed with octagonal grid-blocks. The boundaries are then populated with triangular grid-blocks. Thus, the entire domain will consist of different structured grid-blocks in a system we call the hybrid grid-block (HGB) system. In HGB, flow can progress to four different directions in the octagonal grid-blocks and two in the rectangles. This increase in flow directions is expected to reduce the grid-orientation effect in the model. As a structured grid system, HGB retains the familiar finite-difference discretization of the flow equations.

To test the viability of this grid system, we developed a general purpose implicit pressure explicit saturation (IMPES)-formulated 2D black oil simulator with HGB system using the Visual Basic programming language. The simulator developed is named Sim2D. Furthermore, comparative evaluations are made by comparing several simulation cases between HGB and conventional grid-block systems. This innovative grid-block assignment will help to reduce the grid-orientation effect.

2.6.3 DEVELOPMENT OF SIM2D

Sim2D was developed using the Visual Basic 6.0 programming language and it is then compiled into an executable file with simple interface to make it easier to use. In addition, it is equipped with data control/access and file system.

The Sim2D program simulates isothermal, Darcy flow in two dimensions. It assumes reservoir fluids can be described by three fluid phases (oil, gas, and water) of constant composition with physical properties that depend on pressure only. Sim2D is designed to be an easy-to-use program which would be suited to simulate primary depletion and basic secondary recovery operations (such as waterflooding) in a black-oil reservoir. As an IMPES numerical simulator, Sim2D contains an iterative solution technique (biconjugate gradient) for solving systems of algebraic equations. The well model in Sim2D allows specification of rate or pressure constraints on well performance. Several user-controlled output options are also available.

On top of that, Sim2D provides two types of grid systems, namely the conventional Cartesian grid as well as the proposed HGB grid.

2.6.3.1 Averaging of Flow Equation Terms

In a multiphase system, one or more relative permeabilitites must be assigned that will control the flow of the individual phases from one grid-block to the next. In the case of the Sim2D simulator, upstream permeability is used. Here, mobilities are evaluated at saturations that exist in the block from which the fluid phases are moving. For instance, if the flow is from left to right, the relative permeability from the i-1 grid-block will be considered the "upstream block," so $(k_{ro})_{i-1}$ is used for $(k_{ro})_w$. Similarly, if flow is from right to left, the i+1 grid-block will be upstream instead.

2.6.3.2 Boundary Conditions

The boundary conditions used in reservoir simulators can be very complicated, as the differential equations solved by the simulators require that all boundaries be specified. This includes both internal and external boundaries.

External boundaries are the physical boundaries of the flow domain, while for internal boundaries, either well rates or bottomhole pressures can be specified. If a rate is specified for a well, a Neumann-type boundary condition is generated. Conversely, if the pressure is speficied for the wellbore, then a Dirichlet-type boundary condition is obtained.

Sim2D assumes that a no-flow outer boundary exists. To model no-flow boundaries, phase transmissibilities across the boundary interfaces are set to zero. This implies no communication or "flux contribution" across the adjacent boundary blocks.

2.6.3.3 Well Models

A reservoir simulation uses an analytical model to represent flow within a grid-block as it enters or leaves a well. This model is called the well model. The pressure of the wellblock is different from the bottomhole well flowing pressure at the well. This is because in general, the grid-block dimensions are significantly greater than the wellbore radius. The flow rate in the well is proportional to the difference between the block and well pressures. The coefficient of proportionality is known as the productivity or injectivity index. The geometric part of this term is usually called the well index, and the model used to determine the well index is known as the well model.

Peaceman's Well Model. The well model presented by Peaceman[30] can be used for wells located in the center of a rectangular grid-block. Peaceman's model assumes:

- (Pseudo)steady-state flow.
- Homogeneous reservoir.
- Isolated wells.
- Incompressible flow.

Peaceman found that the pressure calculated for a well block is the same as the flowing pressure at an equivalent radius, r_o, where he defined r_o as "the radius at which the steady-state flowing pressure for the actual well is equal to the numerically calculated pressure for the well block." This definition of r_o gives:

$$P_{wf} - P_o = \frac{q\mu}{2\pi} \ln \frac{r_w}{r_o} . \quad \text{..... (2.6.1)}$$

Using uniform square Cartesian grid-blocks ($\Delta x = \Delta y$), Peaceman showed that if $\Delta x = \Delta y$ and $k_x = k_y$ then:

$$r_o = 0.2\Delta x\,. \quad \text{(2.6.2)}$$

In a subsequent paper, Peaceman[31] derived an expression for r_o for an isotropic reservoir with nonsquare grid blocks:

$$r_o = 0.14(\Delta x^2 + \Delta y^2)^{1/2}\,. \quad \text{(2.6.3)}$$

For an anisotropic reservoir, Peaceman[36] determined that r_o is given by:

$$r_o = \frac{0.28\left[\sqrt{k_y/k_x}\,(\Delta x)^2 + \sqrt{k_x/k_y}\,(\Delta y)^2\right]^{1/2}}{(k_y/k_x)^{1/4} + (k_x/k_y)^{1/4}}\,. \quad \text{(2.6.4)}$$

Palagi's Well Model. In using the HGB grid model, we need an additional well model as Peaceman's well model is formulated only for square grid-blocks. Palagi[32] presented an analytical well model based on Peaceman's work which can be applied to grids of any geometry. This model assumes that the pressure at all grid-blocks that are neighbors of the well block can be evaluated by the radial flow equation around the well. Also, flow is assumed to be radial around the well block despite the location of the well. The wells can be placed in the square and octagonal grid-blocks as illustrated in Fig. 2.6.2. The equation is expressed by:

$$r_o = \exp\left(\frac{\sum_j \left(\frac{b}{d}\right)_{ij} - \theta_{ij}}{\sum_j \left(\frac{b}{d}\right)_{ij}}\right). \quad \text{(2.6.5)}$$

Palagi derived a special case for Eq. 2.6.5 when the polygon of interest has equal sides, where:

$$(b/d)_{ij} = \tan(\pi/N)\,. \quad \text{(2.6.6)}$$

Substituting Eq. 2.6.6 into Eq. 2.6.5 (with θ = 2π) and solving for r_o gives:

$$r_o = d_{ij} \exp\left(\frac{-2\pi}{N \tan(\pi / N)}\right), \quad \text{(2.6.7)}$$

where N is number of sides of the polygonal grid-block containing the well.

2.6.4 IMPLEMENTATION OF HYBRID GRID-BLOCK (HGB) SYSTEM

In employing the HGB grid system, several modifications were made for integrating into Sim2D. Changes occur in the areas of calculating intergrid-block transmissibilities, the grid-block numbering, and the well model.

2.6.4.1 Grid-Block Generation

Grid-block generation involves using a unique grid-block assignment where rectangular grid-blocks are interspersed with octagonal grid blocks. The boundaries are then populated with triangular grid-blocks. Thus, the entire domain will consist of a "structured" grid-block system. This arrangement is shown in Fig. 2.6.3, with the black dots representing the center of each grid block. The fluid will flow to four directions in each of the octagons and two directions in each of the rectangles and triangles.

The basic elements are generated from input data, including the number of grid blocks and the interval length in each direction. Based on this predefined information, parameters such as the total grid blocks, the internal length between each grid block, and the number of flow directions can be calculated.

2.6.4.2 Transmissibility Calculations

Since HGB assumes a block-centered geometry, transmissibility calculations are based upon the distances between the centers of each grid-block. Using Fig. 2.6.4 as an example, Cell 1 is connected to Cell 3 "through" cross-sectional area A13. Its transmissibility can be calculated as follows.

$$T_{13} = \frac{0.00633 k A_{13}}{\Delta L_{13}}. \quad \text{(2.6.8)}$$

2.6.4.3 Grid Numbering and Structure of Matrix Forms.

The structure of the coefficient matrix depends on the dimensions of the problem and the ordering of the grid-blocks. The objective of using different grid-block ordering schemes is to reduce the computational work involved in solving a system of finite-difference equations. Numbering system for the 2D grid and the corresponding non-zero co-efficient in the matrix equation for $AP = B$. Therefore, we should order the points in such a way that the bandwidth is the minimum possible.

Using the HGB model, several numbering systems were tested. Grid numbering is an important factor that controls the matrix coefficient band width.

Fig. 2.6.5 shows a type of "diagonal ordering" where the cells are numbered consecutively along the diagonals starting with the shortest direction, as shown by the direction of the arrows. This method groups the cells by "diagonal count," and increases as we move from the lower left through the grid to the upper right. This is the best numbering system tested, resulting in minimum matrix coefficient band width as shown in Fig. 2.6.6. This matrix coefficient gives us a computing advantage as it requires less arithmetic to solve the matrix equation.

2.6.5 GRID ORIENTATION EFFECT IN RECTANGULAR GRID

Various authors have demonstrated that 2D simulations of immiscible displacements with unfavorable mobility ratio exhibit the grid-orientation effect. Even if the reservoir is isotropic and homogeneous with favorable mobility ratio, there can still be an effect of grid-orientation. To examine this effect, we conducted simulations using Eclipse™ 100 of a quarter five-spot waterflood using parallel and diagonal grid systems, as defined and illustrated in Fig. 2.6.7.

A parallel grid system is a grid that is oriented parallel to injector-producer pairs, a diagonal grid system is oriented at 45° between injector and producer pairs. The distance of a producer to an injector and the size of the grid-blocks are the same for both grid systems. Waterflood simulations were performed for oil/water mobility ratios (M) of 0.5, 1.0, and 10. The input data and the grid sizes are shown in Tables 2.6.1 and 2.6.2. The porosities and permeabilities of the boundary blocks are modified so that a five-spot

pattern can be simulated using a block-centered model. The well index was also modified to reflect these changes.

Since the distance of injector to producer is the same, we expect to get similar recovery performance from both grid systems. However, when we compare the recovery performance of parallel grid-blocks of 8x8 and diagonal of 6x6, the recovery performances from both grid-blocks are different, as seen in Fig. 2.6.8. This is because rotation of the coordinate axes results in differing amounts of truncation error.[25] As pointed out by previous authors, the grid-orientation effect can be reduced by increasing the resolution of the grid-blocks for cases with favorable mobility ratio ($M \leq 1.0$).[11] Thus, we increased the number of grid-blocks in diagonal and parallel grid-blocks at $M = 0.5$. We found that recovery performance is not very sensitive to the number of grid-blocks in the diagonal model. However, as the number of the parallel grid-blocks is increased, the recovery performance changes gradually until it converges to a single recovery curve.

We compared the recovery performances of finer grid-blocks in both models (diagonal 21x21 vs. parallel 29x29). We found that the grid-orientation effect was reduced (Fig. 2.6.9) as the difference in the recovery performance curve between the diagonal 21x21 and parallel 29x29 was reduced, compared to those results from the parallel 8x8 and diagonal 6x6 grid-blocks.

When the mobility ratio is increased to 10, the performance of the diagonal does not follow a certain trend (Fig. 2.6.10). On the other hand, for the parallel grid, the solution does not seem to converge to a single curve even when a large number of grid-blocks were used, as seen in Fig. 2.6.11. Thus, as the grid spacing is refined, the performance of diagonal and parallel models actually diverges for the grid spacings investigated here.

The saturation map for diagonal grid model shows viscous fingering at the saturation front while the parallel model also shows a distorted front (Fig. 2.6.12).

Based on this study, we can conclude that grid refinement can help to minimize the grid-orientation effect when we have favorable mobility ratios, of M=1 or less. However, at an unfavorable mobility ratio of M=10 for displacement problems as shown, neither the parallel nor diagonal orientation can be used reliably.

2.6.6 PERFORMANCE OF HGB MODEL

Examples of problems are presented to validate the Sim2D simulator, illustrate of the grid-orientation effects in conventional Cartesian grid, and to show the application of HGB model. Whenever possible, the Sim2D solution is compared with a commercially available black oil simulator from GeoQuest and Eclipse. Single-point upstream weighting of mobility and IMPES solution mode were used in all runs.

To test the viability of the HGB grid, we developed a 2D IMPES simulator and incorporated an HGB grid. Since the HGB grid cannot be validated directly with any commercial simulators, we validated the Cartesian grid model in Sim2D with rectangular Cartesian grid models in Eclipse as shown in an earlier section. Once the algorithm was validated, we applied it to the HGB grid.

2.6.6.1 Program Validation

The example case is based on a conventional 2D reservoir model grid of 5x5. The two-phase model contains one producer and one injector well. Both injector and producer are under a constant-rate constraint. The well is rate constrained to a 100-scf/day oil production. The reservoir is homogeneous and is initially at 5,000 psi of undersaturated oil and connate water.

The simulation was run until the minimum bottomhole pressure (BHP) of 2,000 psi is reached. Other reservoir and simulation data is shown in Table 2.6.3 and Fig. 2.6.13. The oil and water rates as well as the water-cut performance are shown in Fig. 2.6.14 while the Sim2D pressure solutions are presented in Figs. 2.6.15 to 20 along with the results of the same problem runs on ECL™ 100.

2.6.6.2 Use of HGB Grid to Reduce the Grid Orientation Effect

Using the HGB scheme, one-half of a five-spot model with a four-well, diagonal HGB grid (145 grid-blocks), and one-quarter of a five-spot pattern model were chosen to run a two-well, parallel HGB grid (85 grid-blocks) as defined and shown in Fig. 2.6.21.

The reservoir is assumed to be homogeneous and isotropic. Additional rock and fluid properties as well as relevant simulation data are given in Table 2.6.4. Other reservoir and simulation data is shown in Fig. 2.6.13. Mobility ratios of 0.5, 1.0, 10.0 and 50.0

were used in these cases. Porosity and permeability modifications were also performed on the boundary blocks so that the five-spot pattern could be simulated. The locations of the injectors and producers coincide with the locations of the block centers. The well model is also modified to reflect this.

From Fig. 2.6.22, we can see that the parallel and diagonal HGB grid model give very similar results for both the favorable and unfavorable mobility ratios cases. This is because flow can progress in several different directions in the octagonal grid-blocks. The result is that the differences between the parallel and diagonal orientation are greatly reduced. The parallel HGB grid always predicted a higher areal sweep efficiency than the diagonal HGB grid. At lower mobility ratios, the pore volume recovered is higher as the sweep mimics a piston-like displacement. Even so, the discrepancies between these two grids in HGB have a maximum relative difference of approximately 6% (Table 2.6.5) and it is believed to be caused by the presence of the square grid-blocks.

Figs. 2.6.23 to 24 show the saturation distribution map for the parallel and diagonal HGB grid, respectively. The movement of the saturation front is faster when the mobility ratio increases because the displacing fluid is moving at a much higher velocity than oil, the displaced fluid. Fingering of the displacing fluid also results in faster breakthrough times. This result shows that HGB can significantly reduce the grid-orientation effect by reducing the rotational variance in the model, and hence the differences in results between the parallel and diagonal HGB grids.

2.6.6.3 HGB Sensitivity

In the previous example, we showed that the HGB grid is less sensitive to grid-orientation than the conventional Cartesian grid, especially at unfavorable mobility ratios. The next point for investigation is the sensitivity of the HGB grid to the grid dimension, or in other words, its sensitivity to the number of grid subdivisions in the model. We have seen that in Cartesian grids, the parallel grid is more sensitive to the effect of grid size than the diagonal grid. We also show how the performance of the HGB grid compares to the Cartesian grid at a similar number of grid-blocks.

Four different sets of grid numbers were run in HGB (diagonal HGB and parallel HGB) and the results compared to similar models run in Cartesian grid (diagonal

Cartesian and parallel Cartesian). Since the size of each grid-block in the HGB model is dependent upon its shape, i.e. whether it is octagonal or rectangular, an average area per grid-block is calculated for each set of runs. The closest possible average area per grid-block and the number of grid-blocks are then applied to the corresponding Cartesian grid.

For a given set of grid dimension, HGB and its Cartesian grid counterpart have the same pore volume and well locations. Furthermore, since we have shown that the grid-orientation effect can be reduced by refining the grid at a lower mobility ratio, all these cases are run at $M = 0.5$. The reservoir and rock properties are similar to those shown in Fig. 2.6.13 and Table 2.6.4.

Fig. 2.6.25 shows an example of the calculated performance for the HGB grids and their corresponding Cartesian grids. Results using the HGB grids are always in between those calculated on Cartesian grids. However, the differences between the diagonal HGB and parallel HGB were reduced as the number of grid blocks in the model increased. In fact, the performances of the parallel and diagonal HGB grid models tend to converge as the grid spacing is refined.

Likewise, the differences between diagonal Cartesian and parallel Cartesian plots are reduced as a smaller grid dimension is used. As we have shown in the previous section, at low mobility ratios, i.e., $M = 0.5$, the diagonal Cartesian grid is insensitive to the number of grid-blocks in the model. In contrast, when more refined grid blocks are used in the parallel Cartesian grid, oil recovery increased and the results converged to a single recovery curve after an increase in a certain number of grid blocks.

The results between the HGB and Cartesian grid models are summarized in Table 2.6.6. For reasons mentioned earlier, these two models are compared at a similar averaged area per grid block. As the number of grid blocks is increased and the size of grid blocks is reduced, we can see that both models give a smaller relative difference in pore volume recovered between the parallel and diagonal grid than when coarser grids are used. More importantly, the HGB grid performs better by consistently giving a smaller relative difference in pore volume recovered than the Cartesian grid at similar average area per grid block for all the cases studied. This indicates that the HGB is more effective in reducing the grid-orientation error than the conventional Cartesian grid.

Results of simulation runs at M=0.5 are summarized in Figs. 2.6.26 and 2.6.27 for the parallel and diagonal HGB grid, respectively. Performance of the parallel HGB grid is not sensitive to the number of grid blocks in the model, as all four models give similar results. On the other hand, oil recovery predicted by the diagonal HGB model increased as the number of grid blocks increased, and the results converged when the number of grid blocks reached 200 and higher.

2.6.7 DISCUSSION

We have shown the effect of grid-orientation in conventional Cartesian parallel and diagonal grids. Also, we have successfully developed the HGB grid system and we have shown that HGB is more effective in reducing the grid-orientation effect than the Cartesian grid. This is attributed to the increase of flow connections in the octagonal grid-blocks of HGB grid. On the other hand, the increase in flow connections also means that there would be more terms to solve, and this would increase the computational time compared to Cartesian grid. Moreover, the construction and numbering or indexing of the HGB grid is not as intuitive as the Cartesian grid. Extension of the HGB grid to a 3D model would also be a challenging task. However, we would recommend the use of the HGB grid for simulations of displacement problems especially at unfavorable mobility ratios.

2.6.8 CONCLUSIONS

The following conclusions can be derived from this study:

1. The grid orientation effect was observed in rectangular Cartesian grid models even in an isotropic, homogeneous reservoir of M = 1.0.
2. Based on this study, grid refinement can help to reduce the grid-orientation effect in rectangular Cartesian grid models when there are favorable mobility ratios, i.e. M=1.0 or less. However, at an unfavorable mobility ratio of M=10.0, we found that neither parallel nor diagonal orientation can be used reliably. This is because as the number of grid blocks is increased, the performance of diagonal and parallel models actually diverges for the grid spacings investigated in this study.

3. With the increased number of connections in the octagonal grid-blocks in the HGB grid compared to the Cartesian grid, HGB is able to reduce the grid-orientation effect even for unfavorable mobility ratio displacement problems (M = 10.0), with maximum relative difference of 6% in pore volume recovered between parallel and diagonal HGB grid models for all the cases run. However, the grid-orientation effect in the HGB model is believed to be caused by the presence of the square grid-blocks.
4. Contrary to the Cartesian parallel grid, HGB parallel grid is less sensitive to the number of grid-blocks in the model compared to the HGB diagonal grid for M = 0.5. Also, at a favorable mobility ratio of M = 0.5, the performance of the parallel and diagonal HGB grid models converged as the number of grid-blocks is increased.
5. The HGB grid performs better by consistently giving a smaller relative difference between the HGB parallel grid and the HGB diagonal grid in pore volume recovered (6.0, 4.5, 3.3, and 2.2%) compared to the relative difference between the Cartesian parallel grid and the Cartesian diagonal grid in pore volume recovered (17.0, 13.0, 9.3, 7.9%) at similar averaged area per grid-block for all four comparison cases studied. This indicates that the HGB is more effective in reducing the grid-orientation error than the conventional Cartesian grid.

NOMENCLATURES

A = cross-sectional area

b_{ij} = length of one equal side of polygon

d_{ij} = distance between the centers of neighboring grid-blocks i and j

i = center of grid-block containing the well

j = center of grid-block that is neighbor of well block i

k = absolute permeability

k'_r = end-point relative permeability

ΔL = length between two adjacent centroids

M = Mobility ratio

N = number of equal sides

P_{wf} = wellbore flowing pressure

P_o = oil pressure

q = flow rate

r_o = effective wellbore radius

r_w = wellbore radius

S = saturation

T = transmissibility

VP = pore volume

Δx = size of block in x-direction

Δy = size of block in y-direction

μ = viscosity

ϕ = porosity

θ_{ij} = 2π for a well located in the center of the block

Subscripts

inj =injection

o = oil

w = water

x = x-direction

y = y-direction

REFERENCES

1. Pedrosa, O.A. and Aziz, K.: "Use of Hybrid Grid in Reservoir Simulation", paper SPE 13507, presented at the 1985 SPE Symposium on Reservoir Simulation, Dallas, Texas, 10-13 February.
2. Nacul, E.C.: Use of Domain Decomposition and Local Grid Refinement in Reservoir Simulation, Ph.D. Dissertation, Stanford University, Palo Alto, California (March 1991).
3. Ding, Y. and Lemonnier, P.: "Use of Corner Point Geometry in Reservoir Simulation", paper SPE 29933 presented at the 1995 International Meeting on Petroleum Engineering held in Beijing, PR China, 14 -17 Nov..

4. Peaceman, D.W.: “Calculation of Transmissibilities of Grid blocks Defined by Arbitrary Corner Point Geometry”, paper SPE 37306 presented at the 1996 SPE Reservoir Simulation Symposium, New Orleans, Louisiana, 31 Jan - 3 Feb.
5. Heinemann, Z.E. and Brand, C.W.: “Modeling Reservoir Geometry with Irregular Grids”, paper 18412 presented at the 1989 SPE Symposium on Reservoir Simulation, Houston, Texas, 6-8 February.
6. Palagi, C.L. and Aziz, K.: “Use of Voronoi Grid in Reservoir Simulation”, paper SPE 22889 presented at the 1991 SPE Reservoir Simulation Symposium held in New Orleans, Louisiana, 31 Jan - 3 Feb.
7. Gunasekera, D., Cox, J. and Lindsey, P.: “The Generation and Application of K-Orthogonal Grid Systems”, paper SPE 37998 presented at the 1997 SPE Symposium on Reservoir Simulation, Dallas, Texas, 8-11 June.
8. Kocberber, S.: “An Automatic, Unstructured Control Volume Generation System for Geologically Complex Reservoirs”, paper SPE 38001 presented at the 1997 SPE Symposium on Reservoir Simulation, Dallas, Texas, 8-11 June.
9. Aavatsmark, I., Barkve, T., Boe, O., and Mannseth, T.: “Discretization on Nonorthogonal, Quadrilateral Grids for Inhomogeneous, Anisotropic Media”, J. Computational Physics (1996) 127, 2-14.
10. Verma, S. and Aziz, K.: “A Control Volume Scheme for Flexible Grids in Reservoir Simulation”, paper SPE 37999 presented at the 1997 SPE Symposium on Reservoir Simulation, Dallas, Texas, 8-11 June.
11. Todd, M.R., O’Dell, P.M. and Hirasaki, G.J.: “Methods for Increased Accuracy in Numerical Simulation”, paper SPE 3516 presented at the 1971 PE Annual Fall Meeting, New Orleans, Louisiana, 3-6 October.
12. Holloway, C.C., Thomas, L.K., and Pierson, R.G.: “Reduction of Grid Orientation Effects in Reservoir Simulation”, paper SPE 5522 presented at the 1975 Annual Fall Meeting of the Society of Petroleum Engineers of AIME, Dallas, Texas, 28 September 28 – 1 October.
13. Frauenthal, J.C., Rolaud, B. and Towler, B.F.: “Reduction of Grid-Orientation Effects in Reservoir Simulation with Generalized Upstream Weighting”, paper SPE 11593

presented at the 1983 SPE Symposium on Reservoir Simulation, San Francisco, California, 15-18 November.

14. Vinsome, P.K. and Au A.K.: “One Approach to the Grid Orientation Problem in Reservoir Simulation,” paper SPE 8247 presented at the 1979 Annual Fall Technical Conference and Exhibition of the Society of Petroleum Engineers of AIME, Los Angeles, California, 23-26 September.
15. Yanosik, J.L. and McCracken, T.A.: “A Nine-Point, Finite-Difference Simulator for Realistic Prediction of Adverse Mobility Ratio Displacements”, paper SPE 5734 presented at the 1976 SPE-AIME Symposium of Numerical Simulation of Reservoir Performance, Los Angeles, California, 19-20 February.
16. Ko, S.C.M. and Au, A.D.K.:“A Weighted Nine-Point Finite-Difference Scheme for Eliminating the Grid Orientation Effect in Numerical Reservoir Simulation”, paper SPE 8248 presented at the 1979 SPE Annual Fall Meeting, Las Vegas, Nevada, 23-26 September.
17. Coats, K.H. and Modine, A.D.: “A Consistent Method for Calculating Transmissibilities in Nine-Point Difference Equations”, paper SPE 12248 presented at the 1983 Reservoir Simulation Symposium, San Francisco, California, 15-18 November.
18. Shah, P.C.: “A Nine-Point Finite Difference Operator for Reduction of the Grid Orientation Effect,” paper SPE 12251 presented at the 1983 Reservoir Simulation Symposium, San Francisco, California, 15-18 November.
19. Ostebo, B. and Kazemi, H: “Mixed Five-Point/Nine-Point Finite-Difference Formulation of Multiphase Flow in Petroleum Reservoirs”, paper SPE 21227 presented at the 1991 Reservoir Simulation Symposium, Anaheim, California, 17-20 February.
20. Shiralkar, G.S. and Stephenson, R.E.: “A General Formulation for Simulating Physical Dispersion and a New Nine-Point Scheme”, paper SPE 16975 presented at the 1987 Annual Technical Conference and Exhibition, Dallas, Texas, 27-30 September.
21. Vinsome, P.K. and Au A.K.: “One Approach to the Grid Orientation Problem in Reservoir Simulation,” paper SPE 8247 presented at the 1979 Annual Fall Technical

Conference and Exhibition of the Society of Petroleum Engineers of AIME, Los Angeles, California, 23-26 September.

22. Brand, C.W., Heinemann, J.E., and Aziz, K.: "The Grid Orientation Effect in Reservoir Simulation", paper SPE 21228 presented at the 1991 SPE Symposium on Reservoir Simulation, Anaheim, California, 17-20 February.
23. Chen, W.H. and Durlofsky, L.J.: "Minimization of Grid Orientation Effects Through Use of Higher-Order Finite Difference Methods", paper SPE 22887 presented at the 1991 Annual Technical Conference and Exhibition, Dallas, Texas, 6-9 October.
24. Pinto A.C.C. and Correa, A.C.F.: "High-Resolution Schemes for Conservation Laws: Applications to Reservoir Engineering," paper SPE 24262 presented at the 1992 European Petroleum Computer Conference, Stavanger, Norway, 25-27 May.
25. Wolcott, D.S., Kazemi, H., and Dean, R.H.: "A Practical Method for Minimizing the Grid Orientation Effect in Reservoir Simulation", paper SPE 36723 presented at the 1996 Annual Technical Conference and Exhibition, Denver, Colorado, 6-9 October.
26. Shin, D. and Merchant, A.R.: "Higher-Order Flux Update Function Method for Reduction of Numerical Dispersion and Grid Orientation Effect in Reservoir Simulation", paper SPE 25600 presented at the 1993 Middle East Oil Technical Conference and Exhibition, Bahrain, 3-6 April.
27. Pruess, K. and Bodvarsson, G.S.: "A Seven-Point Finite Difference Method for Improved Grid Orientation Performance in Pattern Steamfloods," paper SPE 12252 presented at the 1983 Reservoir Simulation Symposium, San Francisco, California, 15-18 November.
28. Heinemann, Z.E. and Brand, C.W.: "Modeling Reservoir Geometry with Irregular Grids", paper 18412 presented at the 1989 SPE Symposium on Reservoir Simulation, Houston, Texas, 6-8 February.
29. Mattax, C.C. and Dalton R.L.: Reservoir Simulation, Monograph #13, SPE, Richardson, Texas (1990).
30. Peaceman, D.W.: "Interpretation of Well-Block Pressures in Numerical Reservoir Simulation", paper SPE 6893 presented at the 1977 SPE-AIME Annual Fall Technical Conference and Exhibition, Denver, Colorado, 9-12 Oct.

31. Peaceman, D.W.: "Interpretation of Well-Block Pressures in Numerical Reservoir Simulation with Nonsquare Grid Blocks and Anisotropic Permeability", paper SPE 10528 presented at the 1982 SPE Reservoir Simulation Symposium New Orleans, Louisiana, 31 Jan - 3 Feb.
32. Palagi, C.L.: Generation and Application of Voronoi Grid to Model Flow in Heterogeneous Reservoirs, Ph.D. Dissertation, Stanford University, Palo Alto, California, (May 1992).

Table 2.6.1 – Reservoir Parameters for Rectangular Grid

Properties	Values
Rock Permeability, k, mD	100
Porosity, ϕ, fraction	0.20
Net Pay Thickness, ft	10
Producer-Injector Distance, ft	≈ 933.4
Production Rate, q_o, STB/D	18
Injection Rate, q_w, STB/D	18
Initial Pressure, psi	5000
Area of Reservoir (Parallel), acres	20
Area of Reservoir (Diagonal), acres	10

Table 2.6.2 – Grid Sizes Used in Rectangular Grid Models

Diagonal Grid	Grid Block Size (Δx=Δy)	Parallel Grid	Grid Block Size (Δx=Δy)
6 x 6	132.0 ft	8 x 8	133.34 ft
11 x 11	66.0 ft	15 x 15	66.67 ft
21 x 21	33.0 ft	29 x 29	33.36 ft
41 x 41	16.5 ft	57 x 57	16.67 ft

Table 2.6.3 – Reservoir Data for HGB Grid

Properties	Values
Area of Reservoir, ft^2	50000
Grid Block Dimension, $\Delta x = \Delta y$ (ft)	100
Reservoir Thickness (ft)	10
Permeability (mD)	100
Porosity	0.20
Initial Water Saturation	0.20
Initial Oil Saturation	0.80
Well Radius (ft)	0.33
Initial Pressure (psi)	5000
Minimum Bottomhole Pressure (psi)	2000
Rock Compressibility (1/psi)	3E-06

Table 2.6.4 – Data Used for HGB Pattern Simulations

Properties	Values
Rock Permeability, k, mD	100
Porosity, ϕ, fraction	0.20
Net Pay Thickness, ft	10
Producer-Injector Distance, ft	825
Production Rate, q_o, STB/D	18
Injection Rate, q_w, STB/D	18
Initial Water Saturation, S_{wi}, fraction	0.20
Initial Oil Saturation S_{oi}, fraction	0.80
Initial Pressure, psi	5000
Area of Reservoir (Parallel), acres	15
Area of Reservoir (Diagonal), acres	7.5

Table 2.6.5 – Relative Difference Between Parallel and Diagonal Grid for Both HGB and Cartesian Grids at *M* = 0.5

M	Relative Difference (%)
50.0	5.92
10.0	4.59
1.0	2.24
0.5	1.11

Table 2.6.6 – Relative Difference Between Parallel and Diagonal Grid for Both HGB and Cartesian Grids at *M* = 0.5

	Averaged area per grid-block (ac)		Relative Difference in Pore Volume Recovered (%)
	Diagonal	Paralel	
HGB Grid	0.159 (98)*	0.156(50)*	6.0
	0.078 (200)	0.080 (98)	4.5
	0.040 (392)	0.039 (200)	3.3
	0.020(800)	0.020 (392)	2.2
Cartesian Grid	0.156 (100)	0.159 (49)	17.0
	0.080 (196)	0.078 (100)	13.0
	0.039 (400)	0.040 (196)	9.3
	0.020 (784)	0.020 (400)	7.9

* number in bracket indicates the number of grid-blocks used

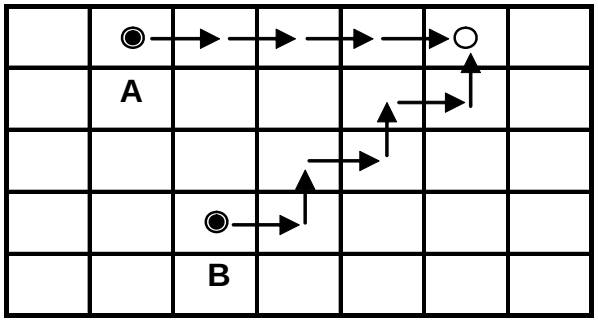

Fig. 2.6.1 – Flow paths for parallel and diagonal flow in a Cartesian grid (after Mattax and Dalton)[11].

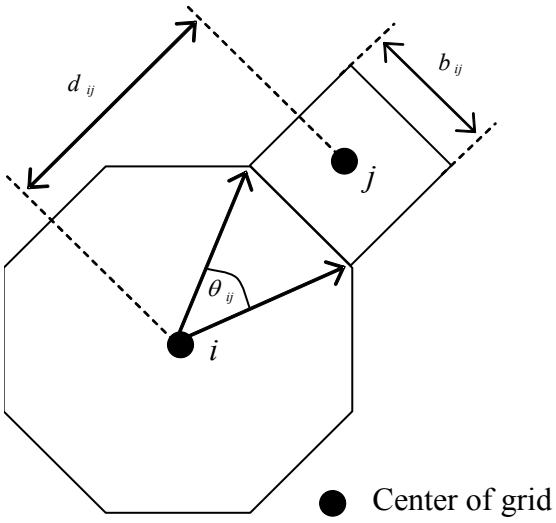

Fig. 2.6.2 – Well model for a polygon.

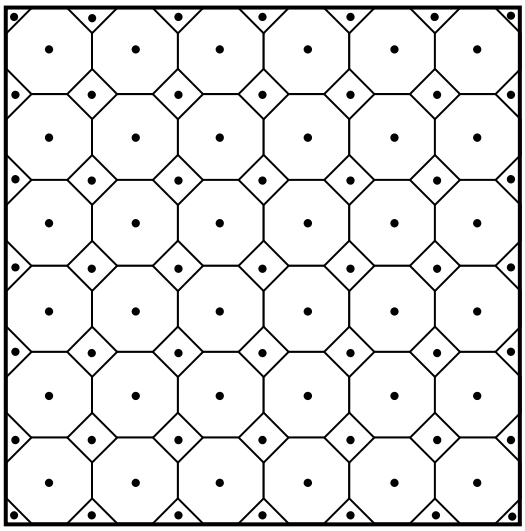

Fig. 2.6.3 – HGB grid model.

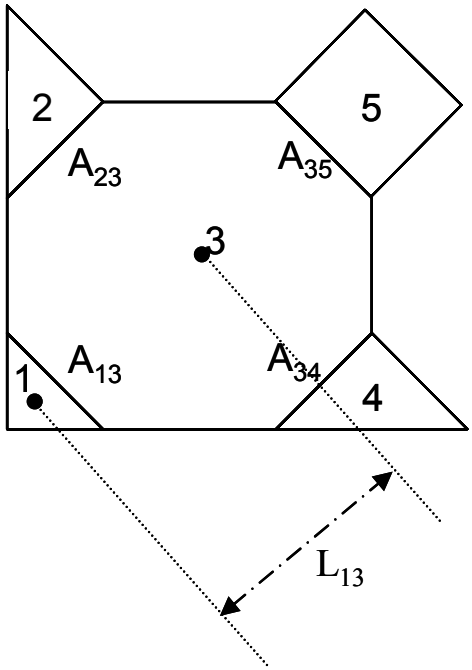

Fig. 2.6.4 – Example of transmissibility calculations in HGB.

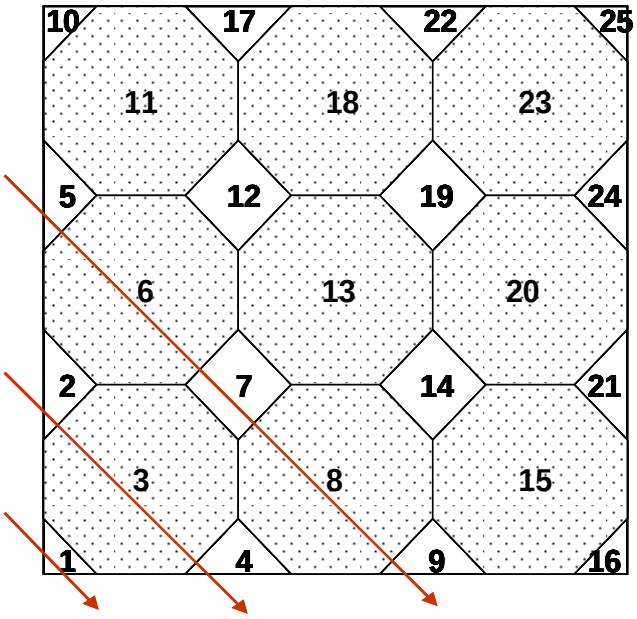

Fig. 2.6.5 – Diagonal ordering of grid-blocks to reduce band width.

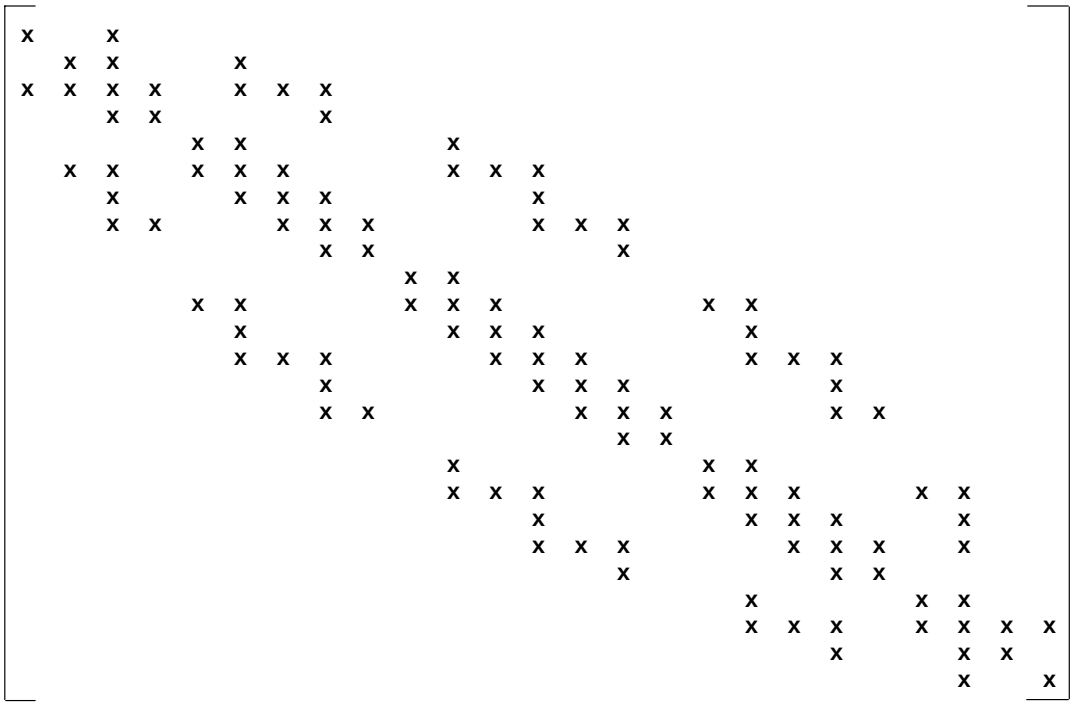

Fig. 2.6.6 – Locations of matrix elements for diagonal ordering.

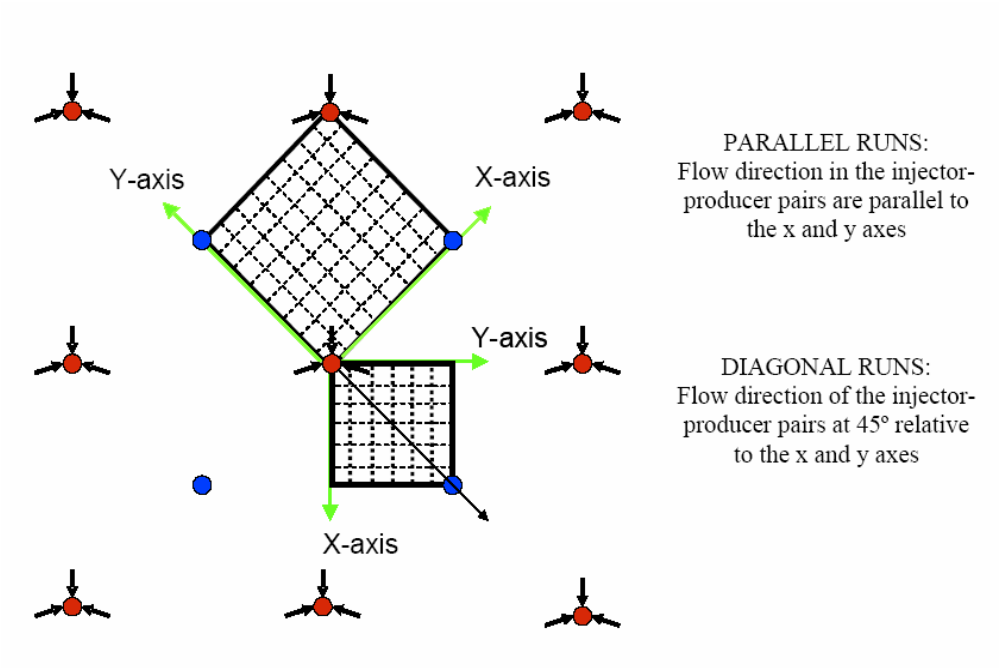

Fig. 2.6.7 – Parallel and diagonal orientation for simulations of waterflooding in five-spot symmetry elements

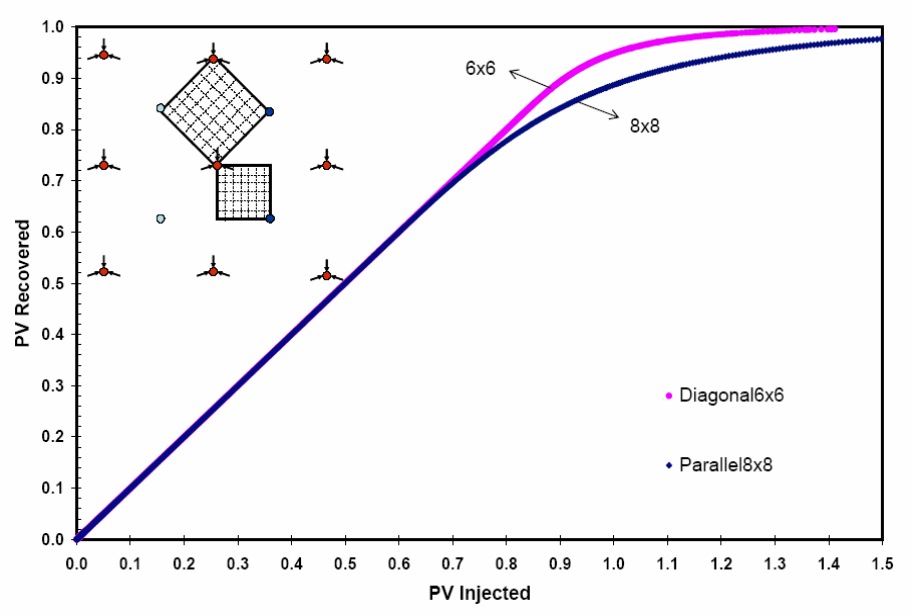

Fig. 2.6.8 – M = 0.5 coarse grid

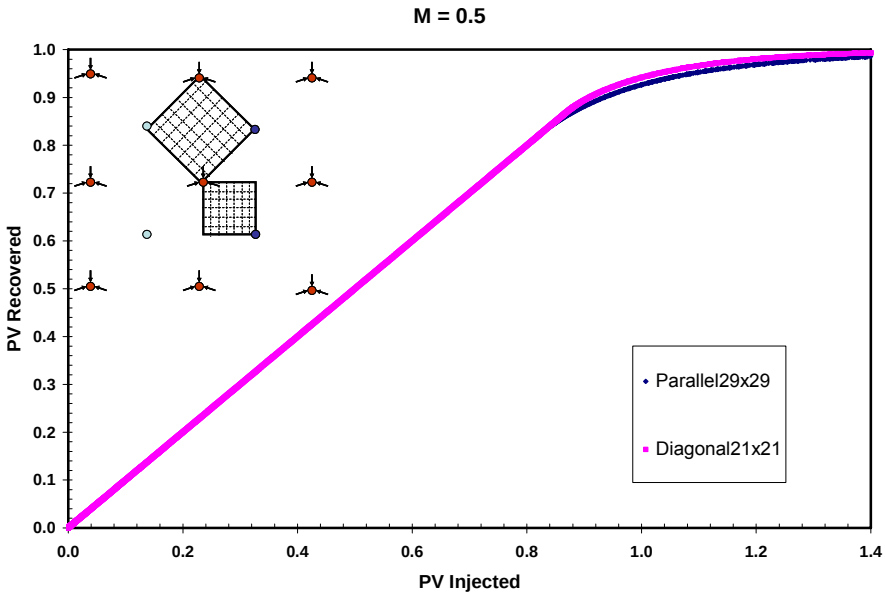

Fig. 2.6.9 – M = 0.5 fine grid

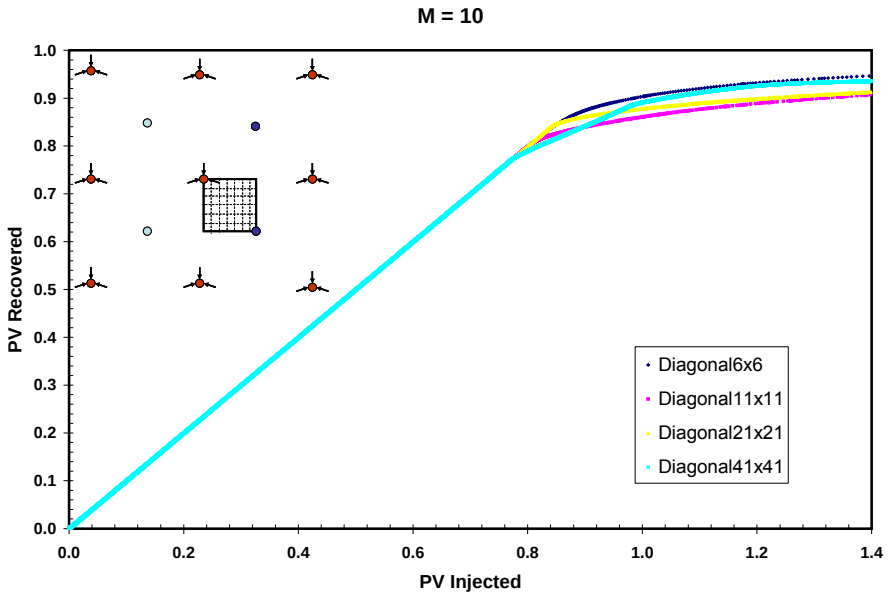

Fig. 2.6.10 – M = 10 diagonal

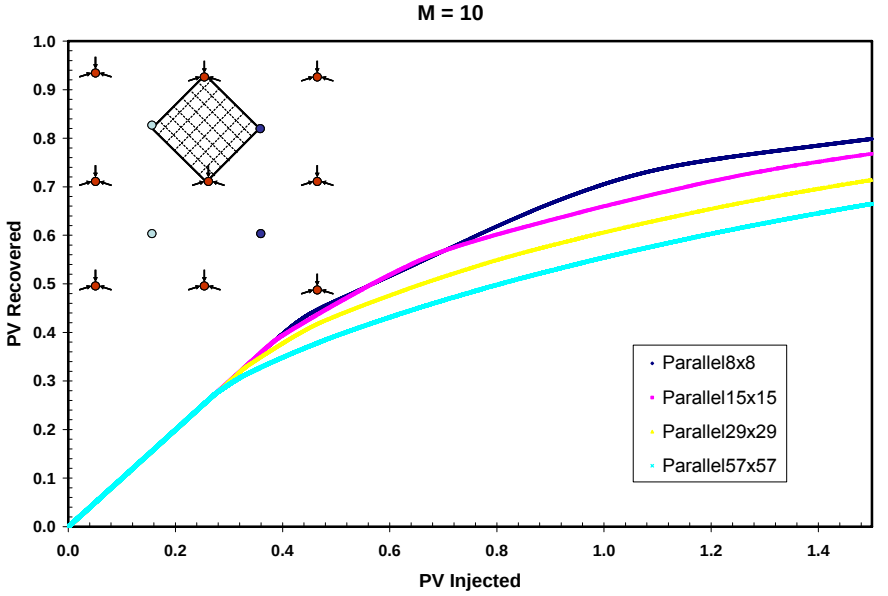

Fig. 2.6.11 – M = 10 parallel

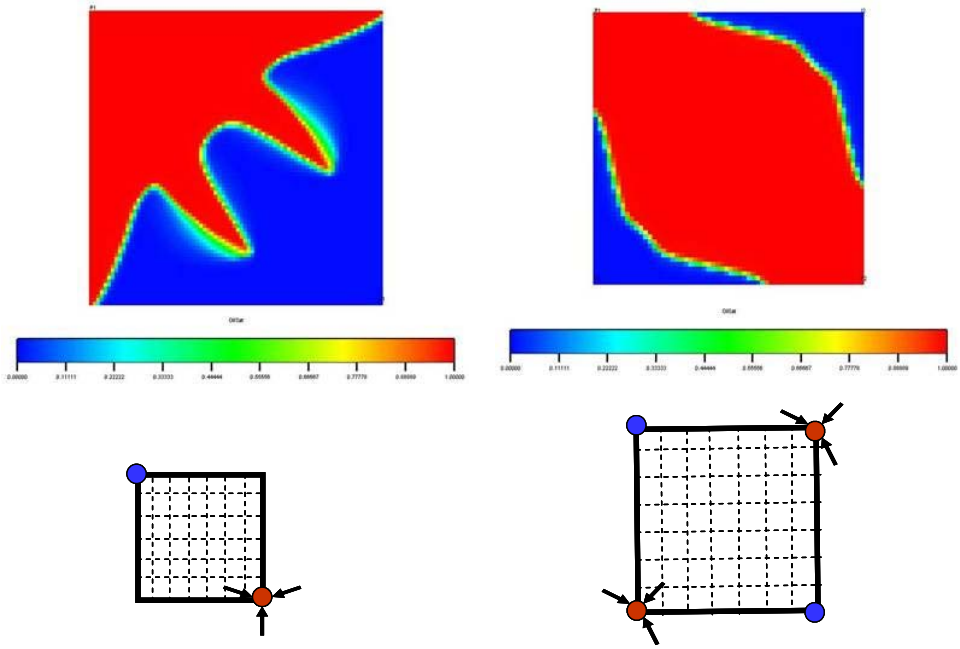

Fig. 2.6.12 – Saturation distribution map for (a) diagonal model, and (b) parallel model at PV_{inj} = 1.0 for M = 10.

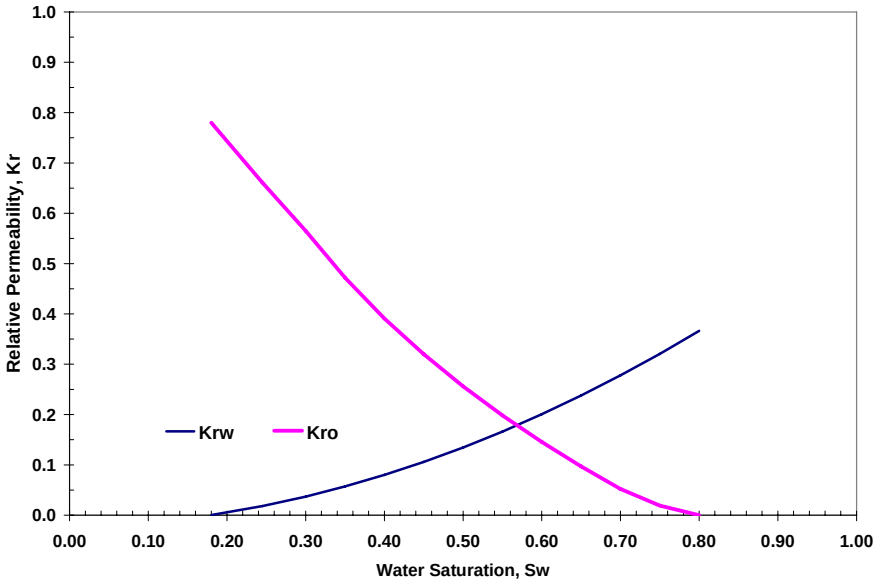

Fig. 2.6.13 – Relative permeability curve.

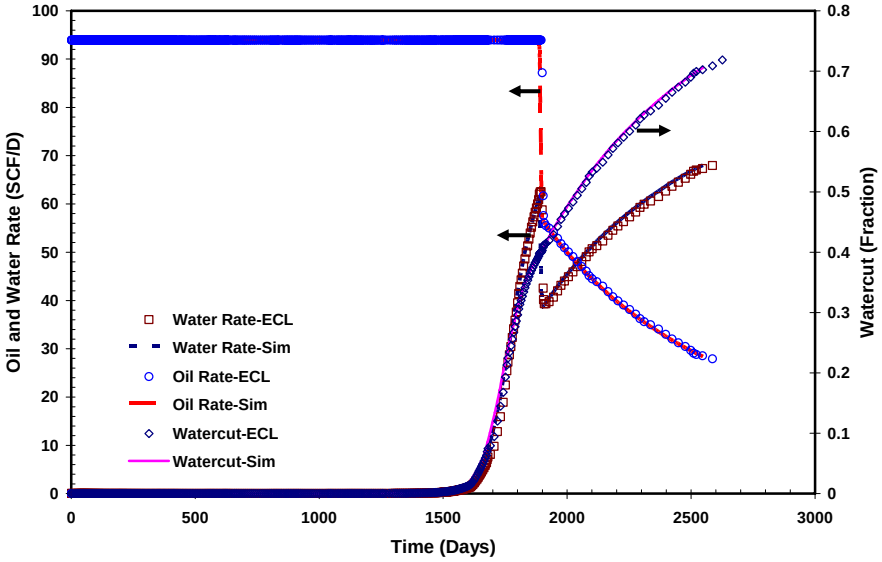

Fig. 2.6.14 –Comparison of Sim2D oil and water rates and watercut with ECL™ 100 showing good agreement the two simulators.

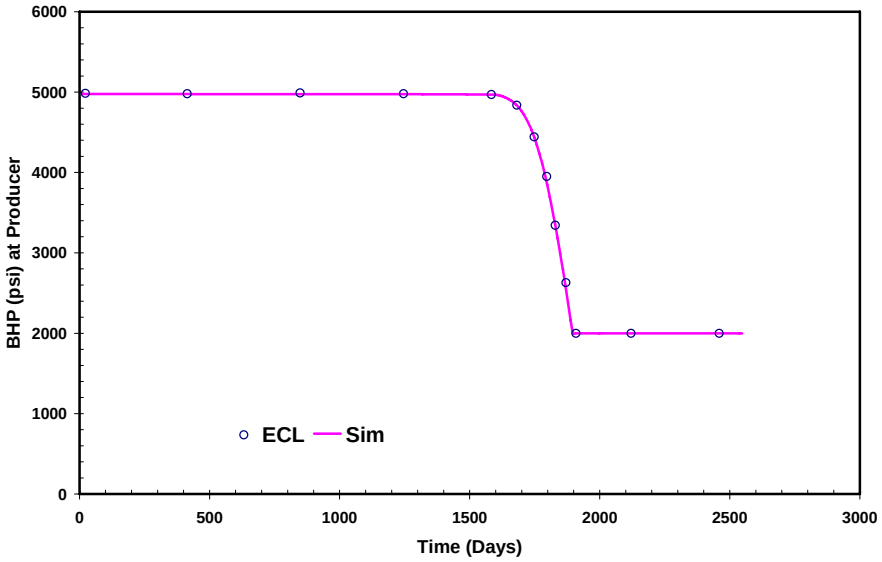

Fig. 2.6.15 – Comparison of Sim2D well bottomhole pressure at producer with ECL™ 100.

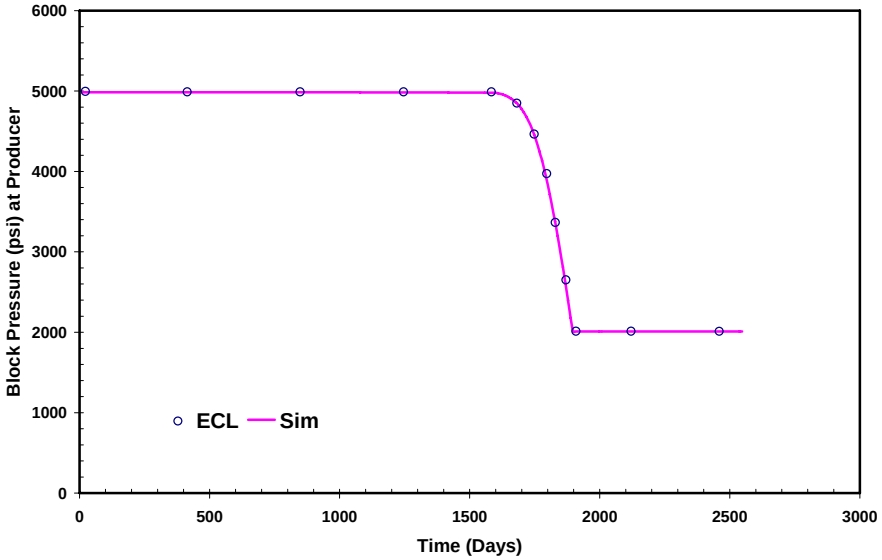

Fig. 2.6.16 – Comparison of Sim2D well block pressure at producer with ECL™ 100.

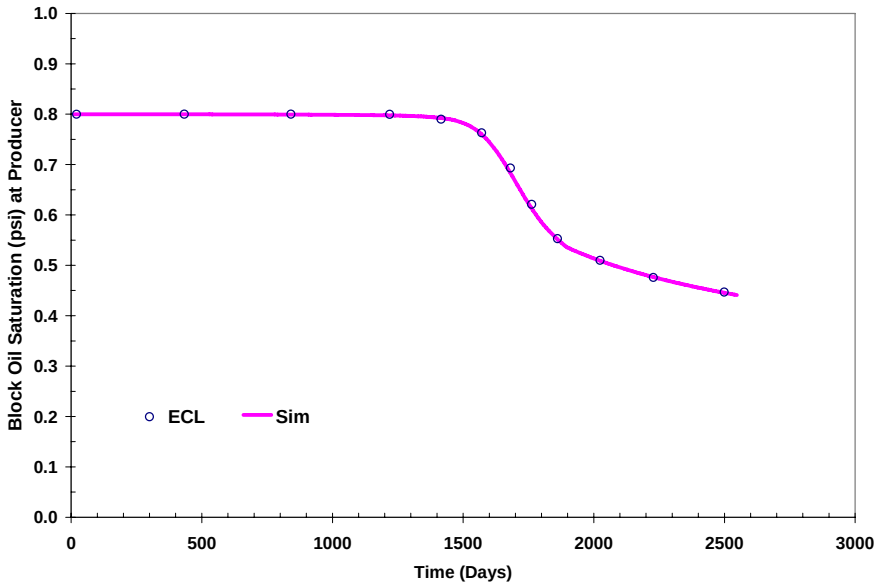

Fig. 2.6.17 – Comparison of Sim2D well block oil saturation at producer with ECL™ 100.

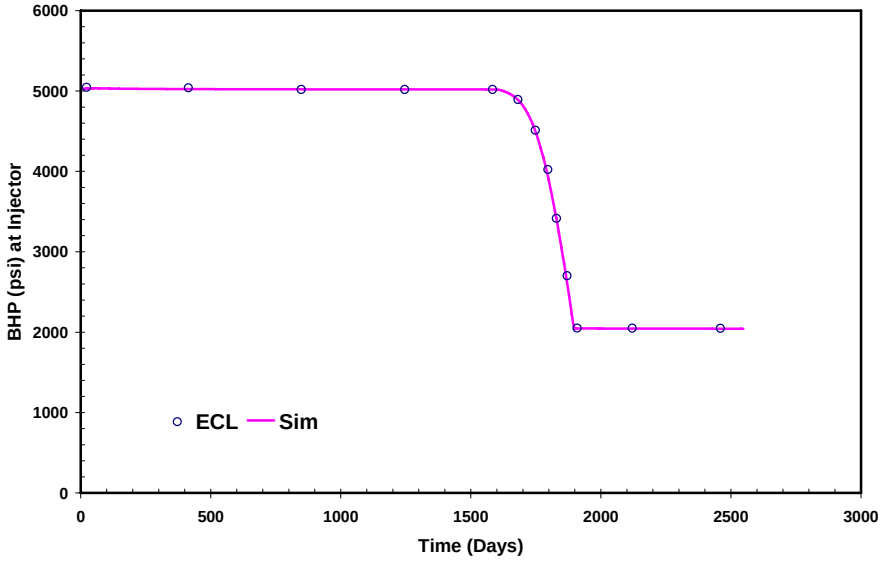

Fig. 2.6.18 – Comparison of Sim2D well bottomhole pressure at injector with ECL™ 100.

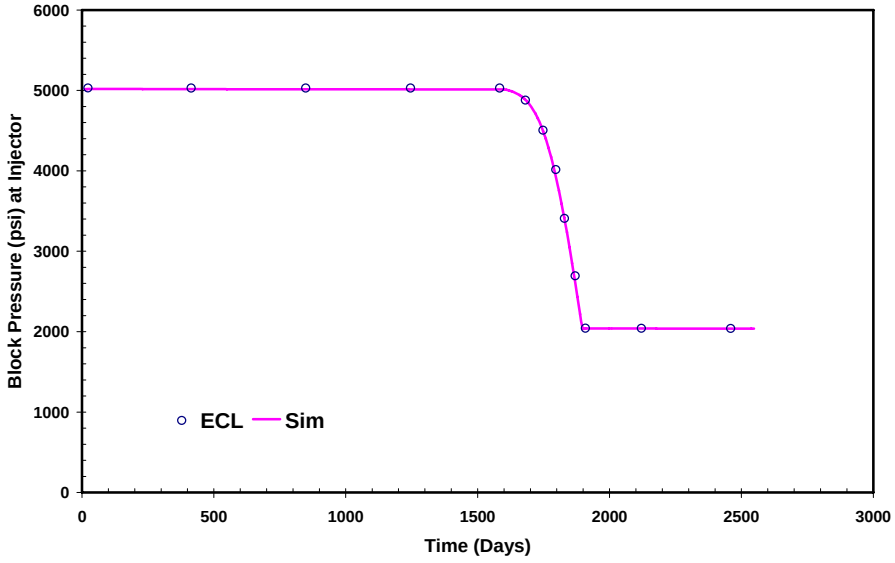

Fig. 2.6.19 – Comparison of Sim2D well block pressure at injector with ECL™ 100.

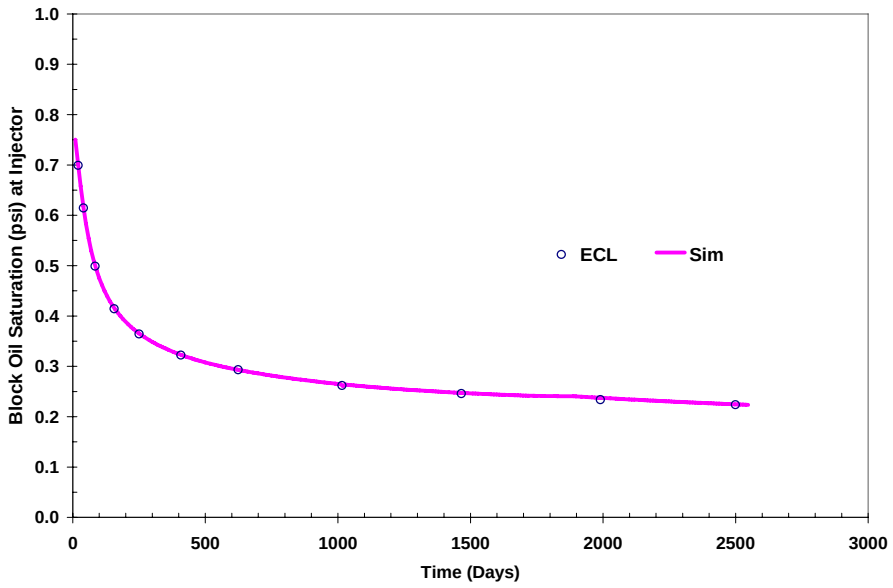

Fig. 2.6.20 – Comparison of Sim2D well block oil saturation at injector with ECL™ 100.

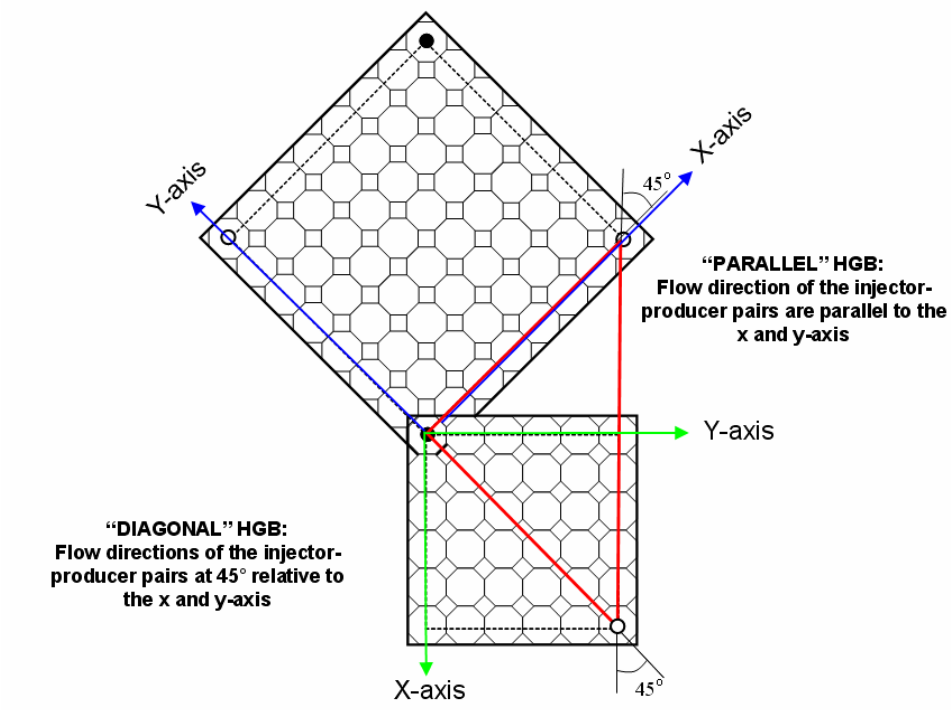

Fig. 2.6.21 – (a) Parallel and (b) diagonal grid-orientation in HGB grid.

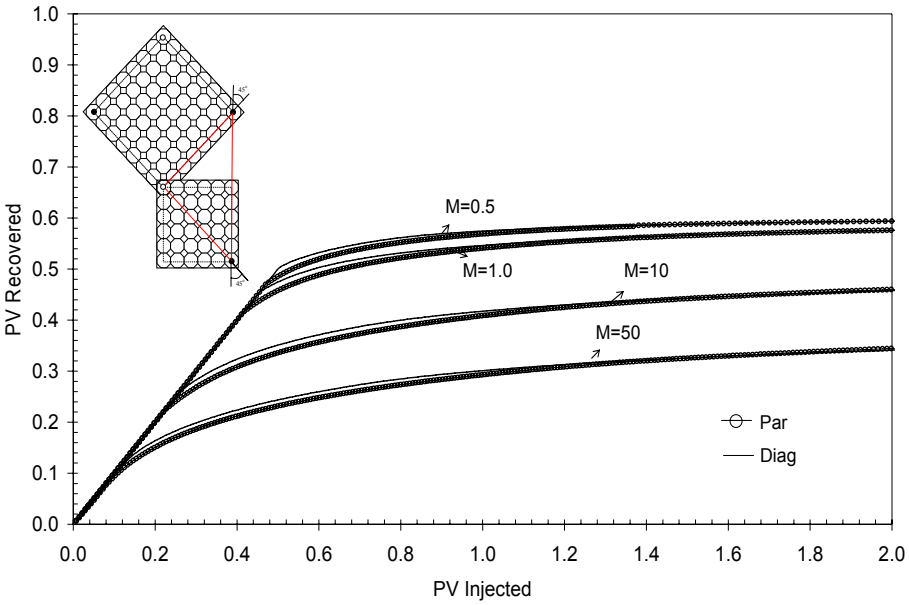

Fig. 2.6.22 – Influence of mobility ratios on the predicted performance of HGB grid.

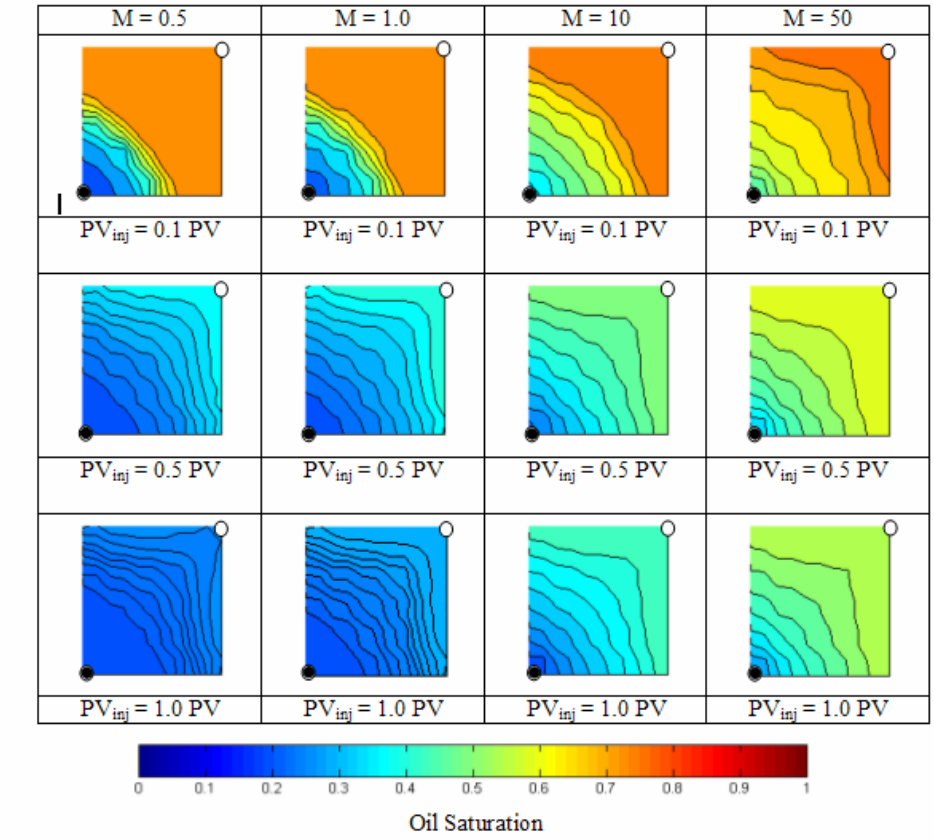

Fig. 2.6.23 – Saturation distribution map for diagonal HGB grid as shown in Fig. 2.6.21 (b) at various mobility ratios.

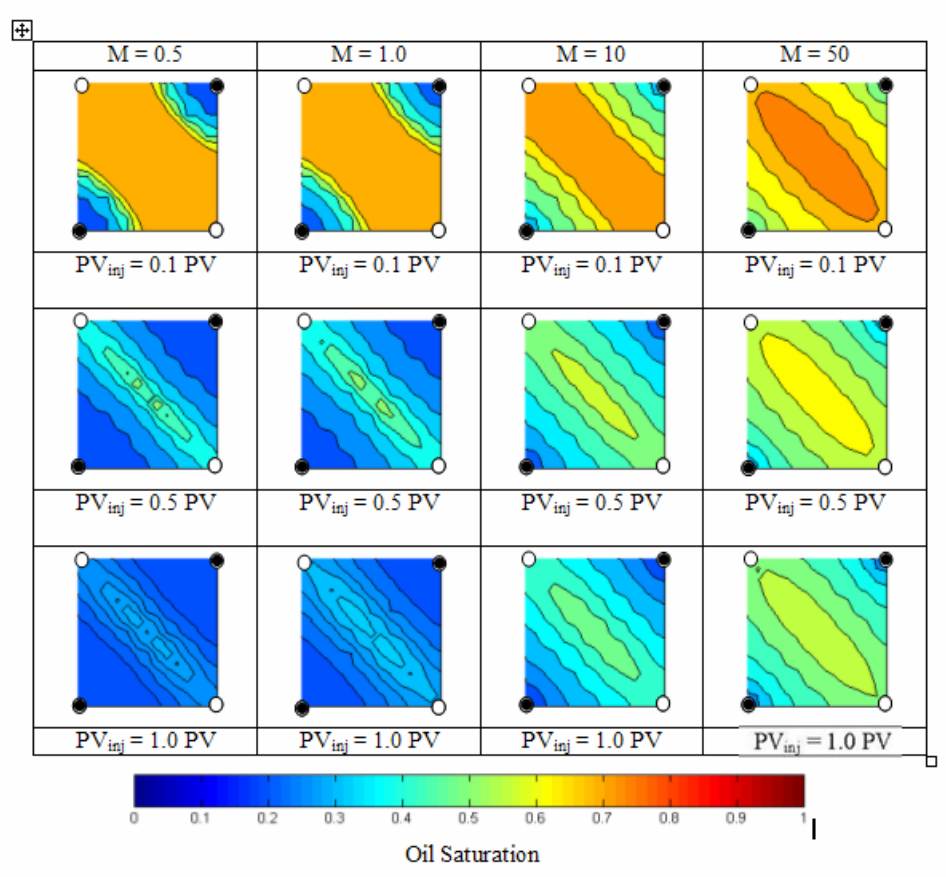

Fig. 2.6.24 – Saturation distribution map for parallel HGB grid as shown in Fig. 2.6.21 (a) at various mobility ratios.

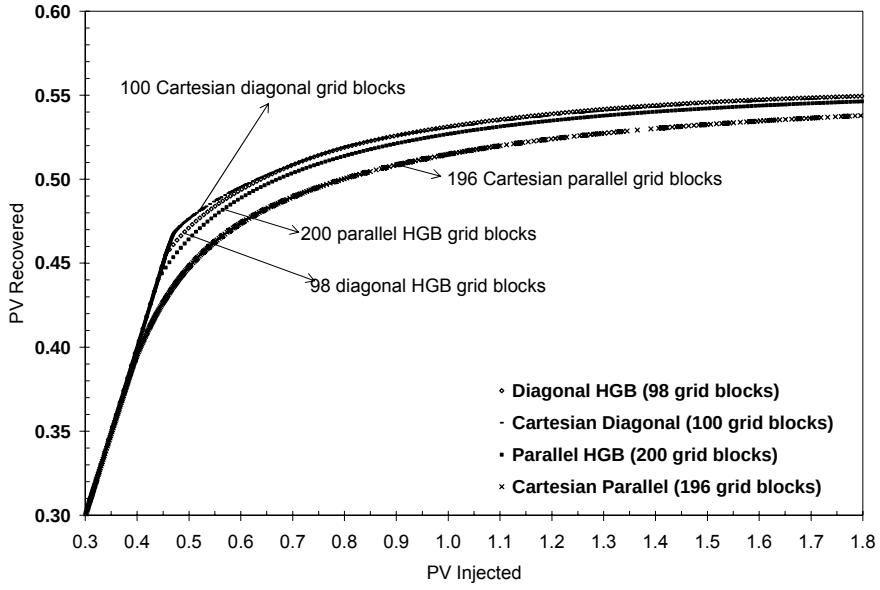

Fig. 2.6.25 – Comparison between HGB grid (98 and 200 grid-blocks) and Cartesian grid (100 and 186 grid-blocks) at M = 0.5.

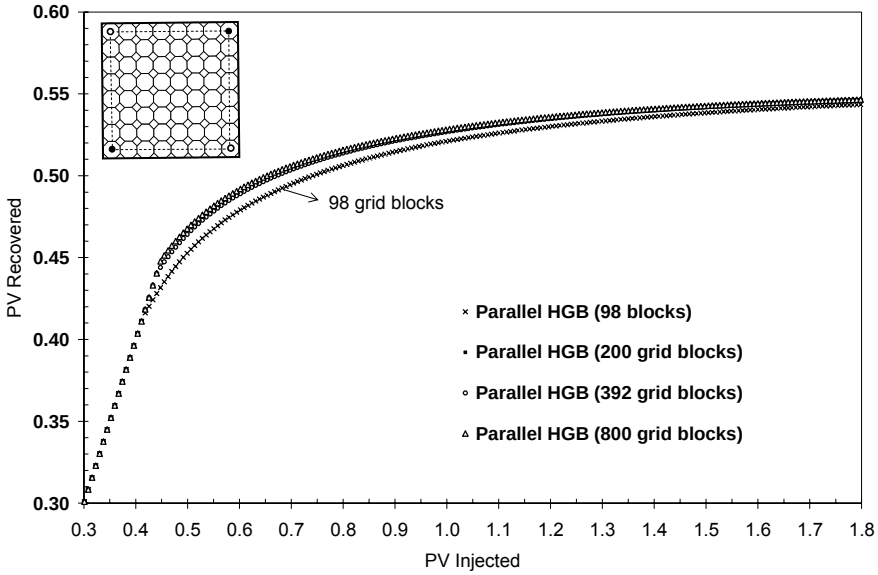

Fig. 2.6.26 – Effect of grid spacing on parallel HGB grid for M=0.5.

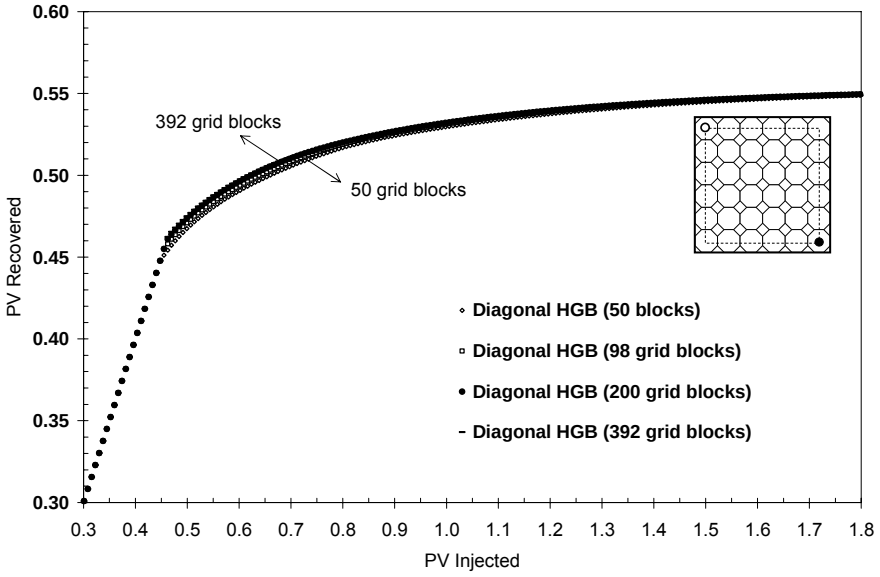

Fig. 2.6.27 – Effect of grid spacing on diagonal HGB grid for M=0.5.

Chapter II-7
Reduced CO_2 Bypassing and Optimized CO_2 Flood Design

2.7.1 INTRODUCTION

We studied a CO_2 flood pattern is located in the Wasson field in west Texas. The Wasson field is situated in Gaines and Yoakum counties on the southeastern margin of the northwest shelf of the North Basin platform of the Permian Basin in west Texas[1] (Fig. 2.7.1)**.** The production comes from the San Andres formation, which is a middle Permian-aged dolomite located at subsurface depths ranging approximately from 4,800 to 5,200 ft. The oil/water contact (OWC) varies from -1,250 ft to -2,050 ft below sea level. The gas/oil contact (GOC) is estimated to be -1,325 ft. The CO_2 flood pattern had been under waterflood for 14 years before carbon dioxide (CO_2) injection commenced. Considerable oil saturation (35 to 65%) was not effectively recovered by primary production and waterflooding because of formation heterogeneity. This remaining oil saturation has been the target of CO_2 enhanced oil recovery.[2-4]

We modeled the effects of heterogeneity on the overall sweep efficiency. A compositional simulation model was used to optimize CO_2 flood performances. We optimized the injection rate, flood patterns, slug sizes, and water-alternating-gas (WAG) ratio and explored the uses of a viscous agent in WAG application and polymer injection in conformance control to improve oil recovery.

2.7.2 SIMULATION MODEL CONSTRUCTION

The reservoir model for the simulation study is a quarter of an 80-acre inverted nine-spot pattern. The model covers 20 acres and contains three production wells and one injection well (Fig. 2.7.2). Production and injection wells are vertical and completed in all the layers of the simulation model. The reservoir properties can be seen in Table 2.7.1. The grid sensitivities were conducted to obtain minimum requirement of the grid block

numbers. We found that the 20x20 grid number provided satisfactory results when compared to finer gridded models.

We used an exisiting geologic description to define the layers of the simulation model (Fig. 2.7.3). Simulation layers were constructed to represent the actual reservoir zonation and resemble actual flow units. Layer thicknesses, porosity, and permeability were taken from an existing petrophysical evaluation of the area (Figs. 2.7.4 and 2.7.5). There are no areal variations of thickness, porosity, and permeability across each single simulation layer.

2.7.2.1 PVT EQUATION OF STATE CHARACTERIZATION

An essential part of a compositional reservoir simulation of a miscible EOR method is the prediction of the complex phase equilibria during enhanced oil recovery (EOR) processes.[5] An equation of state (EOS) was tuned to reproduce the observed fluid behavior and to predict the CO_2 /oil phase behavior in the compositional simulation.[6]

PVT laboratory sample data of the San Andres formation were used in the tuning of the EOS. PVT laboratory data consisted of differential liberation (DL) experiments, constant-composition-expansion (CCE), and swelling tests. These data were used to tune an EOS that is capable of characterizing the CO_2/reservoir-oil system above the minimum miscibility pressure (MMP).

Each laboratory experiment was simulated with the cubic Peng-Robinson EOS and compared to the laboratory pressure/volume/temperature (PVT) observations.[7] The Peng-Robinson EOS was used to reproduce the PVT experiments.

This was a multistep process that was started by splitting the heavy component into three pseudocomponents based on its relative mole fraction (Table 2.7.2). Regressions were performed against pseudocomponents to tune the EOS. The regression parameters were basically the pseudocomponents critical pressure, critical temperature, acentric factor, and binary interaction coefficients. The shift parameters and the CO_2/hydrocarbon binary interaction parameters of the pseudocomponents were numerically regressed to match the oil density and the swelling test experimental data, respectively. Figs. 2.7.6 through 2.7.11 show the results of the tuning of the EOS. After a satisfactory match of all the experimental data, a grouping procedure was performed with

some of the components of the EOS to get an EOS acceptable for a compositional simulation. By doing this reduction, we expected to minimize the computational time constraint and the numerical complexity of the simulation.

2.7.2.2 RELATIVE PERMEABILITY

Relative permeability is an important petrophysical parameter as well as a critical input parameter in simulation of miscible floods. However, relative permeability is a lumping parameter that includes the effects of wetting characteristics, heterogeneity of reservoir fluids, and rock and fluid saturations.[8]

Laboratory floods attempting to emulate CO_2 flood[9] experienced appreciable water relative permeability reductions after CO_2 injection. In addition, the data showed significant hysteresis effects in the water relative permeability between the drainage and imbibition curves.[8]

The two phase oil/water at $S_g = 0$ and gas/oil relative permeability curves used for the waterflood simulation are shown in Figs. 2.7.12 and 2.7.13. The relative permeability data are based on laboratory analyses.

During a WAG injection, each cycle of water injection is of an imbibition type, whereas as soon as gas injection begins the process will switch to the drainage flow. Therefore, the hysteresis effects have to be considered. Hysteretic effects on the relative permeability curves were included in the simulation model to consider the impact of saturation cycles as water and gas slugs move through the reservoir. Fig. 2.7.13 shows the imbibition and secondary drainage curves used in the simulation model for the WAG process. The major characteristic of the hysteresis curve is the increase in the connate water saturation from 15% on imbibition to 25% on secondary drainage. This increase occurs because the water is trapped by the wetting oleic phase during the secondary drainage. This trapped water reduces the water relative permeability on secondary drainage and also reduces the oil end-point relative permeability.

2.7.3 HISTORY MATCHING

The pattern was history matched for both waterflood and CO_2 flood. The oil production and injection rates were specified in each well and the model reproduced the reservoir pressure and the gas and water production. The quality of the history match was judged from how well the simulated water and gas production compared to the hystorical data. For the history match, the relative permeability curves were slightly adjusted to obtain a better producing water-to-oil ratio (WOR).

Additionally, well connections factor to the simulation grid were modified because most of the wells have been fractured and the wells' permeability-thickness product, *kh*, and the skin factor, *S*, were unknown. Since the connection factor is calculated from the cell properties, cell geometry, and completion information, modification of the connection factor was accomplished by enlarging the completion interval of the production wells to account for the effect of hydraulic stimulation.

During the WAG process, equal volumes of water and gas (at reservoir conditions) were injected during each slug resulting in a WAG ratio (volume of water to that of gas in a slug) of approximately 1. This WAG ratio was kept constant for the CO_2 flood history match.

During the waterflood period, water cut match deviates at early times. However, the overall water production matches very well. A reasonable match of gas production was also obtained. Figs. 2.7.14 through 2.7.16 show the comparison between historical data and simulation results of gas and water production during the history-match period.
Oil and water production matches from individual wells were also very good. These indicate that the simulation model was properly calibrated and can be used to predict reservoir performance.

At the end of the history-match period, the average remaining oil saturation was 45%. Fig. 2.7.17 shows the distribution of oil saturation at the end period. It identified many unswept areas between injectors and producers. The channeling of the injected fluids within the reservoir is clearly seen in the cross sections (Fig. 2.7.18). The channeling causes a nonuniform movement of the front and thus creates poor sweep efficiency. High-permeability layers breakthrough earlier than the low-permeability layers, leaving some untapped reserves behind.

The pattern experienced a severe breakthrough which reduced its overall sweep efficiency. Additionally, little oil displacement was observed in the upper layers of the simulation model. The sweep efficiency of the patterns was merely impacted by the contrast in permeability between the upper and lower layers of the formation. As a result, most of the injected fluids moved into the lower layers even though the upper layers have commercial permeability.

Results of the simulation do not only highlight reservoir areas with high oil saturation to the future CO_2 flooding but also reveal that mobility ratio needs to be improved, and the breakthrough has to be controlled to improve the sweep efficiency and increase the incremental oil recovery of the pattern.

2.7.4 PARAMETRIC STUDY

2.7.4.1 CO_2 INJECTION RATE OPTIMIZATION

To investigate the effect of the injection rate on the WAG process, we performed four sensitivities at a WAG ratio of 1:1 using constant rates of 100, 200, 300 and 500 RB/D (233.5, 467, 762 and 1167 Mscf/day respectively) of CO_2. We injected 3% HCPV half cycle of CO_2 and 3% HCPV half cycle of water until a fixed total CO_2 slug of 30% HCPV was reached. The recovery from WAG changes as a function of the injection rate; Fig. 2.7.19 indicates that the optimum injection rate for a 1: 1 WAG ratio is between 200 and 300 RB/D.

2.7.4.2 OPTIMUM WATER-ALTERNATING-GAS (WAG) RATIO

Two of the most important design issues for WAG process optimization are the WAG ratio and the amount of gas injection or slug size. Various compositional simulations were conducted to determine the optimum WAG ratio and the optimum slug size.

A series of WAG ratio sensitivities were compared. We injected water alternating with CO_2 at four different WAG ratios (1:1, 1:2, 2:1, and 4:1). The runs evaluated CO_2 slug sizes up to 100% HCPV. The gas and water injection were carried out in cycles injecting both fluids in the same well.

Results indicate that injecting a 100% hydrocarbon pore volume (HCPV) slug of CO_2 with a 1:1 WAG ratio would yield the maximum incremental oil recovery. The design included injection of alternating volumes (3.0% HCPV) of CO_2 and water into each pattern until the target 100% slug size was reached.

Fig. 2.7.20 shows the CO_2 flood performance for the different WAG ratios as a function of total CO_2 injection. It also shows a continuous CO_2 flood and waterflooding recovery profiles. The recovery profiles obtained indicates that the best incremental oil recovery is obtained at a WAG ratio of 1:1. The incremental oil recovery obtained with the continuous flood was low due to early breakthrough of CO_2 through high-permeability layers of the pattern.

Fig. 2.7.21 shows the residual oil saturation in the reservoir for all the cases after 100% HCPV have been injected. As expected, the 1:1 WAG ratio exhibits the lowest remaining oil saturation.

2.7.4.3 CONFORMANCE CONTROL

Channeling of the injected CO_2 during a WAG process has been a major area of concern in the oil industry.[8] During the course of CO_2 injection, multiple profile-control treatments have been conducted to improve the sweep efficiency.

To reduce the CO_2 mobility and delay the breakthrough of the CO2, we simulated a blocking agent and a polymer injection treatment with a WAG ratio of 1:1. This simulation allowed for the investigation of the effect of these treatments on the sweep efficiency and conformance control.

A blocking agent, such as gel, must be selectively injected so that it flows to the most permeable zones. After a certain amount of time, the gel stiffens and blocks fluid through those zones. Polymer injection reduces CO2 cycling through a high permeability layer between the injection well and offset producing wells.

To simulate the effect of placing the blocking agent in the “thief” zone, a high permeability layer was identified in the simulation model and the gridblock next to the injector well was plugged by assigning it a zero permeability value (Fig. 2.7.22).

For the polymer injection treatment, the injected water viscosity was increased from 1 to 20 cp. For this run, care was taken not to increase the injection pressure above the

formation parting pressure in order to avoid an induced fracture. The incremental recovery obtained from the polymer injection and the viscous water treatments were compared to the recovery obtained from a WAG 1:1 ratio injection process without any treatment. The oil production rate of the pattern exhibited a significant response to the profile control treatments performed on the injection well (Fig. 2.7.23).

Even though results indicate that the application of these treatments can significantly increase the oil production, the success of this technique in the field will depend on the correct placement of the polymer without damaging other adjacent layers. Additionally, it depends on the periodic repetition of the treatment to positively affect areal sweep efficiency.

2.7.4.4 OPTIMUM WELL PATTERN

We analyzed the effect of pattern reconfiguration on the CO_2 displacement. Pattern conversion is a viable option to achieve an incremental recovery in a mature field with high remaining oil saturations.

A pattern reconfiguration can improve the performance by improving the geometry, decreasing the spacing of the patterns, reducing the producer/injector ratio, and improving areal and vertical efficiency. This sensitivity includes infill drilling and well conversion from producer to injector to achieve a better CO_2 displacement throughout the reservoir and ultimately obtain a substantial increase in production from the existing CO_2 flood.

Different well-pattern configurations were simulated and analyzed. The inverted nine-spot pattern was converted to a staggered line-drive pattern, line-drive pattern, and a nine- spot pattern in the simulation model. The new patterns were forecast using the saturations and pressures at the end of the history match**.** Figs. 2.7.24 shows the geometric patterns considered in this work. The gridded zone represents the simulated area of the full pattern

Figs. 2.7.25 and 2.7.26 compare the production performance obtained from each pattern investigated. The sharp rise in the production rate is very evident after redefining the well-pattern geometry to staggered line-drive and line-drive patterns. Simulation results showed both the staggered line-drive pattern and the line-drive pattern create an

immediate peak above 100 STB/D in the production rate, which represents approximately 26% of increment in production as a result of the pattern reconfiguration.

The production rate obtained from the inverted nine-spot pattern is the lowest one among the patterns compared here. Extremely low rates clearly indicate that this pattern configuration does not perform well for this particular drainage area and does not improve the CO_2 displacement.

2.7.5 CONCLUSIONS

1. Recovery from a WAG process is a function of the injection rate as well as WAG ratio and the CO_2 slug.
2. WAG injection is effective in increasing the sweep efficiency of the injected CO_2 in the reservoir.
3. The injection of viscous water and polymer resulted in a positive production response that yielded an incremental oil recovery of 32% and 20% respectively.
4. Modeling suggests that pattern conversion from the inverted nine-spot pattern to staggered line-drive improves the production oil rate up to 26%.

REFERENCES

1. Mathis, R.L.: "Reservoir Geology of the Denver Unit–Wasson San Andres Field, Gaines and Yoakum Counties, Texas," Permian Basin SEPM Publication 86-26, 1986, 43-47.
2. Hsu, C.F., Morell, J.I. and Falls, A.H.: "Field Scale CO_2 Flood Simulations and Their Impact on the Performance of the Wasson Denver Unit," paper SPE 29116 presented at the 1995 SPE Symposium on Reservoir Simulation, San Antonio, TX, 12-15 February.
3. Ghauri, W.K.: "Production Technology Experience in a Large Carbonate Waterflood, Denver Unit, Wasson San Andres Field," paper SPE 8406 presented at the 54th Annual Technical Conference and Exhibition held in Las Vegas, Sept. 23-26, 1979.
4. Thai, B.N., Hsu, C.F., Bergersen, B.M., Albrecht, S,L., and Richardson, T.W.: "Denver Unir Infill and Pattern Reconfiguration Program," paper SPE 59548

presented at the 2000 SPE Permian Basin Oil and Gas Recovery Conference, Midland, TX, 21-23 March.

5. Merrill, R.C., Hartman, K.J. and Creek, J.L.: "A Comparison of Equation of State Tuning Methods," paper SPE 28589 presented at the 69th Annual Technical and Exhibition held in New Orleans, LA, 25-28 September.
6. Khan, S.A., Pope, G.A. and Sepehrnoori, K.: "Fluid Characterization of Three-Phase CO_2/Oil Mixtures," paper SPE/DOE 24130 presented at the Eighth Symposium Oil Recovery held in Tulsa, OK, 22-24 April, 1992.
7. Peng, D.Y. and Robinson, D.B.: "A New Two-Constant Equation of State," Ind. & Eng. Chem. Fund. (1976) 15, No. 1, 59-64.
8. Rogers, J.D. and Reid B. Grigg, R.B.: "A Literature Analysis of the WAG Injectivity Abnormalities in the CO_2 Process," paper SPE 73830, original paper SPE 59329 presented at the 2000 Improved Oil Recovery Symposium, Tulsa, 3-5 April.
9. Christman, P.G. and Gorell, S.B.: "A Comparison of Laboratory and Field-Observed CO_2 Tertiary Injectivity," paper SPE/DOE 17335 presented at the 1988 Improved Oil Recovery Symposium., Tulsa, OK,17-20 April.

Table 2.7.1—Basic Reservoir Properties

Formation	San Andres
Top of Pay (Ft)	5000
Pay Thickness (Ft)	292.5
OOIP (MMSTB)	>2.0
Average Porosity (%)	0.115
Average Permeability (md)	5.67
Initial Reservoir Pressure (psi)	1805
Bubble Point Pressure (psi)	1805
Reservoir Temperature (°F)	105

Table 2.7.2—EOS Characterization

Original Composition	"After Split" Composition	Tuning of EOS	"After Grouping" Composition
CO_2	CO_2	Regressions on the C_7+ pseudo components	6 components
N_2	N_2		CO_2
C_1	C_1		$(N_2 - C1)$
C_2	C_2		$(C_2 - C_3)$
C_3	C_3		$(iC_4 - {}_nC4)$
iC_4	iC_4		$(C_5 - C_6)$
nC_4	nC_4		C_{7+}
iC_5	iC_5		
nC_5	nC_5		
C_6	C_6		
C_{7+}	C7+(1)	Regressed Variables: Critical Temp. Critical Press. Acentric Factors BIC's	
	C7+(1)		
	C7+(1)		

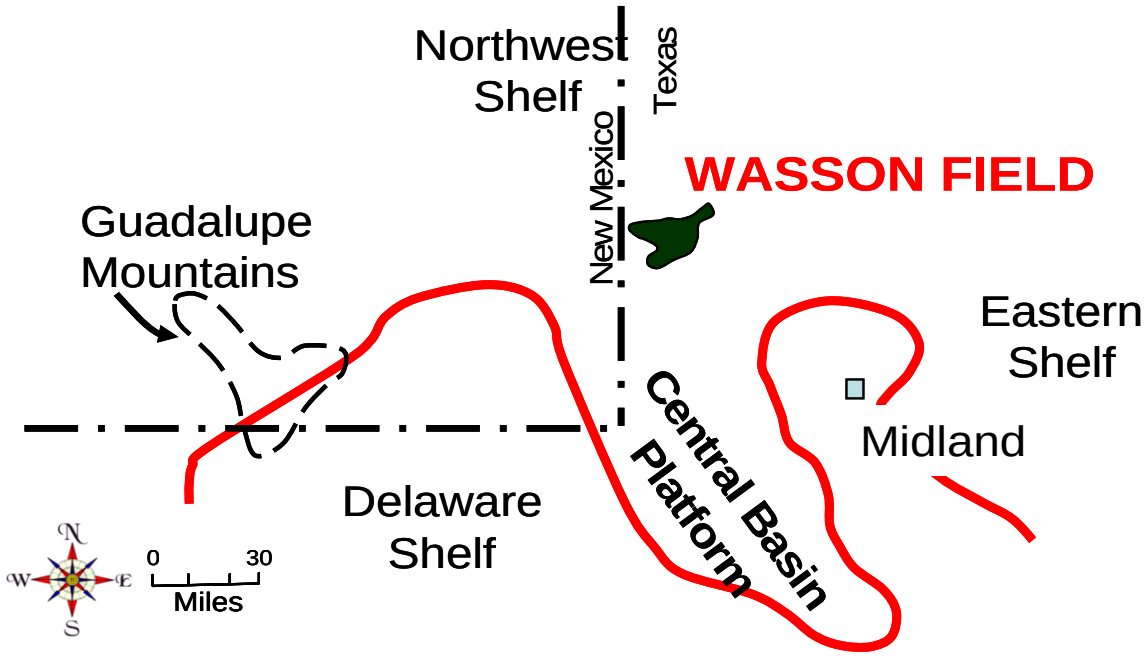

Fig. 2.7.1—Location of Wasson field in the Permian Basin

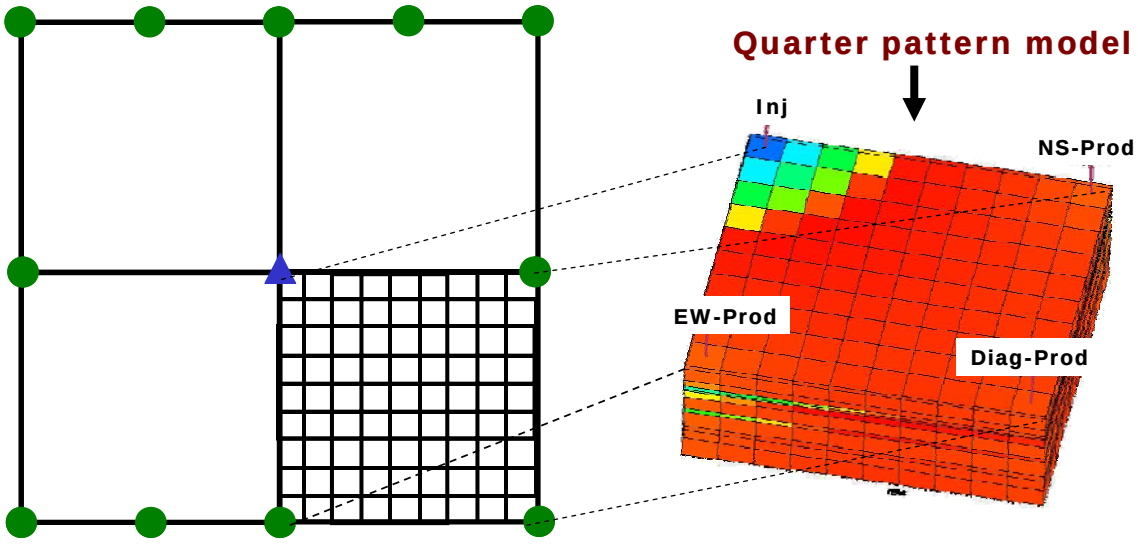

Fig. 2.7.2—Well pattern geometry

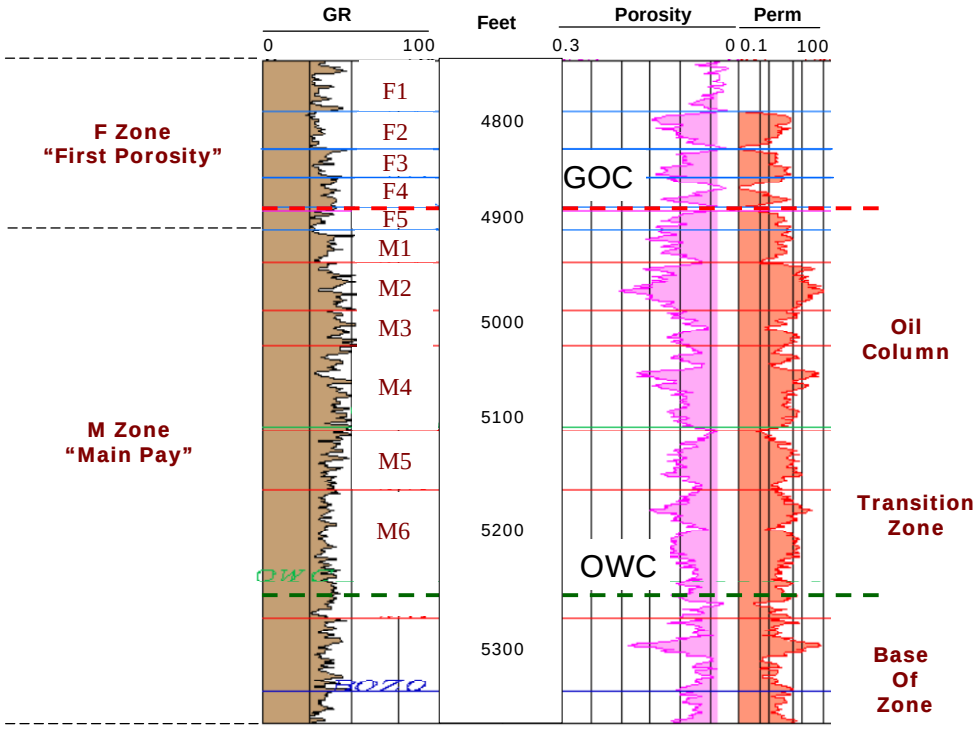

Fig. 2.7.3—Type log Denver unit[1]

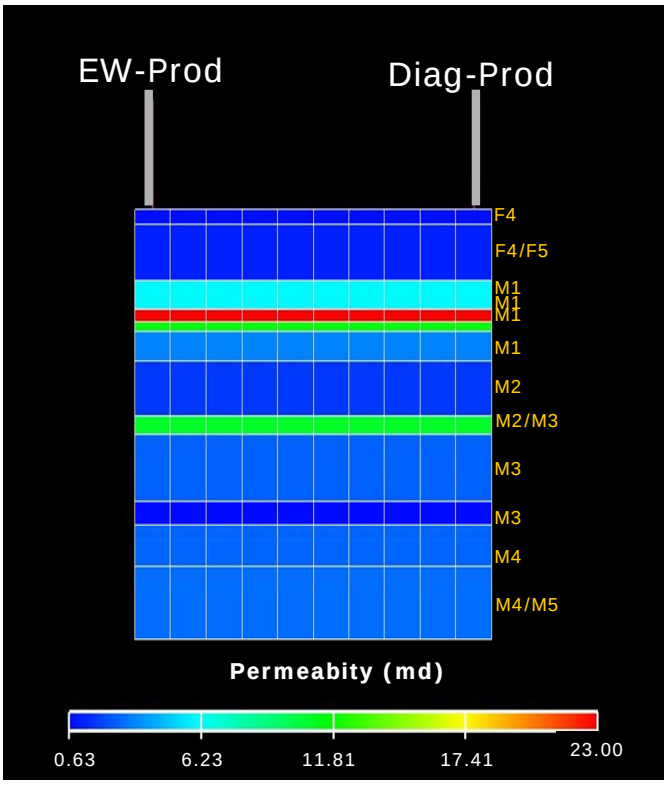

Fig. 2.7.4 —Variation of permeability values at each layer

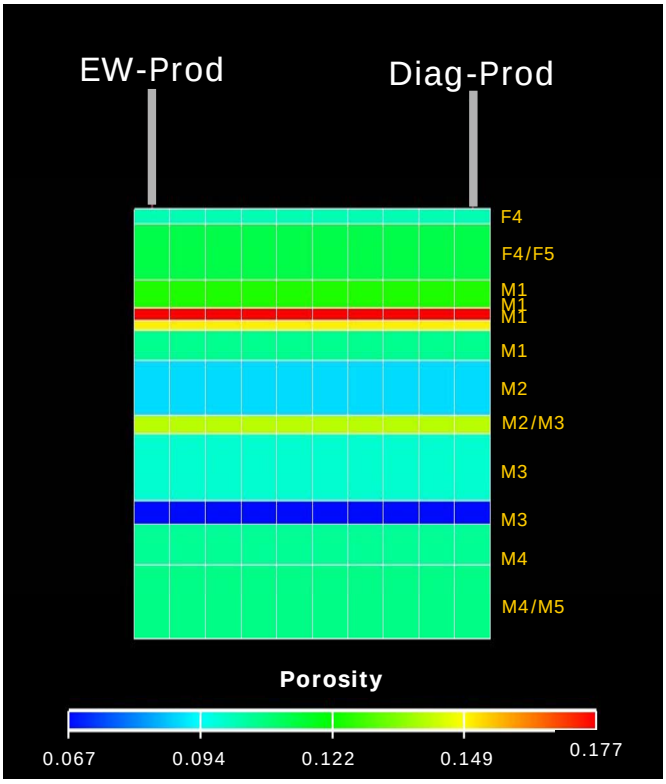

Fig. 2.7.5—Variation of porosity values at each layer

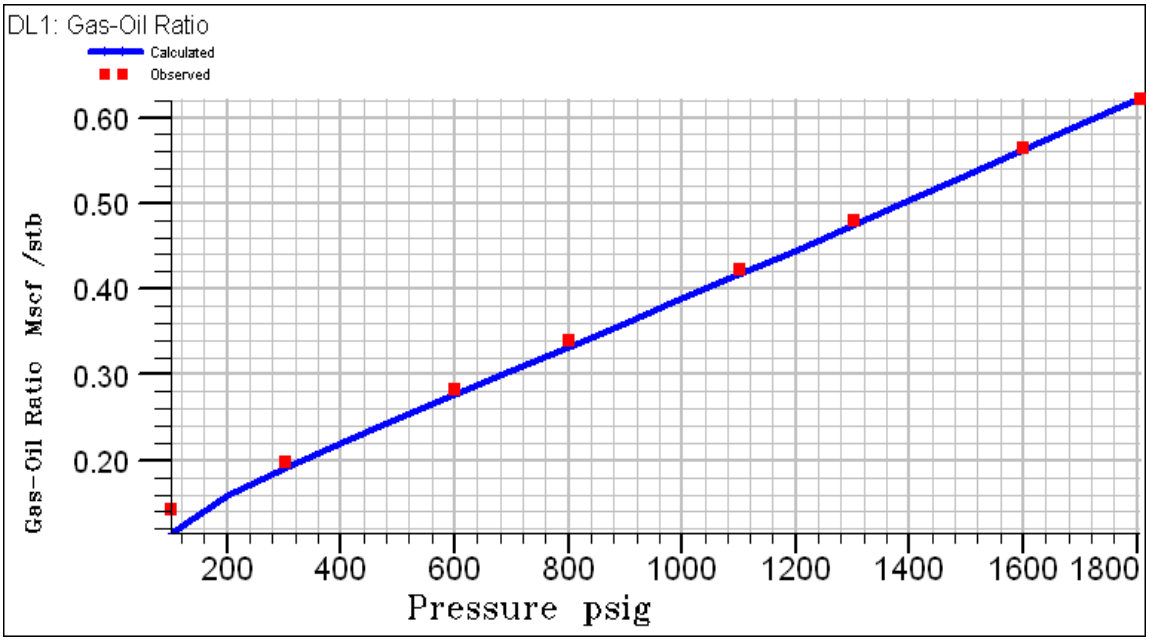

Fig. 2.7.6—GOR comparison between PVT EOS results and observed data

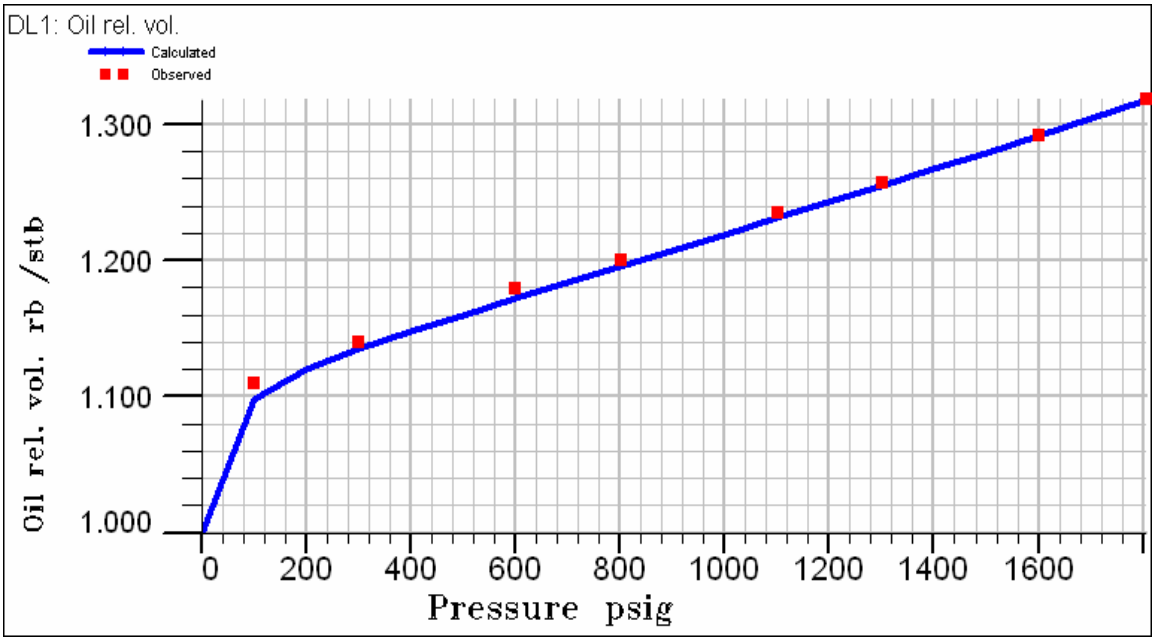

Fig. 2.7.7— FVF comparison between PVT EOS results and observed data

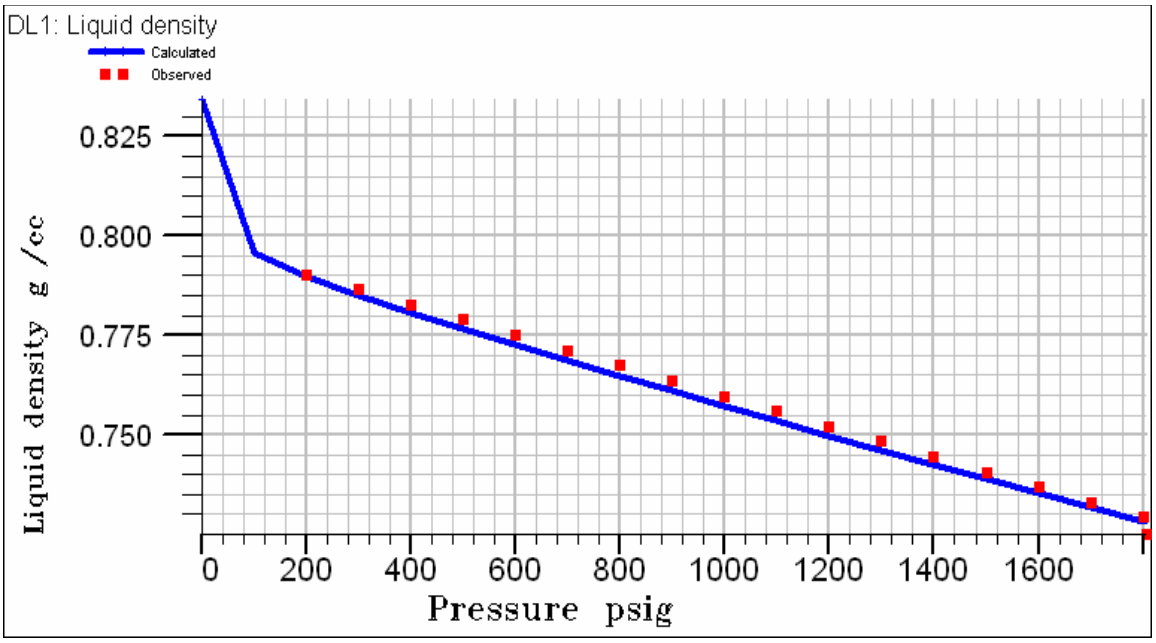

Fig. 2.7.8— Oil density (ρ_o) comparison between PVT EOS results and observed data

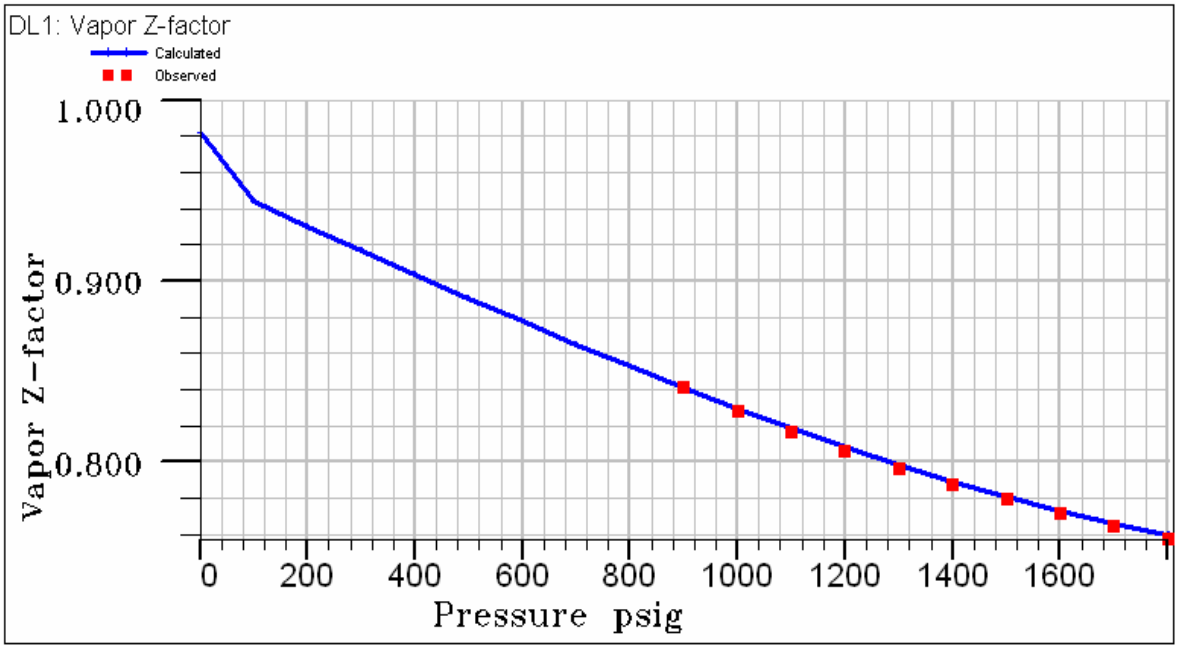

Fig. 2.7.9—Gas deviation factor (Z) comparison between PVT EOS results and observed data

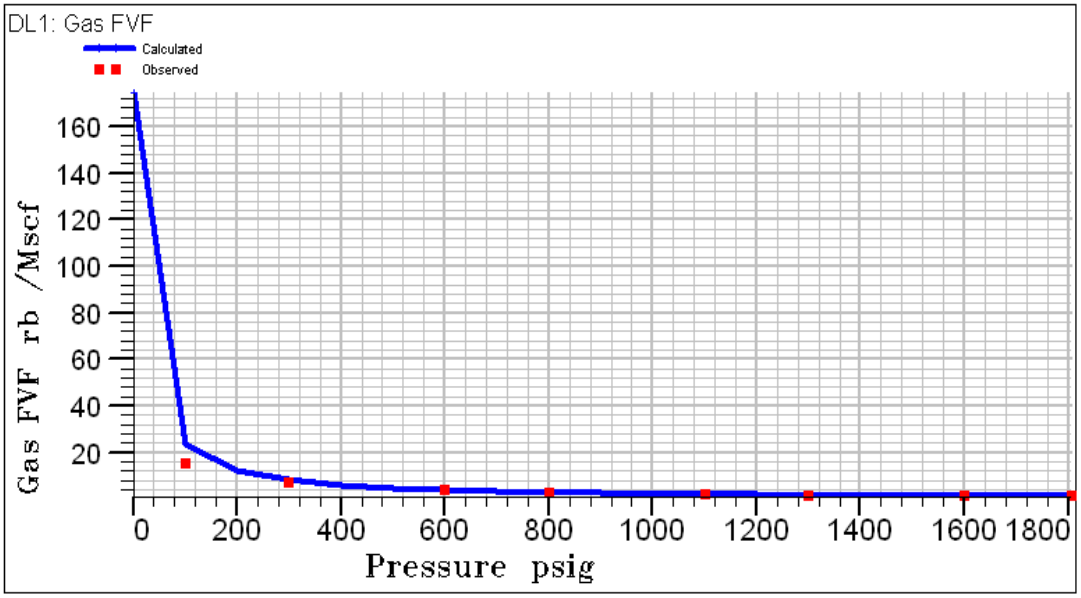

Fig. 2.7.10— Gas FVF comparison between PVT EOS results and observed data

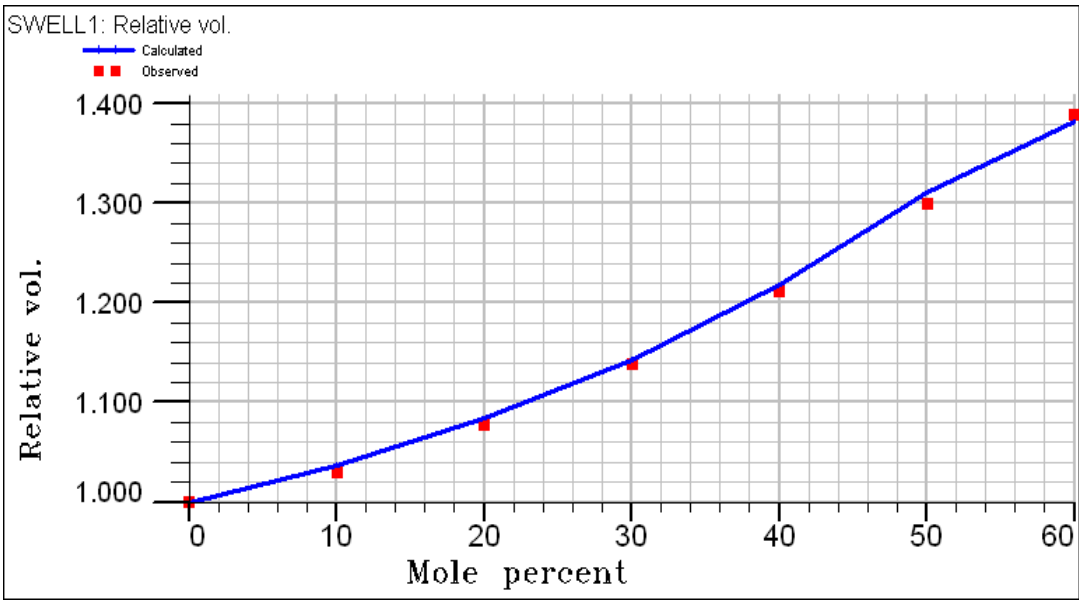

Fig. 2.7.11— CO_2 swelling factor comparison between PVT EOS results and observed data

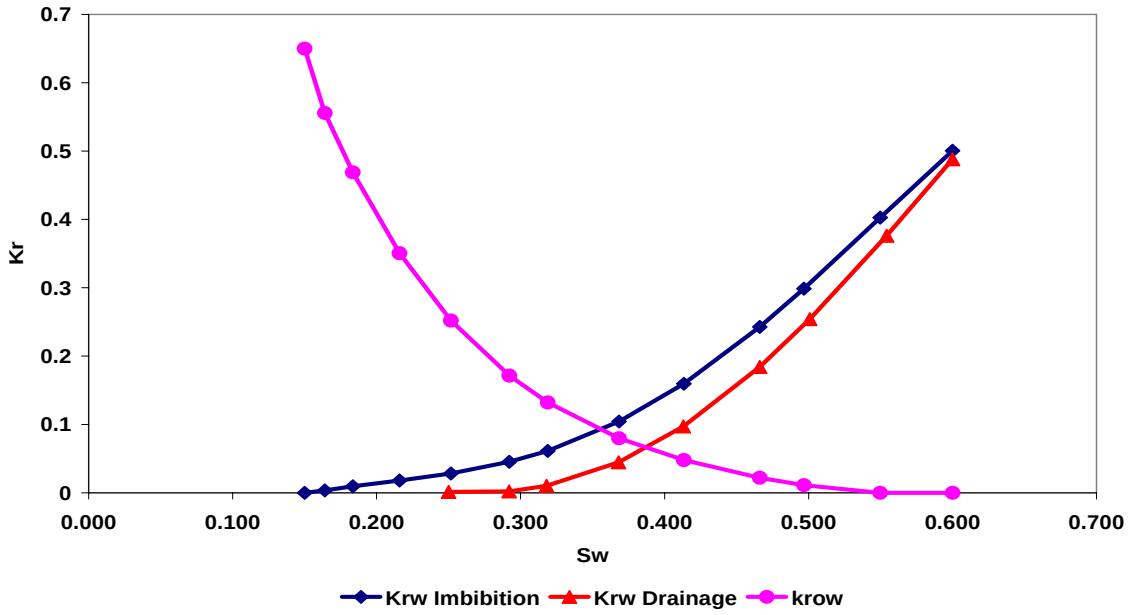

Fig. 2.7.12—Imbibition and secondary drainage water relative permeability curves (hysteresis)

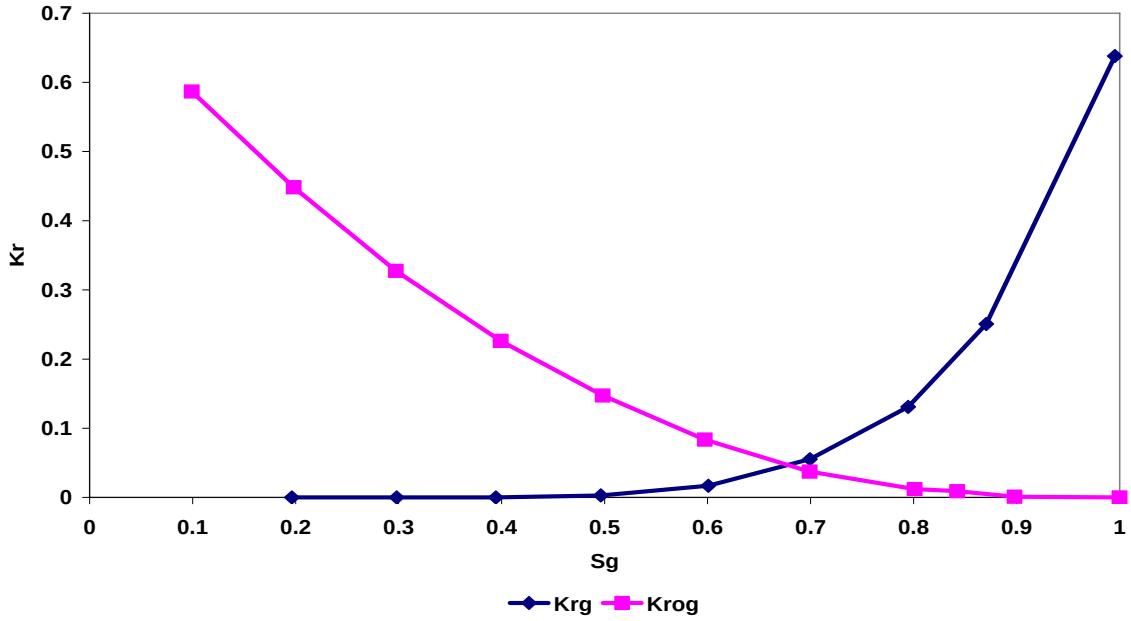

Fig. 2.7.13—Gas and oil relative permeability curves as a function of gas saturation

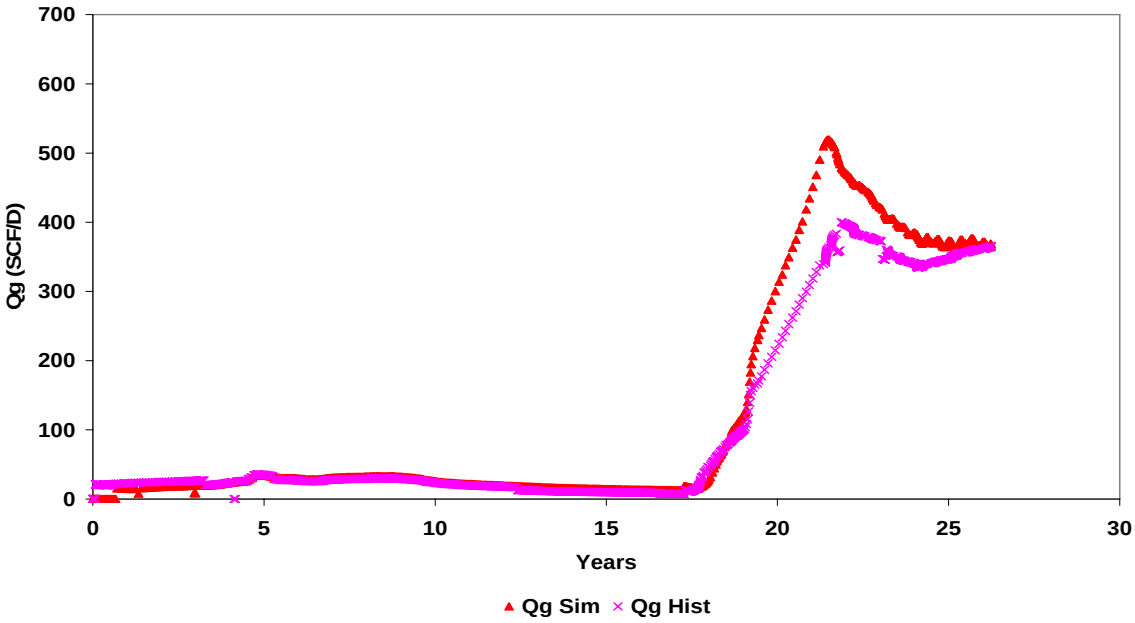

Fig. 2.7.14—Gas production rate comparison between simulation result and observed data

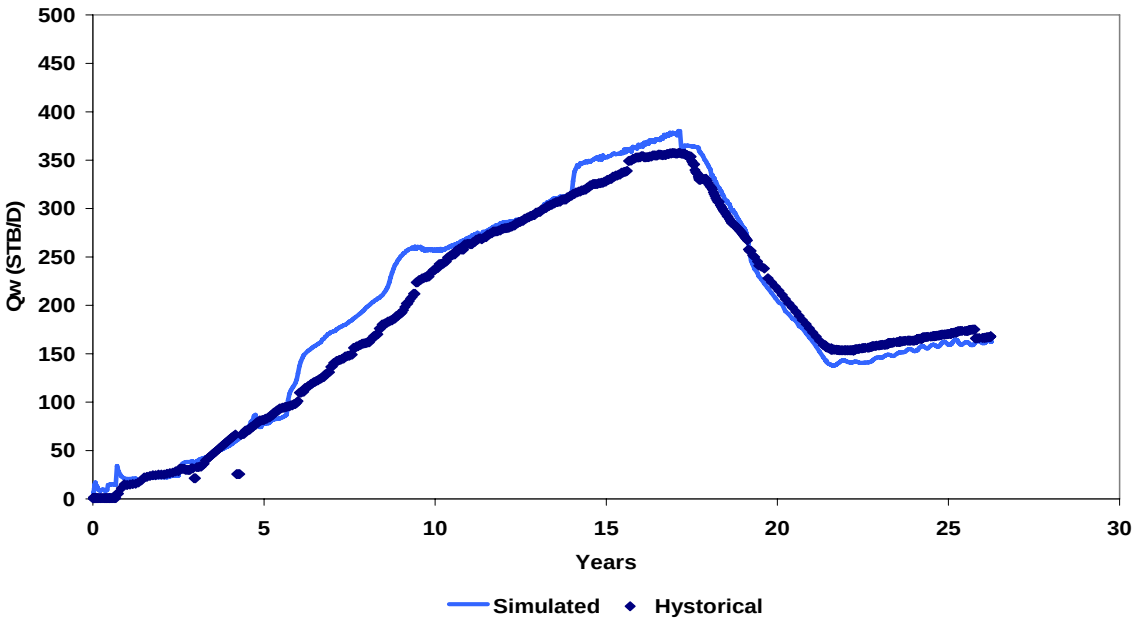

Fig. 2.7.15—Water production rate comparison between simulation result and observed data

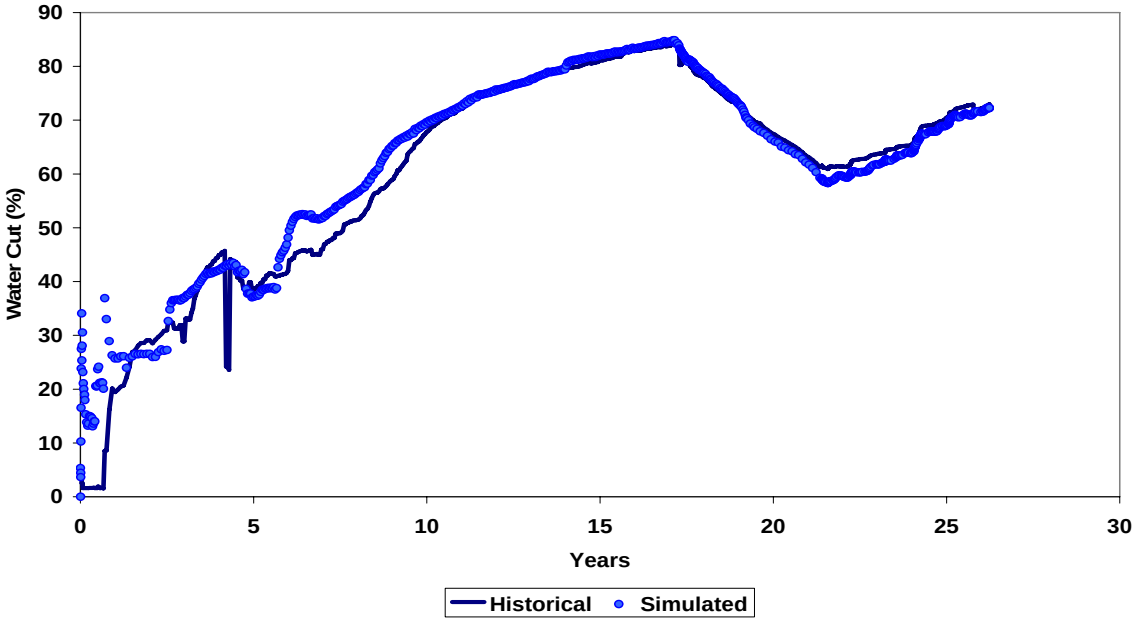

Fig. 2.7.16—Water cut comparison between simulation result and observed data

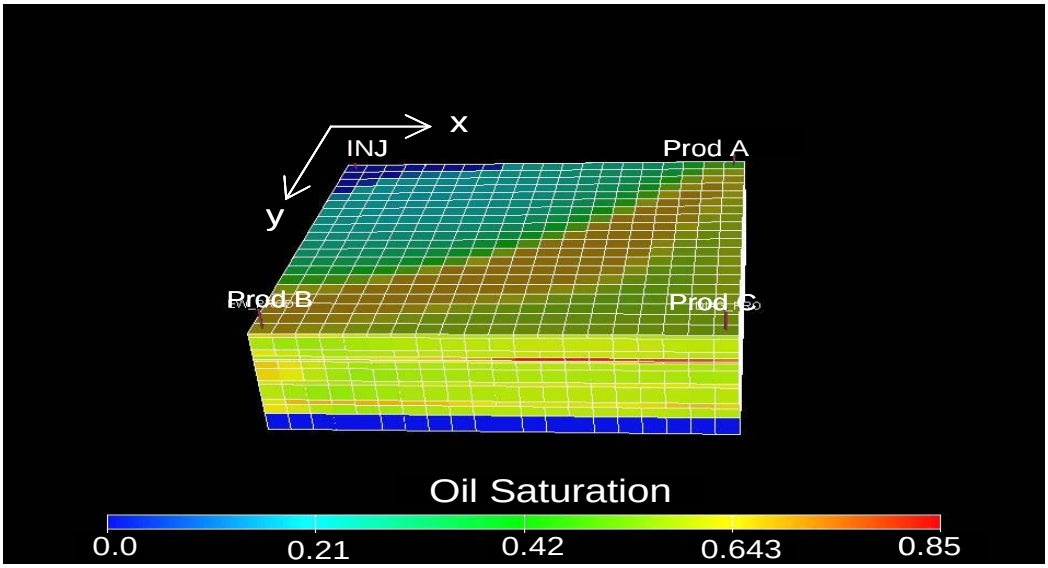

Fig. 2.7.17—Areal view of oil saturation distribution showing oil bypassed after CO_2 injection

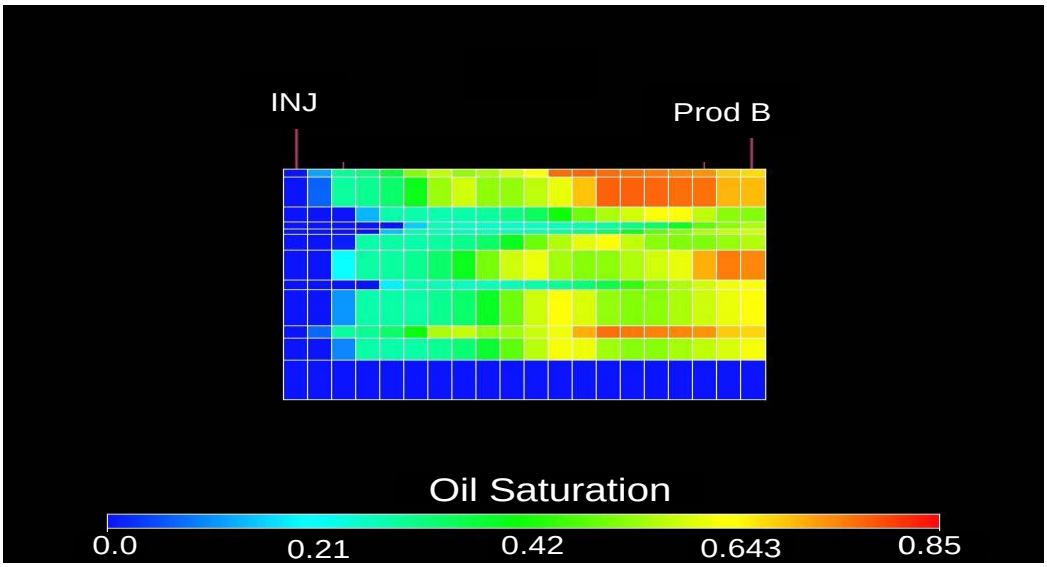

Fig. 2.7.18—E-W cross section view of the oil saturation distribution showing oil bypassed after CO_2 injection

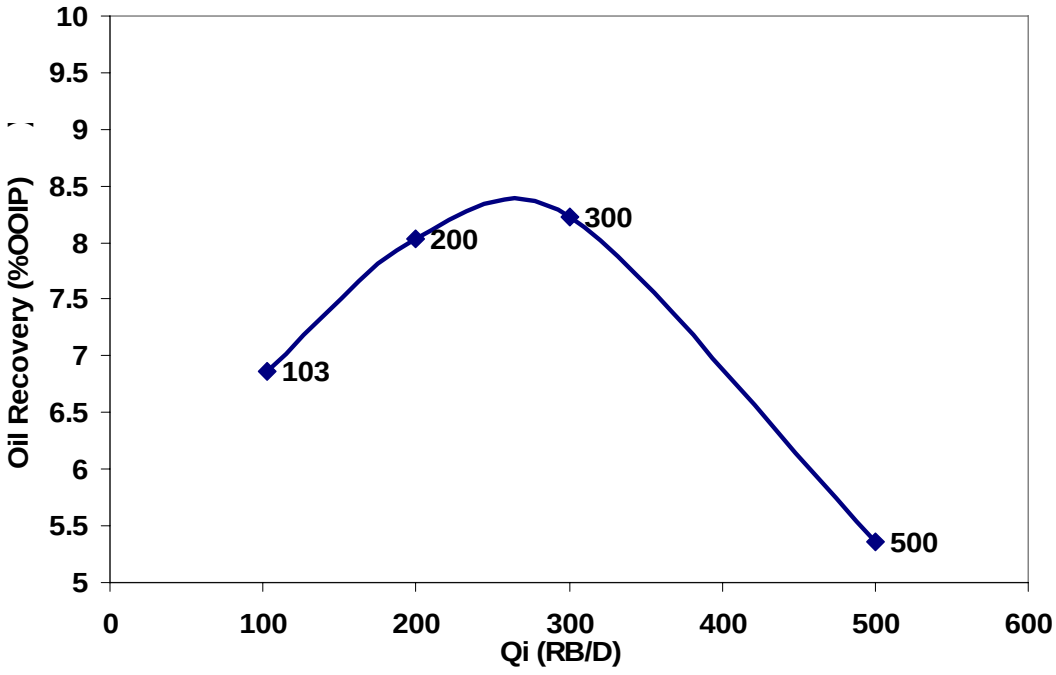

Fig. 2.7.19—Oil recovery comparison at different injection rates with similar 1:1 WAG ratio

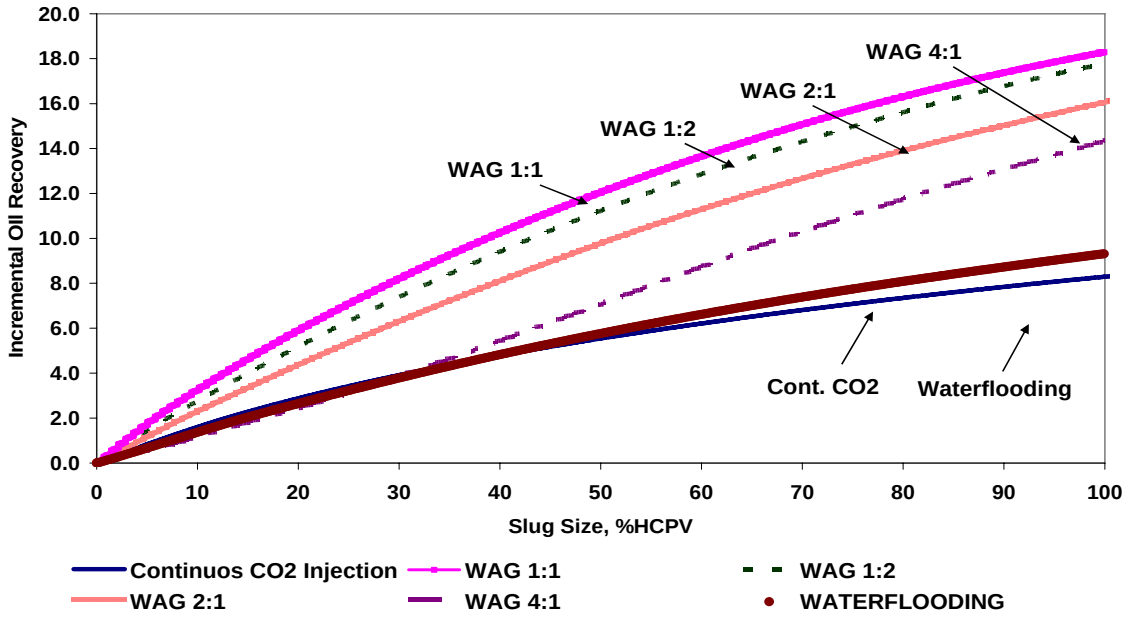

Fig. 2.7.20—Comparison of incremental oil recovery at different WAG ratios

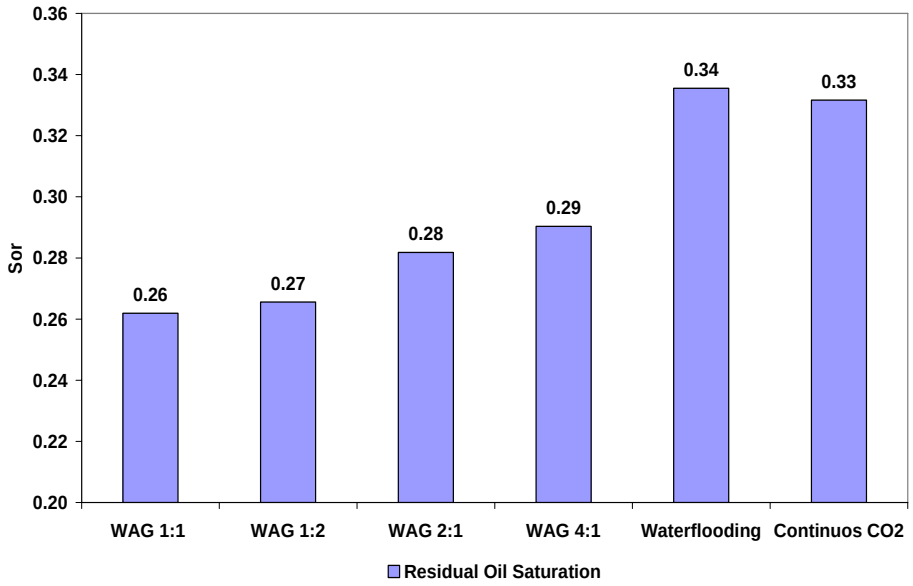

Fig. 2.7.21—Comparison of residual oil saturation for different WAG ratios at 100% HCPV injection

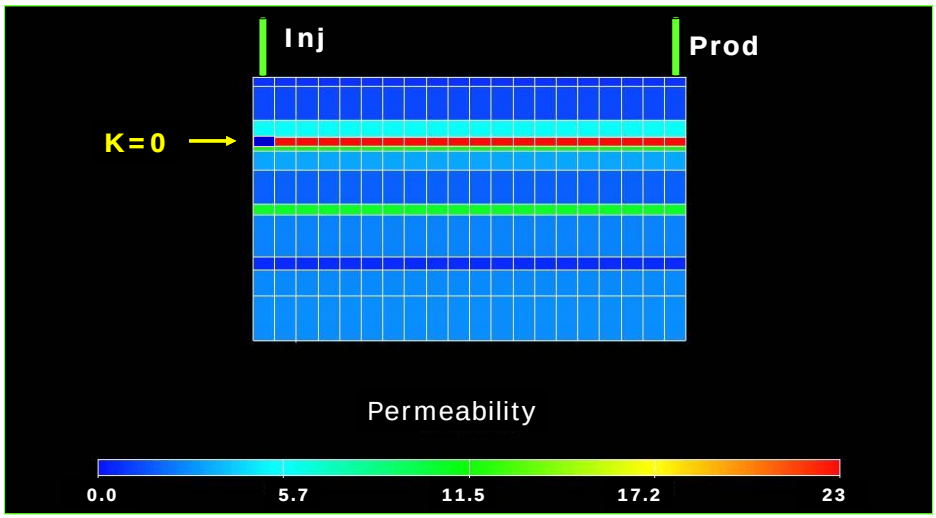

Fig. 2.7.22—East–West cross section view of the model showing the location of zero permeability treated by polymer.

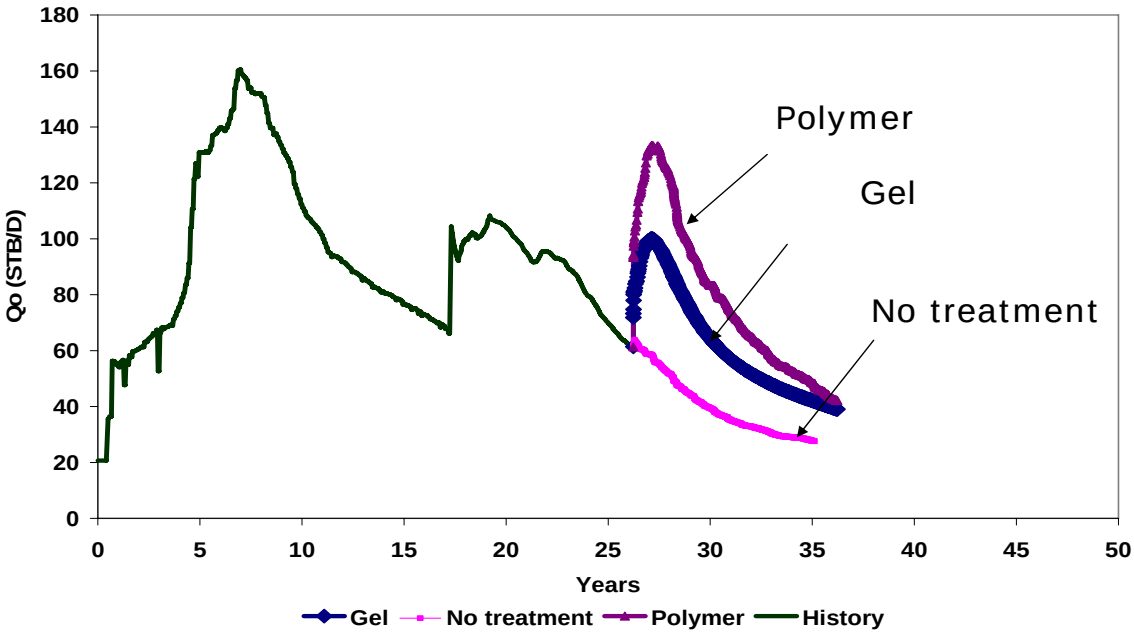

Fig. 2.7.23—Estimated future oil production rate comparison with and without conformance control treatments

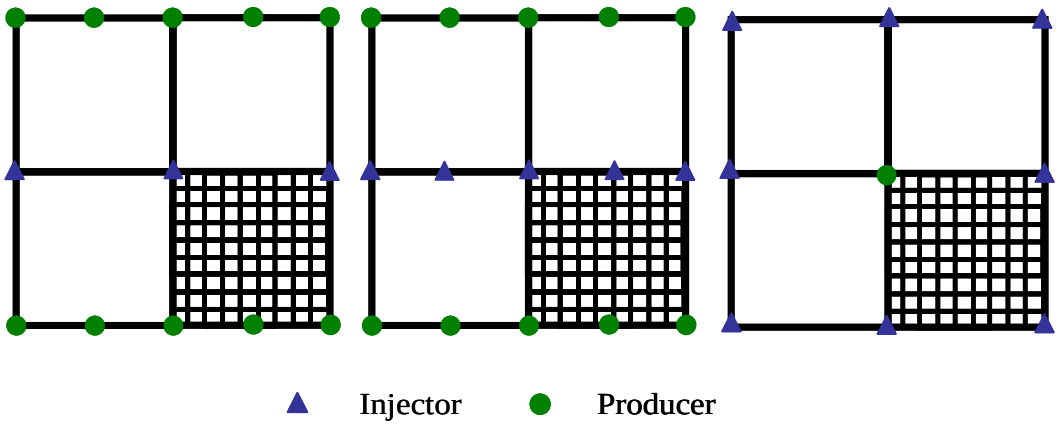

Fig. 2.7.24—(a) Staggered line drive, (b) line drive and (c) nine-spot well pattern

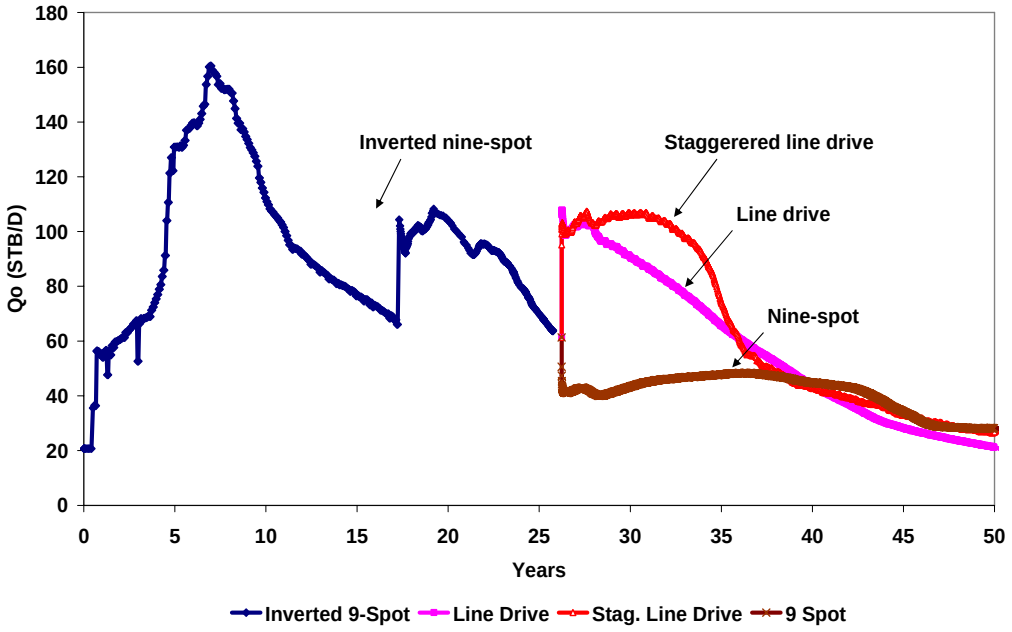

Fig. 2.7.25— Estimated future oil production rate comparison between staggered line drive, line drive and nine-spot well patterns

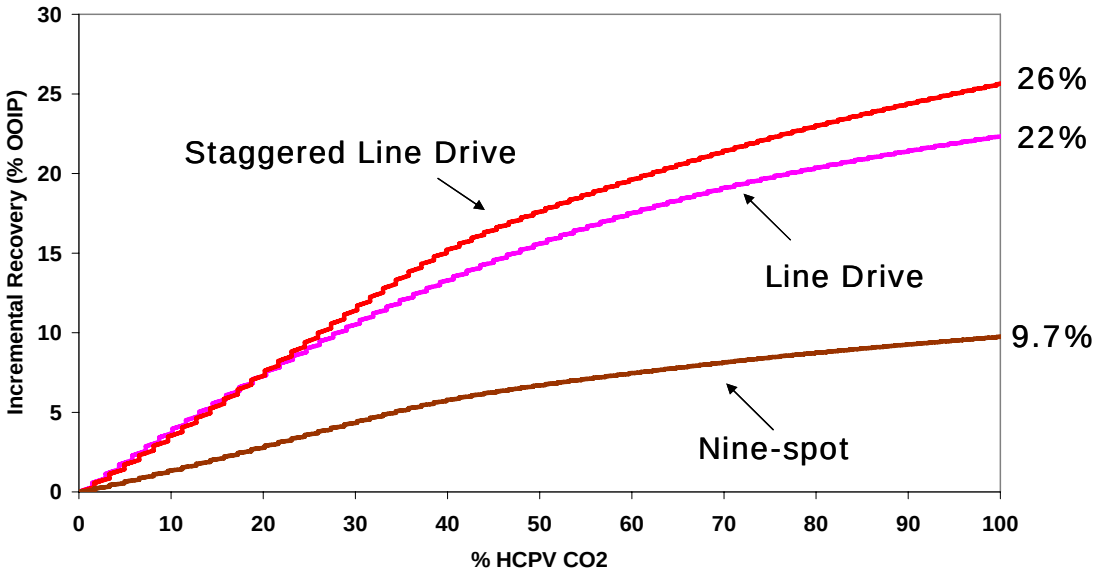

Fig. 2.7.26—Estimated incremental oil recovery comparison between different well pattern configurations

Investigation of Efficiency Improvement during CO_2 Injection in Hydraulically and Naturally Fractured Reservoirs

DE-FC26-01BC15361

Program

This project was in response to DOE's solicitation DE- PS26-01NT41048, Reservoir Efficiency Process. The goal of this solicitation was to reduce the amount of oil bypassed due to the poor sweep of carbon dioxide and to increase oil predictability and improve oil extraction using new technologies.

Project Goal

Perform unique laboratory experiments with Artificial fractured cores (AFCs) and X-ray CT to examine the physical mechanisms of bypassing in HFR and NFR that eventually result in less efficient CO_2 flooding in heterogeneous or fracture-dominated reservoirs.

Performer

Texas Engineering Experiment Station, Texas A&M University

322 Wisenbaker Engineering Research Center, College Station, TX 77843

Results

The project has used X-Ray CT scanner to image saturation profiles of flow patterns for direct measurement of bypassing mechanisms and to measure bypassed oil in order to optimize CO_2 flooding efficiency. With this equipment, we have established the relationship between fracture aperture distribution and overburden pressures. We found that CO_2 gravity drainage still plays an important role in oil recovery even in a short matrix block. Significant CO_2 sweep efficiency improvement was achieved by controlling the CO_2 mobility in the fracture with viscosified water and placing a cross-linked gel placed in the fracture.

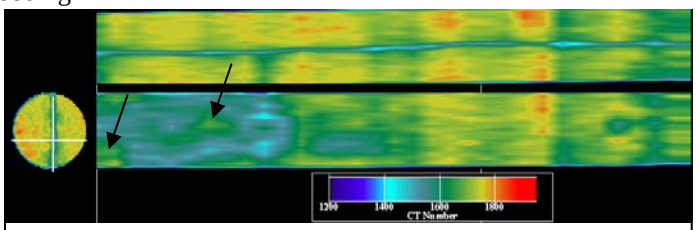

CT images show CO_2 bypasses oil at certain fracture surface areas (shown by arrows) Top view is longitudinal cross section showing fracture. Bottom view is slice across fracture surface.

Benefits

In the United States, oil that is potentially producible by advanced methods amounts to approximately 200 of the remaining 351 billion barrels. Of the available advanced oil recovery methods, gas injection has the greatest potential for additional oil recovery from light oil reservoirs located in the United States. Carbon Dioxide (CO_2) flooding is the most promising gas injection technique for widespread use in improved oil recovery (IOR).

New CO_2 projects are commencing in the U.S. and internationally each year. CO_2 suppliers are drilling new CO_2 production wells, to increase available CO_2 for delivery, and plans are under way to increase current pipeline capacities. Also, other areas in North

America, such as the Wyoming-to-Canada corridor, California, and the Mississippi region, continue development or consideration of extending the current pipeline networks to more distant reservoirs. However, there are many reservoirs that are not being considered for CO_2 flooding or any type of IOR methods because of extreme heterogeneity, or natural fractures. Thus, the developments from our present and future projects are an asset to the economic and strategic future of the United States of America.

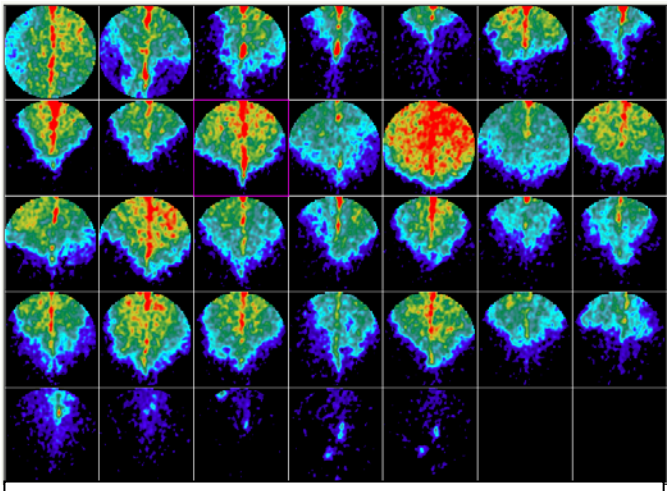

X-Ray images of a CO_2 front movement through a fractured core showing the influence of gravity segregation

Background

The primary goal of this research is to maximize the potential of CO_2 flooding in the domestic U.S. As more technical knowledge accumulates it becomes clear that natural and hydraulically induced fractures often dominate pattern reservoir or sweep efficiency. As the level of sophistication grows, low permeability reservoirs become more amenable to Enhanced Oil Recovery (EOR) via CO_2. Low permeability reservoirs are usually characterized by brittle matrix rock, which cracks under natural or induced conditions.

Many of the issues involved in saturation distribution during CO_2 injection have been tested in Berea cores above and below miscibility pressure. However, the level of heterogeneity rarely, if ever, includes the presence of natural fractures. This is not coincidental since the level of experimentation required is high in order to develop useful interpretations. The fact remains, however, that reservoir heterogeneity dominates the performance of gas injection. Hydraulic or natural fractures can exert a major influence on the economics of CO_2 injection projects. However, the fundamental mechanisms of transfer in fracture systems are virtually unexplored. The transfer of injected gas from HF or NF determines the ultimate displacement and sweep efficiency. It is the intent of this proposed work to advance the understanding of this dynamic process and determine the implications on the ultimate performance of bypassing reserves during CO_2 injection.

Project Summary

- Advanced imaging technology has been employed (1) to characterize matrix and fracture systems, (2) to image

saturation profile and (3) to investigate transfer and bypassing mechanisms in order to optimize CO_2 flooding efficiency.

- The new laboratory experiments have been developed (1) to demonstrate the effect of different overburden pressures and injection rates on fracture aperture and matrix and fracture productivities and (2) to mitigate bypassing mechanisms that will result in less bypassing and more efficient CO_2 flooding in fracture-dominated reservoirs.
- Different CO_2 injection rates and WAG injection ratios along with increasing water viscosity in WAG process and placing gel-polymer in fracture system were conducted in laboratory scale to improve CO_2 flooding efficiency.
- The laboratory techniques has been used to reduced CO_2 bypassing and optimized CO_2 flood design in the Wasson Field, west Texas.
- Several analytical and numerical modeling have been performed (1) to investigate the effect of fracture aperture at variable overburden pressure, (2) to investigate the effect of different rock heterogeneity on flow path contributors, (3) to validate the use of cubic law equation, (4) to investigate the transfer mechanism during core flooding in fractured core and (5) to investigate the effect of grid orientation in different mobility ratio.
- A new discrete fracture simulator with flexible and unstructured gridding techniques was developed to accurately model the fluid flow through fracture networks with multiple orientations.

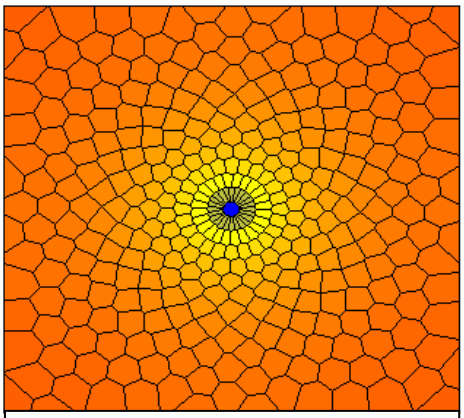

Pressure distribution map with unique gridding technique

Current Status

All the proposed works have been completed in time. The current status of the project is the preparation for the final report due on Sept 2005.

Publication

- Schechter, D.S. *et al.*: "Investigation of Efficiency Improvement during CO_2 Injection in Hydraulically and Naturally Fractured Reservoirs" Semi-Annual Progress Report (DOE Contract No.: DE-FC26-01BC15361), Oct 2001-March 2002, April 2002-October 2002, October 2002-March 2002, April 2003-October 2003, Nov 2003-March 2004, April 2004-October 2004, October 2004-April 2005.
- Kaul, S.P., Putra, E., and Schechter, D.S.: "Spontaneous Imbibition Simulation with Rayleigh-Ritz Finite Element Method," paper SPE 90053 presented at the 2004 SPE International Petroleum Conference, Puebla, Mexico, 8–9 November.
- Muralidharan, V., Chakravarthy, D., Putra, E., and Schechter, D.S.: "Simulation of Fluid Flow through Rough Fractures," paper SPE 89941 presented at the 2004 SPE International Petroleum Conference, Puebla, Mexico, 8–9 November.
- Muralidharan, V., Chakravarthy, D., Putra, E., and Schechter, D.S.: "Simulation and Imaging Experiments for Flow through a Fracture Surface: A New Perspective" paper SPE presented at 2004 International Student Paper Contest, Houston, Texas, 26-29 September.
- Chong, E., Syihab, Z., Putra, E. and Schechter, D.S.: "A Unique Grid-Block System for Improved Grid Orientation," paper SPE 88617 presented at 2004 Asia Pacific Oil and Gas Conference and Exhibition (APOGCE), Perth, Australia, 18-20 October.
- Muralidharan, V., Putra, E., and Schechter, D.S.: "Experimental and Simulation Analysis of Fractured Reservoir Experiencing Different Stress Conditions," paper CIPC 2004-229 presented at 2004 Annual Technical Meeting of the Petroleum Society, Calgary, Canada, 8-10 June.
- Muralidharan, V., Chakravarthy, D., Putra, E., and Schechter, D.S.: "Investigating Fracture Aperature Distributions under Various Stress Conditions Using X-Ray CT Scanner," paper CIPC 2004-230 presented at 2004 Annual Technical Meeting of the Petroleum Society, Calgary, Canada, 8-10 June.
- Chakravarthy, D., Muralidharan, V., Putra, E., and Schechter, D.S.: "Application of X-Ray CT for Investigating CO_2 and WAG Injection in Fractured Reservoirs," paper CIPC 2004-232 presented at 2004 Annual Technical Meeting of the Petroleum Society, Calgary, Canada, 8-10 June.
- Tellapaneni, P.K., Putra, E., and Schechter, D.S.: "Usage of X-Ray CT for Empirical Transfer Functions in Dual Porosity Simulation," paper CIPC 2004-246 presented at 2004 Annual Technical Meeting of the Petroleum Society, Calgary, Canada, 8-10 June.
- Kaul, S.P., Putra, E., and Schechter, D.S.:"Simulation of Spontaneous Imbibition Using Rayleigh-Ritz Finite Element Method-A Discrete Fracture Approach," paper CIPC 2004-228 presented at 2004 Annual Technical Meeting of the Petroleum Society, Calgary, Canada, 8-10 June.
- Alfred, D., Putra, E., and Schechter, D.S.: "Modeling Fluid Flow through Single Fractures Using Experimental, Stochastic and Simulation Approaches," paper SPE/DOE 89442 presented at 2004 Improved Oil Recovery Symposium, OK, Tulsa, 17–21 April.
- Alfred, D., Putra, E., and Schechter, D.S., Modeling Fluid Flow Through a Single Fracture Using Experimental, Stochastic and Simulation Approaches, Saudi Aramco J. of Tech., Spring, 2004.
- Putra, E., Muralidharan, V., and Schechter, D.S., Overburden Pressure Affects Fracture Aperture and Fracture Permeability in a Fractured Reservoir, Saudi Aramco, J. of Tech., Fall 2003.

Project Start: 9/28/2001
Project End: 9/27/2005
Anticipated DOE Contribution: $
Performer Contribution: $ (% of Total)

Other Government Organizations Involved:

Contact Information:
NETL – Daniel J. Ferguson (dan.ferguson@npto.doe.gov or 918- 699-2047)
TEES-TAMU – David Schechter (schech@pe.tamu.edu or 979- 845-2275)